



National Technical University of Athens
School of Mechanical Engineering
Fluids Sector
Laboratory of Thermal Turbomachines

Development of an Integrated System for Preliminary Design of Aircraft Gas Turbines

PhD Thesis

Ioannis Koliás

Dipl. Mechanical Engineering, NTUA

Supervisor:

Nikolaos Aretakis

Associate Professor, NTUA

June 2023, Athens



National Technical University of Athens
School of Mechanical Engineering
Fluids Sector
Laboratory of Thermal Turbomachines

Development of an Integrated System for Preliminary Design of Aircraft Gas Turbines

PhD Thesis
Ioannis Kolias

Thesis Examination Committee:

1. Nikolaos Aretakis**, Associate Professor, NTUA
School of Mechanical Engineering
2. Konstantinos Mathioudakis*, Professor, NTUA
School of Mechanical Engineering
3. Kyriakos Giannakoglou*, Professor, NTUA
School of Mechanical Engineering
4. Ioannis Anagnostopoulos, Professor, NTUA
School of Mechanical Engineering
5. Vasileios Riziotis, Associate Professor, NTUA
School of Mechanical Engineering
6. Ioannis Templalexis, Professor, Hellenic Air Force Academy
Division of Thermodynamics, Propulsion and Energy Systems
7. Ioannis Nikolos, Professor, Technical University of Crete
School of Production Engineering and Management

** Supervisor

* Member of the Advisory Committee

June 2023, Athens

Part of the research study presented in this PhD thesis was supported by the NTUA Research Committee, which provided the author with a four-year full scholarship (February 2017-2021).

Μέρος της έρευνας που παρουσιάζεται σε αυτή τη διδακτορική διατριβή υποστηρίχτηκε οικονομικά από τον Ειδικό Λογαριασμό Κονδυλίων Έρευνας ΕΜΠ, που παρείχε στον συγγραφέα πλήρη υποτροφία διάρκειας τεσσάρων ετών (Φεβρουάριος 2017-2021).

Copyright © 2023 by Ioannis Kolias

All rights reserved. No part of this publication may be reproduced, distributed, or transmitted in any form or by any means, including photocopying, recording, or other electronic or mechanical methods, without the prior written permission of the author, except in the case of brief quotations embodied in critical reviews and certain other noncommercial uses permitted by copyright law (Law 2121/1993). For permission requests, e-mail the author at: johnkolias87@gmail.com or ikolias@mail.ntua.gr.

The PhD thesis approval from the School of Mechanical Engineering of NTUA does not imply acceptance of the opinions of the author (Law 5343/1932, Article 202).

Acknowledgements

Concluding this journey, I would like to thank all those who have contributed towards completing the present thesis.

First and foremost, I would like to sincerely thank my academic advisor, Nikolaos Aretakis, Associate Professor NTUA, for giving me the opportunity to conduct research in the interesting and very challenging field of the design of gas turbine engines. His valuable scientific and personal guidance and support were essential for successfully completing this thesis. I would also like to thank him for the diligent proofreading of the thesis text.

Next, I would like to thank Konstantinos Mathioudakis, Professor NTUA, for his constant presence and guidance throughout these years. His spot-on comments and advice on our joint publications and his corrections and suggestions for improving the quality of the thesis manuscript and presentation, were of paramount importance.

I would also like to thank Kyriakos Giannakoglou, Professor NTUA, for his comments, suggestions, and corrections on the thesis presentation and manuscript. His participation in the advisory committee of my thesis and his immediate response in reading and correcting the thesis manuscript were truly valuable.

Special thanks are due to Ioannis Anagnostopoulos (Professor NTUA), Vasileios Riziotis (Associate Professor NTUA), Ioannis Templelexis (Professor HAFSA), and Ioannis Nikolos (Professor TUC), for their participation in the examination committee of the present thesis.

At this point, I would like to express my special thanks and my deep gratitude to Dr. Alexios Alexiou. Without his priceless advice and his constant moral support, the completion of my PhD would have been impossible.

I also owe special thanks to my colleague and friend Dr. Konstantinos Ntonas for our collaboration, his help, and suggestions. But, more importantly, I owe him special thanks for our friendship and the mutual support which pulled us through our doctoral research in LTT/NTUA.

Finally, I would like to express the gratitude I feel for my parents, Alekos and Matoula, and my brother Lambros, who supported me morally throughout this PhD thesis. My special thanks are also due to my close friends, Sofia, Konstantinos, and Stavros, who were there whenever I felt like whining and drinking (a lot of) beer to compensate for the long weeks of hard work.

Last but not least, I want to express my gratitude to Anna Maria for being by my side, and for her patience. Without her material and moral support, the last two months prior to defending my thesis would have been unbearable.

Abstract

Development of an Integrated System for Preliminary Design of Aircraft Gas Turbines

The development of new gas turbine engines formally begins with the engine performance, geometry, and weight requirements, imposed by a customer or the manufacturer itself trying to fulfill a new market need. The first step after defining the project's specific needs is the preliminary design phase where the potential of a new engine design in terms of fuel efficiency, stable operation, production, operational, and maintenance costs, is assessed. In aircraft engines, the design should also comply with the aircraft's top-level requirements and with environmental regulations. To fulfill this objective, a preliminary design framework is required which integrates robust, fast, and reliable predictive models and tools for different design and analysis disciplines.

This thesis is concerned with the development of an integrated system for the preliminary, multi-disciplinary design and assessment of gas turbine aircraft engines. Therefore, in the scope of the present thesis, a number of computational tools, appropriate for such calculations, were developed under the same, user-friendly coding, modelling, and simulation environment (PROOSIS). The term "appropriate" means tools of lower-fidelity (0D/1D) which exhibit a number of advantages compared to higher-fidelity (2D/3D) tools when used in the context of preliminary design studies: 1) they are time efficient, 2) require very few and very basic performance and geometry inputs which are typically available during a preliminary calculation, 3) they are relatively easy in setting-up a calculation model and, finally, 4) they are easy to integrate in a design workflow.

Although there is not a single general recipe, the preliminary design phase should, at least, comprise modules for the aerothermodynamic design of turbomachinery components, for performance calculations at off-design conditions, for the mechanical design and analysis of critical structural components and parts, and for weight estimations. Therefore, in the context of the present thesis, corresponding computational tools and models (0D/1D) were developed which are organized in the following four (4) libraries:

- **TURBO1D:** Includes models for the preliminary aerothermodynamic design of gas turbine components, which are appropriate for multi-point design studies.
- **GTMD:** Includes models and tools for the preliminary design and analysis of critical structural parts.
- **GTWC:** Includes models for the preliminary weight estimation of gas turbine components and generic turbofan engines.
- **MLC:** Includes models and tools for the preliminary aerothermodynamic design (MLDC) and off-design performance estimation (MLAC) of multi-stage, axial-flow compressors.

All the above tools were initially validated individually against publicly available data of real-engine configurations or against predictions produced by higher-fidelity (3D) tools. Then, they were combined under the PROOSIS environment for developing an integrated system for the preliminary design of aircraft engines, which allows the efficient preliminary design and assessment of new engine concepts by easily defining any combination of design metrics and constraints, at any operating point, and for any of the involved design and analysis disciplines.

The capabilities, fidelity, and efficiency of the developed tools are demonstrated through trade-off optimization studies at component and at engine level, considering an ultra-high bypass ratio turbofan engine for a short-range aircraft mission. The design studies were formulated considering different objectives and conducted for two (2) values of the engine overall pressure ratio split between the low- and high-pressure compressors (0.30 and 0.40), which are of current industrial interest.

It is important to note that some of the tools presented in this thesis were developed as part of LTT/NTUA's collaboration with European gas turbine and aircraft industries, while the novel contributions of the present work are supported by five (5) peer-reviewed international scientific conference and journal papers.

Keywords: Aircraft gas turbines, preliminary design, lower-fidelity models (0D/1D), performance analysis, aerothermodynamic design, mechanical design, weight estimation, ultra-high bypass ratio turbofan engines, trade-off optimization studies

Περίληψη

Ανάπτυξη Συστήματος Υπολογιστικών Εργαλείων για τον Προκαταρκτικό Σχεδιασμό Αεροπορικών Αεριοστροβίλων

Η ανάπτυξη ενός νέου αεριοστροβίλου ξεκινά επίσημα με τις προδιαγραφές για τις επιδόσεις, τη γεωμετρία, και το βάρος της μηχανής που τίθενται από τον πελάτη ή από τον ίδιο τον κατασκευαστή της μηχανής προσπαθώντας να ερευνήσει και να ικανοποιήσει κάποια καινούργια ανάγκη της αγοράς. Το πρώτο βήμα ύστερα από τον ορισμό των προδιαγραφών της μηχανής είναι η φάση του προκαταρκτικού σχεδιασμού όπου αποτιμούνται οι προοπτικές ενός νέου σχεδιασμού ως προς την κατανάλωση καυσίμου, την ευσταθή λειτουργία, και τα κόστη παραγωγής, λειτουργίας και συντήρησης της μηχανής. Στις αεροπορικές μηχανές, ο σχεδιασμός θα πρέπει επίσης να συμμορφώνεται με τις απαιτήσεις του φακέλου πτήσης του αεροσκάφους στο οποίο πρόκειται να τοποθετηθεί η νέα μηχανή, αλλά και με περιβαλλοντικούς περιορισμούς. Για την επίτευξη αυτών των στόχων, απαιτείται η ανάπτυξη ολοκληρωμένων συστημάτων προκαταρκτικού σχεδιασμού τα οποία θα πρέπει να ενσωματώνουν στιβαρά, γρήγορα, και αξιόπιστα υπολογιστικά μοντέλα και εργαλεία για τις διαφορετικές αρχές σχεδιασμού και ανάλυσης που λαμβάνουν χώρα στον προκαταρκτικό σχεδιασμό.

Στη διατριβή αυτή γίνεται η ανάπτυξη ενός ολοκληρωμένου συστήματος για τον προκαταρκτικό, πολυκριτηριακό σχεδιασμό και την αξιολόγηση αεροπορικών αεριοστροβίλων. Συνεπώς, στο πλαίσιο της παρούσας διατριβής, αναπτύχθηκαν υπολογιστικά εργαλεία κατάλληλα για προκαταρκτικούς υπολογισμούς. Η ανάπτυξη και ο προγραμματισμός των εργαλείων αυτών έγινε στο ίδιο περιβάλλον προγραμματισμού, μοντελοποίησης, και προσομοίωσης (PROOSIS). Ο όρος «κατάλληλα» σημαίνει εργαλεία χαμηλής πιστότητας (0D/1D) που παρουσιάζουν ένα πλήθος πλεονεκτημάτων έναντι εργαλείων υψηλότερης πιστότητας (2D/3D) όταν χρησιμοποιούνται σε μελέτες προκαταρκτικού σχεδιασμού: 1) είναι υπολογιστικά γρήγορα, 2) απαιτούν πολύ λίγα (και πολύ βασικά) δεδομένα εισόδου που, τυπικά, είναι διαθέσιμα κατά τη διάρκεια ενός προκαταρκτικού υπολογισμού, 3) μπορούν να χρησιμοποιηθούν απροβλημάτιστα για τη δημιουργία μιας νέας υπολογιστικής περίπτωσης και, τέλος, 4) μπορούν να ενσωματωθούν εύκολα σε μια ροή εργασιών για τον ολοκληρωμένο προκαταρκτικό σχεδιασμό μιας μηχανής.

Αν και δεν υπάρχει μια γενική «συνταγή», το στάδιο του προκαταρκτικού σχεδιασμού πρέπει, κατ' ελάχιστον, να περιλαμβάνει εργαλεία για τον αεροθερμοδυναμικό σχεδιασμό των στροβιλοσυνιστωσών της μηχανής, για τον υπολογισμό των επιδόσεων των συνιστωσών της μηχανής σε σημεία λειτουργίας εκτός του σημείου σχεδιασμού τους, για τη μηχανολογική ανάλυση και το σχεδιασμό κρίσιμων δομικών στοιχείων της μηχανής όπως οι άτρακτοι και οι δίσκοι, και για την εκτίμηση του δομικού βάρους των συνιστωσών και της ίδιας της μηχανής. Συνεπώς, στο πλαίσιο της διατριβής, αναπτύχθηκαν αντίστοιχα υπολογιστικά εργαλεία και μοντέλα (0D/1D) που οργανώνονται στις ακόλουθες τέσσερις (4) βιβλιοθήκες:

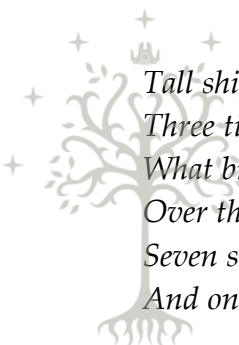
- **TURBO1D:** Στη βιβλιοθήκη αυτή περιλαμβάνονται μοντέλα για τον προκαταρκτικό αεροθερμοδυναμικό σχεδιασμό συνιστωσών ενός αεριοστροβίλου, που είναι κατάλληλα για ταυτόχρονο σχεδιασμό σε πολλά σημεία λειτουργίας της μηχανής.
- **GTMDC:** Στη βιβλιοθήκη αυτή περιλαμβάνονται μοντέλα και εργαλεία για τον προκαταρκτικό σχεδιασμό και την ανάλυση κρίσιμων δομικών μερών και εξαρτημάτων μιας μηχανής.
- **GTWC:** Στη βιβλιοθήκη αυτή περιλαμβάνονται μοντέλα για την προκαταρκτική εκτίμηση βάρους συνιστωσών ενός αεριοστροβίλου και για γενικές διατάξεις στροβιλοαντιδραστήρων διπλού ρεύματος.
- **MLC:** Στη βιβλιοθήκη αυτή περιλαμβάνονται μοντέλα και εργαλεία για τον προκαταρκτικό αεροθερμοδυναμικό σχεδιασμό (MLDC) και την εκτίμηση των επιδόσεων σε σημεία εκτός σχεδιασμού (MLAC) πολυβάθμιων, αξονικών συμπιεστών.

Τα προαναφερθέντα εργαλεία αρχικά πιστοποιήθηκαν ξεχωριστά χρησιμοποιώντας διαθέσιμα δεδομένα για πραγματικές μηχανές και συγκρίσεις με προβλέψεις από εργαλεία υψηλότερης πιστότητας (3D). Στη συνέχεια, συνδυάστηκαν στο ίδιο περιβάλλον μοντελοποίησης και προσομοίωσης (PROOSIS) για τη δημιουργία ενός ολοκληρωμένου συστήματος, κατάλληλου για τον προκαταρκτικό σχεδιασμό αεροπορικών κινητήρων. Το σύστημα αυτό επιτρέπει τον αποδοτικό σχεδιασμό και την αξιολόγηση νέων διατάξεων αεροπορικών κινητήρων ορίζοντας εύκολα διαφορετικούς συνδυασμούς μετρικών και περιορισμών σχεδιασμού, που μπορούν να οριστούν σε οποιοδήποτε σημείο λειτουργίας της μηχανής και για οποιαδήποτε αρχή σχεδιασμού και ανάλυσης που περιλαμβάνεται στο σύστημα.

Οι υπολογιστικές δυνατότητες, η απόδοση, και η ακρίβεια των αναπτυχθέντων εργαλείων επιδεικνύονται μέσω μελετών βελτιστοποίησης σε επίπεδο συνιστώσας και κινητήρα, θεωρώντας έναν στροβιλοαντιδραστήρα διπλού ρεύματος υπέρ-υψηλού λόγου παράκαμψης, που μελετάται σε μια αποστολή μικρής εμβέλειας. Για τις μελέτες σχεδιασμού διατυπώθηκαν διαφορετικές αντικειμενικές συναρτήσεις, ενώ θεωρούνται δύο (2) διαφορετικές τιμές του λόγου διαμοιρασμού του ολικού λόγου πίεσης της μηχανής μεταξύ των συμπιεστών χαμηλής και υψηλής πίεσης (0.30 και 0.40), που είναι τρέχοντος βιομηχανικού ενδιαφέροντος.

Είναι σημαντικό να τονιστεί ότι κάποια από τα εργαλεία που παρουσιάζονται σε αυτήν τη διατριβή αναπτύχθηκαν στο πλαίσιο της συνεργασίας του ΕΘΣ/ΕΜΠ με Ευρωπαϊκές βιομηχανίες κατασκευής αεροπορικών αεριοστροβίλων και αεροσκαφών. Τέλος, οι καινοτόμες συνεισφορές της παρούσας διατριβής υποστηρίζονται από πέντε (5) δημοσιεύσεις σε διεθνή επιστημονικά συνέδρια και περιοδικά με κριτές.

Λέξεις κλειδιά: Αεροπορικοί αεριοστροβίλοι, προκαταρκτικός σχεδιασμός, μοντέλα χαμηλής πιστότητας (0D/1D), θερμοδυναμική ανάλυση επιδόσεων, αεροθερμοδυναμικός σχεδιασμός, μηχανολογικός σχεδιασμός, εκτίμηση βάρους, στροβιλοαντιδραστήρες διπλού ρεύματος υπέρ-υψηλού λόγου παράκαμψης, βελτιστοποίηση



*Tall ships and tall kings
Three times three,
What brought them from the foundered land
Over the flowing sea?
Seven stars and seven stones
And one white tree.*

– J.R.R. Tolkien, LotR, The Two Towers

Table of Contents

Chapter 1. Preliminary Multi-Disciplinary Design of Aircraft Gas Turbines	27
1.1 Introduction	27
1.1.1 Enabling Technologies for UHBR Engines	29
1.1.1.1 Discussion on Gearbox	30
1.1.1.2 Discussion on VPF and VAN	31
1.2 Tools for the Preliminary Design of Aircraft Gas Turbines	32
1.2.1 State-of-the-art	33
1.2.2 Mean-Line Methods for Compressor Preliminary Design and Analysis	34
1.2.2.1 Compressor Design	35
1.2.2.2 Compressor Off-Design Performance Prediction	37
1.2.2.3 Compressor Choke Prediction	39
1.2.2.4 Compressor Stall Prediction	40
1.2.3 Methods for Preliminary Mechanical Design	40
1.2.3.1 Design of Shafts	41
1.2.3.2 Design of Casings	41
1.2.3.3 Design of Ducts	41
1.2.3.4 Design of Disks	41
1.2.4 Methods for Preliminary Weight Estimations	43
1.2.4.1 Whole Engine-Based Approaches	43
1.2.4.2 Component-Based Approaches	44
1.2.4.3 Other Weight Estimation Approaches	47
1.3 Motivation and Objectives	47
1.4 Thesis Outline	48
Chapter 2. The Developed System of Tools	51
2.1 Introduction	51
2.2 A Brief Introduction to PROOSIS	51
2.2.1 History of PROOSIS	51
2.2.2 The PROOSIS Coding, Modelling, and Simulation Environment	51
2.2.3 LTT/NTUA and PROOSIS	54
2.3 The Developed Design and Analysis Workflow	55
2.4 Summary and Discussion	57

Chapter 3. Turbomachinery 1D Aerothermodynamic Design	59
3.1 Introduction	59
3.2 Fundamentals	62
3.2.1 Fluid and Thermodynamic Flow Properties Modelling	62
3.2.2 Mean-Line Flow Representation	63
3.2.3 Flow Station Calculation	65
3.2.4 Stage Performance Parameters	66
3.2.5 Euler Pump and Turbine Equations	67
3.2.6 3D Flow Approximation	68
3.2.7 Solidity, Blade Count, and Aspect Ratio	68
3.3 Axial Compressor 1D Aerothermodynamic Design	69
3.3.1 Stage-by-Stage Calculation	70
3.3.2 Mass Flow Calculation	71
3.3.3 Area Blockage Calculation	71
3.3.4 Compressor Inlet Calculation	73
3.3.5 Compressor Exit Calculation	74
3.3.6 Mean-Line Distribution	76
3.3.7 Rotational and Blade Speed Calculation	78
3.3.8 Stage Performance Parameters Calculation	78
3.3.8.1 Flow Coefficient	78
3.3.8.2 Loading Coefficient	79
3.3.8.3 Stage Reaction	79
3.3.9 Aspect Ratio Calculation	80
3.3.10 Velocity Triangles Calculation	80
3.3.10.1 Mean-Line Velocity Triangles	81
3.3.10.2 Hub and Tip Velocity Triangles	82
3.3.11 Blade Row Solidity Calculation	83
3.3.12 Blade Row Total Pressure Loss Calculation	84
3.3.12.1 Profile Losses	84
3.3.12.2 Endwall Losses	85
3.3.12.3 Secondary Losses	86
3.3.12.4 Shock Losses	86
3.3.12.5 Total Loss	86
3.3.13 Stage Isentropic Efficiency Calculation	86
3.3.14 Stage Radial Positioning	88
3.3.15 Next Stage Aerodynamic Design and Overall Compressor Performance	88
3.4 Compressor Axial Positioning and Gas-Path Visualization	89
3.4.1 Blade Dimensions Calculation	90
3.4.1.1 Blade Count	90
3.4.1.2 Stagger Angles	90
3.4.1.3 Chord Lengths	91
3.4.2 Axial Coordinates Calculation	91
3.4.2.1 Axial Gap Calculation	91

3.4.2.2 Compressor Axial Positioning	92
3.4.2.3 Compressor Gas-Path Visualization	95
3.5 Axial Turbine 1D Aerothermodynamic Design	96
3.5.1 Stage-by-Stage Calculation	97
3.5.2 Mass Flow Calculation	98
3.5.3 Turbine Inlet and Exit Calculation	100
3.5.4 Mean-Line Distribution	100
3.5.5 Rotational and Blade Speed Calculation	101
3.5.6 Stage Performance Parameters Calculation	102
3.5.6.1 Flow Coefficient	102
3.5.6.2 Loading Coefficient	102
3.5.6.3 Stage Reaction	103
3.5.6.4 Rotor Swirl Parameters	103
3.5.7 Velocity Triangles Calculation	104
3.5.7.1 Mean-Line Velocity Triangles	104
3.5.7.2 Hub and Tip Velocity Triangles	105
3.5.8 Isentropic Efficiency Calculation for Uncooled Stages	105
3.5.8.1 Aungier's Method	105
3.5.8.2 Glassman's Method	106
3.5.9 Cooled Stages Isentropic Efficiency Calculation	108
3.5.10 Model for Stage Cooling	109
3.5.11 Stage Radial Positioning	110
3.5.12 Next Stage Aerodynamic Design and Overall Turbine Performance	110
3.6 Turbine Axial Positioning and Gas-Path Visualization	111
3.6.1 Blade Dimensions Calculation	111
3.6.1.1 Solidities and Stagger Angles	111
3.6.1.2 Chord Lengths	112
3.6.1.3 Blade Count	113
3.6.2 Axial Coordinates Calculation	113
3.6.2.1 Axial Gap Calculation	113
3.6.2.2 Turbine Axial Positioning	113
3.6.2.3 Turbine Gas-Path Visualization	116
3.7 Axial Fan 1D Aerothermodynamic Design and Gas-Path Visualization	116
3.7.1 Fan Rotor Inlet Calculation	117
3.7.2 Rotational Speed Estimation	117
3.7.3 Fan Performance Estimation	118
3.7.4 Fan Rotor Exit Calculation	118
3.7.5 Fan Radial and Axial Positioning and Gas-Path Visualization	119
3.7.6 Blade Count	122
3.8 TURBO1D PROOSIS Library	122
3.9 TURBO1D Validation Studies	123
3.9.1 Compressor Component Validation	123
3.9.2 Turbine Component Validation	128
3.9.3 Fan Component Validation	133

3.10 Summary and Discussion	136
Chapter 4. Mechanical Design of Critical Structural Components	137
<hr/>	
4.1 Introduction	137
4.2 Materials Database	138
4.3 Power Transmitting Shafts	141
4.3.1 Shaft Simplified Stress Model (S-SSM)	142
4.3.2 S-SSM Validation	143
4.4 Rotating Shafts	145
4.4.1 Disk Geometry Modelling	146
4.4.1.1 Ring Disk	148
4.4.1.2 Web Disk	148
4.4.1.3 Hyperbolic Disk	149
4.4.2 Disk Stress Modelling	149
4.4.2.1 Disk Simplified Thermal Model (D-STM)	149
4.4.2.2 D-STM Validation	151
4.4.2.3 Disk Simplified Stress Model (D-SSM)	153
4.4.2.4 D-SSM Validation	157
4.4.3 Rotating Disk Optimizer (RDO) for Minimum Weight	165
4.4.3.1 Optimization Algorithm	166
4.4.3.2 Selection of Design Variables	166
4.4.3.3 Initializing the Disk Geometry	168
4.4.3.4 Calculation of Disk Mass	170
4.4.3.5 Calculation of Stress Margins	170
4.4.3.6 Objective Function Formulation	170
4.4.3.7 Constraints Formulation	171
4.4.3.8 Optimization Procedure Validation	173
4.4.3.9 Optimization of a Ten-Stage Compressor Disks	175
4.5 Interconnecting Ducts	182
4.6 Turbomachinery Casings	183
4.7 Summary and Discussion	184
Chapter 5. Weight Estimation of Aircraft Gas Turbines	185
<hr/>	
5.1 Introduction	185
5.2 Component-Based, Semi-Empirical (CB-SE) Weight Estimation	186
5.2.1 Fan Weight	187
5.2.2 Compressor Weight	188
5.2.3 Burner Weight	189
5.2.4 Turbine Weight	190
5.2.5 Structural Weight	191
5.2.6 Gearbox Weight	191

5.2.7 VPF Pitch-Changing Mechanism Weight	192
5.2.8 Controls and Accessories Weight	194
5.2.9 VAN Area-Changing Mechanism Weight	194
5.2.10 Bare Engine Weight	195
5.2.11 Nacelle Weight	195
5.2.12 Thrust Reversal System Weight	197
5.2.13 Engine Total Weight	197
5.3 Component-Based, Analytical (CB-GM) Weight Estimation	198
5.3.1 Frames Weight	198
5.3.2 Ducts Weight	201
5.3.3 Shafts Weight	201
5.3.4 Structural Weight	201
5.3.5 Connecting Hardware Weight	201
5.3.6 Disks Weight	202
5.3.7 Casings Weight	204
5.3.8 Blading Weight	205
5.3.8.1 GasTurb Details 5 Modelling Approach	205
5.3.8.2 NASA's WATE Modelling Approach	206
5.3.9 Compressor and Turbine Weights	207
5.3.10 Fan Weight	209
5.3.11 Burner Weight	210
5.3.12 Engine Total Weight	212
5.4 GTWC PROOSIS Library	212
5.5 GTWC Validation Studies	213
5.5.1 Partial Validation of Component for Compressor Weight Estimation	213
5.5.2 Qualitative Validation of Component for Engine Weight Estimation	215
5.5.3 Quantitative Validation of Component for Engine Weight Estimation	219
5.6 Summary and Discussion	224
Chapter 6. Axial Compressor 1D Off-Design Performance Modelling (MLAC)	225
<hr/>	
6.1 Introduction	225
6.2 Fundamentals	226
6.2.1 Fluid and Thermodynamic Flow Properties Modelling	227
6.2.2 Mean-Line Flow Modelling	228
6.2.3 Flow Station Calculation	229
6.2.4 Compressor Overall Performance	229
6.3 Compressor Performance Modelling	231
6.3.1 BRM Modelling	233
6.3.2 IVM Modelling	235
6.4 Blade Row Geometry Modelling	236
6.5 Design Incidence and Deviation Models	239
6.5.1 Design Incidence Angle and Angle of Attack	239

6.5.1.1 Lieblein's Model	239
6.5.1.2 Herrig's Model	241
6.5.2 Design Deviation Angle	241
6.5.2.1 Lieblein's Model	241
6.5.2.2 Howell's Model	242
6.6 Aerodynamic Performance of Diffusing Rows	242
6.7 Off-Design Deviation Angle Models	243
6.7.1 Deviation Angle Models for Diffusing Rows	243
6.7.1.1 Lieblein's Model	243
6.7.1.2 Swan's Model	244
6.7.2 Deviation Angle Model for IGVs	244
6.8 Loss Models for Diffusing Rows	246
6.8.1 Equivalent Drag Coefficient Loss	247
6.8.2 Endwall Loss Models	247
6.8.2.1 Howell's Model	247
6.8.2.2 Vavra's Model	248
6.8.3 Secondary Loss Models	248
6.8.3.1 Howell's Model	248
6.8.3.2 Vavra's Model	248
6.8.4 Clearance Loss Model	248
6.8.5 Shock Loss Models	249
6.8.6 Reynolds Number Effects	250
6.8.6.1 Aungier's Model	250
6.8.6.2 Wright et al.'s Model	250
6.8.6.3 Koch et al.'s Model	251
6.8.7 Design Profile Loss Models	251
6.8.7.1 $\Omega_{pr} = f(DF)$ Model	252
6.8.7.2 $\Omega_{pr} = f(DF_{eq})$ Model	252
6.8.8 Mach Number Effects	253
6.8.9 Off-Design Profile Loss Model	255
6.8.10 Blockage Modelling	256
6.9 Loss Model for IGVs	256
6.10 Choke Modelling	258
6.10.1 Indices for Annulus Choke Modelling	258
6.10.2 Index for Throat Passage Choke Modelling	259
6.10.2.1 Subsonic Choke Modelling	259
6.10.2.2 Supersonic Choke Modelling	260
6.10.3 Estimating the Choke Mass Flow Rate	261
6.10.4 Choked Part of a Speed-Line	261
6.11 Stall Modelling	262
6.11.1 Stalling Incidence Criterion	263
6.11.2 Diffusion Factor Criterion	263
6.11.3 Minimum Velocity Ratio Criterion	264
6.11.4 Stall Margin Criterion (Maximum Static Pressure Rise Criterion)	265

6.11.5 Estimating the Stall Mass Flow Rate	266
6.12 MLAC PROOSIS Library Components for Off-Design Simulations	267
6.13 MLAC Validation Studies	269
6.13.1 MLAC Tuning Test Case	269
6.13.2 Choke Modelling Test Case	275
6.13.3 MLAC Integration in 0D Cycle Calculations Test Case	280
6.13.4 Multi-Stage Compressor Performance Map Validation Test Case	283
6.14 Summary and Discussion	284
Chapter 7. Axial Compressor 1D Design Modelling (MLDC)	287
<hr/>	
7.1 Introduction	287
7.2 Compressor Design Modelling, Options, and Inputs	287
7.2.1 General Design Approach	287
7.2.2 Definition of the Compressor Work Distribution	288
7.2.3 Definition of the Axial Velocity Distribution	288
7.2.4 Definition of the Rotor Inlet Absolute Flow Angle	289
7.2.5 Compressor Mean-Line Definition	289
7.2.6 Compressor Axial Positioning and Gas-Path Visualization	290
7.3 Blade Row Design Modelling, Options, and Inputs	290
7.3.1 IVM Modelling	290
7.3.2 BRM Modelling	290
7.3.2.1 BRM Flow Modelling	291
7.3.2.2 BRM Geometry Modelling	291
7.4 MLDC PROOSIS Library Component for Design Calculations	293
7.5 MLDC Validation Study	293
7.6 Summary and Discussion	296
Chapter 8. Compressor Trade-Off Design Studies	297
<hr/>	
8.1 Introduction	297
8.2 Inputs for Aerodynamic, Performance, and Weight Calculations	298
8.3 LPC and HPC Design Studies	302
8.3.1 PROOSIS Design Model Setup and ISIGHT Implementation	302
8.3.2 Sensitivity Design Studies	303
8.3.2.1 Influence of Aspect Ratio	304
8.3.2.2 Influence of Solidity	305
8.3.2.3 Influence of Stage Count	306
8.3.2.4 Influence of 1st Rotor Tip Speed	307
8.3.2.5 Influence of Exit Mach Number	308
8.3.2.6 Influence of Axial Velocity Shape Factor	309
8.3.2.7 Influence of Average Absolute Flow Angle	309
8.3.3 Optimization Studies	310

8.3.3.1 Selection of Design Variables and Constants	311
8.3.3.2 Optimization Results	312
8.4 HPC Design and Off-Design Optimization Studies	326
8.4.1 PROOSIS Design Model Setup and ISIGHT Implementation	326
8.4.2 Optimization Studies	327
8.4.3 Optimization Results	328
8.5 Summary and Discussion	335
Chapter 9. Engine Trade-Off Design Studies at Aircraft Mission Level	337
<hr/>	
9.1 Introduction	337
9.2 Multi-Disciplinary Design Workflow Setup and ISGHT Implementation	337
9.2.1 Engine Cycle Analysis Module (TDP)	338
9.2.2 Compressor Design (CMD) and Off-Design Analysis (CMM) Modules	339
9.2.3 Engine Multi-Point Design Module (MPD)	340
9.2.4 Engine Off-Design Performance Module (ODS)	342
9.2.5 Aircraft Mission Analysis Module (ACS)	343
9.2.6 ISIGHT Implementation	344
9.3 Calculation Inputs and Design Assumptions	344
9.4 Optimization Setup	348
9.5 Optimization Results	350
9.6 Summary and Discussion	358
Chapter 10. Closure	359
<hr/>	
10.1 Summary	359
10.2 Conclusions	361
10.3 Novel Contributions	364
10.4 List of Publications and Technical Reports	364
10.5 Suggestions for Future Work	366
Appendix A. Turbomachinery Design Guidelines	369
Appendix B. Polytropic Efficiency for Consistent Preliminary Design	373
Appendix C. Annular Combustor Preliminary Sizing	377
Appendix D. NASA/GE E3 HPC Inputs for Mechanical Design and Weight Estimation Validations	385
Appendix E. Blade and Blade Attachment Sizing	395
Appendix F. Proof and Validation of Eq. (4.53)	399

Appendix G. Nacelle Dimensions and Installed Engine Profile Drag Estimation for Unmixed Turbofans	401
Appendix H. Polar Moments of Inertia Estimation	405
Appendix I. 2-Spool Unmixed Flow Turbofan Engine Station Designation	407
Abbreviations	409
Nomenclature	413
References	421

1 Preliminary Multi-Disciplinary Design of Aircraft Gas Turbines

1.1 Introduction

To fulfill the short-term ACARE Vision 2020 [see European Commission (2001)] and the long-term ACARE SRIA 2050 [see ACARE (2012)] aviation targets (Table 1.1), several innovative steps should be materialized at the engine and aircraft levels, as well as in the air traffic management and operations.

Table 1.1: ACARE short- and long-term aviation targets [adapted from Sieber (2015)]

CO ₂ Emissions		Vision 2020	SRIA 2020	SRIA 2035	SRIA 2050
Air traffic per passenger and kilometer		-50%	-43%	-60%	-75%
Contribution	Airframe	-25%	-20%	-30%	-34%
	Engine	-20%	-20%	-30%	-34%
	Air traffic management	-12%	-7%	-12%	-12%
	Operation	-4%	-4%	-7%	-12%
					-68%
NO _x Emissions		Vision 2020	SRIA 2020	SRIA 2035	SRIA 2050
Air traffic per passenger and kilometer		-80%	N/A	-84%	-90%
Margin relative to ICAO LTO CAEP6		-60%	N/A	-65%	-75%
Acoustic Emissions		Vision 2020	SRIA 2020	SRIA 2035	SRIA 2050
Aircraft		-10 EPNdB (-50%)	N/A	-11 EPNdB (-55%)	-15 EPNdB (-65%)

According to Sieber (2015), the near-term ACARE objectives (EIS of 2025) with respect to engine performance and noise are expected to be met by ducted ultra-high bypass ratio (UHBR) turbofan engines with high overall pressure ratios and small cores. As it can be seen in Figure 1.1, UHBR turbofans are expected to offer high thermal and propulsive efficiencies resulting to improved overall efficiency and fuel consumption [see Epstein (2014)]. According to Leylekian et al. (2014), UHBR engines are additionally expected to offer significantly reduced noise levels, according to Figure 1.2.

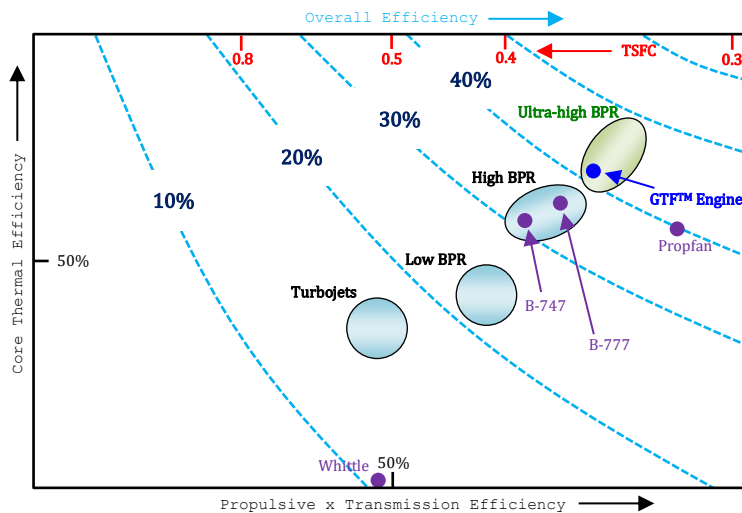


Figure 1.1: Evolution of efficiencies for different engine configurations¹.

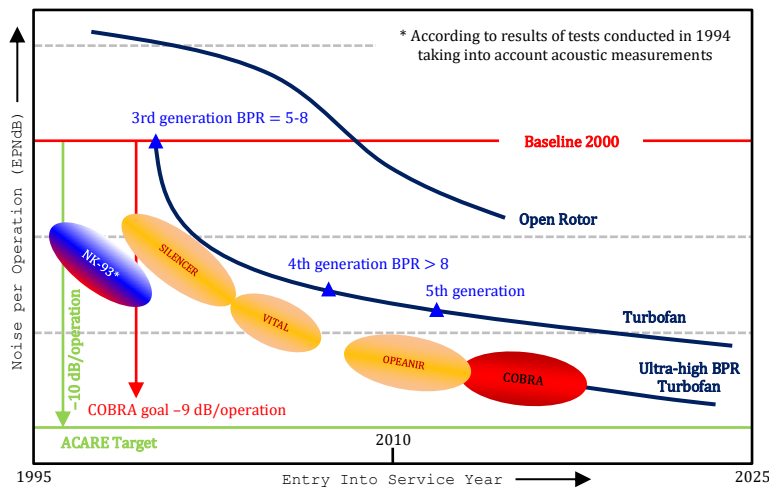


Figure 1.2: Noise level evolution for different engine configurations [adapted from Leylekian et al. (2014)].

Regarding NO_x , dry-low- NO_x combustors used in land-based gas turbines for more than two decades are now mitigating to aircraft gas turbines for compensating the high turbine inlet temperatures and overall pressure ratios used in modern engines which, in turn, promote NO_x production. Lean-burn combustion systems can offer improved NO_x performance in comparison to rich-burn quick-quench lean-burn combustors, especially when they are coupled with turbine NGVs of variable geometry that can help in the modulation of the combustor primary zone fuel-to-air ratio during part-load operation [see Kyprianidis et al. (2017)].

It is common ground that to move to ultra-high bypass ratios the development and maturation of a number of core technologies is crucial. As discussed by McKay et al. (2012), UHBR engines are expected to be equipped with compressor flow and

¹Adapted from a presentation made by Winter M. in AIAA Aerospace Today and Tomorrow in June 2013: "A View Into the Next Generation of Commercial Aviation (2025 Timeframe)". The presentation can be found in the following link: https://www.aiaa.org/uploadedFiles/Events/Other/Corporate/2013_-_Aerospace_Todayand_Tomorrow/Winter.pdf (accessed: December 21st, 2017)

clearance control [see Alexiou et al. (2010)], cooling flows, lean-burn combustion systems [see Kyprianidis et al. (2017)], and turbines constructed by ceramic matrix composites (CMCs). CMCs will significantly improve the engine performance and reduce the engine weight because of the increased blade temperatures and the reduced material densities compared to materials currently used in gas turbine applications.

1.1.1 Enabling Technologies for UHBR Engines

It is well understood that increasing the bypass ratio of a direct-drive turbofan engine to ultra-high values will result to limitations in both the fan and LPT performance and weight. According to Kurzke (2009), the aerodynamic loading of the LPT is increased significantly as the bypass ratio is increased due to the reduction in the fan tip speed. In turn, the increased loading results to a decrease in turbine efficiency and to an increase in stage count if the engine configuration is to remain unchanged. Furthermore, the torque transmitted by the low-pressure shaft will also increase [see Borradaile (1988)], leading to structural problems in the absence of vastly improved materials.

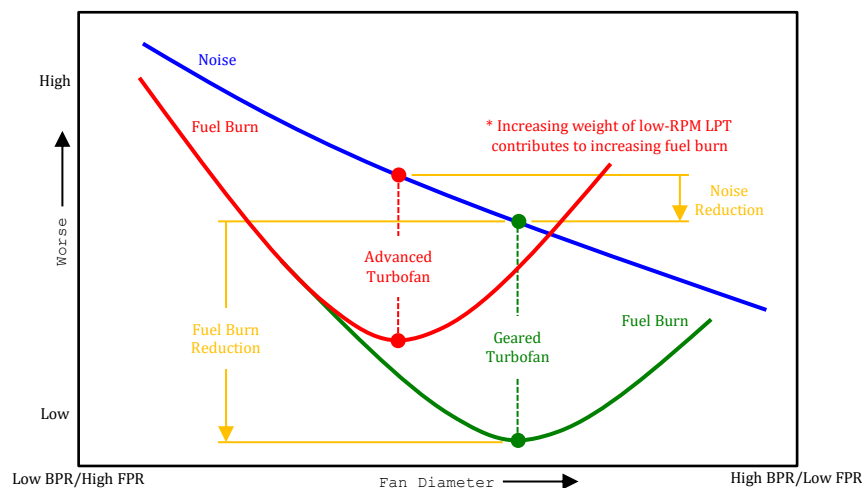


Figure 1.3: Propulsion system performance².

To achieve high bypass ratio and high overall efficiency, a gearbox between the LPT/LPC and fan shafts was opted as the optimal solution and applied to the P&W high bypass ratio GTF PurePower™ family of engines³. As seen in Figure 1.3, the introduction of a gearbox allows the two shafts (LPT/LPC and fan) to rotate at their optimal speed in terms of efficiency, stage loading, stage count, and noise. Furthermore, the increased speed of the low-pressure shaft allows the splitting of the overall pressure ratio to be done more easily between the LPC and HPC components [see Epstein (2014)].

²Adapted from a presentation made by Winter M. in AIAA Aerospace Today and Tomorrow in June 2013: “A View Into the Next Generation of Commercial Aviation (2025 Timeframe)”. The presentation can be found in the following link: https://www.aiaa.org/uploadedFiles/Events/Other/Corporate/2013_-_Aerospace_Todayand_Tomorrow/Winter.pdf (accessed: December 21st, 2017)

³<https://www.prattwhitney.com/en/products/commercial-engines/pratt-and-whitney-gtf/> (accessed: March 30th, 2023)

It is obvious that if the bypass ratio is to be increased well above 10, then the geared turbofan engine becomes more attractive and the direct-drive turbofan design is no longer a viable option. Increasing the bypass ratio results in increased propulsive efficiencies, but the specific thrust reduces, leading, in turn, to increased engine and nacelle diameters and, thus, weight and installation drag. Direct-drive engines become unattractive for bypass ratios greater than 13 according to a study by Bijewitz et al. (2014). To compensate for this increase in engine diameter, a shorter intake will be required, while special care should be given to ground clearance. Shorter intake ducts, however, suffer from reduced diffusion capability which, in turn, can lead to flow separation around the nacelle causing fan stability and performance problems.

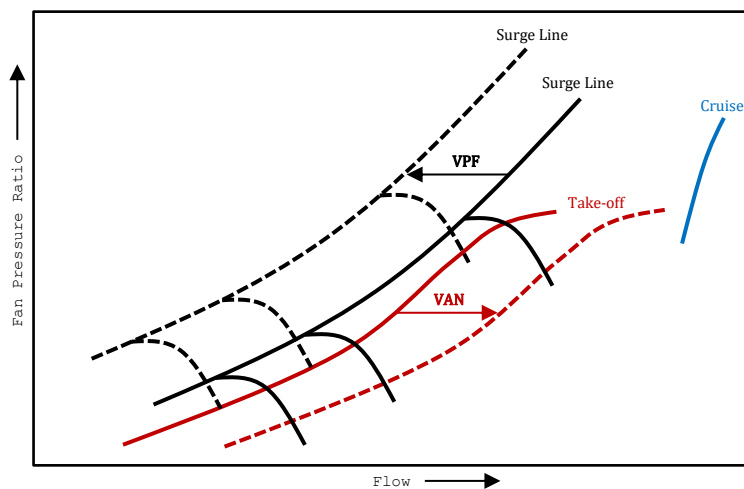


Figure 1.4: VAN and VPF configurations on fan operation [adapted from Borradaile (1988)].

The main stability issue of UHBR engines is expected to emanate from the fan component. The fan working line is controlled by the bypass nozzle characteristic. At take-off where the fan pressure ratio is low, the nozzle pressure ratio will fall below the critical value for choking in the absence of sufficient ram recovery and the bypass nozzle will unchoke. The unchoked bypass nozzle will shift the operating line of the fan towards reduced mass flows and closer to the surge line. To avoid this problem, two solutions are proposed: 1) a variable area bypass nozzle (VAN) or 2) a variable pitch fan (VPF). According to Figure 1.4, VPF moves the surge line away from the operating line, while the VAN configuration shifts the operating line to higher mass flows and lower pressure ratios, away from surge.

In conclusion, the gearbox, bypass VAN, and VPF are expected to offer performance benefits that will allow the design, development, and production of UHBR engines, but with significant weight, installation complexity, and maintenance cost penalties. Next, a brief insight on the application status and research advances for all three technologies is given.

1.1.1.1 Discussion on Gearbox

As we saw above, in high bypass ratio engines gearboxes allow the shafts of the fan and LPC/LPT to rotate at their optimal speeds in terms of component efficiencies, while they also allow the easier split of the engine pressure ratio in the compression system.

The gear ratio is expected to lie between 2 and 4 [see Borradaile (1988)], although ratios lower than 3 can be difficult to attain according to Dominy (1987). In the P&W GTF PurePower™ engines the value 3:1 was applied and was also selected as the optimum in several studies [see Kurzke (2009) and Hall et al. (2006)]. The value 3.3:1 was selected by Alexiou et al. (2010), while a ratio of 4:1 was used in the studies by Bijewitz et al. (2014). Regarding the weight penalty, the gearbox weight is estimated to account between 6% to 8% of the engine total weight [see Hall et al. (2006); Larsson et al. (2011a); Edkins et al. (1972); Larsson et al. (2011b)].

1.1.1.2 Discussion on VPF and VAN

Low pressure ratio-high bypass ratio fans are expected to have stability issues during take-off since, for fixed engine geometry, the fan is choked at high altitudes and flight Mach numbers, but unchokes at low speeds. Hence, the mass flow reduces and the fan operating line is moved towards the surge line. As we saw, the VAN and/or VPF utilization will provide an additional parameter for handling the operating line of the fan component. During take-off, the fan could be operated away from surge by opening the nozzle area or closing the fan blades. Likewise, an optimal efficiency could be achieved in any flight regime by selecting the optimal VAN or VPF setting. According to Zimbrick et al. (1990), engines with fan pressure ratios less than 1.40-1.45 will require the installation of a VPF or VAN configuration, while the simultaneous use of both has also been explored [see Edkins et al. (1972) and Willis (1979)].

The VPF concept was extensively used in propeller-driven aircrafts and helicopters and tested in turbofan engines in the early 1970's [see Denning (1972) and Dawson et al. (1972)]. The high hub-to-tip ratio required for its application, the weight penalty, reliability, and complexity of the pitch changing mechanism have put this concept on hold until recently due to the interest in UHBR engines. It is expected that novel pitch changing mechanisms can lift most of its drawbacks [see Violette et al. (2010) and Mazzawy (2010)]. Theoretically, the VPF could be utilized for thrust reversing as well, thus reducing the nacelle weight. However, tests and calculations have shown that the required reverse thrust is difficult to be attained [see Willis (1979)]. Regarding the weight penalty of the pitch changing mechanism, this was between 23% and 24% of the fan total weight for the fans described by Ryan et al. (1977) and Willis (1979), respectively.

VAN is a concept that is being used extensively in military engines. Similarly to the VPF, the VAN use is also limited by the weight and complexity penalties introduced by the area changing mechanism. However, contrary to the VPF concept, the VAN one is more mature. P&W patented a nozzle system with adjustable panels which was ready to be implemented on some of its PurePower™ GTF models if fan stability issues occurred [see Krishnan et al. (2013) and Leylekian et al. (2014)]. Boeing also tested VAN configurations in full-scale test flights, by utilizing shape memory alloy actuators to achieve the necessary nozzle area change [see Calkins et al. (2006)]. The VAN weight was modelled via a 10% penalty on the engine total weight in the studies conducted by Guynn et al. (2009) [a figure also adopted by both Krishnan et al. (2013) and Rousis (2011)].

According to McKay et al. (2012), for bypass ratios between 12 and 15, the VAN is necessary for regulating the fan stall margin at off-design conditions. For bypass ratios

greater than 25, the weight of the VAN will become prohibitive while an area increase larger than 30% would be needed. In their study, Krishnan et al. (2013) concluded that the crossover point at which a VPF becomes necessary is for bypass ratios between 20 and 27.

Regarding the optimal value of bypass and fan pressure ratios for a GTF, the result depends on the technology level assumptions and the metrics taken into account. For instance, the optimal bypass ratio of a GTF engine for both small and larger aircrafts without the need of a VAN is 14.3 (for a fan pressure ratio equal to 1.45) [see Daggett et al. (2003)]. The studies conducted by Guynn et al. (2011) showed that there is no single engine configuration that can achieve the best performance over all the metrics considered. More specifically, for minimum block fuel is required a GTF with bypass and fan pressure ratio equal to 14.7 and 1.5, respectively, while for minimum block NO_x production the optimal engine is a GTF with bypass and fan pressure ratio equal to 12.4 and 1.6, respectively. Both engines are without a VAN. On the other hand, a GTF with VAN is the optimal engine for minimum LTO noise and NO_x emissions, with a bypass ratio of 17.6 and a fan pressure ratio equal to 1.4. Finally, in their study Berton et al. (2010) minimized the block fuel with a low fan pressure ratio (~1.36) UHBR GTF engine equipped a VAN, while a moderate fan pressure ratio (~1.48) GTF engine without a VAN was identified as an excellent design compromise over all the metrics considered.

1.2 Tools for the Preliminary Design of Aircraft Gas Turbines

From the preceding discussion, it is evident that in order to explore the design space of current, future, and novel aircraft engines (such as GTFs, UHBR engines with variable geometries, etc.), an integrated system of tools is required for the multi-disciplinary, preliminary design and assessment of an engine's potential in terms of fuel efficiency, weight, stable operation, production cost, operational cost, maintenance cost, and environmental characteristics.

As it can be seen from Figure 1.5, the engine design is a highly iterative procedure that involves a number of different engineering disciplines such as thermodynamics, aerodynamics, mechanical design, weight estimation, and off-design performance prediction. Thus, a modular approach is required comprising fast, robust, and accurate models which will allow for any gas turbine engine configuration, any discipline, and any level of modelling fidelity to be simulated.

Visualization of the results is also an essential requirement for both the designer and the analyst to be able to quickly assess the impact of different design parameters on the overall engine design.

Finally, for reducing the model and calculation sequence setup times, the definition and combination of different calculation types (e.g., steady-state, transient, sensitivity, optimization, multi-point design, etc.) in a consistent way and under the same, user-friendly coding, modelling, and simulation environment is desirable.

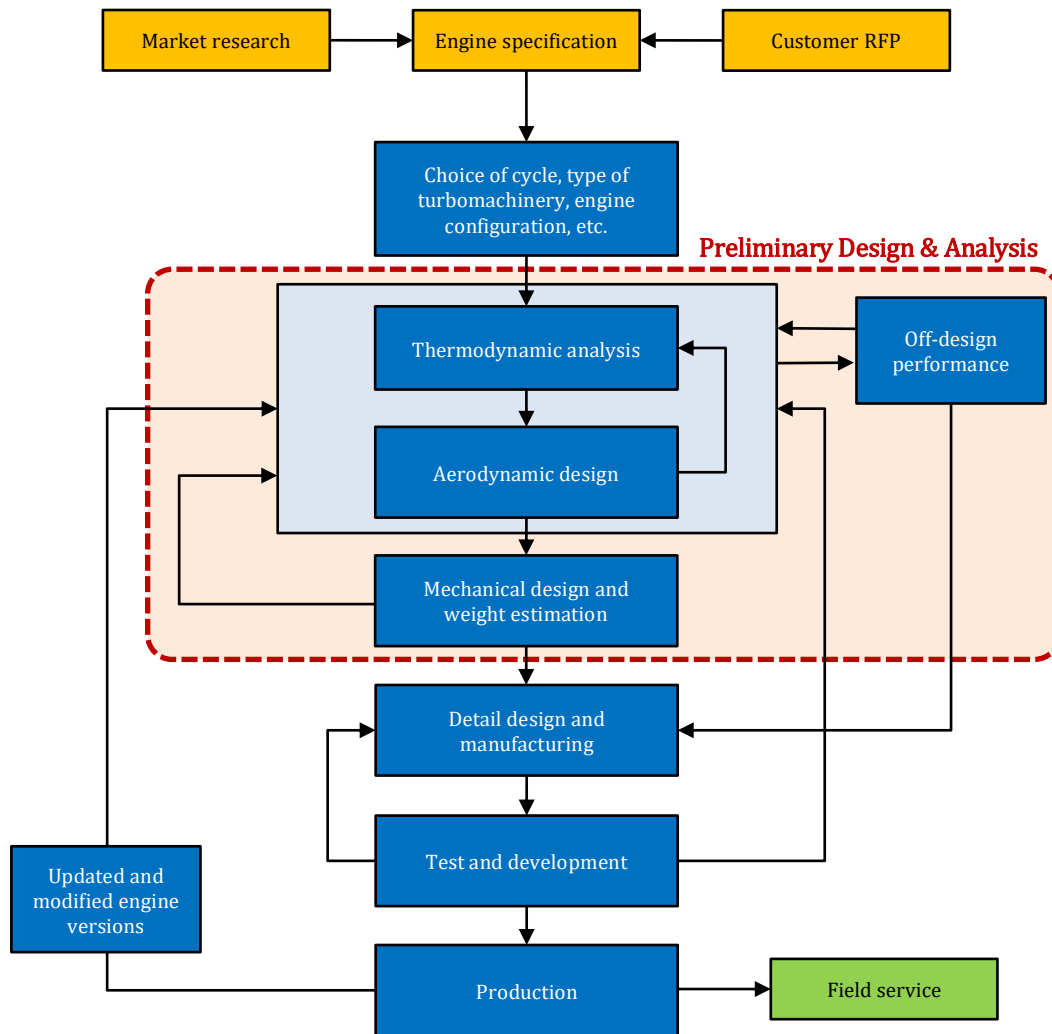


Figure 1.5: Simplified flow-chart representing the development course of a new gas turbine engine [adapted from Mattingly et al. (2002)].

1.2.1 State-of-the-art

Tools with the above modelling and computational capabilities are available in both industry and research community. In industry, the most profound examples are MTU’s MOPEDS [see Jeschke et al. (2002)] and P&W’s PMDO [see Panchenko et al. (2002)]. Within the research community, such platforms have also been described for the multi-disciplinary design and assessment of future propulsion concepts. These include TERA [see Bretschneider et al. (2007) and Ogaji et al. (2009)], GISMO [see Avellan et al. (2007)], EDS [see Kirby et al. (2008)], EVA [see Kyprianidis et al. (2008)], and DLR’s GTlab [see Becker et al. (2015); Reitenbach et al. (2018); Vieweg et al. (2019); Vieweg et al. (2020)].

Note that all the above as well as other industrial and research tools^{4,5,6} are of proprietary nature and the author of the present thesis could not review further the underlying physics, assumptions, and modelling fidelity employed in them. From the

⁴GasTurb: <https://www.gasturb.de/> (accessed: March 9th, 2023)

⁵Gas Turbine Simulation Program: <https://www.gspteam.com/> (accessed: March 9th, 2023)

⁶GitHub-NASA/T-MATS: <https://www.github.com/nasa/T-MATS/> (accessed: March 9th, 2023)

above literature survey, however, it was seen that almost all tools present deficiencies in terms of the physical and numerical modelling. These include:

- The different design and analysis modules may use different working fluid properties, thermodynamic functions, and numerical solvers which, in turn, may result in physical inconsistencies and numerical instabilities.
- The integration of the various modules is not in all cases transparent (use of codes in executable or dll form).
- Some of them use an independent central system for managing the calculation sequence and the interchange of data.
- Some tools lack the necessary modularity and flexibility to define new design cases.
- Some of them are too complex for this stage of the engine design. They use higher-fidelity tools (e.g., 2D or 3D flow codes) which require an increased amount of inputs (typically not available during the preliminary design phase), while they also slow down the speed of calculation without necessarily improving the overall calculation accuracy.

To enable the assessment of the design potential of an engine, all the above platforms (as well as any other platform for the preliminary design and assessment of gas turbine engines that would like to consider itself “complete”), at the very least, include computational tools for the aerothermodynamic design and off-design analysis of gas turbine components, the mechanical design of critical structural parts, and the estimation of weight of engine components⁷.

1.2.2 Mean-Line Methods for Compressor Preliminary Design and Analysis

Aerodynamically, compressors are the most challenging components for the operation and life of gas turbines due to the flow physics involved. During the preliminary design phase of a gas turbine engine where new engine concepts are assessed not only at design, but also at off-design conditions, it is clear that both the compressor design aspects and off-design performance must be available to the designer at a very early stage. The extensive literature available on the subject matter reveals that the understanding of the flow aerodynamics through compressors continues to trouble numerous teams of researchers and engineers throughout industry and academia. This difficulty in fully understanding the physics of the flow across compressors makes their design and off-design performance modelling and prediction, as well as their structural design, challenging tasks [see Gallimore (1999)].

Nowadays, the flow through multi-row compressors can be accurately predicted at different operating conditions using higher fidelity tools, ranging from 2D streamline curvature codes [see Pachidis (2006); Templalexis et al. (2006); Petrovic et al. (2009); Zhu et al. (2013); Xiaoxiong et al. (2016); Li et al. (2018); Banjac et al. (2018b)], to 3D CFD/(U)RANS codes for analysis and optimization [see Ntanakas et al. (2018) and Ricci

⁷Although they are not part of the present work, other modules typically included in such platforms are for engine transient analysis, engine off-design performance, aircraft mission analysis, emissions and noise prediction, and costs estimation, among other.

et al. (2019)]. However, even today with high computing power being easily accessible, higher fidelity tools are considered expensive for preliminary calculations due to their high computational cost, the need for input data, and the expertise required to set up the model and the simulation case. Their use is thus left for the later stages in the design process. In the preliminary design phase simulation time is more important than detailed flow predictions and the designer must resort to lower- or mid-fidelity tools, like 0D or 1D.

In 0D models, the compressor performance (and that of other components) is modelled by generic maps in the form of 2D tables of mass flow, efficiency, and pressure ratio versus compressor rotational speed and an auxiliary interpolation parameter [see Kurzke et al. (2018)]. These maps can then be scaled accordingly to match the component design point. Although using 0D models for preliminary design studies is a good compromise between accuracy and simulation time, they use simple thermodynamic relations to link the component inlet and outlet conditions, they provide no information about the flow physics through the compressor whatsoever, while secondary effects affecting the compressor performance are simulated using user-defined scalars that modify/scale appropriately the compressor map. Finally, 0D models require a database of generic compressor maps so that the designer can select one that will best resemble the compressor performance and its operating limits.

During the early design stages, the need for developing fast and reliable multi-fidelity and multi-disciplinary platforms for gas turbine design and optimization [see Panchenko et al. (2002) and Vieweg et al. (2019)], studying the effects of heat transfer [see Kiss et al. (2018)], novel combustion concepts [see Neumann et al. (2019)], and low-power engine operation on compressor aerodynamics [see Vidal et al. (2020)], has made 1D (or “mean-line”) models for evaluating the compressor performance at design and off-design conditions a valuable tool for the designer. In contrast to higher fidelity tools (such as 2D or fully 3D CFD), 1D tools are fast, have acceptable accuracy if appropriately tuned [see Neumann et al. (2019)], need only a few geometry inputs, and don’t require an expert user to set-up the model and the calculation case. In contrast to 0D performance models, the physical representation they use to describe the flow field (i.e., algebraic correlations and high-level indices to describe the performance of the blade rows) allows them to provide information about the flow across the compressor and to capture the effect of secondary flow phenomena on the compressor performance. Therefore, 1D tools allow designers to test and assess fast the influence of various parameter changes on the compressor design and performance, to easily capture compressor design and performance trends, and to identify and evaluate the effect of compressor aerodynamics on the overall engine design at a very early stage in the engine design chain. For this reason, even though they have first appeared a long time ago, they remain of current interest and are the subject of modern-day research efforts [see Neumann et al. (2019); Vidal et al. (2020); Zhang et al. (2020a); Zhang et al. (2020b); Zhang et al. (2021)].

1.2.2.1 Compressor Design

Engineering teams from both industry and academia have put significant efforts in the development of tools for the accurate modelling and prediction of the on- and off-design performance of compressors. During the preliminary design phase, these tools

should be fast, reliable, and sufficiently accurate. They should also require the minimum number of inputs and the minimum effort to set-up a calculation case. Finally, their integration in frameworks for the overall design and assessment of new engines should be easy.

A 1D design code should produce the compressor gas-path for the specified mass flow and design pressure ratio with the maximum efficiency and the minimum number of stages. This should be done while producing consistent blade dimensions to be used as inputs for the detailed design of a machine, thus minimizing the iterations between the preliminary and detail design stages. However, due to the the flow physics involved, these objectives can only be met if a code is sufficiently versatile by including the possibility for different design options and inputs, blade models, loss sources and/or models, etc. An analysis mode is also a desirable feature for the consistent prediction of the compressor off-design performance over a range of working conditions, after the compressor design has been concluded.

In the past, many design methodologies and tools for teaching, research, and industrial use have been described in the open literature. All these tools, implement the same design philosophy where the compressor design is conducted in a stage-by-stage manner where the number of stages is pre-defined by the user.

In the code presented by Mattingly et al. (2002) and Mattingly (2005) for teaching turbomachinery classes (COMPR), some of the design inputs are hard-coded (e.g., blade gaps and blockage). That is, the entire code must be re-compiled if its user wishes to modify some of them. The compressor design also relies on the simplifying assumption of repeating compressor stages, while the blade row losses across the compressor are a user input. The same attributes are also true for the mean-line code presented by Denton (2017), which was also meant for teaching purposes (MEANGEN).

Tomita et al. (2012) presented a code for teaching the basic aspects of turbomachinery design. In this code, the compressor efficiency is a given input by the user. The blade row losses are modelled assuming only two basic loss sources, that is, profile and shock losses.

Another code originally developed for teaching turbomachinery design is T-C_DES, which was developed at the university of Cincinnati [see, Bruna et al. (2007) and Turner et al. (2006, 2007, 2010)]. As its authors state, their code is based on COMPR, but it was improved by lifting most of its drawbacks regarding the hard-coded inputs used in COMPR. In T-C_DES, however, the blade row losses are still a user input and not estimated by appropriate loss models.

Becker et al. (2015) described a code for the design of multi-stage, axial-flow compressors, which is part of DLR's integrated environment (GTlab). In their code, the compressor overall efficiency is an input (that is, it is not a result of the aerothermodynamic design) while the compressor is designed assuming constant enthalpy rise across the compressor.

He et al. (2018) and Lei et al. (2021a, 2021b) presented 1D design codes which they used to explore the design space of multi-stage compressors with industrial and aeronautical interest. In their codes, blade losses from only two sources are considered (profile and shock), while the compressor blades are modelled using either NACA-65 (for subsonic flow modelling) or DCA (for transonic flow modelling) profile shapes. Finally, in the code presented by Lei et al. (2021a), the work distribution is an input,

that is, it is not estimated from aerodynamic criteria regarding the loading capacity of the blades⁸.

Other tools for the mean-line design of compressors have been described by Veres (2009), Banjac et al. (2018a), and Wells et al. (2021). These tools have more-or-less the same attributes and calculation options as the ones described above and, therefore, they will not be reviewed further. However, all compressor design tools reviewed by the author of this thesis present modelling and numerical aspects which could otherwise limit their versatility and automation if they were to be used as part of an integrated platform for the preliminary design of gas turbine engines:

- In all codes, the number of stages is a user input, that is, it is not obtained on physical principles based on the stage-wise loading and loss distributions for achieving the desired design pressure ratio.
- The compressor design is limited to three gas-path shapes (constant hub, constant mean, constant tip), while in some codes, e.g., in COMDES by Veres (2009), the user must also specify the value of certain gas-path diameters (that is, the gas-path is not entirely obtained from the aerothermodynamic design).
- In the codes where the blade losses are estimated based on loss models, these are pre-defined and the user cannot select from different models.
- Finally, some codes do not combine an analysis mode for producing consistent performance maps after the compressor design has been completed. The only exception is the codes by Veres (2009) and Banjac et al. (2018a) which both combine design and analysis modes, but even for these there is no indication by their authors that the design and analysis modes cooperate or that they use consistent physical assumptions, fluid models, thermodynamic functions, and numerical solvers.

1.2.2.2 Compressor Off-Design Performance Prediction

Apart from the special care the designer must put in designing a compressor, its performance at off-design (steady and transient) conditions must also be accurately evaluated and accounted for when assessing a new engine concept. This implies that the off-design performance (in the form of maps of pressure ratio and efficiency) must be available to the designer at a very early stage in the design chain of a new engine.

In the past, different 1D modelling approaches for compressor off-design performance estimation and map generation have been formulated and presented in the public domain. For instance, Howell et al. (1978), Steinke (1982), and Tsalavoutas et al. (1994) formulated and presented a stage-stacking approach for predicting the characteristics field of multi-row, axial-flow compressors, while Mathioudakis et al. (1994) formulated an adaptive version of this approach for compressor fault diagnoses. In the stage-stacking approach, generic stage characteristics along with a few geometry inputs are used to obtain the compressor performance map in a stage-by-stage calculation manner. As with 0D approaches, however, stage-stacking techniques also have the drawback of requiring a good bank of generic maps for stage characteristics.

⁸For instance, by using a maximum loading coefficient value, a minimum De Haller or maximum diffusion factor value, or by defining the maximum flow turning.

More recently, Mishra et al. (2017, 2018) formulated a quasi-1D method for steady and unsteady compressor performance predictions. In their work, the performance of a compressor blade row is modelled thermodynamically as that of a diffuser, whereas mean-line flow velocity changes at the interface of stationary and rotating blade rows are accounted for with velocity “addition junctions”.

In more traditional 1D approaches, however, the compressor performance is estimated in a row-by-row manner where the through-flow field is modelled by velocity triangles and flow properties being calculated at a single representative radius running through the compressor, the span-wise variations of the flow are neglected, and the flow conditions at the blade row outlet are established using loss and deviation models. Denton (1993) gives a thorough account for the different loss sources encountered in turbomachines.

Most researchers and engineers have (more or less) relied on “traditional” loss and deviation models for developing performance prediction codes. The term “traditional” is used here for loss and deviation models that were formulated during the 1950’s by conducting 2D cascade tests in subsonic wind tunnels [see Carter (1950); Lieblein et al. (1953); Lieblein (1957); Lieblein (1960); Johnsen et al. (1965)]. In his book, Aungier (2003) presents a thorough account of the traditional loss and deviation models he used and modified during his career for the development of design and analysis codes. Another good source that includes a detailed presentation of traditional loss and deviation models for subsonic and supersonic flows across compressor blades, is the book by Cumpsty (1989).

Example of codes that relied on the above philosophy are the ones developed and presented by Koch et al. (1976), Daini (1986), Casey (1987), Miller et al. (1987), Wright et al. (1991), Smith (1999), Falck (2008), Madadi et al. (2008), Eftari et al. (2011), Peyvan et al. (2016) and, more recently, by Zhang et al. (2020a, 2020b, 2021), who made use and/or modified traditional loss and deviation models to develop performance calculation codes for axial-flow compressors.

Cetin et al. (1989) analyzed a number of known loss and deviation models and proposed corrections based on available transonic compressor measurements to improve their accuracy [see also AGARD (1987)]. On the other hand, White et al. (2002) used different combinations of loss and deviation models available in the public literature to identify that combination that would give the best on- and off-design performance for a number of different compressors modelled with conventional blade profiles (circular- or parabolic-arc).

Schnoes et al. (2015) presented an automated method for re-calibrating traditional loss and deviation models utilizing CFD simulation results. In the same direction, Peng et al. (2019) utilized measured data to present a calibration procedure for various loss and deviation models based on an error-minimization computation using the Nelder-Mead SIMPLEX method [Nelder et al. (1965)].

In contrast to the above, there are efforts by researchers to develop new loss and deviation models, or to extend existing ones, to better predict the performance of current technology transonic and supersonic compressors. Konig et al. (1994a, 1994b) extended well-established loss and deviation models to quasi-2D conditions, separately for subsonic and supersonic inlet flow conditions, to improve the accuracy of performance predictions across transonic compressor rows.

Schobeiri (1997a, 1997b) developed a new loss model that accounted for blade profile and shock losses, and was based on a modified diffusion factor that incorporates flow compressibility effects. Other such examples, are the ones by Bloch et al. (1999), Sun et al. (2015), and Liu et al. (2017a), who all formulated analytical models for predicting the losses that result from the shock system that develops across the passage of a compressor blade row.

Dickens et al. (2011) formulated a profile loss model from first principles by constructing an appropriate velocity distribution around the compressor airfoil, suitable for both conventional and high stage loadings.

Liu et al. (2017b) formulated models for the minimum loss incidence and deviation angles based on numerical predictions for the flow over blades with splitter vane arrangements.

Both Veres (2009) and Neumann et al. (2019) formulated their own loss and deviation correlations based on measured performances of well-documented NASA transonic compressors. In the first part of their two-part paper, Kidikian et al. (2018a) first stressed out and then demonstrated the importance of appropriately tuning blade loss and deviation in order to accurately predict the performance of highly-loaded transonic compressors. In the second part [Kidikian et al. (2018b)], they devised a generalized 1D loss and deviation model utilizing measured data of well-documented single-stage, transonic compressors by NASA.

Banjac et al. (2014) used CFD flow simulations to formulate loss and deviation correlations for estimating the performance of compressor IGVs for NACA-65 and NACA-63 A4K6 airfoil shapes.

Finally, Wu et al. (2018) conducted statistical analyses using open-source performance reports by NASA, and they developed a span-wise model for the prediction of the off-design deviation flow angle.

1.2.2.3 Compressor Choke Prediction

Mean-line codes use physically consistent modelling to capture compressor flow physics and predict performance at different conditions, using correlations and high-level indices of blade row performance. The nature of the equations they use often leads to convergence problems when the compressor works at, or beyond, choking conditions.

Even modern, state-of-the art 1D codes, still employ the approach introduced long ago by Galvas (1973) and use a “manual” pre-processing step for determining the conditions where a compressor becomes choked: the inlet mass flow rate changes incrementally until the code producing a compressor map fails to converge as the inlet mass flow approaches or reaches the choking value. One such example is the NASA code OTAC [see Jones (2014, 2015)], that conducts mean-line or stream-line design and off-design performance calculations, for radial- or axial-flow turbomachines. For a speed-line, the flow where one (or more) compressor blade rows choke is taken equal to the value for which the code fails to converge [Jones (2015)]. In another code for compressor mean-line calculations (COMDES), also developed at NASA [see Veres (2009)], the working mass flow range is determined iteratively by varying the incidence angle of the first rotor row and for any given speed the maximum flow is identified when the code fails to converge.

Attempts to modify the set of mean-line equations so that turbomachinery performance models can work without convergence problems within the choked portion of the map have been demonstrated successfully only on multi-stage turbines [see Hendricks (2016)]. Because of the more complicated nature of the flow involved, Hendricks states that the real challenge in modelling compressor choke “lies primarily in understanding the mechanisms causing it”.

In the above direction, various efforts were made to model compressor choking. Arolla et al. (2008) described a low-order approach for modelling the blade row throat passage choke for subsonic and supersonic inlet conditions. They also proposed a method for producing the vertical portion on the characteristics map, by introducing additional losses at the last choked blade row until the compressor back pressure was attained or a downstream blade row choked. Finally, Cadrecha et al. (2018), used simple flow equations to first identify the conditions (in terms of the flow Mach number) that lead blade rows and ducts to choke. Then, based on the work of Chaquet et al. (2017), they formulated a bisection method for solving the system of mean-line equations at subsonic, supersonic, and choke conditions. They also described a modelling approach for extending the choked portion of the map characteristics where they increased the losses of the duct following a choked blade row, until the last row or the compressor exit chokes.

1.2.2.4 Compressor Stall Prediction

Due to the adverse pressure gradients and the flow deceleration, compressors are prone to stall phenomena which, in high-speed machines, can be disastrous. Stall is a highly three-dimensional and unsteady phenomenon and, therefore, its modelling and prediction in the scope of mean-line design and analysis codes is inherently difficult.

At blade row level, stall is modelled using high-level indices and empirical criterions that express the maximum attainable flow deceleration (or static pressure rise) across blade rows. To estimate the onset of stall, most researchers make use of diffusion factors [see Aungier (2003)], De Haller-like metrics [see Banjac et al. (2015)], and criterions on the flow incidence [see Aungier (2003) and Miller et al. (1987)].

At component level, statistical correlations have also been presented. For instance, Schweitzer et al. (1984) developed a semi-empirical correlation for estimating the surge margin of compressors. For doing so, they utilized the resemblance of the flow across the passages of compressor blades to that of diffusers, and correlated the maximum permissible static pressure rise a blade can attain to blade row geometry and flow characteristics [see, also, Glassman et al. (1995)]. Finally, they used existing compressor performances to calibrate their model. He et al. (2018) used this criterion to conduct design studies, where one of the two objectives they considered was the maximization of the compressor surge margin.

1.2.3 Methods for Preliminary Mechanical Design

Mechanical design is one of the most critical areas of design when it comes to gas turbine engines, both at component and at engine level. The mechanical design of critical structural parts (both rotating and stationary) provides the necessary dimensions so that those parts can withstand the severe mechanical and thermal loads

developed within gas turbines. Also, an accurate mechanical design as early as possible not only provides an assessment for the engine's safe operation, production, and maintenance costs, but also provides consistent inputs for the detail design, thus minimizing the iterations between the preliminary and detail design phases.

1.2.3.1 Design of Shafts

One of the most critical parts in any gas turbine are the shafts. Shafts are mainly designed for transferring the necessary torque between the components they connect while maintaining their structural integrity. The latter is expressed in terms of the material yield strength and a safety factor [see Drydale (1978); Pera et al. (1977a); Loewenthal (1984); Becker et al. (2015)].

1.2.3.2 Design of Casings

Another critical part for the safety of gas turbines are the casings. Casings are commonly designed to contain the high-pressure flows, but they also designed to withstand the high-energy impacts occurring by blade fragments in case of blade failures [see Bretschneider et al. (2008) and Schaber et al. (2019)].

1.2.3.3 Design of Ducts

In gas turbine engines, ducts are used to transfer smoothly the flow between different components with the minimum flow loss and distortion. Typically, ducts are designed to occupy both minimum length and weight, while satisfying flow and structural criteria.

The design of ducts is extremely complicated considering their effect on the engine performance and dimensions. For this reason, in all approaches for the preliminary design of gas turbines, ducts are simply designed as pressure vessels containing the pressure of the gas flowing between different components [see Onat et al. (1979a) and Lolis (2014)]. Regarding their length, typical empirical values have been proposed in gas turbine textbooks [see, e.g., Walsh et al. (2004)], while the shape of their walls is typically approximated by 1st, 2nd, or 3rd degree polynomials [see Lolis (2014) and Anastasiou (2021)].

1.2.3.4 Design of Disks

However, probably one of the most significant parts during the mechanical design of turbomachines is the design of rotating disks. Disks occupy a significant part on the overall weight of gas turbines, and in that matter are especially critical for aircraft engines. Therefore, disks are commonly designed for minimum weight while satisfying a number of geometry and stress criteria.

In their paper for optimizing the design of a single-stage compressor, Lim et al. (1989) used an analytical stress model to identify the disk thickness shape by utilizing the mechanical design principles described by Kerrebrock (1992). For doing so, Lim et al. assumed a constant stress distribution along the disk radius to obtain an exponential variation for the disk thickness from bore to rim.

Armand (1995) presented an optimization approach for obtaining web-type disks of minimum weight. Armand imposed constraints on both the disk geometry and stresses, where the latter were expressed by appropriately defined design and burst margins. For estimating the necessary radial and tangential stress distributions along

the disk radius, Armand utilized a 1D plane stress equilibrium model which he solved numerically using an FD approach. Finally, thermal loads were modeled by a user-defined, 5th order polynomial for the radial distribution of temperature.

In the context of NASA's WATE, Tong et al. (2004) developed and presented a novel disk design methodology for minimizing the weight of ring-, web-, and hyperbolic-type disks, while taking into account lifing considerations. In their approach, the disk design is also subjected to both geometry and stress constraints. Similarly to Armand (1995), Tong et al. utilized the same 1D plane stress equilibrium model for obtaining the necessary radial and tangential stress distributions along the disk radius, which they solved numerically using a self-adaptive iterative scheme. Finally, in their methodology, the radial distribution of temperature is estimated using an approximate, analytical solution of Fourier's law for heat conduction assuming disks of constant thickness.

In GasTurb Details 5 [see Kurzke (2007)], the approach by Tong et al. (2004) is utilized for finding the minimum weight of web- or hyperbolic-shaped disks. In contrast to Tong et al., in GasTurb Details 5 the thermal loads along the disk radius are estimated assuming a linear variation of temperature from bore to rim. Finally, the user can utilize two methods to conduct the disk shape optimization, an adaptive random method search strategy or a gradient-based one.

In the context of the T-Axi flow solver developed for educational purposes at the university of Cincinnati, Gutzwiller et al. (2010a) [see also Gutzwiller (2009); Gutzwiller et al. (2009); Gutzwiller et al. (2010b)] developed and presented a complementary code for the design of turbomachinery disks. The available disk shapes in their code include ring-, web-, and hyperbolic-type disks, while they also formulated a parameterization for modelling disks having "continuous slope" shapes. The stresses developed along a disk are obtained by solving numerically a 1D plane stress equilibrium model [the same as in Armand (1995) and Tong et al. (2004)] using an FV approach. In Gutzwiller et al.'s code, however, the plane stress model is formulated to take into account both isotropic and anisotropic materials. Finally, for obtaining the disk shape which gives the minimum weight disk while satisfying both geometry and stress constraints, Gutzwiller et al. implemented a genetic algorithm.

In his PhD thesis, Lolis (2014) presented a methodology for the design of ring-, web-, and hyperbolic-type disks using a gradient-based optimization method. As with all the above mentioned codes, the disk design is also subjected to geometry and stress constraints. For solving the 1D plane stress equilibrium model, however, Lolis utilized a semi-analytical approach of poor accuracy where the disk is discretized in a very small number (typically ~5) of disk segments assumed of having constant thickness [see, e.g., Saravanamuttoo et al. (2017)], while the thermal loads are modelled by an empirical curve for the radial temperature distribution.

Other disk design tools that are part of conceptual design platforms, are the ones included in DLR's GTlab [see Becker et al. (2015)] and MTU's MOPEDS [see Schaber et al. (2019) and Salpingidou et al. (2020)]. In GTlab, the disk design tool was developed after the works of Armand (1995) and Tong et al. (2004), where the disk optimization is achieved using a direct-search algorithm or an evolutionary one. In MOPEDS, the optimal disk geometry is obtained iteratively until the produced disk geometry fulfills the imposed stress constraints, where the radial and tangential stresses along the disk

radius are estimated using approximate, analytical equations [similar to the ones used by Lolis (2014)].

Finally, other (much) older references for the design and analysis of turbomachinery disks can be found by Manson (1947), Millenson et al. (1948), De Silva (1969), and Luchi et al. (1980). The above references basically provide the fundamentals for disk design and stress calculations.

1.2.4 Methods for Preliminary Weight Estimations

Engine weight⁹ is a key figure when designing new aircraft gas turbines. Weight affects the fuel burn efficiency of the engine itself, as well as the aircraft performance, range, and DOC. Also, weight is a direct indicator of the engine initial and maintenance costs. Therefore, reliable weight estimations are of the utmost importance during the preliminary design and assessment of new gas turbine engines.

In the past, the need for estimating the weight of an aircraft engine during the preliminary design phase led to the development of methods that consider different parameters and, often, different assumptions physics-wise. The formulation of methods with different levels of fidelity is dictated primarily by the following criteria:

- the available geometry/performance inputs,
- the lack of publicly available weight data for correlation/validation purposes,
- the computational speed required, and
- the desired accuracy.

The different methods for the estimation of aircraft engines during a preliminary design calculation can, in general, be divided into two (2) major categories according to Lolis (2014):

1. Whole Engine-Based Approaches (WEB), and
2. Component-Based Approaches (CB).

As their name implies, WEB approaches estimate the weight of an engine as a whole, while CB methods estimate the weight by summing-up the weight of the individual engine components.

1.2.4.1 Whole Engine-Based Approaches

The confidentiality restrictions imposed by OEMs regarding individual component weight values, not only makes the development of semi-empirical, component-based approaches difficult (if possible, at all), but they also render the validation of methods that estimate the weight by taking into account the geometry of the components and the material selection prohibitive.

The above reasons have led to the development of WEB approaches, which rely on simple physical assumptions linking the variation of the engine weight to basic engine geometrical and cycle parameters which, in turn, are easily available during the preliminary design phase. Such parameters include, for example, the fan diameter (D_{FAN}) and the engine bypass ratio (BPR), overall pressure ratio (OPR), and thrust

⁹The terms “weight” and “mass” will be used interchangeably in the present text.

(F_N), among other parameters. WEB approaches are simple algebraic equations correlating only few (often just one) parameters and, therefore, can give weight predictions with minimal computational cost. Table 1.2 lists some of the publicly available WEB models.

Table 1.2: Summary of WEB approaches for turbofan dry weight estimation

Author(s)	Correlation
Gerend et al. (1970) ¹⁰	$W_{KG,BENG} = f(BPR, OPR, TET, \dot{m}, M, \dots)$
Waters et al. (1977)	$W_{KG,BENG} = f(BPR, F_N)$
Torenbeek (1982)	$W_{KG,BENG} = f(BPR, OPR, F_{N,TO}, \dot{m}_{TO})$
Raymer (1992) ¹¹	$W_{KG,BENG} = \begin{cases} f_{dry}(BPR, F_{N,TO}) \\ f_{ab}(BPR, F_{N,TO}, M_{max}) \end{cases}$
Jenkinson et al. (1999)	$W_{KG,BENG} = f(BPR, F_{N,TO})$
Svoboda (2000)	$W_{KG,BENG} = f(F_{N,TO})$
Clavier (2008) ¹²	$W_{KG,BENG} = f(BPR, OPR, \dot{m})$
Donus et al. (2010)	$W_{KG,BENG} = f(PR, OPR, F_{N,TO}, \dot{m}_{TO})$
Guha et al. (2012)	$W_{KG,BENG} = f(D_{FAN})$

On the other hand, the applicability of WEB approaches is restricted by the engine weight databases used for their calibration. In other words, each of the methods given in Table 1.2 is more-or-less suitable for predicting the weight of engines which have similar geometry and performance characteristics as the ones used for its formulation and calibration. Moreover, the physical assumptions used in their development are, in most cases, not quoted by their authors or they are ambiguous in nature and, thus, WEB approaches tend to be, in general, unable to correctly capture the expected weight trends. A detailed quantitative and qualitative presentation of several WEB approaches is given by Lolis (2014).

In conclusion, although WEB approaches are computationally cheap and require a small number of inputs, their range of validity and accuracy is very limited [see Lolis (2014)]. Therefore, methods that are physically more consistent are used for calculating weight and capturing weight trends with better accuracy.

1.2.4.2 Component-Based Approaches

In contrast to WEB approaches that deal with the engine as a unit, CB approaches consider that an engine can be broken down to the components and parts it consists of,

¹⁰Apart from the thermodynamic cycle data, Gerend et al.'s (1970) correlation also includes corrections that take into account the engine manufacturer, the EIS year, the fan duct configuration, noise and lifing considerations, among other.

¹¹In Raymer's (1992) correlations "dry" is for turbofans without afterburners while "ab" stands for afterburning turbofan engines.

¹²The author of the present thesis did not have access to the original material by Clavier (2008) where the quoted weight correlation was first presented, but the correlation can be found in Lolis (2014). Nevertheless, the original author is credited here.

calculate the individual component weights, and then they sum them up to produce the total weight of the engine.

Obviously, CB approaches require geometry and cycle data at component level in order to calculate the individual component weights and, typically, those are obtained by the preliminary aerothermodynamic and mechanical calculations. The calculation of the individual engine weights and the need for aerothermodynamic and mechanical calculations in order to produce the necessary inputs, increases significantly the computational time compared to WEB approaches, while the validation of the individual component weights is impossible due to the disclosure policies followed by OEMs regarding individual component weight values.

On the other hand, CB approaches produce weight estimations and trends that are physically more accurate and meaningful, since the weight is calculated based on “detailed” engine geometry and cycle inputs, and not by “rough” correlations on engine overall geometry and/or performance data. Also, their applicability range is not as limited as that of their WEB counterparts since the necessary inputs are obtained by aerothermodynamic and mechanical calculations. For the above reasons, CB approaches are preferred over WEB methods for preliminary design purposes although they require more inputs and greater computational effort.

One of the first (if not the first) CB methods that appeared in the public domain, is the semi-empirical method by Sagerser et al. (1971). The method of Sagerser et al. is dedicated primarily in estimating the weight of VTOL and STOL aircraft powerplants, but the authors also provide calibration factors for cruise engines as well. Sagerser et al. developed expressions for estimating the weight of major engine components that include, among other, the fan, the compressor, the burner, and the turbine. These expressions were devised based on physical principles that correlate component geometry and cycle parameters, and their calibration was conducted using available engine data including engines in the stages of production, testing, and preliminary design. Regarding accuracy, the authors state that their method produces accuracy levels in the range of $\pm 10\%$ for the test cases they used to validate it against.

Another known CB method is NASA’s WATE code for the preliminary sizing and weight estimation of aircraft gas turbine engines. The first version of the method (WATE-1), was first developed by Pera et al. (1977a). In contrast to the Sagerser et al. (1971) method which makes use of correlations for the total weight of individual engine components, WATE goes a step further and breaks a component down to its elemental structural parts. For instance, an axial-flow compressor is considered to comprise a series of rotor and stator rows, the rotating disks, the connecting hardware, and the casings. For each individual part, a volume is calculated which multiplied by the material density gives the part mass. Summing up the individual masses, the component total weight is then established. The volume is correlated to the basic dimensions of the part considered, while for rotating parts (e.g., disks) and container-type components (such as casings and ducts), their volume is established based, additionally, to structural design correlations which consider the allowable mechanical stresses developed on those parts. These correlations were formulated based on fundamental physical intuition and their calibration was conducted using a database of 29 engines (including turbojets and turbofans), in the stages of production and design. Finally, the authors of the method claimed that their code achieves better accuracy than

the $\pm 10\%$ margin by Sagerser et al. method, that is, in the range of $\pm 5\%$ for the test cases they used to validate it. Klees et al. (1978) modified the method to allow quick, hand-based estimations.

The original code (WATE-1) was later followed by several improved editions. The first of those chronologically was WATE-2 by Onat et al. (1979a) who modified and corrected WATE-1 to include the estimation of the weight of small gas turbine components such as centrifugal compressors and radial-inflow turbines. More recently, Tong et al. (2004) modified the code to include a database of materials and they also added a novel method for calculating the weight of the rotating disks. Finally, in order to enable the direct interaction with the engine performance model within NASA's NPSS framework, Tong et al. (2008) developed WATE++, which is the object-oriented version of the WATE-2 code written originally in FORTRAN.

Sanghi et al. (1998) developed a method for estimating the weight of engine systems which, basically, utilizes the same correlations and approaches developed and used in NASA's WATE for establishing the volumes of various structural parts and components. Through a test-case example where the authors recalculated the weight of an existing engine, their method showed to deviate by $\sim 4\%$ from the actual engine weight. A similar approach to the one by Sanghi et al. (1998) was followed also by Rolls Royce's Genesis preliminary design tool [see Jones et al. (2002)]. Genesis weight estimation module was validated against the weight of seven (7) existing engines and showed an average error of about 3.9% and a maximum deviation of about 10.4%.

In MTU's MOPEDS, the engine weight estimation follows the CB philosophy where the weight of some structural parts (e.g., disks, blades and vanes, rotor attachments, casings) is assessed analytically through their estimated volumes, whereas for some components (e.g., for the fan) semi-empirical correlations [such as the ones provided by Sagerser et al. (1971)] are used to estimate their weight [see Jeschke et al. (2002) and Donus et al. (2010)]. For the parts for which their volume is estimated analytically, simplified mechanical design methods are used to establish their dimensions and, thus, their volumes [see Schaber et al. (2019) and Salpingidou et al. (2020)].

In the context of the TERA framework [see Bretschneider et al. (2007) and Ogaji et al. (2009)], the WeiCo software was developed which comprises two parts: one for engine weight analyses and one for engine system cost assessments. The first part, developed by the Chalmers University, is used to conduct basic engine sizing. Then, it estimates the weight of the engine following the methodology and modelling approaches used in NASA's WATE. The second part of WeiCo was developed by the Stuttgart University and is used for estimating the production cost of an engine design.

Finally, Lolis (2014) presented a new CB approach for the preliminary sizing and weight estimation of turbofan engines. Similarly to the NASA's WATE philosophy, the engine components are broken down into basic structural parts the volume of which is calculated first, and then multiplied by the selected material density to give the required mass. In contrast, however, to WATE that uses semi-empirical correlations to estimate the volume, Lolis' method calculates the volume analytically by considering the actual dimensions of a part which, in turn, are obtained after an aerothermodynamic and/or mechanical design. The author validated his method against the known weight of two widely used commercial turbofan engines, one 2-

spool and one 3-spool, and his method gave predictions of the order of 5%. Lolis also used his method to conduct feasibility studies on future GTF configurations.

1.2.4.3 Other Weight Estimation Approaches

Other methods for preliminary weight estimation that should be mentioned, include the works of Greitzer et al. (2010b) and Pantalone et al. (2016). In the context of the TASOPT code, both teams used WATE++ to produce surrogate weight estimation models to conduct studies on contemporary and future technology direct-drive and geared turbofan engines. Greitzer et al. ran approximately 450 WATE++ simulations by varying the engine inlet mass flow, BPR , and OPR , to produce a best-fit WEB correlation of the form $W_{KG,BENG} = f(BPR, OPR, \dot{m})$, while Pantalone et al. varied the same parameters to run WATE++ simulations for producing best-fit weight correlations for components including the fan, the burner, and the engine nacelle.

Finally, the commercial software for gas turbine performance design and analysis GasTurb [see Kurzke (2012)], estimates the weight of an engine in a component-based manner but limited or no information at all is given by its author regarding the process and the assumptions that take place during this calculation.

1.3 Motivation and Objectives

Following the literature review above on the different platforms and tools for the preliminary design of gas turbine engines, it was decided that the present thesis should focus on the following three main objectives:

1. The development and improvement, by proposing more efficient and novel approaches, of tools to be used in the preliminary design of gas turbine engines. These will include 1) models for the aerothermodynamic design and analysis of gas turbine components, 2) models and methods for the mechanical design of critical structural parts, and 3) models for estimating the weight of aircraft gas turbines. These tools should additionally be fast, robust, and appropriate for this kind of calculation by requiring the minimum set of inputs and the minimum user expertise to set them up.
2. The development and combination of the above tools under the same, user-friendly programming, modelling, and simulation environment to construct an integrated system for the preliminary, multi-disciplinary design and assessment of aircraft gas turbines. The system should additionally be sufficiently modular allowing for any gas turbine configuration and any design discipline to be easily modelled and studied.
3. To demonstrate the capabilities of the developed system of tools by conducting trade-off studies for aircraft engine configurations of current and future industrial interest.

To meet the above objectives, a number of tools (0D/1D) appropriate for preliminary studies were first developed and, then, combined under the same computational environment. This way, some of the modelling “gaps” present in similar research and

industrial tools and systems for the preliminary design of gas turbine components and engines are intended to be filled in and remedied, as will be explained in more detail during the course of the present text.

The development of the system and of the tools comprising it, as well as the engine trade-off studies, were conducted within the PROOSIS environment, which is the tool currently used by the European gas turbine industry.

1.4 Thesis Outline

The present text is organized in chapters and appendices as follows:

Chapter 2 gives a brief description of the system of tools developed in this thesis and described in more detail in the subsequent chapters and appendices. Also, the reader is offered a short introduction to the PROOSIS environment, which was used for the materialization of the computational tools described in this text.

Chapter 3 describes the development of the TURBO1D library. In this chapter, the equations, methods, and assumptions used to formulate new components for the aerothermodynamic design of gas turbine components, are presented. The validation of the components and of their capability to correctly represent the performance and gas-path geometry of fans, compressors, and turbines is also demonstrated by utilizing publicly available data of real-engine configurations.

Chapter 4 describes the development of the GTMDC library. In this chapter, the equations, methods, and assumptions used for developing computational tools for the design and analysis of critical structural components, are summarized. Methods for the structural design and analysis of ducts, casings, rotating shafts, and turbomachinery disks are presented. The validation and performance of the tools for the design and analysis of disks and shafts is demonstrated by utilizing publicly available data from real-engine geometries and by comparisons with a higher-fidelity (3D FEA) tool.

Chapter 5 describes the development of the GTWC library. This chapter presents the equations and assumptions used to develop methodologies for estimating the weight of aircraft gas turbine components and whole engines. The validity of these methods is demonstrated both qualitatively and quantitatively using publicly available data from real components and engines.

Chapter 6 describes the development of the MLAC library. In this chapter the equations, assumptions, and methods utilized to develop components for the off-design performance prediction (map generation) of axial-flow, multi-stage compressors are summarized. The performance and the capabilities of the developed components are exemplified and validated through the use of publicly available data about real-engine configurations.

Chapter 7 describes the development of the MLDC library. Since the component(s) defined in the MLDC library adopt most of the models, equations, methods, and

assumptions used in the development of the MLAC library described in Chapter 6, in this chapter only the different modelling aspects between the two libraries are presented. The capability of the developed component(s) is validated by utilizing publicly available information about a real compressor configuration.

Chapter 8 presents trade-off design studies for the low- and high-pressure compressors of an ultra-high bypass ratio turbofan engine. The studies conducted in this and Chapter 9 serve as an illustration of the capabilities of the developed tools. For this reason, in this chapter the tools described in Chapters 4, 5, 6, and 7 are utilized to conduct constrained optimization studies to identify the relative influence of various design variables on the on- and off-design performance of the engine compressors. The optimization studies are formulated considering different objectives and are conducted for two (2) values of the engine overall pressure ratio split between the low- and high-pressure compressors (0.30 and 0.40), which are of current industrial interest.

Chapter 9 presents trade-off design studies for an ultra-high bypass ratio turbofan engine (the same considered in Chapter 8) at aircraft mission level. The studies presented demonstrate the capabilities of the tools described throughout this text (Chapters 3, 4, 5, 6, and 7) by utilizing the developed system of tools illustrated in Figure 2.3. For the demonstration, the engine constrained optimization is considered aiming at minimum fuel burn and maximum surge margin of the high-pressure compressor at low-power conditions. Similarly to Chapter 8, the optimization studies are conducted for the same two values of the engine overall pressure ratio split (0.30 and 0.40). In the studies, design variables and constraints are considered at different operating points on the flight envelope.

Chapter 10 summarizes the conclusions of the thesis together with some ideas and recommendations for future developments and improvements regarding the developed tools.

Finally, the **Appendices** provide supplementary material which may help the reader to better understand the developed methods and models presented throughout the text.

2 The Developed System of Tools

2.1 Introduction

The present chapter gives a brief description of the (computational) tools developed during this thesis, and of how these were combined to construct an integrated workflow for the preliminary, multi-disciplinary design and analysis of aircraft gas turbine engines. A novel aspect of the present thesis is the use of the PROOSIS environment for the development of the aforementioned system of tools.

2.2 A Brief Introduction to PROOSIS

2.2.1 History of PROOSIS

PROOSIS is an acronym for **P**ropulsion **O**bject **O**riented **S**imulation **S**oftware, and is the Greek word for “propulsion”. PROOSIS is a state-of-the-art, stand-alone coding, modelling, and simulation environment, originally developed by a consortium of European industry companies and academic and research institutes during the European project VIVACE¹³. It is based on EcosimPro¹⁴, a simulation tool developed by EAI S.A. for modelling physical processes that can be modelled in terms of ODEs, DAEs, and discrete events.

2.2.2 The PROOSIS Coding, Modelling, and Simulation Environment

PROOSIS can perform steady-state and transient simulations, single- or multi-point design and off-design calculations, sensitivity analyses, parametric studies, optimization studies, etc. It can also perform multi-system, multi-physics, multi-fidelity, and multi-disciplinary simulations, and it can be connected easily to external tools (commercial or in-house), for instance CFD and FEA software. The modelling of any

¹³https://cordis.europa.eu/result/rcn/47814_en.html (accessed: May 11th, 2022)

¹⁴<https://www.ecosimpro.com> (accessed: May 11th, 2022)

physical process is enabled by a high-level, object-oriented programming language (named EL) that resembles C++. EL offers all the advantages of an object-oriented programming language such as inheritance, polymorphism, and encapsulation, but at the same time its syntax is easy enough for anyone who uses PROOSIS to be focusing solely on the modelling aspects of their problem and not on the programming ones.

The fundamental concepts of PROOSIS are Components and Ports. Components contain pieces of code that model mathematically the physical function(s) of real-life components (e.g., a compressor, a turbine, etc.). Ports, on the other hand, allow the connection and the interaction between different components by defining a set of variables to be communicated. Components and ports can be developed “from scratch”. Alternatively, some (or all) parts of their mathematical modelling and attributes could be inherited by existing components and ports through the inheritance capability offered by EL. Finally, components (and ports) can have icons. Figure 2.1 illustrates an example compressor component with its ports and the underlying code used to model its physical function.

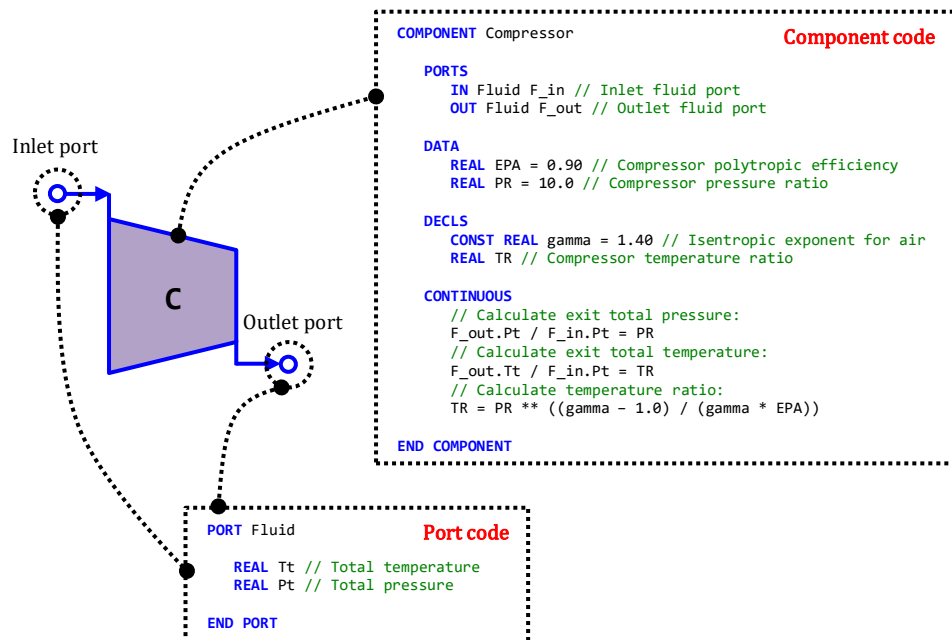


Figure 2.1: Icon of component and ports that represents a compressor, and the example underlying code that models the physical function of the compressor. The fluid port in this example is used to communicate the flow total temperature and pressure conditions. Equations under the “CONTINUOUS” block of components can be written symbolically and with any order; then the equations and the unknowns are re-ordered automatically by PROOSIS according to the boundary conditions and data specified by the user when constructing the partition of a model.

Components and ports are stored in reusable Libraries. In PROOSIS, libraries that model different physical processes can be developed and exist under the same workspace. Through the software GUI, different components from different libraries can be dragged-and-dropped into a “canvas” and can then be connected through their ports to create the schematic model of an engine and its sub-systems. This way, mathematical models for multi-disciplinary calculations can be defined. Note that, in

the present thesis, the most important library is the TURBO library which defines components for turbomachinery performance calculations (0D) [see Alexiou (2020)].

After a schematic model has been created, the user can create the associated mathematical model. In PROOSIS this procedure is called a “Partition”. In a partition, the user can select the boundary values of their problem. Then, PROOSIS built-in algorithms sort the equations of the models to solve for the unknowns, resolve high-index problems, solve the linear and non-linear algebraic sub-problems created automatically, etc.

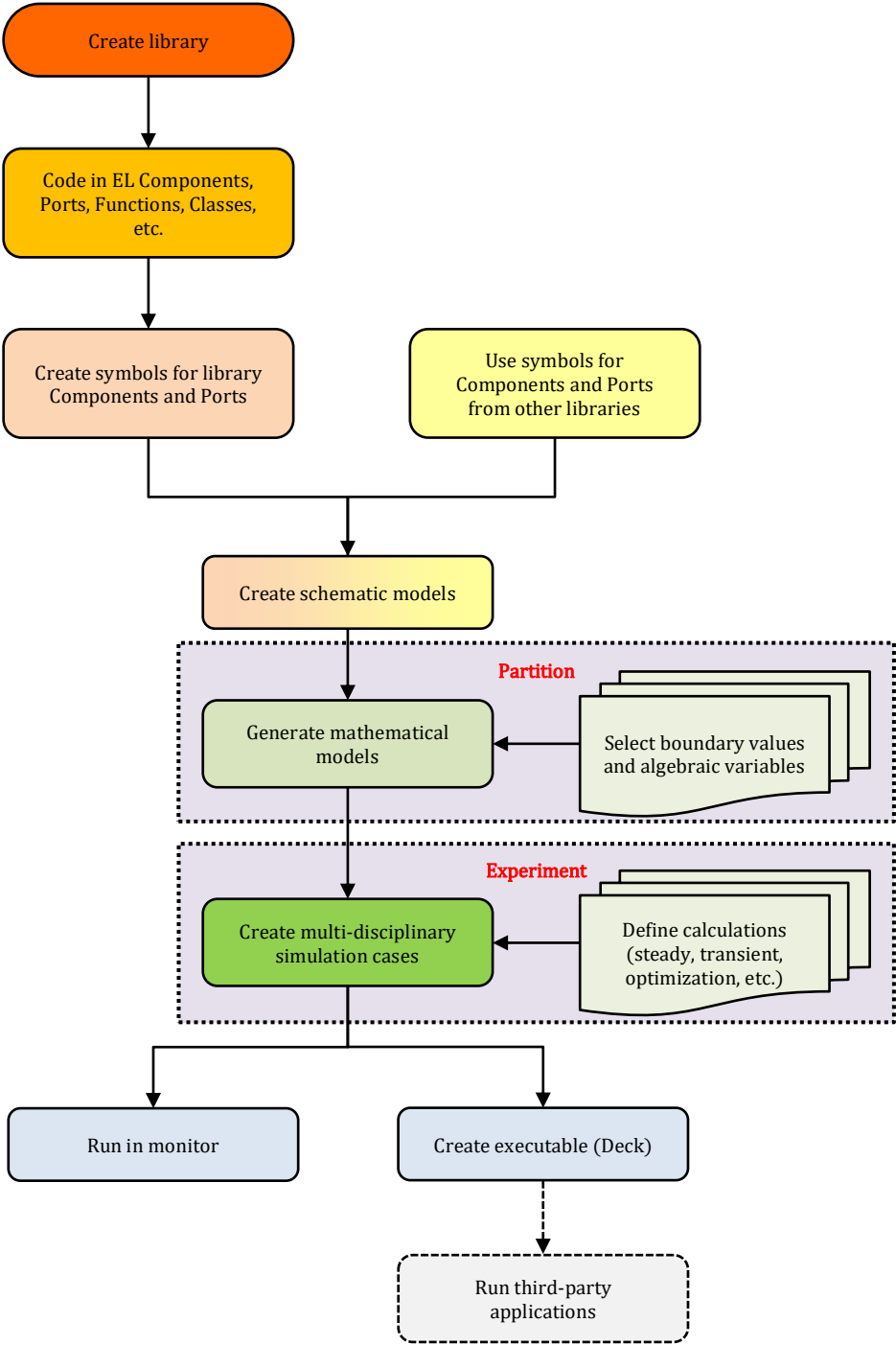


Figure 2.2: Model creation steps in PROOSIS.

For a given partition, the user can define different calculation cases (called “Experiments”). In experiments, the user can initialize variables, define the value of the boundary variables, modify component attributes, run single or multiple steady and transient simulations, generate reports, etc. Using internal (in EL) or external functions (in C, C++, and FORTRAN), the user can create advanced, multi-fidelity, and multi-disciplinary simulation cases. Experiments can be run and post-processed through the PROOSIS monitor, where the user can plot a variety of graphs and tables. Finally, the user can export experiments as executable programs (Decks) which can then be used from third-party software to define even more sophisticated simulations.

The steps followed from creating a PROOSIS library to generating an experiment deck, are shown diagrammatically in Figure 2.2.

2.2.3 LTT/NTUA and PROOSIS

The Laboratory of Thermal Turbomachines of the NTUA was one of the leading partners in developing the TURBO library during the VIVACE programme. Ever since, the LTT has a leading role in developing libraries for gas turbine modelling and simulation, both for land-based and aero-engine applications. Most of the works that the LTT has carried out have been published in peer-reviewed international journals and conferences, thus verifying both the experience that the LTT has acquired over the years on PROOSIS as well as the response that PROOSIS has in the scientific and industrial community as a modelling and simulation tool. The LTT experience with PROOSIS can be found on the LTT’s website^{15,16}. Next, examples of published works that highlight the modelling and computational capabilities of PROOSIS, are presented.

In 2005, Alexiou et al. (2005) presented an early version of the PROOSIS environment and exemplified the flexibility offered by its object-oriented architecture by conducting steady-state and transient performance simulations of a turbofan engine model. In the following year, Alexiou et al. (2006) further demonstrated the capabilities of PROOSIS by presenting the development and integration of a component modelling the performance of cooled turbines. In the same work, the possibility of PROOSIS models to run as deck applications from third-party software was also demonstrated.

The capability of PROOSIS to conduct multi-fidelity calculations was demonstrated by Alexiou et al. (2007) who, using a 1D stage-stacking code for compressor off-design performance calculations, they tested different zooming implementations to conduct cycle (0D) calculations of an industrial gas turbine engine. In the same context, Templalexis et al. (2016) demonstrated the integration of a through-flow (2D) fan model in a turbofan engine performance (0D) model.

Alexiou et al. (2008) used PROOSIS to develop and validate a library that defined components for modelling the secondary air system of gas turbine engines. They then demonstrated the capability of PROOSIS to combine components from different libraries to conduct multi-system calculations, by using said components to model the secondary air system in a turbofan cycle (0D) model. In 2012, Alexiou et al. (2012) showcased again the capability of PROOSIS to conduct multi-system calculations. In their work, they investigated the effect of different fuel options on the performance of a

¹⁵<https://www.ltt.ntua.gr/index.php/en/publication/modelling> (accessed: May 23rd, 2022)

¹⁶<https://www.ltt.ntua.gr/index.php/en/publication/emisenvimpactmnu> (accessed: May 23rd, 2022)

helicopter for a typical mission specification. In doing so, they modelled both the helicopter performance as well as the performance of the helicopter engine (turboshaft). A year later, Alexiou et al. (2013) considered the same models to optimize the turboshaft engine design for achieving minimum fuel burn over a specified mission.

The capability of PROOSIS to conduct multi-physics calculations was also demonstrated by Alexiou et al. (2010). By modelling a geared turbofan engine with active core technologies, they assessed the benefits in terms of NO_x and noise emissions for two typical, short- and long-range, aircraft missions.

In 2014, Aretakis et al. (2014) presented the capability of PROOSIS models to adapt to engine data to reproduce the performance of existing engines. They basically utilized PROOSIS to construct engine performance models of different adaptation quality using a semi-automated adaptation method, which they then utilized to investigate different methods for engine health assessments.

In 2017, Kalathakis et al. (2017) presented and validated a stand-alone PROOSIS library for modelling the performance of solar-powered gas turbine systems. Utilizing the components of this library, he assessed different solar-powered gas turbine configurations [see Kalathakis et al. (2016a, 2016b)].

Finally, in the works by Ntonas et al. (2021, 2022), PROOSIS was used to conduct gas turbine studies oriented towards maritime applications.

2.3 The Developed Design and Analysis Workflow

In this thesis a number of tools were developed, appropriate for the preliminary design and analysis of gas turbine engines. The formulation of the tools, their novel aspects, and their application to study engine configurations of current industrial interest are presented in the following chapters. The present section gives a brief description of the libraries developed within PROOSIS and of the tools they include. Note that, some of the tools presented in this PhD thesis were developed as part of LTT/NTUA's collaboration with European gas turbine and aircraft industries.

Overall, five (5) PROOSIS libraries were developed including PROOSIS components and computational tools and models for the preliminary design and analysis of gas turbine components. These are:

1. **TURBO1D:** Extends the components of the standard PROOSIS TURBO library (0D) to define components (0D/1D) for the preliminary design of gas turbine components (fans, compressors, turbines, and burners), which are appropriate for multi-point design studies.
2. **GTMDC:** Defines PROOSIS models and computational tools (0D/1D) for the preliminary design and analysis of gas turbine structural parts (shafts, disks, ducts, and casings).
3. **GTWC:** Defines PROOSIS components and models (0D/1D) for the preliminary weight estimation of gas turbine components (fans, compressors, turbines, and burners) and generic turbofan engines.

4. **MLAC:** Defines PROOSIS components (0D/1D) and experiments for the off-design performance prediction and map generation of compressors.
5. **MLDC:** Extends the functionalities of the MLAC library to define component(s) (0D/1D) and experiments for the aerothermodynamic design of compressors.

Note that, the MLAC and MLDC libraries will sometimes be referred to as the design (MLDC) and off-design (MLAC) MLC (Mean-Line Code) libraries.

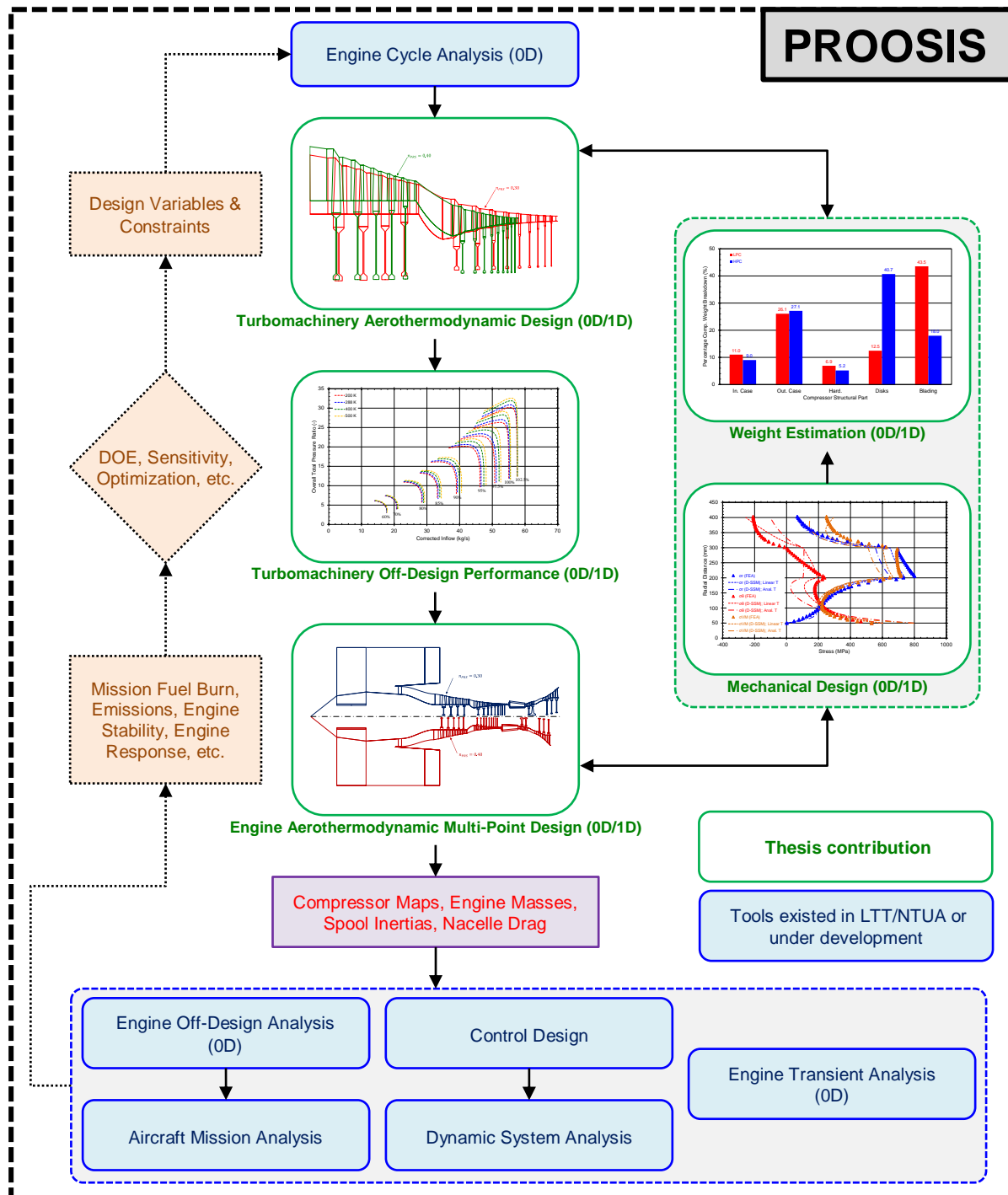


Figure 2.3: Layout of the developed design and analysis workflow for the preliminary, multi-disciplinary design of aircraft gas turbine engines.

Finally, the above tools were combined under the PROOSIS environment to construct an integrated system for the preliminary design and analysis of aircraft gas turbine engines. The general layout of the system is shown in Figure 2.3. Note that, other tools shown in Figure 2.3 either pre-existed or they continue to being developed and integrated into the system from the LTT/NTUA team.

2.4 Summary and Discussion

The present chapter gave a brief insight into the developed system of tools which will be presented in more detail in the following chapters. The tools themselves as well as the workflow for the preliminary design and analysis of aircraft gas turbine engines were developed in PROOSIS. In the beginning of this chapter, the reader can also find a short introduction to what is PROOSIS and what are its capabilities.

3 Turbomachinery 1D Aerothermodynamic Design

3.1 Introduction

The development of new aero- or industrial gas turbine engines formally begins with the engine performance specifications and geometry and/or weight requirements. These specifications are either imposed by a customer in the form of an RFP document, or by the manufacturer itself trying to fulfill a new market need [see Mattingly et al. (2002)]. The development of a gas turbine engine comprises designing steps the number and sequence of which are dictated primarily by manufacturer's experience and the project unique features (see Figure 3.1).

Although there is not a single general recipe, engine specification is typically followed by the conceptual design phase where the engine cycle and configuration are selected, among other. Then, the preliminary design phase follows. The first step during this phase is the thermodynamic cycle analysis where several parameters, including the turbomachinery components isentropic or polytropic efficiency, are selected based on manufacturer's experience or assumed based on current technology level. The second step, following that of the cycle analysis, is the aerodynamic design of turbomachinery (and other engine) components. It is in this step where the stage number, the rotational speed, the efficiency, etc., are estimated considering the engine performance requirements and thermal, mechanical, and aerodynamic constraints. Turbomachinery efficiencies, however, are affected by the design choices made during this step. Therefore, efficiencies are validated and if needed (or decided), the obtained values are fed back to the cycle analysis step which in turn produces new values of parameters for the aerodynamic design step. Taking into account that within the industrial environment the thermodynamic and aerodynamic studies are conducted by different engineering teams, a time-consuming iterative procedure is thus established that typically concludes when the efficiencies assumed at the outset of the cycle analysis match the values calculated during the aerodynamic design step (Figure 3.4).

In order to avoid unnecessary iterations between the thermodynamic and aerodynamic design disciplines, the present chapter presents a novel modelling approach for the direct coupling of 0D and 1D models for axial-flow compressor and turbine components. The existing thermodynamic (0D) performance models directly integrate 1D aerodynamic design and gas-path generation/visualization capabilities, all

at the same modelling level and within the same, user-friendly, simulation environment (i.e., PROOSIS). This way, a consistent, transparent, robust, and single-step calculation procedure is established that requires only a small number of inputs.

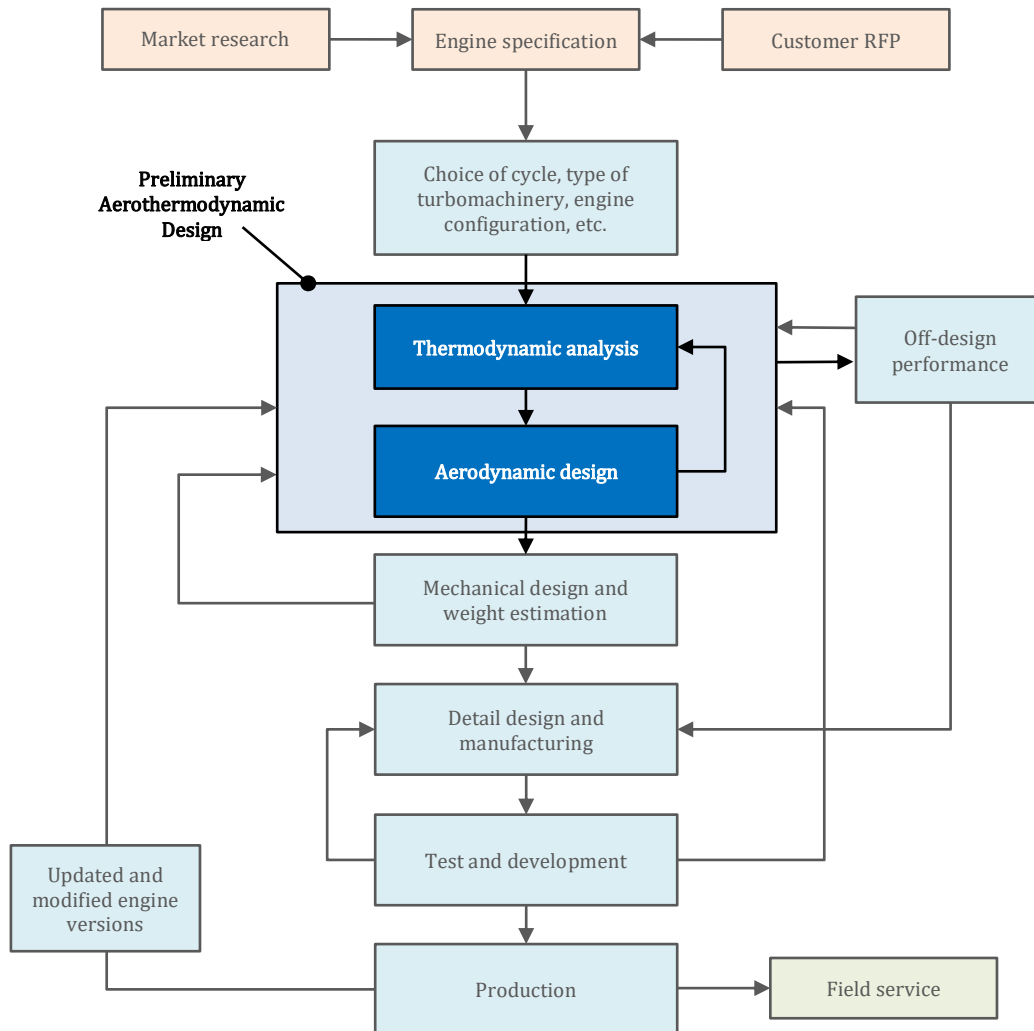


Figure 3.1: Simplified flow-chart representing the development course of a new gas turbine engine [adapted from Mattingly et al. (2002)]. The present chapter is concerned only with the “Preliminary Aerothermodynamic Design” box.

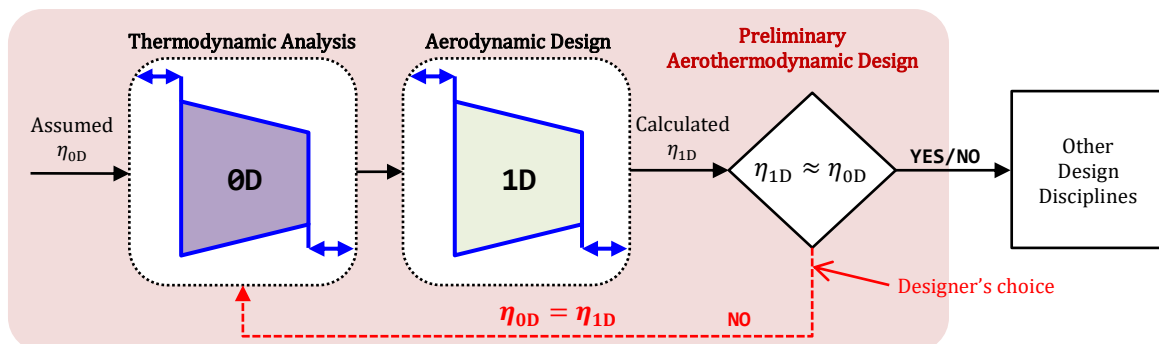


Figure 3.2: Diagrammatic representation of the preliminary aerothermodynamic design phase, where the iterations on turbomachinery efficiency between the cycle analysis and aerodynamic design modules is shown.

In this thesis, new compressor and turbine components were developed that integrate 1D aerodynamic design and gas-path generation functionalities which inherit directly the entire mathematical model (e.g., variables, equations, etc.) for performance calculations of the PROOSIS TURBO library ones (see Figure 3.3), resulting in the development of a dedicated TURBO1D library.

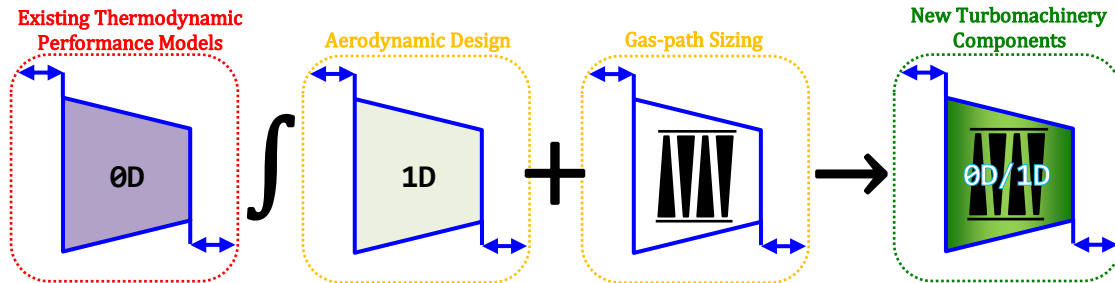


Figure 3.3: Conceptualization of the development of new turbomachinery components (green-colored) for preliminary design purposes. The existing compressor and turbine components for 0D performance calculations now integrate 1D aerodynamic design and gas-path sizing functionalities at the same modelling level and within the same simulation environment.

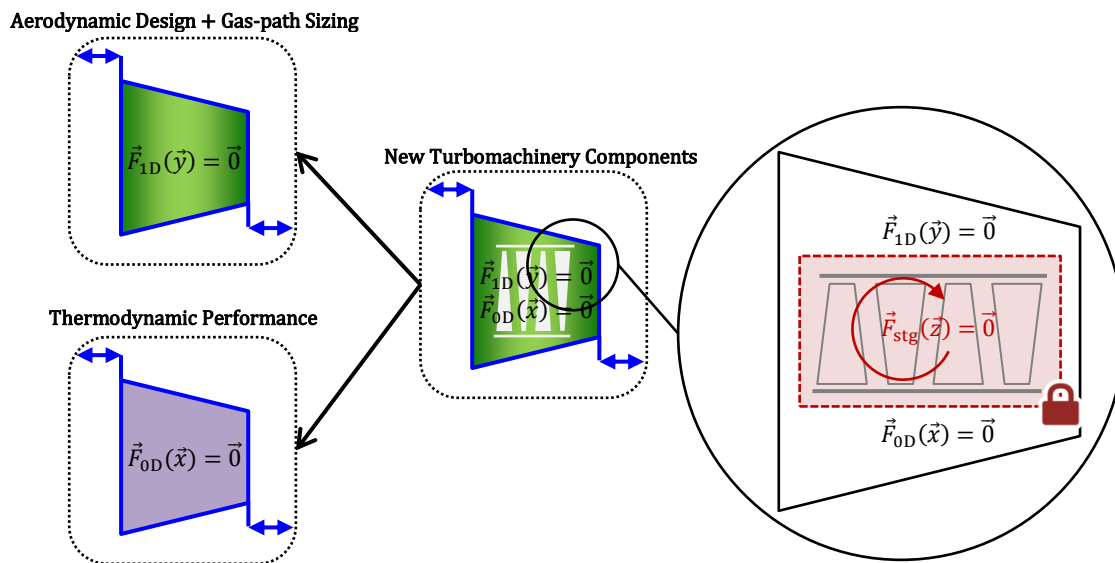


Figure 3.4: Conceptualization of the mathematical modelling of the new turbomachinery components (green-colored). The new compressor and turbine components inherit the mathematical model of the existing 0D ones and are extended to include 1D aerodynamic design and gas-path sizing calculations. Iterative solutions to establish stage-wise performance are confined at stage level and, therefore, the mathematical models of the components and the engine are not altered or affected.

By utilizing the concept of PROOSIS functions¹⁷, iterative procedures that may be employed in order to compute the performance of a stage (e.g., the stage isentropic efficiency and pressure ratio) are performed at stage level and, therefore, the mathematical models at component and engine level are not altered (Figure 3.4). This way, a novel single-step preliminary design procedure is established where continuous

¹⁷The equivalent, for example, of subroutines in FORTRAN.

data interchange between the different disciplines is not required at component level, while the existing mathematical formulations (number of non-linear equation systems and/or algebraic variables) for performance simulations of components and the whole engine remain unaffected and at the same level of robustness and speed of execution as for typical performance calculations.

The 1D aerodynamic design for establishing a component's overall efficiency is accomplished for both multi-stage compressor and turbine components through a mean-line, stage-by-stage calculation approach, where the stage-wise isentropic or polytropic efficiency is calculated by employing either loss or semi-empirical correlations linking the stage efficiency with other stage performance parameters. Next, the 1D aerodynamic modelling and gas-path sizing for axial-flow compressor, turbine, and fan components is presented.

3.2 Fundamentals

Before moving on to describe the basic methodology and equations comprising the 1D aerodynamic and gas-path modelling, some basic equations, models, and notation applicable to all turbomachinery components are given first.

3.2.1 Fluid and Thermodynamic Flow Properties Modelling

The calculations described in this chapter consider variable gas properties. The fluid and thermodynamic flow properties (gas constant, specific enthalpy, specific entropy function, specific heats ratio, and viscosity) at a flow station are established using the standard fluid and thermodynamic model functions provided by the PROOSIS TURBO library. These functions obtain the flow properties from 3D tables in terms of the fuel model (e.g., Jet-A, diesel, etc.), temperature, and gas composition (FARB and WAR), while "inverse" functions are also defined from which the flow temperature can be obtained given the flow enthalpy or entropy function. For simplicity reasons, the dependence on gas composition (FARB and WAR) will be omitted hereafter and only that on temperature will be highlighted unless otherwise specified.

For calculations with variable gas properties, the pressure ratio of an arbitrary isentropic process 1 → 2 is calculated using Gibbs' equation:

$$\frac{p_2}{p_1} = e^{\frac{\phi_2 - \phi_1}{Rg}} \quad (3.1)$$

with

$$\phi(T) = \int_{T_{ref}}^T c_p(t) \frac{dt}{t}$$

being the entropy function.

Note here, that since for variable gas properties the thermodynamic and flow relationships do not have analytical forms, then whenever deemed necessary the

relevant equations will be presented (without loss of generality) considering constant gas properties (c_p and γ) for clarity.

For more information about the default fluid and thermodynamic flow models in PROOSIS TURBO library, the reader is referred to Alexiou (2014).

3.2.2 Mean-Line Flow Representation

For initial design purposes when the detailed geometry of a machine is not yet known and there is need for fast performance and sizing calculations, designers usually resort to 1D (or “mean-line”) flow models for design and analysis. These models assume that the 3D flow phenomena taking place at a station across the machine can be represented by appropriately defined “average” flow conditions (temperatures, velocities, pressures, etc.) over the flow station in study. These “average” flow properties are typically defined at a mean radius running through the turbomachine, as it can be seen in Figure 3.5. The flow is additionally assumed to be invariant in the circumferential direction while the spanwise (in the radial direction) flow variations are neglected. Note that in the present implementation, the local mean radius is taken equal to the average of the local hub and tip radii.

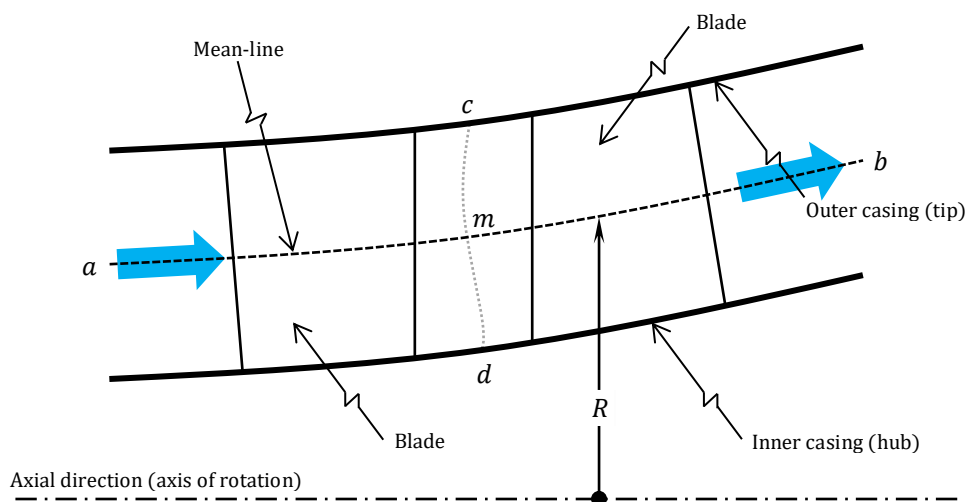


Figure 3.5: One-dimensional representation of the flow across a generic mixed-flow turbomachine. Curve “a-b” is a representative mean-line along which the 1D calculation takes place. According to the mean-line flow model, the flow conditions across an arbitrary station “c-d” are represented by average values defined on a point “m” along the “a-b” line.

In mean-line models, the flow is represented by velocity triangles which are used to analyze the performance of the blade rows and to establish the work interchanges that take place between the working fluid and the machine. The basic vector equation that relates the flow absolute and relative velocities is given by:

$$\vec{V} = \vec{W} + \vec{U} \quad (3.2)$$

where, the blade velocity has a magnitude expressed by:

$$U = \frac{2\pi N_{mech}}{60} R \quad (3.3)$$

Figure 3.6 and Figure 3.7 illustrate the velocity diagrams and the 1D station numbering across a compressor stage and across a turbine stage, respectively. Note that the flow angles are defined w.r.t. the axial direction and, unless otherwise stated, they are always considered positive in the context of this thesis. The relationships between the components of the velocity triangles can be found in any introductory turbomachinery textbook [see, e.g., Papailiou et al. (2000)] and, thus, they will not be presented any further in the present paragraph.

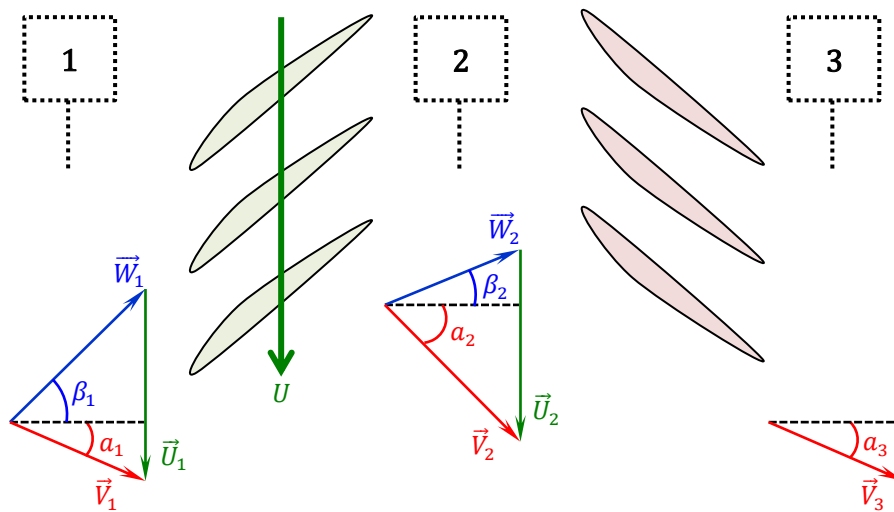


Figure 3.6: Velocity triangles across a compressor stage and 1D calculation station numbering.

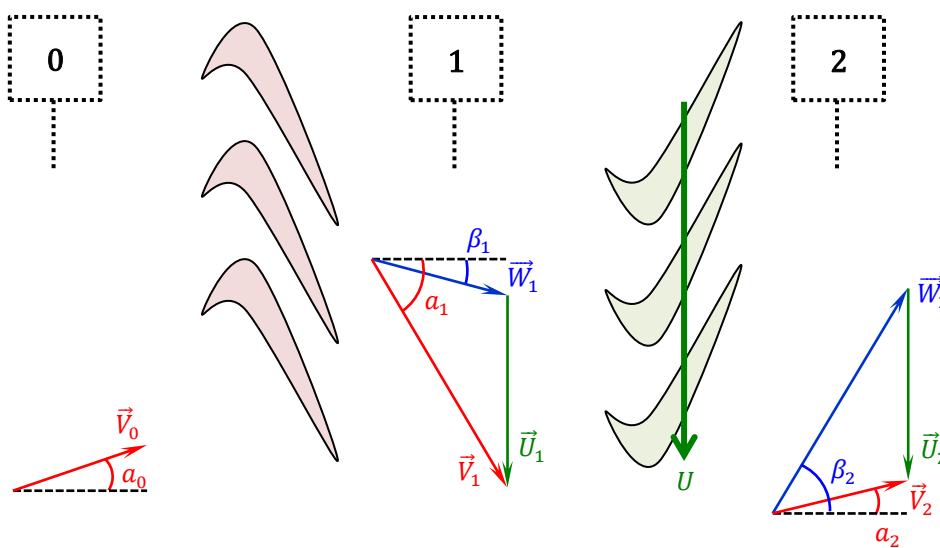


Figure 3.7: Velocity triangles across a turbine stage and 1D calculation station numbering.

3.2.3 Flow Station Calculation

The present paragraph presents the equations used to fully define the flow conditions at a flow station. To present the calculation procedure and the equations involved, gas properties are considered constant for clarity but the same procedure is employed when variable gas properties are assumed. The only difference is that instead of using temperatures, the static and total (stagnation) conditions are interrelated using enthalpies, while isentropic processes are expressed by Eq. (3.1) which makes use of the entropy function.

The mass flow rate across a station is given by:

$$\dot{m} = \rho^s A W \cos \beta \quad (3.4)$$

where $A = \pi(R_t^2 - R_h^2)$ is the flow-annulus cross-sectional area.

In Eq. (3.4), ρ^s is the fluid density, which is given by the equation of state:

$$\rho^s = \frac{p^s}{R_g T^s} \quad (3.5)$$

The total and static temperatures are related by:

$$\frac{T_r^0}{T^s} = 1 + \frac{\gamma - 1}{2} M_r^2 \quad (3.6)$$

while the total-to-static pressure ratio, p_r^0/p^s , is given by the isentropic relationship expressed by:

$$\frac{p_r^0}{p^s} = \left(\frac{T_r^0}{T^s} \right)^{\frac{\gamma}{\gamma-1}} \quad (3.7)$$

In Eq. (3.6), the flow Mach number is defined by:

$$M_r = \frac{W}{\sqrt{\gamma R_g T^s}} \quad (3.8)$$

For known gas properties (R_g and γ), Eqs (3.4) through (3.8) constitute a system of five (5) equations with ten (10) unknowns. Typically, at a station the mass flow \dot{m} , the cross sectional area A , the flow angle β , and the total conditions T_r^0 and p_r^0 are known and, therefore, the system of Eqs (3.4)–(3.8) can be solved (e.g., iteratively on T^s) to give the static conditions (T^s , p^s , ρ^s), the flow velocity (W), and the Mach number (M_r) of the flow.

Another possible situation is when instead of the flow-annulus area A , the flow velocity W or the Mach number M_r is known. Then the system of equations can again be solved to determine the area A which is required for passing the specified mass flow rate \dot{m} for the given flow conditions T_r^0 and p_r^0 and angle β .

Note that Eqs (3.4)–(3.8) are expressed in terms of relative (to the frame of reference studied) flow properties, meaning that the system of equations applies equally to both absolute and relative frames of reference.

3.2.4 Stage Performance Parameters

In the present paragraph some basic dimensionless parameters characterizing the performance of a compressor or turbine stage are given. Figure 3.8 shows the compression and expansion processes that take place across a single-stage compressor and turbine on an enthalpy-entropy diagram, respectively.

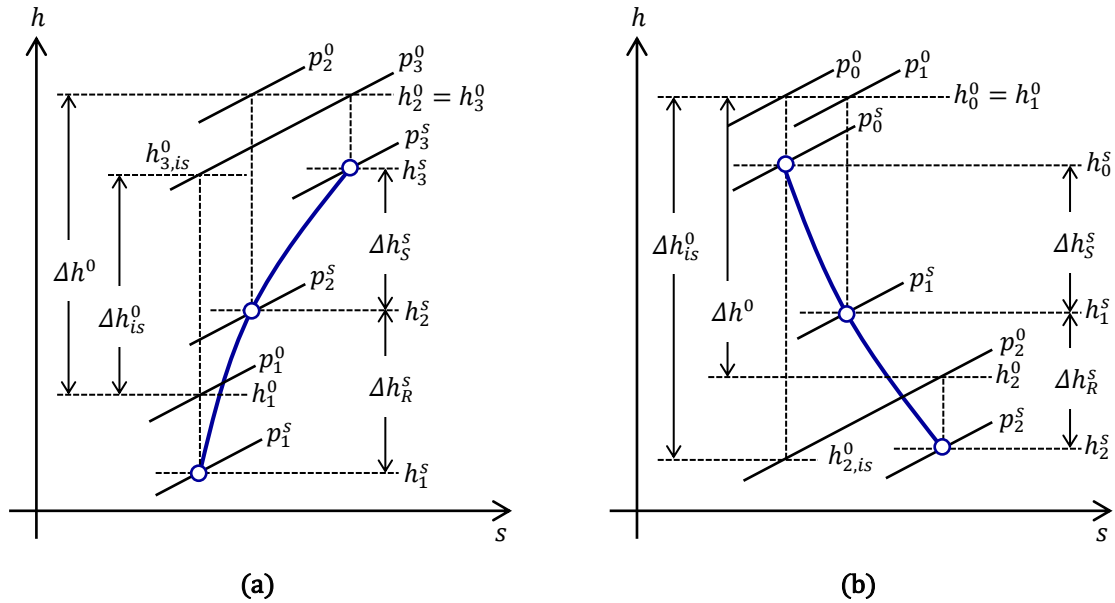


Figure 3.8: Entropy-enthalpy diagram for a single-stage (a) compressor and (b) turbine [adapted by Papailiou et al. (2000)].

Two parameters of interest to both the designer and the user of a turbomachine are the isentropic and polytropic efficiencies, expressed in terms of total conditions. For a compressor stage, isentropic (η_{is}) and polytropic (η_p) efficiencies are given by:

$$\eta_{is,CMP} = \frac{\Delta h_{is}^0}{\Delta h^0} \quad (3.9)$$

$$\eta_{p,CMP} = \frac{R_g}{\phi_3^0 - \phi_1^0} \ln \frac{p_3^0}{p_1^0} \quad (3.10)$$

In Eq. (3.9), Δh^0 is the actual work done on the working fluid, while Δh_{is}^0 is the work required for achieving the same compression ratio, p_3^0/p_1^0 , if the compressor worked ideally (adiabatically and frictionless).

For a turbine stage, isentropic and polytropic efficiencies are given by:

$$\eta_{is,TRB} = \frac{\Delta h^0}{\Delta h_{is}^0} \quad (3.11)$$

$$\eta_{p,TRB} = \frac{\phi_0^0 - \phi_2^0}{R_g} \ln \frac{p_0^0}{p_2^0} \quad (3.12)$$

with Δh^0 being the actual work extracted from the working fluid, and Δh_{is}^0 is the work extracted for the same expansion ratio, p_0^0/p_2^0 , if the turbine worked isentropically.

Another parameter of interest is the stage flow coefficient. Flow coefficient, φ , is defined as the ratio of the axial velocity to the blade speed, or:

$$\varphi = \frac{V_x}{U} \quad (3.13)$$

The flow coefficient is an indicator of the swallowing capacity of the component and, thus, a direct indication of the component size.

The stage loading coefficient, ψ , is defined as the total enthalpy change across a stage, divided by the blade speed squared, or:

$$\psi = \frac{\Delta h^0}{U^2} \quad (3.14)$$

The loading coefficient is a measure of the work delivered to the working fluid or extracted from it and, thus, it is an indirect index of the technology level.

Finally, the stage reaction, Λ , is a stage performance parameter that describes the work split in a stage between the rotor and the stator. Stage reaction is defined as the ratio of the static enthalpy rise or drop to the one achieved across the whole stage, and is expressed as:

$$\Lambda = \frac{\Delta h_R^s}{\Delta h_R^s + \Delta h_S^s} \quad (3.15)$$

3.2.5 Euler Pump and Turbine Equations

For a 1D, steady flow, implementation of the law of moment of momentum on a control volume defining a general turbomachine that encloses a rotating blade row states that the net sum of external moments with respect to the axis of rotation equals the time change of angular momentum. The time rate of the work interchange between the working fluid and the axis of the machine can then be expressed by the Euler pump or turbine equation [more information about the mathematical formulation can be found in Dixon et al. (2014)]:

$$P_{wr} = \dot{m}\Delta(UV_\theta) = \dot{m} \begin{cases} (U_2V_{\theta,2} - U_1V_{\theta,1}), & \text{for compressors} \\ (U_1V_{\theta,1} - U_2V_{\theta,2}), & \text{for turbines} \end{cases} \quad (3.16)$$

where the nomenclature introduced in Figure 3.6 and Figure 3.7 is used.

Finally, implementation of the energy equation for a 1D, steady-state, adiabatic flow, can express Eq. (3.16) in terms of the total enthalpy change, Δh^0 , according to the following equation:

$$P_{wr} = \dot{m}\Delta h^0 \quad (3.17)$$

3.2.6 3D Flow Approximation

Mean-line approaches are more accurate when the machines considered comprise blades with small height (or high hub-to-tip ratio) compared to the mean radius selected, and the flow can be approximated as 2D. Nevertheless, both compressors and turbines often include stages where the blade height is significant (blades of low hub-to-tip ratio) and 3D phenomena can no longer be neglected. Typical such examples are the first stages of HPCs and the last stages of LPTs in aircraft gas turbine engines.

For describing the flow along the blade span, the radial equilibrium flow approximation is used according to which the pressure forces exerted by the flow on a fluid element balance out the inertial forces developed in the fluid element. This flow condition is expressed as [see Saravanamuttoo et al. (2017)]:

$$\frac{1}{\rho^s} \frac{dp^s}{dr} = \frac{1}{r} V_\theta^2$$

Using Gibbs' equation ($Tds = dh - dp/\rho$), the definition for absolute total enthalpy ($h^0 = h^s + V^2/2$), and the simplifying assumption that $ds/dr = 0$, the above gives the vortex-energy equation [see Saravanamuttoo et al. (2017)]:

$$\frac{dh^0}{dr} = V_x \frac{dV_x}{dr} + V_\theta \frac{dV_\theta}{dr} + \frac{1}{r} V_\theta^2$$

Solving the above [see Lewis (1996) for different solution strategies] gives the variation of the flow along the annulus span. In this thesis, approximate analytical solutions of the vortex-energy equation above are used for simplicity. More specifically, the free-vortex flow assumption is utilized, described by [see Saravanamuttoo et al. (2017)]:

$$\frac{dh^0}{dr} = 0 \tag{3.18}$$

$$\frac{dV_x}{dr} = 0 \tag{3.19}$$

$$\frac{d}{dr}(rV_\theta) = 0 \tag{3.20}$$

3.2.7 Solidity, Blade Count, and Aspect Ratio

The number of blades comprising a blade row is calculated by the ceiling function expressed by:

$$Z_b = \left\lceil \frac{2\pi R}{s} \right\rceil = \left\lceil \frac{2\pi \sigma R}{c} \right\rceil \tag{3.21}$$

where σ is the blade row solidity given by:

$$\sigma = \frac{c}{s} \tag{3.22}$$

and s is the blade row spacing (or pitch length). For blades with negligible taper ratio (≈ 1), application of Eq. (3.21) between the mean-line (subscript “ m ”) and an arbitrary radius, R , gives:

$$\sigma \approx \sigma_m \frac{R_m}{R} \quad (3.23)$$

where the assumption was made that the blade chord remains radially constant.

Finally, the blade aspect ratio is defined as the blade (average) height divided by the blade chord length:

$$AR = \frac{\bar{h}_b}{c} \quad (3.24)$$

The blade average height (\bar{h}_b) in Eq. (3.24) is given by:

$$\bar{h}_b = \frac{R_{t,1} - R_{h,1} + R_{t,2} - R_{h,2}}{2} \quad (3.25)$$

where the subscripts 1 and 2 correspond to the blade inlet and outlet, respectively.

3.3 Axial Compressor 1D Aerothermodynamic Design

The present section presents the methodology and equations employed for estimating the isentropic and polytropic efficiencies of axial-flow, multi-stage compressors. Figure 3.9 shows a schematic of the meridional view for an axial-flow machine.

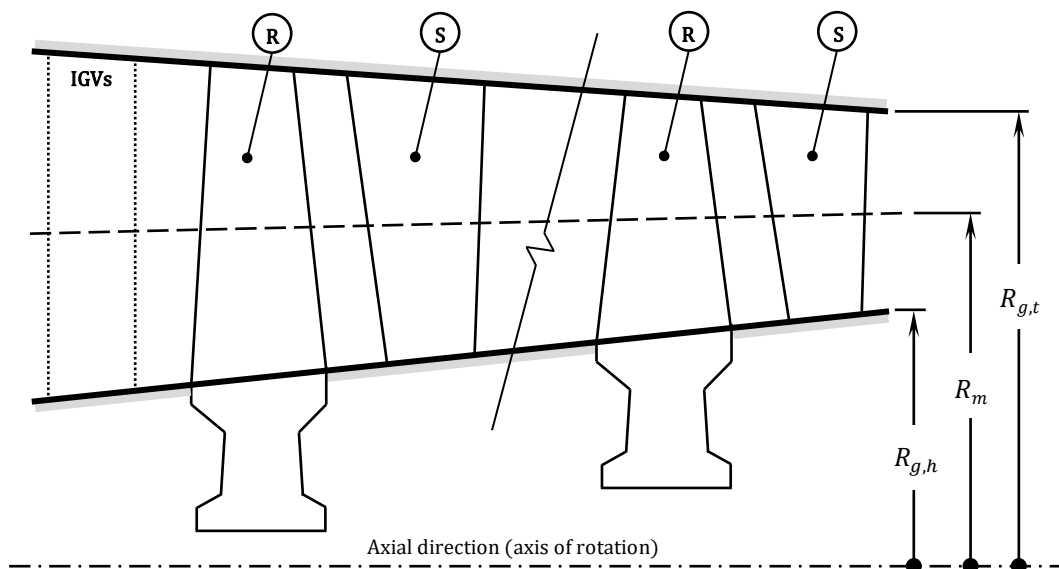


Figure 3.9: Axial-flow compressor flow-annulus, blading, and geometry nomenclature, where R stands for rotor and S for stator.

The compressor design is performed by a mean-line approach in a stage-by-stage manner. To simplify the calculation process and the number of required design inputs, each compressor stage is designed following the next two design assumptions:

1. Constant mean diameter ($D_m = \text{const} \rightarrow U_m = \text{const}$), and
2. constant axial velocity ($V_x = \text{const}$).

Note that the above assumptions do not necessarily hold across the compressor, meaning that both the mean diameter and the axial velocity can vary throughout the compressor, but they remain constant across a stage.

Finally, to account for 3D effects, all necessary stage parameters are calculated at the two blade span extremes, the hub and the tip, using the free-vortex flow approximation of Eqs (3.18)–(3.20). The stage geometry, nomenclature and station numbering used in the present and the following paragraphs are shown in Figure 3.10.

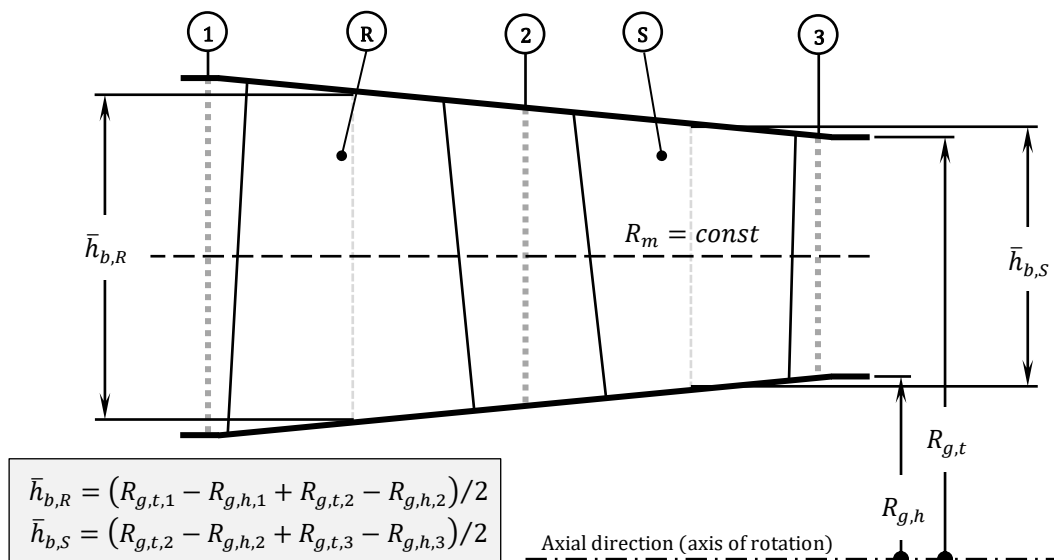


Figure 3.10: Compressor stage meridional view, station numbering, and nomenclature for mean-line calculation. As is the common design practice, compressor stages comprise a rotor blade (R) followed by a stator vane (S). For simplicity reasons and for minimizing the necessary design inputs, it is assumed that the rotor outlet and the stator inlet flow stations coincide thermodynamically and kinematically thus, the common station numbering “2”.

3.3.1 Stage-by-Stage Calculation

The term “stage-by-stage” means a “marching” approach that commences at compressor’s inlet and terminates at compressor’s outlet. The calculation is performed sequentially through every stage of the compressor. Therefore, for the calculation to continue with the next stage, the calculation of the upstream stage must have been completed and so forth. Basically, the above calculation aims at determining the outlet flow conditions and dimensions of a stage which, in turn, are used for defining the inlet conditions and dimensions for the next compressor stage. This way, at the end of the stage-by-stage calculation the compressor geometry and the compressor exit conditions (and, thus, performance) are fully defined.

The calculation of a stage is summarized as follows. With the total conditions being known at the stage inlet ($\dot{m}_1, T_1^0, p_1^0, a_1, M_1$), the exit ones ($\dot{m}_3, T_3^0, p_3^0, a_3, M_3$) are calculated. If we know the stage work input ($h_3^0 = h_1^0 + \Delta h^0$) and if the stage isentropic efficiency (η_{is}) is known, then stage pressure ratio is given by:

$$PR = \frac{p_3^0}{p_1^0} = e^{\frac{\phi_{3,is}^0 - \phi_1^0}{Rg}} \quad (3.26)$$

The value of $h_{3,is}^0$ required for calculating $\phi_{3,is}^0$ in Eq. (3.26) is obtained from the definition of the isentropic efficiency [see also Eq. (3.9)]:

$$h_{3,is}^0 = h_1^0 + \eta_{is} \Delta h^0 \quad (3.27)$$

Having determined the stage exit total temperature and pressure as $T_3^0 = h^{-1}(h_3^0)$ and $p_3^0 = p_1^0 \times PR$, respectively, the stage exit flow-annulus area (and thus dimensions) are estimated according to the methodology described in paragraph 3.2.3 given, additionally, the mass flow and the velocity triangle (flow angle and Mach number) at the stage outlet (\dot{m}_3, a_3, M_3). Therefore, both the stage performance and geometry are fully defined.

Next, the equations and methodology followed for establishing the stage work input and isentropic efficiency for establishing the stage outlet conditions and geometry are presented in the paragraphs that follow.

3.3.2 Mass Flow Calculation

In the present methodology, mass flow rate at compressor inlet is a design input. Then, the mass flow across a stage, j , is assumed constant and equal to the mass flow rate at the stage inlet which, in turn, is estimated by the following recursive formula:

$$(\dot{m}_1)_j = \dot{m}_{in} - \sum_{k=1}^{k=j-1} (\dot{m}_{gb})_k \quad (3.28)$$

where the stage bleed, \dot{m}_{gb} , is assumed to occur at the respective stage exit. The gas bleed is either a user input or a cycle parameter determined, e.g., from turbine cooling, aircraft power requirements, etc.

3.3.3 Area Blockage Calculation

Blockage factor, λ_B , is a number less than unity that accounts for the geometric flow area reduction due to flow phenomena, such as the boundary layer growth along the compressor annulus walls. Due to the flow capacity reduction, blockage has a considerable effect on the axial velocity of the flow across the compressor and, hence, has to be accounted for in the design process according to Saravanamuttoo et al. (2017).

Designating the geometric quantities of the flow-annulus area with the subscript “ g ” and the effective ones with “ e ”, the blockage factors accounting for the flow capacity

reduction at the annulus hub and the tip, expressed as unblocked fractions of the flow-annulus area, δ_B , are given by [see Creveling et al. (1968a)]:

$$\delta_{B,h} = \frac{D_{g,t}^2 - D_{e,h}^2}{D_{g,t}^2 - D_{g,h}^2} \quad (3.29)$$

$$\delta_{B,t} = \frac{D_{e,t}^2 - D_{g,h}^2}{D_{g,t}^2 - D_{g,h}^2} \quad (3.30)$$

In this formulation, it is assumed that the flow capacity reduction distributes evenly at the hub and the tip, or $\delta_{B,h} = \delta_{B,t} = \delta_B$. Blockage factor (λ_B) is defined by:

$$\lambda_B = \frac{A_e}{A_g} \leq 1 \quad (3.31)$$

From the above definition it is easily seen that λ_B can be expressed in terms of the geometric and the effective flow-annulus diameters by:

$$\lambda_B = \frac{D_{e,t}^2 - D_{e,h}^2}{D_{g,t}^2 - D_{g,h}^2} \quad (3.32)$$

Combining Eqs (3.29), (3.30), and (3.32), we get:

$$\lambda_B = \delta_{B,h} + \delta_{B,t} - 1 = 2\delta_B - 1 \quad (3.33)$$

In the present design process, λ_B either takes on a user-defined value in every stage or can be calculated from Eq. (3.33) using default values for the fractions $\delta_{B,h}$ and $\delta_{B,t}$. Typical values for $\delta_{B,h}$ and $\delta_{B,t}$ are given by Glassman et al. (1995) in terms of the stage number, j , at the rotor and stator exit in Table 3.1.

Table 3.1: Blockage fraction values at rotor and stator exit [see Glassman et al. (1995)]

Stage number	Blockage Fractions @ Rotor Exit (-)	Blockage Fractions @ Stator Exit (-)
1	0.990	0.985
2	0.985	0.980
3	0.980	0.975
4	0.975	0.970
5	0.970	0.965
6	0.965	0.960
7	0.960	0.955
8	0.955	0.950
9	0.950	
>9		

Here, the individual values for $\delta_{B,h}$ and $\delta_{B,t}$ given in Table 3.1 are expressed analytically by the following recursive formula:

$$(\delta_B)_j \approx \max\left(0.99 - \frac{j-1}{200}, 0.95\right)$$

In the present 1D modelling approach, every compressor stage is assumed to have a single λ_B value throughout. Substituting the above recursive expression in Eq. (3.33), we get Eq. (3.34) for estimating the blockage factor value for a compressor stage:

$$(\lambda_B)_j = 2\max\left(0.99 - \frac{j-1}{200}, 0.95\right) - 1 \quad (3.34)$$

Knowing the value for λ_B in every compressor stage [specified or calculated from Eq. (3.34)] and having established the geometric diameters of the flow-annulus, the effective diameters at the same flow station are estimated from Eq. (3.32) and one additional equation correlating the two sets of diameters. Using the assumption that $\delta_{B,h} = \delta_{B,t}$ and equating Eqs (3.29) and (3.30), this equation reads:

$$D_{e,t}^2 + D_{e,h}^2 = D_{g,t}^2 + D_{g,h}^2 \quad (3.35)$$

Solving the system of Eqs (3.32) and (3.35) for the effective diameters, $D_{e,h}$ and $D_{e,t}$, we get:

$$D_{e,h} = \sqrt{\frac{1}{2}[(\lambda_B + 1)D_{g,h}^2 - (\lambda_B - 1)D_{g,t}^2]} \quad (3.36)$$

$$D_{e,t} = \sqrt{\frac{1}{2}[(\lambda_B + 1)D_{g,t}^2 - (\lambda_B - 1)D_{g,h}^2]} \quad (3.37)$$

3.3.4 Compressor Inlet Calculation

For known cycle parameters at compressor's inlet, that is, mass flow rate \dot{m} , absolute total temperature T^0 and pressure p^0 , absolute flow angle α , and absolute flow Mach number M (a user input), the static conditions (T^s and p^s), flow velocity (V), and geometric flow-annulus area (A_g) at the compressor inlet are established by solving the system of Eqs (3.4) through (3.8) as described in paragraph 3.2.3.

The dimensions (hub, mean, and tip diameters) of the flow-annulus at compressor's inlet are then estimated for a specified hub-to-tip ratio, $HTR = D_h/D_t$, using the following equations:

$$D_{g,t} = \sqrt{\frac{4A_g}{\pi(1 - HTR^2)}} \quad (3.38)$$

$$D_{g,h} = HTR \times D_{g,t} \quad (3.39)$$

$$D_m = \frac{D_{g,h} + D_{g,t}}{2} \quad (3.40)$$

Note that having established A_g , then the effective flow-annulus area (A_e) at compressor's inlet is estimated from the definition of the blockage factor, Eq. (3.31), as: $A_e = \lambda_B A_g$.

3.3.5 Compressor Exit Calculation

Similarly to computing the compressor inlet flow station, for known cycle parameters (\dot{m} , T^0 , p^0 , a) and a user-specified absolute flow Mach number (M) at compressor's outlet, the static conditions (T^s and p^s), flow velocity (V), and geometric flow-annulus area (A_g) at compressor outlet are again established by solving the system of Eqs (3.4)–(3.8) given in paragraph 3.2.3.

In order to calculate the flow-annulus diameters at compressor's exit, a design choice should be made regarding the definition of the flow-annulus shape. In the present design approach, there are four (4) design options for the distribution of the mean-line, as listed below:

- Constant mean diameter
- Constant tip diameter
- Constant hub diameter
- Mean diameter distribution

Next, the calculation procedure followed to establish the flow-annulus diameters for each one of the above four design options is described in more detail.

Constant Mean Diameter

Here, the mean diameter along the compressor is held constant from compressor inlet to outlet, or $D_{m,in} = D_m = D_{m,out} = \text{const}$ and, therefore, D_m is known. Then, hub and tip diameters are determined by solving the set of equations:

$$\begin{cases} A = \frac{\pi}{4}(D_t^2 - D_h^2) \\ D_m = \frac{D_h + D_t}{2} \end{cases} \quad (3.41)$$

for the geometric quantities, or:

$$D_{g,h} = D_m - \frac{A_g}{\pi D_m} \quad (3.42)$$

$$D_{g,t} = D_m + \frac{A_g}{\pi D_m} \quad (3.43)$$

$$HTR = \frac{D_{g,h}}{D_{g,t}} \quad (3.44)$$

Constant Tip Diameter

Here, the tip diameter is held constant from compressor's inlet to compressor's outlet, $D_{g,t,in} = D_{g,t} = D_{g,t,out} = const$, and, thus, $D_{g,t,out}$ is a known value. The calculation of the other two diameters ($D_{g,h}$ and D_m) is then a simple task. Finally, these diameters are given by:

$$D_{g,h} = \sqrt{D_{g,t}^2 - \frac{4A_g}{\pi}} \quad (3.45)$$

$$D_m = \frac{D_{g,h} + D_{g,t}}{2} \quad (3.46)$$

The hub-to-tip ratio is calculated from Eq. (3.44).

Constant Hub Diameter

Here, the hub diameter is held constant across the compressor, that is, $D_{g,h,in} = D_{g,h} = D_{g,h,out} = const$, and, thus, $D_{g,h,out}$ is known. Similarly to the case of the constant tip diameter above, the calculation of the remaining two diameters (D_m and $D_{g,t}$) is easily done, where the tip diameter is calculated and is given by:

$$D_{g,t} = \sqrt{D_{g,h}^2 + \frac{4A_g}{\pi}} \quad (3.47)$$

Finally, the mean diameter is calculated by Eq. (3.46) and the hub-to-tip ratio is given by Eq. (3.44).

Mean Diameter Distribution

For the fourth and final design option, a distribution for the mean diameter throughout the compressor, between the (already) known mean diameter at the compressor inlet and the unknown (at this point) mean diameter at the compressor outlet, is specified. Evidently, at this point of the calculation there is not enough data at the outlet and, thus, the compressor exit geometry and the mean-line distribution cannot be fully defined. For this case an extra design input is given, namely the hub-to-tip ratio (HTR). Then, the annulus tip diameter can be obtained using Eq. (3.38), which is repeated here for completeness:

$$D_{g,t} = \sqrt{\frac{4A_g}{\pi(1 - HTR^2)}} \quad (3.48)$$

The remaining two diameters, $D_{g,h}$ and D_m , are then established using Eqs (3.45) and (3.46).

Similarly to the case of calculating the compressor inlet flow station, the effective area is established from the geometric one using the definition of the blockage factor, Eq. (3.31), as: $A_e = \lambda_B A_g$.

3.3.6 Mean-Line Distribution

As already described in paragraph 3.3.5, one of the available design options is to specify a mean-line distribution between the compressor inlet (first stage rotor inlet) and exit (last stage stator outlet) mean diameters. In this design modelling approach, the stage diameter is constant and is assumed equal to that at the respective rotor inlet. Figure 3.11 depicts a diagrammatic example of a linear mean diameter distribution.

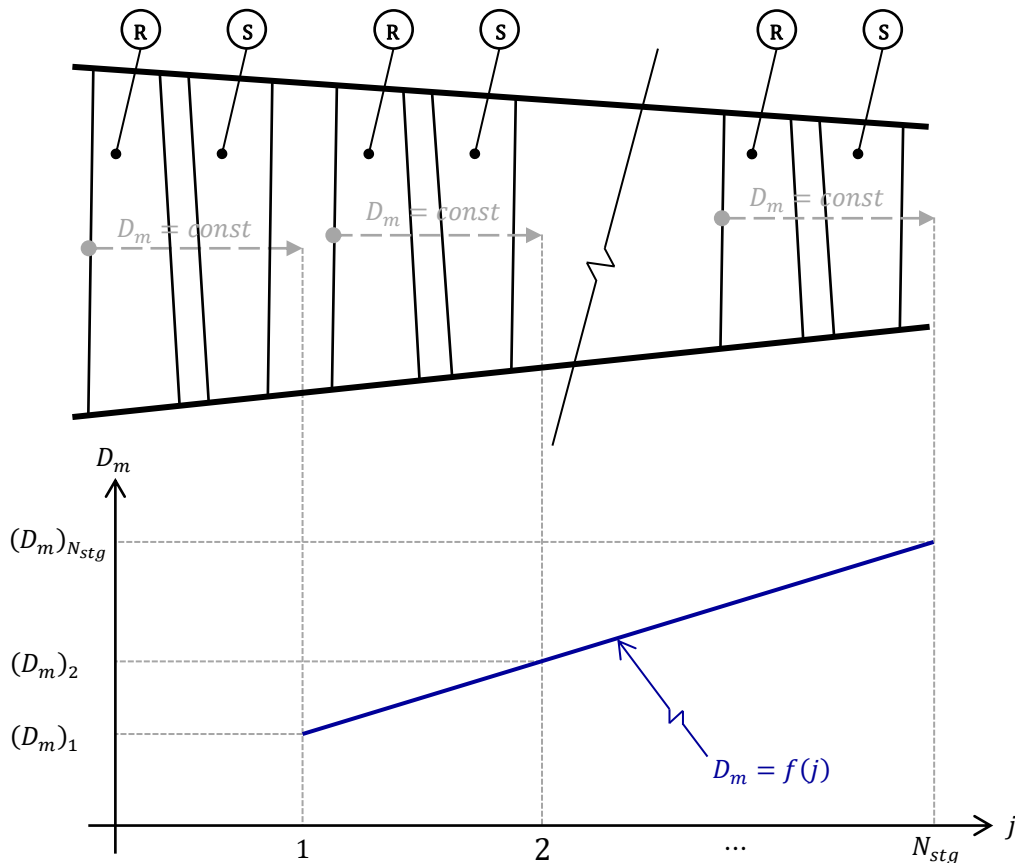


Figure 3.11: Diagrammatic example of a linear mean diameter distribution for specifying the mean-line shape of a compressor component. In the present modelling approach, it is assumed that the stage mean diameter is constant and equal to the diameter at the respective rotor inlet.

In the present modelling approach, there are four (4) possible mean-line distributions:

- Linear from compressor inlet to compressor exit
- Constant from compressor inlet up to a stage and then linear up to the exit
- Linear from compressor inlet up to a stage and then constant up to the exit
- Parabolic from compressor inlet to compressor exit

Option 1: Linear from Inlet to Outlet

For the first design option, the mean diameter distribution is given by:

$$(D_m)_j = \frac{D_{m,out} - D_{m,in}}{2N_{stg} - j_{IGV}} (2j - 1 - j_{IGV}) + D_{m,in} \quad (3.49)$$

Option 2: Constant from Inlet up to Stage, then Linear up to Exit

For the second design option, the mean diameter distribution is given by:

$$(D_m)_j = \begin{cases} D_{m,in}, & j \leq j^* \\ 2 \frac{D_{m,out} - D_{m,in}}{2(N_{stg} - j^*) - 1} (j - j^*) + D_{m,in}, & j > j^* \end{cases} \quad (3.50)$$

Option 3: Linear from Inlet up to Stage, then Constant up to Exit

For the third design option, the mean diameter distribution is given by:

$$(D_m)_j = \begin{cases} \frac{D_{m,out} - D_{m,in}}{2j^* - 1 - j_{IGV}} (2j - 1 - j_{IGV}) + D_{m,in}, & j \leq j^* \\ D_{m,out}, & j > j^* \end{cases} \quad (3.51)$$

Option 4: Parabolic from Inlet to Outlet

Finally, for the fourth and final design option, the mean diameter distribution is given by:

$$(D_m)_j = c_1(2j - 1)^2 + c_2(2j - 1) + c_3 \quad (3.52)$$

where the coefficients c_1 , c_2 , and c_3 in Eq. (3.52) are given by the following set of equations:

$$c_1 = 2 \frac{D_{m,in} + D_{m,out} - 2\bar{D}_m}{(2N_{stg} - j_{IGV})^2} \quad (3.53)$$

$$c_2 = \frac{D_{m,out} - D_{m,in}}{2N_{stg} - j_{IGV}} - c_1(2N_{stg} + j_{IGV}) \quad (3.54)$$

$$c_3 = D_{m,in} - c_1 j_{IGV}^2 - c_2 j_{IGV} \quad (3.55)$$

$$\bar{D}_m = D_{CLICO} \times \frac{D_{m,in} + D_{m,out}}{2} \quad (3.56)$$

where D_{CLICO} a user-defined shape factor for the parabolic mean-line distribution.

In Eqs (3.49)–(3.56), j and j^* are the stage number and the number of the stage where the distribution slope changes, respectively, while j_{IGV} accounts for the absence or presence of IGVs: $j_{IGV} = 0$ for a compressor with IGVs and $j_{IGV} = 1$ for a compressor without them.

Finally, in case a constant tip or a constant hub design option is selected, then the mean diameter is again calculated by Eq. (3.49) assuming linear variation from compressor's inlet to compressor's exit.

To conclude, once the calculation of the inlet and outlet compressor sections has been completed, the mean diameter along the compressor can be computed and, thus, to whatever follows it is a known quantity in every stage and station of the compressor.

3.3.7 Rotational and Blade Speed Calculation

With the mean diameter distribution along the compressor being known, the blade speed at the mean-line is also known and constant in every stage (since every stage is designed assuming constant mean diameter). Blade speed is calculated according to Eq. (3.3). Equation (3.3) involves the component rotational speed (N_{mech}) which is either an input (imposed, e.g., by an external load, by the turbine component with which the compressor is mechanically coupled, etc.) or, is estimated based on stress and/or aerodynamic criteria.

It is well known that one of the options for increasing the specific work done by the compressor stages is by increasing the blade speed¹⁸ or, equivalently, N_{mech} . However, the maximum value of N_{mech} is constrained by both the maximum mechanical stresses developed on compressor blades and disks, as well as by the losses associated with high Mach number flows and compressibility phenomena developing near the tip region of rotating blades (where the blade speed is maximum). Typical mechanical and aerodynamic criteria are the maximum blade speed and relative flow Mach number developed at the tip of the first rotating blade, or:

$$U_t \leq (U_t)_{max} \text{ and } M_{r,t} \leq (M_{r,t})_{max}$$

Both $(U_t)_{max}$ and $(M_{r,t})_{max}$ express current technology limits and typical values for both can be found in many technical reports and turbomachinery textbooks (see Appendix A). For instance, Walsh et al. (2004) quote $(U_t)_{max} \leq 500$ m/s and $(M_{r,t})_{max} \leq 0.9 - 1.3$ for compressors.

3.3.8 Stage Performance Parameters Calculation

In this paragraph, the available options on imposing values for the stage flow coefficient, loading coefficient, and reaction are presented and commented on. Fixing the values of (φ, ψ, Λ) on every compressor stage (j) fixes the mean-line velocity diagrams and, thus, the flow velocities and angles are known in every station and stage across the compressor.

3.3.8.1 Flow Coefficient

The stage flow coefficient is given by Eq. (3.13). Because every stage is designed assuming constant mean diameter and axial velocity, from Eq. (3.13) it follows that φ is also constant across a stage.

There are two (2) options for imposing φ on every stage of the compressor. In the first, φ is linearly distributed between inlet and outlet values according to:

$$\varphi_j = \frac{\varphi_{out} - \varphi_{in}}{N_{stg} - 1} (j - 1) + \varphi_{in} \quad (3.57)$$

The second design choice is a linear distribution of the axial velocity between inlet and exit values:

¹⁸The specific work that a (constant mean diameter) stage does on the working fluid is given by Euler's pump equation: $\Delta h^0 = U\Delta V_\theta$.

$$(V_x)_j = \frac{V_{x,out} - V_{x,in}}{N_{stg} - 1} (j - 1) + V_{x,in} \quad (3.58)$$

The calculation of φ then follows from definition [see Eq. (3.13)] or $\varphi_j = (V_x)_j / U_j$. The inlet and outlet axial velocities are calculated from the known velocity triangles: $V_{x,in} = V_{in} \cos \alpha_{in}$ and $V_{x,out} = V_{out} \cos \alpha_{out}$.

Note that for the flow across IGVs, $V_{x,in}$ is multiplied by a user-defined factor greater than unity to account for the corresponding flow acceleration.

3.3.8.2 Loading Coefficient

The stage loading coefficient is given by Eq. (3.14). In the present modelling approach there are three (3) options available for imposing ψ on every compressor stage. The first one assumes a constant average value $\bar{\psi}$ in every stage:

$$\psi_j = \bar{\psi} = \frac{1}{\sum_{j=1}^{j=N_{stg}} U_j^2} \Delta h_{CMP}^0 \quad (3.59)$$

where Δh_{CMP}^0 is the total specific enthalpy rise across the compressor.

The second option assumes a constant stage Δh^0 distribution across the compressor ($\Delta h^0 = \overline{\Delta h^0}$). Then ψ is calculated from:

$$\psi_j = \frac{\overline{\Delta h^0}}{U_j^2} = \frac{1}{N_{stg} U_j^2} \Delta h_{CMP}^0 \quad (3.60)$$

In the third and last option, a variable stage Δh^0 is imposed as a fraction of the overall Δh_{CMP}^0 . Thus, ψ is now given by:

$$\psi_j = \frac{(\Delta h^0)_j}{U_j^2} = \frac{(K_{\Delta h})_j}{U_j^2} \Delta h_{CMP}^0 \quad (3.61)$$

with $\sum_{j=1}^{j=N_{stg}} (K_{\Delta h})_j = 1$.

Finally, with ψ being known in every stage, the specific work a stage can perform is calculated from definition:

$$\Delta h^0 = \psi U^2 \quad (3.62)$$

Then, the stage outlet enthalpy is calculated as: $h_3^0 = h_1^0 + \Delta h^0$.

3.3.8.3 Stage Reaction

In the present modelling approach, stage reaction can either be specified directly across the compressor, or a distribution for the absolute flow angle at the stage inlet, α_1 , can be assumed.

For the first case, reaction Λ is enforced on every stage except the first one where Λ is calculated from the known flow angle and the known flow and loading coefficients by [see Dixon et al. (2014)]:

$$\Lambda = 1 - \varphi \tan a_1 - \frac{\psi}{2} \quad (3.63)$$

In case a distribution for the inlet flow angle is given, then reaction is fixed by (φ, ψ, a_1) according to Eq. (3.63).

3.3.9 Aspect Ratio Calculation

The last class of inputs required by the present design procedure is related to the blade dimensions. More specifically, the aspect ratios, AR , for the first and the last stage rotor and stator blades are given and the aspect ratios for the intermediate stage rotor and stator blades are calculated by simple linear interpolation [similarly to the practice by Glassman et al. (1995)].

Let AR_1 and $AR_{N_{stg}}$ be the first and last stage aspect ratio, respectively, either for the rotor or the stator blades. Then, the aspect ratio for the respective blade at stage j is given by:

$$AR_j = AR_1 + \frac{AR_{N_{stg}} - AR_1}{N_{stg} - 1} (j - 1) \quad (3.64)$$

Note that, the aspect ratio of IGVs is set equal to a user-defined input value.

3.3.10 Velocity Triangles Calculation

In this paragraph, the equations and relationships used for calculating the dimensionless (i.e., in terms of φ, ψ, Λ) velocity triangles at the mean, hub, and tip annulus spans, at every stage station, are presented. For compressor stages of arbitrary degree of reaction Λ , the dimensionless velocity triangles nomenclature is shown in Figure 3.12. Note that, Λ determines the degree of the triangle asymmetry.

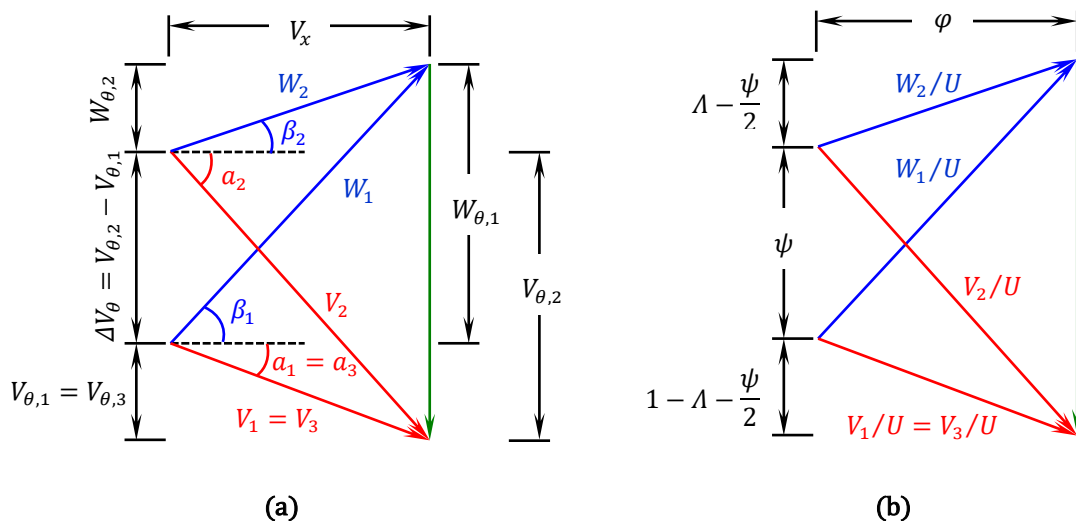


Figure 3.12: Compressor stage velocity triangles in (a) dimensional and (b) dimensionless form for arbitrary degree of reaction, assuming a repeating stage and constant axial velocity and blade speed [adapted from Lewis (1996)].

3.3.10.1 Mean-Line Velocity Triangles

The basic equations describing the velocity vectors across a compressor stage can be found in several introductory turbomachinery textbooks [see Papailiou et al. (2000)]. Most expressions are obtained using the vector equation (3.2) and simple trigonometry to link the different velocity components and flow angles. Making use of the design assumptions of constant axial velocity and constant blade speed (see Section 3.3), and assuming a repeating stage ($\vec{V}_1 = \vec{V}_3$), the different velocity components and flow angles are expressed in non-dimensional form in terms of φ , ψ , and Λ [see Lewis (1996) and Papailiou et al. (2000)].

The absolute flow velocity peripheral component at compressor's inlet ($V_{\theta,1}$) is calculated by:

$$\frac{V_{\theta,1}}{U} = \varphi \tan a_1 \quad (3.65)$$

since the flow angle, a_1 , is imposed. For every other compressor stage, V_{θ} at station 1 is given by:

$$\frac{V_{\theta,1}}{U} = 1 - \Lambda - \frac{\psi}{2} \quad (3.66)$$

Using Euler's pump equation, V_{θ} at station 2 is calculated from:

$$\frac{V_{\theta,2}}{U} = \psi + \frac{V_{\theta,1}}{U} \quad (3.67)$$

At every station 3, V_{θ} is calculated using:

$$\frac{V_{\theta,3}}{U} = \varphi \tan a_3 \quad (3.68)$$

Using the vector equation (3.2), the relative flow velocity peripheral component, W_{θ} , at stations 1 and 2 is given by:

$$\frac{W_{\theta}}{U} = 1 - \frac{V_{\theta}}{U} \quad (3.69)$$

The absolute flow velocity magnitude, V , is then obtained by:

$$\frac{V}{U} = \sqrt{\varphi^2 + \left(\frac{V_{\theta}}{U}\right)^2} \quad (3.70)$$

The above holds at stations 1, 2, and 3. Similarly to Eq. (3.70), the relative flow velocity magnitude, W , is given by:

$$\frac{W}{U} = \sqrt{\varphi^2 + \left(\frac{W_{\theta}}{U}\right)^2} \quad (3.71)$$

at stations 1 and 2.

Finally, the flow absolute and relative angles (α and β , respectively) at stations 1 and 2, are given by:

$$\alpha = \tan^{-1} \frac{V_{\theta}/U}{\varphi} \quad (3.72)$$

$$\beta = \tan^{-1} \frac{W_{\theta}/U}{\varphi} \quad (3.73)$$

Note that, α_3 is assumed equal to α_1 of the following stage, except for the last compressor stage where α_3 is imposed.

3.3.10.2 Hub and Tip Velocity Triangles

In this paragraph, the expressions for the velocity triangles components at the two blade span extremes, namely the annulus hub and the tip, are presented. For this reason, the free-vortex flow approximation described by Eqs (3.19) and (3.20), is utilized. For grouping equations, subscript RP is used which takes the values h for hub and t for tip.

For calculating the blade speed at hub and tip, Eq. (3.3) expressed at the mean (subscript “ m ”) and an arbitrary radial position RP gives:

$$U_{RP} = U \frac{D_{e,RP}}{D_m}$$

Using the above and Eq. (3.19), the definition of the flow coefficient [see also Eq. (3.13)] expressed between the mean and an arbitrary radial position gives:

$$\varphi_{RP} = \varphi \frac{D_m}{D_{e,RP}}$$

The absolute flow velocity peripheral component, V_{θ} , at stations 1, 2, and 3 is given by:

$$\frac{V_{\theta,RP}}{U_{RP}} = \frac{V_{\theta}}{U} \left(\frac{D_m}{D_{e,RP}} \right)^2, \quad RP = h, t \quad (3.74)$$

Using the vector equation (3.2), the relative flow velocity peripheral component, W_{θ} , at stations 1 and 2 is given by:

$$\frac{W_{\theta,RP}}{U_{RP}} = 1 - \frac{V_{\theta,RP}}{U_{RP}}, \quad RP = h, t \quad (3.75)$$

The absolute flow velocity magnitude, V , is then calculated by:

$$\frac{V_{RP}}{U_{RP}} = \sqrt{\left(\varphi \frac{D_m}{D_{e,RP}} \right)^2 + \left(\frac{V_{\theta,RP}}{U_{RP}} \right)^2}, \quad RP = h, t \quad (3.76)$$

at stations 1, 2, and 3. Similarly, the relative flow velocity magnitude, W , is given by the following equation:

$$\frac{W_{RP}}{U_{RP}} = \sqrt{\left(\varphi \frac{D_m}{D_{e,RP}}\right)^2 + \left(\frac{W_{\theta,RP}}{U_{RP}}\right)^2}, \quad RP = h, t \quad (3.77)$$

at stations 1 and 2.

Finally, the flow absolute and relative angles (a and β , respectively) at stations 1 and 2, are given by:

$$a_{RP} = \tan^{-1} \frac{V_{\theta,RP}/U_{RP}}{\varphi(D_m/D_{e,RP})}, \quad RP = h, t \quad (3.78)$$

$$\beta_{RP} = \tan^{-1} \frac{W_{\theta,RP}/U_{RP}}{\varphi(D_m/D_{e,RP})}, \quad RP = h, t \quad (3.79)$$

Note that, a_3 at the annulus hub and tip is taken equal to a_1 of the downstream stage hub and tip, respectively, except for the last compressor stage where a_3 is imposed and is assumed equal to the mean-line value.

3.3.11 Blade Row Solidity Calculation

For calculating the solidity of the rotor and stator blades, which is needed in establishing both the blade count and the blade row total pressure loss, the approach used by Glassman et al. (1995) is followed. Based on values used in the design and development of five transonic core compressors, Glassman et al. correlated the rotor tip solidity with the rotor tip relative Mach number at the stage inlet ($M_{r,t,1}$), and the stator hub solidity with the stator hub turning (Δa_h) which is a measure of the flow diffusion. These correlations read:

$$\sigma_{t,R} = 0.5M_{r,t,1} + 0.7$$

for the rotor, and

$$\sigma_{h,S} = \begin{cases} 0.0206\Delta a_h + 0.794, & \Delta a_h < 44^\circ \\ 0.080\Delta a_h - 1.82, & 44^\circ \leq \Delta a_h < 60^\circ \\ 3, & \Delta a_h \geq 60^\circ \end{cases}$$

for the stator, where: $\Delta a_h = a_{h,2} - a_{h,3}$.

In this design process, the rotor and stator solidities at the mean diameter are required and, therefore, the above correlations are approximated at the mean-line by employing Eq. (3.23) as:

$$\sigma_R \approx \frac{D_{e,t,1}}{D_m} \sigma_{t,R} \quad \text{and} \quad \sigma_S \approx \frac{D_{e,h,1}}{D_m} \sigma_{h,S}$$

for the rotor and the stator, respectively.

Using the above, the rotor (σ_R) and stator (σ_S) solidities are given by:

$$\sigma_R = \frac{D_{e,t,1}}{D_m} (0.5M_{r,t,1} + 0.7) \quad (3.80)$$

$$\sigma_S = \frac{D_{e,h,1}}{D_m} \begin{cases} (0.0206\Delta a + 0.794), & \Delta a < 44^\circ \\ (0.080\Delta a - 1.82), & 44^\circ \leq \Delta a < 60^\circ \\ 3, & \Delta a \geq 60^\circ \end{cases} \quad (3.81)$$

Note that, in Eq. (3.81) the approximation $\Delta a_h \approx \Delta a = a_2 - a_3$ was made in order to avoid iterative solutions since, at this stage of the calculation, the hub values for a_2 and a_3 are not yet known.

Finally, note that for IGVs the row solidity is a direct input value given by the user.

3.3.12 Blade Row Total Pressure Loss Calculation

In this paragraph the equations and relationships used for obtaining the rotor and stator cascade total pressure losses are presented. These equations have the same expression in both the relative (for rotors) and absolute (for stators) frame of reference and, therefore, they are listed here only once. For writing the cascade loss expressions in a uniform way, a local station numbering system is adopted with subscripts 1 and 2 corresponding to the blade row inlet and outlet, respectively. In the stage-wise station numbering system introduced in Figure 3.10, stations 1 and 2 of this local system correspond to stations 1 and 2 for rotors, and stations 2 and 3 for stators.

There are many loss sources across a blade row. Here, it is assumed that the total pressure loss across a cascade comprises the following four (4) loss sources:

- Profile losses
- Endwall losses
- Secondary losses
- Shock losses

3.3.12.1 Profile Losses

Profile losses are associated with the boundary layer development around a blade. Profile losses are correlated with the wake momentum thickness, θ_w , and, in the form of an equivalent drag coefficient they are given by¹⁹:

$$C_{D,pr} = 2 \frac{\theta_w}{c} \left(\frac{\cos \bar{\beta}}{\cos \beta_2} \right)^3 \quad (3.82)$$

where $\bar{\beta}$ is a “mean” flow angle given by [see Aungier (2003)]:

$$\bar{\beta} = \tan^{-1} \left[\frac{1}{2} (\tan \beta_1 + \tan \beta_2) \right] \quad (3.83)$$

¹⁹Cf. equations (6-27) and (6-40) by Aungier (2003) for constant axial velocity across the blade row.

From 2D cascade tests conducted by Lieblein in 1959, θ_w/c is correlated to the blade equivalent diffusion factor, DF_{eq} , where the equivalent diffusion factor of a blade row is defined by [see Dixon (1998)]:

$$DF_{eq} = \frac{\cos \beta_2}{\cos \beta_1} \left[1.12 + \frac{0.61}{\sigma} (\tan \beta_1 - \tan \beta_2) \cos^2 \beta_1 \right] \quad (3.84)$$

For approximating the experimental results of Lieblein, $\theta_w/c = f(DF_{eq})$, Dixon developed an analytical correlation given by:

$$\frac{\theta_w}{c} = \frac{0.004}{1 - 1.17 \ln DF_{eq}} \quad (3.85)$$

According to Dixon, Eq. (3.85) can be used up to $DF_{eq} = 1.9 - 2.0$ for efficient blade row operation. Figure 3.13 shows the experimental relationship $\theta_w/c = f(DF_{eq})$ established by Lieblein as adapted from Aungier (2003), as well as the predictions obtained by Dixon's model. Note that both the practical and diffusion limits are also shown in Figure 3.13.

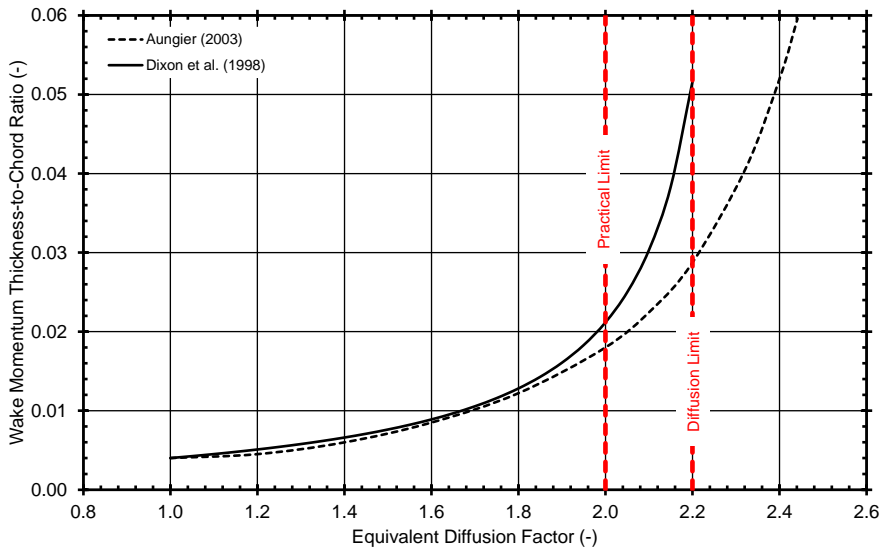


Figure 3.13: Wake momentum thickness-to-chord ratio in terms of equivalent diffusion factor [adapted from Aungier (2003)]. The predictions of Dixon's (1998) model as well as the practical and diffusion limits are also shown on the graph.

3.3.12.2 Endwall Losses

As the name implies, endwall losses arise due to the boundary layers developing along the compressor annulus walls. In terms of a drag coefficient, annulus losses are expressed as [see Aungier (2003)]:

$$C_{D,ew} = 0.02 \frac{s}{\bar{h}_b} = \frac{0.02}{\sigma AR} \quad (3.86)$$

where the definitions for aspect ratio, Eq. (3.24), and solidity, Eq. (3.22), were used.

3.3.12.3 Secondary Losses

Typically, secondary losses include all loss sources that are not part of profile and endwall losses. Secondary losses arise due to secondary flow phenomena along the blade span and they are associated with the 3D nature of the flow inside a blade row. In the form of an equivalent drag coefficient, secondary losses are expressed by [see Aungier (2003)]:

$$C_{D,sc} = 0.018C_L^2 \quad (3.87)$$

where the lift coefficient of the blade is given as:

$$C_L = \frac{2}{\sigma} \cos \bar{\beta} (\tan \beta_1 - \tan \beta_2) \quad (3.88)$$

In the above, $\bar{\beta}$ is calculated using Eq. (3.83).

3.3.12.4 Shock Losses

Shock losses are associated with supersonic flow phenomena. They arise when the flow at the blade inlet is supersonic and shock waves are forming. For calculating the total pressure loss coefficient for shock losses, the model presented by Dixon et al. (2014)²⁰ is used, described by:

$$\omega_{sh} = \begin{cases} 0, & M_{r,1} \leq 1 \\ -0.2599M_{r,1}^3 + 1.4183M_{r,1}^2 - 2.1176M_{r,1} + 0.9605, & M_{r,1} > 1 \end{cases} \quad (3.89)$$

3.3.12.5 Total Loss

Finally, the total loss of a blade row is obtained by summing up the individual losses described above²¹:

$$\omega = \omega_{sh} + \sigma \frac{\cos^2 \beta_1}{\cos^3 \bar{\beta}} [C_{D,sc} + C_{D,ew} + C_{D,pr}] \quad (3.90)$$

Regarding the IGVs, total loss is a user input and is defined as $\omega = (p_2^0 - p_1^0)/(p_1^0 - p_1^s)$. From the latter, p_2^0 is estimated from the known inlet conditions.

3.3.13 Stage Isentropic Efficiency Calculation

Using dimensional analysis, it can be shown that the isentropic (total-to-total conditions) efficiency of a compressor stage depends on five stage parameters according to Lewis (1996). These are φ , ψ , A , and the rotor and stator total pressure loss coefficient ω_R and ω_S , respectively. This correlation can be expressed analytically and is given by [see Lewis (1996)]:

$$\eta_{is} = TF \left\{ 1 - \frac{1}{2\psi} \left[\omega_R \left(\frac{W_1}{U} \right)^2 + \omega_S \left(\frac{V_2}{U} \right)^2 \right] \right\} \quad (3.91)$$

²⁰See figure 5.12 by Dixon et al. (2014).

²¹For casting the equivalent drag coefficient back to the corresponding physical total pressure loss coefficient, equation (6-40) by Aungier (2003) is used.

where W_1/U and V_2/U are given in terms of φ , ψ , and Λ as described in paragraph 3.3.10. In the above, TF is a user-specified technology factor.

Equation (3.91) is only one of the two methods available for establishing the isentropic efficiency of a compressor stage. The second method (if opted by the user) utilizes an iterative procedure on the stage isentropic efficiency η_{is} , and exploits the known stage total enthalpy rise Δh^0 . First, a guess on the value of the isentropic efficiency is made and along with the known Δh^0 the stage pressure ratio p_3^0/p_1^0 is computed using Eqs (3.26) and (3.27). Then, the stage pressure ratio is used to calculate the stage polytropic efficiency η_p using Eq. (3.10) which, in turn, is compared against the polytropic efficiency (let η'_p) predicted by the pressure ratio-polytropic efficiency correlations presented by Glassman (1992a). This procedure is repeated until the two polytropic efficiencies are matched within a prescribed tolerance $|\eta'_p - \eta_p| \leq \varepsilon$.

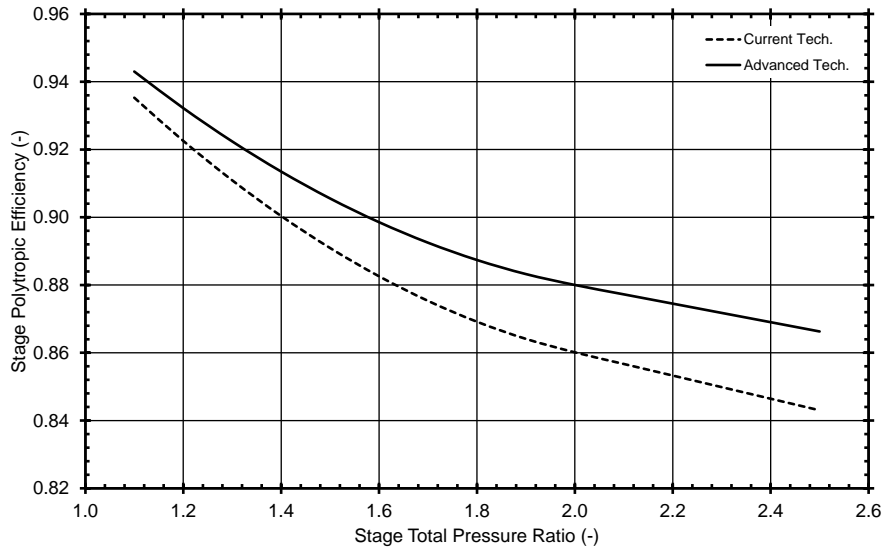


Figure 3.14: Correlations for stage polytropic efficiency versus stage pressure ratio for current- and advanced technology compressor stages [adapted by Glassman (1992a)].

The stage pressure ratio-polytropic efficiency correlations used by Glassman in his studies are depicted in Figure 3.14, and are given by:

$$\eta_p = \begin{cases} 0.054795 \times PR^2 - 0.25337 \times PR + 1.1477, & PR \leq 2 \\ -0.03419 \times PR + 0.9285, & PR > 2 \end{cases} \quad (3.92)$$

for current technology compressor stages, and:

$$\eta_p = \begin{cases} 0.047322 \times PR^2 - 0.21668 \times PR + 1.1241, & PR \leq 2 \\ -0.027392 \times PR + 0.93478, & PR > 2 \end{cases} \quad (3.93)$$

for advanced technology compressor stages. In the above equations, $PR = p_3^0/p_1^0$ is the stage (total) pressure ratio.

3.3.14 Stage Radial Positioning

At this point of the calculation procedure the mass flow across the stage, the stage outlet total temperature and pressure, and the flow velocities and angles across the stage are established. Thus, the stage outlet flow-annulus area ($A_{e,3}$) can be obtained according to paragraph 3.2.3. Knowing $A_{e,3}$, $A_{g,3}$ is then calculated from Eq. (3.31) and the radial positioning of the stage exit is performed easily as follows.

If a constant tip design has been adopted, then the tip diameter at the stage outlet equals the one at the compressor inlet and the hub diameter is calculated from:

$$D_{g,h,3} = \sqrt{D_{g,t,in}^2 - \frac{4A_{g,3}}{\pi}} \quad (3.94)$$

If, on the other hand, a constant hub design is assumed, then the hub diameter at the stage outlet equals the one at compressor's inlet and the tip diameter is calculated from:

$$D_{g,t,3} = \sqrt{\frac{4A_{g,3}}{\pi} + D_{g,h,in}^2} \quad (3.95)$$

Finally, for the case of a mean diameter distribution (see paragraph 3.3.6), the tip ($D_{g,t,3}$) and hub ($D_{g,h,3}$) diameters at the stage outlet are given by:

$$D_{g,t,3} = D_m + \frac{A_{g,3}}{\pi D_m} \quad (3.96)$$

$$D_{g,h,3} = D_m - \frac{A_{g,3}}{\pi D_m} \quad (3.97)$$

Finally, the hub and tip diameters at station 2 are approximated as the average of the respective stage inlet (station 1) and outlet (station 3) diameters, according to the following equations:

$$D_{g,h,2} = \frac{D_{g,h,1} + D_{g,h,3}}{2} \quad (3.98)$$

$$D_{g,t,2} = \frac{D_{g,t,1} + D_{g,t,3}}{2} \quad (3.99)$$

Having established the geometric diameters, the effective ones are obtained by employing Eqs (3.36) and (3.37).

3.3.15 Next Stage Aerodynamic Design and Overall Compressor Performance

The above calculation procedure (paragraphs 3.3.2 through 3.3.14) continues with the next stage, j , where the inlet total temperature and pressure equal the ones at the exit of the previous stage, $j - 1$, or:

$$(T_1^0)_j = (T_3^0)_{j-1} \text{ and } (p_1^0)_j = (p_3^0)_{j-1}$$

For geometry continuity²², the same applies for the stage inlet diameters:

$$(D_{g,h,1})_j = (D_{g,h,3})_{j-1} \text{ and } (D_{g,t,1})_j = (D_{g,t,3})_{j-1}$$

At the end of this calculation process, the compressor exit is reached and the compressor radial positioning is completed. Also, the compressor overall work input and total pressure ratio are obtained allowing for the calculation of the compressor isentropic (η_{is}) and polytropic (η_p) efficiencies. These are given by the following equations:

$$\eta_{is} = \frac{h_{out,is}^0 - h_{in}^0}{h_{out}^0 - h_{in}^0} \quad (3.100)$$

$$\eta_p = \frac{R_g}{\phi_{out}^0 - \phi_{in}^0} \ln \frac{p_{out}^0}{p_{in}^0} \quad (3.101)$$

For calculating the isentropic temperature and enthalpy at the compressor exit, the following equation is used:

$$\phi_{out,is}^0 = \phi_{in}^0 + R_g \ln \frac{p_{out}^0}{p_{in}^0} \quad (3.102)$$

Note here, that apart from the aerodynamic design for establishing the compressor efficiencies, another method was also implemented and is the one presented by Samuelsson et al. (2015) (see Appendix B). In this case, the aerodynamic design could still be employed for establishing the compressor dimensions, but the component overall efficiency is obtained based on overall correlations which correct a nominal efficiency for EIS, component size, and Reynolds number effects.

3.4 Compressor Axial Positioning and Gas-Path Visualization

Having determined the compressor radial positioning in Section 3.3, the next step is to calculate the basic blade dimensions (e.g., blade count, chord lengths, etc.) and, ultimately, to establish the compressor gas-path axial coordinates and to visualize the

²²Since the flow velocities and angles are determined by imposing (different, in general) φ , ψ , and Λ values on every stage, the flow velocity and angle at the inlet of a stage are not necessarily equal to those exiting the previous stage. Thus, the inlet area of a stage will not, in general, be equal to the outlet area of the previous stage, even when we consider the same total temperature and pressure conditions across both flow stations. Therefore, hub and tip diameters will also differ between the two flow stations. The same rationale applies when a mean diameter distribution is considered [see Eqs (3.96) and (3.97)] where successive stages will, in general, have different mean diameters. For the above reasons, and in order to ensure geometrical continuity, equality on the hub and tip radii between the inlet and outlet of successive stages is imposed.

compressor meridional view. In the present section, the relevant methodology is presented.

3.4.1 Blade Dimensions Calculation

Here the equations used to estimate basic blade dimensions are presented. Since the equations used have the same expression for both rotors and stators, they are listed only once. For this reason, the local numbering convention adopted in paragraph 3.3.12 is also used here, according to which subscripts 1 and 2 are used for the blade row inlet and outlet, respectively. Again, in the stage-wise station numbering system (see Figure 3.10), stations 1 and 2 of the local system correspond to stations 1 and 2 for rotors, and stations 2 and 3 for stators.

3.4.1.1 Blade Count

The number of blades comprising a blade row is estimated using Eq. (3.21) applied at the mean-line. Equation (3.21) can be rewritten in terms of the blade aspect ratio instead of the blade chord in the form:

$$Z_b = \left[\frac{\pi AR \sigma D_m}{\bar{h}_b} \right] \quad (3.103)$$

where Eq. (3.24) was used to replace the chord with AR . The blade (average) height, \bar{h}_b , is expressed (in the local numbering system) by:

$$\bar{h}_b = \frac{D_{g,t,1} - D_{g,h,1} + D_{g,t,2} - D_{g,h,2}}{4} \quad (3.104)$$

3.4.1.2 Stagger Angles

In the present design method it is assumed that the airfoils comprising a blade are constructed by circular- or equivalent circular-arc camber lines. For these types of camber lines, the stagger angle can be expressed as the average of the LE and TE metal angles [see Aungier (2003)]:

$$\gamma = \frac{\kappa_{LE} + \kappa_{TE}}{2}$$

where κ_{LE} and κ_{TE} are the camber line tangent angles w.r.t. the axial direction at the blade LE and TE, respectively. For preliminary design purposes, the flow incidence and deviation are assumed zero and, therefore, κ_{LE} and κ_{TE} are assumed approximately equal to the flow angles at the blade row inlet (β_1) and outlet (β_2), respectively. Therefore:

$$\gamma = \frac{\beta_1 + \beta_2}{2} \quad (3.105)$$

at the mean-line.

Likewise, the stagger angles at the blade hub (γ_h) and tip (γ_t) are estimated by using the values of the hub and tip flow angles into Eq. (3.105).

3.4.1.3 Chord Lengths

The blade true chord length at the mean-line is estimated by Eq. (3.21) which, rearranged, gives:

$$c = \frac{\pi \sigma D_m}{Z_b} \quad (3.106)$$

where Z_b has been estimated by Eq. (3.103). Note that, in this design procedure the chord is assumed constant along the blade height ($c_h = c_t = c$), i.e., blades without taper are assumed ($TR = 1$).

From simple trigonometry, the blade axial chord length at the mean-line is calculated using:

$$c_x = c \cos \gamma \quad (3.107)$$

Equation (3.107) is used at the blade hub and tip to establish the respective axial chord lengths using γ_h and γ_t , respectively, and also utilizing the fact that $c_h = c_t = c$.

Figure 3.15 illustrates the axial chord lengths across a compressor stage at the three characteristic radial positions (hub, mean, tip), which are used to axially position the compressor gas-path.

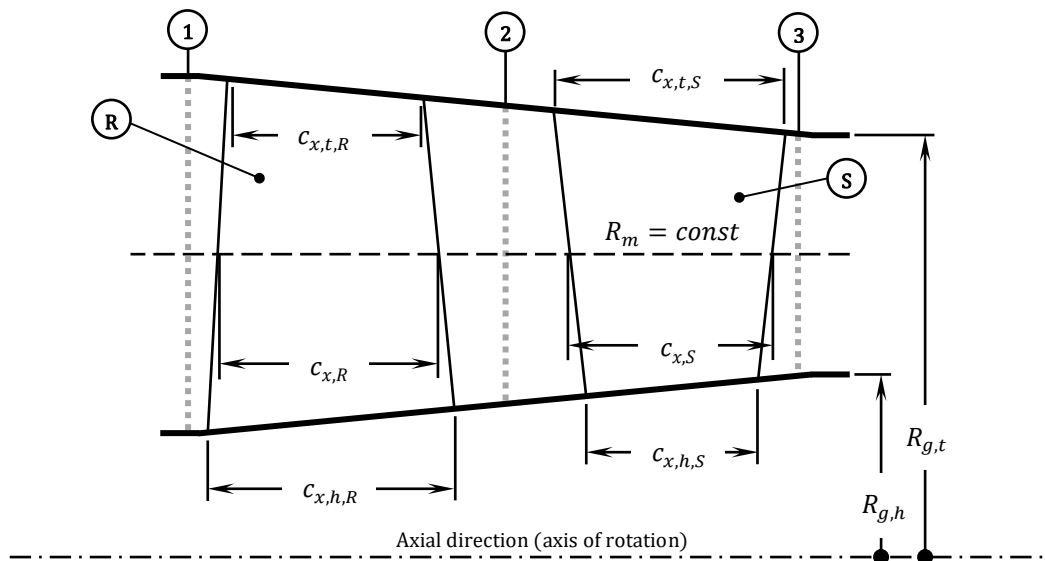


Figure 3.15: Compressor stage rotor (R) and stator (S) axial chord lengths along the blade span.

3.4.2 Axial Coordinates Calculation

In the present paragraph, the axial coordinates of a stage and, in a latter step, of the whole compressor, are estimated following primarily the procedure described by Mattingly (2005).

3.4.2.1 Axial Gap Calculation

First, the axial gaps between successive rows are set. According to Walsh et al. (2004), the axial gap between two adjoining blade rows must be large enough to minimize

vibratory excitation and to avoid clipping, while it should be maintained small enough for obtaining minimum engine length and weight.

In the present design process, the gap percentage (g_x) between a rotor and its downstream stator (referred to as the “rotor gap”), and the gap between a stator and its downstream rotor (referred to as the “stator gap”), are calculated from simple linear interpolation between an inlet and an outlet value according to:

$$(g_x)_j = (g_x)_1 + \frac{(g_x)_{N_{stg}} - (g_x)_1}{N_{stg} - 1} (j - 1) \quad (3.108)$$

where j is the stage number and $(g_x)_1$ and $(g_x)_{N_{stg}}$ is the rotor and stator gap percentage for the first and the last stage, respectively.

Here, the rotor and the stator gap percentages are defined with respect to the axial chord length at the rotor hub and the stator tip, $c_{x,h,R}$ and $c_{x,t,S}$, respectively. For the case of a compressor with IGVs, the corresponding gap percentage between the IGVs and the first compressor rotor is a user-specified input and is defined with respect to the axial chord length at the IGVs tip.

Examining real compressor 2D cutaways, values for the first and the last stage rotor gaps were found equal to 30% and 72%, respectively, while for the stator gap the inlet and exit values were equal to 30% and 60%, respectively. For stages where a mass bleed occurred, the stator gap was found equal to 90%. This value means that the stator and its downstream rotor were almost one axial width apart for facilitating the necessary mass extraction. Note that, Walsh et al. (2004) quote a typical value of 20% for the gap percentage between any two blade rows.

3.4.2.2 Compressor Axial Positioning

Here, the axial positioning of the compressor gas-path is described. To what follows, a stage-wise station numbering is adopted as illustrated in Figure 3.16.

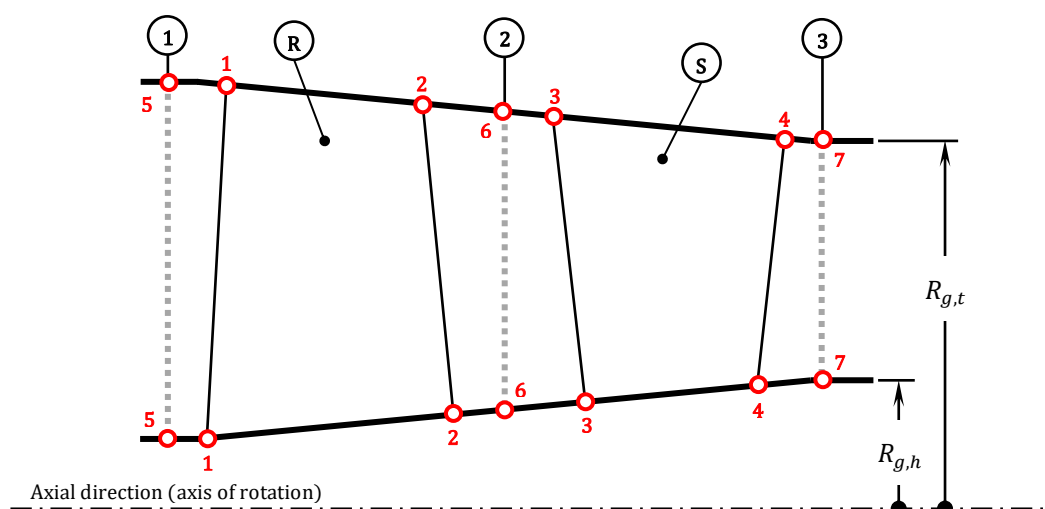


Figure 3.16: Numbering system used in the estimation of the axial coordinates of the rotor (R) and the stator (S) of a compressor stage. For convenience, the same indices (i.e., 1, 2, 3, 4, 5, 6, and 7) are used for both the annulus hub and tip, and each number identifies uniquely a gas-path station: 1 → rotor inlet, 2 → rotor outlet, 3 → stator inlet, 4 → stator outlet; indices 5, 6, and 7 correspond to stations 1, 2, and 3 of the 1D calculation.

First, an origin is selected, let $x_{h,1}$. For every compressor stage with $j > 1$, $x_{h,1}$ is calculated from the recursive formula:

$$(x_{h,1})_j = (x_{h,1})_1 + \sum_{k=1}^{j-1} \left\{ [1 + (g_{x,R})_k] (c_{x,h,R})_k + [1 + (g_{x,S})_k] (c_{x,t,S})_k \right\} \quad (3.109)$$

where, for the first compressor stage ($j = 1$), $(x_{h,1})_1$ is given by:

$$(x_{h,1})_1 = \begin{cases} \frac{1}{4} [(c_{x,h,R})_1 + (c_{x,t,R})_1], & \text{no IGVs} \\ (1 + g_{x,IGV}) c_{x,t,IGV}, & \text{with IGVs} \end{cases} \quad (3.110)$$

Next, the axial coordinates of the hub at station 2, the tip at station 3, and the tip at station 4 are calculated sequentially (see Figure 3.17) at every stage using Eqs (3.111)–(3.113).

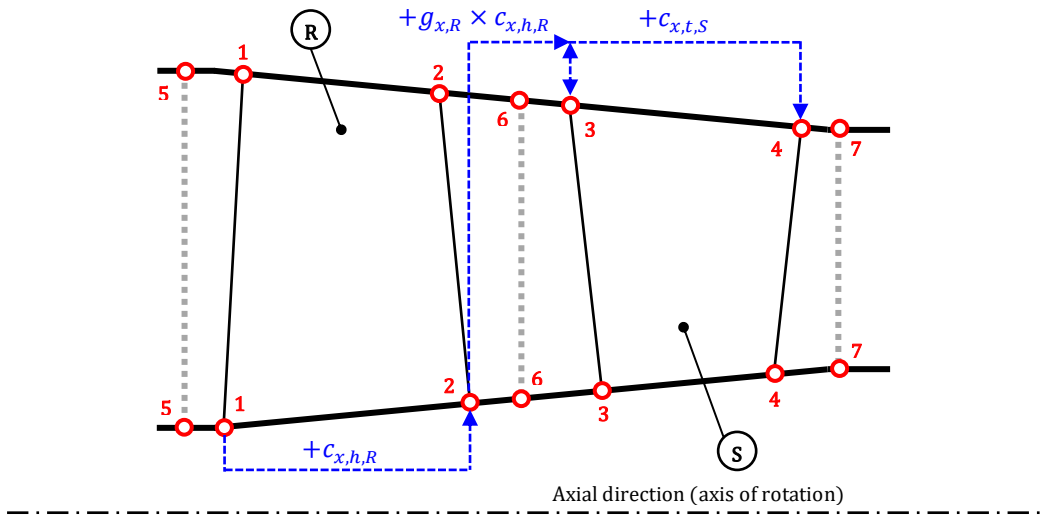


Figure 3.17: Rotor (R) hub and stator (S) tip axial coordinates calculation. Arrows indicate the sequence of the calculation.

$$x_{h,2} = x_{h,1} + c_{x,h,R} \quad (3.111)$$

$$x_{t,3} = x_{h,2} + g_{x,R} \times c_{x,h,R} \quad (3.112)$$

$$x_{t,4} = x_{t,3} + c_{x,t,S} \quad (3.113)$$

With the hub axial coordinates of the rotor and the tip axial coordinates of the stator fully defined, the remaining blade coordinates are calculated according to the calculation sequence presented in Figure 3.18. Therefore, the rotor tip and the stator hub axial coordinates are given for every compressor stage (j) by Eqs (3.114) through (3.117).

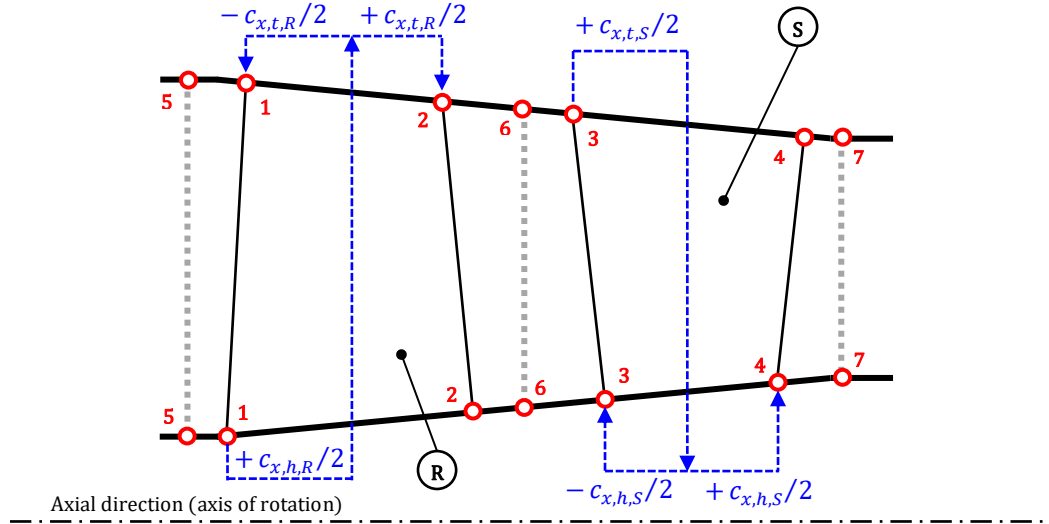


Figure 3.18: Rotor (R) tip and stator (S) hub axial coordinates calculation. Arrows indicate the sequence of the calculation.

$$x_{t,1} = x_{h,1} + \frac{1}{2}(c_{x,h,R} - c_{x,t,R}) \quad (3.114)$$

$$x_{t,2} = x_{h,1} + \frac{1}{2}(c_{x,h,R} + c_{x,t,R}) \quad (3.115)$$

$$x_{h,3} = x_{t,3} + \frac{1}{2}(c_{x,t,S} - c_{x,h,S}) \quad (3.116)$$

$$x_{h,4} = x_{t,3} + \frac{1}{2}(c_{x,t,S} + c_{x,h,S}) \quad (3.117)$$

The axial coordinates of the tip at stations 5, 6, and 7 are given for every stage by:

$$x_t = x_h \quad (3.118)$$

where the hub coordinates are given by:

$$(x_{h,5})_j = \begin{cases} 0, & j = 1, \text{ no IGVs} \\ \frac{1}{4}[c_{x,h,IGV} + c_{x,t,IGV} + (x_{h,1})_j + (x_{t,1})_j], & j = 1, \text{ with IGVs} \\ \frac{1}{4}[(x_{h,4})_{j-1} + (x_{t,4})_{j-1} + (x_{h,1})_j + (x_{t,1})_j], & j > 1 \end{cases} \quad (3.119)$$

$$x_{h,6} = \frac{1}{4}(x_{h,2} + x_{t,2} + x_{h,3} + x_{t,3}) \quad (3.120)$$

$$(x_{h,7})_j = \begin{cases} (x_{h,5})_{j+1}, & j < N_{stg} \\ (x_{h,4})_j + \frac{1}{4}[(c_{x,h,S})_j + (c_{x,t,S})_j], & j = N_{stg} \end{cases} \quad (3.121)$$

Finally, since IGVs are stator blades, the same station numbering introduced in Figure 3.16 applies (for calculation convenience) but only stations 3, 4, and 7 are considered. Then, the axial positioning of the IGVs is achieved using the following set of equations:

$$x_{h,3} = 0 \quad (3.122)$$

$$x_{t,3} = x_{h,3} \quad (3.123)$$

$$x_{h,4} = x_{t,3} + \frac{1}{2}(c_{x,t,IGV} + c_{x,h,IGV}) \quad (3.124)$$

$$x_{t,4} = x_{t,3} + c_{x,t,IGV} \quad (3.125)$$

with $x_{t,7} = x_{h,7}$ and $x_{h,7}$ equal to $x_{h,5}$ of the first stage.

3.4.2.3 Compressor Gas-Path Visualization

For producing a smooth compressor gas-path for visualization purposes, the radii at stations 1, 2, 3, and 4 in Figure 3.16 are estimated according to the following set of equations:

$$R_{g,RP,1} = \frac{x_{RP,1} - x_{RP,5}}{x_{RP,6} - x_{RP,5}}(R_{g,RP,6} - R_{g,RP,5}) + R_{g,RP,5}, \quad RP = h, t \quad (3.126)$$

$$R_{g,RP,2} = \frac{x_{RP,2} - x_{RP,5}}{x_{RP,6} - x_{RP,5}}(R_{g,RP,6} - R_{g,RP,5}) + R_{g,RP,5}, \quad RP = h, t \quad (3.127)$$

$$R_{g,RP,3} = \frac{x_{RP,3} - x_{RP,6}}{x_{RP,7} - x_{RP,6}}(R_{g,RP,7} - R_{g,RP,6}) + R_{g,RP,6}, \quad RP = h, t \quad (3.128)$$

$$R_{g,RP,4} = \frac{x_{RP,4} - x_{RP,6}}{x_{RP,7} - x_{RP,6}}(R_{g,RP,7} - R_{g,RP,6}) + R_{g,RP,6}, \quad RP = h, t \quad (3.129)$$

where, according to Figure 3.16, the radius at stations 5, 6, and 7 is equal to the radius obtained by the 1D calculation at stations 1, 2, and 3, respectively.

Finally, for IGVs, the respective hub and tip radii are obtained according to the following equations:

$$R_{g,RP,3} = \frac{1}{2}D_{RP,in}, \quad RP = h, t \quad (3.130)$$

$$R_{g,RP,4} = \frac{x_{RP,4} - x_{RP,3}}{x_{RP,7} - x_{RP,3}}(R_{g,RP,7} - R_{g,RP,3}) + R_{g,RP,3}, \quad RP = h, t \quad (3.131)$$

In the above, $R_{g,h,7}$ and $R_{g,t,7}$ are equal to $R_{g,h,5}$ and $R_{g,t,5}$ of the first stage, respectively.

3.5 Axial Turbine 1D Aerothermodynamic Design

Here, the methodology and equations employed for estimating the isentropic and polytropic efficiencies of axial-flow, multi-stage, cooled or uncooled turbines is presented. As a guideline, the design procedure developed by Glassman (1992b) is used with several modifications, additions, and improvements. Figure 3.19 shows a schematic of the meridional view for an axial-flow turbine.

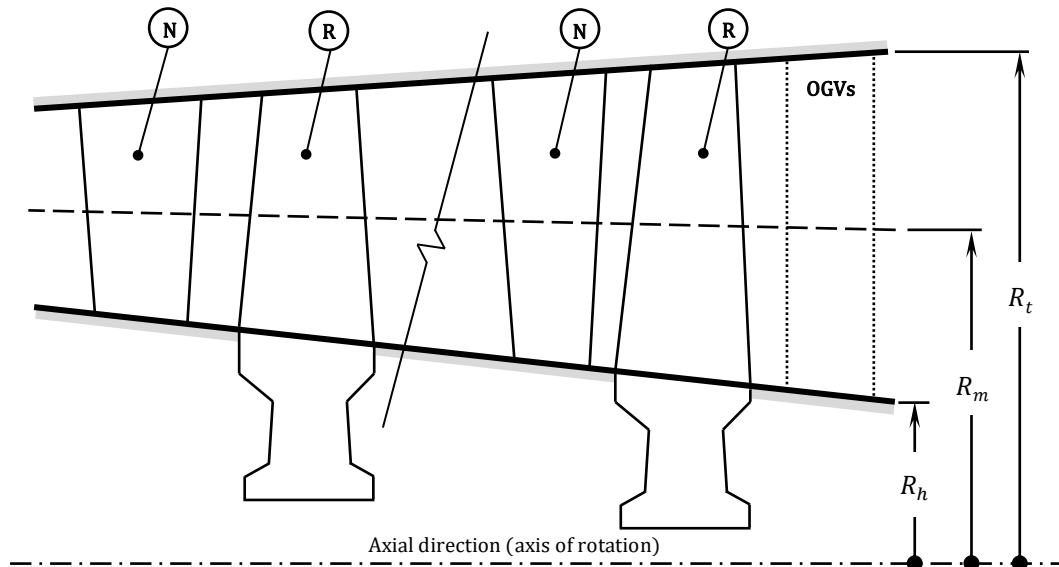


Figure 3.19: Axial-flow turbine flow-annulus, blading, and geometry nomenclature, where R stands for rotor and N for nozzle.

Similarly to the compressor component design, turbines are also designed by a mean-line approach in a stage-by-stage manner following (again) the next two design assumptions:

1. Constant mean diameter ($D_m = const \rightarrow U_m = const$), and
2. constant axial velocity ($V_x = const$).

Again, the above do not necessarily hold across the turbine, meaning that both the mean diameter and the axial velocity can vary throughout the turbine but they remain constant across a stage.

To perform necessary calculations along the blade span, the free-vortex flow approximation expressed by Eqs (3.18)–(3.20), is employed. The stage geometry, nomenclature and station numbering used in the present and following paragraphs are shown in Figure 3.20.

Before moving on to describe the design procedure for turbine components, note that some calculations are identical to the ones presented in Section 3.3 for the aerothermodynamic design of compressors and, therefore, they will only be referenced here. The only difference in the stage-wise nomenclature between turbine and compressor stages is the station numbering notation. For uniformity, the station numbering across the rotor blades where the work interchange between the machine and the flow takes place in a stage, is maintained between compressors and turbines.

Therefore, in turbine stages the station numbers 0, 1, and 2 are used instead of 1, 2, and 3, respectively.

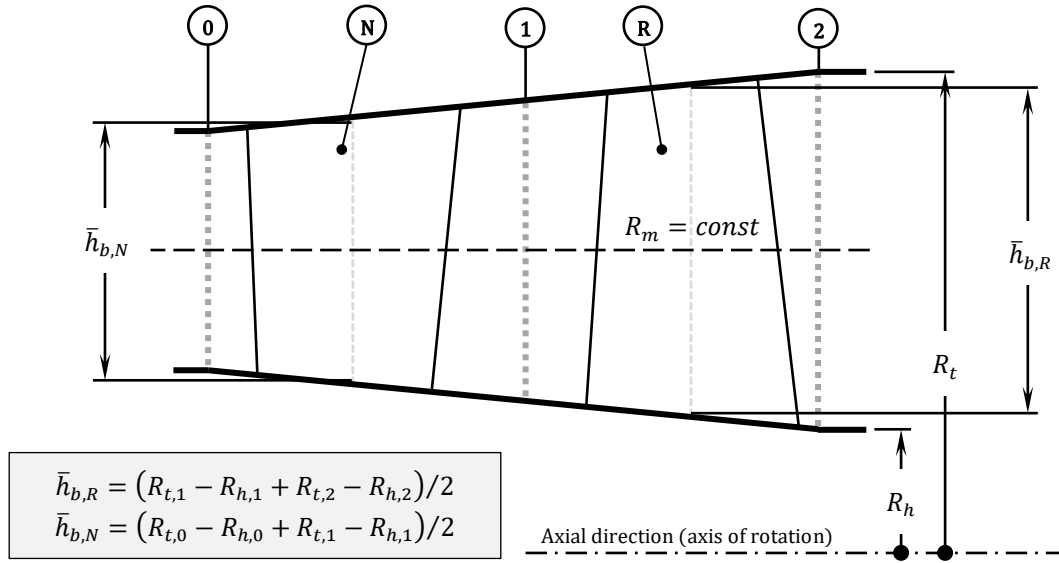


Figure 3.20: Turbine stage meridional view, station numbering, and nomenclature for mean-line calculation. As is the common design practice, turbine stages comprise a nozzle blade (N) followed by a rotor blade (R). For simplicity reasons and for minimizing the necessary design inputs, it is assumed that the nozzle outlet and the rotor inlet flow stations coincide thermodynamically and kinematically thus, the common station numbering “1”.

3.5.1 Stage-by-Stage Calculation

Similarly to the compressor stage-by-stage calculation described in paragraph 3.3.1, the stage-by-stage calculation for a turbine component starts at the turbine inlet and terminates at turbine’s exit. The calculation is performed sequentially through every turbine stage assuming that the stage inlet flow conditions and geometry are known, and aims at determining the stage outlet flow conditions and geometry which, in turn, are used for carrying the calculation on with the downstream stage. At the end of this procedure, the calculation of the turbine exit conditions (and, thus, performance) and the turbine radial positioning are accomplished.

The calculation across a stage is summarized as follows. Knowing the total conditions at the stage inlet ($\dot{m}_0, T_0^0, p_0^0, a_0, M_0$), the exit ones ($\dot{m}_2, T_2^0, p_2^0, a_2, M_2$) are calculated. With known the stage work input, $h_2^0 = h_0^0 + \Delta h^0$, the stage pressure ratio is given by:

$$PR = \frac{p_2^0}{p_0^0} = e^{\frac{\phi_{2,is}^0 - \phi_0^0}{R_g}} \quad (3.132)$$

The value of $h_{2,is}^0$ required for calculating $\phi_{2,is}^0$ in Eq. (3.132) is obtained from the definition of the isentropic efficiency [see Eq. (3.11)]:

$$h_{2,is}^0 = h_0^0 - \frac{\Delta h^0}{\eta_{is}} \quad (3.133)$$

where it is assumed that the stage isentropic efficiency (η_{is}) is known.

Having determined the stage exit total temperature and pressure as $T_2^0 = h^{-1}(h_2^0)$ and $p_2^0 = p_0^0 \times PR$, respectively, the stage exit flow-annulus area (and thus dimensions) are estimated according to the methodology described in paragraph 3.2.3 given, additionally, the mass flow and the velocity triangle (flow angle and Mach number) at the stage outlet (\dot{m}_2, a_2, M_2). Therefore, both the stage performance and geometry are fully defined.

In the following paragraphs the equations and methodology followed for establishing the stage work input and isentropic efficiency are described and commented upon.

3.5.2 Mass Flow Calculation

In this design methodology, turbines with one (1) returning bleed, \dot{m}_{rb} , are considered. The mass flow rate at the inlet of each blade row is calculated by the simple mass balance illustrated in Figure 3.21 and, for every turbine stage j , this is given by the recursive formulas expressed by Eq. (3.134) and Eq. (3.135) for the nozzle and rotor blades, respectively.

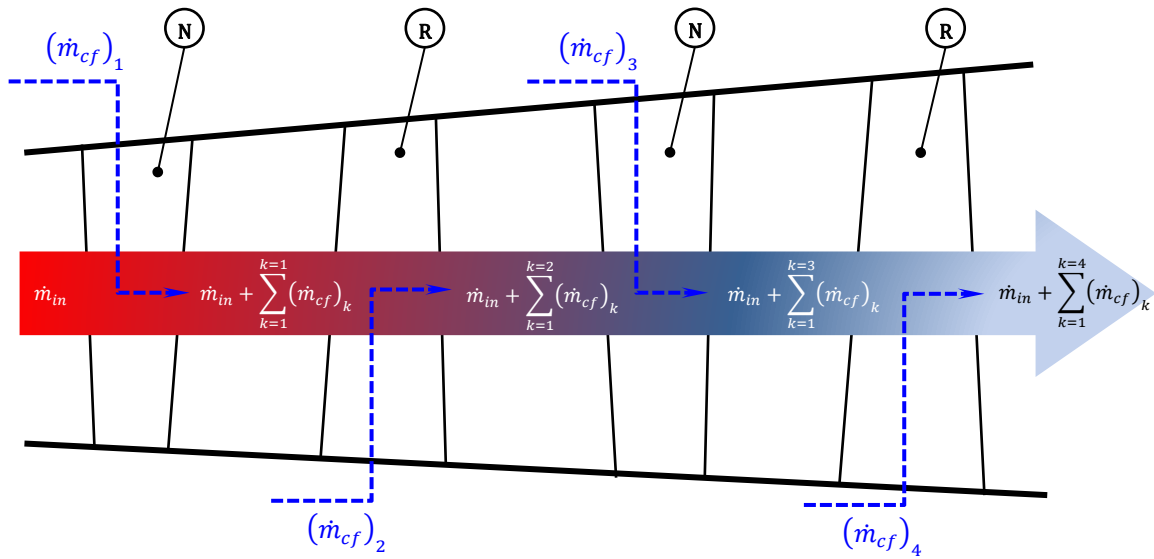


Figure 3.21: Example of mass balance for a two stage turbine (four blade rows in total) with returning bleeds for nozzle (N) and rotor (R) cooling.

$$(\dot{m}_0)_j = \dot{m}_{in} + \sum_{k=1}^{k=j-1} [(\dot{m}_{cf})_{2k-1} + (\dot{m}_{cf})_{2k}] \quad (3.134)$$

$$(\dot{m}_1)_j = \dot{m}_{in} + \sum_{k=1}^{k=2j-1} (\dot{m}_{cf})_k \quad (3.135)$$

In Eqs (3.134) and (3.135), \dot{m}_{cf} is the blade row cooling mass flow rate, with $\sum \dot{m}_{cf} = \dot{m}_{rb}$ over the $2 \times N_{stg}$ blade rows.

For defining the cooling flow for each blade row (\dot{m}_{cf}), the methodology described by Wilcock et al. (2005) is applied according to which the required cooling mass flow rate is determined from:

$$\frac{\dot{m}_{cf}}{\dot{m}_g} = \frac{K_{cool} \varepsilon_0 - \varepsilon_f [1 - \eta_{int} (1 - \varepsilon_0)]}{1 + B \eta_{int} (1 - \varepsilon_0)} \quad (3.136)$$

The mainstream gas flow, \dot{m}_g , equals \dot{m}_0 for nozzles and \dot{m}_1 for rotors. In Eq. (3.136) the parameter B is given by:

$$B = \text{Bi}_{tbc} - \frac{\varepsilon_0 - \varepsilon_f}{1 - \varepsilon_0} \text{Bi}_{met} \quad (3.137)$$

and the blade cooling effectiveness ε_0 is estimated by:

$$\varepsilon_0 = \frac{T'_g - T_{met}}{T'_g - T_{cf}} \quad (3.138)$$

In Eq. (3.138), T_{met} is the allowable external surface metal temperature for the blade (assumed constant over the blade) which is a user-defined input, T_{cf} is the coolant temperature (input or equal to that of the gas bleed taken from the compressor), and the mainstream gas temperature, T'_g , is calculated according to:

$$T'_g = T_g + K_{comb} \Delta T_{comb} \quad (3.139)$$

In the above, T_g equals T_0^0 and $T_{r,1}^0$ for nozzles and rotors, respectively, ΔT_{comb} is the combustion temperature rise, and K_{comb} is a combustion pattern factor (0.15 for the first cooled nozzle and reduces progressively in subsequent cooled rows).

Table 3.2: Cooling technology constants in terms of cooling technology level [see Wilcock et al. (2005)]

Cooling Technology Level	K_{cool} (-)	η_{int} (-)	ε_f (-)	Bi_{met} (-)	Bi_{tbc} (-)
Current	0.045	0.70	0.40	0.15	0.30
Advanced	0.045	0.75	0.45	0.15	0.40
Super-advanced	0.045	0.80	0.50	0.15	0.50

In conclusion, given the allowable metal temperature for a blade (T_{met}), Wilcock et al.'s method estimates the required mass flow required for cooling²³ based on five cooling technology constants, namely: (a) the cooling flow factor (K_{cool}), (b) the internal cooling efficiency (η_{int}), (c) the film cooling effectiveness (ε_f), (d) the metal Biot number (Bi_{met}), and (e) the thermal barrier coating Biot number (Bi_{tbc}). Typical values for the cooling constants are given in Table 3.2 in terms of the cooling technology level.

²³The method could be used in reverse, that is, for a specified cooling mass flow the blade metal temperature is estimated.

3.5.3 Turbine Inlet and Exit Calculation

The turbine inlet flow-annulus dimensions (hub, mean, and tip diameters) are estimated similarly to compressor's following the methodology described in paragraph 3.3.4 given, additionally, the flow Mach number and hub-to-tip ratio.

Likewise, the turbine exit dimensions are estimated following the calculations described in paragraph 3.3.5 for establishing the compressor exit hub, mean, and tip diameters. Again, the flow Mach number and the hub-to-tip ratio (if required) at the exit station are specified. Similarly to the compressor component, the same four (4) design options for establishing the mean-line shape across the turbine are available: (a) constant mean diameter, (b) constant tip diameter, (c) constant hub diameter, and (d) specified mean-line distribution.

3.5.4 Mean-Line Distribution

One of the available design options for specifying the turbine mean-line shape is by imposing a mean-line distribution between the inlet (first stage nozzle inlet) and exit (last stage rotor outlet) mean diameters. Here, the stage diameter is constant and assumed to be equal to that at the respective rotor outlet. Figure 3.22 shows an example of a linear mean diameter distribution.

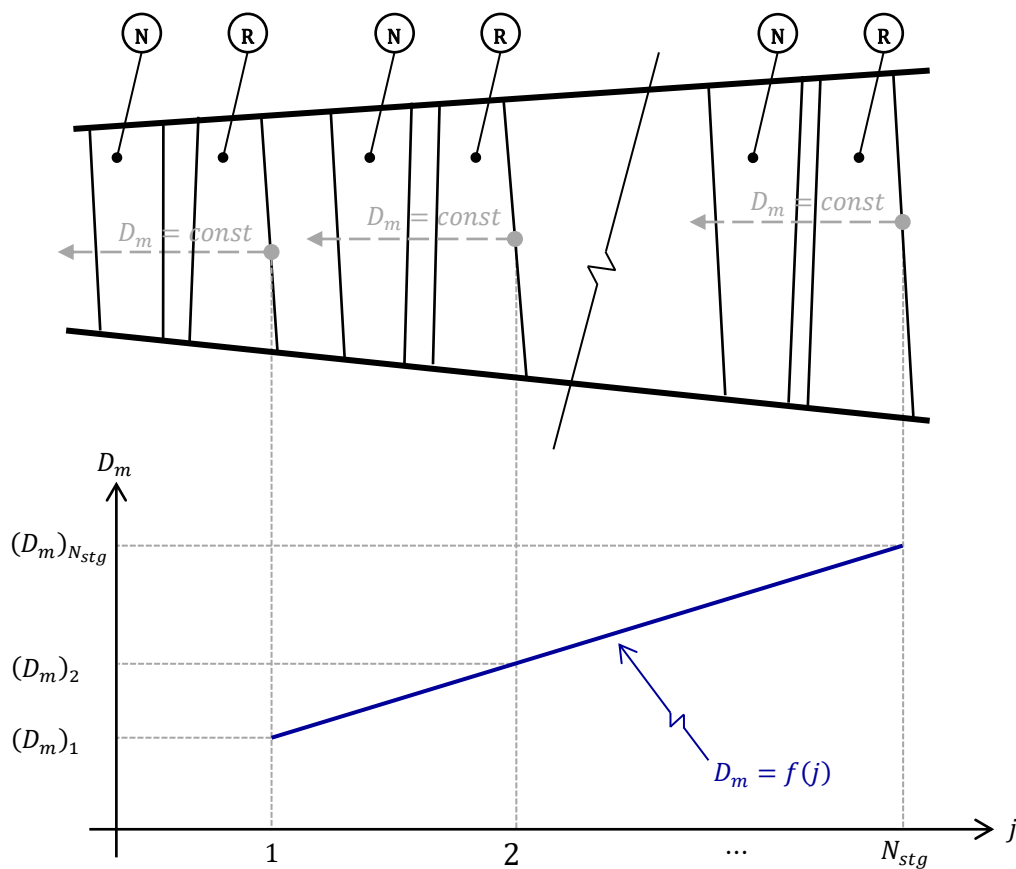


Figure 3.22: Diagrammatic example of a linear mean diameter distribution for specifying the mean-line shape of a turbine component. In the present modelling approach, is assumed that the stage mean diameter is constant and equal to that at the respective rotor outlet.

In the present modelling approach, there are three (3) possible mean-line distributions:

- Linear from turbine inlet to turbine exit
- Constant from turbine inlet up to a stage and then linear up to exit
- Linear from turbine inlet up to a stage and then constant up to exit

Option 1: Linear from Inlet to Outlet

For the first design option, the mean diameter distribution is given by:

$$(D_m)_j = \frac{D_{m,out} - D_{m,in}}{N_{stg}} j + D_{m,in} \quad (3.140)$$

Option 2: Constant from Inlet up to Stage, then Linear up to Exit

For the second design option, the mean diameter distribution is given by:

$$(D_m)_j = \begin{cases} D_{m,in}, & j \leq j^* \\ \frac{D_{m,out} - D_{m,in}}{N_{stg} - j^*} (j - j^*) + D_{m,in}, & j > j^* \end{cases} \quad (3.141)$$

Option 3: Linear from Inlet up to Stage, then Constant up to Exit

For the third design option, the mean diameter distribution is given by:

$$(D_m)_j = \begin{cases} \frac{D_{m,out} - D_{m,in}}{j^*} j + D_{m,in}, & j \leq j^* \\ D_{m,out}, & j > j^* \end{cases} \quad (3.142)$$

In Eqs (3.140)- (3.142), j and j^* is the stage number and the number of the stage where the distribution slope changes, respectively.

Finally, for the case where a constant tip or constant hub design option is selected, then the mean diameter is again calculated by Eq. (3.140) assuming linear variation from turbine's inlet to turbine's exit.

Concluding, after the calculation of the inlet and outlet turbine sections has been completed, the mean diameter along the turbine can be computed and thus, is to what follows, a known quantity in every stage and station of the turbine.

3.5.5 Rotational and Blade Speed Calculation

With the mean diameter distribution along the turbine being known, blade speed at the mean-line is calculated according to Eq. (3.3), and is hereafter a known quantity and constant across a stage. Equation (3.3) involves the component rotational speed (N_{mech}) which is either an input (e.g., is imposed by an external load) or it is estimated based on disk and blade stress criteria. For the later, mechanical integrity reasons dictate that:

$$AN_{mech}^2 \leq (AN_{mech}^2)_{max}$$

where AN_{mech}^2 is the product of the flow-annulus area mid-way along the rotor blade and the blade rotational speed, and expresses the maximum mechanical stress exerted at the root of the blade [see Saravanamuttoo et al. (2017)].

The product AN_{mech}^2 poses a limit with respect to current material and cooling technologies, and typical values for it can be found in various turbomachinery handbooks (see Appendix A). For instance, according to Walsh et al. (2004) $(AN_{mech}^2)_{max} \leq (20 - 50) \times 10^6 \text{ m}^2 \cdot \text{rpm}^2$ for the last stage rotor of a turbine component, where the lower values are used for small, low-technology uncooled turbines, and the higher values for heavyweight, modern-technology cooled turbines.

3.5.6 Stage Performance Parameters Calculation

Similarly to the compressor component design, in the present paragraph the available options on imposing values for the stage performance parameters (φ, ψ, Λ) are presented.

3.5.6.1 Flow Coefficient

For calculating the stage flow coefficient, φ , the stage axial velocity V_x is imposed across every stage using linear interpolation between the turbine inlet and exit values according to Eq. (3.58).

The inlet and outlet axial velocities are calculated from the known velocity triangles, $V_{x,in} = V_{in} \cos a_{in}$ and $V_{x,out} = (V_{out} / \sqrt{E_a}) \cos a_{out}$, with E_a being a user-defined quantity that expresses the squared ratio of the stage exit to the stage average axial velocities [see Glassman (1992b)]:

$$\sqrt{E_a} = \frac{V_{x,2}}{(V_{x,0} + V_{x,1} + V_{x,2})/3} \approx \frac{V_{x,2}}{V_x} \quad (3.143)$$

Then, the calculation of φ follows from definition [see Eq. (3.13)].

3.5.6.2 Loading Coefficient

In this design approach, there are available three (3) options for imposing ψ on every turbine stage. The first one assumes a constant average value $\bar{\psi}$ in every stage, given by:

$$\psi_j = \bar{\psi} = \frac{P_{wr,TRB}}{\sum_{j=1}^{j=N_{stg}} (\dot{m}_1)_j U_j^2} \quad (3.144)$$

with \dot{m}_1 calculated according to Eq. (3.135).

The second option assumes a constant $\overline{\Delta h^0}$ distribution across the turbine with ψ calculated from Eq. (3.60), and $\overline{\Delta h^0}$ calculated using:

$$\overline{\Delta h^0} = \frac{P_{wr,TRB}}{\sum_{j=1}^{j=N_{stg}} (\dot{m}_1)_j} \quad (3.145)$$

with \dot{m}_1 given again by Eq. (3.135).

In the third and last option, a variable stage Δh^0 is imposed and the corresponding loading coefficient is obtained by definition [see Eq. (3.14)]:

$$\psi_j = \frac{(\Delta h^0)_j}{U_j^2} \quad (3.146)$$

With ψ being known in every turbine stage, the specific total enthalpy drop a stage performs is given by Eq. (3.62) ($\Delta h^0 = \psi U^2$), and the stage outlet enthalpy is calculated as: $h_2^0 = h_0^0 - \Delta h^0$.

Finally, the swirl velocity difference between the rotor inlet and outlet, ΔV_θ , is calculated from Euler's equation for turbines according to:

$$\Delta V_\theta = V_{\theta,1} - V_{\theta,2} = \psi U \quad (3.147)$$

3.5.6.3 Stage Reaction

In the present design procedure, stage reaction Λ can either be a user-defined input in every turbine stage or, alternatively, a velocity diagram type can be selected. Table 3.3 summarizes the four (4) possible options for defining the stage reaction.

Table 3.3: Stage reaction calculation options for turbine stages

Velocity Diagram	Λ (-)
Symmetrical	0.5
Zero exit swirl ²⁴	$1 - \psi/2$
Impulse	0
General	User input

3.5.6.4 Rotor Swirl Parameters

The rotor inlet and outlet swirl parameters, $V_{\theta,1}/\Delta V_\theta$ and $V_{\theta,2}/\Delta V_\theta$, respectively, depend on the type of velocity diagram and are key parameters for establishing the stage efficiency according to Glassman (1992b). For a stage with $U_m = const$, $V_x = const$, and $V_0 \approx V_2$, it is easily proven that the stage inlet swirl parameter is expressed in terms of the stage reaction and loading coefficient according to [see Glassman (1972a)]:

$$\frac{V_{\theta,1}}{\Delta V_\theta} = \frac{1 - \Lambda}{\psi} + \frac{1}{2} \quad (3.148)$$

for every turbine stage, or:

$$\frac{V_{\theta,1}}{\Delta V_\theta} = \frac{1}{\Delta V_\theta} \sqrt{E_a} V_{x,out} \tan a_{out} + 1 \quad (3.149)$$

²⁴The proof that $\Lambda = 1 - \psi/2$ for a zero exit swirl turbine stage designed for constant axial velocity and blade speed, and assuming a repeating stage, can be found in Chapter 3 by Glassman (1972a).

for the last stage in case no exit vanes are considered for turning the turbine exit flow towards the axial direction.

It is evident that for different sets of ψ and Λ , Eq. (3.148) obtains the value of $V_{\theta,1}/\Delta V_{\theta}$. The different calculation options available for estimating $V_{\theta,1}/\Delta V_{\theta}$, are summarized in Table 3.4.

Table 3.4: Calculation options for estimating the inlet swirl parameter for a turbine stage

ψ (-)	Velocity Diagram	Λ (-)	$V_{\theta,1}/\Delta V_{\theta}$ (-)
Arbitrary	Symmetrical	0.5	$(1 + \psi)/(2\psi)$
Arbitrary	Zero exit swirl	$1 - \psi/2$	1
Arbitrary	Impulse	0	$(2 + \psi)/(2\psi)$
Arbitrary	General	User input	$(1 - \Lambda)/\psi + 1/2$
≤ 2	Zero exit swirl	$1 - \psi/2$	1
> 2	Impulse	0	$(2 + \psi)/(2\psi)$
Arbitrary	General	From Eq. (3.148)	User input

Having established $V_{\theta,1}/\Delta V_{\theta}$, the value of the stage outlet swirl parameter, $V_{\theta,2}/\Delta V_{\theta}$, is then given by:

$$\frac{V_{\theta,2}}{\Delta V_{\theta}} = \frac{V_{\theta,1}}{\Delta V_{\theta}} - 1 \quad (3.150)$$

From Eqs (3.148) and (3.150), the velocity swirl components at the rotor inlet and outlet can be established, respectively, as:

$$V_{\theta,1} = (V_{\theta,1}/\Delta V_{\theta})\Delta V_{\theta} \text{ and } V_{\theta,2} = (V_{\theta,2}/\Delta V_{\theta})\Delta V_{\theta}$$

where ΔV_{θ} is obtained from Eq. (3.147).

3.5.7 Velocity Triangles Calculation

From paragraphs 3.5.5 and 3.5.6, V_{θ} , V_x , and U have been established across the turbine stage and, therefore, the mean-line velocity triangles can now be estimated. In the present paragraph, the equations used to calculate the flow velocities and angles at the annulus hub, mean, and tip are presented.

3.5.7.1 Mean-Line Velocity Triangles

Apart from the axial velocity, V_x , and the rotor swirl velocities, V_{θ} , which were calculated with the means presented in paragraph 3.5.6, the remaining components of the velocity triangles are calculated in every stage and station using the vector Eq. (3.2) and simple trigonometry. At stations 1 and 2 across the rotor, the following equations apply:

$$W_{\theta} = V_{\theta} - U \quad (3.151)$$

$$V = \sqrt{V_x^2 + V_\theta^2} \quad (3.152)$$

$$W = \sqrt{V_x^2 + W_\theta^2} \quad (3.153)$$

$$a = \tan^{-1} \frac{V_\theta}{V_x} \quad (3.154)$$

$$\beta = \tan^{-1} \frac{W_\theta}{V_x} \quad (3.155)$$

Note that, at station 2 the axial velocity V_x in Eqs (3.152)–(3.155) is replaced by $V_{x,2} = V_x \sqrt{E_a}$ [see also Eq. (3.143)]. Finally, the flow angle at the nozzle inlet (station 0) is calculated as $(a_0)_j = -(a_2)_{j-1}$, except for the first turbine stage where a_0 is equal to the imposed inlet flow angle, a_{in} .

3.5.7.2 Hub and Tip Velocity Triangles

For establishing the velocity triangles at the annulus hub and tip across the rotor (stations 1 and 2) Eqs (3.151)–(3.155) are again used, but applied at the annulus hub and tip. For this reason, the free-vortex flow approximation is used [see Eqs (3.19) and (3.20)] to first establish V_x and V_θ at the two blade span extremes. Thus, having determined V_x and V_θ at the mean radius (subscript “ m ”), V_x and V_θ at hub and tip are estimated from the following expressions:

$$V_{x,RP} = V_{x,m} \text{ and } V_\theta = \frac{D_m}{D_{g,RP}} V_{\theta,m}$$

with $RP = h, t$.

Finally, the blade speed at hub and tip is calculated using Eq. (3.3), which expressed between the mean radius and an arbitrary radial position RP gives:

$$U_{RP} = \frac{D_{g,RP}}{D_m} U$$

3.5.8 Isentropic Efficiency Calculation for Uncooled Stages

This paragraph presents the two methods available for estimating the isentropic efficiency (total-to-total conditions) for uncooled turbine stages. The isentropic efficiency for a cooled stage can then be obtained after appropriate correction of the uncooled efficiency, as will be described in the following paragraph.

3.5.8.1 Aungier’s Method

The first method adopted here is the one presented by Aungier (2005), where the uncooled (subscript “ uc ”) stage isentropic efficiency is estimated through the use of a Smith-type chart. More specifically, Aungier developed an analytical correlation for the Kacker & Okapuu [see Kacker et al. (1982)] efficiency chart, where the isentropic efficiency (for zero tip leakage) is approximated by:

$$\eta_{is,uc} = TF \left[\eta_{opt} - K_{\psi} (\varphi - \varphi_{opt})^2 \right] \quad (3.156)$$

with $TF \geq 1$ being a user-specified technology factor accounting for the increase in the efficiency due to the technological progress, φ is the stage flow coefficient, and φ_{opt} is the optimal flow coefficient that yields the maximum efficiency. In Eq. (3.156), K_{ψ} , η_{opt} , and φ_{opt} are given in terms of the stage loading coefficient, ψ , according to the following equations:

$$K_{\psi} = \begin{cases} 0.375 - 0.125\psi, & \psi \leq 2.2 \\ 0.22/\psi, & \psi > 2.2 \end{cases} \quad (3.157)$$

$$\eta_{opt} = \begin{cases} 0.913 + 0.103\psi - 0.0854\psi^2 + 0.0154\psi^3, & \psi \leq 2.8 \\ 1.01 - 0.05\psi, & \psi > 2.8 \end{cases} \quad (3.158)$$

$$\varphi_{opt} = 0.375 + 0.25\psi \quad (3.159)$$

Figure 3.23 illustrates the efficiency chart predicted by Eqs (3.156) through (3.159). Note that, like most Smith-type charts, Kacker & Okapuu's chart is also based on 50% stage reaction, justifying the fact that Eqs (3.156)–(3.159) show no dependence on Λ . Kacker & Okapuu's model is also based on stages comprising moderate- to high-aspect ratio blades.

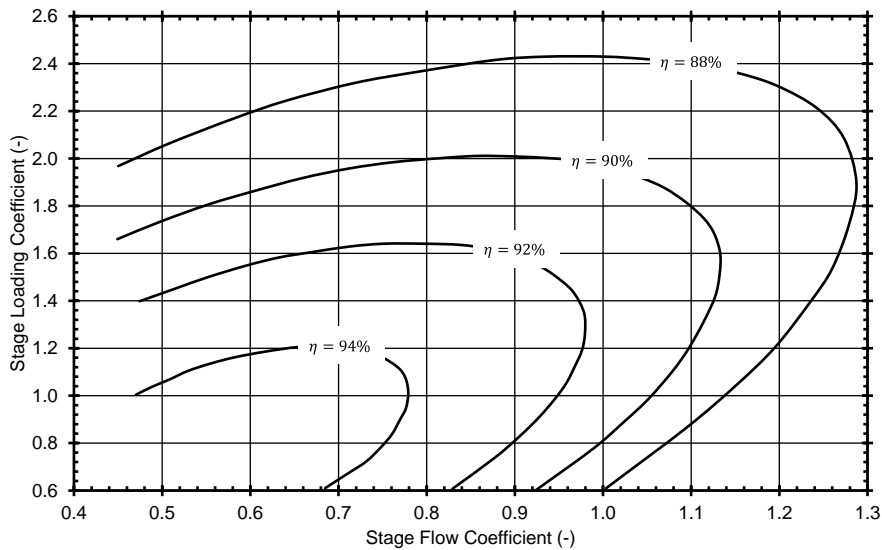


Figure 3.23: Turbine stage efficiency chart produced using Kacker & Okapuu model [adapted from Aungier (2005)].

3.5.8.2 Glassman's Method

In contrast to Aungier's method presented in the previous paragraph, which is a semi-empirical method, the method presented here establishes the stage efficiency based on estimates of the stage losses. According to this method [originally presented by Stewart (1961) and later used by Glassman (1992b) to develop his code for the preliminary

design of axial-flow turbines], the isentropic efficiency of an uncooled turbine stage is given in terms of the stage loading coefficient (ψ) and the stage losses by:

$$\eta_{is,uc} = \frac{1}{1 + \frac{A_\omega}{2} \psi} \quad (3.160)$$

In Eq. (3.160), A_ω is the stage loss parameter given by:

$$A_\omega = K_\omega \text{Re}^{-0.2} \tan a_1 (F_{\omega,N} C_{\omega,N} + F_{\omega,R} C_{\omega,R} + C_{\omega,OGV}) \quad (3.161)$$

The proportionality constant, K_ω , referred to as the turbine loss coefficient by Glassman, is an empirical constant which in the absence of additional information claims the value $K_\omega = 0.3$ [see Glassman (1992b)]. The Reynolds number in Eq. (3.161) is defined as:

$$\text{Re} = \frac{2\dot{m}_{in}}{\mu_{in}^0 D_{m,in}} \quad (3.162)$$

and is assumed constant throughout the turbine. Thus, it is calculated only once in terms of the turbine inlet quantities.

The remaining terms in the right-hand side of Eq. (3.161) depend on the stage location and the velocity diagram type (through the stage swirl parameters). The rotor loss weighting factor, $F_{\omega,R}$, and the rotor loss parameter, $C_{\omega,R}$, have the same expression regardless of the stage position and are given by:

$$F_{\omega,R} = 2 \quad (3.163)$$

$$C_{\omega,R} = \frac{2}{\tan^2 a_1} \left(\frac{V_{\theta,1}}{\Delta V_\theta} \right)^2 + \left(\frac{V_{\theta,1}}{\Delta V_\theta} - \frac{1}{\psi} \right)^2 + \left(\frac{V_{\theta,2}}{\Delta V_\theta} - \frac{1}{\psi} \right)^2 \quad (3.164)$$

The stator loss weighting factor and loss parameter, $F_{\omega,N}$ and $C_{\omega,N}$, respectively, depend on the stage position and are given by:

$$F_{\omega,N} = \begin{cases} 1 - \frac{3 \tan a_0}{\tan a_1}, & j = 1 \\ 1 - \frac{\tan a_0}{\tan a_1} \\ 3 - 2 \frac{V_{\theta,1}}{\Delta V_\theta}, & j > 1 \end{cases} \quad (3.165)$$

$$C_{\omega,N} = \begin{cases} \left(1 + \frac{2 + \tan^2 a_0}{\tan^2 a_1} \right) \left(\frac{V_{\theta,1}}{\Delta V_\theta} \right)^2, & j = 1 \\ \left(1 + \frac{2}{\tan^2 a_1} \right) \left(\frac{V_{\theta,1}}{\Delta V_\theta} \right)^2 + \left(\frac{V_{\theta,2}}{\Delta V_\theta} \right)^2, & j > 1 \end{cases} \quad (3.166)$$

Finally, for last stages with OGVs the loss parameter is given by:

$$C_{\omega,OGV} = \begin{cases} \frac{2}{\tan^2 a_1} \left(\frac{V_{\theta,1}}{\Delta V_{\theta}} \right)^2 + \left(\frac{V_{\theta,2}}{\Delta V_{\theta}} \right)^2, & j = N_{stg} \\ 0, & j < N_{stg} \end{cases} \quad (3.167)$$

Note that, in Eqs (3.164)–(3.167) the stage swirl parameters are calculated according to the methodology described in paragraph 3.5.6.

3.5.9 Cooled Stages Isentropic Efficiency Calculation

In order to calculate the isentropic efficiency of a cooled turbine stage, the method applied by Glassman (1994) is followed. Glassman obtains the cooled stage efficiency by correcting the uncooled one [calculated using either Eq. (3.156) or Eq. (3.160)] according to:

$$\eta_{is} = \eta_{is,uc} \left[1 - \left(\delta_{c,N} \frac{\dot{m}_{cf,N}}{\dot{m}_0} + \delta_{c,R} \frac{\dot{m}_{cf,R}}{\dot{m}_1} \right) \right] \quad (3.168)$$

In the above, the cooling fractions for the nozzle and the rotor blade, $\dot{m}_{cf,N}/\dot{m}_0$ and $\dot{m}_{cf,R}/\dot{m}_1$, respectively, are obtained according to the methodology presented in paragraph 3.5.2.

As it can be seen from Eq. (3.168), the mixing and heat-transfer phenomena that develop due to the re-introduction of the coolant flows in the hot mainstream gas flow, cause a reduction in the stage efficiency (compared to the uncooled stage). This reduction in efficiency is accounted for by including a specific loss parameter due to cooling ($\delta_c \geq 0$) for the nozzle and the rotor blades.

Table 3.5: Specific cooling losses for turbine stages in terms of cooling method [see Gaunter (1980)]

Cooling Configuration	% TE Ejection	Impingement	$\delta_{c,N}$ (-)	$\delta_{c,R}$ (-)
Uncooled	–	–	0	0
Convection	100	No	0	0
Convection with coat	100	No	0	0
Advanced convection	100	Yes	0.10	0.20
Film with convection	75	Yes	0.12	0.24
Film with convection	50	Yes	0.15	0.30
Film with convection	25	Yes	0.18	0.36
Transpiration with convection	25	Yes	0.50	1.0
Full cover film	0	Yes	0.35	0.80
Transpiration	0	Yes	1.0	1.50

Indicative values for δ_c are tabulated in Table 3.5, as taken from Gaunter (1980). Although these correspond to > 40 year old technology, they serve well as a starting point for preliminary design purposes. The author of this thesis could not identify any other source of the public domain quoting values for δ_c for modern-day cooling

technologies and, therefore, this topic is left for future research for extending the present design methodology.

3.5.10 Model for Stage Cooling

Considering the most widely used stage isentropic efficiency definition [e.g., see Kurzke (2002) and Walsh et al. (2004)], each coolant flow is considered whether it does work on the rotor or not. For the cooling model depicted in Figure 3.24, the nozzle coolant flow (A) is considered doing work on the rotor, while the rotor coolant flow (B) cannot do any useful work on the rotor itself. Secondary cooling flows, such as the platform cooling air (b), disk rim sealing air (c), and liner cooling air (a) normally are not considered doing work on the rotor due inadequate momentum.

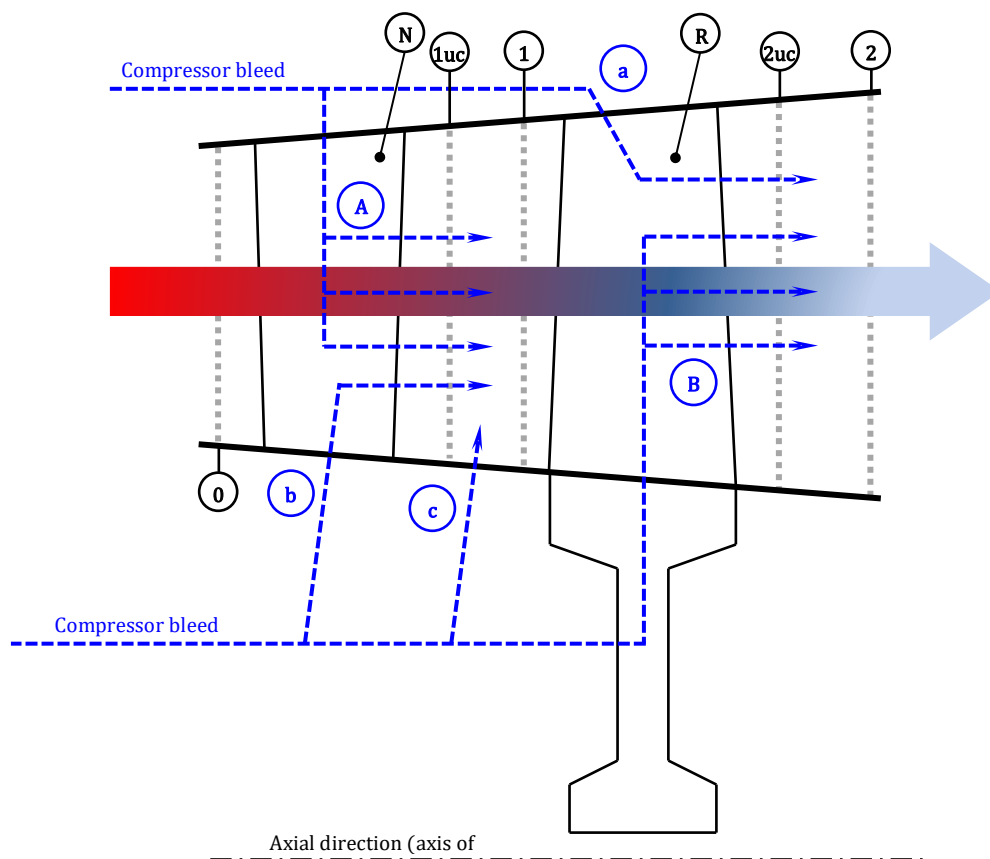


Figure 3.24: Cooling model for turbine stage nozzle (N) and rotor (R) blades and station numbering [adapted from Kurzke (2002)].

In the present analysis, five (5) flow state stations are considered for expressing the flow enthalpy, as indicated in Figure 3.24: station “0” denotes the stage inlet and coincides with station “2” of the upstream stage, station “1uc” denotes the state before the addition of the stator coolant flow, station “1” denotes the state after the addition of the stator coolant flow, station “2uc” denotes the state before the addition of the rotor coolant flow and, finally, station “2” denotes the state after the addition of the rotor coolant flow.

Note that no work is performed across the stator while for simplicity and modelling reasons, before the mixing of the mainstream and the coolant flows, the flow through the stator is considered adiabatic and, hence, $h_{1,uc}^0 = h_0^0$. Applying appropriate control volumes, the total enthalpies at stations 1 and 2 in every stage (j) are calculated through mass and energy balances, which are expressed by the following set of equations:

$$h_1^0 = \frac{\dot{m}_0 h_{1,uc}^0 + \dot{m}_{cf,N} h_{rb}^0}{\dot{m}_0 + \dot{m}_{cf,N}} \quad (3.169)$$

$$h_2^0 = \frac{\dot{m}_1 h_{2,uc}^0 + \dot{m}_{cf,R} h_{rb}^0}{\dot{m}_1 + \dot{m}_{cf,R}} \quad (3.170)$$

In Eqs (3.169) and (3.170), the mainstream gas flows at the nozzle and rotor inlet, \dot{m}_0 and \dot{m}_1 , respectively, as well as the coolant flows $\dot{m}_{cf,N}$ and $\dot{m}_{cf,R}$, are obtained according to paragraph 3.5.2. Finally, the total specific enthalpy at station 2uc is given from the known enthalpy drop as: Δh^0 , as $h_{2,uc}^0 = h_1^0 - \Delta h^0$.

3.5.11 Stage Radial Positioning

Similarly to the compressor design, at this point of the calculation the mass flow across the stage, the stage outlet total temperature and pressure, and the flow velocities and angles across the stage are already established. Thus, the stage outlet flow-annulus area (A_2) can be obtained according to paragraph 3.2.3 and the radial positioning of the stage (stations 1 and 2, assuming that the stage inlet is known) is performed easily following the formulation presented in paragraph 3.3.14 for compressor components.

3.5.12 Next Stage Aerodynamic Design and Overall Turbine Performance

The above calculation procedure (paragraphs 3.5.2 through 3.5.11) continues with the next stage, j , where the inlet total temperature and pressure equal the ones at the exit of the previous stage, $j - 1$, or:

$$(T_0^0)_j = (T_2^0)_{j-1} \text{ and } (p_0^0)_j = (p_2^0)_{j-1}$$

For geometry continuity, the same applies for the stage inlet diameters:

$$(D_{g,h,0})_j = (D_{g,h,2})_{j-1} \text{ and } (D_{g,t,0})_j = (D_{g,t,2})_{j-1}$$

At the end of this procedure, the turbine exit is reached and the turbine radial positioning is completed. Then, the turbine overall work input and total pressure ratio are obtained allowing for the calculation of the overall isentropic and polytropic efficiencies. These are given by:

$$\eta_{is} = \frac{h_{in}^0 - h_{out}^0}{h_{in}^0 - h_{out,is}^0} \quad (3.171)$$

$$\eta_p = \frac{\phi_{in}^0 - \phi_{out}^0}{R_g} \ln \frac{p_{in}^0}{p_{out}^0} \quad (3.172)$$

For calculating the isentropic temperature and enthalpy at the turbine exit, Eq. (3.102) is used.

Note here, that apart from the aerodynamic design for establishing the turbine efficiencies, another method was also implemented, and is the one presented by Samuelsson et al. (2015) (see Appendix B). In this case, the aerodynamic design is still employed for establishing the turbine dimensions, but the component overall efficiency is obtained based on overall correlations which correct a nominal efficiency for EIS, component size, and Reynolds number effects.

3.6 Turbine Axial Positioning and Gas-Path Visualization

After we have determined the turbine radial positioning according to Section 3.5, the next step is to establish the basic blade dimensions (e.g., blade count, chord lengths, etc.) and, ultimately, to calculate the turbine gas-path axial coordinates and to visualize its meridional view.

3.6.1 Blade Dimensions Calculation

In the present paragraph, the equations used to estimate basic blade dimensions are presented. Since the equations used have the same expression for both rotors and stators, they are listed only once. For this reason, a local numbering system convention is adopted according to which subscripts 1 and 2 are used for the blade row inlet and outlet, respectively. In comparison to the stage-wise station numbering system (see Figure 3.20), stations 1 and 2 of the local system correspond to stations 0 and 1 for nozzles, and stations 1 and 2 for rotors.

3.6.1.1 Solidities and Stagger Angles

For the calculation of the blade axial solidity the method by Zweifel, as adopted by Glassman (1993), is used. Zweifel derived an expression for the axial solidity of a blade in terms of the inlet and outlet flow angles by equating the tangential force exerted by a fluid flowing through a 2D cascade to the tangential force due to the blade pressure loading. This condition is expressed by:

$$\sigma_x = \frac{2 \cos \beta_2}{\psi_z \cos \beta_1} \sin(\beta_1 - \beta_2) \quad (3.173)$$

where ψ_z is the tangential loading coefficient, which is the ratio of the actual blade loading to Zweifel's ideal loading. For minimum losses: $\psi_z = 0.8$.

Equation (3.173) is used for calculating the axial solidity at the mean-line. At the blade hub and tip, σ_x is estimated using again Eq. (3.173) but for the hub and tip flow angles (again: $\psi_z = 0.8$).

In order to determine the blade chord length and the optimal actual solidity of the blade row, it is first necessary to calculate the blade stagger angle γ . Using the analytical blading model of Miser et al. (1956), the blade stagger angle is calculated using sequentially the following system of equations:

$$a_\theta = \frac{\sigma_x - \sin \beta_1 \cos \beta_1 + \sin \beta_2 \cos \beta_2}{\sin \beta_1 - \sin \beta_2} \quad (3.174)$$

$$c_\theta = \sin^2 \beta_1 - a_\theta (\cos \beta_1 - \cos \beta_2) - \sin^2 \beta_2 \quad (3.175)$$

$$\gamma = \tan^{-1} \frac{c_\theta}{\sigma_x} \quad (3.176)$$

where σ_x is obtained by Eq. (3.173).

For the calculation of the blade stagger angles at the two span extremes (hub and tip), the same equations apply but using the hub and tip flow angles, respectively.

Finally, for calculating the blade row actual solidity, the following equation is used:

$$\sigma = \frac{\sigma_x}{\cos \gamma} \quad (3.177)$$

3.6.1.2 Chord Lengths

The present design calculation assumes that stator and rotor blades have equal (mean-line) axial chord lengths (c_x) which, in turn, are correlated to the stage mean diameter (D_m) according to [see Glassman (1992b)]:

$$c_x = K_{AR,1} D_m + K_{AR,2} D_m^2 + K_{AR,3} + K_{AR,4} \frac{1}{D_m} \quad (3.178)$$

In Eq. (3.178), the values of $K_{AR,1}$ – $K_{AR,4}$ are given by Glassman (1992b) in terms of the blade aspect ratio (see Table 3.6).

Table 3.6: Coefficients for axial chord length model [see Glassman (1992b)]

Aspect Ratio	$K_{AR,1} \times 10^2$	$K_{AR,2} \times 10^3$	$K_{AR,3} \times 10^2$	$K_{AR,4} \times 10^3$
High	0.5716	7.8984	1.4911	-0.7498
Mid	3.0740	9.9323	1.4714	-0.7411
Low	6.6559	8.7134	1.1949	-0.5580

The blade actual chord length is then calculated by rearranging Eq. (3.107), where the known values for γ and c_x are used. Similarly to the compressor blade design, chord is assumed constant along the blade height ($c_h = c_t = c$), that is, blades without taper ratio are assumed.

Finally, the blade axial chord length at the two blade span extremes (hub and tip) is calculated by using Eq. (3.107) for the values of γ_h and γ_t , respectively, and making use of the fact that $c_h = c_t = c$. Figure 3.25 illustrates the axial chord lengths across a

turbine stage at the three characteristic radial positions (hub, mean, tip). In the following, these will be used to axially position the turbine gas-path.

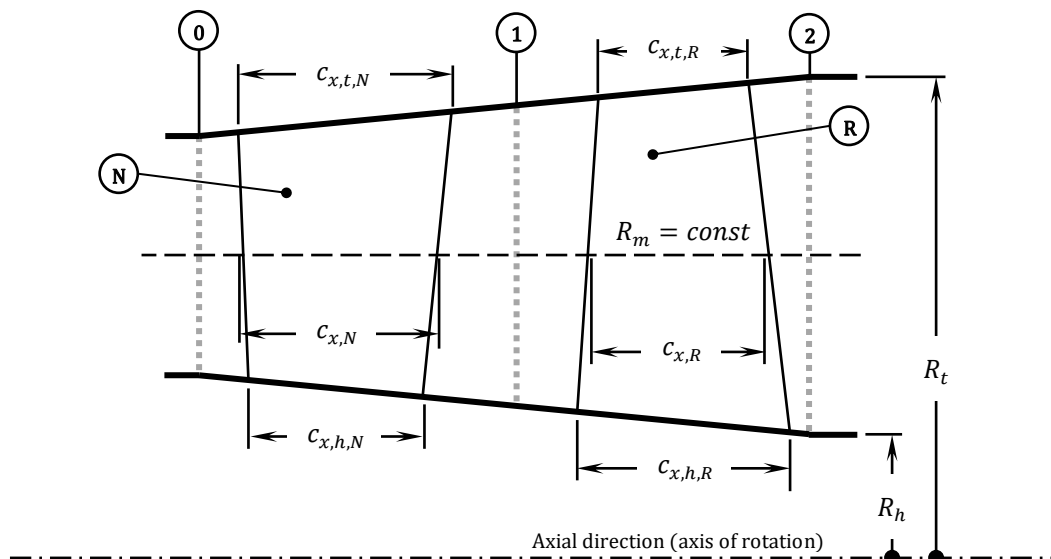


Figure 3.25: Turbine stage nozzle (N) and rotor (R) axial chord lengths along the blade span.

3.6.1.3 Blade Count

Having determined the actual chord length (paragraph 3.6.1.2) and actual solidity (paragraph 3.6.1.1) at the mean-line, the number of blades for both the nozzle and the rotor of a stage is estimated using Eq. (3.21).

3.6.2 Axial Coordinates Calculation

In the following paragraphs, the axial coordinates of a stage and, later, of the whole turbine are estimated following, similarly to the compressor stages, the procedure described by Mattingly (2005).

3.6.2.1 Axial Gap Calculation

Axial gaps are defined as for compressor stages (see paragraph 3.4.2.1), and are calculated for both nozzles and rotors using Eq. (3.108) for given values of inlet and exit stator and rotor gaps. Note that, Walsh et al. (2004) quote a typical value of 25% for both stator and rotor gaps.

3.6.2.2 Turbine Axial Positioning

The present paragraph describes the axial positioning of the turbine gas-path. To what follows, the stage-wise station numbering, illustrated in Figure 3.26, is adopted. Note that, most of the equations and the calculation procedure described for compressor components in paragraph 3.4.2.2 applies in a similar manner for the axial positioning of turbine components and, therefore, only the different equations are highlighted and commented here.

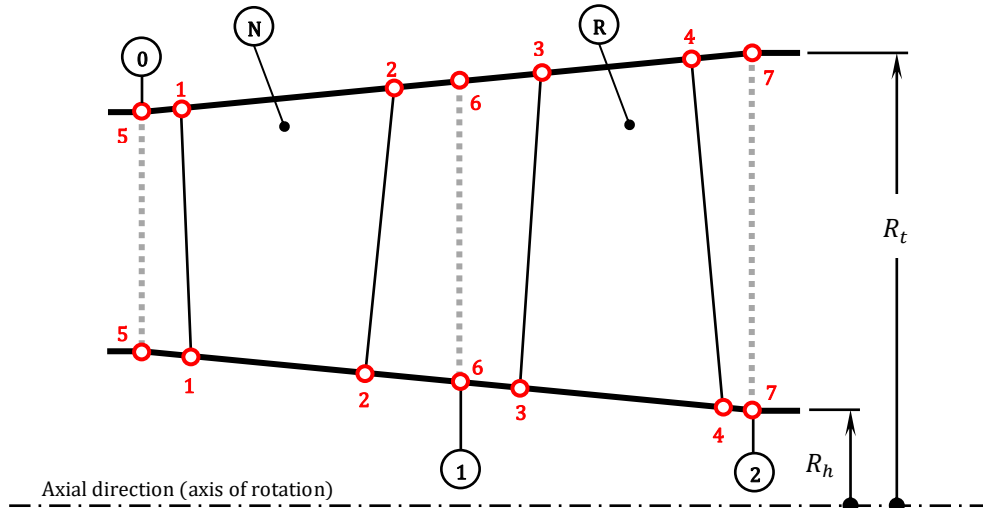


Figure 3.26: Numbering system used in the estimation of the axial coordinates of the nozzle (N) and the rotor (R) of a turbine stage. For convenience, the same indices (i.e., 1, 2, 3, 4, 5, 6, and 7) are used for both the annulus hub and tip, and each number identifies uniquely a gas-path station: 1 → nozzle inlet, 2 → nozzle outlet, 3 → rotor inlet, 4 → rotor outlet, while 5, 6, and 7 correspond to stations 0, 1, and 2 of the 1D calculation, respectively.

First, an origin is selected, let $x_{t,1}$ be the one. For every turbine stage, $x_{t,1}$ is calculated from the recursive formula:

$$(x_{t,1})_j = \begin{cases} \frac{1}{2} [(c_{x,h,N})_j + (c_{x,t,N})_j], & j = 1 \\ (x_{t,1})_1 + \sum_{k=1}^{j-1} \{ [1 + (g_{x,R})_k] (c_{x,h,R})_k + [1 + (g_{x,N})_k] (c_{x,t,N})_k \}, & j > 1 \end{cases} \quad (3.179)$$

Next, the axial coordinates at the tip of station 2 and the hub of stations 3 and 4 are calculated sequentially (see Figure 3.27) at every stage using Eqs (3.180)–(3.182).

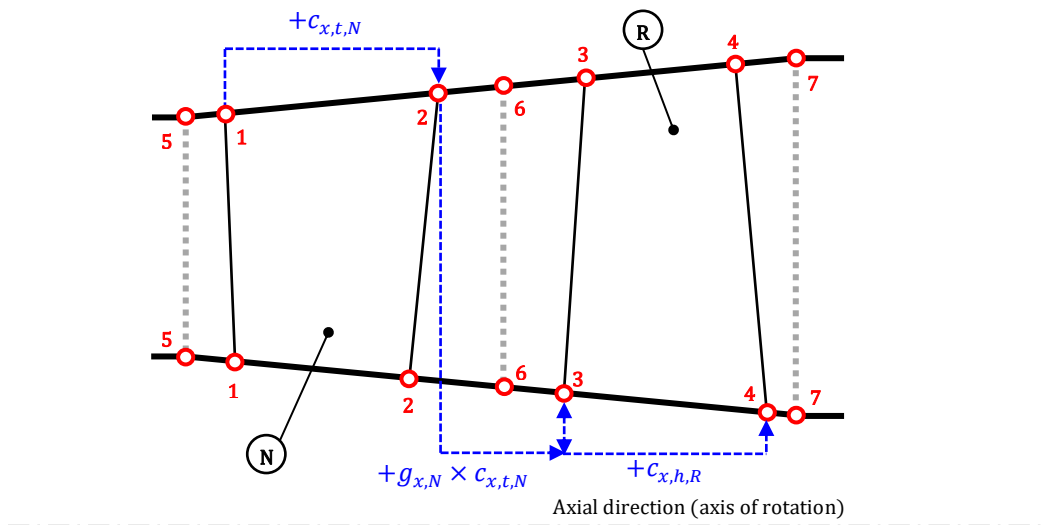


Figure 3.27: Nozzle (N) tip and rotor (R) hub axial coordinates calculation. Arrows indicate the sequence of the calculation.

$$x_{t,2} = x_{t,1} + c_{x,t,N} \quad (3.180)$$

$$x_{h,3} = x_{t,2} + g_{x,N} \times c_{x,t,N} \quad (3.181)$$

$$x_{h,4} = x_{h,3} + c_{x,h,R} \quad (3.182)$$

With the tip axial coordinates of the nozzle and the hub axial coordinates of the rotor known, the remaining blade coordinates are calculated according to the calculation sequence illustrated in Figure 3.28. Therefore, the rotor tip and nozzle hub axial coordinates, are obtained for every turbine stage (j) by Eqs (3.183)–(3.186).

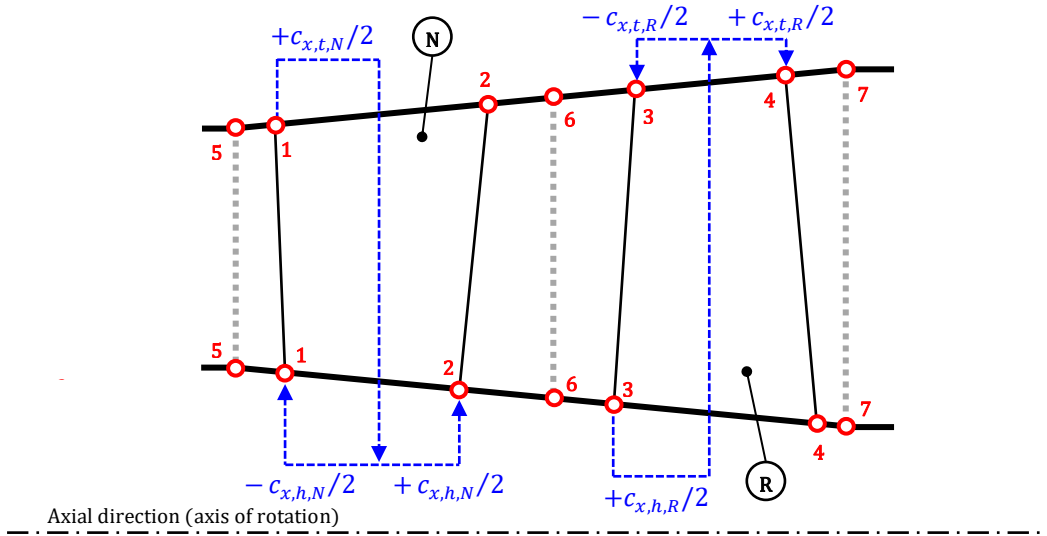


Figure 3.28: Rotor (R) tip and nozzle (N) hub axial coordinates calculation. Arrows indicate the sequence of the calculation.

$$x_{h,1} = x_{t,1} + \frac{1}{2}(c_{x,t,N} - c_{x,h,N}) \quad (3.183)$$

$$x_{h,2} = x_{t,1} + \frac{1}{2}(c_{x,t,N} + c_{x,h,N}) \quad (3.184)$$

$$x_{t,3} = x_{h,3} + \frac{1}{2}(c_{x,h,R} - c_{x,t,R}) \quad (3.185)$$

$$x_{t,4} = x_{h,3} + \frac{1}{2}(c_{x,h,R} + c_{x,t,R}) \quad (3.186)$$

Finally, the tip axial coordinates of stations 5, 6, and 7 are calculated for every turbine stage similarly to the compressor stages by applying Eq. (3.118), where the hub coordinate at station 5 is given by:

$$(x_{h,5})_j = \begin{cases} 0, & j = 1 \\ \frac{1}{4}[(x_{h,4})_{j-1} + (x_{t,4})_{j-1} + (x_{h,1})_j + (x_{t,1})_j], & j > 1 \end{cases} \quad (3.187)$$

The hub coordinates of stations 6 and 7 are estimated using the same equations formulated for compressor stages, i.e., Eqs (3.120) and (3.121), respectively.

3.6.2.3 Turbine Gas-Path Visualization

For producing a smooth turbine gas-path for visualization purposes, the radii of stations 1, 2, 3, and 4 in Figure 3.26 are calculated using the same Eqs (3.126)–(3.129) formulated, originally, for compressor stages. Note that, according to Figure 3.26 the radius at station 5, 6, and 7 is equal to that of the 1D calculation station 0, 1, and 2, respectively.

3.7 Axial Fan 1D Aerothermodynamic Design and Gas-Path Visualization

In the present section, a brief description of the basic equations used to model the performance and gas-path geometry of an axial-flow fan is presented. The term “fan” is used for describing the first compressor component in a turbofan engine. In Figure 3.29 a schematic of the meridional view of an axial-flow, single-stage fan is shown.

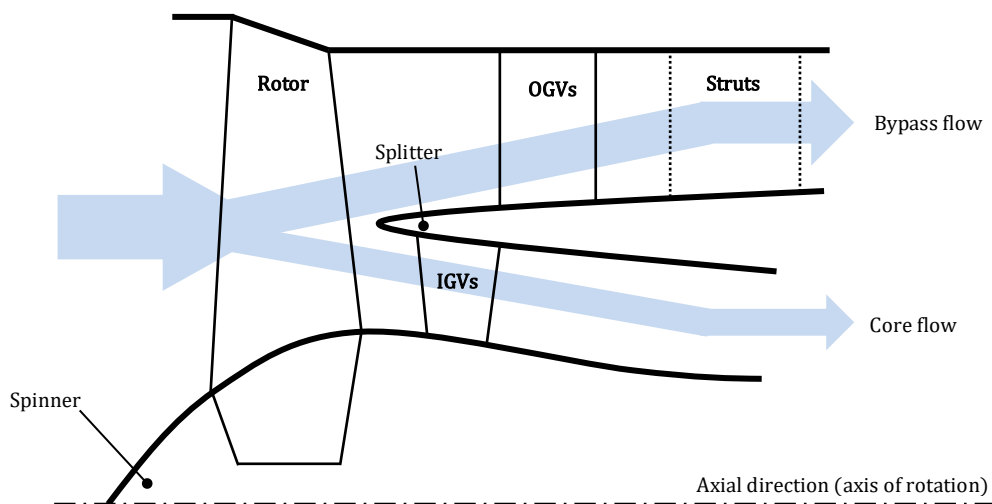


Figure 3.29: Axial-flow, single-stage fan flow-annulus and blading nomenclature.

Fans are high-flow, low-pressure ratio compressors. The primary functional purpose of fans is to split the flow into two (2) downstream flows, namely the bypass (secondary or cold) flow and core (primary or hot) flow. Fans (and in general turbofan engines) are classified based on the value of the bypass ratio:

$$BPR = \frac{\dot{m}_{cold}}{\dot{m}_{hot}}$$

where \dot{m}_{cold} and \dot{m}_{hot} are the bypass and core stream flows, respectively. Turbofan engines can roughly be classified into three (3) categories based on their BPR value: 1) low-bypass ratio engines ($BPR \sim 1$), 2) high-bypass ratio engines ($BPR \sim 5$), and 3)

ultra-high bypass ratio engines ($BPR \sim 15$). Note that low-bypass ratio engines are typically used in fighter-jet airplanes and typically comprise multi-stage fans. In this thesis, we will only deal with single-stage fans which are typically used in high- and ultra-high bypass ratio turbofans employed in civil applications.

As it can be seen from Figure 3.29, the typical arrangement of a single-stage fan is a rotor followed by the tip and root stators, which are typically placed downstream of the splitter. Throughout the present text, the tip stators will be called “OGVs” while the root stators will be called “IGVs”. In some fan designs there is also another set of stator blades placed at the exit of the bypass stream, the struts. These are typically part of the engine’s main frame and serve as structural support for the engine’s accessory drive, oil pipes, etc.

3.7.1 Fan Rotor Inlet Calculation

For known cycle parameters (\dot{m} , T^0 , p^0) at the fan rotor inlet and a user-specified absolute flow Mach number (M), static conditions (T^s , p^s), flow velocity (V), and flow-annulus area (A) are established by solving the system of Eqs (3.4) through (3.8) (see paragraph 3.2.3). Note that, at the rotor inlet the flow is assumed to be purely axial ($\alpha = 0^\circ$) and uniform along the annulus span.

The dimensions (hub and tip diameters) of the flow-annulus at the rotor inlet are then established for a user-specified hub-to-tip ratio ($HTR = D_h/D_t$) using:

$$D_t = \sqrt{\frac{4A}{\pi(1 - HTR^2)}} \quad (3.188)$$

$$D_h = HTR \times D_t \quad (3.189)$$

3.7.2 Rotational Speed Estimation

In the present design procedure, the fan rotational speed (N_{mech}) can either be an input (by, e.g., the turbine component with which the fan is mechanically coupled) or can be established based on structural integrity and/or aerodynamic criteria. Typical mechanical and aerodynamic criteria are the maximum rotor speed and relative flow Mach number at the rotor (inlet) tip:

$$U_t \leq (U_t)_{max} \text{ and } M_{r,t} \leq (M_{r,t})_{max}$$

The above quantities express technology limitations. According to Walsh et al. (2004), the values $(U_t)_{max} \leq 500$ m/s and $(M_{r,t})_{max} \leq 1.4 - 1.8$ could be assumed for current technology fan components (see Appendix A).

Note that, for calculating the Mach number at the tip, the flow velocity at the rotor inlet is assumed constant along the blade span and the flow direction is assumed axial (see paragraph 3.7.1). Therefore, the relative flow velocity at the rotor tip can be expressed by the local velocity triangle as: $W_t = \sqrt{U_t^2 + V_t^2}$.

3.7.3 Fan Performance Estimation

For estimating the fan pressure ratio (FPR) and polytropic efficiency (η_p), the correlations presented by Felder et al. (2011) in graphical form are adopted. These are shown in Figure 3.30, and basically correlate FPR and η_p with the fan corrected tip speed.

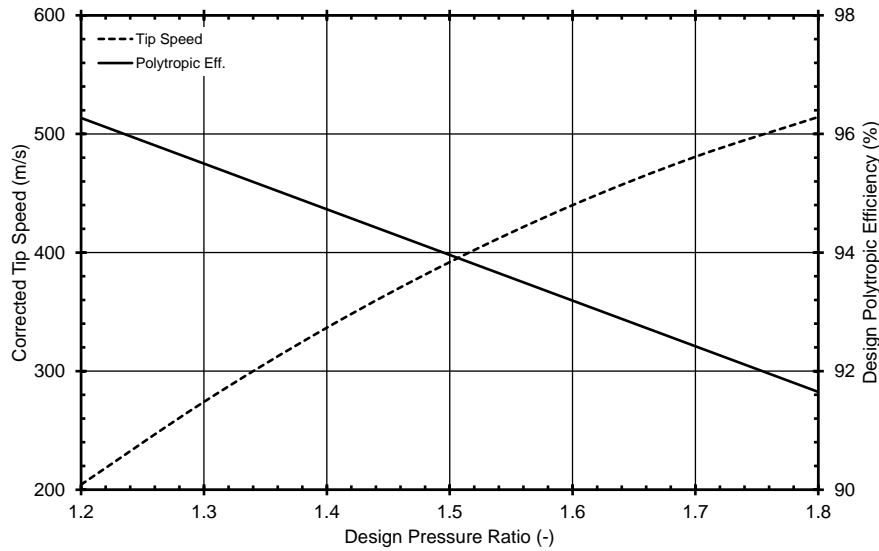


Figure 3.30: Fan design corrected tip speed and polytropic efficiency versus design pressure ratio [adapted by Felder et al. (2011)].

The curves shown in Figure 3.30 were expressed and used in the design code as polynomial best-fits:

$$U_{t,c} = -362.31 \times FPR^2 + 1603.8 \times FPR - 1198.6 \quad (3.190)$$

$$\eta_p = -0.077 \times FPR + 1.0551 \quad (3.191)$$

Note here that, apart from Eq. (3.190), another method was implemented for establishing the component efficiency. This is the one presented by Samuelsson et al. (2015) (see Appendix B).

3.7.4 Fan Rotor Exit Calculation

Having established the fan rotor exit conditions from the known pressure ratio and efficiency values obtained in the preceding paragraph, the exit flow-annulus area (and flow static conditions and velocity) is established following the procedure of paragraph 3.2.3 for user-specified flow Mach numbers. Here, it is assumed that the flow conditions (total pressure and total temperature) remain constant along the blade span. The procedure for estimating the rotor exit diameters is as follows.

First, the flow-annulus area that corresponds to the bypass stream (let A_{sec}) is obtained for a user-specified Mach number (M_{sec}). In the present design procedure, it is assumed that the fan tip diameter at the rotor exit is obtained by the inlet one multiplied by a user-defined exit-to-inlet ratio less or equal to 1.0 (the default value is

unity). Therefore, the diameter of the fan splitter (let D_s) can be established from the known D_t and A_{sec} as:

$$D_s = \sqrt{D_t^2 - \frac{4A_{sec}}{\pi}} \quad (3.192)$$

Similarly, the flow-annulus area that corresponds to the core stream (let A_{pri}) is estimated assuming a user-defined Mach number (M_{pri}). Then, from D_s and A_{pri} the hub diameter at the rotor exit is computed by:

$$D_h = \sqrt{D_s^2 - \frac{4A_{pri}}{\pi}} \quad (3.193)$$

3.7.5 Fan Radial and Axial Positioning and Gas-Path Visualization

For producing the meridional view of a single-stage fan, the station numbering shown in Figure 3.31 is used. Note that, for simplicity (since this is a preliminary design calculation), the flow-annulus walls are assumed straight lines while the axial chord lengths of the blades are assumed radially constant. For completing the task, a number of user inputs is also necessary: the axial aspect ratio for all blades (AR_x), the spinner semi-angle (α_0), the hade angles for the bypass and core ducts (α_2 , α_3 , and α_5), and the axial gap percentages between the blades ($g_{x,2-s}$, $g_{x,2-3}$, $g_{x,2-5}$, and $g_{x,6-7}$). Typical values for these variables can be found from 2D cutaways of contemporary turbofan engines. For the default values of these parameters see Table 3.7.

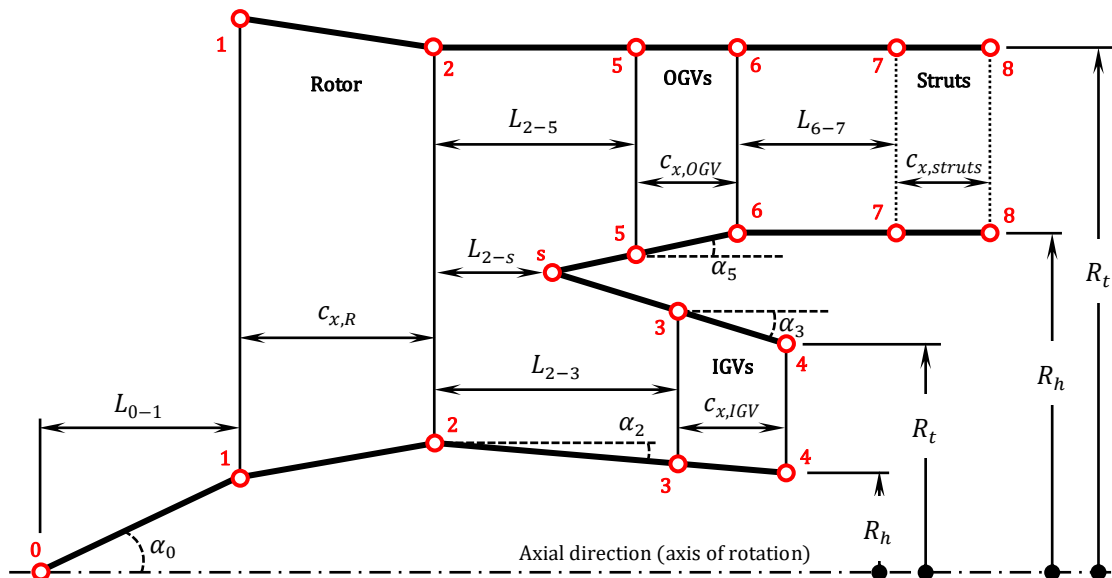


Figure 3.31: Numbering system and nomenclature used in the estimation of the radial and axial coordinates of a single-stage fan. For convenience, the same indices (i.e., 1, 2, 3, 4, 5, 6, 7, and 8) are used for the both the annulus hub and tip across a blade row, and each number identifies uniquely a gas-path station: 1 → rotor inlet, 2 → rotor outlet, 3 → IGVs inlet, 4 → IGVs outlet, 5 → OGVs inlet, 6 → OGVs outlet, 7 → struts inlet, 8 → struts outlet. Also, 0 is used for the nose cone (spinner) and “s” for the splitter. Angles are positive if they are directed above the horizontal axis.

Table 3.7: Default values for fan gas-path calculation

Parameter	Value
α_0	45°
α_2, α_3	-5°
α_5	5°
$AR_{x,R}$	2.0
$AR_{x,IGV}, AR_{x,OGV}, AR_{x,struts}$	3.0
$g_{x,2-s}, g_{x,6-7}$	100%
$g_{x,2-5}$	200%
$g_{x,2-3}$	110%

First of all, the radii at stations 1, 2, and “s” are known and were obtained as explained in paragraphs 3.7.1 and 3.7.4. Making the assumption that the fan tip diameter remains constant between stations 2 and 8, it follows also that:

$$R_{t,5} = R_{t,6} = R_{t,7} = R_{t,8} = R_{t,2} \quad (3.194)$$

From the given aspect ratio for the rotor ($AR_{x,R}$), the rotor blade axial chord length can be established according to:

$$c_{x,R} = \frac{\bar{h}_{b,R}}{AR_{x,R}} = \frac{R_{t,1} - R_{h,1} + R_{t,2} - R_{h,2}}{2AR_{x,R}} \quad (3.195)$$

Then, the axial lengths L_{2-s} , L_{2-3} , and L_{2-5} are estimated from the user-defined axial gap percentages $g_{x,2-s}$, $g_{x,2-3}$, and $g_{x,2-5}$, respectively, as:

$$L_{2-s} = g_{x,2-s}c_{x,R}, \quad L_{2-3} = g_{x,2-3}c_{x,R}, \quad L_{2-5} = g_{x,2-5}c_{x,R} \quad (3.196)$$

From simple geometry, the hub radii at stations 5 and 6 are established according to the following set of equations:

$$R_{h,5} = R_s + (L_{2-5} - L_{2-s}) \tan \alpha_5 \quad (3.197)$$

$$R_{h,6} = \frac{(R_{t,5} + R_{t,6}) \tan \alpha_5 + (2AR_{x,OGV} - \tan \alpha_5)R_{h,5}}{2AR_{x,OGV} + \tan \alpha_5} \quad (3.198)$$

while the hub radii at stations 7 and 8 follow from the assumption that the hub radius between stations 6 and 8 remains constant:

$$R_{h,7} = R_{h,8} = R_{h,6} \quad (3.199)$$

From the given aspect ratio for the OGVs ($AR_{x,OGV}$) and the struts ($AR_{x,struts}$), the axial chord length for the OGVs and the struts are estimated from:

$$c_{x,OGV} = \frac{\bar{h}_{b,OGV}}{AR_{x,OGV}} = \frac{R_{t,5} - R_{h,5} + R_{t,6} - R_{h,6}}{2AR_{x,OGV}} \quad (3.200)$$

$$c_{x,struts} = \frac{\bar{h}_{b,struts}}{AR_{x,struts}} = \frac{R_{t,7} - R_{h,7} + R_{t,8} - R_{h,8}}{2AR_{x,struts}} \quad (3.201)$$

The axial length between the OGVs and the struts (L_{6-7}) can be estimated from the following equation and the user-defined value for $g_{x,6-7}$:

$$L_{6-7} = g_{x,6-7}c_{x,OGV} \quad (3.202)$$

From simple geometry and some tedious algebraic manipulations, the hub and tip radii at stations 3 and 4 are established according to:

$$R_{h,3} = R_{h,2} + L_{2-3} \tan \alpha_2 \quad (3.203)$$

$$R_{t,3} = R_s + (L_{2-3} - L_{2-s}) \tan \alpha_3 \quad (3.204)$$

$$R_{h,4} = R_{h,2} + \left[L_{2-3} + \frac{2(R_{t,3} - R_{t,3})}{2AR_{x,IGV} + \tan \alpha_3 - \tan \alpha_5} \right] \tan \alpha_2 \quad (3.205)$$

$$R_{t,4} = R_s + \left[L_{2-3} - L_{2-s} + \frac{2(R_{t,3} - R_{t,3})}{2AR_{x,IGV} + \tan \alpha_3 - \tan \alpha_5} \right] \tan \alpha_3 \quad (3.206)$$

while the axial chord length of the IGVs is established using the known $AR_{x,IGV}$ value from:

$$c_{x,IGV} = \frac{\bar{h}_{b,IGV}}{AR_{x,IGV}} = \frac{R_{t,3} - R_{h,3} + R_{t,4} - R_{h,4}}{2AR_{x,IGV}} \quad (3.207)$$

Finally, the nose cone axial length (L_{0-1}) is estimated according to:

$$L_{0-1} = R_{h,1}(\tan \alpha_0)^{-1} \quad (3.208)$$

For defining the axial positions for all stations (0, 1, 2, 3, 4, 5, 6, 7, 8, and "s"), an origin is required. Let $(x_0, R_0) = (0,0)$ be the one. Then, the axial coordinates for all other stations follow easily from Figure 3.31:

$$x_{h,1} = x_{t,1} = x_0 + L_{0-1} \quad (3.209)$$

$$x_{h,2} = x_{t,2} = x_0 + L_{0-1} + c_{x,R} \quad (3.210)$$

$$x_{h,3} = x_{t,3} = x_0 + L_{0-1} + c_{x,R} + L_{2-3} \quad (3.211)$$

$$x_{h,4} = x_{t,4} = x_0 + L_{0-1} + c_{x,R} + L_{2-3} + c_{x,IGV} \quad (3.212)$$

$$x_{h,5} = x_{t,5} = x_0 + L_{0-1} + c_{x,R} + L_{2-5} \quad (3.213)$$

$$x_{h,6} = x_{t,6} = x_0 + L_{0-1} + c_{x,R} + L_{2-5} + c_{x,OGV} \quad (3.214)$$

$$x_{h,7} = x_{t,7} = x_0 + L_{0-1} + c_{x,R} + L_{2-5} + c_{x,OGV} + L_{6-7} \quad (3.215)$$

$$x_{h,8} = x_{t,8} = x_0 + L_{0-1} + c_{x,R} + L_{2-5} + c_{x,OGV} + L_{6-7} + c_{x,struts} \quad (3.216)$$

$$x_s = x_0 + L_{0-1} + c_{x,R} + L_{2-s} \quad (3.217)$$

3.7.6 Blade Count

Concluding this section, the blade count for the fan blade rows is given. The number of blades for the various blade rows is estimated according to Eq. (3.21) using the respective axial chord lengths and (average) mean radii:

$$Z_b = \left\lceil \frac{2\pi\sigma\bar{R}_m}{c_x} \right\rceil \quad (3.218)$$

In the above, the blade solidity is an input and typical values can be found in Appendix A.

3.8 TURBO1D PROOSIS Library

As mentioned in the chapter introduction, the methods and equations presented in the previous sections were used to develop a dedicated PROOSIS library for aerothermodynamic calculations of turbomachinery components (named TURBO1D). Apart from components for compressor, turbine, and fan 0D/1D calculations, a component that conducts basic aerothermodynamic calculations for annular combustors is also defined (the mathematical modelling can be found in Appendix C). The PROOSIS symbols defined in the TURBO1D library are shown in Figure 3.32. As it can be seen from Figure 3.32, two (2) compressor components are defined with two (2) and three (3) gas bleeds, but components with more (or less) gas bleeds can easily be defined by utilizing the PROOSIS EL's inheritance capability.

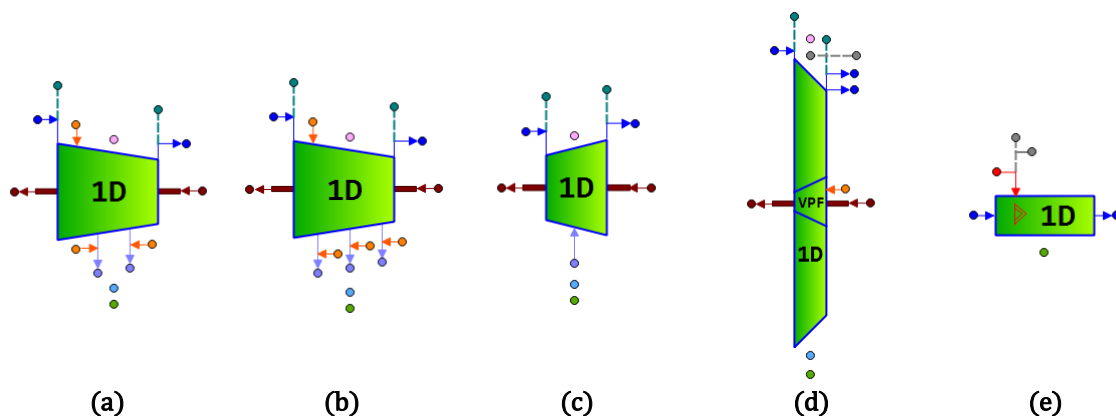


Figure 3.32: TURBO1D palette defining PROOSIS symbols for the aerothermodynamic design of (a) axial-flow compressors with two (2) gas bleeds, (b) axial-flow compressors with three (3) gas bleeds, (c) axial-flow turbines with one (1) returning bleed, (d) axial-flow fans, and (e) burners.

The symbols shown in Figure 3.32, can be dragged-and-dropped into a PROOSIS schematic canvas for modelling the aerothermodynamic design of turbofan engines. Note that, more than one symbols of the same TURBO1D component seen in Figure 3.32 can be dragged-and-dropped into the same canvas and connected together.

3.9 TURBO1D Validation Studies

In this paragraph, the components for the aerothermodynamic design of the compressor, turbine, and fan are validated against publicly available data. For this reason, information about major components of the NASA Energy Efficient Engine (E³) was utilized.

3.9.1 Compressor Component Validation

For the validation of the compressor component of the TURBO1D library, the NASA/GE E³ 10-stage, high-pressure compressor is considered [see Holloway et al. (1982) and Cline et al. (1983)]. This is an advanced technology, high-speed and -aerodynamic loading compressor, the aerodynamic and mechanical design of which took place during the late 1970's-early 1980's. Its basic configuration and design features were selected during a NASA/GE preliminary design and optimization study in the mid-1970's. The inlet guide vanes and the first four stator rows are variable while two gas bleeds are located at the exit of stages 5 (customer needs and turbine cooling) and 7 (starting and turbine cooling). The aerodynamic design of the compressor was performed at 100% corrected speed and corrected inlet mass flow rate (maximum climb flight conditions) for an overall pressure ratio of 25 (referred to as the "original design"), and standard-day, sea-level inlet static conditions (288.15 K, 101,325 Pa). The efficiency goal for the E³ HPC was set at 85.7%. However, the two rig-tests conducted in the early 1980's, did not reach 100% speed nor this efficiency goal. The aerodynamic design point data for the compressor are summarized in Table 3.8.

Table 3.8: NASA/GE E³ HPC aerodynamic design point data [see Holloway et al. (1982)]

Parameter	Value
Corrected inlet tip speed	456.0 m/s
Corrected inflow	54.4 kg/s
Mechanical rotational speed	12,416.5 rpm
Overall pressure ratio	25.0

Next, the necessary inputs as calculated and/or extracted from Holloway et al. (1982), are described.

The rotor inlet absolute flow angle and the total enthalpy rise fraction per stage are illustrated in Figure 3.33. The compressor inlet and exit absolute flow angles are

both equal to 0° . The compressor characteristic flow-annulus dimensions are given in Table 3.9.

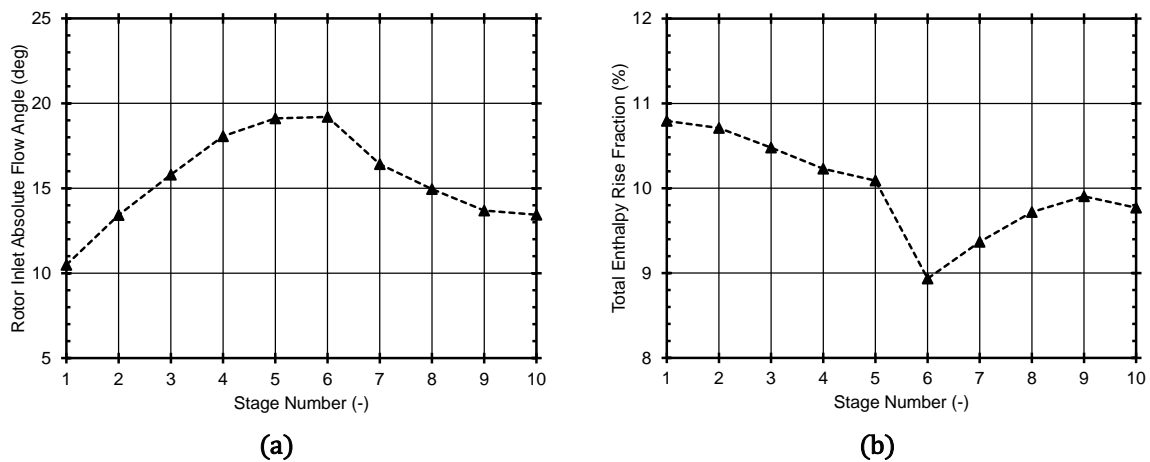


Figure 3.33: NASA/GE E³ HPC stage-wise distribution of (a) rotor inlet absolute flow angle and (b) total enthalpy rise fraction [see Holloway et al. (1982)].

Table 3.9: NASA/GE E³ HPC characteristic flow-annulus dimensions [see Holloway et al. (1982)]

Parameter	Value
Inlet flow-annulus area	0.318 m ²
Exit flow-annulus area	0.035 m ²
Inlet hub-to-tip ratio	0.48
Exit hub-to-tip ratio	0.93
1 st rotor axial gap percentage	4.2%
1 st stator axial gap percentage	46.0%
10 th rotor axial gap percentage	59.6%
10 th stator axial gap percentage	52.2%
IGVs axial gap percentage	23.4%
Axial gap percentage at bleeding stages (average)	100.5%

Two gas bleeds are extracted from the compressor. The first is at the exit of the 5th stage and the other at the exit of the 7th stage. The magnitude (as percentage of the compressor inlet mass flow rate) and the position of the bleeds expressed as fraction of the overall enthalpy rise are given in Table 3.10.

Table 3.10: NASA/GE E³ HPC gas bleeds magnitudes and positions [see Holloway et al. (1982)]

Parameter	Value
5 th stage gas bleed magnitude	1.3%
5 th stage gas bleed position	52.3%
7 th stage gas bleed magnitude	2.3%
7 th stage gas bleed position	70.6%

The blade dimensions are given in Table 3.11, while the IGVs performance characteristics (losses and axial velocity ratio) are given in Table 3.12.

Table 3.11: NASA/GE E³ HPC blade dimensions [see Holloway et al. (1982)]

Parameter	Value
1 st rotor aspect ratio	1.52
1 st stator aspect ratio	2.75
10 th rotor aspect ratio	0.92
10 th stator aspect ratio	0.95
IGVs aspect ratio	3.54
IGVs solidity	1.004

Table 3.12: NASA/GE E³ HPC IGVs performance [see Holloway et al. (1982)]

Parameter	Value
Total pressure losses	3.8%
Axial velocity ratio	1.104

The blockage factor required to establish the effective from the geometric flow-annulus areas is distributed approximately linearly from an inlet value of 0.97 to an exit value of 0.9 [Holloway et al. (1982)]. Therefore, its value can readily be estimated for intermediate compressor stages and is used as an input for this validation case (see Figure 3.34).

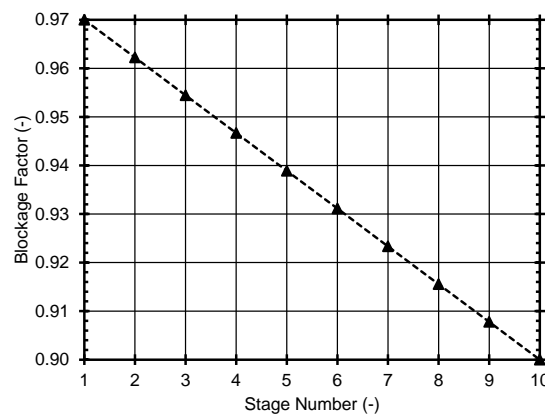


Figure 3.34: NASA/GE E³ HPC stage-wise blockage factor distribution [Holloway et al. (1982)].

The last input required for the validation is the shape of the compressor mean-line. Currently, the TURBO1D compressor component considers that the stage(-wise) constant mean diameter equals that at the respective rotor inlet (see paragraph 3.3.6). In this context, the mean diameter at the inlet of each stage is calculated and its distribution is plotted in Figure 3.35.

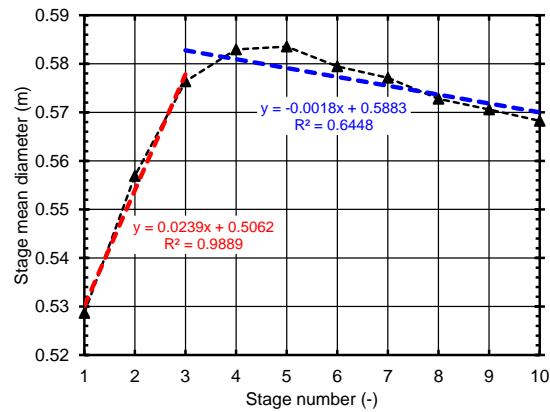


Figure 3.35: NASA/GE E³ HPC mean-line distribution [Holloway et al. (1982)].

As it can be seen from Figure 3.35, the NASA/GE E³ HPC mean-line shape can be approximated as linear through the first three stages (1-3) and as constant through the remaining seven stages (4-10).

Using as inputs the values outlined in the preceding paragraph, the overall isentropic efficiency of the compressor is calculated using both the losses ($TF = 1.0$) and Glassman's correlations for current and advanced level technology compressor stages (see paragraph 3.3.13). The results, as well as their comparison against the NASA/GE E³ HPC goal efficiency (85.7%) are summarized in Table 3.13, where the relative difference is defined as $100 \times (\eta_{is}^{E3} - \eta_{is}^{TURBO1D}) / \eta_{is}^{E3}$.

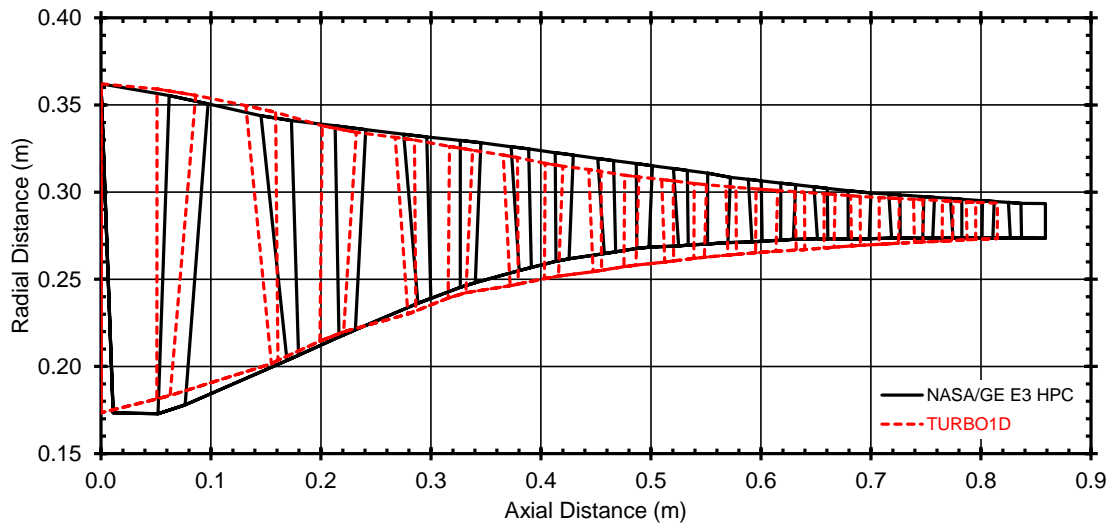
As it can be seen from Table 3.13, all three efficiency estimation methods predict the NASA/GE E³ HPC goal efficiency within a $\pm 2\%$ error. The losses method gives the best efficiency prediction ($\sim 0.8\%$ error) among the three. Here, it is worth noting that the losses method is more meaningful physics-wise compared to Glassman's method, and this fact probably justifies the better prediction.

Table 3.13: Comparison between the actual NASA/GE E³ HPC overall isentropic efficiency and the one calculated by the TURBO1D compressor component for different calculation methods

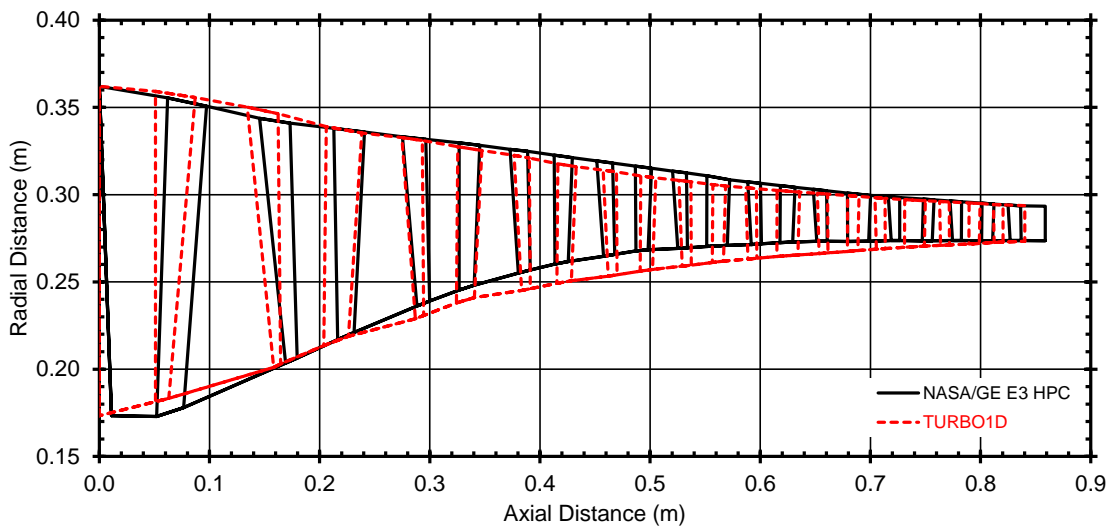
Calculation Method	Actual Efficiency	Estimated Efficiency	Relative Difference
Losses		85.0%	+0.81%
Glassman's current	85.7%	84.4%	+1.51%
Glassman's advanced		86.5%	-0.95%

In Figure 3.36, the comparison between the calculated and the NASA/GE E³ HPC gas-paths is illustrated for the losses, Glassman current, and Glassman advanced methods. For completeness, the RMS error between the calculated and the actual gas-path coordinates is also presented for all efficiency calculation methods in Table 3.14.

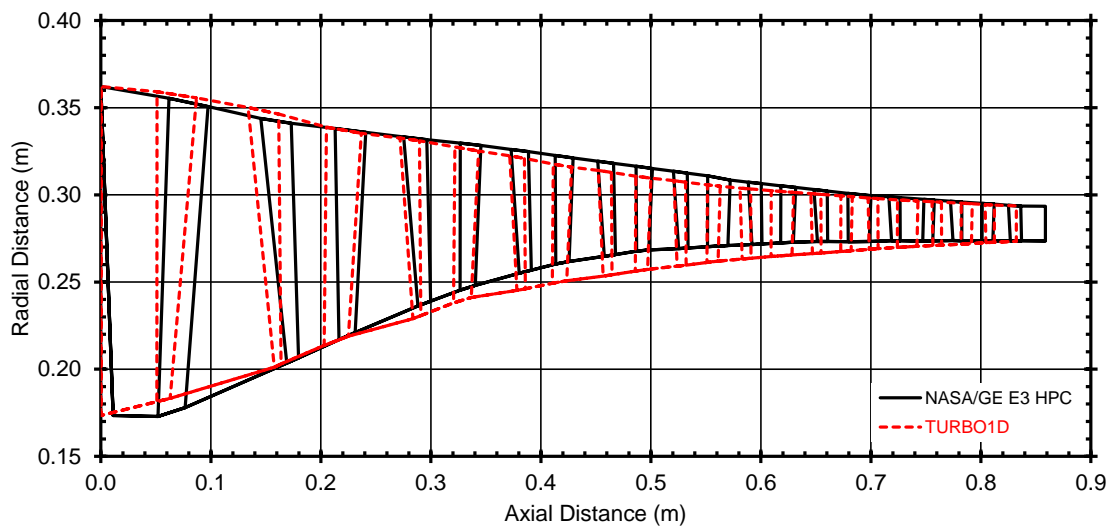
As it can be seen from both Figure 3.36 and Table 3.14, a good agreement between the actual and the estimated gas-paths exists for all three efficiency calculation methods. However, note that although the losses method gives the best efficiency prediction, it is Glassman's method for current technology level stages that gives the best prediction for gas-path geometry overall (see Table 3.14).



(a)



(b)



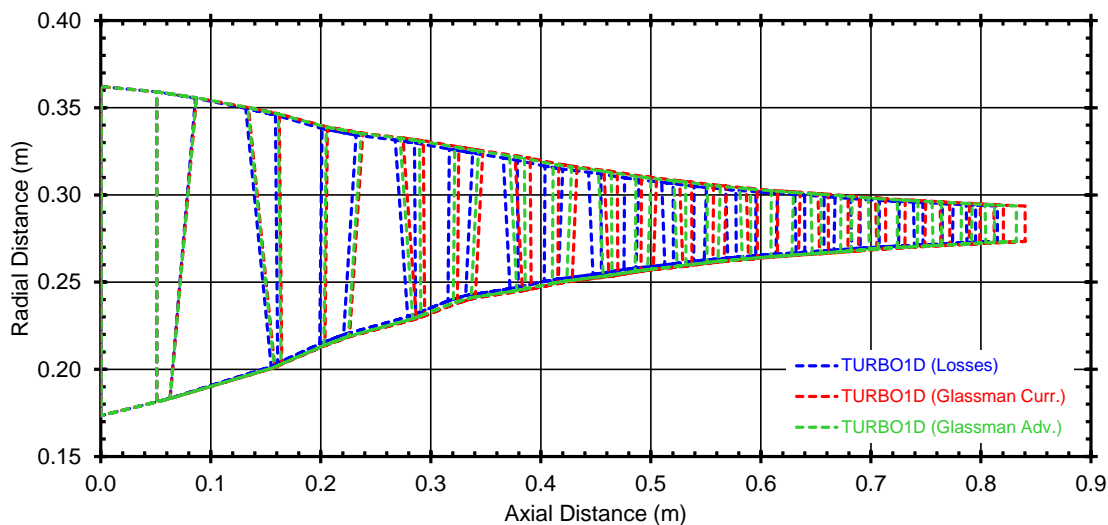
(c)

Figure 3.36: Comparison between the actual NASA/GE E³ HPC gas-path and the one obtained by the TURBO1D compressor component using the (a) losses, (b) Glassman current, and (c) Glassman advanced method.

Table 3.14: RMS errors between the actual NASA/GE E³ HPC and the estimated axial and radial gas-path coordinates

Calculation Method	Hub Axial	Hub Radial	Tip Axial	Tip Radial
Losses	5.03%	2.58%	2.30%	1.20%
Glassman's current	3.50%	2.84%	0.83%	1.03%
Glassman's advanced	3.79%	2.82%	1.20%	1.04%

Finally, Figure 3.37 shows the comparison between the meridional views produced by the three methods.

**Figure 3.37:** Comparison between the calculated meridional views obtained by the TURBO1D compressor component for the different calculation methods.

The validation of the component model was carried out utilizing information about a turbomachinery component that has been through almost all the stages of the development course up to actual manufacturing and testing. The NASA/GE E³ HPC was even scaled up in size and a 9-stage derivative of it was employed as the high-pressure compressor of the GE90 engine [see Gunston (2004)]. Keeping this in mind, it is concluded that the comparison between the predicted and the actual component isentropic efficiencies and gas-path coordinates are deemed satisfactory for a preliminary design tool exploiting only semi-empirical methods and correlations.

3.9.2 Turbine Component Validation

For the validation of the turbine component included in the TURBO1D library, the NASA/GE E³ 5-stage, low-pressure Block II scaled air-turbine is considered [see Bridgeman et al. (1983)]. The NASA/GE E³ LPT is a high-aerodynamic loading turbine featuring high outer wall slope, controlled vortex aerodynamics, and reduced clearances. It was designed and tested during the late 1970's-early 1980's. The turbine performance assessment was conducted in a series of scaled air-turbine rig-tests

divided into two phases: Block I and Block II. The final 5-stage, scaled air-model was tested as Block II in the early 1980's and its efficiency prior to any corrections for edge blockage, Reynolds number, and purge air was measured to be up to 92% [see Bridgeman et al. (1983)]. The aerodynamic design point data for the Block II scaled air-model are summarized in Table 3.15.

Table 3.15: NASA/GE E³ LPT Block II scaled air-model aerodynamic design point data [see Bridgeman et al. (1983)]

Parameter	Value
Inlet total temperature	416.17 K
Inlet total pressure	310.0 kPa
Inflow	24.4 kg/s
Mechanical rotational speed	3208.7 rpm
Overall pressure ratio	4.37

Next, the necessary inputs as calculated and/or extracted from Bridgeman et al. (1983), are described.

The stage-wise total enthalpy drop fraction and reaction are illustrated in Figure 3.38. The turbine inlet and exit absolute flow angles are equal to 0° and 12.5°, respectively. The turbine characteristic flow-annulus dimensions are given in Table 3.16.

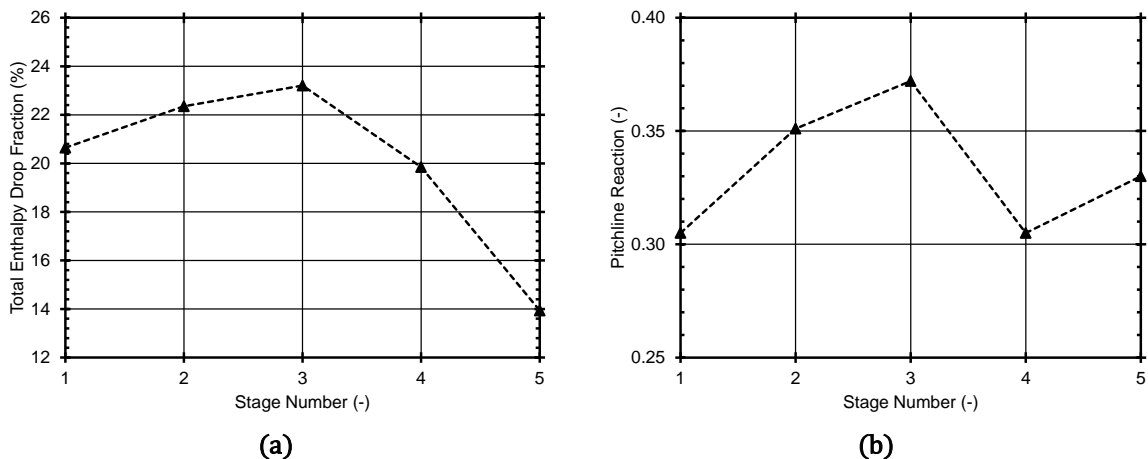


Figure 3.38: NASA/GE E³ LPT Block II scaled air-model stage-wise distribution of (a) total enthalpy drop fraction and (b) reaction [see Bridgeman et al. (1983)].

Table 3.16: NASA/GE E³ LPT Block II scaled air-model characteristic flow-annulus dimensions [see Bridgeman et al. (1983)]

Parameter	Value
Inlet flow-annulus area	0.086 m ²
Exit flow-annulus area	0.305 m ²

Table 3.16 (cont.): NASA/GE E³ LPT Block II scaled air-model characteristic flow-annulus dimensions [see Bridgeman et al. (1983)]

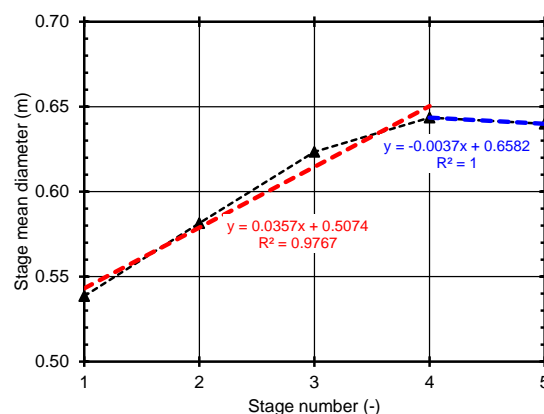
Parameter	Value
Inlet hub-to-tip ratio	0.80
Exit hub-to-tip ratio	0.62
1 st rotor axial gap percentage	49.1%
1 st nozzle axial gap percentage	18.6%
5 th rotor axial gap percentage	42.5%
5 th nozzle axial gap percentage	33.4%

Regarding the blade geometry, the average value of nozzle and rotor aspect ratios are equal to 3.802 and 5.952, respectively. From these values, Glassman's mid- and high-aspect ratio correlations are assumed for the nozzle and rotor blades, respectively. Finally, the average Zweifel loading coefficient is equal to 0.873 and 1.066 for the nozzles and the rotors, respectively. These values are summarized in Table 3.17.

Table 3.17: NASA/GE E³ LPT Block II scaled air-model blade dimensions [Bridgeman et al. (1983)]

Parameter	Value
Nozzles aspect ratio	Glassman's mid-
Rotors aspect ratio	Glassman's high-
Nozzles Zweifel coefficient (average)	0.873
Rotors Zweifel coefficient (average)	1.066

The last input required for the validation of the turbine component is the shape of the mean-line. Currently, the TURBO1D turbine component considers that the stage(-wise) constant mean diameter equals that at the respective rotor exit (see paragraph 3.5.4). In this context, the mean diameter at the outlet of each stage is calculated from Bridgeman et al. (1983) and its distribution is plotted in Figure 3.39.

**Figure 3.39:** NASA/GE E³ LPT Block II scaled air-model mean-line distribution [Bridgeman et al. (1983)].

As it can be seen from Figure 3.39, the NASA/GE E³ LPT Block II scaled air-model mean-line shape can be approximated as linear through the first four stages (1-4) and, then, as constant.

Using as inputs the values outlined above, the overall isentropic efficiency of the turbine is calculated using both Aungier's (with $TF = 1.0$) and Glassman's methods (see paragraph 3.5.8). The results, as well as their comparison against the uncorrected measured efficiency (92%) for the NASA/GE E³ LPT Block II scaled air-model are summarized in Table 3.18, where the relative differences are expressed as $100 \times (\eta_{is}^{E3} - \eta_{is}^{TURBO1D}) / \eta_{is}^{E3}$.

Table 3.18: Comparison between the actual NASA/GE E³ LPT Block II scaled air-model overall isentropic efficiency and the one calculated by the TURBO1D turbine component for different calculation methods

Calculation Method	Actual Efficiency	Estimated Efficiency	Relative Difference
Aungier	92%	89.02%	+3.24%
Glassman		91.38%	+0.68%

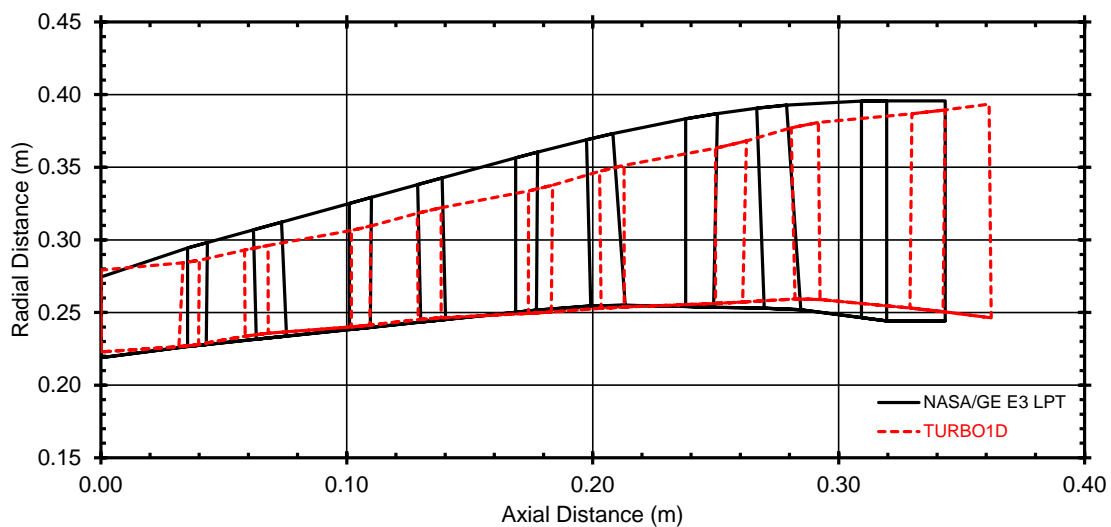
As it can be seen from Table 3.18, both efficiency methods predict the NASA/GE E³ LPT efficiency within a $\pm 3.5\%$ error, where Glassman's method gives the best efficiency prediction between the two. Here, it is worth noting that Glassman's method is more meaningful physics-wise compared to Aungier's method as it is actually a losses method probably, justifying, the better prediction. Moreover, Aungier's method is highly dependent on the value of the technology factor (TF) which is introduced in order to capture the improvement in turbine efficiency. Although the NASA/GE E³ LPT's installed efficiency was expected to be around the 91.5% value (a value higher than that for engines developed around the 1980's), here a technology factor value of 1.0 was assumed. It is noted that according to Bellocq et al. (2015), turbines with an EIS of 2020 are expected to have an efficiency of about 93%. Thus, a technology factor value of 1.02 is suggested. Considering that the NASA/GE E³ LPT measured efficiency is very close to this value, using a higher TF would have been justified and would have led to a better prediction.

In Figure 3.40, the comparison between the calculated and the NASA/GE E³ LPT Block II scaled air-model gas-paths is illustrated for Aungier's and Glassman's methods. In Figure 3.41, the comparison between the meridional views produced by the two calculation methods is shown. For completeness, the RMS error between the calculated and the actual gas-path coordinates is also presented for both methods in Table 3.19.

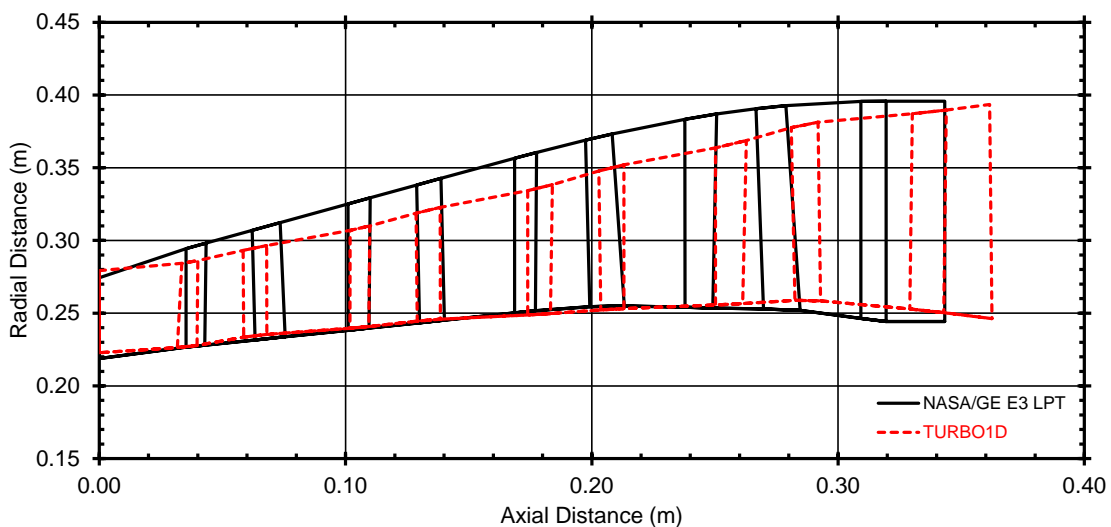
As it can be seen from Figure 3.40 and Table 3.19, an acceptable agreement between the actual and the estimated gas-paths exists for both efficiency estimation methods. Regarding the difference between the two, as we see from Figure 3.41 and Table 3.19, both methods produce gas-paths that are very close to each other, while both methods produce gas-paths which are slightly lengthier than the actual one.

It is worth noting that both methods predict the radial coordinates of the hub annulus wall very well, in contrast to the tip (see Table 3.19). One reason for this discrepancy is due to the fact that the NASA/GE E³ LPT was designed with high outer wall slopes to facilitate active clearance control technologies. Note that the present

design methodology does not model these technologies and their effect on both the turbine performance and gas-path shape. Additionally, as we have already explained in paragraph 3.5.4, the design methodology applied to turbines assumes that the mean radius remains constant across a stage. Taking into account that the flow-annulus area across a turbine experiences an abrupt widening due to the flow involved (accelerating flow and large density decreases), the latter may not be an appropriate design assumption. In future adaptations of the method, keeping the mean radius constant across a row should be investigated instead so that the rapid annulus changes be taken into account at the blade row level.



(a)



(b)

Figure 3.40: Comparison between the actual NASA/GE E³ LPT Block II scaled air-model gas-path and the one obtained by the TURBO1D turbine component using (a) Glassman's method and (b) Aungier's method.

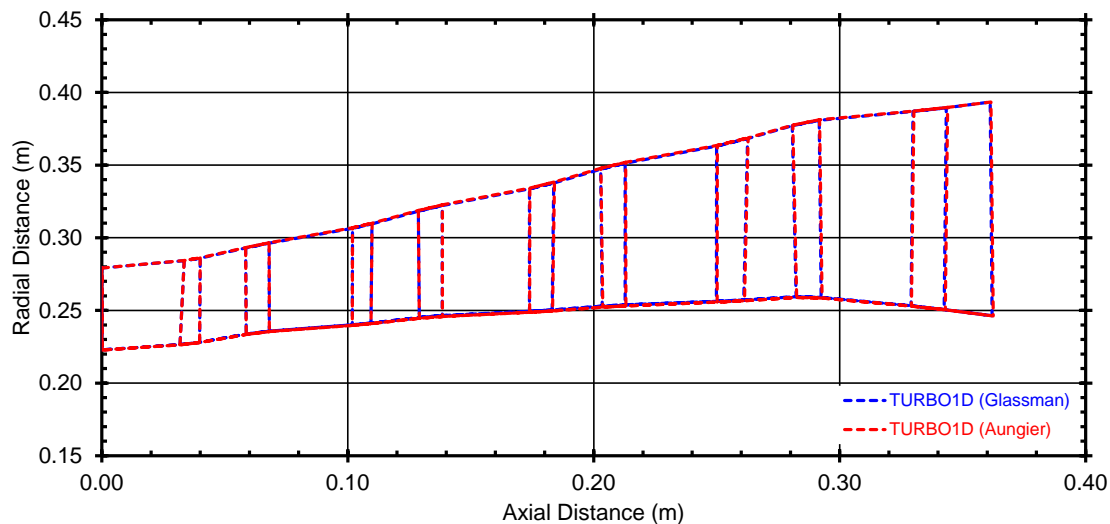


Figure 3.41: Comparison between the calculated meridional views obtained by the TURBO1D turbine component for the different calculation methods.

Table 3.19: RMS errors between the actual NASA/GE E³ LPT Block II scaled air-model and the estimated axial and radial gas-path coordinates

Calculation Method	Hub Axial	Hub Radial	Tip Axial	Tip Radial
Aungier	5.20%	1.34%	4.72%	4.61%
Glassman	5.15%	1.41%	4.65%	4.73%

The validation for the turbine model was carried out utilizing information about a turbomachinery component that has been through almost all the stages of the development course up to actual manufacturing and testing. Keeping this in mind, it is concluded that the comparison between the predicted and the actual component isentropic efficiencies and gas-path coordinates are deemed satisfactory for a preliminary design tool exploiting only semi-empirical methods and correlations.

3.9.3 Fan Component Validation

For the validation of the TURBO1D fan component, information about the NASA/P&W E³ fan was utilized. The NASA/P&W E³ fan is a high-performance, single-stage machine which was designed based on advanced technologies in the areas of aerodynamics and structural mechanics [see Halle et al. (1981)]. During the design phase, two fan components were originally designed and evaluated, one with shrouded rotor blades and one without shrouds. The aerodynamic design for both fan configurations was conducted at flight altitude of 10,668 m and for a cruise Mach number of 0.8. For the shroudless design, which will be used here for validation purposes, an efficiency of 87.3 was predicted²⁵. Table 3.20 summarizes the aerodynamic design point data for the NASA/P&W shroudless fan configuration.

²⁵This refers to the bypass efficiency.

Table 3.20: NASA/P&W E³ shroudless fan aerodynamic design point data [see Halle et al. (1981)]

Parameter	Value
Bypass ratio	6.51
Corrected inlet tip speed	456.0 m/s
Corrected inflow	622.7 kg/s
Corrected mechanical rotational speed	4215 rpm
Fan bypass pressure ratio	1.74
Fan core pressure ratio	1.61

Next, the necessary inputs as calculated and/or extracted from Halle et al. (1981) are given. The fan characteristic flow-annulus dimensions are summarized in Table 3.21, while the blade dimensions in Table 3.22.

Table 3.21: NASA/P&W E³ shroudless fan main flow-annulus dimensions [see Halle et al. (1982)]

Parameter	Value
Inlet flow-annulus area	2.938 m ²
Exit flow-annulus area (bypass)	2.180 m ²
Inlet hub-to-tip ratio	0.34
Bypass hub hade angle	6.1°
Core tip hade angle	-7.5°
Core hub hade angle	18.3°
Rotor-splitter axial gap percentage	31.4%
Rotor-OGVs axial gap percentage	300.9%
Rotor-IGVs axial gap percentage	42.6%
Rotor exit-to-inlet tip ratio	0.992

Table 3.22: NASA/P&W E³ shroudless fan main blade dimensions [see Halle et al. (1982)]

Parameter	Value
Rotor axial aspect ratio	3.41
OGVs axial aspect ratio	2.64
IGVs axial aspect ratio	1.63

Using as inputs the values summarized above, the fan polytropic efficiency is calculated. The result, as well as its comparison against the predicted efficiency (87.3%) for the NASA/P&W E³ shroudless fan model are summarized in Table 3.23, where the relative difference in the table is expressed as $100 \times (\eta_p^{E3} - \eta_p^{TURBO1D}) / \eta_p^{E3}$.

Table 3.23: Comparison between the actual NASA/P&W E³ shroudless fan efficiency and the one calculated by the TURBO1D fan component

Actual Efficiency	Estimated Efficiency	Relative Difference
87.3%	92.11%	-5.51%

As we see from Table 3.23, the difference between the actual and the estimated efficiencies is ~5.5%. This difference is obviously attributed to the correlation used for estimating the fan efficiency (see paragraph 3.7.3). As we can see from Figure 3.30, for pressure ratios in the range 1.60-1.75 (as the ones of the NASA/P&W E³ fan, see Table 3.20), the efficiency is indeed expected to lie in the range 92-93.5%. The correlations presented by Felder et al. (2011) were, at the time, reflecting the anticipated efficiency trends by the year 2015, and were further enhanced to reflect efficiency trends up to the year 2025 (N+3 readiness level). Therefore, the difference in efficiencies of ~5.5% is reasonable and expected, since the NASA/P&W E³ fan is a > 40 year old design. In future adaptations of the fan modelling a technology factor should be introduced in both Eqs (3.190) and (3.191) so that the performance of older designs can be estimated with greater precision (only for validation/comparison reasons).

Finally, Figure 3.42 presents the comparison between the estimated and the NASA/P&W E³ shroudless fan configuration gas-paths.

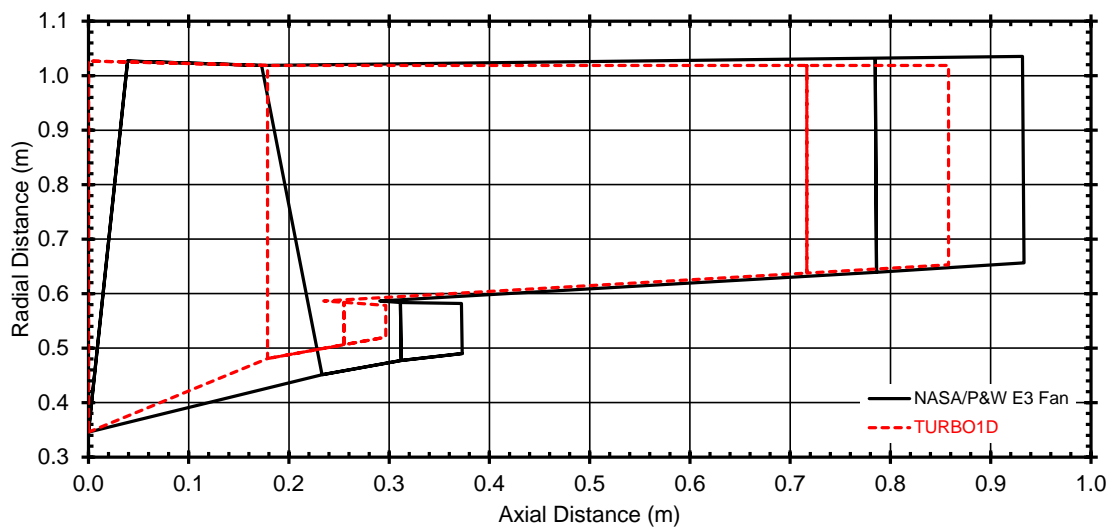


Figure 3.42: Comparison between the actual NASA/P&W E³ shroudless fan gas-path and the one obtained by the TURBO1D fan component.

As we can observe in Figure 3.42, the major discrepancy between the two gas-paths is caused by the shape of the rotor blades. In the actual fan, the rotors are tapered while in the present modelling approach the axial chord length of the blades is assumed constant, for simplicity. It is obvious that if the blade taper “matched” the actual one, then the shift of the (calculated) axial coordinates to the right would match closely the actual ones. The other reason for this discrepancy is, of course, the difference in fan efficiency, as we saw earlier. This difference produces different total conditions at the

rotor exit and, thus, a difference in area and radial dimensions (which is noticeable at the hub wall of the core stream). Nevertheless, the comparison between the two gas-paths is deemed acceptable for the needs of the present work.

Apart from the observations made above in terms of both the efficiency and gas-path geometry predictions, one should also keep in mind another aspect of the fan design. High bypass ratio fans are typically machines that are characterized by highly 3D flow phenomena, especially along the rotor span (low hub-to-tip ratios). These flow phenomena are, in turn, accommodated by highly twisted blades in modern turbofan engines. Of course, this level of modelling fidelity is not applicable in a preliminary design calculation. Therefore, the predictions obtained by the TURBO1D fan component are deemed satisfactory for the needs of this thesis.

3.10 Summary and Discussion

In the present chapter, a novel modelling approach for the aerothermodynamic design of axial-flow compressors, turbines, and fans was presented. This modelling approach led to the development of a dedicated PROOSIS library including components for the aerothermodynamic design of axial-flow gas turbine components (TURBO1D). The components defined in the TURBO1D library inherit the basic fluid models, thermodynamic functions, and numerical solvers from the standard TURBO library, thus enabling consistent calculations between the thermodynamic analysis and the aerodynamic design calculations. The newly developed components integrate performance (0D) calculations, mean-line (1D) aerodynamic design, and gas-path generation/visualization capabilities at the same modelling level, leading to single-step and transparent calculations. Iterative procedures that are needed at stage level for estimating the stage efficiency and/or pressure ratio are confined to the stage level and, therefore, the mathematical models of the component and of the engine are not changed. Finally, the aerothermodynamic design is accomplished through a stage-by-stage calculation approach, where the stage performance (efficiency and pressure ratio) is established using either loss or semi-empirical (e.g., Smith-type charts for turbines) methods, among other options, while the user can select from several options for defining the mean-line shape of a component.

Finally, the components for the aerothermodynamic design of fans, compressors, and turbines were validated against publicly available data for existing engine components. From the validation studies, it was shown that the 1D aerothermodynamic design can reproduce the meridional geometry and performance of existing machines, which have been through almost all the stages of the development course up to actual manufacturing and testing.

4 Mechanical Design of Critical Structural Components

4.1 Introduction

The completion of the aerothermodynamic design presented in Chapter 3 is followed by mechanical design (see Figure 4.1). Mechanical design is obviously one of the most critical stages in the design chain of gas turbines both at component and at engine level. Aerothermodynamic design provides the necessary rotational speeds, dimensions, and cycle data (e.g., pressures, temperatures, mass flow rates), which are then fed to mechanical design for establishing the size of critical structural components and parts, both rotating and stationary. Such parts include compressor and turbine disks and casings, and interconnecting machinery such as rotating shafts and ducts, among other. Structural components are designed primarily to withstand the severe mechanical and thermal loads developed within a gas turbine engine for ensuring the engine longevity and safe operation, but also to minimize the engine production, operational, and maintenance costs.

The mechanical and thermal stresses developed within gas turbine components are both of steady and unsteady nature, the latter owed to intermittent aerodynamic loads. Centrifugal, bending, vibratory forces, and thermal loads are examples of loads developed in gas turbine components [e.g., Saravanamuttoo et al. (2017) and Ntonas et al. (2021)], that create a complicated and severe stress environment that designers should consider when developing a new engine.

This chapter, the equations, models, and procedures developed and used for the preliminary sizing of rotating shafts and disks, casings, and interconnecting ducts, are presented, which led to the development of a dedicated mechanical design and analysis PROOSIS library (Gas Turbine Mechanical Design Code, GTMDC).

In this thesis, the term “preliminary” is used to emphasize the fact that these models are of simplified nature requiring few geometry and cycle data inputs, since we just seek to identify basic design constraints, dimensions, and sizing trends. Sizing is achieved by fulfilling both geometry and stress constraints. Unsteady effects (due to, e.g., vibratory forces), production, manufacturability, and detail design aspects are not in the scope of GTMDC. At the very least, the vibratory response of rotating components should also be considered during a preliminary design process [e.g., in terms of

Campbell diagrams according to Ntonas et al. (2022)] for ensuring structural integrity in both steady and unsteady loadings, but this topic is left for future research.

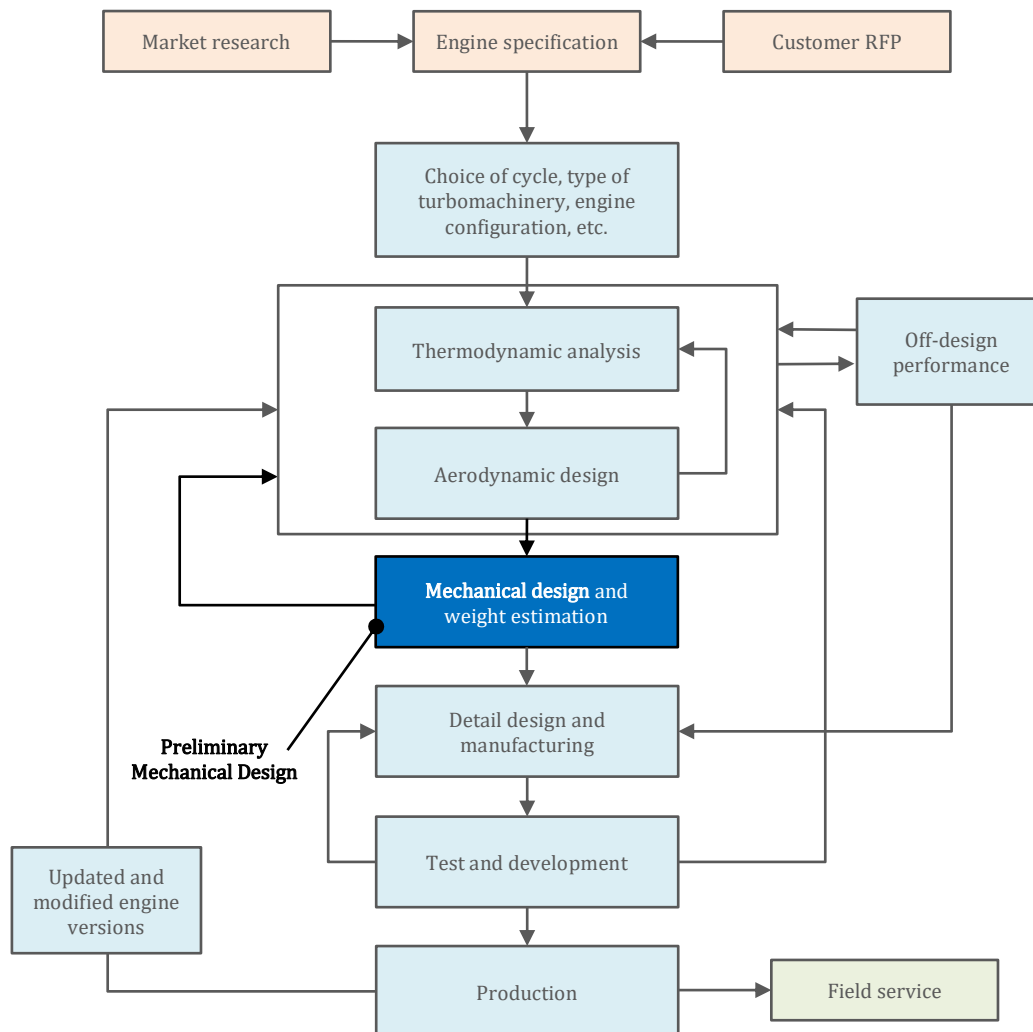


Figure 4.1: Simplified flow-chart representing the development course of a new gas turbine engine [adapted from Mattingly et al. (2002)]. The present chapter is concerned with the “Preliminary Mechanical Design” box.

4.2 Materials Database

Mechanical design cannot be performed without a database of structural materials. For this reason, in the present thesis a database of engineering materials commonly used in gas turbine applications was developed in PROOSIS based on information gathered from online material databases²⁶ and vendor^{27,28,29} datasheets. For each material in the database, its density (ρ), modulus of elasticity (E), yield strength at 0.2% strain (σ_Y),

²⁶<http://www.matweb.com> (accessed: May 11th, 2022)

²⁷<http://www.specialmetals.com> (accessed: May 11th, 2022)

²⁸<http://www.aubertduval.com> (accessed: May 11th, 2022)

²⁹<http://www.americanelements.com> (accessed: May 11th, 2022)

ultimate tensile strength (σ_{UTS}), Poisson's ratio (ν), and coefficient of thermal expansion (α_{CTE}), are available. Take note that mechanical properties (E , σ_Y , σ_{UTS} , ν , α_{CTE}) are stored in the database in the form of 1D tables in terms of the material temperature.

Table 4.1 tabulates all materials available in the database and their mechanical properties at room temperature, while Table 4.2 shows their typical uses in gas turbine applications as identified in vendor datasheets, online material databases, gas turbine design tools [see Kurzke (2007)], gas turbine textbooks [see Rolls-Royce plc (1996) and Gunston (2004)], and gas turbine engines currently in operation.

Table 4.1: Database materials and their mechanical properties at room temperature (20 °C)

Material	ρ (kg/m ³)	E (GPa)	σ_Y (MPa)	σ_{UTS} (MPa)	ν (-)	α_{CTE} ($\mu\text{m}/\text{m}/^\circ\text{C}$)
A-286	7916	199	660	998	0.30	16.3
AM-350	7920	202	1170	1394	0.30	10.9
Aluminum-2050	2710	76	441	490	0.30	21.4
Gr. Ascoloy-418	7870	199	1019	1218	0.30	10.2
Hastelloy-S	8750	197	304	763	0.30	12.7
Haynes-188	8980	232	432	940	0.30	11.4
Haynes-282	8270	217	710	1146	0.30	12.2
Incoloy-800	7940	197	695	776	0.34	13.2
Incoloy-907	8330	165	1120	1341	0.36	7.8
Incoloy-925	8080	199	787	1159	0.29	12.4
Inconel-601	8110	207	240	706	0.27	13.3
Inconel-706A	8050	211	1022	1293	0.39	12.6
Inconel-706B	8050	211	1101	1356	0.39	12.6
Inconel-718	8220	201	1202	1401	0.30	13
Inconel-738	8110	201	952	1096	0.28	11.3
Inconel-740	8050	221	722	1170	0.30	11.9
Inconel-783	7810	177	779	1194	0.31	9.9
Kevlar-149	1470	179	1240	3450	0.36	-4.0
Kevlar-49	1440	179	1240	3000	0.36	-4.0
Mar-M-247	8540	205	861	989	0.30	10.9
N-155	8249	202	412	808	0.30	13.6
Nimonic-105	8010	221	751	1140	0.30	11.7
Rene-41	8250	218	1041	1396	0.30	11.9
Rene-N4	8400	128	1000	1036	0.30	12.9
Rene-N5	8600	128	855	1078	0.30	12.9
Ti-6Al-4V	4430	114	880	970	0.33	8.6
Ti-8-1-1	4370	120	900	1020	0.32	8.5
Udimet-720	8080	213	888	1103	0.30	12.1
Waspaloy	8190	215	764	1264	0.30	12.5

Table 4.2: Typical uses of database materials in gas turbine applications

Material	Fan	Compressor	Turbine	Burner	Other
A-286	Blades Casings	Blades Casings	Blades Casings Disks	Burner parts	Ducts
AM-350		Blades Disks			Shafts
Aluminum-2050	Blades Bypass Casings				
Gr. Ascoloy-418		Blades Disks			Hardware Shafts
Hastelloy-S					Ducts
Haynes-188					Hardware
Haynes-282			Turbine parts	Burner parts	
Incoloy-800					Hardware
Incoloy-907	Casings	Casings	Casings		Shafts
Incoloy-925					Hardware
Inconel-601				Burner parts	Ducts
Inconel-706A	Casings	Casings Disks	Casings Disks		Shafts
Inconel-706B	Casings	Casings Disks	Casings Disks		Shafts
Inconel-718	Blades Casings Disks	Blades Casings Disks	Blades Casings Disks		Ducts Shafts
Inconel-738				Burner parts	Ducts
Inconel-740					Hardware
Inconel-783	Casings	Casings	Casings		
Kevlar-149	Bypass casings				Fan OGVs
Kevlar-49	Bypass casings				Fan OGVs
Mar-M-247	Blades	Blades	Blades		
N-155		Casings	Blades	Burner parts	
Nimonic-105	Blades Disks	Blades Disks	Blades Disks		Shafts
Rene-41			Blades Disks	Burner parts	Hardware
Rene-N4			Blades		
Rene-N5			Blades		
Ti-6Al-4V	Blades Disks	Blades Disks			Ducts Shafts
Ti-8-1-1	Blades Disks	Blades Disks			Ducts
Udimet-720		Blades Disks	Blades Disks		
Waspaloy	Disks	Disks	Disks		Shafts

As it can be seen from Table 4.1 and Table 4.2, materials of current and future technological interest for the fabrication of gas turbine components and parts, such as CMCs, are not included in the database since their detailed mechanical and thermal properties at the time of writing this thesis were not available in the public domain. However, CMSs are expected to significantly improve the performance of future engines by offering both lower component weights and better thermal insulation (the latter translates to higher operating temperatures and reduced need for cooling flows in hot-end components). Therefore, it is suggested that the database be extended once the properties of such materials become publicly available.

4.3 Power Transmitting Shafts

Shafts are an essential part of any rotating machine. They are used to connect and support different components and to transmit power between them. Here, shafts are assumed to be concentric cylinders with constant inner and outer diameters (constant thickness) that transmit power from turbines to compressors. Figure 4.2 shows a schematic diagram of a three-spool arrangement, where the shaft length is increased as one moves from the HP to the LP spool. A concentric system of shafts (Figure 4.2) is designed assuming the following:

1. The innermost shaft is assumed solid, that is, having a zero inner diameter, and
2. successive shafts are separated by a radial clearance equal to 0.20 inches according to Pera et al. (1977a).

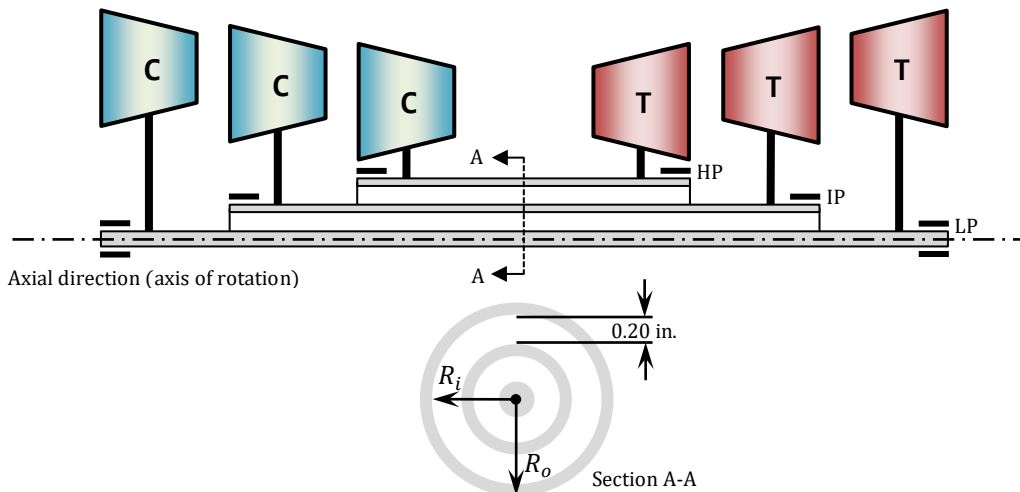


Figure 4.2: Arrangement of shafts in a 3-spool gas turbine, modelled as concentric cylinders.

Although shaft diameters are primarily determined by the requirement for torque transmission, typically shafts are also designed to withstand bending and vibratory loadings. Since these design aspects introduce additional complexity and the need for more inputs, they are omitted as is also the case in other preliminary shaft design methodologies [e.g., Pera et al. (1977a); Lolis (2014); Becker et al. (2015)].

4.3.1 Shaft Simplified Stress Model (S-SSM)

Most design methodologies [Pera et al. (1977a) and Lolis (2014)] estimate the shaft diameters by considering only the requirement for transmitted torque. The torque transmitted by a shaft creates a radial shear stress distribution which has a maximum value at the outer radius of the shaft. This is given by [see Ugural et al. (2003)]:

$$\tau = \frac{2R_o}{\pi(R_o^4 - R_i^4)} T_{rq} \quad (4.1)$$

Here, additionally, the loading due to axial and body (centrifugal) forces are also considered. The axial normal stress exerted on the shaft is expressed by [see Becker et al. (2015)]:

$$\sigma_x = \frac{1}{\pi(R_o^2 - R_i^2)} \sum F_{rc,x} \quad (4.2)$$

where $\sum F_{rc,x}$ is the sum of the axial forces induced by the components that the shaft connects. The axial force a component induces is assumed equal to the total pressure difference between the component inlet and outlet, or: $F_{rc,x} = p_{in}^0 A_{g,in} - p_{out}^0 A_{g,out}$.

Finally, the maximum tangential normal stress developed by centrifugal forces is realized at the shaft outer radius and is given by [see Becker et al. (2015)]:

$$\sigma_\theta = \frac{3 + \nu}{4} \left(R_o^2 + \frac{1 - \nu}{3 + \nu} R_i^2 \right) \rho \omega^2 \quad (4.3)$$

where $\omega = 2\pi N_{mech}/60$ is the shaft angular velocity. Note that, in their work, Becker et al. employed Eq. (4.3) having, however, replaced Poisson's ratio with a typical value of $\nu = 0.30$.

Stresses given by Eqs (4.1)–(4.3) are then combined using the von Mises criterion to yield a maximum equivalent normal stress which is given by:

$$\sigma_{vM} = \sqrt{\sigma_x^2 + \sigma_\theta^2 - \sigma_x \sigma_\theta + 3\tau^2} \quad (4.4)$$

The system of Eqs (4.1) through (4.4) will be collectively called the Shaft-Simplified Stress Model (S-SSM). For structural integrity, the maximum stress expressed by Eq. (4.4) must be less than (or, at most, equal to) the maximum allowable stress imposed by the material yield strength divided by a safety factor ($SF_Y \geq 1.0$). This condition is expressed by:

$$\sigma_{vM} \leq \frac{\sigma_Y}{SF_Y} \quad (4.5)$$

Given the shaft material and the shaft inner radius, R_i , the outer radius, R_o , is estimated by solving iteratively S-SSM on R_o until Eq. (4.5) is satisfied within a user-specified tolerance. For this reason, a Newton-Raphson method (PROOSIS built-in) is utilized to reduce the number of iterations required for obtaining the final answer.

Regarding the value of the safety factor appearing in Eq. (4.5), the following are noted. According to Loewenthal (1984), the value of SF_Y is based on personal judgement. More specifically, Loewenthal states: “... It depends on the consequences of failure, that is, cost, time, safety, etc. Some factors to consider when selecting a value for the safety factor are how well the actual loads, operating environment, and material properties are known... Values typically range from 1.3 to 6.0, depending on the confidence in the prediction technique and the criticality of the application... Values of less than 1.5 are not normally recommended”.

4.3.2 S-SSM Validation

S-SSM was validated both qualitatively and quantitatively. First, S-SSM was validated qualitatively against a commercial higher-fidelity 3D FEA tool³⁰. For this reason, a reference shaft was considered with a radius ratio of $R_i/R_o = 0.8$ and $R_o = 5$ cm, while the shaft material was selected to be a typical for such applications, that is, Inconel-706B. Axial force and torque were considered constant and typical values were adopted after the NASA/GE E³ HPC (see Appendix D), while rotational speed was varied from 2500 rpm to 22,500 rpm. Figure 4.3 shows the von Mises stress comparison between S-SSM and FEA, for different speed ratios ($N_{mech}/2500$).

As it can be seen from Figure 4.3, S-SSM reproduces successfully the physical trend obtained by the higher fidelity FEA tool. It is also worth noting that the average and maximum relative difference between the S-SSM and FEA stresses is 0.86% and 1.41%, respectively, where the relative difference is defined as $100 \times (\sigma_{vM}^{FEA} - \sigma_{vM}^{S-SSM}) / \sigma_{vM}^{FEA}$.

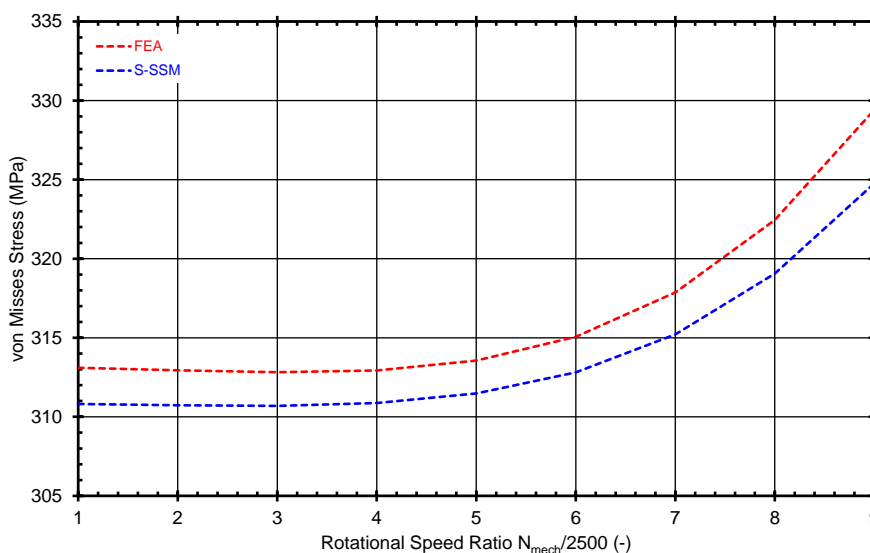


Figure 4.3: von Mises stress comparison between S-SSM and FEA for different speed ratios.

Being confident that the simplified stress model can successfully reproduce the (steady-state) stress trends observed in rotating shafts, next S-SSM was validated quantitatively against the shaft of the NASA/GE E³ HPC [see Holloway et al. (1982)].

³⁰<https://www.ansys.com/products/structures/ansys-mechanical> (accessed: May 11th, 2022)

Digitization of 2D cutaways of the engine that can be found in Holloway et al. (1982), gave a shaft inner radius of $R_i = 6.14$ cm and an outer radius of $R_o = 6.95$ cm. The shaft material was found to be Inconel-718 according to Davis et al. (1985), while E³ HPC rotates at a design speed of 12,416.5 rpm (~ 1300 rad/s). Figure 4.4 illustrates the shaft outer radius and the relative difference (defined as $100 \times |R_o^{E^3} - R_o^{S-SSM}|/R_o^{E^3}$) from $R_o = 6.95$ cm, as obtained using S-SSM, for different safety factor values in the range of 1.0–6.0 [see Loewenthal (1984)]. Apart from Inconel-718, eight (8) other engineering materials were also examined, typically used in the fabrication of shafts in turbomachinery applications (see Table 4.2).

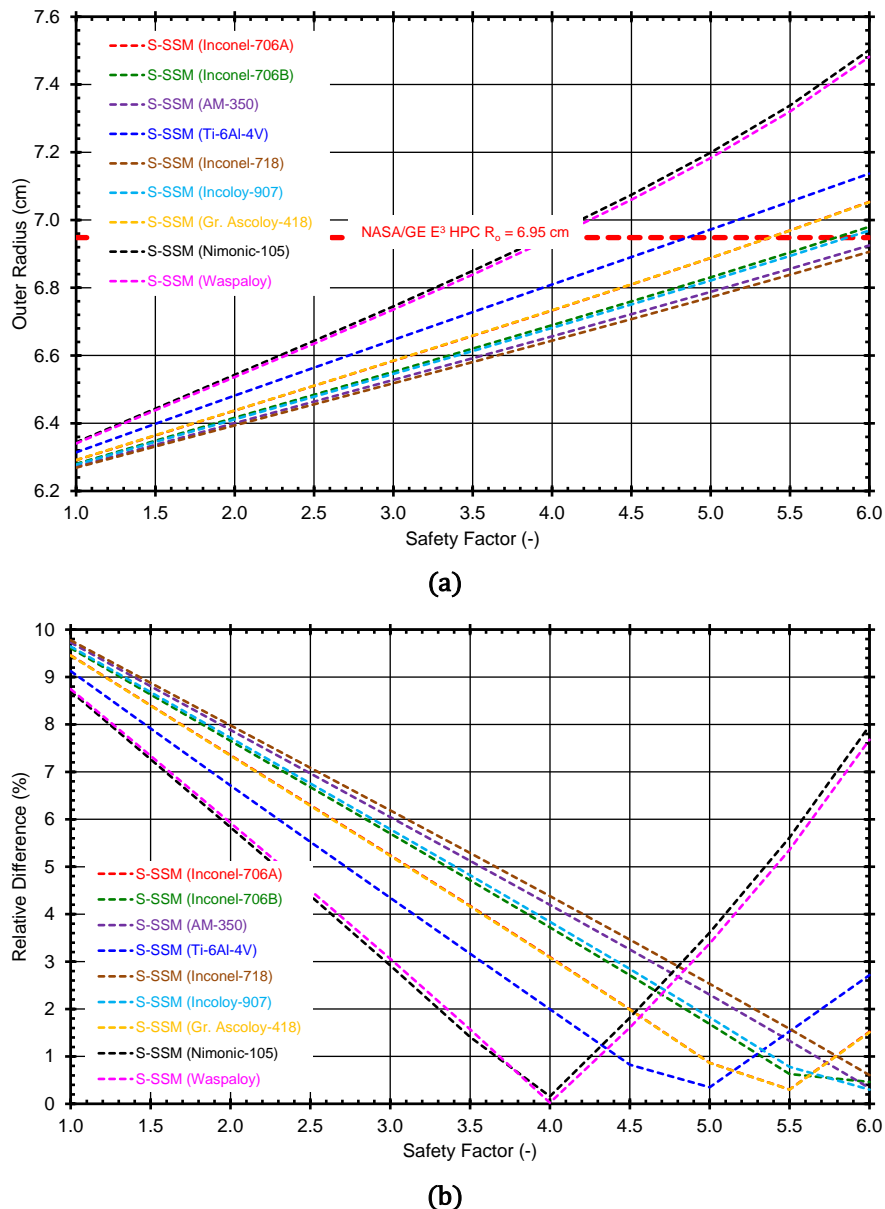


Figure 4.4: S-SSM results for the NASA/GE E³ HPC shaft outer radius, for different shaft materials: (a) shaft radius and (b) absolute value of relative difference vs safety factor value.

As expected, for constant material yield strength the shaft radius increases as the safety factor value is increased. The maximum difference between S-SSM and the actual

radius is 9.77% (for Inconel-718 and $SF_Y = 1.0$) corresponding to a radius difference of about 6.8 mm, while the minimum difference is 0.03% (for Waspaloy and $SF_Y = 4.0$) corresponding to a radius difference less than 0.02 mm. The average difference for all materials and safety factor values is about 5.48%. For $SF_Y \geq 1.5$ the average difference drops below 4.20% (maximum difference is about 8.88% corresponding to a radius difference of about 6.1 mm).

As it can be seen from Figure 4.4, in some material cases both very low and very high values of the safety factor lead to significant differences between the actual shaft radius and the calculated one, while there are combinations of the material and the safety factor value that lead to very low differences. According to Loewenthal, the value of SF_Y is selected based on several criteria including the criticality of the application and the uncertainty of the loads being modelled. Taking into account this and the fact that the present approach 1) models the shaft geometry as a simple cylinder of constant thickness (actual shafts in turbomachines have more complicated shapes which cannot be modelled in a preliminary design approach), and 2) does not account for bending and unsteady (vibrations) loads, then according to the results presented in Figure 4.4 it is concluded that a value of the safety factor in the range of $SF_Y = 4.0 - 5.0$ gives satisfactory results for all materials considered in this parametric study (differences less than 5%). For $SF_Y = 4.0 - 5.0$, the average difference is less than 2.31% with a maximum value of 4.38% (for Inconel-718 and $SF_Y = 4.0$, which corresponds to a radius difference of about 3.0 mm).

In conclusion, the safety factor value is a choice relying both on personal judgment and experience. However, the results presented in Figure 4.4 demonstrate that the simplified stress model formulated for the needs of this thesis can give reasonable quantitative results with good accuracy, even for low or high safety factor values (differences less than 9% are observed).

4.4 Rotating Disks

Another critical part of any modern gas turbine is the disk. Disks are used to support the rotor blades of compressor and turbine components, and to transfer the required torque produced by the turbine rotor to the appropriate compressor blading. Disks should be able to withstand the centrifugal stresses generated by rotor blades (and their attachment) and the centrifugal stresses associated with the inertia of the disk itself (body forces). In turbine components, disks are also designed to withstand the significant temperature gradients. In aero-engines, disks should also be able to withstand landing and thrust forces [see Armand (1995)]. Overall, disks are designed as life-limited parts with overspeed and LCF capabilities [see Kurzke et al. (2018)]. Figure 4.5 illustrates a 2D cutaway of the CFM56-5A turbofan engine³¹, where the different disk shapes, arrangements, and connections can be seen clearly for all turbomachinery components.

³¹<https://eduscol.education.fr/sti/sites/eduscol.education.fr.sti/files/ressources/pedagogiques/11659/11659-ctc-044-basic-engine.pdf> (accessed: May 11th, 2022)

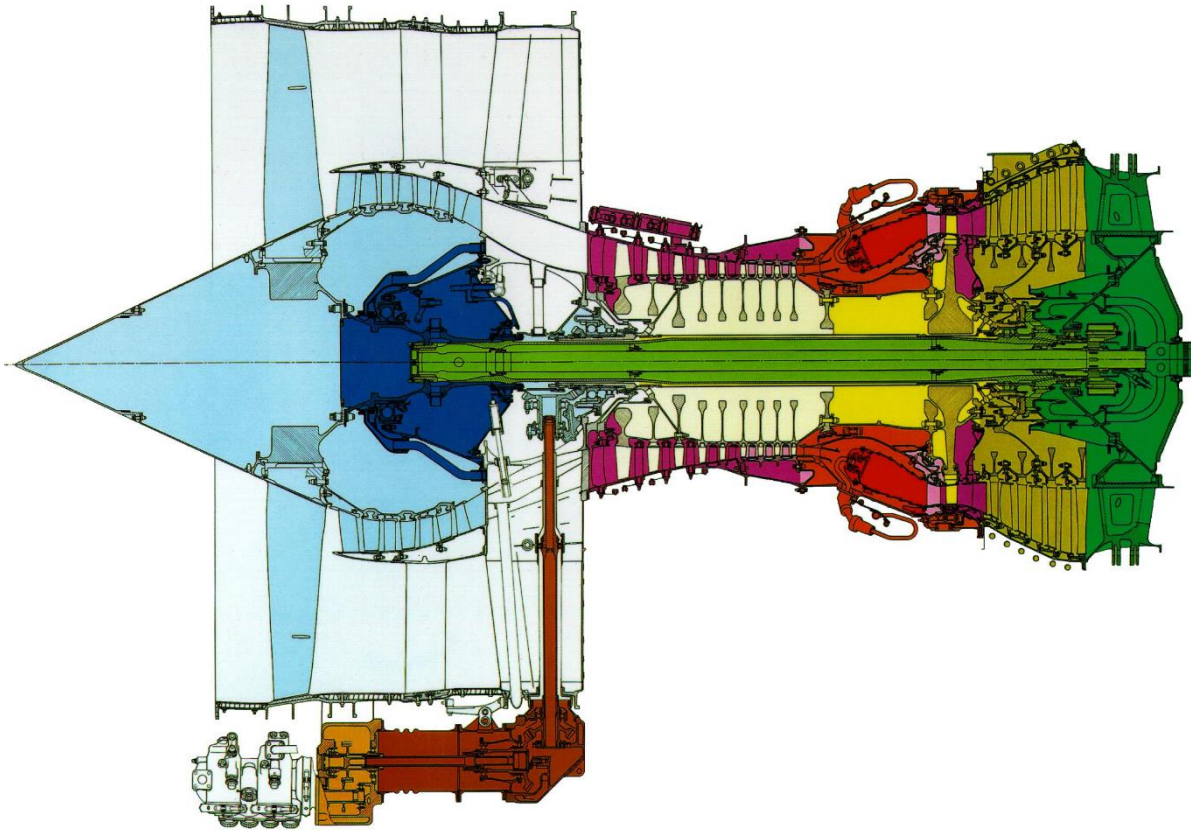


Figure 4.5: 2D cutaway of CFM56-5A turbofan engine showing the disks shapes and connections for all turbomachinery components.

Since disks comprise a significant part of the overall weight of a gas turbine engine, disks are mainly optimized for minimum mass while satisfying a number of geometry and stress criteria. The sizing point can be an on- or an off-design point of the engine cycle. Lifting considerations (in terms of LCF) [e.g., see Tong et al. (2004)] as well as vibratory loadings [see De Silva (1969)] should also be considered.

In the present section, a disk design approach for obtaining the minimum disk mass while not violating a number of geometry and stress constraints, is presented. The approach developed follows the general methods and guidelines proposed by similar, publicly available methodologies [see Armand (1995); Tong et al. (2004); Gutzwiller et al. (2010b); Lolis (2014)] and gas turbine design tools [see GasTurb Details 5, Kurzke (2007)], but several modifications and improvements are also included. In the present thesis, disk life and vibratory loadings are not considered as part of the disk design process but is proposed to be included in future adaptations of the method.

4.4.1 Disk Geometry Modelling

In most gas turbine engines, the geometry of the disks can be recognized and classified into one of the following three shape types [Tong et al. (2004)]: ring, web, and hyperbolic.

Disks with continuous slope sections have also been proposed and studied in the open literature [see Gutzwiller et al. (2010b)], but they are not dealt with in this work.

The disk shapes and the relevant nomenclature are illustrated in Figure 4.6. For simplicity, the hyperbolic part of the hyperbolic-type disks is approximated with a straight line without significant error [see Lolis (2014)].

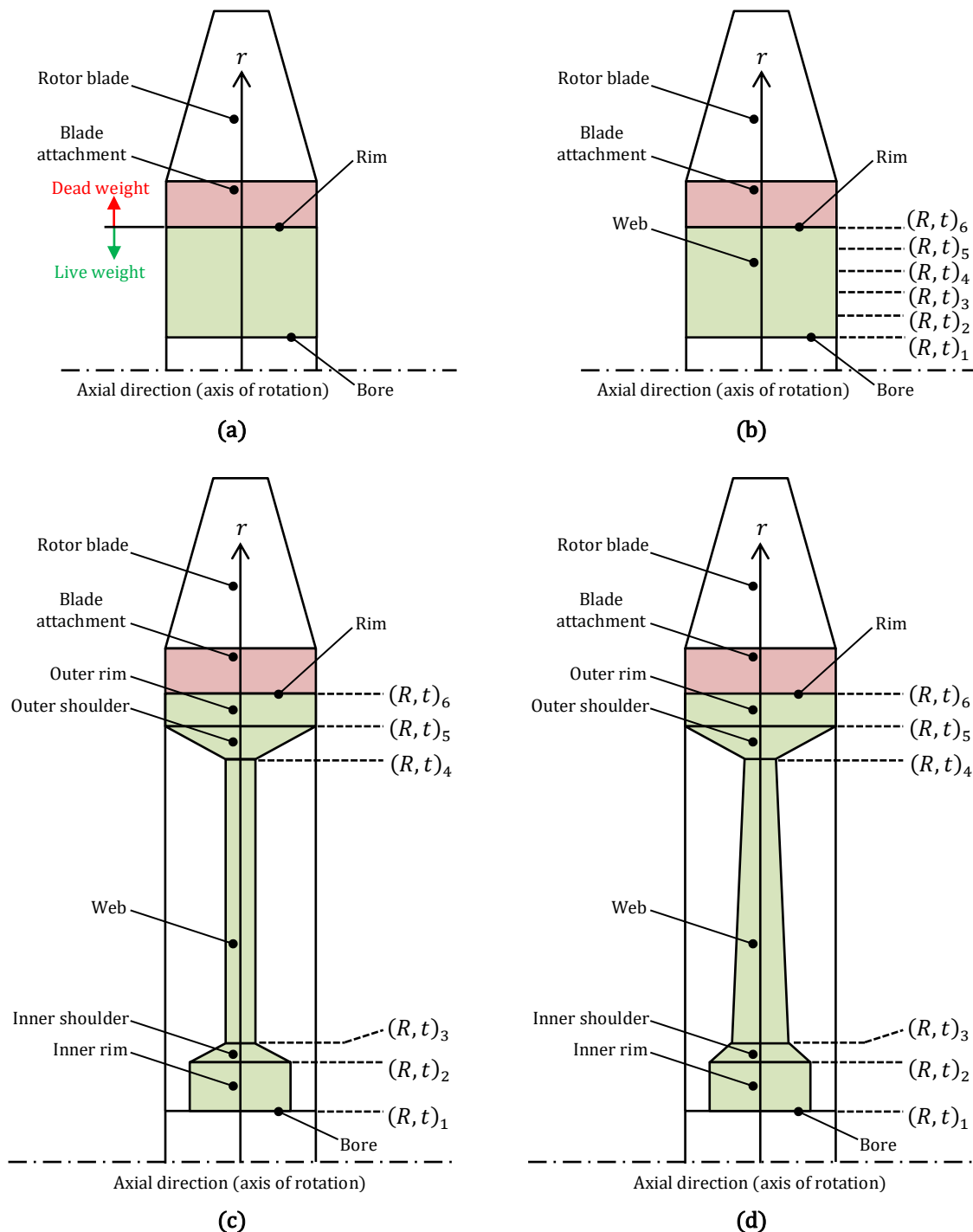


Figure 4.6: Cross-sectional (meridional) view of common use disk shapes in turbomachinery applications and their nomenclature: **(a)** disk/blade assembly defining the disk live and dead weights, **(b)** ring-, **(c)** web-, and **(d)** hyperbolic-type [adapted from Tong et al. (2004)].

As is the common practice [see Tong et al. (2004)], the disk is divided into two portions: the live weight disk and the dead weight (Figure 4.6a). The blades and the

blades attachment (which includes both the blade root – platform + neck + fir tree – and the disk post) constitute dead mass³² that produces most of the pull stress exerted on the rim of the live disk. The present design methodology is concerned with the design of the live disk.

As it can be seen from Figure 4.6, each disk shape is, in general, defined by six (6) radial stations [five (5) radial segments]. Each one of the six radial stations is characterized by the values of a radius, R , and a thickness, t . Note that stations 1 and 6 coincide with the disk bore and rim, respectively and, therefore, for these two stations the subscripts “rim” and “bore” will often be used instead of “1” and “6”.

At each one of the five disk segments, the thickness variation with radius is described by³³:

$$t = n + m(r - R_i)^{dsf}, \quad n = t_i, \quad m = \frac{t_o - t_i}{(R_o - R_i)^{dsf}} \quad (4.6)$$

where the subscripts i and o stand for the inner and the outer station of the segment in question, and $dsf > 0$ is a disk shape factor which may have different values for different disk segments. For $dsf = 1$ a linear thickness variation is defined (e.g., the web segment of hyperbolic-type disks, see Figure 4.6d), while values of $dsf \neq 1$ give the flexibility to define other thickness distributions and, thus, to produce more complex disk shapes.

4.4.1.1 Ring Disk

Although ring-type disks are geometrically defined by only two (2) radial stations (see Figure 4.6b), for nomenclature and software uniformity reasons ring disks are also thought of as comprising six radial stations, where the intermediate stations (2, 3, 4, 5) are calculated by the bore and rim ones using linear interpolation:

$$R_k = R_1 + (k - 1) \frac{R_6 - R_1}{5}, \quad k = 2,3,4,5 \quad (4.7)$$

In ring type disks, the thickness remains constant with radius according to:

$$t_1 = t_2 = t_3 = t_4 = t_5 = t_6 \quad (4.8)$$

4.4.1.2 Web Disk

In web-type disks, the thickness at the inner rim, web, and outer rim segments (see Figure 4.6c), remains constant:

$$t_1 = t_2, \quad t_3 = t_4, \quad t_5 = t_6 \quad (4.9)$$

respectively, while at the inner and outer shoulders it varies linearly with radius or, by applying Eq. (4.6) with $dsf_2 = 1$ and $dsf_4 = 1$, respectively, we obtain:

$$t = t_2 + \frac{t_3 - t_2}{R_3 - R_2}(r - R_2), \quad t = t_4 + \frac{t_5 - t_4}{R_5 - R_4}(r - R_4) \quad (4.10)$$

³²For the estimation of the dimensions of the dead weight (blade + blade attachment) see Appendix E.

³³An adapted version of the expression used for hyperbolic disks only by Gutzwiller et al. (2010b).

4.4.1.3 Hyperbolic Disk

Similarly to web-type disks, the thickness at the inner and outer rim segments of hyperbolic-type disks remains constant (see Figure 4.6d):

$$t_1 = t_2, \quad t_5 = t_6 \quad (4.11)$$

At the inner shoulder, web, and outer shoulder, the thickness varies linearly with radius. Using Eq. (4.6) with $dsf_2 = 1$, $dsf_3 = 1$, and $dsf_4 = 1$, we get:

$$t = t_2 + \frac{t_3 - t_2}{R_3 - R_2}(r - R_2), \quad t = t_3 + \frac{t_4 - t_3}{R_4 - R_3}(r - R_3), \quad t = t_4 + \frac{t_5 - t_4}{R_5 - R_4}(r - R_4) \quad (4.12)$$

4.4.2 Disk Stress Modelling

As described in the introduction of the present section, disks are designed primarily to receive the mechanical stresses developed by blade, body, and thermal loads without failure, while aiming at minimum weight. Therefore, part of any disk design methodology [e.g., see Armand (1995); Tong et al. (2004); Gutzwiller et al. (2010b); Lolis (2014)] is a stress calculation capability. The stress model used must be accurate enough to capture the correct stress trends and magnitudes, but also fast enough (since stress calculation is performed at every optimization cycle) while requiring the minimum number of inputs. In the present work, low fidelity (1D) models for calculating both thermal and mechanical stresses in disks are developed, and their qualitative and quantitative capabilities are validated against a higher fidelity 3D FEA tool using real-life turbomachinery disk geometries.

4.4.2.1 Disk Simplified Thermal Model (D-STM)

Temperature gradients in disks, especially in turbine components, can be high enough to create significant thermal stresses that cannot be ignored. Apart from that, material properties depend also on temperature. Therefore, a Disk-Simplified Thermal Model (D-STM) was formulated for obtaining the temperature distribution along the disk radius.

For calculation simplicity and time efficiency, most disk design approaches assume that temperature varies linearly along the disk span [see GasTurb Details 5, Kurzke (2007)], or they utilize empirical temperature curves of ambiguous origin and accuracy [see Lolis (2014)]. In the present method, temperature along the disk radius is calculated assuming that heat transfer effects can be approximated by the steady-state Fourier's law of heat conduction. Unsteady phenomena and convective heat transfer between the disk surface and its surroundings are not taken into account since they introduce the need for additional inputs that are not available during the preliminary design phase.

The radial temperature distribution in a disk is obtained by the steady-state Fourier's law of heat conduction without heat sources. For simplicity, thermal conductivity is assumed constant and independent from temperature. Then, the 1D Fourier's law for heat conduction takes the form [see Holman (2010)]:

$$\frac{d^2T}{dr^2} + \frac{1}{r} \frac{dT}{dr} = 0 \quad (4.13)$$

Equation (4.13) is a 2nd order, linear, and homogeneous ODE that has an analytical solution. Specifying the temperature value both at the disk rim and bore,

$$T = \begin{cases} T_{rim}, & r = R_{rim} \\ T_{bore}, & r = R_{bore} \end{cases} \quad (4.14)$$

the radial distribution of temperature can be expressed as:

$$\frac{T}{T_{rim}} = 1 + \frac{T_{bore}/T_{rim} - 1}{\ln(R_{bore}/R_{rim})} \ln \frac{r}{R_{rim}} \quad (4.15)$$

Equation (4.13) [and, thus, Eq. (4.15)] does not account for the disk thickness variation, an approximation followed also by NASA's WATE [see Tong et al. (2004)]. However, as will be shown later in paragraphs 4.4.2.2 and 4.4.2.4, this omission not only leads to inaccurate physical solutions, but also introduces significant inaccuracy in the calculation of the mechanical stresses developed in disks. For this reason, in this thesis a second modelling approach was developed and utilized, for the first time in the public literature, that accounts for the radial distribution of the disk thickness, thus leading to more accurate stress results at the same expense of time as Eq. (4.15).

Fourier's law for heat conduction for the same assumptions used in formulating Eq. (4.13), but taking also into account the disk thickness variation is expressed by [see Cengel et al. (2015)]:

$$\frac{d}{dr} \left(A_r \frac{dT}{dr} \right) = 0 \quad (4.16)$$

In the above, A_r is the disk circumferential area at an arbitrary radius r where the disk thickness is t , and is given by:

$$A_r = 2\pi r t \quad (4.17)$$

Equation (4.16) is solved numerically for T using an FD approach, for the same set of boundary conditions as those given by Eq. (4.14).

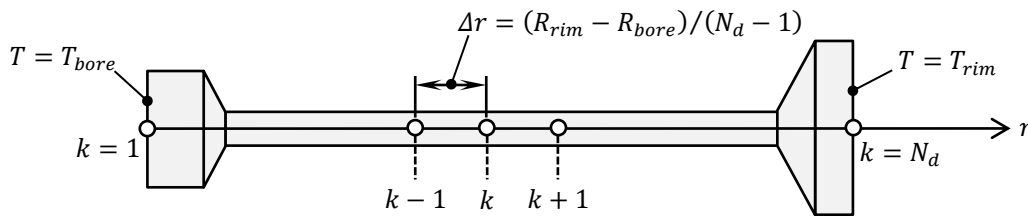


Figure 4.7: Radial discretization of an arbitrary thickness disk using equidistantly spaced nodes, for solving numerically the boundary value problem expressed by Eqs (4.16) and (4.14).

The disk is discretized radially using N_d , equally spaced, nodes (see Figure 4.7). Then, at every node k , the derivatives appearing in Eq. (4.16) are approximated using the following 2nd order accurate finite difference expressions:

$$\left. \frac{dX}{dr} \right|_k = \frac{X_{k+1} - X_{k-1}}{2\Delta r} + O(\Delta r^2), \quad \left. \frac{d^2X}{dr^2} \right|_k = \frac{X_{k+1} - 2X_k + X_{k-1}}{\Delta r^2} + O(\Delta r^2)$$

where the dummy variable X is valid for temperature (T) and area (A_r). Equation (4.16) is finally transformed into a discrete equation for T expressed by:

$$A_k T_{k-1} + B_k T_k + C_k T_{k+1} = 0 \quad (4.18)$$

where the coefficients A , B , and C , are given by:

$$A_k = \frac{1}{\Delta r^2} - \frac{1}{2\Delta r} \left(A_r \frac{dA_r}{dr} \right)_k, \quad B_k = -\frac{2}{\Delta r^2}, \quad C_k = \frac{1}{\Delta r^2} + \frac{1}{2\Delta r} \left(A_r \frac{dA_r}{dr} \right)_k \quad (4.19)$$

Equations (4.18) and (4.19) apply on all internal nodes, $k = 2 \rightarrow N_d - 1$, while at the boundary nodes, $k = 1$ and $k = N_d$, the boundary conditions apply (see Figure 4.7), which in discrete form are:

$$T_1 = T_{bore}, \quad T_{N_d} = T_{rim} \quad (4.20)$$

Given the disk geometry, the set of Eqs (4.18)–(4.20) constitutes a tridiagonal system of N_d linear equations for calculating N_d values of temperature T , which is solved with a tridiagonal system solver.

4.4.2.2 D-STM Validation

Both the analytical and the numerical thermal models, described in the preceding paragraph, were validated against a higher-fidelity 3D FEA tool³⁴. For this reason, the example disk geometry and temperature boundary conditions shown in Table 4.3 were used.

Table 4.3: Disk geometry and temperature boundary conditions for validating D-STMs

Disk Station	R (mm)	t (mm)	T (K)
1 (Bore)	50.0	70.0	398.2
2	100.0	70.0	
3	200.0	12.5	
4	300.0	10.0	
5	375.0	40.0	
6 (Rim)	400.0	40.0	823.2

First, the analytical [given by Eq. (4.15)] and numerical [given by Eq. (4.18)] thermal models were validated against a ring-type disk (constant thickness disk) with the same rim and bore radii as those described in Table 4.3, and assuming a (constant) thickness equal to that at the disk rim (40.0 mm). The comparison between both D-STMs and FEA

³⁴<https://www.ansys.com/products/structures/ansys-mechanical> (accessed: May 11th, 2022)

is shown in Figure 4.8. From this figure it is seen that both D-STMs present excellent agreement with the results obtained by the higher fidelity FEA tool.

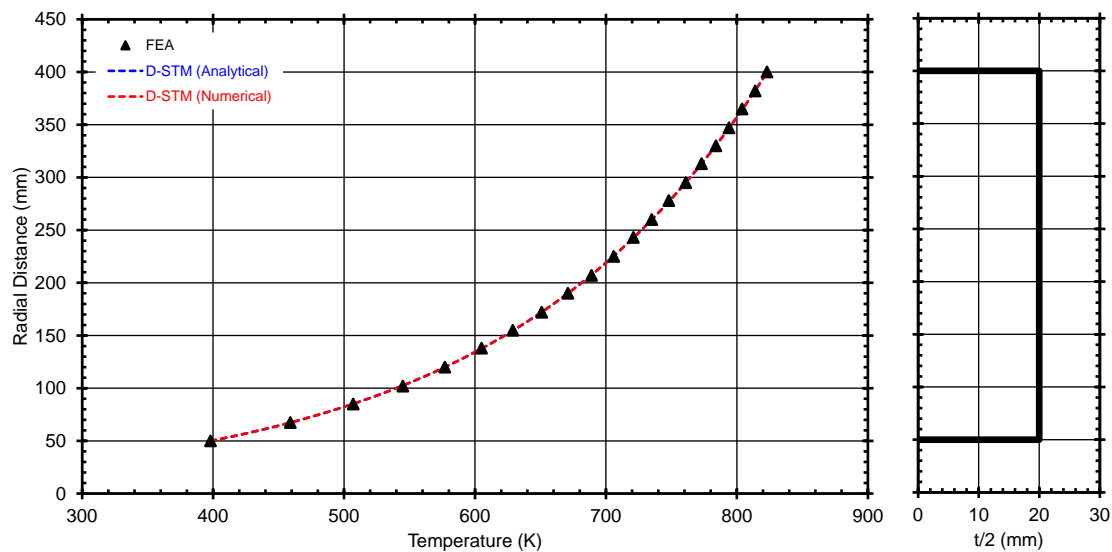


Figure 4.8: Temperature distribution comparison between FEA and the analytical/numerical D-STMs for a constant thickness (ring) disk (the disk semi-contour is shown on the right).

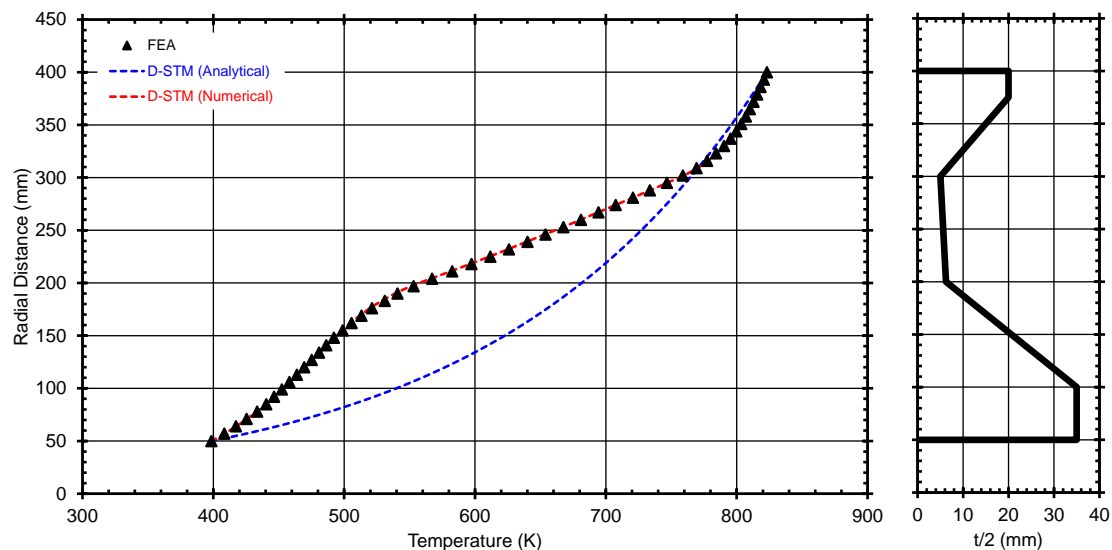


Figure 4.9: Temperature distribution comparison between FEA and the analytical/numerical D-STMs for a variable thickness (hyperbolic) disk (the disk semi-contour is shown on the right).

Figure 4.9 shows the comparison between the analytical and numerical D-STMs against the results obtained by the FEA tool, for the variable thickness disk described in Table 4.3. As it can be seen from Figure 4.9, the analytical D-STM (which does not account for the disk thickness variation) fails to capture both the correct temperature trend and magnitude (differences up to 21% can be observed). As will be demonstrated later (see paragraph 4.4.2.4), this difference can lead to significant errors regarding the estimation of the stresses developed in a disk, potentially compromising both the disk mechanical design and its structural safety. On the other hand, Figure 4.8 demonstrates

the ability of the numerical D-STM to capture correctly both the physics and the magnitudes of the temperature distribution in a disk of variable thickness.

It is worth noting, that on a desktop PC (Windows 7 64-bit, Intel® Core™2 Duo CPU @ 3 GHz with 4GB RAM), both the analytical and numerical D-STMs required about ~70 milliseconds each for calculating the temperature distribution on a grid of the same size (here 101 nodes were used after a mesh independence study). In conclusion, the numerical D-STM offers far greater accuracy with a computational effort not greater than that of the analytical model, and significantly less than the FEA one.

4.4.2.3 Disk Simplified Stress Model (D-SSM)

For developing the model for the estimation of the mechanical stresses developed in disks (will be referred to as D-SSM hereafter) due to blade, body, and thermal loads, the following are assumed [see Armand (1995) and Gutzwiller et al. (2010b)]:

1. The disk thickness is small relative to the disk radius and, therefore, the variation of stresses and displacements along the disk thickness can be neglected ($\partial/\partial x = 0$).
2. The stress problem is assumed axisymmetric ($\partial/\partial\theta = 0$) by eliminating tangential displacements and, thus, $\tau_{r\theta} = 0$ also holds³⁵.
3. In the $r - \theta$ plane, the plane stress assumption is made ($\sigma_x = \tau_{rx} = \tau_{\theta x} = 0$).
4. The displacements are small and, thus, the small angle assumption applies.
5. The supporting structures that connect the disks to each other and to the shaft are flexible thin cylinders or cones that do not impose radial or tangential constraints on the disks.

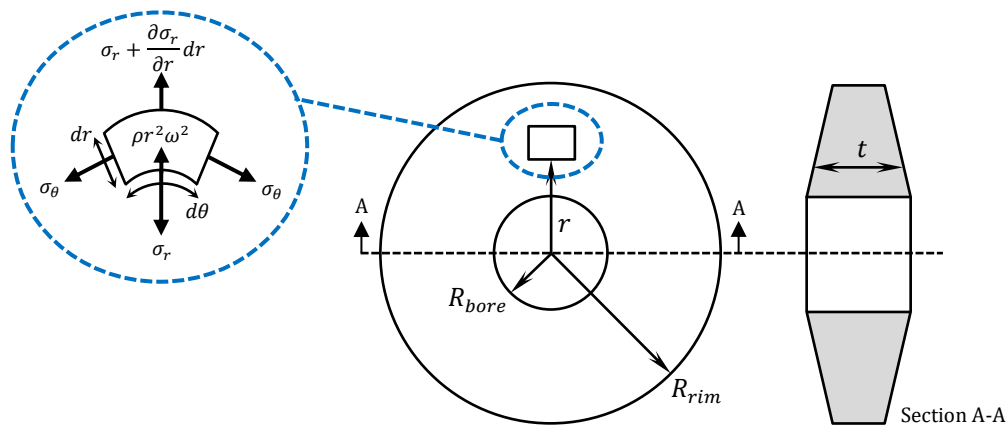


Figure 4.10: Free-body diagram of a differential element of a disk of arbitrarily variable thickness [adapted from Armand (1995)].

The force equilibrium on the differential disk element $dr - d\theta$ shown in Figure 4.10 and the assumptions 1-4 give the following equation, which expresses the equilibrium of stresses developed in a disk of variable thickness [see Ugural et al. (2003)]:

³⁵See Ugural et al. (2003).

$$\frac{d}{dr}(tr\sigma_r) - t\sigma_\theta + t\rho r^2\omega^2 = 0 \quad (4.21)$$

where $\omega = 2\pi N_{mech}/60$ is the disk angular velocity.

For solving Eq. (4.21), boundary conditions both at the disk rim and bore must be specified. In typical bladed disk applications, the disk rim is loaded due to the centrifugal forces developed by the disk dead weight, which are applied on the disk rim as a positive (tensile) stress. On the other hand, application of assumption 5 gives a zero boundary loading at the disk bore. Thus, the boundary conditions at the disk rim and bore are formulated according to:

$$\sigma_r = \begin{cases} \sigma_{r,rim}, & r = R_{rim} \\ 0, & r = R_{bore} \end{cases} \quad (4.22)$$

with $\sigma_{r,rim}$ given by:

$$\sigma_{r,rim} = \frac{Z_b W_{KG,dw} R_{cg,d} \omega^2}{2\pi R_{rim} t_{rim}} \quad (4.23)$$

where $W_{KG,dw}$ is the mass of the disk dead weight which includes the masses of the blade, blade attachment (platform + neck + fir tree), and disk post, and $R_{cg,dw}$ is the center of gravity of the dead weight³⁶.

Note that, Eq. (4.22) claims this specific form only for the needs of the present work. However, the stress calculation code that was developed is general enough so that any combination of boundary conditions on the disk rim and bore can be specified, thus allowing the study of novel disk applications where assumption 5 may not hold.

Given the disk geometry, Eq. (4.21) is an ODE that involves two (2) unknown variables, namely the radial and tangential normal stresses, σ_r and σ_θ , respectively. Therefore, Eq. (4.21) must be expressed in terms of a single variable. For this reason, constitutive expressions interrelating stresses and displacements are used [see Ugural et al. (2003)]. Radial and tangential stresses can be written in terms of mechanical and thermal deformations according to the following equations [see Ugural et al. (2003) and Gutzwiller et al. (2010b)]:

$$\sigma_r = A_{rm} \frac{du}{dr} + B_{rm} \frac{u}{r} + C_{rt}(T - T_{ref}) \quad (4.24)$$

$$\sigma_\theta = A_{\theta m} \frac{du}{dr} + B_{\theta m} \frac{u}{r} + C_{\theta t}(T - T_{ref}) \quad (4.25)$$

where u is the radial disk displacement, and $T_{ref} = (20 + \Delta T)$ °C with ΔT a user-defined temperature difference (for all test cases examined in this thesis, $\Delta T = 0$ °C is used).

In Eqs (4.24) and (4.25), the expressions for the coefficients A , B , and C are given by [see Gutzwiller et al. (2010b)]:

³⁶For the calculation of $W_{KG,dw}$ see paragraph 5.3.8; for the calculation of $R_{cg,dw}$ see Appendix E.

$$A_{rm} = \frac{S_{11}S_{33} - S_{13}^2}{S_{33}} \quad (4.26)$$

$$A_{\theta m} = B_{rm} = \frac{S_{12}S_{33} - S_{13}S_{23}}{S_{33}} \quad (4.27)$$

$$B_{\theta m} = \frac{S_{22}S_{33} - S_{23}^2}{S_{33}} \quad (4.28)$$

$$C_{rt} = -(A_{rm}a_{CTE,r} + B_{rm}a_{CTE,\theta}) \quad (4.29)$$

$$C_{\theta t} = -(A_{\theta m}a_{CTE,r} + B_{\theta m}a_{CTE,\theta}) \quad (4.30)$$

In Eqs (4.26) through (4.28), S_{11} , S_{12} , S_{13} , S_{22} , S_{23} , and S_{33} are the stiffness tensor elements that relate stresses and strains, and are estimated according to [see Gutzwiller et al. (2010b)]:

$$S_{11} = S_{33} = \frac{E_r(E_\theta - E_r\nu^2)}{E_\theta - 2E_r\nu^2} \quad (4.31)$$

$$S_{22} = \frac{E_\theta^2}{E_\theta - 2E_r\nu^2} \quad (4.32)$$

$$S_{12} = S_{23} = \frac{E_rE_\theta\nu}{E_\theta - 2E_r\nu^2} \quad (4.33)$$

$$S_{13} = \frac{E_r^2\nu^2}{E_\theta - 2E_r\nu^2} \quad (4.34)$$

Provision has been made so that disks of both isotropic and anisotropic materials can be calculated. For isotropic materials, $E_r = E_\theta$ and $a_{CTE,r} = a_{CTE,\theta}$ and, therefore, Eqs (4.26)-(4.34) can be simplified to give the familiar stress-strain equations described in many elasticity textbooks [e.g., see Ugural et al. (2003)] and relative technical reports [see Armand (1995) and Tong et al. (2004)].

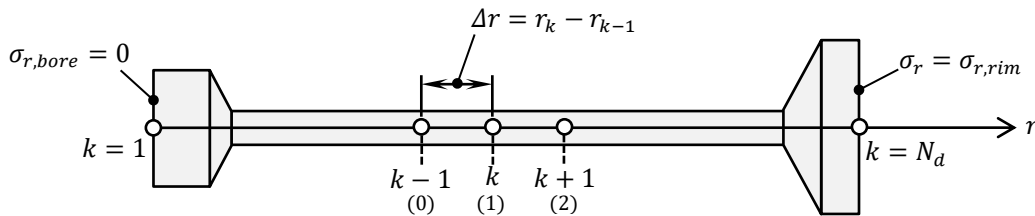


Figure 4.11: Radial discretization of an arbitrary thickness disk, for solving numerically the boundary value problem expressed by Eqs (4.21) and (4.22). In the figure the global and local (in parentheses) nodal schemes used for discretizing the system of equations are also shown.

Given the temperature field along the disk radius, replacement of Eqs (4.24)-(4.34) into Eq. (4.21) results in a 2nd order, linear ODE in one (1) unknown variable, that is,

the radial displacement u . The solution of the resulting boundary value problem is performed numerically. Therefore, the disk is discretized into N_d nodes as shown in Figure 4.11. An FV discretization approach of the system of Eqs (4.21)–(4.34) is followed using 2nd order accurate central difference schemes, that results into a pentadiagonal system of equations. The algebraic formulation is thoroughly presented in Gutzwiller et al. (2010b), and here only the equations comprising the final matrix system are presented. The final matrix system of equations reads:

$$\begin{bmatrix} (4.36) & (4.37) & (4.38) & \dots & 0 & 0 & 0 \\ (4.39) & (4.40) & (4.41) & \dots & 0 & 0 & 0 \\ & & & \vdots & & & \\ & 0 & 0 & \dots & (4.39) & (4.40) & (4.41) \\ & 0 & 0 & \dots & (4.42) & (4.43) & (4.44) \end{bmatrix} \begin{bmatrix} u_1 \\ u_2 \\ \vdots \\ u_{N_d-1} \\ u_{N_d} \end{bmatrix} = \begin{bmatrix} (4.45) \\ (4.46) \\ \vdots \\ (4.46) \\ (4.47) \end{bmatrix} \quad (4.35)$$

where the matrix elements are given by:

$$\text{Coeff. } u_1: \quad \frac{B_{rm,1}}{r_1} - \frac{3A_{rm,1}}{r_3 - r_1} \quad (4.36)$$

$$\text{Coeff. } u_2: \quad \frac{4A_{rm,1}}{r_3 - r_1} \quad (4.37)$$

$$\text{Coeff. } u_3: \quad -\frac{A_{rm,1}}{r_3 - r_1} \quad (4.38)$$

$$\text{Coeff. } u_{k-1}: \quad \frac{2\beta_0}{\beta_0 + \beta_1} \left(\frac{\bar{A}_{rm,10}}{\Delta r_{10}} - \frac{\bar{B}_{rm,10}}{2\bar{r}_{10}} \right) + \frac{\bar{t}_{10}}{\beta_0 + \beta_1} \left(B_{rm,10} - \frac{\bar{B}_{\theta m,10}}{2} \ln \frac{r_1}{r_0} \right) \quad (4.39)$$

$$\begin{aligned} \text{Coeff. } u_k: \quad & \frac{2\beta_2}{\beta_2 + \beta_1} \left(\frac{\bar{B}_{rm,21}}{2\bar{r}_{21}} - \frac{\bar{A}_{rm,21}}{\Delta r_{21}} \right) + \frac{\bar{t}_{21}}{\beta_2 + \beta_1} \left(B_{rm,21} - \frac{\bar{B}_{\theta m,21}}{2} \ln \frac{r_2}{r_1} \right) + \\ & -\frac{2\beta_0}{\beta_0 + \beta_1} \left(\frac{\bar{A}_{rm,10}}{\Delta r_{10}} + \frac{\bar{B}_{rm,10}}{2\bar{r}_{10}} \right) - \frac{\bar{t}_{10}}{\beta_0 + \beta_1} \left(B_{rm,10} + \frac{\bar{B}_{\theta m,10}}{2} \ln \frac{r_1}{r_0} \right) \end{aligned} \quad (4.40)$$

$$\text{Coeff. } u_{k+1}: \quad \frac{2\beta_2}{\beta_2 + \beta_1} \left(\frac{\bar{A}_{rm,21}}{\Delta r_{21}} + \frac{\bar{B}_{rm,21}}{2\bar{r}_{21}} \right) - \frac{\bar{t}_{21}}{\beta_2 + \beta_1} \left(B_{rm,21} + \frac{\bar{B}_{\theta m,21}}{2} \ln \frac{r_2}{r_1} \right) \quad (4.41)$$

$$\text{Coeff. } u_{N_d-2}: \quad \frac{A_{rm,N_d}}{r_{N_d} - r_{N_d-2}} \quad (4.42)$$

$$\text{Coeff. } u_{N_d-1}: \quad -\frac{4A_{rm,N_d}}{r_{N_d} - r_{N_d-2}} \quad (4.43)$$

$$\text{Coeff. } u_{N_d}: \quad \frac{B_{rm,N_d}}{r_{N_d}} + \frac{3A_{rm,N_d}}{r_{N_d} - r_{N_d-2}} \quad (4.44)$$

$$\text{RHS:} \quad -C_{rt,1}(T_1 - T_{ref}) \quad (4.45)$$

$$\begin{aligned}
& \frac{2\beta_2\bar{T}_{21}}{\beta_2 + \beta_1} (\bar{A}_{rm,21}\bar{a}_{CTE,r,21} + \bar{B}_{rm,21}\bar{a}_{CTE,\theta,21}) + \\
& - \frac{\bar{t}_{21}\bar{T}_{21}\Delta r_{21}}{\beta_2 + \beta_1} (\bar{A}_{\theta m,21}\bar{a}_{CTE,r,21} + \bar{B}_{\theta m,21}\bar{a}_{CTE,\theta,21}) + \\
\text{RHS:} \quad & - \frac{2\beta_0\bar{T}_{10}}{\beta_0 + \beta_1} (\bar{A}_{rm,10}\bar{a}_{CTE,r,10} + \bar{B}_{rm,10}\bar{a}_{CTE,\theta,10}) + \\
& - \frac{\bar{t}_{10}\bar{T}_{10}\Delta r_{10}}{\beta_0 + \beta_1} (\bar{A}_{\theta m,10}\bar{a}_{CTE,r,10} + \bar{B}_{\theta m,10}\bar{a}_{CTE,\theta,10}) + \\
& - \frac{\bar{t}_{21}\rho\omega^2}{\beta_1 + \beta_2} \frac{r_2^3 - r_1^3}{3} - \frac{\bar{t}_{10}\rho\omega^2}{\beta_0 + \beta_1} \frac{r_1^3 - r_0^3}{3}
\end{aligned} \tag{4.46}$$

$$\text{RHS:} \quad \sigma_{r,rim} - C_{rt,N_d}(T_{N_d} - T_{ref}) \tag{4.47}$$

In Eqs (4.39)–(4.41) and (4.46) the local nodal system shown in Figure 4.11 was utilized for convenience, while the following substitutions are used:

$$\Delta X_{10} = X_k - X_{k-1}, \quad \Delta X_{21} = X_{k+1} - X_k, \quad \bar{X}_{10} = \frac{X_k + X_{k-1}}{2}, \quad \bar{X}_{21} = \frac{X_{k+1} + X_k}{2}, \quad \beta = tr$$

The dummy variable X is valid for the thickness (t), temperature (T), stiffness terms (A, B), and thermal expansion coefficient (a_{CTE}).

Equation (4.35) is simplified into a tridiagonal system of equations by eliminating the coefficients for u_3 and u_{N_d-2} in the first and last equations, respectively. The resulting tridiagonal system is then solved using a tridiagonal system algorithm.

Take note that provision has been made in the code so that the terms expressing thermal stresses are dropped off of the equations if thermal effects are not considered. After the solution of the system of equations, the displacement field u is obtained which is then used to calculate the radial and tangential stresses, σ_r and σ_θ , respectively, along the disk radius using Eqs (4.24) and (4.25). The derivative du/dr (which expresses the radial normal strain) appearing in Eqs (4.24) and (4.25) is approximated using 2nd order accurate difference expressions. Finally, the von-Mises stress along the radius is easily calculated using [see Gutzwiller et al. (2009)]:

$$\sigma_{vM} = \sqrt{\sigma_r^2 + \sigma_\theta^2 - \sigma_r\sigma_\theta} \tag{4.48}$$

4.4.2.4 D-SSM Validation

In the present paragraph D-SSM is validated against a higher-fidelity 3D FEA tool³⁷, using real-life disk geometries and boundary conditions, both including and not-including heat transfer effects. For demonstrating that D-SSM can predict accurately the stresses developed in gas turbine disks of any shape, the validation is conducted on ring-, web- and hyperbolic-type disk geometries. For this reason, the NASA/GE E³ HPC was considered. A 2D cutaway of the engine is depicted in Figure 4.12.

³⁷<https://www.ansys.com/products/structures/ansys-mechanical> (accessed: May 11th, 2022)

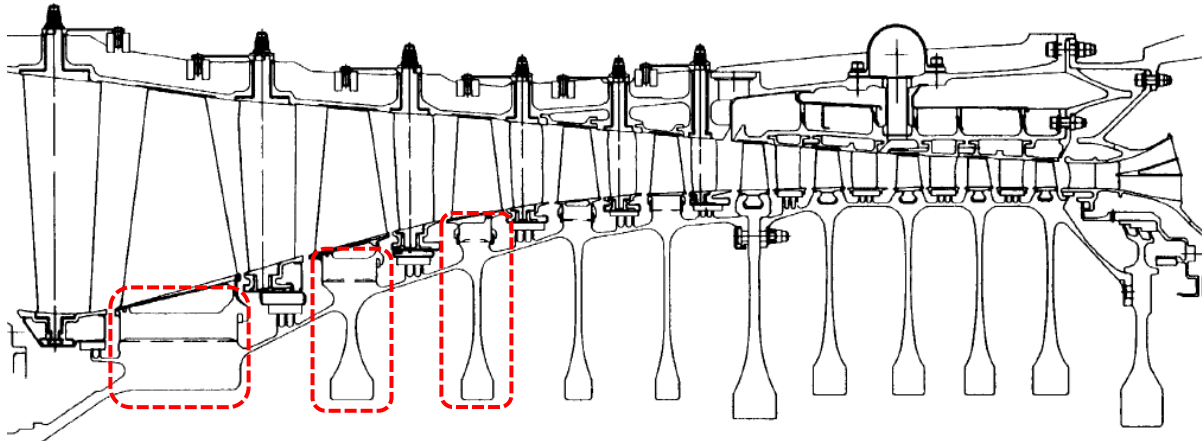


Figure 4.12: 2D cutaway of NASA/GE E³ HPC showing the different disk shapes [Davis et al. (1985)]. For validating D-SSM the first-, second-, and third-stage disk geometries of E³ HPC are considered (shown into the dashed red-line rectangles).

The 1st, 2nd, and 3rd stage disk geometries of the E³ HPC are considered which, as it can be seen from Figure 4.12, approximate disks of ring-, hyperbolic- and web-shape, respectively. The disk dimensions at the six characteristic radial disk stations are given in Table 4.4. Other information necessary to the stress calculation code is presented in Table 4.5 (see also Appendix D). The boundary loading at the disk rim, $\sigma_{r,rim}$, given in Table 4.5, is calculated by applying the E³ HPC inputs to Eq. (4.23) for a design speed of 12,416.5 rpm (~ 1300 rad/s). Finally, 81, 141, and 141 nodes were used for discretizing the ring-, hyperbolic-, and web-type disk geometry, respectively, as obtained by a mesh independence study.

Table 4.4: Disk geometry for stages 1-3 of the NASA/GE E³ HPC [see Holloway et al. (1982)]

Stage (Type):	1 (Ring)		2 (Hyper.)		3 (Web)	
Disk Station	R (mm)	t (mm)	R (mm)	t (mm)	R (mm)	t (mm)
1 (Bore)	104.1	93.7	106.6	32.9	106.3	24.7
2	114.2	93.7	121.0	32.9	120.1	24.7
3	124.3	93.7	140.1	15.3	153.6	6.2
4	134.4	93.7	169.9	7.5	198.6	6.2
5	144.5	93.7	196.7	46.2	217.1	28.1
6 (Rim)	154.6	93.7	202	46.2	230.3	28.1

Table 4.5: Other inputs relative to stages 1-3 of the NASA/GE E³ HPC [see Holloway et al. (1982)]

Stage	Blade Material	Disk Material	T_{rim} (K)	Z_b (-)	$W_{KG,dw}$ (g)	$R_{cg,dw}$ (mm)	$\sigma_{r,rim}$ (MPa)
1	Ti-8-1-1	Ti-8-1-1	323.2	28	865.6	199.1	89.7
2	Ti-8-1-1	Ti-6Al-4V	379.9	38	279.2	231.0	70.6
3	Ti-8-1-1	Ti-6Al-4V	433.2	50	117.1	253.3	61.6

FEA Setup Validation

First, the FEA model setup is validated against the analytical solution that is available for a ring disk (constant thickness disk) for zero rim and bore (stress) boundary conditions, without heat transfer effects. For the validation, the geometry of the 1st stage E³ HPC disk, shown in Table 4.4, is used. The analytical solution for this problem is given by [see Ugural et al. (2003)]:

$$\sigma_r = \frac{3 + \nu}{8} \left(R_{rim}^2 + R_{bore}^2 - \frac{R_{rim}^2 R_{bore}^2}{r^2} - r^2 \right) \rho \omega^2 \quad (4.49)$$

$$\sigma_\theta = \frac{3 + \nu}{8} \left(R_{rim}^2 + R_{bore}^2 + \frac{R_{rim}^2 R_{bore}^2}{r^2} - \frac{1 + 3\nu}{3 + \nu} r^2 \right) \rho \omega^2 \quad (4.50)$$

which express the radial variation of the radial and tangential normal stresses, respectively.

Figure 4.13 depicts the comparison between the radial distributions of the radial and tangential normal stresses obtained by the FEA tool and the analytical solution described by Eqs (4.49) and (4.50). As one observes from Figure 4.13, the FEA tool can successfully reproduce both the physics and the magnitudes obtained by the analytical solution. Therefore, the FEA setup can be used with confidence as a validation tool for D-SSM when studying more complicated problems in terms of both geometry and stress/thermal boundary conditions.

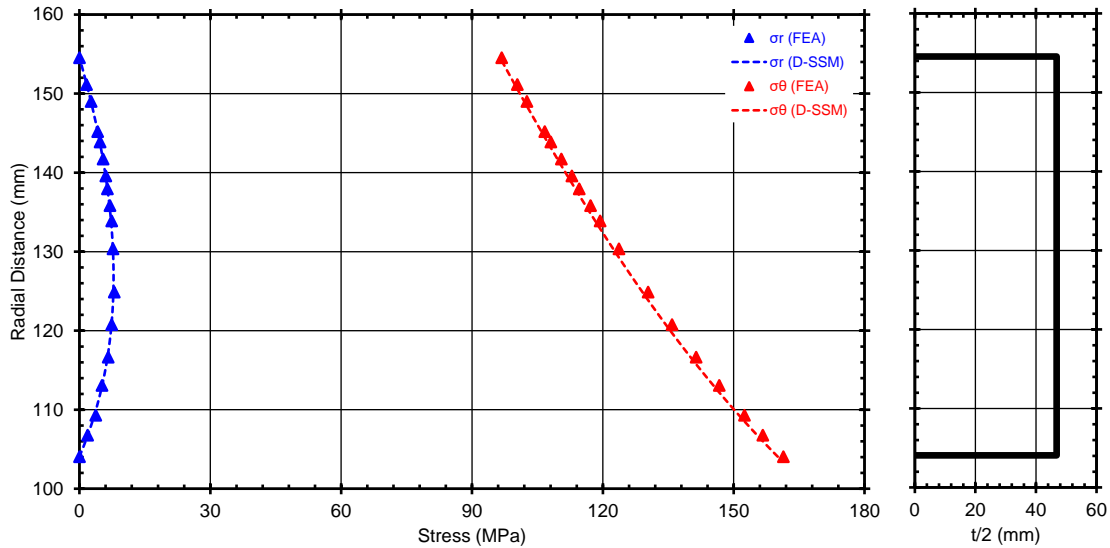


Figure 4.13: Radial and tangential normal stress distributions comparison between FEA and the analytical solution for the case of a ring disk, with zero stress applied at both the disk rim and bore, and considering no heat transfer effects. The disk semi-contour is shown on the right.

D-SSM Validation for Ring-Type Disks

Next, the geometry of the 1st stage (ring) disk of the NASA/GE E³ HPC (Table 4.4) is used to validate D-SSM for the case of ring-shaped disks, for the following two boundary loading cases: 1) zero rim stress, and 2) rim stress according to Table 4.5 (89.7 MPa). Heat transfer effects are not taken into account, while the material

properties are calculated at (a radially constant) room temperature (20 °C). The results of the calculations are shown in Figure 4.14.

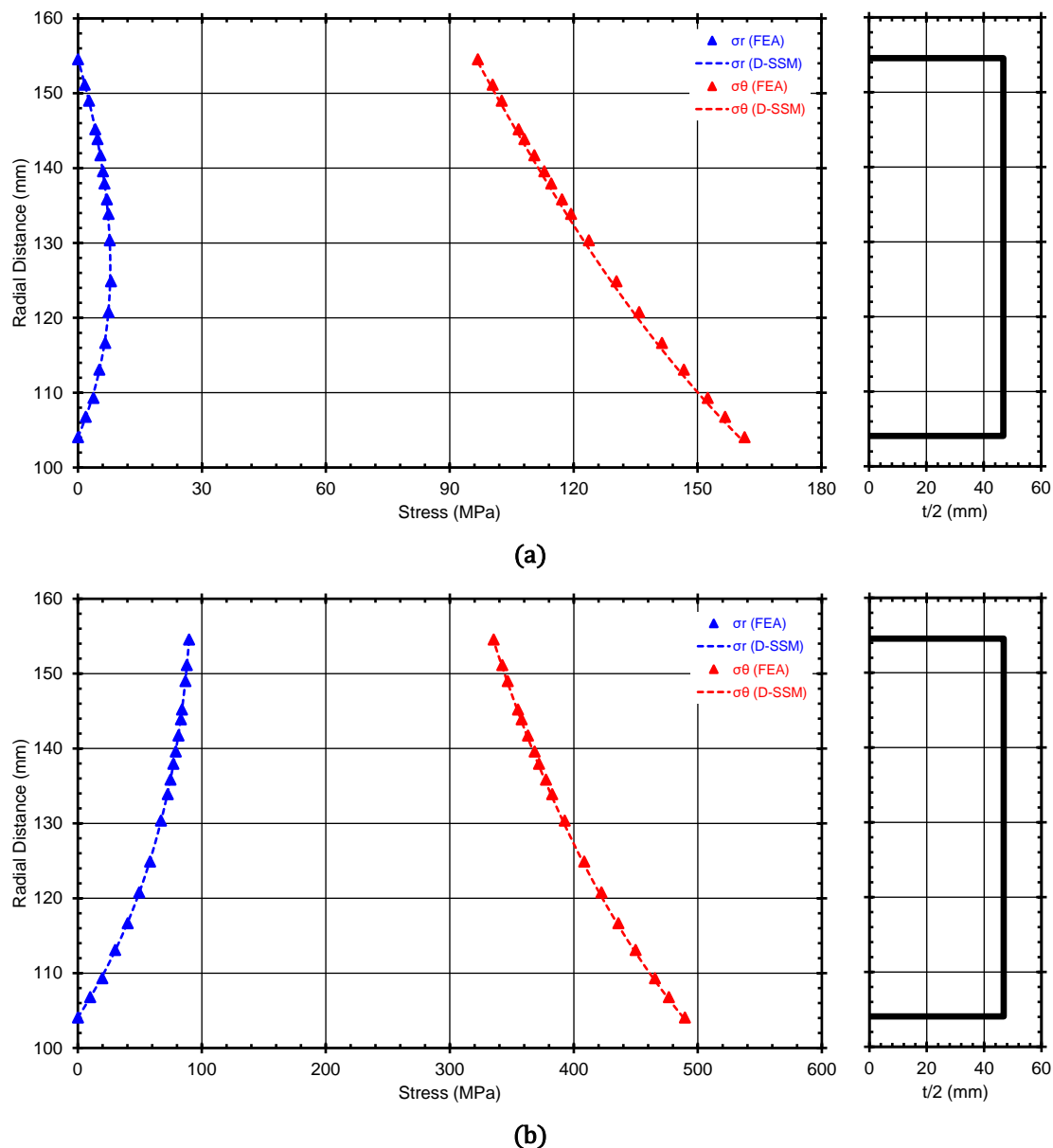


Figure 4.14: Comparison of radial and tangential normal stresses between FEA and D-SSM for a ring-type disk: (a) zero rim stress; (b) non-zero (89.7 MPa) rim stress. No heat-transfer effects are taken into account while material properties are calculated at (radially constant) room temperature (20 °C). The disk semi-contour is shown on the right.

Figure 4.14 depicts the comparison of the radial variations of the radial and tangential normal stresses between D-SSM and FEA. As it can be seen from Figure 4.14, D-SSM captures correctly both the stress trends and magnitudes for both boundary loading cases. It is observed that the maximum (tangential) stress appears at the disk bore, similarly to the physical case for constant thickness, hollow disks [see Saravanamuttoo et al. (2017)]. Notice also, that the non-zero rim stress calculation case gives a maximum tangential normal stress which is almost 3 times greater than that for the zero rim stress case.

D-SSM Validation for Hyperbolic-Type Disks

The geometry of the 2nd stage (hyperbolic) disk of the NASA/GE E³ HPC (Table 4.4) is used to validate D-SSM for the case of hyperbolic-shaped disks, for the following two boundary loading cases: 1) zero rim stress, and 2) rim stress according to Table 4.5 (70.6 MPa). Again, heat transfer effects are not taken into account, and material properties are calculated at constant room temperature (20 °C). The results are shown in Figure 4.15.

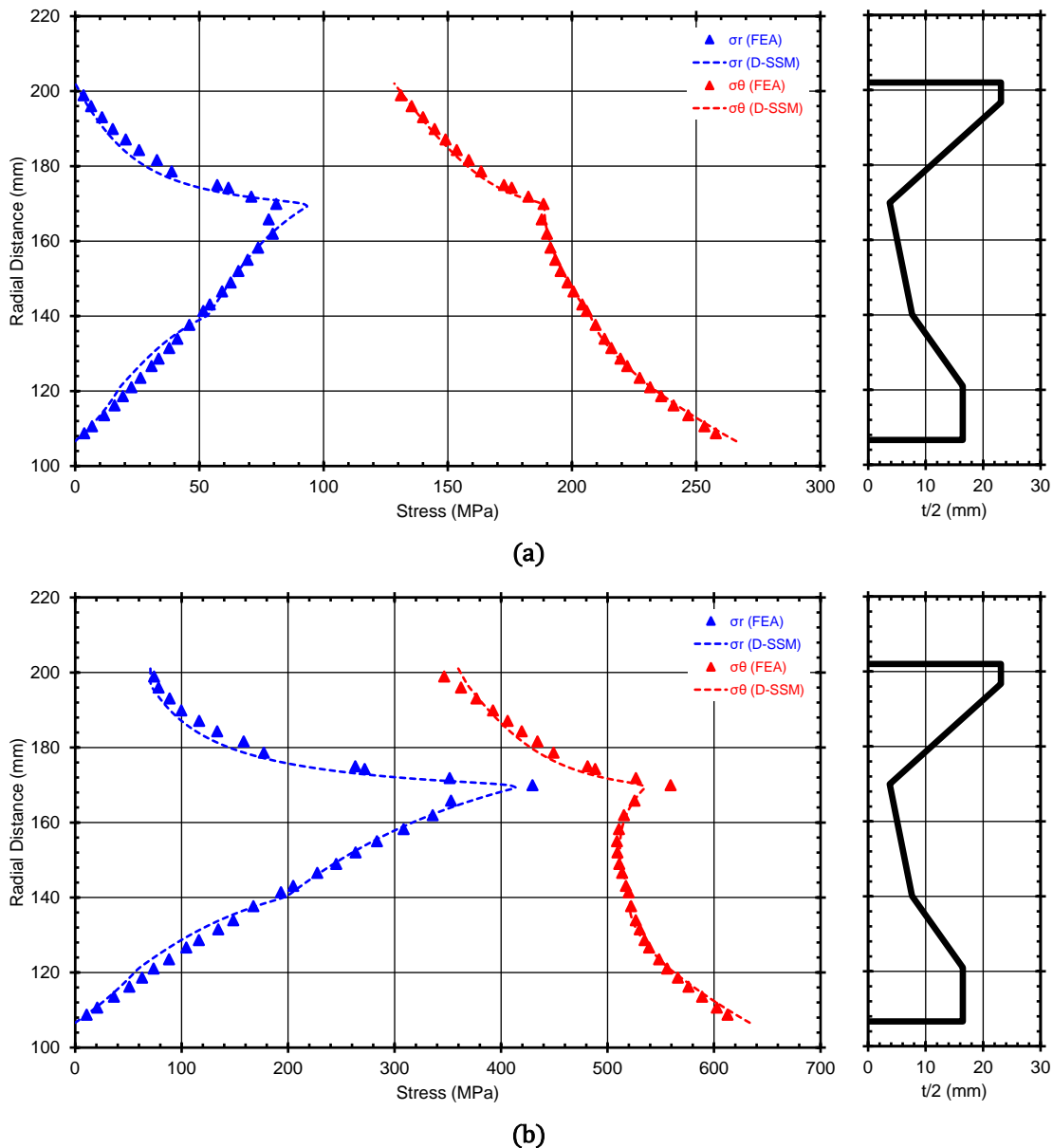


Figure 4.15: Comparison of radial and tangential normal stresses between FEA and D-SSM for a hyperbolic-type disk: **(a)** zero rim stress; **(b)** non-zero (70.6 MPa) rim stress. No heat-transfer effects are taken into account, while material properties are calculated at constant room temperature (20 °C). The disk semi-contour is shown on the right.

Figure 4.15 depicts the comparison between the radial and tangential normal stresses obtained by D-SSM and FEA. As it can be seen from Figure 4.15, D-SSM captures sufficiently both the stress trends and magnitudes for both boundary loading cases. It is

observed that the maximum (tangential) stress appears at the disk bore, with the non-zero rim stress calculation case giving a maximum tangential normal stress which is about 2.5 times greater than that for the zero rim stress case.

D-SSM Validation for Web-Type Disks

The geometry of the 3rd stage (web) disk of the NASA/GE E³ HPC (Table 4.4) is used to validate D-SSM for the case of web-shaped disks, for the following two boundary loading cases: 1) zero rim stress, and 2) rim stress according to Table 4.5 (61.6 MPa). Similarly to the previous two test cases, heat transfer effects are not taken into account, while material properties are calculated at constant room temperature (20 °C). The results are shown in Figure 4.16.

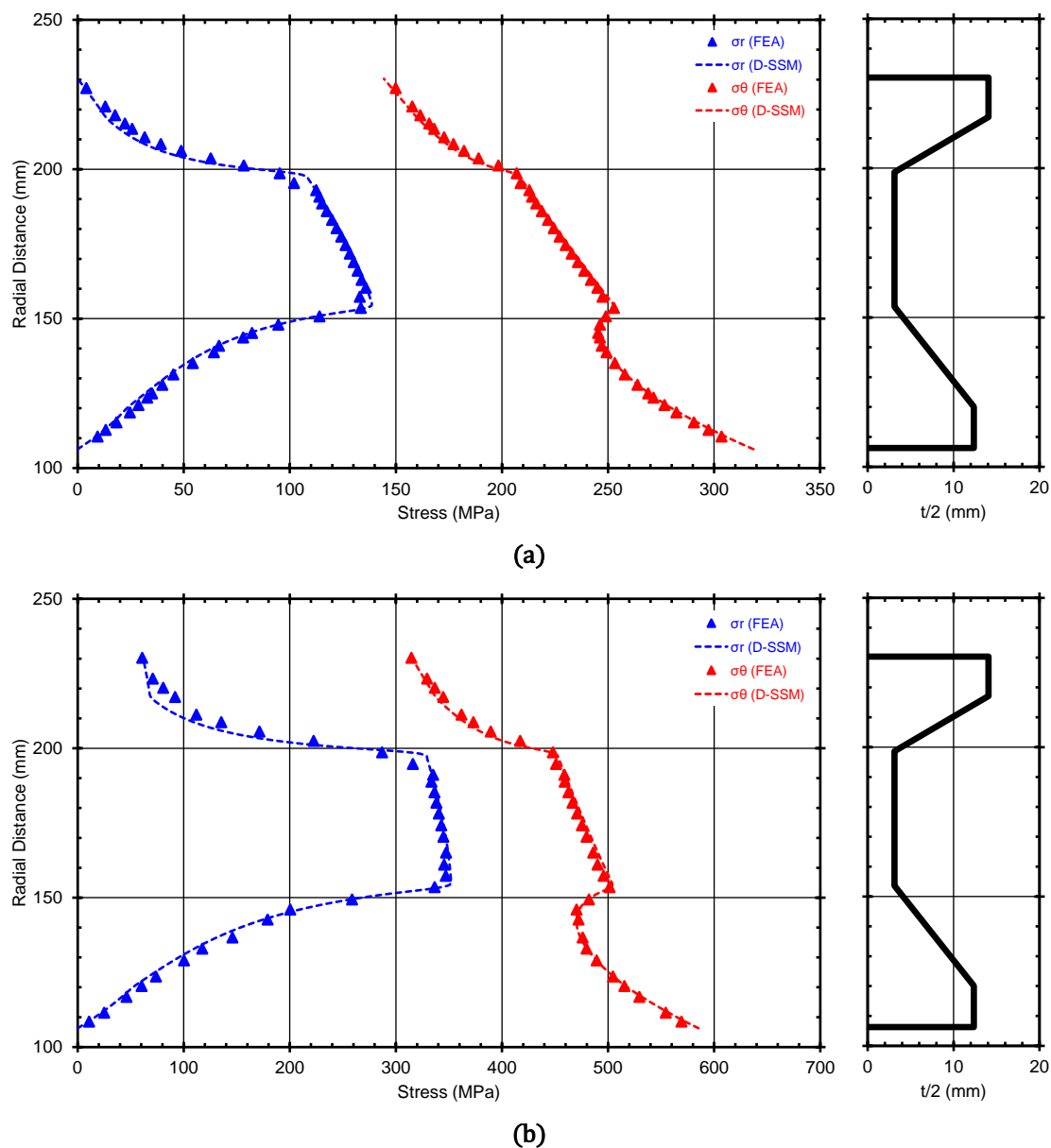


Figure 4.16: Comparison of radial and tangential normal stresses between FEA and D-SSM for a web-type disk: (a) zero rim stress; (b) non-zero (61.6 MPa) rim stress. No heat-transfer effects are taken into account, while material properties are calculated at constant room temperature (20 °C). The disk semi-contour is shown on the right.

Figure 4.16 depicts the comparison between the radial and tangential normal stresses obtained by D-SSM and FEA. As it can be seen from Figure 4.16, D-SSM captures correctly both the stress trends and magnitudes for both boundary loading cases. It is observed that the maximum (tangential) stress appears at the disk bore, with the non-zero rim stress calculation case giving a maximum tangential normal stress which is about 2 times greater than that for the zero rim stress case.

D-SSM Validation with Heat Transfer Effects

Finally, for validating D-SSM when heat transfer effects are also considered, the geometry and temperature boundary conditions given in Table 4.3 are utilized. The hyperbolic-type disk rotates at 3750 rpm (~ 393 rad/s), while the blade and attachment weights exert at the disk rim a boundary loading equal to 66.8 MPa. The disk material is Inconel-718. After a mesh independence study, 141 nodes were used for discretizing the disk geometry. The results are shown in Figure 4.17.

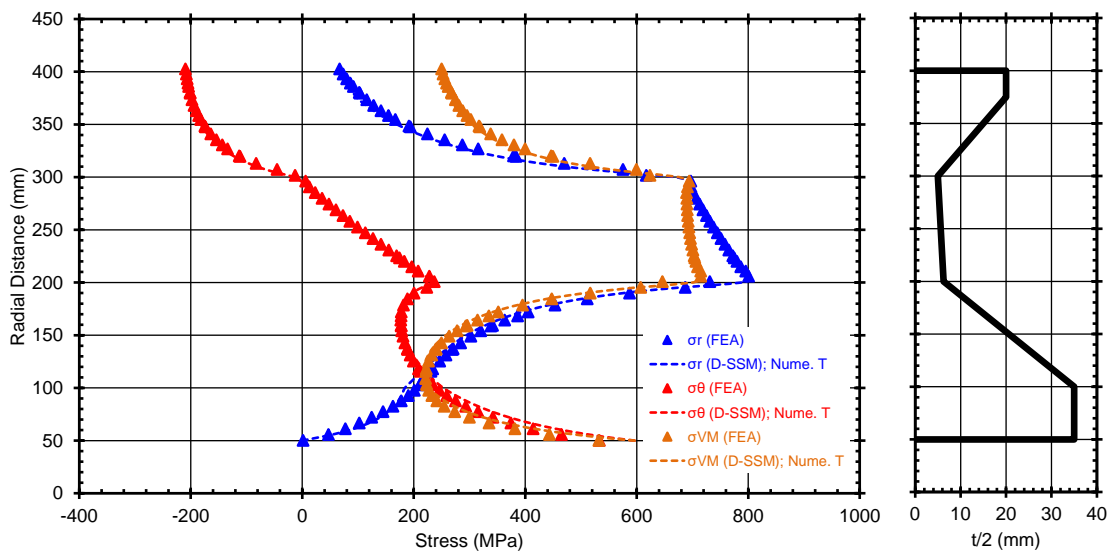


Figure 4.17: Comparison of radial, tangential, and von Mises stresses between FEA and D-SSM for a hyperbolic-type disk considering heat-transfer effects and a non-zero (66.8 MPa) rim stress. Disk temperature is obtained through the numerical D-STM, and material properties are calculated using the local value of temperature. The disk semi-contour is shown on the right.

Figure 4.17 illustrates the comparison between the radial, tangential, and von Mises stresses obtained by D-SSM and FEA. The temperature variation along the disk radius is obtained by the numerical D-STM (see Figure 4.9). Material properties are calculated considering the local value of temperature. As it can be seen from Figure 4.17, excellent agreement between D-SSM and FEA (both qualitatively and quantitatively) is observed. Compared to the previous examined cases, here the maximum stress appears at the inner radius of the disk web (station 3 in Figure 4.6d) and is the radial component of stress. The maximum tangential stress appears also at the disk bore, similarly to the previous test cases.

Next, the above calculation is repeated but this time the variation of temperature along the disk radius is obtained 1) considering the analytical D-STM solution (as shown in Figure 4.9), and 2) considering that temperature varies linearly between the

disk bore and rim. Again, material properties are calculated using the local value of temperature. The results are shown in Figure 4.18.

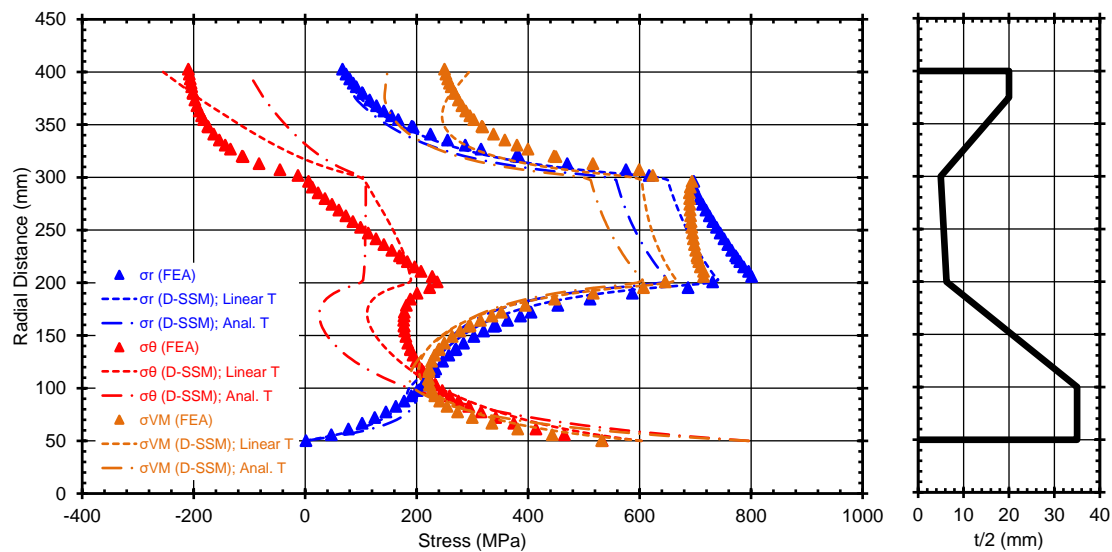


Figure 4.18: Comparison of radial, tangential, and von Mises stresses between FEA and D-SSM for a hyperbolic-type disk considering heat-transfer effects, and a non-zero (66.8 MPa) rim stress. Disk temperature is obtained 1) considering the analytical D-STM and 2) a linear variation of temperature between the bore and rim, while material properties are calculated using the local value of temperature. The disk semi-contour is shown on the right.

From Figure 4.18 one observes that a temperature field that is obtained without taking into account the disk thickness variation produces a stress field that is significantly different from the real one, both in magnitude and trend.

From Figure 4.18, we see that the radial component of stress presents qualitatively the same behavior as the one given by FEA, but the stress magnitudes are significantly off for both temperature fields, especially at the region of the disk web (between 200 and 300 mm). The maximum relative difference [expressed by $100 \times (\sigma_r^{\text{FEA}} - \sigma_r^{\text{D-SSM}}) / \sigma_r^{\text{FEA}}$] is about 9% for the linear variation of temperature, while the analytical D-STM temperature field gives stress differences up to almost 30%. The maximum difference in stress is about 64 MPa for the linear variation of temperature, while the analytical D-STM temperature field produces stress differences up to ~154 MPa! Note that the respective differences do not appear at the same radius.

In contrast to the radial stress component, we observe from Figure 4.18 that the examined temperature fields fail to reproduce, both qualitatively and quantitatively, the FEA variation of the tangential stress component. There are radial regions where even the stress sign is wrong. The maximum stress difference is about 117 MPa for the linear variation in temperature, and 199 MPa for the analytical D-STM temperature field!

Finally, considering the von Mises stress, we see maximum relative differences of about 21.2% for the linear variation of temperature and up to about 46.6% for the analytical D-STM temperature field! The maximum difference in stress is about 86 MPa for the linear variation of temperature, while the analytical D-STM temperature field produces differences up to almost 199 MPa!

Conclusively, not considering the disk thickness variation yields incorrect temperature fields, both qualitatively and quantitatively, as demonstrated in paragraph 4.4.2.2. This, in turn, affects (directly and indirectly) the calculation of the stresses developed in the disk, leading to inaccurate stress results both qualitatively and quantitatively. More specifically, an incorrect temperature field leads to inaccurate thermal strains and, thus, inaccurate stress values directly through Eqs (4.24) and (4.25). Also, an incorrect temperature field results in incorrect estimation of the material properties and thus, gives inaccurate stresses since stresses are linked to (correct mechanical and incorrect thermal) strains through the material E 's, ν 's, and α_{CTE} 's [see Eqs (4.24)–(4.34)]. Potentially, the erroneous estimation of the stress field could compromise both the disk mechanical design and its structural safety.

4.4.3 Rotating Disk Optimizer (RDO) for Minimum Weight

In the past, many researchers have dealt with the design of turbomachinery rotating disks [see De Silva (1969); Armand (1995); Tong et al. (2004); Kurzke (2007); Gutzwiller et al. (2010b); Lolis (2014)]. Disks contribute a significant part to the overall weight of an engine and, therefore, their design aims at minimum weight, while subjected to several geometry and stress constraints. The necessary geometry and stress calculations for a disk were presented in paragraphs 4.4.1 and 4.4.2, respectively. In this paragraph, the formulation used in the Rotating Disk Optimizer (RDO) for obtaining a disk of minimum mass is presented. Figure 4.19 depicts the general workflow applied in RDO for minimizing the disk mass.

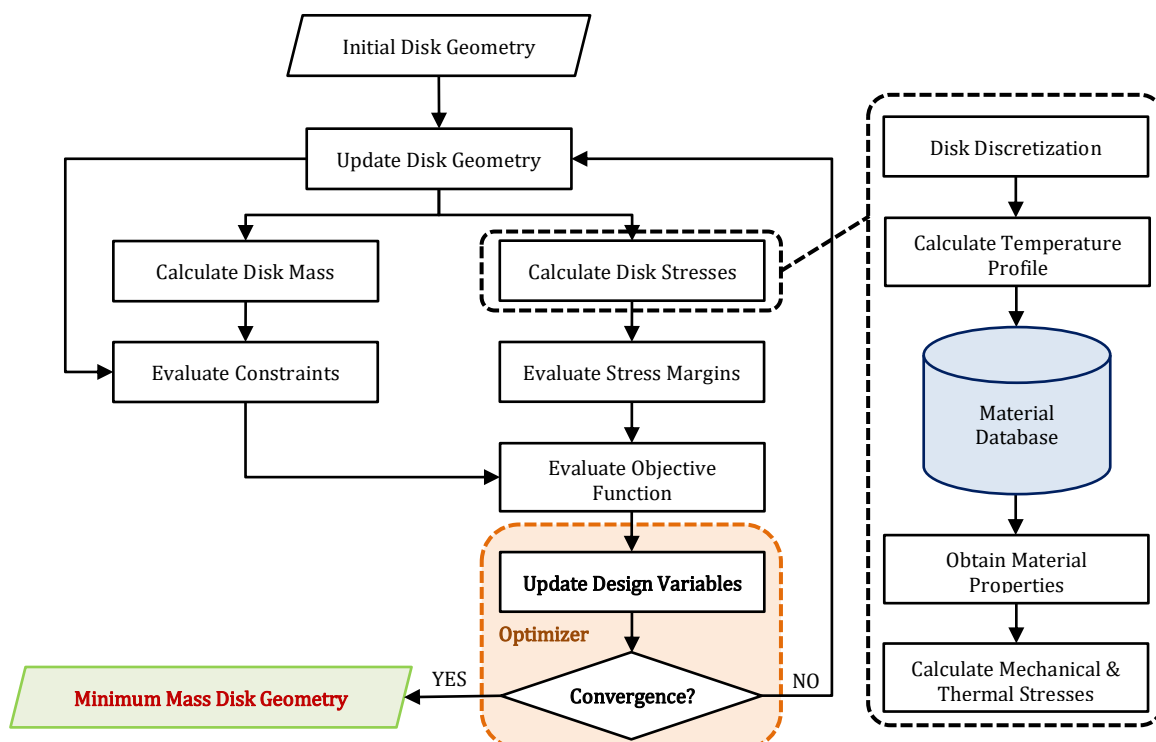


Figure 4.19: RDO flow-chart for obtaining a disk of minimum weight.

4.4.3.1 Optimization Algorithm

To avoid local optima, most researchers resort to non-gradient methods (exploratory methods or methods based on evolutionary strategies) for optimizing the disk geometry. However, these methods require increased calculation times if an engine comprising several disks is to be optimized.

In developing RDO, the Nelder-Mead SIMPLEX [see Nelder et al. (1965)], direct-search, minimization algorithm was used. The choice of SIMPLEX was based on criteria such as: 1) it does not need any information about 1st- and 2nd-order derivatives, 2) it can handle non-continuous and non-smooth functions, 3) it requires very few function evaluations per iteration, and 4) it can produce satisfactory results very quickly³⁸, among other reasons. Also, it's available in PROOSIS as a built-in and validated function.

4.4.3.2 Selection of Design Variables

For optimizing a disk for minimum weight, the disk radii and thicknesses are selected as design variables. The value of these design variables is updated in every optimization cycle until a disk geometry is produced that achieves minimum weight while not violating the imposed constraints.

Each disk shape is modeled by six (6) sets of radius and thickness, $(R, t)_k$, $k = 1, 2, 3, 4, 5, 6$ (see paragraph 4.4.1). However, to ensure numerical stability and speed of execution, the minimum number of R_k 's and/or t_k 's is selected as design variables, while the remaining are fixed or correlated to them. Table 4.6 summarizes the design variables used in this work for the optimization of the geometry of any of the considered disk types.

Table 4.6: Design variables for disk geometry optimization

Disk Type	Nr. of Design Variables	Design Variables
Ring	1	R_1
Web	5	$R_1, (R_2 - R_1)/t_6, (R_6 - R_5)/t_6, t_1/t_6, t_4/t_6$
Hyperbolic	5	$R_1, (R_2 - R_1)/t_6, (R_6 - R_5)/t_6, t_1/t_6, t_4/t_6$

Next, the correlations between the different R_k 's and t_k 's are summarized for the three disk types, giving the necessary number of independent variables shown in Table 4.6.

Ring Disk

In a ring-type disk the thickness remains radially constant [see Eq. (4.8)] and equal to the rotor axial chord length at hub ($t_6 = t_{rim} = c_{x,h,R}$), while the disk rim radius ($R_6 = R_{rim}$) is also fixed (see Appendix E). Therefore, the only free variable for defining the disk geometry is the bore radius ($R_1 = R_{bore}$) since the remaining radii are obtained through Eq. (4.7).

³⁸http://www.scholarpedia.org/article/Nelder-Mead_algorithm (accessed: May 11th, 2022)

Web Disk

Similarly to the ring-type disk, rim radius ($R_6 = R_{rim}$) and rim width ($t_6 = t_{rim}$) are fixed by the blade root geometry.

According to Eq. (4.9), the thickness at the outer rim remains constant and, therefore, $t_5 = t_6 = t_{rim}$. From Eq. (4.9) it is seen that the thickness at the inner rim and web segments of the disk also remains constant ($t_1 = t_2$ and $t_3 = t_4$, respectively) and, therefore, there are two (2) free variables left to choose from t_1 , t_2 , t_3 , and t_4 for defining the thickness distribution along the disk. Here t_1 and t_4 are selected, expressed in dimensionless form in terms of the fixed rim width, t_1/t_6 and t_4/t_6 .

Finally, we are left with five (5) radii (R_1 , R_2 , R_3 , R_4 , and R_5) to fully define the disk geometry. Theoretically, we could have selected all of them [see Armand (1995)], leading to a total of seven (7) design variables. However, to reduce the number of independent variables it is assumed that the radii at stations 2 and 3, and those at stations 4 and 5, are related through a fixed angle correlation. This assumption has been proposed and used by many authors [see Kurzke (2007); Lolis (2014); Schaber et al. (2019)] and adopted also here. Therefore:

$$R_3 = R_2 + \frac{t_2 - t_3}{2} \tan \alpha_{IS}, \quad R_4 = R_5 - \frac{t_5 - t_4}{2} \tan \alpha_{OS} \quad (4.51)$$

where α_{IS} and α_{OS} are user-defined angles. In the present thesis default values of 36° are used for both angles [see Lolis (2014)].

Therefore, there are now three (3) free variables left to fully define the disk geometry (R_1 , R_2 , and R_5) making a total of five (5) design variables (along with t_1 and t_4). Note that, instead of using R_2 and R_5 directly as design variables, R_2 and R_5 are obtained from the dimensionless inner and outer rim heights, $(R_2 - R_1)/t_6$ and $(R_6 - R_5)/t_6$, respectively.

Hyperbolic Disk

Similarly to the other two disk types, the rim radius ($R_6 = R_{rim}$) and rim width ($t_6 = t_{rim}$) are again fixed by the blade root geometry.

According to Eq. (4.11), the thickness at the inner and outer rim remains constant, $t_1 = t_2$ and $t_5 = t_6 = t_{rim}$, respectively. On the other hand, the thickness at the inner shoulder, web, and outer shoulder varies linearly with radius [see Eq. (4.12)]. Therefore, there are three (3) free variables to choose from t_1 , t_2 , t_3 , and t_4 for defining the thickness distribution. Here, t_1/t_6 and t_4/t_6 are again selected, while t_3 is correlated to $t_2 = t_1$ and t_4 by:

$$t_3 = \frac{1}{3}(t_2 + t_4) \quad (4.52)$$

Equation (4.52) is an average value based on existing engine configurations and is used to reduce the number of design variables.

Finally, following the same rational as that for web-type disks, R_1 , $(R_2 - R_1)/t_6$, and $(R_6 - R_5)/t_6$ are selected as design variables to fully define the disk geometry, while R_3 and R_4 are correlated to R_2 and R_5 , respectively, through Eq. (4.51).

4.4.3.3 Initializing the Disk Geometry

For initializing the disk geometry in a consistent way, that is, to assign initial values to the design variables outlined in the preceding paragraph, a digitization of existing engine 2D cutaways was performed for identifying possible correlations between the design variables and gas-path and/or performance parameters.

It is assumed that the disk sizing is due primarily to the boundary loading developed by the blades and exerted on the disk rim. Neglecting the disk post and blade root sections, the stress developed at the disk rim because of the presence of the blade alone is equal to the maximum stress developed at the hub of the blade itself. The latter is proportional to $A_g N_{mech}^2$ [see Saravanamuttoo et al. (2017)], where A_g is the flow-annulus area mid-way along the blade. Due to limited number of engines with both significantly different rotational speeds and legitimate 2D cutaways³⁹ that could be used for producing these correlations, it was assumed (at a first approximation) that the disk dimensions could be related to A_g alone. The latter is proportional to the blade hub-to-tip ratio (HTR).

Figure 4.20 and Figure 4.21 depict the acquired correlations for $(R_2 - R_1)/t_6$, $(R_6 - R_5)/t_6$, t_1/t_6 , and t_4/t_6 in terms of HTR for compressor and turbine components, respectively, while Table 4.7 summarizes the respective min/max values.

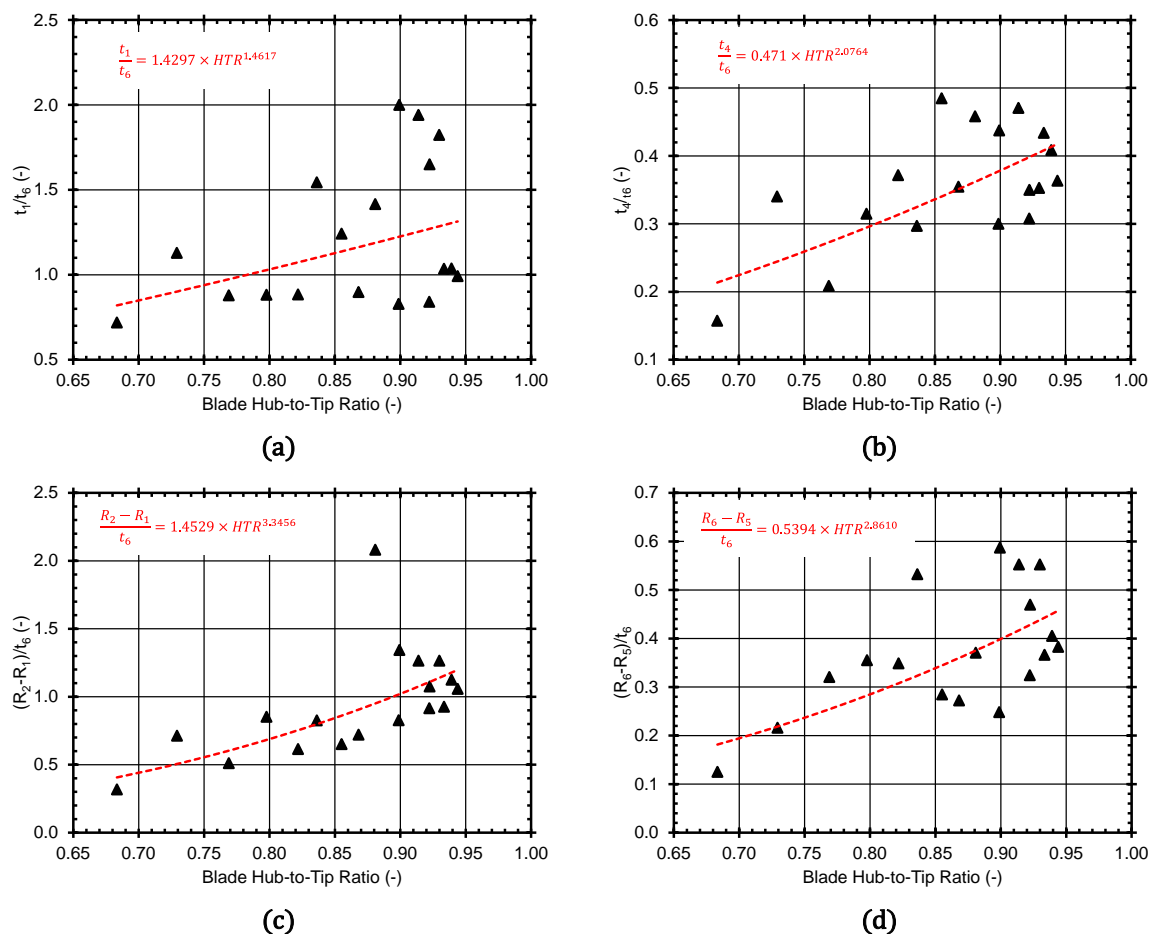


Figure 4.20: Design variables in terms of rotor hub-to-tip ratio for compressor components.

³⁹Digitizations were based on two commercially operational turbofan engines, namely the CFM56-7B27 and CFM56-5A, for which clear 2D cutaways are available in the public domain.

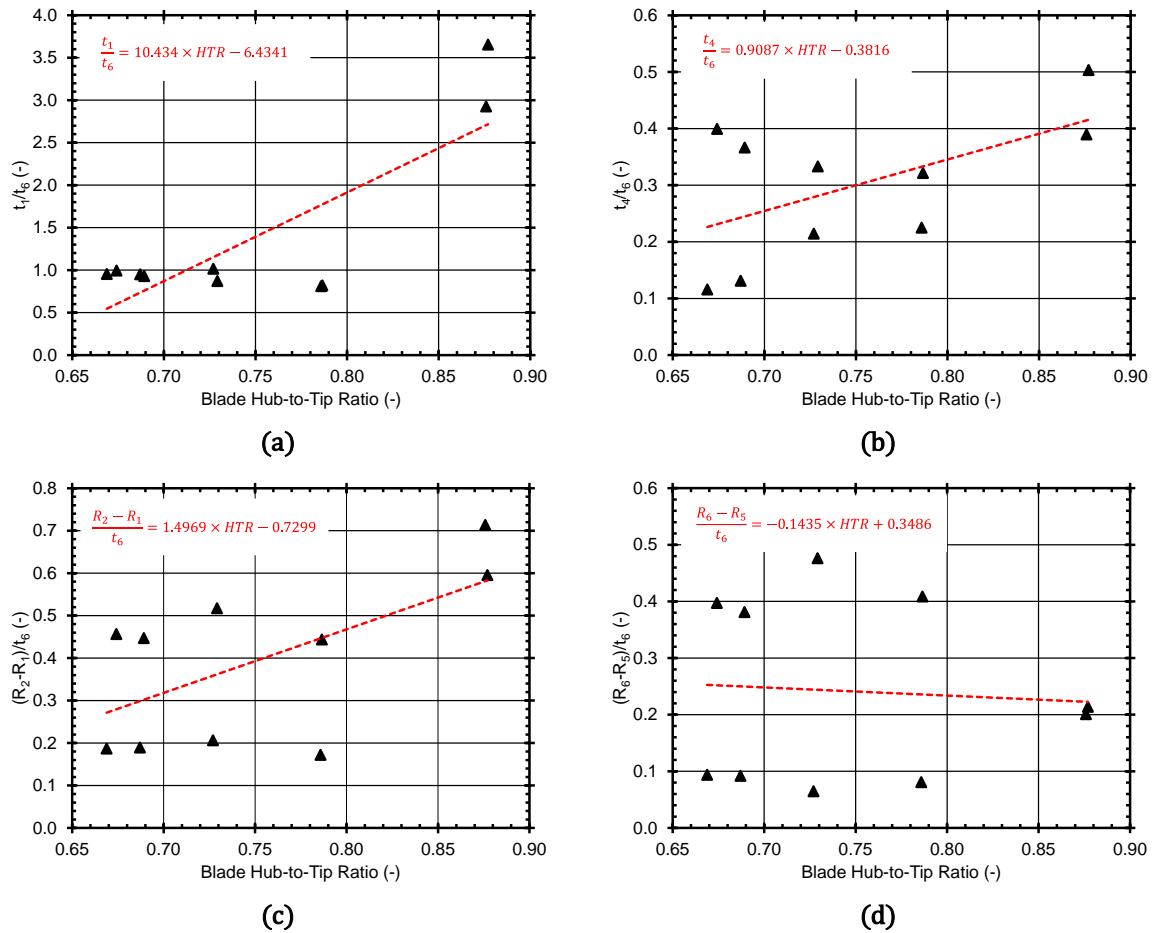


Figure 4.21: Design variables in terms of rotor hub-to-tip ratio for turbine components.

Table 4.7: Disk optimization design variables min/max values

Design Variable	Minimum Value		Maximum Value	
	Compressor	Turbine	Compressor	Turbine
R_1	1.1 times the shaft R_o		N/A	
$(R_2 - R_1)/t_6$	0.3	0.2	3.0	3.0
$(R_6 - R_5)/t_6$	0.1	0.1	0.7	0.5
t_1/t_6	0.7	0.8	2.5	2.0
t_4/t_6	0.1		0.5	

The correlations depicted in Figure 4.20 and Figure 4.21 are used for assigning initial values to the design variables. However, if the computed values are lower or greater than the min/max values tabulated in Table 4.7, then the design variables are assigned the respective min/max values instead. This way an initial disk geometry is obtained that always respects then min/max values given in Table 4.7. Since the same min/max values are also used as geometrical constraints (see paragraph 4.4.3.7) during the optimization, it is obvious that the initial disk geometry lies always in the feasible space.

4.4.3.4 Calculation of Disk Mass

The mass of a disk (W_{KG}) comprising five (5) segments, each of which has a radial thickness distribution described by Eq. (4.6), is estimated by:

$$W_{KG} = 2\pi\rho \sum_{k=1}^{k=5} \left\{ m \left[\frac{(R_o - R_i)^{2+dsf}}{2 + dsf} + \frac{R_i(R_o - R_i)^{1+dsf}}{1 + dsf} \right] + \frac{n}{2}(R_o^2 - R_i^2) \right\}_k \quad (4.53)$$

where ρ is the disk material density (see Appendix F).

4.4.3.5 Calculation of Stress Margins

The stress criteria used for ensuring the structural integrity of the disk at every optimization cycle are given by [see Armand (1995); Tong et al. (2004); Kurzke (2007); Lolis (2014)].

$$RDM = \frac{\sigma_{vM,max}}{\sigma_{Y,min}/SF_Y} \leq 1 \quad (4.54)$$

$$RBM = \frac{\bar{\sigma}_\theta/SF_T}{\bar{\sigma}_{UTS}} \leq 1 \quad (4.55)$$

The design margin, described by Eq. (4.54), requires that the maximum von Mises stress developed in the disk be lower than the minimum value of the disk material yield strength. The minimum value of σ_Y is obtained at the maximum temperature along the disk radius. A typical value for the safety factor ($SF_Y \geq 1.0$) is $SF_Y = 1.1$ [see Armand (1995)], but greater values could be adopted to compensate for inaccuracies in the stress estimations.

The second stress margin (burst margin), described by Eq. (4.55), compares the average tangential stress to the average material ultimate tensile strength. The burst margin is typically evaluated at +120% disk overspeed [see Armand (1995)], but the overspeed factor is an input (designer's choice) in the present formulation. A typical value for the safety factor ($SF_T \leq 1.0$) is $SF_T = 0.9$ [see Armand (1995)], but lower values [e.g., $SF_T = 0.47$ according to Tong et al. (2004)] could be adopted. Finally, to include cases where there are tangential stresses with negative values, $\bar{\sigma}_\theta$ is calculated by the RMS formula:

$$\bar{\sigma}_\theta = \sqrt{\frac{1}{N_d} \sum_{k=1}^{k=N_d} \sigma_{\theta,k}^2}$$

where N_d is the number of nodes used to discretize the disk.

4.4.3.6 Objective Function Formulation

In disk design problems, weight reduction is equivalent to maximizing the developed stresses within the disk according to Gutzwiller et al. (2009). Indicative figures for the maximum stresses developed in a disk are the design and burst margins defined in Eqs (4.54) and (4.55). Hence, the objective function, f_{OBJ} , is formulated as:

$$\min: f_{OBJ} = [\max(RDM, RBM) - 1]^2 \quad (4.56)$$

where we seek to minimize f_{OBJ} or, in other words, to maximize whichever between RDM or RBM is larger such that $RDM \leq 1$ and $RBM \leq 1$.

Note that maximizing the disk stresses instead of directly minimizing the disk mass was opted since it leads to minimum weight, but the mathematical problem formed has some advantages in terms of the minimization procedure. For producing acceptable disk designs, the minimization of the disk mass should be subjected to a number of geometry and stress constraints. For a robust and converging optimization procedure, the initial disk design should fall into the feasible solutions space when using, e.g., direct-search techniques. Initializing the disk dimensions alone, although done in a consistent way, cannot always ensure the fulfillment of both Eqs (4.54) and (4.55) if they are used as constraints. In other words, the initial disk geometry is not a feasible solution by default and, therefore, cannot be used as a suitable starting point.

On the other hand, formulating the minimization problem in the form of Eq. (4.56), leaves as only constraints to be fulfilled by both the initial and optimized disk geometries the constraints related to the disk dimensions alone. For the initial disk, these constraints can be more easily fulfilled (as already explained in paragraph 4.4.3.3), thus producing an appropriate starting disk geometry for the optimization.

The above arguments were tested by the author of this thesis during the formulation, development, and verification of the optimization procedure described in the present section, and it was concluded that formulating the minimization problem in the form of Eq. (4.56) is more robust than minimizing directly the disk mass [expressed by Eq. (4.53)], when using the Nelder-Mead SIMPLEX algorithm.

4.4.3.7 Constraints Formulation

Constraints, f_{CNS} , are formulated as upper-bounded inequalities in the form:

$$f_{CNS} \leq \varepsilon_{CNS} \quad (4.57)$$

where ε_{CNS} it the constraint threshold value.

Whenever a constraint is violated, a penalty value, f_{PNL} , is imposed on the objective function ($f_{OBJ} + f_{PNL}$) in the form:

$$f_{PNL} = \begin{cases} 0, & f_{CNS} \leq \varepsilon_{CNS} \\ s_a, & f_{CNS} > \varepsilon_{CNS} \end{cases} \quad (4.58)$$

or:

$$f_{PNL} = \begin{cases} 0, & f_{CNS} \leq \varepsilon_{CNS} \\ \exp[s_m(f_{CNS} - \varepsilon_{CNS})], & f_{CNS} > \varepsilon_{CNS} \end{cases} \quad (4.59)$$

In Eq. (4.58) s_a is a user-defined scalar adder while in Eq. (4.59) s_m is a user-defined scalar multiplier (default values $s_a = s_m = 1.0$).

Next, the geometry constraints imposed for the different disk types are described. For all disks, the mass should be positive and, therefore, a first constraint imposed is given by:

$$W_{KG} > 0 \quad (4.60)$$

The above constraint is imposed to basically prevent the unlikely production of ring-type disks with $R_1 > R_6$.

Also, the bore radius ($R_1 = R_{bore}$) for all disk types must be greater than the shaft outer radius by a safety factor of 1.1 (see Table 4.7):

$$\frac{R_1}{\text{shaft } R_o} \geq 1.1 \quad (4.61)$$

For web- and hyperbolic-type disks, the design variables must also satisfy the min/max values tabulated in Table 4.7:

$$\begin{cases} 0.3 \leq \frac{R_2 - R_1}{t_6} \leq 3.0, & \text{for compressors} \\ 0.2 \leq \frac{R_2 - R_1}{t_6} \leq 3.0, & \text{for turbines} \end{cases} \quad (4.62)$$

$$\begin{cases} 0.1 \leq \frac{R_6 - R_5}{t_6} \leq 0.7, & \text{for compressors} \\ 0.1 \leq \frac{R_6 - R_5}{t_6} \leq 0.5, & \text{for turbines} \end{cases} \quad (4.63)$$

$$\begin{cases} 0.7 \leq \frac{t_1}{t_6} \leq 2.5, & \text{for compressors} \\ 0.8 \leq \frac{t_1}{t_6} \leq 2.0, & \text{for turbines} \end{cases} \quad (4.64)$$

$$0.1 \leq \frac{t_4}{t_6} \leq 0.5 \quad (4.65)$$

Equation (4.62) ensures that $R_2 > R_1$ and Eq. (4.63) ensures that $R_6 > R_5$. From Eq. (4.65) follows that $t_4 < t_5$, while the combination of Eqs (4.64) and (4.65) yields $t_4 < t_2$ and, therefore, in web-type disks $t_3 < t_2$ is also true. In hyperbolic-type disks, it is easily deduced⁴⁰ from Eq. (4.52) that $t_3 < t_2$ also holds. Thus, from Eq. (4.51), it always follows that $R_3 > R_2$ and $R_5 > R_4$ for both web- and hyperbolic-type disks. Therefore, only an additional constraint, between R_3 and R_4 , is required for producing reasonable (web- and hyperbolic-type) disk shapes with $R_1 < R_2 < R_3 < R_4 < R_5 < R_6$. This is expressed by:

$$R_4 > R_3 \quad (4.66)$$

Finally, for hyperbolic-type disks, an extra constraint between t_3 and t_4 is also imposed in the form:

$$t_4 < t_3 \quad (4.67)$$

⁴⁰ $t_2 > t_4 \rightarrow \frac{1}{3}t_2 > \frac{1}{3}t_4 \rightarrow \frac{2}{3}t_2 > \frac{1}{3}(t_2 + t_4) \rightarrow t_3 < \frac{2}{3}t_2 < t_2$

4.4.3.8 Optimization Procedure Validation

For validating the optimization formulation implemented in RDO, GasTurb Details 5 [see Kurzke (2007)] was utilized. The optimization was conducted for a web-type disk and the results obtained were compared with those produced by GasTurb Details 5. As a baseline, the geometry and performance of the NASA/GE E³ HPC 3rd stage disk were used but, for a fair comparison, these were slightly modified according to the output values produced by GasTurb Details 5 when initializing the disk geometry and boundary loading.

The disk initial geometry is given in Table 4.8. Table 4.9 tabulates other necessary inputs to the optimization procedure. Temperature along the disk radius is set constant and equal to 20 °C (room temperature), i.e., no heat-transfer is considered.

Table 4.8: Initial geometry for validating the disk optimization methodology

Type:	Web	
Disk Station	R (mm)	t (mm)
1 (Bore)	106.3	24.7
2	120.1	24.7
3	134.5	8.0
4	211.3	8.0
5	217.1	28.1
6 (Rim)	230.3	28.1

Table 4.9: Other inputs for validating the disk optimization methodology

Quantity	Value
Blade Material	Ti-8-1-1
Disk Material	Ti-6Al-4V
N_{mech}	12,416.5 rpm
Z_b	50
$W_{KG,dw}$	94.5 g
$R_{cg,dw}$	250.1 mm
$\sigma_{r,rim}$	49.1 MPa

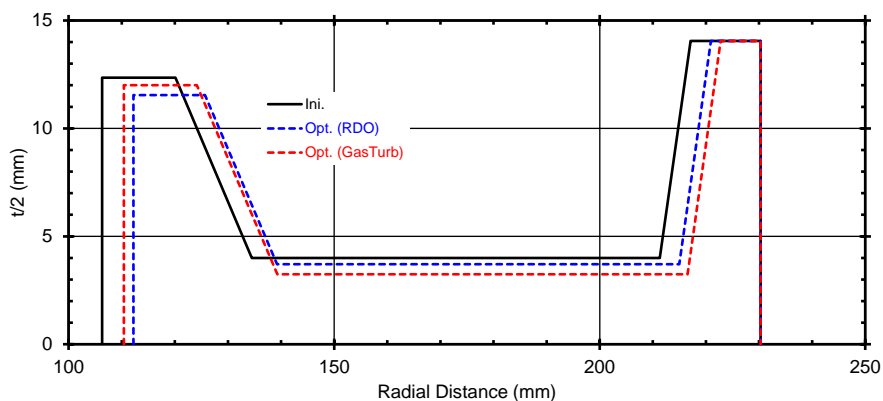
The disk overspeed factor for evaluating the burst margin is set at 100% of the design speed, while the values for the safety factors are set equal to $SF_Y = 1.0$ and $SF_T = 0.47$ (GasTurb Details 5 defaults). Finally, in Eq. (4.51), $\alpha_{IS} = 60^\circ$ and $\alpha_{OS} = 30^\circ$ are used (GasTurb Details 5 defaults).

The optimization results and the comparison between RDO and GasTurb Details 5 are summarized in Table 4.10, where the relative differences seen in the table are defined as $100 \times (X_{Ini.} - X_{Opt.})/X_{Ini.}$

Table 4.10: RDO and GasTurb Details 5 results; the relative difference from initial is also quoted

Quantity	Ini.	RDO		GasTurb Details 5	
		Opt.	Rel. Diff. (%)	Opt.	Rel. Diff. (%)
$R_1/(\text{shaft } R_o)$	1.100	1.161	-5.54	1.142	-3.86
$(R_2 - R_1)/t_6$	0.491	0.480	+2.26	0.489	+0.43
$(R_6 - R_5)/t_6$	0.470	0.333	+29.11	0.268	+42.95
t_1/t_6	0.879	0.822	+6.49	0.854	+2.83
t_4/t_6	0.285	0.264	+7.18	0.231	+18.86
W_{KG}	7.8 kg	6.9 kg	+12.01	6.4 kg	+17.96
RBM	0.937	1.000	-6.76	1.000	-6.76
RDM	0.633	0.667	-5.46	0.651	-2.88

As it can be seen from Table 4.10, both programs minimize the disk weight by maximizing the burst margin (RBM). For achieving this maximization, both programs vary the design variables at the same direction. It is observed that the final values of the design variables are of the same order of magnitude for both RDO and GasTurb Details 5. The greater differences are observed between $(R_6 - R_5)/t_6$ and t_4/t_6 ($\sim 24.3\%$ and $\sim 14.4\%$ between RDO and GasTurb Details 5), which primarily explains why GasTurb Details 5 achieves a slightly larger reduction in disk mass (about 0.46 kg more than RDO). Finally, Figure 4.22 illustrates the disk semi-contour, where the differences between the initial and optimized disks produced by RDO and GasTurb Details 5 are shown.

**Figure 4.22:** Initial disk geometry and optimized geometry comparison between RDO and GasTurb Details 5.

The differences between the two programs are attributed to the different constraints used. GasTurb Details 5 provides no information whatsoever for the optimization method itself or for the penalty value it imposes when a constraint is violated and, therefore, the comparison between the two programs couldn't be altogether fair. Nevertheless, the above study was conducted to verify that RDO can successfully reproduce, both qualitatively and quantitatively, the optimization results provided by a

software which is validated and widely used in preliminary design studies by academia and research institutes.

4.4.3.9 Optimization of a Ten-Stage Compressor Disks

Next, optimization test cases to test RDO's capabilities are provided for ring-, web-, and hyperbolic-type disks. Again, as baseline the 1st, 2nd, and 3rd stage disks of the NASA/GE E³ HPC [see Holloway et al. (1982)] are considered. The baseline geometry and calculation inputs are shown in Table 4.4 and Table 4.5, respectively. The shaft outer radius is equal to $R_o = 6.95$ cm (see paragraph 4.3.2). The disk overspeed factor for evaluating the burst margin is set at 120% of the design speed (12,416.5 rpm), while the values for the safety factors are set equal to $SF_Y = 1.1$ and $SF_T = 0.9$ (RDO defaults). Finally, the disk temperature is set constant along the disk radius and equal to that at the disk rim (see Table 4.5), while heat transfer effects are not taken into account.

According to Armand (1995), NASA/GE E³ HPC's disks were designed but not optimized for minimum weight. Therefore, to first assess how much more can the disk masses be reduced compared to the existing disks, Eqs (4.51) and (4.52) are switched off during the optimization process and the respective dimensions are kept constant and equal to those of the baseline disks: $(R_3, R_4) = (153.6, 198.6)$ mm for the 3rd stage (web) disk and $(R_3, R_4, t_3) = (140.1, 169.9, 15.3)$ mm for the 2nd stage (hyperbolic) disk. That is, only the dimensions directly varied by the design variables are changed during the optimization. The results are shown in Table 4.11, where the relative differences are defined as $100 \times (X_{\text{Base.}} - X_{\text{Opt.}})/X_{\text{Base.}}$.

Table 4.11: RDO results for the re-design of the NASA/GE E³ HPC 1st, 2nd, and 3rd stage disks

Stage (Type):	1 (Ring)			2 (Hyper.)			3 (Web)		
Quantity	Base.	Opt.	Rel. Diff. (%)	Base.	Opt.	Rel. Diff. (%)	Base.	Opt.	Rel. Diff. (%)
$R_1/(\text{shaft } R_o)$	1.498	1.818	-21.34	1.534	1.714	-11.71	1.530	1.803	-17.87
$(R_2 - R_1)/t_6$	N/A	N/A	N/A	0.312	0.305	+2.00	0.491	0.521	-6.12
$(R_6 - R_5)/t_6$	N/A	N/A	N/A	0.115	0.115	-0.52	0.470	0.510	-8.47
t_1/t_6	N/A	N/A	N/A	0.712	0.703	+1.31	0.879	0.826	+6.07
t_4/t_6	N/A	N/A	N/A	0.162	0.164	-0.98	0.221	0.223	-1.07
W_{KG}	16.8 kg	10.2 kg	+39.17	9.7 kg	8.8 kg	+9.40	8.5 kg	7.7 kg	+9.98
RBM	0.631	1.000	-58.48	0.878	1.000	-13.90	0.847	1.000	-18.06
RDM	0.597	0.863	-44.56	0.836	0.927	-10.89	0.825	0.954	-15.64

From Table 4.11 it is seen that the weight reduction achieved by RDO is significant for all three stages, ranging from ~9.4% (2nd stage disk) up to ~39.2% (1st stage disk). In all cases, the disk mass minimization is accomplished by maximizing the burst margin (RBM) with a simultaneous increase in the design margin (RDM) value. As it can be seen from Table 4.11, for all three disks the optimizer tends to minimize the disk

weight by increasing R_1 as much as possible (has the greater relative change compared to the other design variables).

Figure 4.23 depicts the convergence history for all three disk cases, where the logarithm (base 10) of f_{OBJ} (left diagrams) and the values of RDM and RBM (right diagrams) are plotted against the optimization cycle.

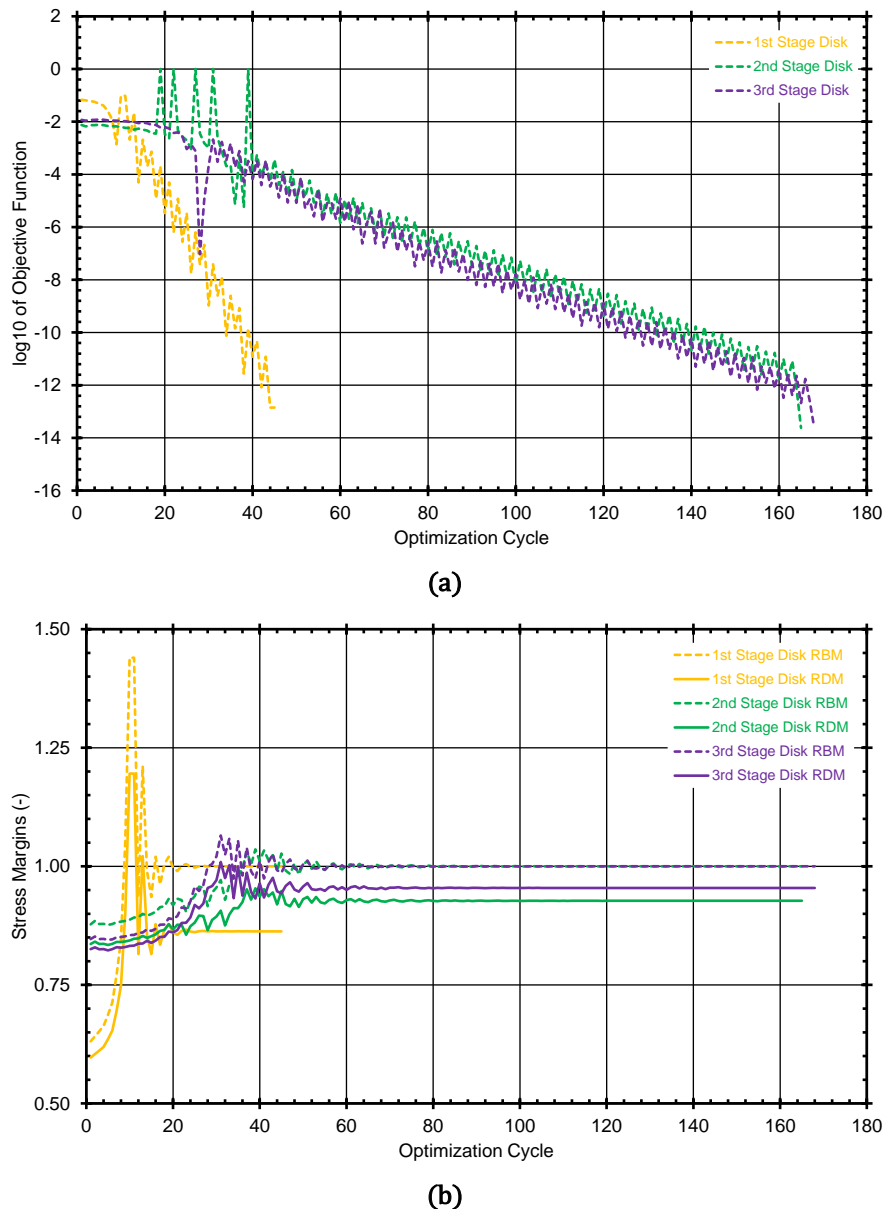
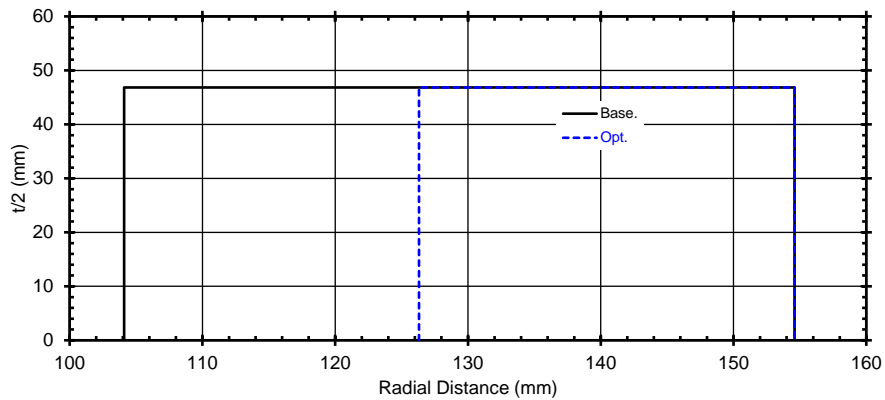


Figure 4.23: RDO convergence history for the re-design of the NASA/GE E³ HPC 1st, 2nd, and 3rd stage disks: (a) value of objective function and (b) value of design margins vs optimization cycle.

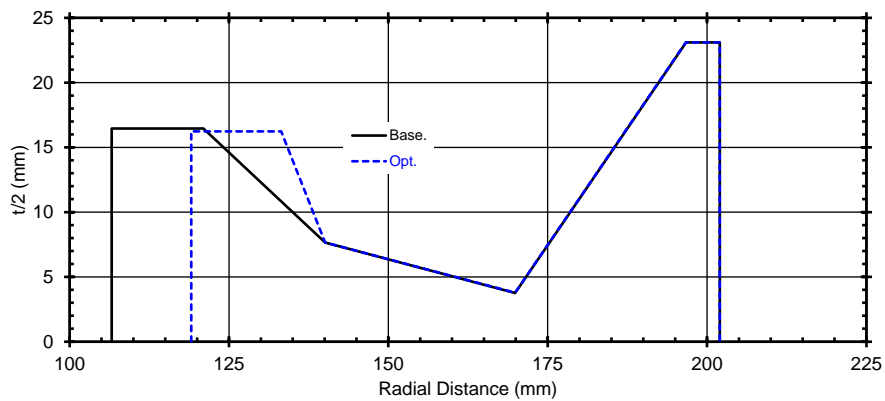
As it can be seen from Figure 4.23a, the ring disk (1st stage) optimization requires less than one third of the number of cycles required for the optimization of the 2nd (hyperbolic) and 3rd (web) stage disks. This, obviously, is due to the fact that there is only one (1) design variable (R_1) for minimizing the mass of a ring-shaped disk, compared to the five (5) design variables (R_1, R_2, R_5, t_1, t_4) required for optimizing the other two disk shapes. For all cases, the convergence is deep ($f_{OBJ} < 10^{-12}$).

As it is also seen from Figure 4.23b, for all optimization cases *RBM* is always greater than *RDM*, thus verifying graphically the results shown in Table 4.11 (according to which the optimizer achieves the mass minimization by maximizing the burst margin value with a subsequent increase in the design margin value).

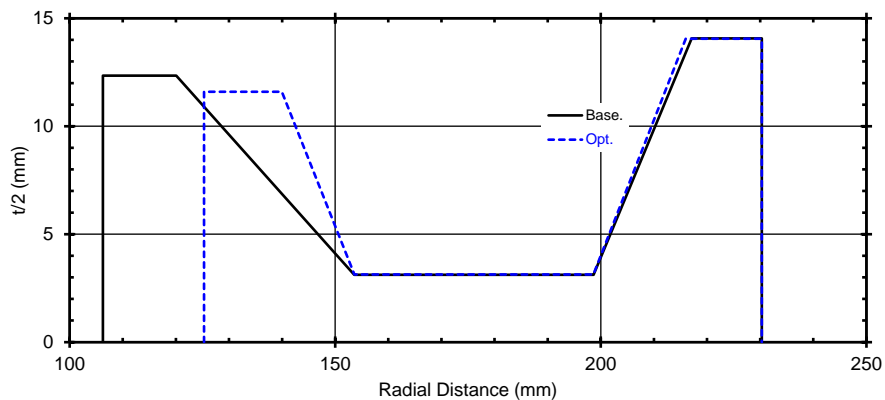
Figure 4.24 illustrates the baseline and optimized disk semi-contours, while Figure 4.25 illustrates the tangential stress ($\sigma_\theta/0.9$) distribution for the baseline and optimized disk geometries, at 100% and 120% of the design speed.



(a)

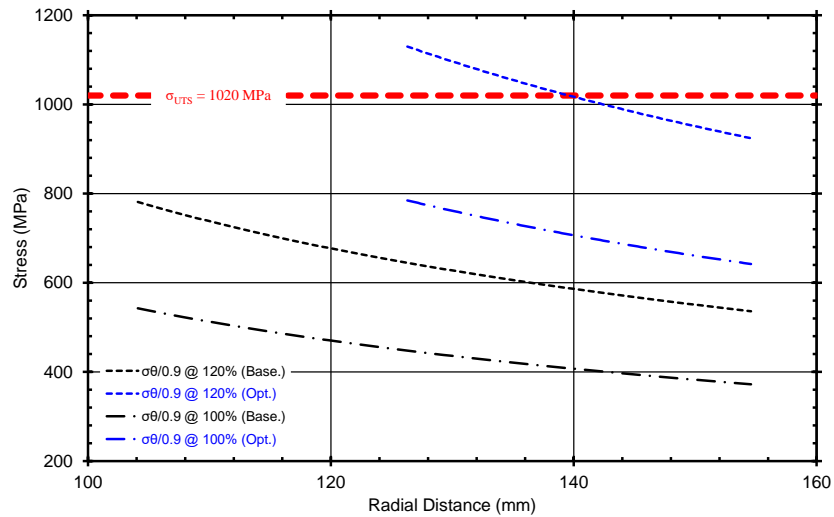


(b)

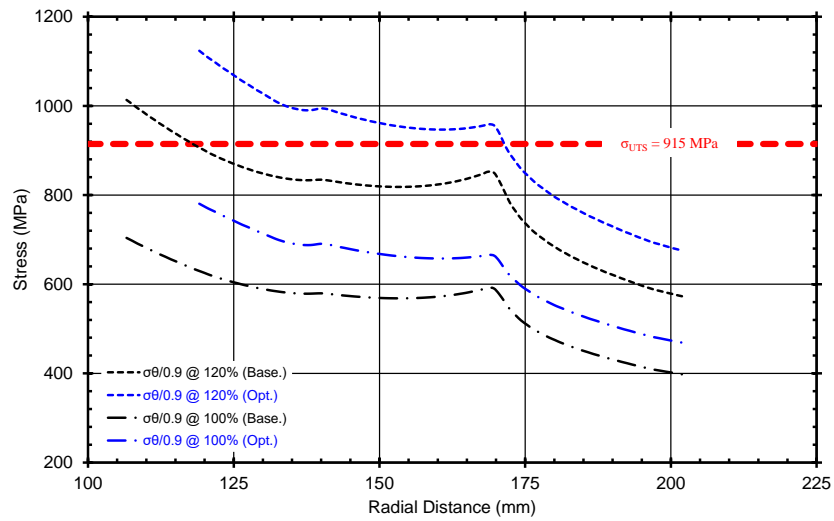


(c)

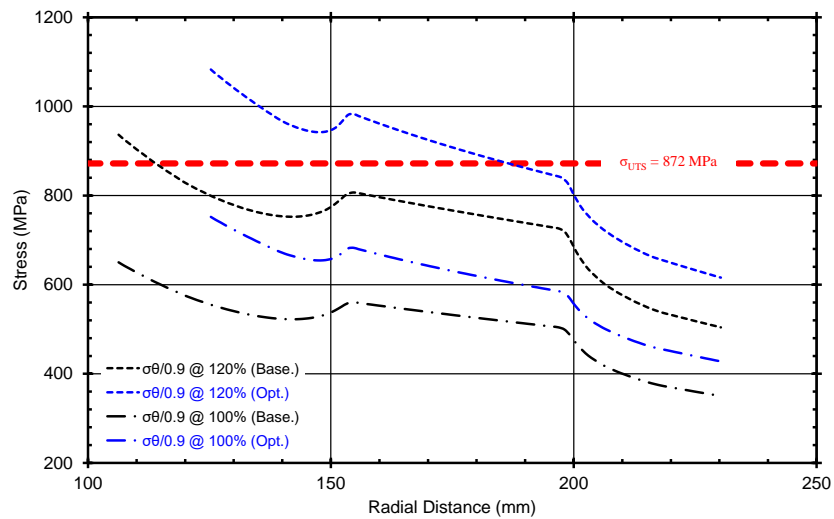
Figure 4.24: Baseline and optimized disk geometry comparison for the NASA/GE E³ HPC: (a) 1st stage ring disk, (b) 2nd stage hyperbolic disk, and (c) 3rd stage web disk.



(a)



(b)



(c)

Figure 4.25: Tangential stress distribution at 100% and 120% of the design speed for the baseline and optimized disk geometry for the NASA/GE E³ HPC: (a) 1st stage ring disk, (b) 2nd stage hyperbolic disk, and (c) 3rd stage web disk. In all cases the UTS limit is also shown.

In Figure 4.25, the UTS limit is also shown. Figure 4.25 demonstrates the shift of the stress curve ($\sigma_\theta/0.9$) at 120% of the design speed towards the UTS line for meeting the *RBM* criterion ($RBM = 1.0$) and the maximization of the disk stress (and, thus, the minimization of the disk mass). For all optimized disk geometries, the tangential stress at 120% of design speed (blue dashed curve) takes both greater and lower values than the respective UTS limit (σ_{UTS}). This is because the burst margin criterion is formulated considering the average values of σ_θ and σ_{UTS} [see Eq. (4.55)]. Therefore, the optimizer updates the disk geometry until the σ_θ curve is shifted to be half above-half below the UTS line.

From Figure 4.25, it is also seen that the tangential stress at 120% of the design speed (black dashed curve) for the 2nd and 3rd stage baseline disks is greater than σ_{UTS} along the inner rim and inner shoulder sections of the disks, contrary to the 1st stage baseline disk where the respective curve ($\sigma_\theta/0.9$ at 120% of design speed) is well below the UTS limit. Therefore, regarding the optimization of the 1st stage disk, there is bigger room for meeting the *RBM* criterion than that required for the optimization of the 2nd and 3rd stage disks. Hence, the greater mass reduction achieved by RDO for the 1st stage disk compared to that for the 2nd and 3rd stage disks (almost 4 times more according to Table 4.11) is justified graphically.

Now, the optimization of all ten (10) stage disks of the NASA/GE E³ HPC (see Appendix D) is conducted again following two approaches. The first is the one followed for the optimization of the 1st, 2nd, and 3rd stage disks presented above (“Re-design” approach). In the second one, Eq. (4.51) with $\alpha_{IS} = \alpha_{OS} = 36^\circ$ (RDO defaults) is again switched on for defining the disk shape (“From scratch” design); that is, the disks are designed anew (from scratch). The RDO results are shown in Figure 4.26, presenting the mass reduction achieved by the two approaches compared to baseline.

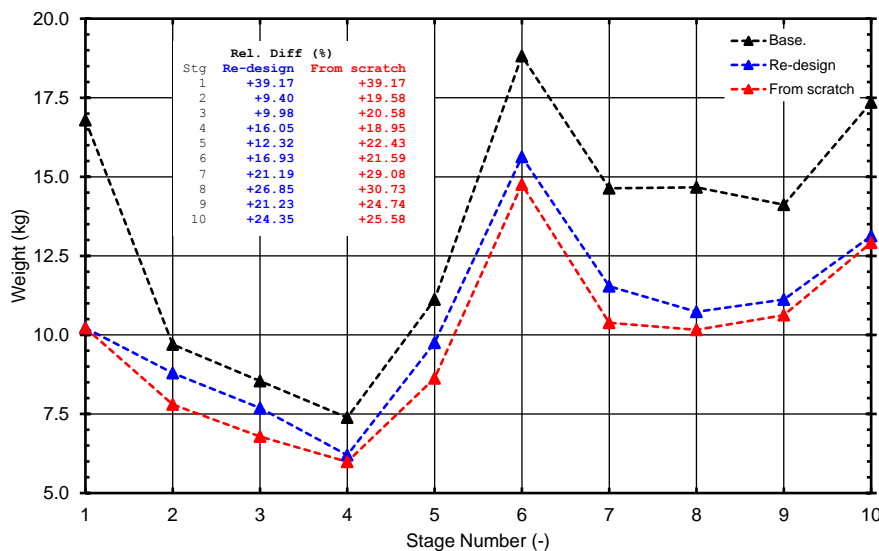


Figure 4.26: Weight comparison between baseline and RDO results for the re-design and “from scratch” design of all ten stage disks of the NASA/GE E³ HPC.

As it can be seen from Figure 4.26, “from scratch” design achieves a greater mass reduction than re-design for all ten stage disks. Design from scratch achieves an overall

mass reduction of about 26.2% (98.3 kg compared to the baseline 133.1 kg) while re-design achieves an overall reduction of about 21.28% (104.8 kg compared to baseline).

Figure 4.27 illustrates the compressor meridional view where the baseline and optimized disk shapes are shown. Regarding the time required for optimizing 10 disks twice, that was less than ~5 seconds on a typical desktop workstation (Windows 7 64-bit, Intel® Core™2 Duo CPU @ 3 GHz with 4GB RAM).

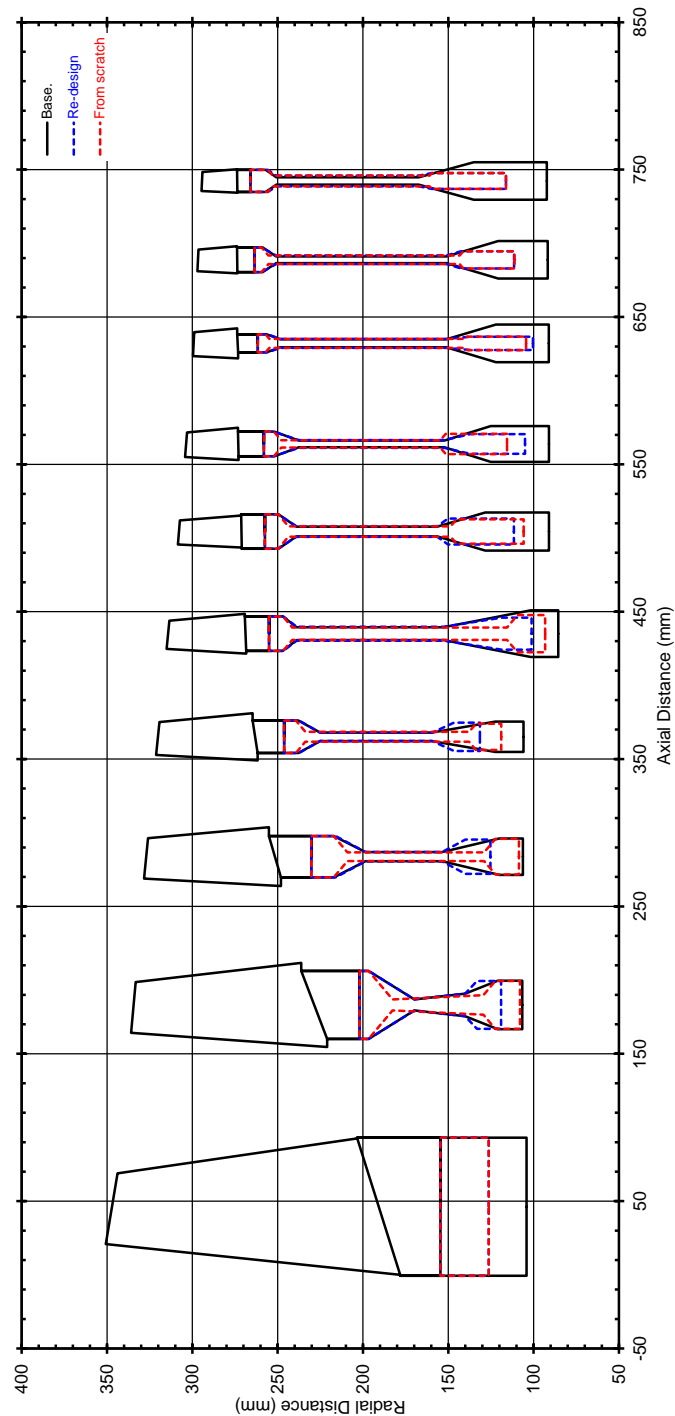


Figure 4.27: NASA/GE E³ HPC meridional view showing the baseline and RDO optimized disk shapes for the re-design and “scratch” design calculations.

Finally, the “from scratch” design is repeated but, this time, heat transfer effects are accounted for by solving the numerical D-STM. For this calculation, the temperature at the bore of the disks is considered constant and equal to 20 °C (room temperature) across the compressor. The meridional view of the compressor after the new design is shown in Figure 4.28. The overall weight reduction is now 16.7% (compared to 26.2% without heat transfer effects). The weight reduction is smaller since more material is required to compensate for the additional thermal stresses.

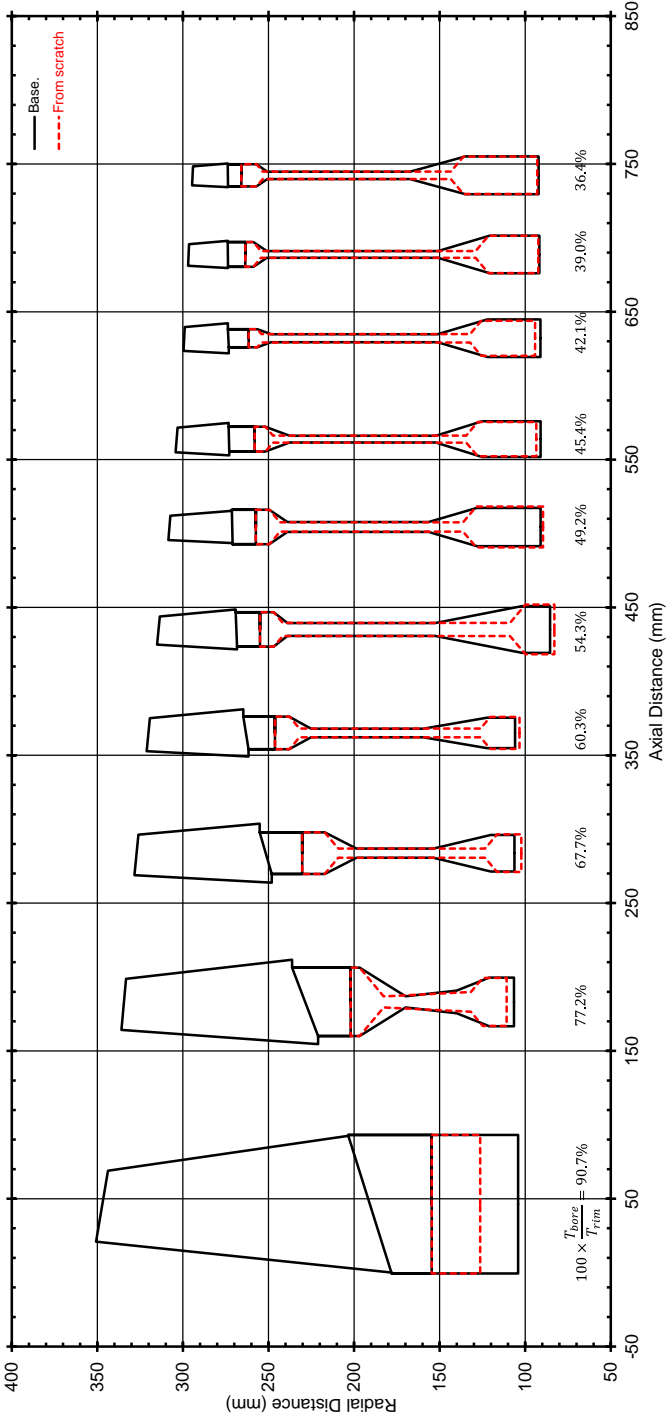


Figure 4.28: NASA/GE E³ HPC meridional view showing the baseline and RDO optimized disk shapes for the “scratch” design calculation including heat transfer effects.

4.5 Interconnecting Ducts

Ducts are structural parts of a gas turbine engine that are used to link different components and to drive the flow between them with minimum loss and flow distortion. Ducts should also occupy minimum space, otherwise they have an adverse impact both on the engine's overall length and weight. Hence, duct design should be conducted aiming to satisfy both flow and structural criteria which, in some cases, lead to conflicting design decisions.

In the present thesis, ducts are designed for containing the pressure of the flow between the components they connect. Although this is a very simplistic approach (having in mind the above discussion), it's the same approach followed by all publicly available preliminary design studies [see Onat et al. (1979a); Lolis (2014)]. Therefore, ducts are treated as pressurized containers of circular shape (see Figure 4.29), the thickness (t) of which is estimated by [Onat et al. (1979a)]:

$$t = \frac{\bar{p}^0 \bar{R}_t}{\sigma_Y} \quad (4.68)$$

In Eq. (4.68), \bar{p}^0 is the average total pressure between the duct inlet and outlet, \bar{R}_t is the duct average wall radius at the annulus tip, and σ_Y is the duct material yield strength. For simplicity, σ_Y is calculated according to Onat et al. (1979a) assuming titanium for temperatures lower than 700 °F, and steel for temperatures greater than 700 °F:

$$\sigma_Y = \begin{cases} 50,000 \text{ psi}, & \bar{T}^0 \leq 700 \text{ °F} \\ 70,000 \text{ psi}, & \bar{T}^0 > 700 \text{ °F} \end{cases}$$

where \bar{T}^0 is the average total temperature between the duct inlet and outlet.

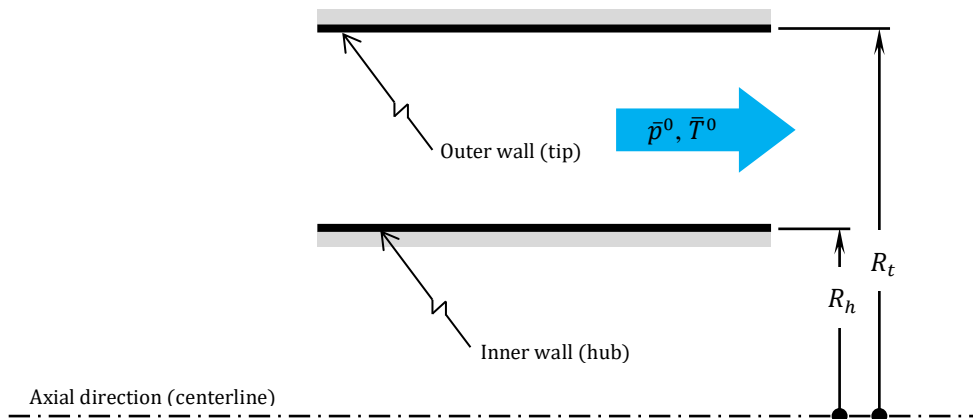


Figure 4.29: Circular annular duct nomenclature [adapted from Onat et al. (1979a)].

In this thesis, the duct length is calculated in terms of a user-specified length-to-height ratio, where the average flow-annulus height between the duct inlet and outlet is used. Typical values for the duct length-to-height ratio can be found in the public literature or from engine 2D cutaways. For instance, a value of 2.85 can be used for inter-

compressor ducts, and a value of 2.28 can be used for inter-turbine ducts [see Walsh et al. (2004)].

Finally, regarding the duct shape, it is assumed that the duct inner and outer wall radius either varies linearly between the inlet and outlet, or according to a 3rd degree polynomial by specifying additionally the inlet and outlet duct angles (user inputs). For S-shaped ducts (typically the ducts connecting the IP to the HP compressor), a third approach is also available where the duct inner and outer wall shapes are approximated by 2nd degree polynomials by specifying only two geometry parameters, namely the duct diameter-to-length ratio and the tip shape coefficient [for more details, see Anastasiou (2021)].

4.6 Turbomachinery Casings

Similarly to ducts, casings are also used to contain high-pressure flows. However, according to Bretschneider et al. (2008), the necessary casing thickness for blade fragment containment surpasses by far the one for pressure containment. Therefore, for outer casing segments over rotor blades, thickness is primarily estimated so that the casing can withstand the high-energy impact of blade fragments in the case of blade failure.

The necessary casing wall thickness, t , is estimated according to the expression formulated by Fedortschenko et al. [cf. Schaber et al. (2019)]. This is given by:

$$t = \sqrt{\frac{E_k}{0.65s_{m,\xi}\xi\sigma_Y(s_{m,\nu}\nu + s_{m,\psi}\psi + 0.5s_{m,\kappa}\kappa)(2t_{b,max} + 2c)}} \quad (4.69)$$

In the above, $t_{b,max}$ and c are the rotor blade maximum thickness and true chord length (at the mean line), σ_Y is the casing material yield strength, and E_k is the kinetic energy of the blade given by:

$$E_k = \frac{1}{2}W_{KG,dw}R_{CG,dw}^2\omega^2 \quad (4.70)$$

where ω is the rotor angular velocity. Here, it is assumed that the blade fragment has the same kinetic energy as that of the intact blade. As it can be seen from Eq. (4.69), t can vary across a component since both the blade dimensions (and, thus, weight and kinetic energy) and casing material also vary.

In Eq. (4.69), ξ , ν , ψ , and κ are empirical coefficients with values [cf. Schaber et al. (2019)]:

$$\xi = 1.3, \quad \nu = 0.7, \quad \psi = 0.05, \quad \kappa = 2.5$$

while $s_{m,\xi}$, $s_{m,\nu}$, $s_{m,\psi}$, and $s_{m,\kappa}$ are user-defined calibration factors (with a default value equal to unity) allowing the user to tune the model.

Note that, in aero- or industrial gas turbine engines, casings serve also as supports and carriers for mechanisms (for instance, the VSV actuators). The design of such cases

introduces complexity that cannot be modelled in a preliminary design study and, therefore, those casing designs were left out in the present work.

For fan casings, Eq. (4.69) may produce large values for the casing thickness t due to the large fan rotor blade weights (and kinetic energies). This, in turn, could lead to heavy fan designs with adverse effects both on the engine's total weight and installed performance. Thus, for fan outer casings lightweight materials are used with high σ_Y and low ρ , such as Kevlar [see Rolls-Royce plc (1996) and Table 4.1].

Finally, for other casing segments (e.g., inner casings or stator casings) the casing thickness can be a user-specified value, or a default value can be assigned to it according to NASA's WATE, equal to 2.54 mm (0.10 inches) [see Pera et al. (1977a)].

4.7 Summary and Discussion

In the present chapter models and procedures for the preliminary mechanical design of turbomachinery structural components and parts were presented, that led to the development of a dedicated PROOSIS library named GTMDC. Essential to any such calculation is the existence of a database of structural materials. Thus, a database of materials, commonly used in turbomachinery applications, was created. Then, models and procedures for the preliminary sizing of rotating shafts, rotating disks, interconnecting ducts, and casings were presented.

Regarding shafts, a simplified structural model was presented that takes into account stresses due to axial, centrifugal, and torque loads. Through the validation test case presented it was shown that the sizing depends on the safety factor considered which, in turn, depends on a number of factors including both personal judgment and experience as well as the criticality of the application considered.

Rotating disks are primarily designed for minimum weight while satisfying several geometry and structural constraints. An optimization formulation was developed and presented (RDO), where the disk mass minimization is achieved by maximizing the stresses developed in the disk. For quantifying the stresses, a design margin and a burst margin were adopted. A consistent initialization technique of the design variables was also developed based on existing engine designs, which ensures a robust optimization procedure. The utility of RDO was showcased through re-design test cases considering the disks of a ten-stage compressor. Furthermore, through the validation cases examined, it was shown that the correct estimation of the thermal and mechanical stresses, essential in any disk optimization procedure, depends on the correct prediction of the disk temperature field. Contrary to the common practice where the radial profile of temperature is calculated assuming constant disk thickness or linear variation for calculation simplicity and time efficiency, it was shown that the inclusion of the disk thickness variation improves significantly the prediction of the stress field. More importantly, this improvement comes at the same expense of computational time as that for the simplified approaches used in the open literature.

Finally, simplified, algebraic models for estimating the thickness of interconnecting ducts and turbomachinery casings were described.

5 Weight Estimation of Aircraft Gas Turbines

5.1 Introduction

Engine weight⁴¹ is a key figure regarding the design of new aircraft gas turbines. Weight not only affects the fuel burn efficiency, but also the aircraft design, performance, range, and DOC requirements, and it is a direct indicator of the engine mechanical integrity and production cost. Therefore, reliable weight estimation at the preliminary design phase is essential for the design and assessment of any new engine concept and its integration on a given aircraft configuration (see Figure 5.1).

In the present chapter, the equations, models, and assumptions used to develop a PROOSIS library named GTWC (Gas Turbine Weight Code) are given. In total, two weight estimation approximations were programmed in GTWC in the context of this thesis (see Figure 5.2), both of which belong in the component-based class of methods (see Chapter 1). The first one presented is a semi-empirical weight estimation method developed using the work conducted by Sagerser et al. (1971). The second is an “analytical” method that considers the component geometry and material selection, and it was developed based both on ATLAS [see Lolis (2014)] and NASA’S WATE [see Pera et al. (1977a)], but with additions and/or modifications/improvements.

Regarding the necessary cycle (rotational speeds, Mach numbers, temperatures, pressures, etc.) and geometry (radii, thicknesses, hub-to-tip ratios, etc.) inputs required by the GTWC components for estimating the weight of various engine components, these are the outputs of the aerothermodynamic design components presented in Chapter 3 and the mechanical design tools presented in Chapter 4.

Finally, note that absolute weight numbers are impossible to obtain at the preliminary design phase [see Kurzke et al. (2018)]. Therefore, in terms of accuracy a $\pm 10\%$ margin is considered acceptable and adopted by most weight estimation methods of the public domain [e.g., in ATLAS and NASA’S WATE]. Hence, the same accuracy goal is also adopted in the present thesis for validating the developed GTWC components.

⁴¹The terms “weight” and “mass” are used interchangeably in this text.

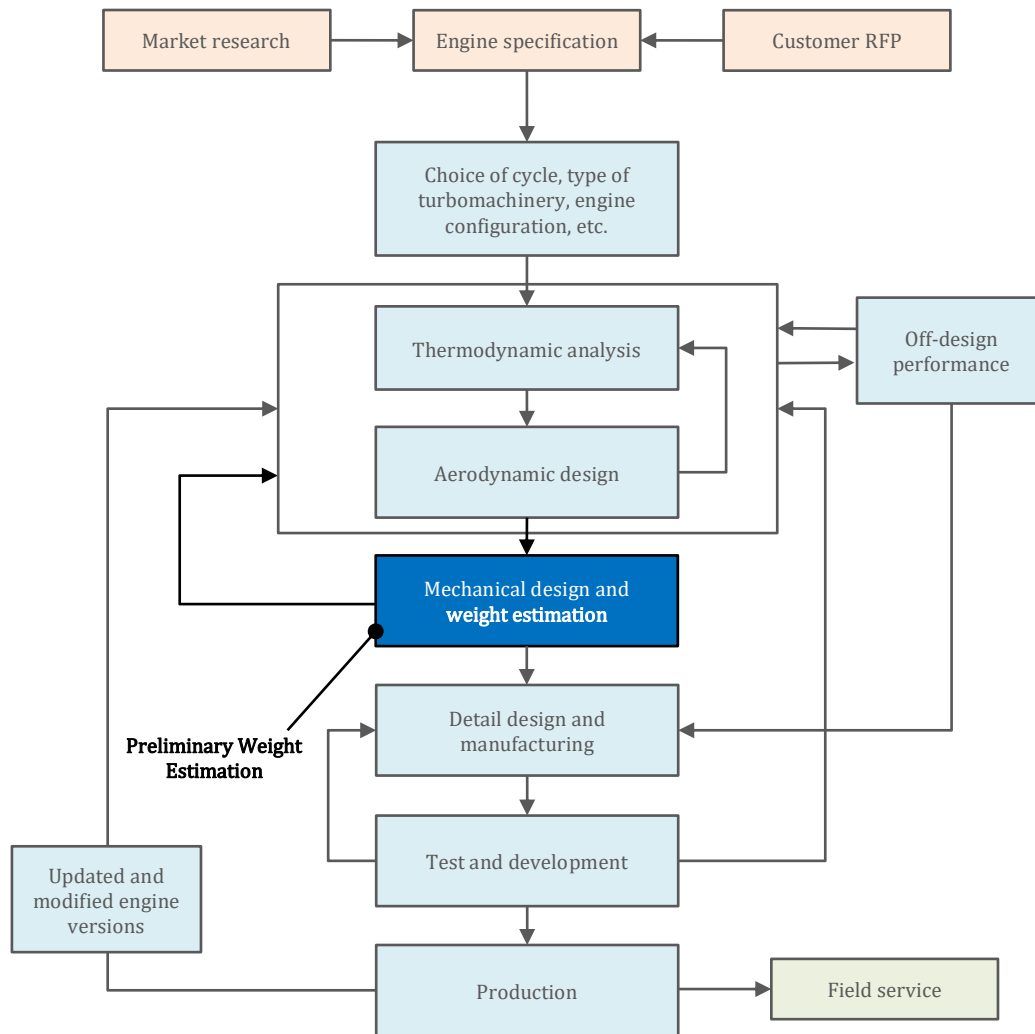


Figure 5.1: Simplified flow-chart representing the development course of a new gas turbine engine [adapted from Mattingly et al. (2002)]. The present chapter is concerned with the “Preliminary Weight Estimation” box.

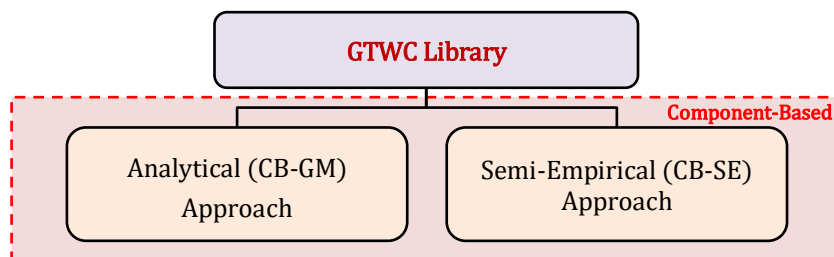


Figure 5.2: Available weight estimation approaches programmed in GTWC.

5.2 Component-Based, Semi-Empirical (CB-SE) Weight Estimation

The first method formulated and programmed for the needs of the present work in GTWC is a semi-empirical method based on the work conducted by Sagerser et al. (1971), but with additions/modifications wherever deemed necessary.

Sagerser et al.'s is an old method (developed in the early 70's) targeted primarily on calculating the weight of V/STOL engines, but the authors also provide calibration factors for cruise engines. Although the technological limits of the correlating variables (see Table 5.1) are considered outdated when we think of turbofan engines currently in operation and production, the method presents a number of advantages that make it an excellent choice for preliminary calculation purposes and, for this reason, it has been used in various recent works and projects [e.g., see Jackson (2009) and Becker et al. (2013)]:

- The correlations present remarkable low scatter.
- The method consists of single-equation algebraic expressions that require very few component and cycle inputs which, in turn, can be obtained after a very basic design calculation (in most cases a simple mass continuity calculation given the flow Mach number and the section hub-to-tip ratio to obtain the component inlet and outlet dimensions suffices).
- It does not need a database of materials.
- Though not a part of the current work, the correlations can easily be calibrated to reflect current technological limits.

Table 5.1: Correlating variables ranges for Sagerser et al. (1971) method

Component	Correlating Variable Range
Fan	$\bar{D}_{t,R} = 0.73 - 2.60 \text{ m}$
	$AR_{x,R} = 2.5 - 7.7$
	$N_{stg} = 1 - 2$
Compressor	$\bar{D}_m = 0.34 - 0.98 \text{ m}$
	$N_{stg} = 2 - 14$
	$L/D_{m,in} = 0.29 - 1.40$
Burner	$\bar{D}_m = 0.40 - 0.91 \text{ m}$
Turbine	$\bar{D}_m = 0.43 - 1.20 \text{ m}$
	$N_{stg} = 1 - 6$
	$\bar{U}_m = 120 - 510 \text{ m/s}$
Controls & Accessories	$F_N = 18,000 - 170,000 \text{ N}$
Structural Supports	Components weight = 100-2000 kg

Next, the expressions for calculating the component and total weights of a turbofan engine are presented and commented upon.

5.2.1 Fan Weight

For fan components, Sagerser et al. formulated Eq. (5.1), which correlates the fan weight with the number of stages, the rotor tip diameter, and the rotor axial aspect ratio:

$$W_{KG,FAN} = s_{m,F} K_F \bar{D}_{t,R}^{s_{m,a}a} \frac{N_{stg}}{AR_{x,R}^{s_{m,c}c}} \quad (5.1)$$

According to Sagerser et al., Eq. (5.1) considers the weight of the rotor blades, rotor disk(s), fan spinner, fan outer casing, stator blades, and support struts. Note that, for the studies conducted in the present thesis, the fan component is assumed to comprise only one stage ($N_{stg} = 1$).

In Eq. (5.1), the value for the proportionality constant, K_F , and the values for the exponents a and c , were established by Sagerser et al. who conducted a regression analysis on a database of 17 existing lift and cruise engines. From that analysis no dependence of the fan weight on the tip speed and/or solidity was found but, since these parameters affect the fan weight, Sagerser et al. corrected Eq. (5.1) by including the effects of both the rotor tip speed and solidity in the form:

$$W_{KG,FAN} = s_{m,F} K_F \bar{D}_{t,R}^{s_{m,a}a} \frac{N_{stg}}{AR_{x,R}^{s_{m,c}c}} \left(\frac{\sigma_{t,R}}{s_{m,\sigma} \sigma_{ref}} \right)^{s_{m,b}b} \left(\frac{\bar{U}_t}{s_{m,U} U_{ref}} \right)^{s_{m,d}d} \quad (5.2)$$

In Eq. (5.2) the blade speed, \bar{U}_t , is calculated as:

$$\bar{U}_{t,R} = \frac{\pi N_{mech}}{60} \bar{D}_{t,R}$$

The default values of the constants appearing in Eqs (5.1) and (5.2) are [cf. Sagerser et al. (1971)]:

$$K_F = 135 \frac{\text{kg}}{\text{m}^{2.7}}, \quad a = 2.7, \quad b = 0.3, \quad c = 0.5, \quad d = 0.3, \quad \sigma_{ref} = 1.25, \quad U_{ref} = 350 \text{ m/s}$$

Finally, both Eqs (5.1) and (5.2) have been introduced with user-defined scalar multipliers, $s_{m,F}$, $s_{m,a}$, $s_{m,b}$, $s_{m,c}$, $s_{m,d}$, $s_{m,\sigma}$, and $s_{m,U}$, with default value of unity, that allow the calibration of the model(s).

Note that the fan weight can be calculated using any one of Eqs (5.1) and (5.2).

5.2.2 Compressor Weight

For the weight of a compressor component, Sagerser et al. correlated the compressor weight with the component average mean diameter, the number of stages, and the component length-to-inlet mean diameter ratio. This expression reads:

$$W_{KG,CMP} = s_{m,C} K_C \bar{D}_m^{s_{m,a}a} N_{stg}^{s_{m,b}b} \left[1 + \frac{\frac{L}{D_{m,in}}}{\left(\frac{L}{D_{m,in}} \right)_{ref}} \right] \quad (5.3)$$

Equation (5.3) includes the weights of the compressor rotor and stator blades, disks, seals, and casings.

In Eq. (5.3), the values of the proportionality constant, K_C , and those of the exponents a and b , were established after a regression analysis taking into account a

total of 26 lift and cruise database engines. From that regression analysis no effect of the blade tip speed on the compressor weight could be found, but since it affects the component weight, Eq. (5.3) was corrected in the form of the following equation to include the tip speed effect:

$$W_{KG,CMP} = s_{m,c} K_C \bar{D}_m^{s_{m,a}} N_{stg}^{s_{m,b}} \left[1 + \frac{\frac{L}{\bar{D}_{m,in}}}{\left(\frac{L}{D_{m,in}}\right)_{ref}} \right] \left(\frac{U_{t,in}}{s_{m,U} U_{ref}} \right)^{s_{m,c}} \quad (5.4)$$

In Eqs (5.3) and (5.4), the compressor average mean diameter, \bar{D}_m , is calculated by:

$$\bar{D}_m = \frac{1}{2} (D_{m,in} + D_{m,out}) \quad (5.5)$$

with $D_{m,in}$ and $D_{m,out}$ being the component inlet and outlet mean diameters, respectively, while the reference length-to-diameter ratio, $(L/D_{m,in})_{ref}$, is given by the following statistical correlation:

$$\left(\frac{L}{D_{m,in}} \right)_{ref} = 0.2 + (0.234 - 0.218 s_{m,HTR} HTR_{ref}) N_{stg} \quad (5.6)$$

In Eq. (5.4), the blade speed at the tip is calculated as:

$$\bar{U}_{t,in} = \frac{\pi N_{mech}}{60} \bar{D}_{t,in}$$

The default values for the constants appearing in Eqs (5.3), (5.4), and (5.6) are [cf. Sagerser et al. (1971)]:

$$K_C = 24.2 \frac{\text{kg}}{\text{m}^{2.2}}, \quad a = 2.2, \quad b = 1.2, \quad c = 0.5, \quad HTR_{ref} = 0.7, \quad U_{ref} = 335 \text{ m/s}$$

Finally, in Eqs (5.3)–(5.6) appropriate scalar multipliers are introduced ($s_{m,c}$, $s_{m,a}$, $s_{m,b}$, $s_{m,c}$, $s_{m,HTR}$, and $s_{m,U}$) that allow the calibration of the model(s), with default values of unity.

Note that the compressor weight can be calculated using any of Eqs (5.3) and (5.4).

5.2.3 Burner Weight

For annular axial-flow combustors, Sagerser et al. developed a statistical correlation that links the burner weight to the burner average mean diameter squared. This expression reads:

$$W_{KG,BRN} = s_{m,B} K_B \bar{D}_m^2 \quad (5.7)$$

The weight for the burner includes the weights of the inner and outer casings, liner, and fuel injection nozzles.

In Eq. (5.7), the proportionality constant, K_B , was determined based on a regression analysis on a total of 21 lift and cruise database engines, where a weight difference between the lift and cruise engines was found. The authors of the model could not identify from the data they used any effect of the length-to-height ratio or the pressure on the burner weight, but they corrected Eq. (5.7) accordingly to reflect the combustor compactness. This was done by including in Eq. (5.7) a length-to-height ratio in the form:

$$W_{KG,BRN} = s_{m,B} K_B \bar{D}_m^2 \left[\frac{\frac{L}{h}}{\left(\frac{L}{h}\right)_{ref}} \right]^{s_{m,a}} \quad (5.8)$$

In Eq. (5.8), the burner height, h , is taken equal to the burner maximum flow-annulus height, while the burner average mean diameter, \bar{D}_m , is calculated by Eq. (5.5).

The default values for the constants appearing in Eqs (5.7) and (5.8) are [cf. Sagerser et al. (1971)]:

$$K_B = 390 \frac{\text{kg}}{\text{m}^{2.2}}, \quad a = 0.5, \quad \left(\frac{L}{h}\right)_{ref} = 3.2$$

Finally, appropriate scalar multipliers ($s_{m,B}$ and $s_{m,a}$) are introduced in the model described by Eqs (5.7) and (5.8) to allow its calibration to different engine data. These scalars have a default value of unity.

Note that the weight of a burner component can be calculated using any of Eqs (5.7) and (5.8).

5.2.4 Turbine Weight

For turbine components, Sagerser et al. (1971) developed the statistical equation described by Eq. (5.9), which expresses the component weight in terms of the turbine average mean diameter, number of stages, and average mean blade speed. Equation (5.9) includes the weight of the turbine rotors and disks, stators, casings, and seals.

$$W_{KG,TRB} = s_{m,T} K_T \bar{D}_m^{s_{m,a}} N_{stg} \bar{U}_m^{s_{m,b}} \quad (5.9)$$

In Eq. (5.9), the proportionality constant, K_T , and the value for the exponents a and b , were established after a statistical regression considering 28 lift and cruise engines. In Eq. (5.9), the turbine average mean blade speed, \bar{U}_m , is calculated as:

$$\bar{U}_m = \frac{\pi N_{mech}}{60} \bar{D}_m$$

where the average mean diameter, \bar{D}_m , is given by Eq. (5.5).

The default values for the constants appearing in Eq. (5.9) are [cf. Sagerser et al. (1971)]:

$$K_T = 7.9 \frac{\text{kg} \cdot \text{s}^{0.6}}{\text{m}^{3.1}}, \quad a = 2.5, \quad b = 0.6$$

As with all other models described in the preceding paragraphs, appropriate scalar multipliers ($s_{m,T}$, $s_{m,a}$, and $s_{m,b}$) were introduced in Eq. (5.9) also, to enable its calibration to different engine data. These scalars have a default value of unity.

5.2.5 Structural Weight

Structural components include the bearings, bearing supports and engine mounts (that is, frames), shafts, fan duct inner wall, and transition sections (i.e., interconnecting ducts). For calculating the structural weight of an engine, Sagerser et al. developed the following equation using a database of 14 engines:

$$W_{KG,STR} = s_{m,S} K_S \left(W_{KG,FAN} + W_{KG,BRN} + \sum_{LP,IP,HP} W_{KG,CMP} + \sum_{LP,IP,HP} W_{KG,TRB} \right) \quad (5.10)$$

where the summation for the compressor and turbine components applies over the LP, IP, and HP spools in a generic 3-spool turbofan configuration.

In Eq. (5.10), the proportionality constant, K_S , has a value of $K_S = 0.18$ for cruise engines, while $s_{m,S}$ is a scalar multiplier used to re-calibrate K_S with a default value of unity. Becker et al. (2013) considered that $K_S = 0.18$ is too low for current technology turbofan engines and replaced it by $K_S = 0.35$ in their study (then, $s_{m,S} \cong 1.944$).

5.2.6 Gearbox Weight

For calculating the weight of a gearbox, two different models were programmed. The first one (which is used in the studies presented here) is the empirical correlation presented by Hendricks et al. (2012), which expresses the weight of the gearbox and its lubrication system in terms of the maximum delivered power output and gear ratio. The correlation was developed by NASA using a database of existing gearbox weight values from over 50 engines, spanning from rotorcraft to turboprop engines. This expression reads:

$$W_{KG,GBX} = -37.4262 + 116.3297 K_{Gp} \quad (5.11)$$

where the auxiliary parameter K_{Gp} is calculated according to:

$$K_{Gp} = \left(\frac{P_{wr,out}}{N_{mech,out}} \right)^{0.75} i_{12}^{0.15} \quad (5.12)$$

and i_{12} is the gear ratio defined by:

$$i_{12} = \frac{N_{mech,in}}{N_{mech,out}} \quad (5.13)$$

Take note, that Eq. (5.11) gives the gearbox weight in pounds mass (lbm), while in Eq. (5.12) the power output ($P_{wr,out}$) is expressed in horsepower (hp).

The second method programmed here is the semi-empirical correlation for simple-offset gearboxes (SO) and planetary systems (PS) used in WATE [see Pera et al. (1977a)]. In this method, the weight of the gearbox is correlated against the torque input and the gear ratio, expressed again by Eq. (5.13). Finally, the gearbox weight is given by:

$$W_{KG,GBX} = s_m K_G T_{rq,in} K_{Gw} \quad (5.14)$$

where the torque, $T_{rq,in}$, is in lbf-ft, and the weight of the gearbox is given in pounds mass (lbm).

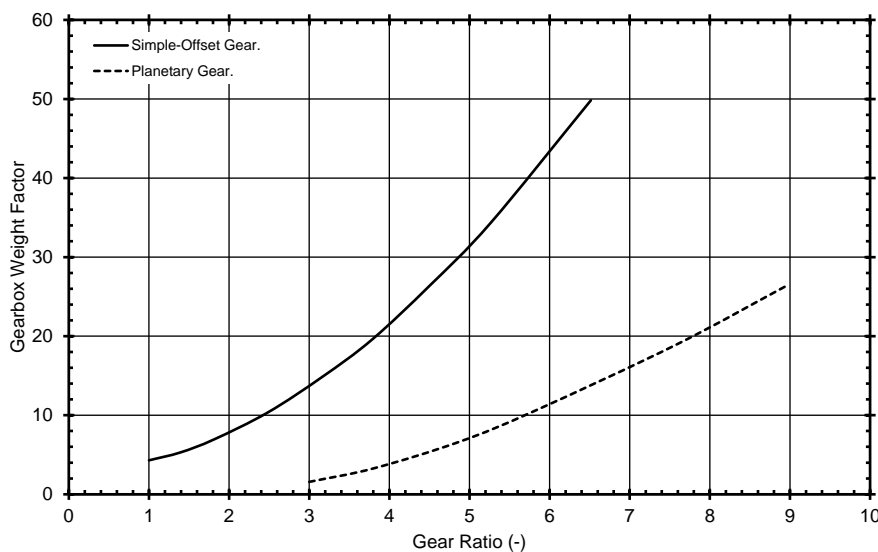


Figure 5.3: Gearbox weight correlation for simple-offset systems and planetary gearboxes [adapted from Pera et al. (1977a)].

In Eq. (5.14), the gearbox weight parameter, K_{Gw} , is depicted in Figure 5.3 in terms of the gear ratio, i_{12} . A 2nd degree polynomial was selected as a best-fit over the data presented by Pera et al. (1977a) in Figure 5.3. More specifically, K_{Gw} is evaluated according to:

$$K_{Gw} = \begin{cases} 0.9968i_{12}^2 + 0.8162i_{12} + 2.3001, & \text{for SO} \\ 0.3159i_{12}^2 + 0.4383i_{12} - 2.7806, & \text{for PS} \end{cases} \quad (5.15)$$

Finally, the constant K_G appearing in Eq. (5.14) claims a value of $K_G = 5 \times 10^{-4}$ for SO systems and $K_G = 8.33 \times 10^{-4}$ for planetary gearboxes (PS). The scalar multiplier s_m has a default value of unity and is introduced for calibrating the model.

5.2.7 VPF Pitch-Changing Mechanism Weight

For calculating the Pitch-Changing Mechanism (PCM) weight of a VPF there was no correlation that could be found by the author of this thesis available in the public

literature. Thus, in this work, it is assumed that the weight of the PCM is equal to a portion of the fan total weight (excluding, obviously, the PCM itself). In other words, the PCM weight is expressed as:

$$W_{KG,PCM} = \frac{K_{PCM}[\%]}{100} W_{KG,FAN} \quad (5.16)$$

where K_{PCM} is the PCM-to-fan weight ratio.

Table 5.2: VPF rotor weight breakdown [see Ryan et al. (1977)]

Fan Component	Weight (kg)
Rotor blades	53.1
Disc	50.8
Spinner	12.7
Pitch change actuator	29.0
Beta regulators ⁴²	5.0
	$\Sigma = 150.6$

Table 5.3: VPF weight breakdown [see Willis (1979)]

Fan Component	Weight (kg)
Fan rotor	217.0
Fan frame	318.0
Variable pitch mechanism	69.0
	$\Sigma = 604.0$

As already mentioned (see paragraph 5.2.1), Sagerser et al. (1971) correlation for estimating the weight of a fan stage [see Eq. (5.1) or Eq. (5.2)] takes into account the weights of the rotor blades, rotor disk, spinner, stator blades, outer casing, and support struts (if any). The first three weights (i.e., the rotor blades, disk, and spinner) comprise what is usually referred to as the “fan rotor weight”, while the remaining make up for the “fan frame weight”. For example, from Table 5.2 that quotes the fan rotor weight breakdown for a research V/STOL aircraft [see Ryan et al. (1977)], the PCM (pitch change actuator + beta regulators) weighs about 22.6% of the fan rotor weight including the PCM, and about 29.2% of the fan rotor weight excluding the PCM. Similarly, from Table 5.3 [see Willis (1979)] which quotes the fan weight breakdown for an experimental short-haul engine, the PCM accounts for about 24.1% and 31.8% of the fan rotor weight including and excluding the PCM weight, respectively. Finally, from the same table the PCM weight is about 11.4% of the fan total weight when the PCM is accounted for in the fan weight, and about 12.9% when it’s excluded from the fan total weight.

⁴²It’s an electrohydraulic control system which changes the blade pitch according to an input command.

5.2.8 Controls and Accessories Weight

Controls and accessories include the fuel, oil, control, and starting systems, and the accessory drive gearbox, but not the variable area mechanisms of VANs [see Sagerser et al. (1971) and Lolis (2014)]. The estimation of the C&A weight of an engine is not a trivial task since there are no correlations for estimating the weight of the individual components. For this reason, Sagerser et al. (1971) developed an “overall” expression that correlates the C&A weight with the engine thrust and *SFC* (fuel flow). They assumed that the oil and starting systems are sized from the engine thrust requirements, while fuel flow affects the size of the fuel pump and the engine control system. Thus, they formulated the following equation for estimating the C&A weight:

$$W_{KG,C\&A} = K_A F_N (1 + a_A SFC)$$

where $K_A = 2 \times 10^{-4}$ and $a_A = 13.2$.

Although the reasoning behind the above expression is legitimate, Sagerser et al.'s correlation was obtained using only data from lift engines and might not be applicable to large turbofan engines. Additionally, it correlates the weight with the engine installed performance which, in turn, will lead to iterative solutions when the engine installed performance is calculated. For these reasons, the C&A weight is calculated as a percentage of the total engine weight, an approach followed also by Lolis (2014). This is done, according to:

$$W_{KG,C\&A} = \frac{K_{C\&A} [\%]}{100} \left(W_{KG,FAN} + W_{KG,PCM} + W_{KG,GBX} + W_{KG,STR} + W_{KG,BRN} \right. \\ \left. + \sum_{LP,IP,HP} W_{KG,CMP} + \sum_{LP,IP,HP} W_{KG,TRB} \right) \quad (5.17)$$

where the summation for the compressor and turbine components applies over the LP, IP, and HP spools in a generic 3-spool turbofan engine.

In Eq. (5.17), $K_{C\&A}$ is the percentage of the C&A weight which, according to Lolis, it can be taken equal to 10%. Lolis argues that although this value is in accordance with the public domain data and other relevant studies [see Onat et al. (1979b)], it might not be representative of current technology engines since, for example, many mechanical systems are being replaced by lighter electrical and electronic systems. According to Sagerser et al. (1971), $K_{C\&A}$ was varying from 9% up to almost 30% for the cruise engines, compared to 2-10% for the lifts engines in their database.

5.2.9 VAN Area-Changing Mechanism Weight

Typically, the Area-Changing Mechanism (ACM) weight of a VAN is modelled via a 10% weight penalty compared to an equivalent fixed-area nozzle. This figure was adopted in a number of recent studies on the subject matter [see Guynn et al. (2009); Rousis (2011); Krishnan et al. (2013)]. Since in the present method the weight of a nozzle is not explicitly calculated, it is assumed that the ACM additional weight is a fraction of the engine total weight or:

$$W_{KG,ACM} = \frac{K_{ACM}[\%]}{100} \left(W_{KG,FAN} + W_{KG,PCM} + W_{KG,GBX} + W_{KG,STR} + W_{KG,BRN} \right. \\ \left. + W_{KG,C\&A} + \sum_{LP,IP,HP} W_{KG,CMP} + \sum_{LP,IP,HP} W_{KG,TRB} \right) \quad (5.18)$$

where the summation for the compressor and turbine components applies over the LP, IP, and HP spools in a generic 3-spool turbofan engine.

In Eq. (5.18) K_{ACM} is the percentage of the ACM weight. According to the studies conducted by Rousis (2011), K_{ACM} accounts for only a small portion of the engine total weight (~5%).

5.2.10 Bare Engine Weight

Having established the engine individual weights as described in paragraphs 5.2.1-5.2.9, the engine bare weight (i.e., the engine weight excluding the nacelle) is calculated simply by summing up the individual weights or:

$$W_{KG,BENG} = W_{KG,FAN} + W_{KG,PCM} + W_{KG,GBX} + W_{KG,STR} + W_{KG,BRN} + W_{KG,C\&A} \\ + \sum_{PRI,SEC} W_{KG,ACM} + \sum_{LP,IP,HP} W_{KG,CMP} + \sum_{LP,IP,HP} W_{KG,TRB} \quad (5.19)$$

where, the summation for the compressor and turbine components applies over the LP, IP, and HP spools in a generic 3-spool turbofan engine, while the summation for the ACMs applies over the primary (core, "PRI") and secondary (bypass, "SEC") engine streams.

5.2.11 Nacelle Weight

The nacelle or "pod" is a streamlined body sized to house the engine with the minimum drag and is typically a component provided by the aircraft manufacturer. In most cases, the nacelle weight is not included in the engine total weight quoted by OEMs. Nevertheless, if the engine installed performance is to be established, then nacelle's weight must be added to the engine bare weight to give the engine total weight. Estimating the nacelle weight is a difficult task since some of the structures concerned are part of the aircraft wing and/or body itself [see Jenkinson et al. (1999)]. Here, the nacelle weight is assumed to include only the weight of the pod and not that of the pylon. In future adaptations of the GTWC, pylon could be approximated as a wing-shaped body and its weight could be calculated given its basic geometrical parameters (chord length, maximum thickness, aspect ratio).

In the present work, the nacelle weight is estimated utilizing the simplified correlation developed by Jackson (2009) in his PhD thesis. In his studies, Jackson assumed that the nacelle can be represented by a series of cylinders where the thickness of the cylinders exposed to the atmosphere is double that of those that are not. Figure 5.4 illustrates the approximate dimensions of the nacelle geometrical model.

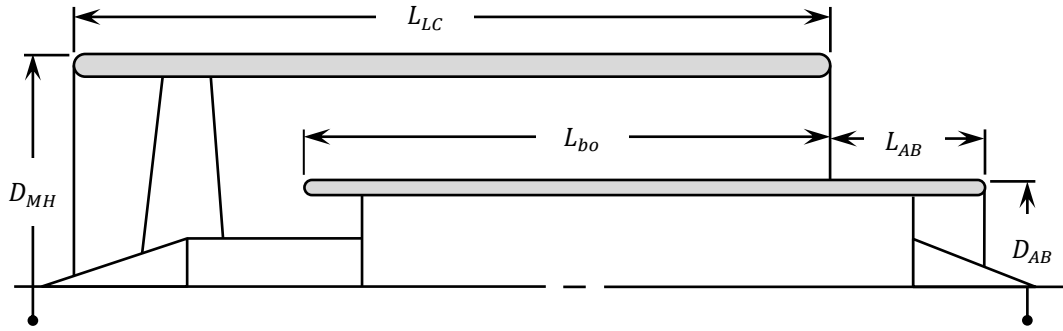


Figure 5.4: Nacelle approximate geometrical model [adapted from Jackson (2009)].

According to Jackson (2009), the nacelle weight can be estimated according to the expression:

$$W_{KG,NCL} = s_m \kappa_\pi (2L_{LC}D_{MH} + L_{bo}D_{AB} + 2L_{AB}D_{AB}) \quad (5.20)$$

Later, Giannakakis (2013) used the same relationship but simplified it by taking into account the volume of the afterbody only once, or:

$$W_{KG,NCL} = s_m \kappa_\pi (2L_{LC}D_{MH} + L_{bo}D_{AB} + L_{AB}D_{AB}) \quad (5.21)$$

Basically, both Eqs (5.20) and (5.21) express the surface area of the cylinders that represent the engine nacelle, multiplied by a coefficient (κ_π) accounting for the nacelle material density per unit area. The coefficient κ_π was estimated by Jackson (2009) who used as reference the nacelle of the Rolls Royce Trent 892 engine, and is equal to $\kappa_\pi = 24.88 \text{ kg/m}^2$. In Eqs (5.20) and (5.21), a scalar multiplier (s_m) has also been introduced for re-calibrating κ_π if necessary (the default value is unity).

For calculating the nacelle dimensions shown in Figure 5.4 the reader is referred to Appendix G. Note that, the core length, L_{bo} , is taken equal to the length between the fan core exit and the low-pressure turbine exit faces.

Another method found by the author of this thesis during the literature survey for nacelle weight estimation methods, is the one formulated by Jenkinson et al. (1999). Since this method correlates the engine nacelle with the engine overall performance (installed take-off thrust, $F_{N,TO}$), it was not implemented in the present study for avoiding iterative solutions when the engine installed performance is established but, it is mentioned here for completeness. The correlation of Jenkinson et al. was developed based on historical engine data and it reads:

$$W_{KG,NCL} = 6.8F_{N,TO}$$

for installed thrusts $F_{N,TO} \leq 600 \text{ kN}$ at SLS conditions, and:

$$W_{KG,NCL} = 2760 + 2.2F_{N,TO}$$

for installed thrusts $F_{N,TO} > 600 \text{ kN}$.

Note that, the above relations refer to the combined nacelle weight for all the engines installed on an aircraft.

5.2.12 Thrust Reversal System Weight

The thrust-reversal system is a mechanism dedicated to provide deceleration to the aircraft at landing conditions (especially on wet or icy runways) by diverting the engine's thrust in such a way to oppose the aircraft's forward motion. On high bypass ratio turbofan engines, thrust-reversal is performed mainly by reversing the cold fan stream since, the majority of the engine thrust, is produced from the bypass stream [Rolls-Royce plc (1996)].

In the past, there have been developed and applied several thrust-reversing systems among which are the "clamshell door" system, the "bucket target" system, and the "cold stream reversal" system, to name a few [for more technical details the interested reader is referred to Rolls-Royce plc (1996)]. For achieving the required redirection of the engine thrust, these systems operate using pneumatic or hydraulic actuators to move some type of deflection buckets or doors. These systems are activated through complicated mechanical systems including air and oil pumps, gearboxes, levers, etc. Thrust-reversing systems are complicated mechanical systems that add weight penalties to the engine total weight and, therefore, their weight should be accounted for.

According to Torenbeek (1982), the thrust-reversal system accounts for about 8% of the engine bare weight for fan reversing systems⁴³, while it may account for 15-20% of the engine bare weight for conventional bucket-type thrust-reversing systems. The author of this thesis could not find any public domain analytical expression for estimating the weight penalty added by such systems and, therefore, in the present weight methodology it was chosen that the thrust-reversal system weight be a fraction of the nacelle weight, or:

$$W_{KG,FNR} = \frac{K_{FNR}[\%]}{100} W_{KG,NCL} \quad (5.22)$$

where K_{FNR} is the thrust-reversing system-to-nacelle weight ratio. According to Jenkinson et al. (1999), the thrust-reversing system may account up to about 10% of the nacelle weight ($K_{FNR} = 10\%$).

5.2.13 Engine Total Weight

Finally, the engine overall weight is calculated by adding the nacelle weight [given by Eq. (5.20) or Eq. (5.21)] and the thrust-reversal system weight [given by Eq. (5.22)] to the engine bare weight [given by Eq. (5.19)]:

$$W_{KG,ENG} = W_{KG,BENG} + W_{KG,NCL} + W_{KG,FNR} \quad (5.23)$$

⁴³A system where the required thrust-reversal is achieved through a negative fan pitch. This method is used mostly in propeller-driven engines.

5.3 Component-Based, Analytical (CB-GM) Weight Estimation

The second method developed and introduced in GTWC is a component-based, “analytical” one. The method presented in this section was primarily adapted from ATLAS [see Lolis (2014)] and NASA’s WATE [see Pera et al. (1977a)], where appropriate modifications, additions, and/or improvements were made.

In contrast to the approach described in Section 5.2, the components comprising the engine are broken down to their elemental structural components and parts for which a volume (V_{M3}) is estimated based on their geometry. The necessary geometry is available after the preliminary aerothermodynamic (Chapter 3) and mechanical (Chapter 4) designs have been concluded. Then, the volume is multiplied by the material density to obtain the corresponding mass:

$$W_{KG} = \rho V_{M3} \quad (5.24)$$

By summing up the individual masses given by Eq. (5.24), the overall component weight is produced and, by adding the different component weights together the engine total weight is finally obtained.

Note that for some components their weight cannot be established in the “analytical” way attempted in the present section. This is because their geometry cannot be established in a straightforward manner (i.e., after a basic aerothermodynamic and/or mechanical design has taken place) without adding too much complexity (e.g., gearbox). For other parts (e.g., actuators, oil pump, pipes, nuts, bolts, etc.), this task is simply impossible at the preliminary design phase. For these components and parts, the methods presented in Section 5.2 are utilized for approximating their contribution to the overall engine weight and, thus, they will not be addressed again in this section. More specifically, the following are noted:

- The gearbox weight is estimated according to Eqs (5.11) and (5.14).
- The VPF pitch-changing mechanism weight is given by Eq. (5.16).
- The VAN area-changing mechanism weight is estimated by Eq. (5.18).
- Controls and accessories weight is estimated according to Eq. (5.17).
- The nacelle weight is estimated according to Eqs (5.20), (5.21), and (5.22).

Next, the equations and models used for estimating the weight of structural components and parts, given their geometry and material selection, are presented. Material is a user-defined input, but in later versions of the method the material of a component is proposed to be optimized for obtaining minimum weight while ensuring structural integrity. Finally, note that an outcome of the present procedure is also the polar moment of inertia of rotating components (see Appendix H).

5.3.1 Frames Weight

Frames are structural parts that serve as bearing supports and/or engine mounts. In a 2-spool boosted turbofan engine, there are typically three (3) types of frames encountered, namely the main (fan), inter-turbine (or center), and rear (at the LPT exit) frames [see Kurzke et al. (2018)]. Figure 5.5 shows the position and configuration of the main and rear frames for the CFM56-5A turbofan engine.

The main frame is located between the LP and HP compressors and spans across the core and bypass ducts. Apart from supporting the front bearings for the LP and HP shafts, the main frame also serves as a structural support for the engine accessory drive (power off-take) and forms an aerodynamic transition duct between the booster and the HP compressor.

The turbine center frame, as the name implies, is located between the HP and LP turbines. The turbine center frame defines the position of the HP shaft's rear bearing. Similarly to the main frame, the inter-turbine frame serves as an aerodynamic transition duct between the HP and LP turbines and, in some engines, also serves as a carrier for the bearing oil tubing.

Finally, the rear frame is an integral part of any turbofan engine. It provides support to the LP shaft rear bearing, connects the LP turbine to the downstream duct (jet pipe), and in separate exhaust engines serves as a mechanism for centering the core gas-path structure [see Kurzke et al. (2018)]. Note that the rear frame usually includes a row of EGVs for cancelling the flow swirl at the LPT exit, thus reducing the losses to the downstream duct.

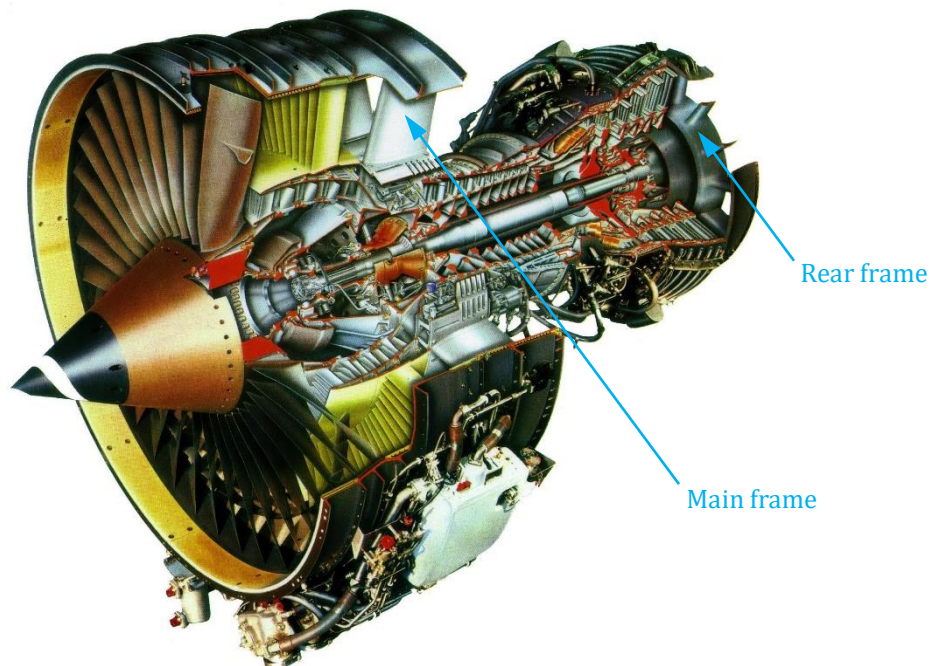


Figure 5.5: CFM56-5A turbofan engine cutaway showing the fan (main) and LPT (rear) frames⁴⁴.

Because they serve as structural supports, the mechanical design of frames requires the detailed knowledge of the loads applied on them under steady and unsteady (transient) operating conditions, as well as under adverse conditions such as hard landing according to Onat et al. (1979a). Apart from being able to carry the developed loads, the frame design aims also at minimum weight. Although frames constitute a significant portion of the engine's overall weight, there were no public domain references during the time of developing/writing this thesis that dealt with the

⁴⁴<https://eduscol.education.fr/sti/sites/eduscol.education.fr.sti/files/ressources/pedagogiques/11659/11659-ctc-044-basic-engine.pdf> (accessed: May 11th, 2022)

preliminary sizing of frames. This is mainly because the design of frames is customized for particular engines and/or engine families [see Lolis (2014)].

For the reasons outlined above, the weight of the frames is estimated using a semi-empirical correlation derived from existing engine databases, an approach followed both by NASA's WATE and ATLAS. The approach adopted here is that developed for NASA's WATE. In WATE, there are four (4) frame types considered:

- Type 1: single-bearing frames with PTO
- Type 2: single-bearing frames without PTO
- Type 3: turbine frames, and
- Type 4: two-bearing intermediate and burner frames.

NASA's WATE model correlates the frame weight (in pounds mass) with its projected area (in ft²). The correlation for each one of the four frame types considered by NASA's WATE is given in a graphical form in Figure 5.6. The curves shown in Figure 5.6 were digitized, smoothed, and introduced into GTWC in a PROOSIS 1D table format. Finally, Table 5.4 lists the possible frame configurations and types in an engine according to NASA's WATE inputs [see Pera et al. (1977b)].

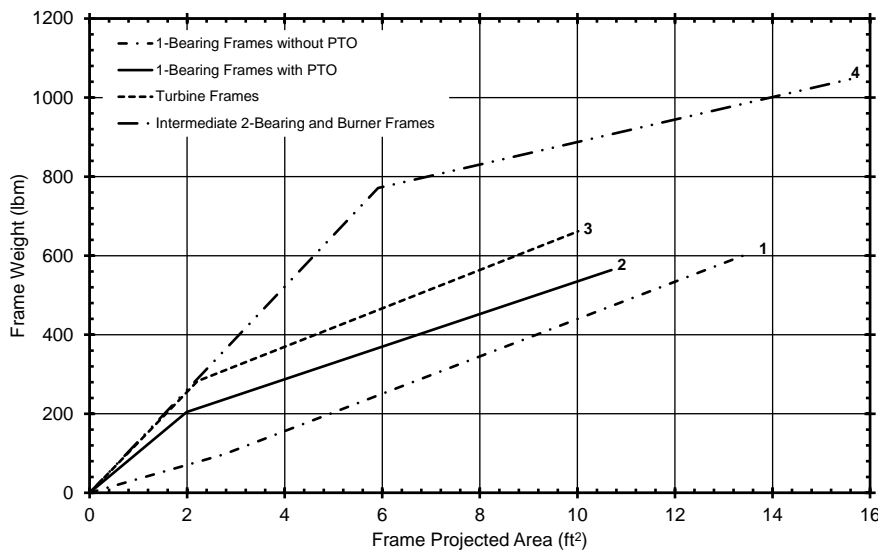


Figure 5.6: NASA's WATE model for frame weight estimation [adapted from Pera et al. (1977a)]. The frame weight is correlated with the frame projected area (radius squared).

Table 5.4: Possible frame configurations and types for different components [see Pera et al. (1977b)]

Component	Frame Type		
	General	@ Front	@ Rear
Fan	N/A	No/Types 1, 2, 4	No/Types 1, 2, 4
Compressor	N/A	No/Types 1, 2, 4	No/Types 1, 2, 4
Burner	No/Type 4	N/A	N/A
Turbine	N/A	N/A	No/Type 3

5.3.2 Ducts Weight

Ducts are engine structures that are used to drive the flow between different components. The mechanical design of ducts was discussed in Chapter 4. Having established the duct length (L), wall thickness (t), and shape of the inner (R_h) and outer (R_t) walls (see Chapter 4), then the volume of the duct is calculated assuming a solid by revolution:

$$V_{M3} = \underbrace{\pi \int_0^L \{R_h^2(x) - [R_h(x) - t]^2\} dx}_{\text{Inner wall volume}} + \underbrace{\pi \int_0^L \{[R_t(x) + t]^2 - R_t^2(x)\} dx}_{\text{Outer wall volume}} \quad (5.25)$$

Equation (5.25) is used for annular ducts of circular shape. For circular tubes, the inner wall volume can be omitted. Having established the duct volume (V_{M3}) the duct weight is then estimated according to Eq. (5.24).

5.3.3 Shafts Weight

Shafts are structural components that are used for transferring rotational motion and torque (power) between the components they connect. The mechanical design of shafts was also presented in detail in Chapter 4.

Having established the shaft inner and outer radius, R_i and R_o , respectively, the shaft volume is obtained easily considering shafts of cylindrical shape:

$$V_{M3} = \pi(R_o^2 - R_i^2)L \quad (5.26)$$

where the shaft length, L , is estimated by summing up the lengths of the components across which the shaft is spanned. Finally, the shaft weight is given by Eq. (5.24).

5.3.4 Structural Weight

The structural weight comprises that of the frames, interconnecting ducts, and rotating shafts (similarly to the Sagerser et al.'s approach, see paragraph 5.2.5). Thus, the total structural weight is obtained by summing up the weight of the frames, ducts, and shafts calculated in paragraphs 5.3.1–5.3.3:

$$W_{KG,STR} = \sum W_{KG,FRM} + \sum W_{KG,DCT} + \sum W_{KG,SHF} \quad (5.27)$$

The summation symbol in Eq. (5.27) implies that each term accounts for all the individual weights of the respective component. For instance, the shaft (total) weight includes the weights of the LP, IP, and HP shaft in a generic 3-spool engine.

5.3.5 Connecting Hardware Weight

In most rotating components (e.g., compressors and turbines), the rotating parts (disks) are connected through nuts, bolts, and spacers. Figure 5.7 shows the NASA/GE E³ LP turbine where the coupling of the disks using bolts can be seen.

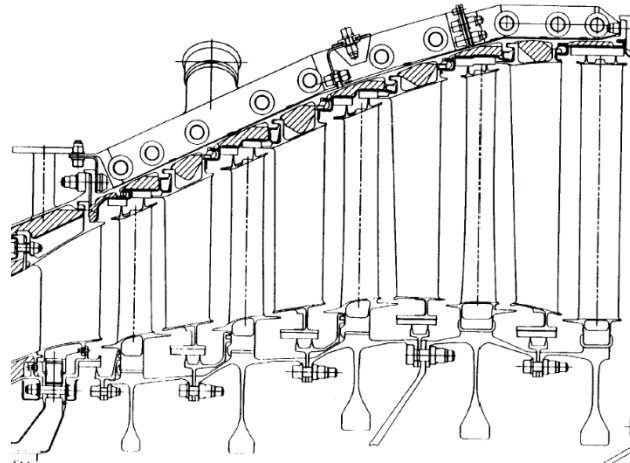


Figure 5.7: NASA/GE E³ LPT configuration showing the connection through bolts of the moving parts [see Davis et al. (1985)].

The connecting hardware weight accounts for a significant part of the engine's total weight. Since the weight of the connecting hardware cannot be calculated analytically, the semi-empirical approach used in NASA's WATE is utilized. The bolts, nuts, and spacers are approximated as thick ($t = 0.075$ inches) hollow cylinders located at the 75% of the stage (average) hub radius. Thus, the volume of the connecting hardware (per stage) is calculated according to [see Pera et al. (1977a)]:

$$V_{M3} = 1.5s_m\pi t\bar{R}_hL \quad (5.28)$$

where \bar{R}_h is the stage average hub radius and L is the stage axial length. In Eq. (5.28), s_m is a user-defined scalar multiplier for calibrating the model with a default value of unity.

The connecting hardware weight is estimated by evaluating Eq. (5.24), and the overall weight of the connecting hardware for a component is calculated by summing up the stage-wise weights.

5.3.6 Disks Weight

The weight of rotating disks is a significant part of the overall engine weight. During the design of a new engine, disks are typically designed last aiming at minimum weight while satisfying geometry and structural constraints. The disk design was discussed in detail in Chapter 4.

Apart from the methodology developed and presented in Chapter 4 for obtaining the minimum weight disk which satisfies both geometry and stress constraints, here another model is presented for estimating the weight of a disk which, instead, is utilized when time efficient calculations are needed, that is, when the costly iterations for optimizing the disk geometry (to achieve minimum weight) must be avoided. Therefore, the approach followed in NASA's WATE [see Pera et al. (1977a)] is implemented, according to which the disk volume is correlated to the maximum pull stress that the rotor blades exert on the hub. The blade pull stress (σ) is, in turn, a function of the blade tip speed, blade material, and blade geometry [taper ratio (TR) and hub-to-tip ratio (HTR)], or:

$$\sigma = \frac{\rho \bar{U}_t^2}{gTR} \left[\frac{1 - \overline{HTR}^2}{2} + \frac{TR - 1}{12} (1 - \overline{HTR})(1 + 3\overline{HTR}) \right] \quad (5.29)$$

where $g = 9.81 \text{ m/s}^2$ is the acceleration due to gravity.

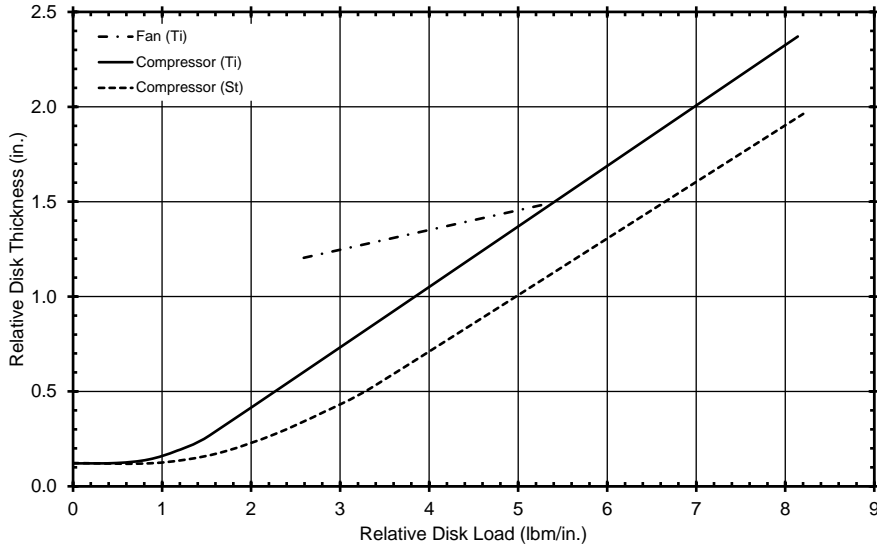


Figure 5.8: NASA's WATE disk volume correlation for fan and compressor disks [adapted from Pera et al. (1977a)].

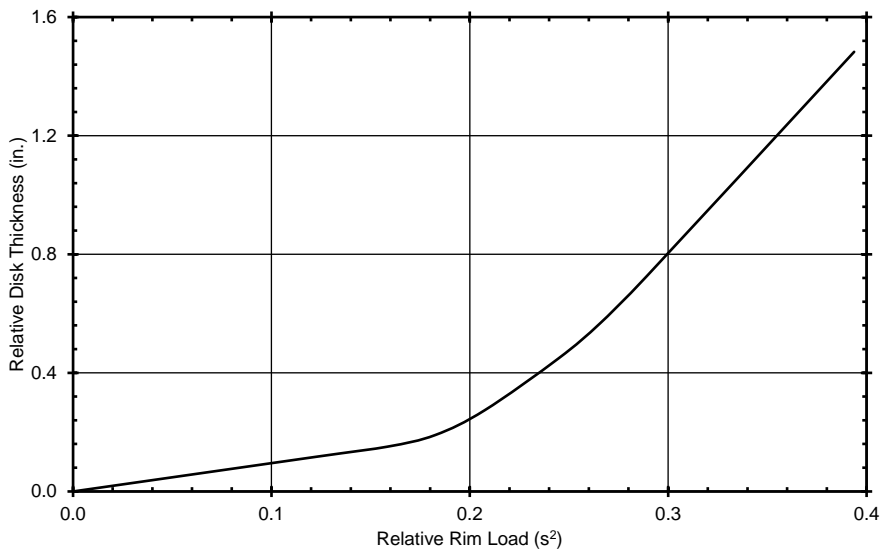


Figure 5.9: NASA's WATE disk volume correlation for turbine disks [adapted from Pera et al. (1977a)].

For fans and compressors, the disk relative thickness, defined as the disk volume divided by the hub diameter squared (V_{M3}/\bar{D}_h^2) is correlated to the relative disk load ($\sigma \times \bar{R}_h \times 10^5$) according to Figure 5.8 for titanium (Ti) and steel (St) disks. Specifically for compressor disks, the disk relative thickness is estimated as a weighted average between the titanium (F_{Ti}) and steel (F_{St}) values obtained from Figure 5.8. Hence:

$$\frac{V_{M3}}{\bar{D}_h^2} = s_m \left\{ \frac{\text{Ti}[\%]}{100} F_{\text{Ti}}(\text{Rel. Disk Load}) + \left(1 - \frac{\text{Ti}[\%]}{100} \right) F_{\text{St}}(\text{Rel. Disk Load}) \right\} \quad (5.30)$$

where Ti is a user-defined titanium percentage with a default value of 50%, and s_m is a user-defined scalar for calibrating the model with a default value of unity.

Similarly to compressor disks, the relative thickness (V_{M3}/\bar{D}_h^2) for turbine disks is correlated to the relative rim loading defined as $(\sigma/\sigma_Y) \times \bar{R}_h$, where σ_Y is the material yield strength at 0.2% strain. The blade pull stress (σ) is again obtained from Eq. (5.29). For the database engines used by NASA, this correlation is shown graphically in Figure 5.9.

Note here, that in contrast to the disk design procedure described in Chapter 4, NASA's WATE model does not produce any kind of disk geometry. Therefore, it is not guaranteed that the obtained disk weight corresponds to a disk geometry which was designed for minimum weight.

Finally, the disk volume is calculated by multiplying V_{M3}/\bar{D}_h^2 (obtained either from Figure 5.8 or Figure 5.9) with \bar{D}_h^2 , and the disk weight is evaluated by Eq. (5.24) given the disk material. The total disk weight for a turbomachinery component is calculated by summing up the individual disk weights for each stage. Note that the curves presented in Figure 5.8 and Figure 5.9 were digitized, smoothed, and introduced into GTWC as a PROOSIS 1D table.

5.3.7 Casings Weight

Casing design was discussed in Chapter 3, where a model for calculating the necessary casing thickness for containing blade fragments in case of blade failure, was presented. After establishing the casing thickness, t , the casing volume is calculated considering a solid of revolution. Therefore, for inner casings:

$$V_{M3} = \pi \int_0^L \{R_h^2(x) - [R_h(x) - t]^2\} dx \quad (5.31)$$

and outer casings:

$$V_{M3} = \pi \int_0^L \{[R_t(x) + t]^2 - R_t^2(x)\} dx \quad (5.32)$$

where L is the casing axial length.

From Eqs (5.31) and (5.32) it is obvious that the term "inner" and "outer" casing is used to describe the annulus wall at the flow-annulus hub and tip, respectively.

Note that, in the present weight methodology, casing contours are approximated as straight lines (in accordance with the stage geometry modelling, presented in Chapter 3). That is, $R_h(x)$ and $R_t(x)$ are linear functions of the axial coordinate x . Equations (5.31) and (5.32), however, are general enough to include casing shapes other than straight lines for future method adaptations.

Finally, the weight of a casing segment is obtained by applying Eq. (5.24), and the total casing weight for a component is obtained by summing up the individual weights of all (inner and outer) casing segments.

5.3.8 Blading Weight

In turbomachines (compressors, turbines, fans), the weight of the blades constitutes a big part of the engine's overall weight. In GTWC, two approximations are available for estimating the weight of individual blades. Both methods can be used in a similar manner to estimate the weight of both rotating and stationary blade elements. These methods are described in the following.

5.3.8.1 GasTurb Details 5 Modelling Approach

The first one utilized in GTWC is the modelling approach developed by Kurzke for GasTurb Details 5 [see Kurzke (2007)]. According to the methodology used in GasTurb Details 5, the total weight of a blade comprises that of the blade itself (aerofoil + shroud), while rotors have an additional weight part that results from the blade root section (platform + neck + fir tree). The blade root is a configuration that is used for attaching the aerofoil onto the rotating disks (disk posts) for transferring the necessary rotational motion and power.

For calculating the aerofoil volume ($V_{M3,af}$) the following equation is used:

$$V_{M3,af} = \frac{K_{VM3}[\%]}{100} \times (|R_{tip} - R_{root}| t_{max} c) \quad (5.33)$$

where t_{max} and c is the maximum thickness and the chord of the aerofoil, respectively, which are assumed constant along the aerofoil height and equal to their value at the mean-line. In Eq. (5.33), t_{max} is a user input given as percentage of chord, while c is a result of the mean-line calculation(s) presented in Chapter 3.

Blade shrouds, if exist, have a volume ($V_{M3,srd}$) approximated by:

$$V_{M3,srd} = \frac{K_{VM3}[\%]}{100} \times \left(0.05 t_{rim}^2 \frac{2\pi R_{tip}}{Z_b} \right) \quad (5.34)$$

For rotor blades, additional volumes are estimated that correspond to the root platform ($V_{M3,plt}$), neck ($V_{M3,nck}$), and fir tree ($V_{M3,fir}$). These are given by the following equations:

$$V_{M3,plt} = \frac{K_{VM3}[\%]}{100} \times \left(0.05 t_{rim}^2 \frac{2\pi R_{root}}{Z_b} \right) \quad (5.35)$$

$$V_{M3,nck} = \frac{K_{VM3}[\%]}{100} \times [2 t_{max} t_{rim} (R_{nck,o} - R_{nck,i})] \quad (5.36)$$

$$V_{M3,fir} = \frac{K_{VM3}[\%]}{100} \times \left[\frac{\pi t_{rim} (R_{nck,i}^2 - R_{rim}^2)}{2Z_b} \right] \quad (5.37)$$

The total volume for a single blade is estimated by appropriately summing up the individual volumes given by Eqs (5.33)–(5.37). This volume is then multiplied with the density corresponding to the given blade material to obtain the blade mass according to Eq. (5.24).

For the case where the disk mass is calculated using the design methodology described in Chapter 4 instead of the WATE correlations presented in paragraph 5.3.6,

then the weight of a rotor blade is increased by the weight of the disk post. The disk post volume, $V_{M3,pst}$, is approximated by:

$$V_{M3,pst} = \frac{K_{VM3}[\%]}{100} \times \left[\frac{\pi t_{rim} (R_{pst,o}^2 - R_{pst,i}^2)}{2Z_b} \right] \quad (5.38)$$

The weight of the post is obtained from Eq. (5.24) by multiplying $V_{M3,pst}$ with the disk material density.

In Eqs (5.33) through (5.38), the necessary dimensions are calculated according to Appendix E. In the above, K_{VM3} is a user-defined volume factor ($0 \leq K_{VM3} \leq 100\%$) accounting for the volume reduction resulting from, e.g., cooling channels in turbine blades, hollow rotor and/or bypass strut blades in fan components, etc. The default value of K_{VM3} in GTWC is 100%.

Note that, for rotor blades, the sum of the blade weight and that of the post weight gives the disk dead weight:

$$\underbrace{W_{KG,dw} = W_{KG,af} + W_{KG,srd} + W_{KG,plt} + W_{KG,nck} + W_{KG,fir} + W_{KG,pst}}_{\text{for a single blade}}$$

required in the design calculations presented in Chapter 4.

Finally, the weight of a blade row is obtained by multiplying the weight of a single blade with the blade count, Z_b .

5.3.8.2 NASA's WATE Modelling Approach

The second method programmed in GTWC for estimating the weight of blades uses the statistical correlations developed by NASA and implemented in the WATE code. Note here, that the author of this thesis deduced (from test calculations) that WATE's correlations suit better for estimating the weight of rotor and bypass blades (OGVs or struts) in fan components, since GasTurb's correlations tend to overestimate it significantly (unless an appropriate K_{VM3} value is used). This is because WATE's correlations are already calibrated based on the database engines used for their formulation (in other words, they inherently implement a K_{VM3} factor).

The volume of a single blade is obtained by the statistical correlation [see Pera et al. (1977a)]:

$$V_{M3,bld} = s_m \frac{K_{VM3}[\%]}{100} \frac{\bar{h}_b^3}{AR^2} \quad (5.39)$$

where s_m is a user-defined calibration scalar with a default value of $s_m = 1$. Basically, Eq. (5.39) models the blade as a square prism with height equal to the blade height (\bar{h}_b) and side equal to the blade chord length ($c = AR \times \bar{h}_b$). A volume factor ($K_{VM3} < 100\%$) is applied to account for the fir-tree mount volume, the blade taper ratio, and the blade thickness-to-chord variation according to Pera et al. (1977a).

The value of the factor K_{VM3} is given for turbine blades by:

$$K_{VM3} = \begin{cases} 19.5\%, & \text{for rotors} \\ 14.4\%, & \text{for stators} \end{cases} \quad (5.40)$$

where the above values are multiplied by a factor of 0.8 for cooled turbine blades.

For compressor and fan blades with $\overline{HTR} \leq 0.8$, K_{VM3} is obtained by:

$$K_{VM3} = \begin{cases} 55\%, & \text{for fans} \\ 12\%, & \text{for compressors} \end{cases} \quad (5.41)$$

while for fan and compressor blades with $\overline{HTR} > 0.8$, K_{VM3} is calculated in terms of \overline{HTR} according to:

$$K_{VM3}[\%] = 12 + 40(\overline{HTR} - 0.8) \quad (5.42)$$

Note that, Eq. (5.39) can be used alike for stators and rotors. For rotor blades, however, the blade volume estimated by Eq. (5.39) includes both the aerofoil and root (platform + neck + fir tree) volumes [see Tong et al. (2004)]. To distinguish between the two volumes, empirical volumetric factors are applied in terms of the disk shape used to support the rotor blades [see Tong et al. (2004)]: 1) for ring and web type disks the aerofoil volume is assumed to occupy 80% of the volume obtained by Eq. (5.39), while for 2) hyperbolic type disks the aerofoil is 50% of the volume given by Eq. (5.39). Therefore, for rotor blades, the aerofoil volume is obtained according to:

$$V_{M3,af} = s_m \frac{K_{VM3}[\%] \bar{h}_b^3}{100 \text{ Eq.(5.39)} AR^2} \times \begin{cases} 0.8, & \text{for ring type disks} \\ 0.8, & \text{for web type disks} \\ 0.5, & \text{for hyperbolic type disks} \end{cases} \quad (5.43)$$

Then, the volumes for the platform, neck, fir tree, and disk post can be obtained from Eq. (5.35), (5.36), (5.37), and (5.38), respectively, while the shroud volume (if exists) is obtained by Eq. (5.34).

Finally, to obtain the weight of a single blade, Eq. (5.24) is used by replacing the given blade and disk (if the disk post is included in the blade volume for calculating the disk dead weight) material densities. The weight of a blade row is obtained by multiplying the weight of a single blade with the blade count (Z_b).

5.3.9 Compressor and Turbine Weights

For estimating the total weight of compressors and turbines, the same procedure is followed for both components. Compressors and turbines comprise a number of stages (N_{stg}) each of which is assumed to include a number of structural parts and sub-components. The weight for a stage is estimated by adding together the weights of the individual structural parts that make up the stage and, then, the compressor or turbine total weight is obtained by summing the weights of the individual stages.

In GTWC, each compressor or turbine stage is assumed to include the blading (rotors, stators, IGVs, OGVs), the rotating disks, the connecting hardware, and the outer and inner casing walls. Figure 5.10 depicts the weight break-down for a typical compressor or turbine stage. Figure 5.11 shows the stage structural parts and sub-components that are taken into account by the weight estimation formulation.

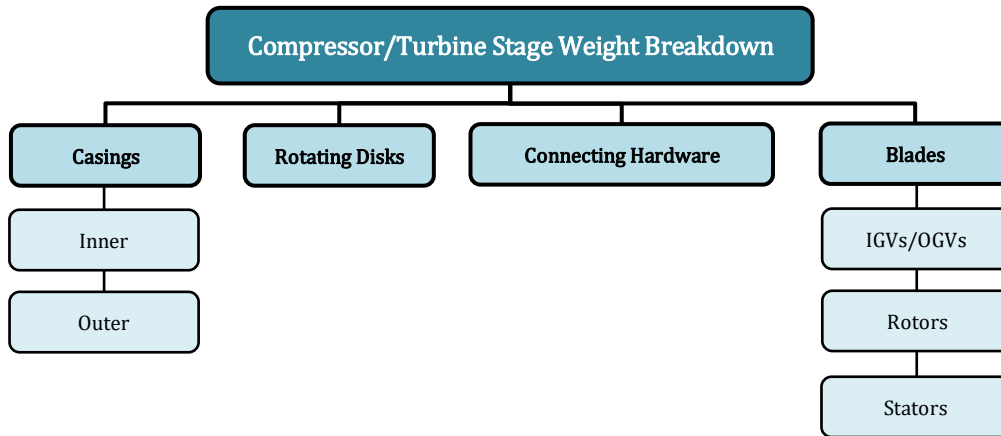


Figure 5.10: Compressor and turbine stage weight breakdown in GTWC.

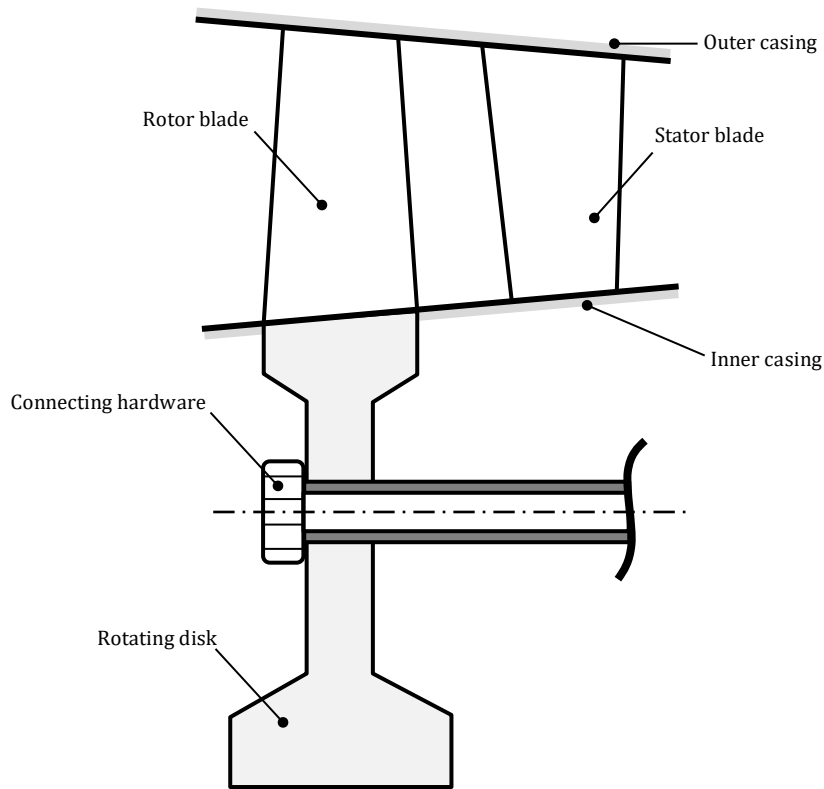


Figure 5.11: Structural parts comprising a compressor or turbine stage.

The compressor or turbine total weight is, therefore, obtained by:

$$W_{KG,CMP \text{ or } TRB} = \sum_{j=1}^{j=N_{stg}} (W_{KG,ics} + W_{KG,ocs} + W_{KG,hw} + W_{KG,dsk} + W_{KG,bld})_j \quad (5.44)$$

where $W_{KG,ics}$, $W_{KG,ocs}$, $W_{KG,hw}$, $W_{KG,dsk}$, and $W_{KG,bld}$ is the weight of the inner casing, outer casing, connecting hardware, disk, and blading (including both the weight of the rotor and stator rows), respectively. The respective weight is calculated according to the models and methodologies outlined in paragraphs 5.3.5 through 5.3.8.

Note that, GTWC gives the flexibility to the user to assign different materials to each structural part at every single stage. Apart from directly assigning a material, the user is also offered the possibility to assign a material in an automated way in terms of a limiting temperature value. In the latter case, the user specifies 1) a temperature value, and 2) the material to be assigned automatically by GTWC when the stage operating (maximum total) temperature is below and above the specified limiting value. For example, a titanium alloy could be used for temperatures less than 650 K, and steel alloys for temperatures greater than 650 K [see Pera et al. (1977a)].

5.3.10 Fan Weight

Similarly to the compressor (or turbine) weight estimation philosophy presented in the preceding paragraph, fan components are also assumed to comprise a number of structural parts and sub-components.

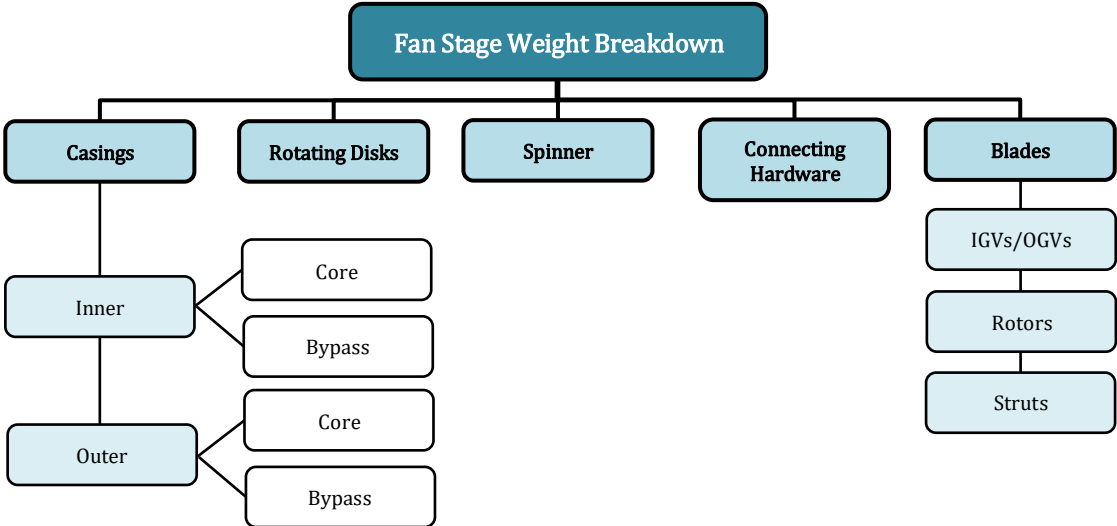


Figure 5.12: Fan stage weight breakdown in GTWC.

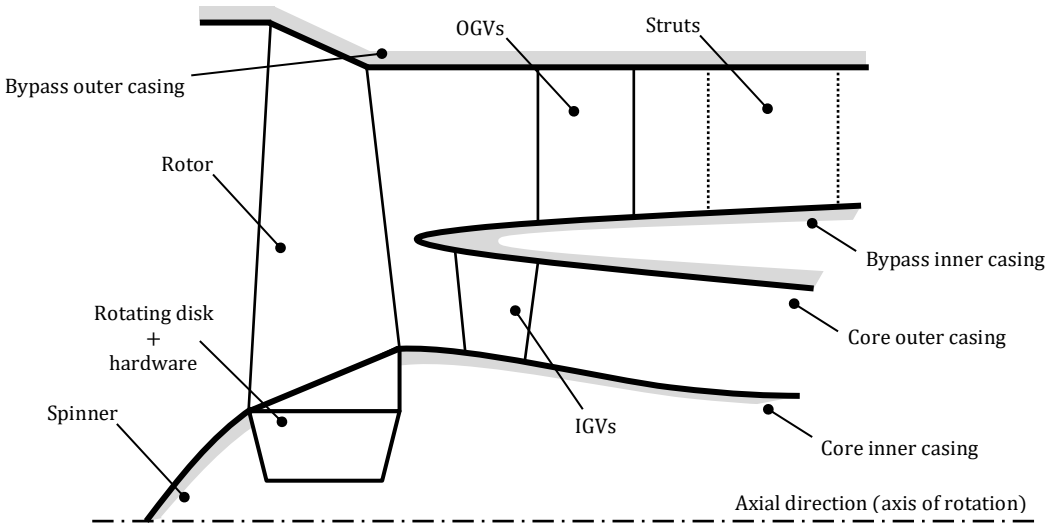


Figure 5.13: Structural parts comprising a single-stage fan component.

In GTWC, fans are treated as single-stage compressors. The stage of a fan component comprises the rotor blades, the IGVs, the bypass OGVs, the bypass strut-like structures, the connecting hardware, the rotating disk, the core and bypass inner and outer casing walls, and the spinner. Figure 5.12 illustrates the weight break-down for a typical fan stage, while Figure 5.13 shows a diagrammatic representation of a fan component and the various structural parts comprising it. The fan total weight is, therefore, obtained by:

$$W_{KG,FAN} = W_{KG,ics} + W_{KG,ocs} + W_{KG,hw} + W_{KG,dsk} + W_{KG,blt} + W_{KG,spn} \quad (5.45)$$

where the inner ($W_{KG,ics}$) and outer casing ($W_{KG,ocs}$) weights include the respective weights for the bypass and core walls, whereas the blading weight ($W_{KG,blt}$) includes the weights of the rotors, IGVs, OGVs, and struts (if exist).

Regarding the spinner, its volume ($V_{M3,spn}$) is calculated assuming that of a right circular cone and is obtained according to:

$$V_{M3,spn} = \frac{\pi}{3} [LR^2 - (L - t)(R - t)^2] \quad (5.46)$$

In the above, L and R are the cone axial length and base radius, respectively, and t is the cone thickness. The latter is assumed equal to $t = 5$ mm [see Lolis (2014)]. Regarding the cone material, fiberglass is assumed [see Lolis (2014)] with a density equal to 2550 kg/m³.

In terms of material selection, different materials can be specified for the different structural parts comprising the fan. Because of their unique nature in terms of both the aerothermodynamic design and structural design, fans usually employ non-traditional (some would use the word “exotic”) materials compared to other conventional components such as compressors or turbines. For instance, lightweight, high strength materials are usually selected for the bypass outer casing such as Kevlar [see Rolls-Royce plc (1996)], while current operation turbofan engines employ aluminum alloys (usually iridium-aluminum alloys) both for the rotor blades (e.g., the PW1000G engine family⁴⁵) and the bypass outer casing [e.g., the CFM56-7B27 engine according to Gunston (2004)].

5.3.11 Burner Weight

Burner weight is assumed to comprise the weight of the pre-diffuser, dump-diffuser, casing, liner, and those of the burner dome, fuel manifold, and fuel nozzles. In GTWC, only single annular combustors are assumed. The basic dimensions of single annular combustors are estimated according to the simplified design methodology described in Appendix C. Figure 5.14 shows the burner weight breakdown applied in GTWC, while Figure 5.15 illustrates the meridional view of a single annular combustor where the various sections and the relevant nomenclature are shown.

⁴⁵<https://www.ainonline.com/aviation-news/air-transport/2014-07-28/pratt-alcoa-pioneer-use-aluminum-fan-blades> (accessed: May 11th, 2022)

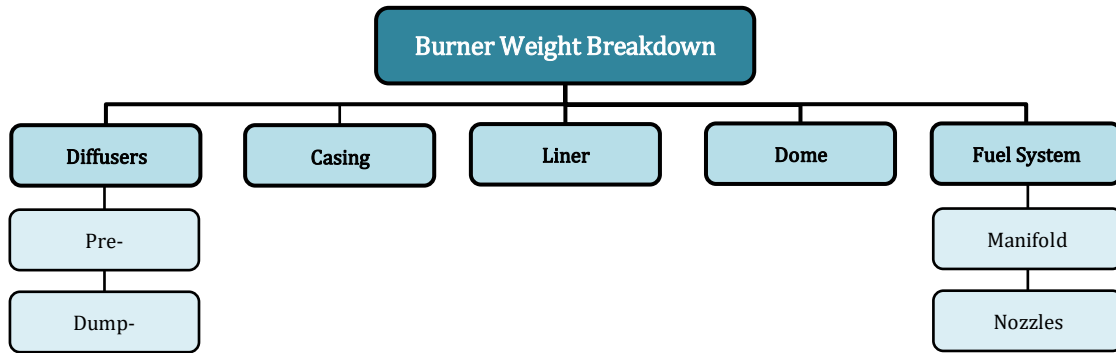


Figure 5.14: Burner weight breakdown in GTWC.

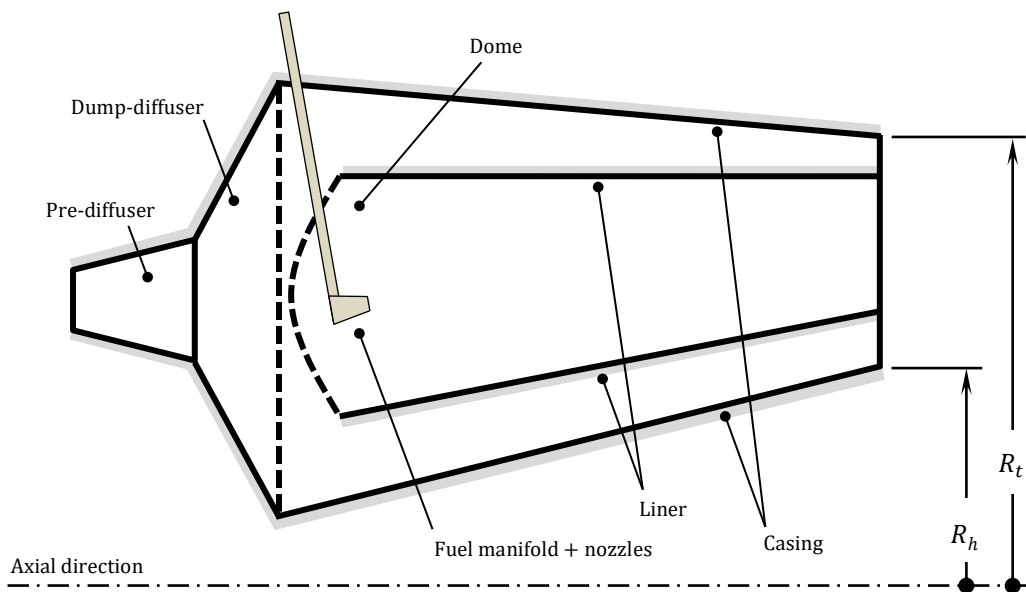


Figure 5.15: Single annular combustor meridional view and nomenclature.

First, the volumes of the different burner sections are estimated. Note that the casing and liner thicknesses are estimated according to Appendix C, and that the pre- and dump-diffusers are assumed to have the same wall thickness as that calculated for the burner casing.

The pre-diffuser ($V_{M3,CPD}$), dump-diffuser ($V_{M3,CDD}$), casing ($V_{M3,CC}$), and liner ($V_{M3,CL}$) volumes are estimated from:

$$V_{M3} = \underbrace{\pi \int_0^L \{R_h^2(x) - [R_h(x) - t]^2\} dx}_{\text{Inner wall volume}} + \underbrace{\pi \int_0^L \{[R_t(x) + t]^2 - R_t^2(x)\} dx}_{\text{Outer wall volume}} \quad (5.47)$$

where L and t is the pre-diffuser, dump-diffuser, casing, and liner axial length and wall thickness, respectively. Note that the thicknesses at the hub and tip walls of the respective part are assumed equal.

As can also be seen from Figure 5.15, all burner annulus walls are approximated as straight lines. That is, the functions $R_h(x)$ and $R_t(x)$ that appear in Eq. (5.47) are linear functions of x . Equation (5.47), however, is general enough to include wall shapes other than straight lines in future adaptations of the burner weight estimation methodology. The respective burner weights are estimated from Eq. (5.24) and the material assigned to each burner part.

Finally, the weight of the burner dome, fuel manifold, and fuel nozzles is estimated using the statistical correlation developed by NASA and used in WATE [see Onat et al. (1979a)]:

$$W_{KG,CD} = 0.0106(\bar{R}_t^2 - \bar{R}_h^2) \quad (5.48)$$

where \bar{R}_h and \bar{R}_t is the average hub and tip radius of the burner casing, respectively.

The burner total weight is then obtained by summing up the individual weights:

$$W_{KG,BRN} = W_{KG,CPD} + W_{KG,CDD} + W_{KG,CC} + W_{KG,CL} + W_{KG,CD} \quad (5.49)$$

5.3.12 Engine Total Weight

Similarly to the CB-SE approach, the engine total weight is estimated from Eq. (5.23) where the bare engine weight is obtained by Eq. (5.19).

5.4 GTWC PROOSIS Library

As mentioned in the chapter introduction, the methods and equations presented in the previous two sections (5.2 and 5.3) resulted in the development of a dedicated PROOSIS library named GTWC. GTWC includes PROOSIS components (see Chapter 2) for estimating the weight of individual turbomachinery components (fans, compressors, turbines, burners), as well as a component for estimating the overall weight of generic, 3-spool turbofan engines with separate exhausts. All GTWC components obtain the respective weight by utilizing either the CB-SE or the CB-GM approach (based on the user's choice through a dedicated calculation switch). The PROOSIS symbols defined in GTWC are shown in Figure 5.16.

The symbols shown in Figure 5.16 can be dragged-and-dropped into a PROOSIS schematic canvas for estimating the weight of individual components or that of a turbofan engine model. The necessary performance (cycle) and geometry inputs required by the GTWC components are obtained through the aerothermodynamic and mechanical design tools presented in Chapters 3 and 4, and are communicated between the TURBO1D and the GTWC components through dedicated PROOSIS ports (see Chapter 2) that have also been developed for the needs of the present work. This way, the aerothermodynamic (and mechanical) design and the weight estimation can take place at the same modelling and simulation levels, in a transparent way.

Note that, more than one symbols of the same GTWC component seen in Figure 5.16 can be dragged-and-dropped into the same schematic canvas and connected to the

same TURBO1D component. This, for instance, allows the estimation of weight using simultaneously the CB-SE and -GM approaches.

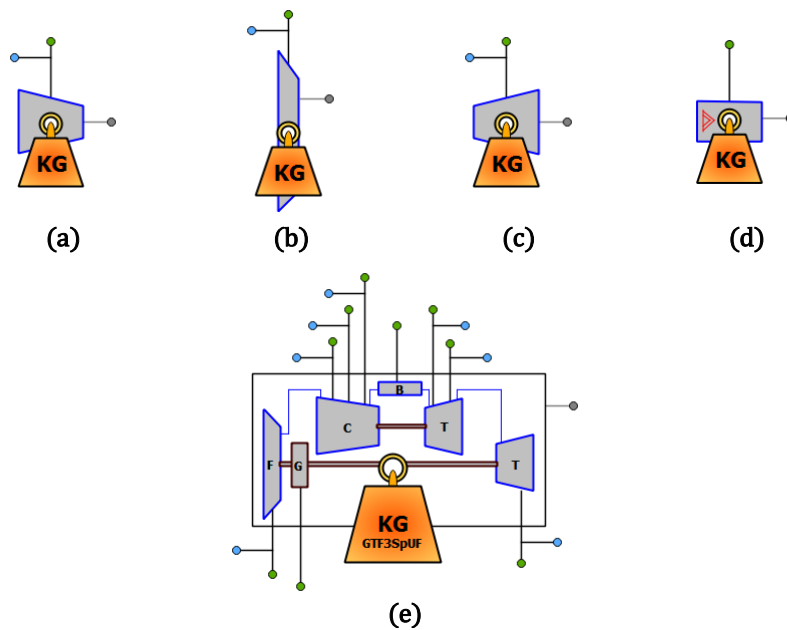


Figure 5.16: GTWC palette defining PROOSIS symbols for the components estimating the weight of (a) compressors, (b) fans, (c) turbines, (d) burners, and (e) generic, 3-spool, unmixed turbofan engines.

5.5 GTWC Validation Studies

In the present section, validation studies are presented. Because of the disclosure policies followed by all OEMs, there is a lack of publicly available data for the detailed geometry (e.g., blade count), materials, and weight of individual turbomachinery components (compressors, fans, turbines, burners) which, in turn, renders the quantitative validation of the GTWC components impossible. Therefore, the validation of the GTWC library was conducted at engine level, where figures for the total weight of turbofan engines are, in general, publicly accessible. Note, however, that the GTWC component for estimating the weight of compressors was partially validated in the CB-GM mode, as will be explained in the following paragraph.

5.5.1 Partial Validation of Component for Compressor Weight Estimation

For validating the GTWC component for compressor weight, information about the NASA/GE E³ 10-stage HPC [see Holloway et al. (1982)] was used⁴⁶. More specifically,

⁴⁶The CB-SE correlations presented in paragraph 5.2.2 estimate the overall weight of compressors. However, the overall weight of the NASA/GE E³ HPC is not publicly available. To be more precise, Davis et al. (1985) quote values for the NASA/GE E³ HPC rotor (blades + disks) weight (215 kg) and stator weight (234 kg), which give a combined weight of 449 kg. This figure seems quite high, and the author of this thesis speculates (since there is no further information provided by Davis et al.) that the stator weight includes also the weight of structural components (probably that of the frames) which are not taken into account by the CB-SE correlations. For the sake of completeness, Eq. (5.4) estimates a weight

the materials for both the rotor blades and rotating disks are known [see Holloway et al. (1982)]. The weight for every single of the 10 rotor blades is explicitly quoted by Holloway et al., while the volume (and, hence, weight) for every single disk can be estimated from the 2D compressor cutaways also provided by Holloway et al. Table 5.5 shows the NASA/GE E³ HPC rotor (blades + disks) weight breakdown according to the information provided/extracted by Holloway et al. (see Table D.6, Table D.11, and Table D.12). Note that the blade weight includes the weights of the blade aerofoil and root (platform + neck + fir tree), while the disk weight includes the weight of the live disk and that of the disk post.

Table 5.5: NASA/GE E³ HPC rotor actual weight breakdown

Stage	Blade Row Weight (kg)	Disk Weight (kg)
1	15.4	24.9
2	7.0	13.5
3	4.1	10.6
4	2.9	8.8
5	4.4	12.9
6	3.6	21.0
7	3.6	16.4
8	2.5	15.7
9	1.7	15.4
10	1.5	18.2
	$\Sigma = 46.5$	$\Sigma = 157.4$
	$\Sigma = 203.9$	

A partial validation was therefore performed, considering only the combined weight of the E³ HPC rotor. The weights of the blades were calculated using the GasTurb models (see paragraph 5.3.8), while the disk weights were calculated according to the NASA's WATE correlations (see paragraph 5.3.6). The results are presented in Table 5.6, where the relative difference quoted in the table is defined as $100 \times (W_{KG}^{E3} - W_{KG}^{GTWC}) / W_{KG}^{E3}$.

Table 5.6: Comparison between the actual NASA/GE E³ HPC rotor weight and the one calculated by the GTWC compressor component

Actual Rotor Weight	Estimated Rotor Weight	Relative Difference
203.9 kg	201.9 kg	0.98%

equal to ~312 kg (~29% less than that by Davis et al.), while Eq. (5.3) gives a weight equal to ~267 kg (~39% less than that by Davis et al.).

As it can be seen from Table 5.6, GTWC estimates a rotor weight which is $\sim 1\%$ less than the actual E³ rotor weight⁴⁷. Considering that the disks and blades make-up most of the weight of a compressor component, the comparison is considered excellent. Finally, the quoted difference falls well within the $\pm 10\%$ accuracy goal set at the beginning of this chapter.

In the future, an attempt should be made to validate GTWC using 3D CAD engine cutaways by comparing the volumes calculated by GTWC and those obtained from the CAD drawings.

5.5.2 Qualitative Validation of Component for Engine Weight Estimation

First, the GTWC component for estimating the weight of generic, 3-spool turbofan engines will be validated qualitatively considering a 2-spool, unmixed flow turbofan engine with a booster. The PROOSIS schematic model of the engine is shown in Figure 5.17. Note that the necessary dimensions for estimating the weight of the engine components are obtained from the TURBO1D components that conduct the aerothermodynamic design of the fan, LPC, HPC, HPT, LPT, and burner engine components. The GTWC component will be validated for both the CB-SE and CB-GM modes. The baseline engine design is performed at cruise conditions ($alt_f = 11,000$ m, $M_f = 0.8$), where the engine performance parameters are given in Table 5.7⁴⁸.

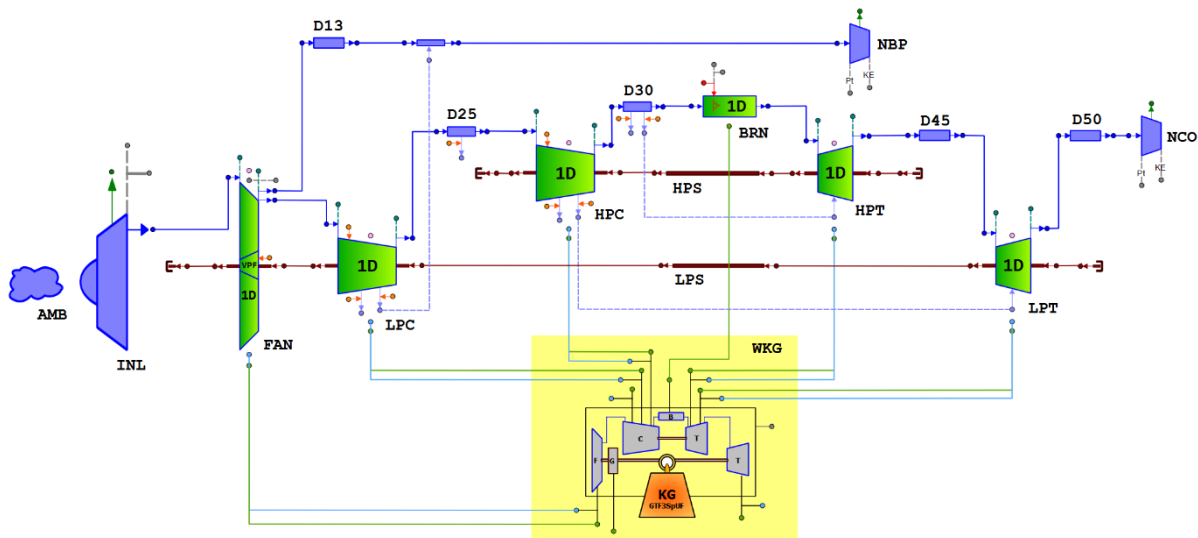


Figure 5.17: Schematic model of a 2-spool, unmixed turbofan engine in PROOSIS, where the GTWC component for evaluating the weight of the engine is shown inside the yellow rectangle (WKG). The engine model comprises components for: Atmosphere (AMB), engine inlet (INL), fan (FAN), low-pressure (LPC) and high-pressure (HPC) compressors, high-pressure (HPT) and low-pressure (LPT) turbines, burner (BRN), core (NCO) and bypass (NBP) nozzles, low-pressure (LPS) and high-pressure (HPS) shafts, and ducts (D13-D50). The conventional 0D TURBO components for the fan, LPC, HPC, HPT, LPT, and burner have been replaced by the respective TURBO1D components (green-colored) for aerothermodynamic calculations.

⁴⁷Davis et al. (1985) quote a value of 215 kg for the rotor (blades + disks) weight. Considering this value, GTWC underestimates the rotor weight by $\sim 6.1\%$ which, however, falls again within the $\pm 10\%$ accuracy goal adopted in this chapter.

⁴⁸Note that the values in Table 5.7 are arbitrary (but reasonably selected) and do not correspond to any commercial turbofan engine currently in operation.

Table 5.7: Selected baseline engine performance parameters at cruise conditions

Parameter	Value
Net thrust	30 kN
Overall pressure ratio	28.9
HPC pressure ratio	10
LP spool rotational speed	5000 rpm
HP spool rotational speed	15,000 rpm

The engine configuration is 1-3-9-2-3, that is, the fan comprises 1 stage, the LPC and HPC 3 and 9 stages (both have IGVs), respectively, and the HPT and LPT 2 and 3 stages, respectively. The basic design inputs for the fan, LPC, HPC, HPT, LPT, and burner are given in Table 5.8, and have been selected according to the guidelines given in Appendix A and Appendix C.

Table 5.8: Turbomachinery design inputs for the baseline engine

Component	Parameter	Value
Fan	Inlet hub-to-tip ratio	0.32
	Inlet Mach number	0.60
	Exit Mach number	0.40
LPC	Configuration	Const. hub
	Inlet hub-to-tip ratio	0.75
	Inlet Mach number	0.45
HPC	Exit Mach number	0.45
	Configuration	Const. mean
	Inlet hub-to-tip ratio	0.70
Burner	Inlet Mach number	0.45
	Exit Mach number	0.25
	Liner-to-casing wall gap ratio	5%
HPT	Dome gas velocity	12 m/s
	Passage gas velocity	60 m/s
	Inlet Mach number	0.10
LPT	Configuration	Const. mean
	Inlet hub-to-tip ratio	0.85
	Inlet Mach number	0.20
LPT	Exit Mach number	0.30
	Configuration	Const. hub
	Inlet hub-to-tip ratio	0.85
LPT	Inlet Mach number	0.30
	Exit Mach number	0.30

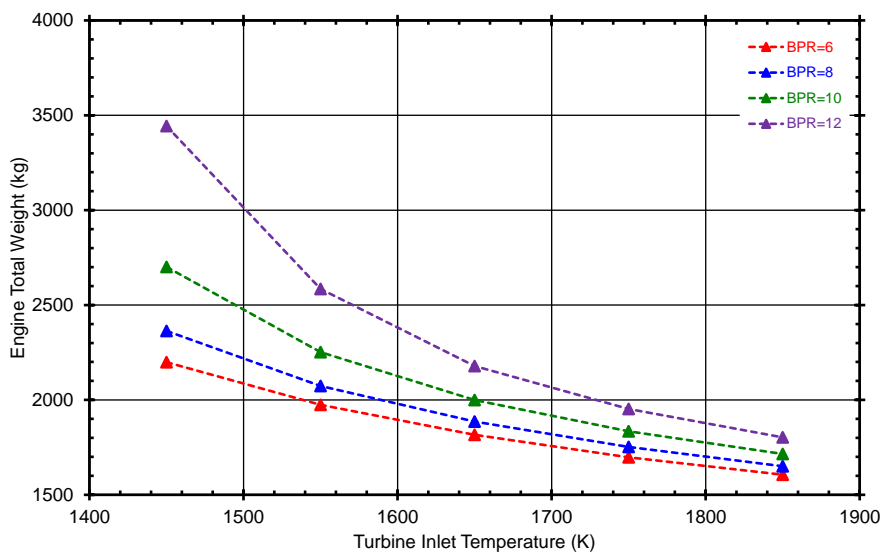
Regarding the materials required when the GTWC components are executed in the CB-GM mode, these are given in Table 5.9 and have been selected after materials that are typically used in such applications (see Table 4.2).

Table 5.9: Material selection for the baseline engine

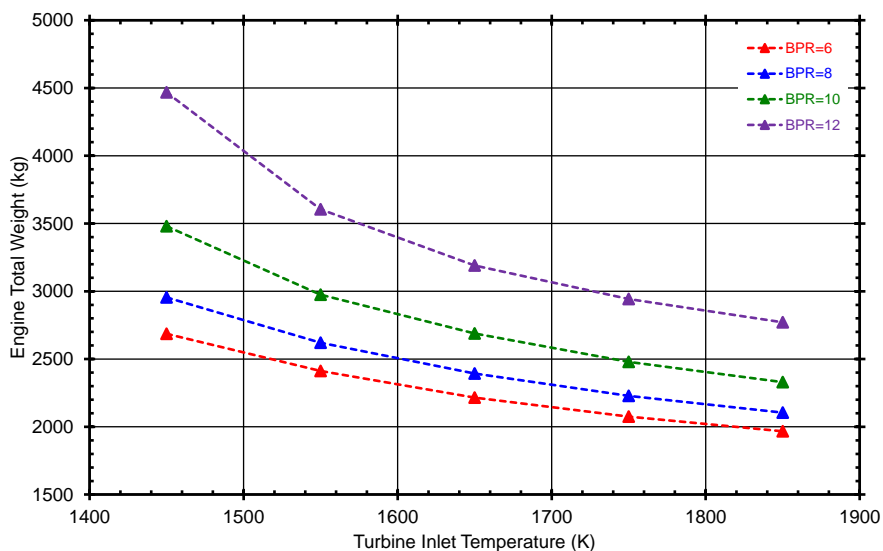
Component	Structural Part	Material (Stages)
Fan	Rotor blades	Ti-6Al-4V
	IGVs	A-286
	OGVs	Kevlar-149
	Disk	Ti-6Al-4V
	Hardware	Rene-41
	Casings (inner & outer)	A-286
LPC	Hardware	Rene-41 (1-3)
	Rotor blades	Ti-6Al-4V (1-3)
	Stator blades	A-286 (1-3)
	IGVs	A-286
	Disks	Ti-6Al-4V (1-3)
	Casings (inner & outer)	A-286 (1-3)
HPC	Hardware	Rene-41 (1-9)
	Rotor blades	Ti-6Al-4V (1-3); Inconel-718 (4-9)
	Stator blades	A-286 (1-9)
	IGVs	A-286
	Disks	Ti-6Al-4V (1-3); Inconel-718 (4-9)
	Casings (inner & outer)	A-286 (1-5); Inconel-718 (6-8); N-155 (9)
HPT	Hardware	Rene-41 (1-2)
	Blading (rotors & stators)	Rene-41 (1-2)
	Disks	Rene-41 (1-2)
	Casings (inner & outer)	Inconel-718 (1-2)
LPT	Hardware	Rene-41 (1-3)
	Blading (rotors & stators)	Rene-41 (1-3)
	Disks	Rene-41 (1-3)
	Casings (inner & outer)	Inconel-718 (1-3)
Ducts		A-286
Shafts	Low-pressure	Inconel-706A
	High-pressure	Ti-6Al-4V

Finally, the weight of the disks is calculated following the semi-empirical approach of NASA's WATE (see paragraph 5.3.6), while the engine is assumed to comprise a fan rear frame (Type 2), a LPT rear frame (Type 3), and a burner frame (Type 4). All other inputs required by the GTWC component for estimating the engine weight are set to their default values.

Using the design and calculation inputs described above, a parametric study is conducted next to evaluate the GTWC component ability to correctly capture the weight prediction trends. For this reason, the engine bypass ratio (BPR) and turbine inlet temperature (TET) are varied, while all other cycle parameters (pressure ratios, component efficiencies, thrust, etc.) are kept constant. The weight trends produced by the GTWC component when executed in both the CB-SE and -GM modes are shown in Figure 5.18. Note that BPR and TET are varied in the range 6-12 and 1450-1850 K, respectively, which represent values of contemporary high-bypass ratio turbofan engines.



(a)



(b)

Figure 5.18: Parametric weight predictions produced by the GTWC component for engine weight estimations when executed in the (a) CB-SE and (b) CB-GM mode. In the vertical axis the engine total weight (bare engine weight + nacelle weight) is plotted.

The engine bypass ratio and turbine inlet temperature are two parameters that influence directly the engine size since, for a given engine thrust requirement, they determine the engine specific thrust (SF_N) and, hence, the air flow at the engine inlet. The engine BPR and TET have opposite effects on SF_N . More specifically, for a given TET the increase in BPR results in a reduction in SF_N , while for a given BPR the increase in TET increases SF_N . In other words, for a given thrust requirement increasing the BPR increases the air flow at the engine inlet, while increasing TET results in a reduction in the air flow at the engine inlet. For given Mach numbers and hub-to-tip ratios across the engine, this mass flow variation produces engines with different sizes and, thus, different weights. From the above discussion it is clear that increasing BPR will produce heavier engine designs while increasing TET will produce lighter engine designs. It is seen from Figure 5.18 that these physical trends are reproduced successfully by the GTWC component for estimating the weight of turbofan engines, by both calculation modes (CB-SE and CB-GM). From Figure 5.18, it is seen that the CB-SE mode calculates engine weights which are lighter than those obtained by the CB-GM mode.

Being confident enough that the GTWC component for engine weight estimations can successfully reproduce the physical weight trends when the key engine cycle parameters are varied, in the following paragraph the same component is validated quantitatively against the CFM56-5A engine.

5.5.3 Quantitative Validation of Component for Engine Weight Estimation

In the present paragraph the CFM56-5A turbofan engine is used to validate quantitatively the GTWC component for engine weight estimations.

The CFM56-5A is a commercial 2-spool, high-bypass ratio turbofan engine. CFM56-5A was developed by CMF International (CFMI)⁴⁹, and the first engine of the CFM56-5A family entered service in 1988 to power the short-to-medium range Airbus A320 aircraft family⁵⁰. More information about the CFM56-5A engine family is given in Table 5.10.

Table 5.10: CFM56-5A engine family information [see Gunston (2004)]

Parameter	Value (Variants)	
	Min.	Max.
Take-off thrust (kN)	~98 (-5A4)	~118 (-5A3)
Bypass ratio (-)	6.0 (-5A1, -5A3, -5A5)	6.2 (-5A4)
Dry bare weight (kg)	2266 (-5A3, -5A4, -5A5)	2337 (-5A1)

⁴⁹A joint venture between the GE Aviation (US) and Safran Aircraft Engines (France). In developing the CFM56 engine family (US military designation F108), Safran was responsible for the fan, LPC, LPT, and accessory gearbox components, while GE developed the HPC and HPT, and the main fuel control system [see Gunston (2004)].

⁵⁰<https://www.cfmaeroengines.com/engines/legacy> (accessed: May 11th, 2022)

The CFM56-5A comprises a 1-stage fan, a 3-stage LPC, a 9-stage HPC, a 1-stage HPT, a 4-stage LPT, and a single- or double-annular burner [see Gunston (2004)]. Note that the HPC component comprises 1 row of variable IGVs, while the first three (3) rows of stators are also of variable geometry. The low-pressure spool rotates at a maximum speed of 5100 rpm (at 102%) while the high-pressure spool rotates at a maximum speed of 15,183 rpm (at 105%) [see EASA (2018)]. Figure 4.5 illustrates a 2D cutaway of the CMF56-5A engine, but is repeated here for completeness (Figure 5.19). Finally, as can it be seen from both Figure 5.5 and Figure 5.19, the CFM56-5A engine comprises two (2) frames, namely the fan (main frame with PTO) and LPT (rear) frames.

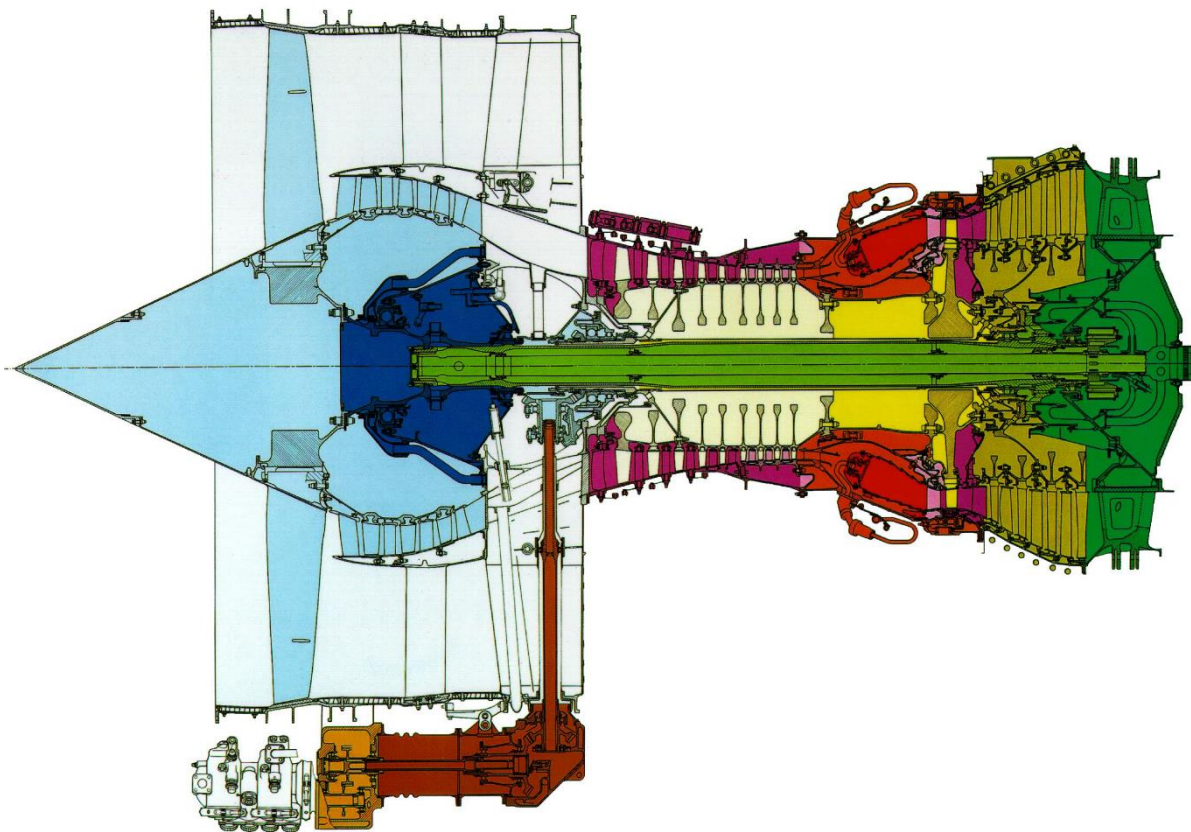


Figure 5.19: 2D cutaway of the CFM56-5A turbofan engine family. The engine comprises a 1-stage fan, a 3-stage LPC, a 9-stage HPC, a 1-stage HPT, a 4-stage LPT, and comes with a single- or double-annular combustor.

The main performance inputs (e.g., shaft rotational speeds) which were used by the GTWC component for estimating the weight of the CFM56-5A engine can be found in Gunston (2004) and EASA (2018). The basic engine dimensions (e.g., lengths, radii, blade counts, etc.) and materials were found by digitizing the engine 2D cutaway (see Figure 5.19) as well as in the available (online) training manual of the engine⁵¹.

The execution of the GTWC component for estimating the weight of turbofan engines in both the CB-SE and CB-GM modes, gave the results shown in Table 5.11. Note that, in the CB-SE mode, the fan weight was estimated using Eq. (5.2), the weights

⁵¹<https://eduscol.education.fr/sti/sites/eduscol.education.fr.sti/files/ressources/pedagogiques/11659/11659-ctc-044-basic-engine.pdf> (accessed: May 11th, 2022)

of the compressors were estimated according to Eq. (5.4), and the burner weight was obtained using Eq. (5.8). In all CB-SE and -GM weight models where calibration scalars are introduced, these claimed their default values; the only exception was Eq. (5.10) where $s_{m,S} \cong 1.944$ (for obtaining $K_S = 0.35$). Finally, for controls and accessories, $K_{C\&A}$ was set equal to 10% [see Eq. (5.17)].

Table 5.11: Bare weight comparisons for the CFM56-5A turbofan engine

GTWC mode	Estimated Weight (kg)	Relative Difference (%)	
		From Min.	From Max.
CB-SE	1728.8	23.71	26.02
CB-GM	2219.8	2.04	5.01

In Table 5.11, the GTWC weight results are compared with both the minimum and maximum values for the CFM56-5A weight quoted in Table 5.10, giving relative differences expressed by $100 \times (W_{KG}^{CMF56} - W_{KG}^{GTWC}) / W_{KG}^{CMF56}$. As it can be seen from Table 5.11, the estimated weight obtained by the CB-GM mode is about 2% less than the minimum real weight of the engine (2266 kg), and ~5% less than the maximum one (2337 kg). These figures fall well within the $\pm 10\%$ accuracy goal set at the beginning of this chapter. On the contrary, the CB-SE mode produces an engine weight which is significantly less than the real ones (relative differences no less than about ~24%). This discrepancy between the two calculation approaches is in accordance with the results presented by other researchers [see Haβy et al. (2002)]. The weight breakdown produced by both calculation modes is shown in Table 5.12.

Table 5.12: Breakdown of the estimated bare weight for the CFM56-5A turbofan engine

Component/ Structural Part	CB-SE Mode		CB-GM Mode	
	Weight (kg)	Percentage (%)	Weight (kg)	Percentage (%)
Fan	814.8	36.71	247.2	14.30
LPC	112.1	5.05	89.3	5.17
HPC	171.9	7.74	192.6	11.14
Burner	65.2	2.94	108.3	6.27
HPT	112.1	5.05	136.0	7.87
LPT	265.0	11.94	391.0	22.60
Ducts	98.0	4.42	N/A	N/A
Frames	337.4	15.20	N/A	N/A
Shafts	41.6	1.87	N/A	N/A
Structures	477.0	21.49	407.5	23.57
C&A	201.8	9.09	157.2	9.09
Core turbo-components	661.0	29.78	808.6	46.77
Turbo-components	1475.8	66.48	1055.9	61.07

Firstly, concerning the controls and accessories weight, we see from Table 5.12 that in both modes this contributes $\sim 9.1\%$ to the engine total weight. This is less than the 10% value used for $K_{C\&A}$. This is simply because the results in Table 5.12 are obtained by dividing the individual component weight with the engine total weight which, in turn, includes the weight of the controls and accessories itself according to Eq. (5.19).

Secondly, from Table 5.12 we see that the CB-GM mode produces components weights which seem reasonable, but there are no publicly available data to do the comparison. However, the percentage weights are of the same order of magnitude as those quoted in other weight studies regarding the CFM56-7B27 engine which has the same configuration as the CFM56-5A engine used here [see Lolis (2014)].

Thirdly, regarding the CB-SE mode, we can see from Table 5.12 that, in most cases, it produces component weights which contribute more to the engine total weight compared to those obtained by the CB-GM mode. The only exception is the fan component where the CB-SE mode produces a fan weight that contributes about 14.3% to the engine total weight, whereas the CB-GM mode produces a fan weight that contributes almost 2.6 times this value ($\sim 36.7\%$). In physical numbers, the CB-SE mode gives a fan weight of about 248 kg while the CB-GM mode gives a fan weight of about 815 kg. Table 5.13 summarizes the CB-SE correlating parameters values as obtained for the CFM56-5A engine.

Table 5.13: Correlating parameters values for estimating the CFM56-5A weight using the CB-SE mode

Component	Correlating Variable Value
Fan	$\bar{D}_{t,R} = 1.72 \text{ m}$
	$AR_{x,R} = 4.33$
	$N_{stg} = 1$
LPC	$\bar{D}_m = 0.8392 \text{ m}$
	$N_{stg} = 3$
	$L/D_{m,in} = 0.30$
HPC	$\bar{D}_m = 0.5073 \text{ m}$
	$N_{stg} = 9$
	$L/D_{m,in} = 1.08$
Burner	$\bar{D}_m = 0.5780 \text{ m}$
HPT	$\bar{D}_m = 0.6941 \text{ m}$
	$N_{stg} = 1$
	$\bar{U}_m = 525.5 \text{ m/s}$
LPT	$\bar{D}_m = 0.7662 \text{ m}$
	$N_{stg} = 4$
	$\bar{U}_m = 200.6 \text{ m/s}$

As we see from Table 5.13, all correlating variables are within the valid range of values given in Table 5.1 except for \bar{U}_m for the HPT which is slightly greater than the upper limit given in Table 5.1 for turbine components (510 m/s). This difference (about 3%)

could be attributed in the error during the digitization of the engine 2D cutaway from which the value of \bar{D}_m is obtained ($\bar{U}_m = \pi N_{mech} \bar{D}_m / 60$). Since from Table 5.12 we see that the HPT component contributes only a small part to the engine total weight (about 7.9% in the CB-SE mode and about 5.1% in the CB-GM mode), we will not deal with it further. The component of interest is the fan which, in high-bypass ratio engines, contributes the largest portion to the engine total weight. From the preceding discussion it is obvious that Sagerser et al.'s (1971) correlations underestimate significantly the weight of the fan component [all correlating parameters in Eq. (5.2) are well within the valid range of values given in Table 5.1]. This conclusion comes rather reasonably since Sagerser et al.'s correlations were developed primarily considering V/STOL engines which are low-bypass ratio engines. Hence, the above study shows the importance of having a more physical weight model that relies on the engine "detailed" dimensions and material selection than having a semi-empirical one that relies on historical data. However, Sagerser et al.'s method is still of great use in conceptual/preliminary design studies where the absolute weight figures are not of so much importance in contrast to obtaining the correct physical trends.

Finally, Figure 5.20 presents the weight breakdown for the fan, low- and high-pressure compressors, and low- and high-pressure turbines as obtained by the CB-GM mode of the GTWC component, demonstrating the fidelity of the developed method.

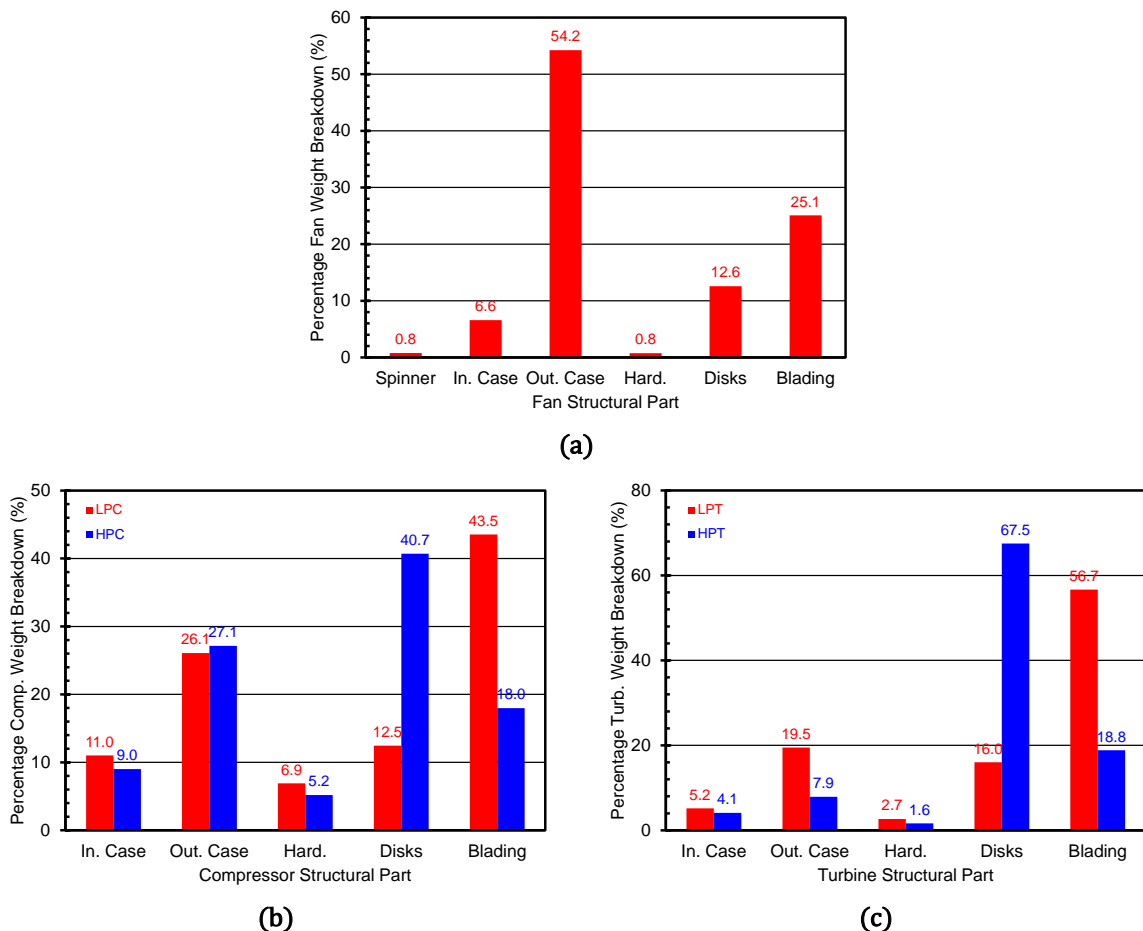


Figure 5.20: CFM56-5A estimated (CB-GM mode) percentage weight breakdown for the (a) fan, (b) LPC and HPC, and (c) HPT and LPT components. The weight of the different structural parts is divided by the respective component weight.

5.6 Summary and Discussion

In the present chapter models, methodologies, and assumptions were presented for estimating the weight of turbofan engines. For the needs of the present thesis, two approximations were programmed that resulted in the development of a PROOSIS library (called GTWC). GTWC defines components for the preliminary weight estimation of turbomachinery components, as well as a component for the estimation of the overall weight of generic 3-spool turbofan engines.

Both approximations used in the development of the GTWC library belong in the component-based class of methods. The first one is a semi-empirical weight estimation method that correlates the weight of individual components with historical data (CB-SE), while the other is a part-based, “analytical” one, that estimates the weight of individual components given their dimensions and materials (CB-GM). In both CB-SE and -GM methods, the overall weight of an engine is obtained by summing up the weights of the individual components that comprise the engine (hence, the term “component-based methods”).

The GTWC component for estimating the weight of turbofan engines was validated both qualitatively and quantitatively in both the CB-SE and -GM calculation modes. Assuming a 2-spool turbofan engine for which the bypass ratio and turbine inlet temperature were varied, we saw that both the CB-SE and -GM modes reproduce successfully the weight trends expected. For the quantitative validation, the CFM56-5A, 2-spool turbofan engine was used as a reference. We saw that the CB-GM calculation mode estimated successfully the engine’s real weight (well within the $\pm 10\%$ accuracy goal adopted in the present chapter), while the CB-SE mode underestimated it significantly. Nevertheless, the CB-SE mode is still useful in conceptual/preliminary design studies where physical trends are more important than absolute figures.

Finally, the GTWC component for estimating the weight of compressors was partially validated in the CB-GM calculation mode using the NASA/GE E³ HPC rotor (blades + disks) geometry. The estimated rotor weight was found to be well within the $\pm 10\%$ accuracy goal adopted in this chapter.

6 Axial Compressor 1D Off-Design Performance Modelling (MLAC)

6.1 Introduction

The development of gas turbine engines is a highly iterative procedure that involves different disciplines and their interactions [see Mattingly et al. (2002)]. The first step in the development of a new engine is the preliminary design phase, where different engine concepts and configurations are assessed both at design and off-design (steady-state and transient) conditions, for identifying the optimum that fulfills the respective performance and installation requirements. The choice is guided by seeking optimality, while not violating a number of performance, aerodynamic, structural, and installation constraints.

Of all components comprising a gas turbine engine, the compressor is probably the most important and critical one due to the flow physics involved. A good compressor design is essential for achieving the desired engine performance and operating range. A poor compressor design not only affects the engine performance, but in the most extreme cases can even damage the engine due to stalling phenomena. Therefore, on- and off-design performance at a wide range of operating conditions should be accurately evaluated and accounted for as early as possible during the design phase of a new engine (see Figure 6.1).

In the present chapter a mean-line (1D) modelling approach is described for evaluating the off-design performance of axial-flow, multi-row compressors, called MLAC (Mean-Line Analysis Code). MLAC was developed and validated in the same environment as the conventional 0D components for turbomachinery performance simulations, namely the PROOSIS TURBO library (see Chapter 2). The existing 0D compressor components were extended to add the 1D capability for off-design performance calculations. This way, 1D compressor components were developed that inherit the same fluid and mechanical interfaces that enable the interconnection between different components and/or systems, and the same functions for numerical, fluid flow, and thermodynamic properties calculations. Thus, a transparent integration in any 0D cycle analysis calculation is ensured, without affecting the mathematical formulation and the simulation robustness.

Finally, an integral part of any compressor off-design simulation tool should be the accurate prediction of stall and choke. In this direction, MLAC implements a novel

approach where appropriately defined indices are introduced to quantify how far the current operating point is from stall and/or choke. The mass flow rate corresponding to stall and choke conditions is obtained by numerically zeroing these indices, utilizing a robust numerical procedure. Overall, a physically consistent, transparent and, more importantly, fully automated procedure is developed for producing the compressor map in the entire operating regime.

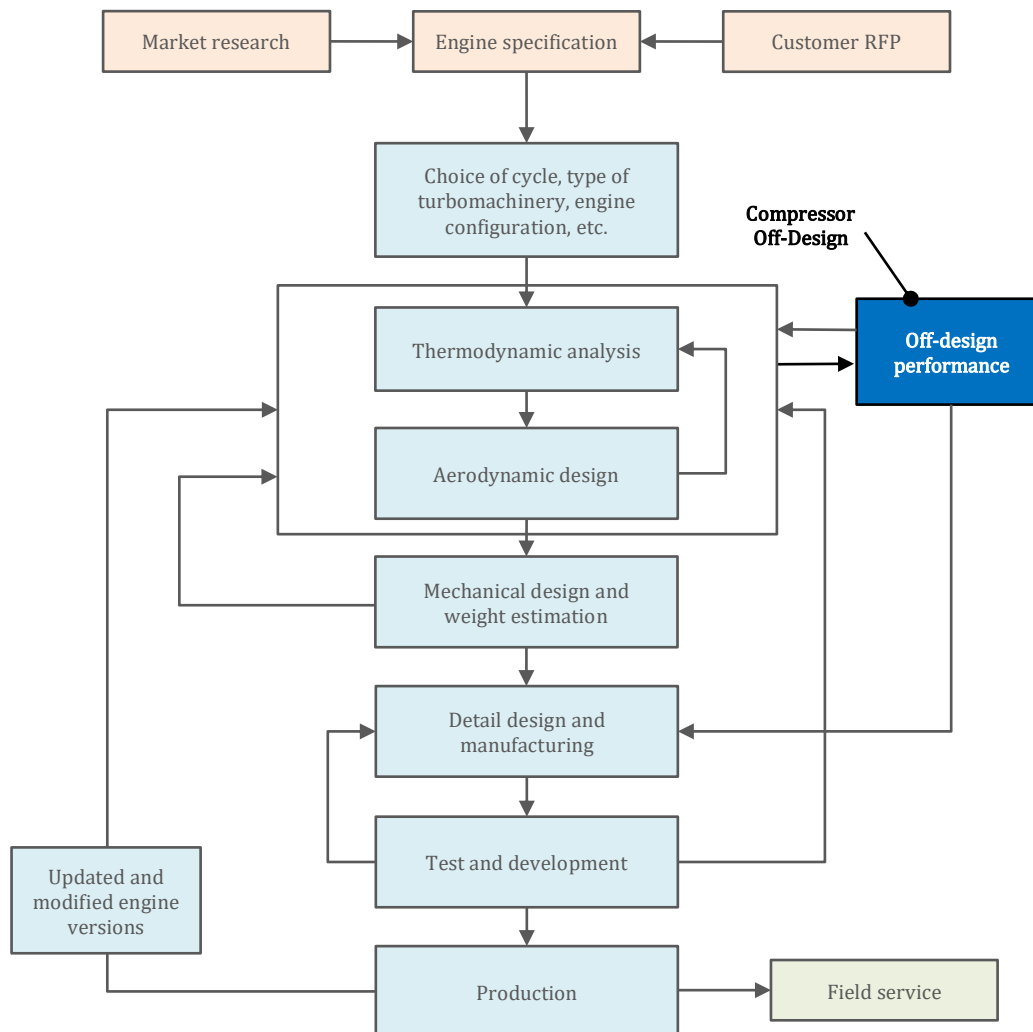


Figure 6.1: Simplified flow-chart representing the development course of a new gas turbine engine [adapted from Mattingly et al. (2002)]. The present chapter is concerned with the “Compressor Off-Design” box.

6.2 Fundamentals

This section summarizes fundamental equations, models, and calculation procedures that are used in MLAC for establishing the compressor off-design performance. Among other, the mean-line flow representation, the modelling of the gas properties across the compressor, and the equations used to estimate the compressor overall performance are presented.

6.2.1 Fluid and Thermodynamic Flow Properties Modelling

MLAC can perform calculations considering both variable and constant gas properties across the compressor. For calculations with variable gas properties (c_p and γ), the reader is referred to paragraph 3.2.1.

To improve the speed of execution when, e.g., parametric or optimization studies are conducted, the possibility to perform calculations with constant c_p and γ across a blade row is also implemented in MLAC. In this case, γ and R_g are calculated based on an appropriate local temperature and gas composition (FARB and WAR), and c_p is obtained from the known relationship for ideal gases:

$$c_p = \frac{\gamma}{\gamma - 1} R_g$$

Considering the flow through a rotor or a stator row (process 1 \rightarrow 2), it was found that the results of such calculations are very close to those using the full gas model (see paragraph 3.2.1) when the row inlet temperature for stators (T_1^0) and the average inlet/outlet temperature for rotors [that is, $(T_1^0 + T_2^0)/2$] are used to obtain the local value of γ . The temperature ratio, T_2^0/T_1^0 , across any rotor is estimated by the recursive formula:

$$\left(\frac{T_2^0}{T_1^0}\right)_k = \frac{N_R + k(\overline{TR} - 1)}{N_R + (k - 1)(\overline{TR} - 1)} \quad (6.1)$$

Equation (6.1) assumes that each compressor rotor achieves the same temperature rise, where k is the rotor row number, and the total temperature ratio (\overline{TR}) is calculated from Eq. (6.2):

$$\overline{TR} = \frac{\overline{PR}^{\frac{\gamma-1}{\eta_p \gamma}}}{\overline{PR}^{\eta_p \gamma}} \quad (6.2)$$

In the above, a polytropic efficiency of $\eta_p = 90\%$ and $\gamma = 1.4$ are assumed, while the average total pressure ratio (\overline{PR}) is taken equal to the compressor design pressure ratio.

Then, enthalpy is calculated from:

$$h = h_{ref} + c_p(T - T_{ref}) \quad (6.3)$$

with $T_{ref} = 298.15$ K and $h_{ref} = 0$ J/kg.

Total and static temperatures are related analytically from:

$$T_r^0 = T^s + \frac{1}{2c_p} W^2 \quad (6.4)$$

or by:

$$\frac{T_r^0}{T^s} = 1 + \frac{\gamma - 1}{2} M_r^2 \quad (6.5)$$

When required, total and static pressures are related using the isentropic relationship given by:

$$\frac{p_r^0}{p^s} = \left(\frac{T_r^0}{T^s} \right)^{\frac{\gamma}{\gamma-1}} = \left(1 + \frac{\gamma-1}{2} M_r^2 \right)^{\frac{\gamma}{\gamma-1}} \quad (6.6)$$

In general, any arbitrary isentropic process ($1 \rightarrow 2$) is represented by:

$$\frac{p_2}{p_1} = \left(\frac{T_2}{T_1} \right)^{\frac{\gamma}{\gamma-1}} \quad (6.7)$$

Finally, for calculating the flow dynamic viscosity, μ , which is used in Reynolds number calculations, Sutherland's law for viscosity is used [see White (2016)]:

$$\mu = \mu_{ref} \left(\frac{T}{T_{ref}} \right)^{1.5} \frac{T_{ref} + T_s}{T + T_s} \quad (6.8)$$

The values of the coefficients appearing in Eq. (6.8) are: $\mu_{ref} = 1.711 \times 10^{-5}$ Pa·s, $T_{ref} = 273.15$ K, and $T_s = 110.4$ K.

6.2.2 Mean-Line Flow Modelling

The mean-line approach used in MLAC models the through-flow field across the compressor using velocity diagrams and flow properties calculated at a single representative radius (referred to as the “mean”), while spanwise flow variations are neglected (see Figure 3.5). In MLAC, the mean radius, R_m , at any flow station across the compressor can be defined using any of the three following equations:

$$R_m = \frac{1}{2} (R_{g,h} + R_{g,t}) \quad (6.9)$$

$$R_m = \sqrt{\frac{1}{2} (R_{g,h}^2 + R_{g,t}^2)} \quad (6.10)$$

$$R_m = \tilde{R}_{IMM} R_{g,h} + (1 - \tilde{R}_{IMM}) R_{g,t} \quad (6.11)$$

where \tilde{R}_{IMM} is a user-specified immersion from tip given by:

$$\tilde{R}_{IMM} = (R_{g,t} - r) / (R_{g,t} - R_{g,h}) \quad (6.12)$$

In the above, $0.0 \leq \tilde{R}_{IMM} \leq 1.0$ (0.0 corresponds to tip and 1.0 to hub). Equation (6.9) considers that the mean-line passes through the geometrical mid-point between the compressor hub and tip walls, while Eq. (6.10) assumes that the mean-line divides any flow station into two parts of equal area. Finally, through the use of Eq. (6.11) the mean-line can be placed at any radial position along a flow annulus by imposing the immersion from tip (\tilde{R}_{IMM}).

Similarly to the mean-line models presented in Chapter 3, the flow across a compressor is represented by a vector equation that relates the absolute (\vec{V}) and relative (\vec{W}) flow velocities at any flow station. This equation is described by Eq. (3.2), but is repeated here for completeness:

$$\vec{V} = \vec{W} + \vec{U} \quad (6.13)$$

In the above, \vec{U} is the blade velocity with its magnitude obtained by Eq. (3.3).

The expansion of vector Eq. (6.13) into its components and the relationships between the different velocity components and flow angles can be found in any introductory textbook for turbomachines [e.g., see Lewis (1996); Dixon et al. (2014); Saravanamuttoo et al. (2017); Papailiou et al. (2000)] and, thus, they will not be analyzed in more detail here. Note, however, that similarly to the mean-line modelling presented in Chapter 3, the flow angles w.r.t. the axial direction are always taken as positive angles (unless otherwise stated).

6.2.3 Flow Station Calculation

The equations and calculation procedures used to define the flow conditions (i.e., T^s , p^s , ρ^s , W , M_r for known gas properties and \dot{m} , A , β , T_r^0 , p_r^0) across a flow station are described in paragraph 3.2.3. Note that in MLAC the flow situation often appears (see paragraph 6.3.2) where the flow angle (β) is an unknown but the peripheral component of the velocity (W_θ) is known instead. Then, the system of Eqs (3.4)–(3.8) is closed by adding Eq. (6.14) into the system. The new system of equations is again solved following the procedures described in paragraph 3.2.3.

$$W_\theta = W \sin \beta \quad (6.14)$$

6.2.4 Compressor Overall Performance

In MLAC a number of parameters are calculated that express the compressor overall performance. The compressor isentropic (η_{is}) and polytropic (η_p) efficiencies are given by:

$$\eta_{is} = \frac{h_{out,is}^0 - h_{in}^0}{h_{out}^0 - h_{in}^0} \quad (6.15)$$

$$\eta_p = \frac{R_g}{\phi_{out}^0 - \phi_{in}^0} \ln \frac{p_{out}^0}{p_{in}^0} \quad (6.16)$$

where for calculating the isentropic temperature and enthalpy at the compressor exit, Eq. (3.101) is used.

Another performance quantity calculated by MLAC is the compressor specific enthalpy change, $\Delta h/T$, which is obtained by:

$$\frac{\Delta h}{T} = \frac{h_{out}^0 - h_{in}^0}{T_{in}^0} \quad (6.17)$$

The compressor performance is also expressed in the widely used MFT format [see Sethi et al. (2013)]. Among other, the compressor flow coefficient (φ_{MFT}) and work coefficient (ψ_{MFT}) are given by the following equations:

$$\varphi_{MFT} = \frac{V_{x,in}}{U_{in}} \quad (6.18)$$

$$\psi_{MFT} = \frac{h_{out}^0 - h_{in}^0}{\frac{1}{2} U_{c,t,in}^2} \quad (6.19)$$

In the MFT format, the compressor overall aerodynamic loss (ω_{MFT}) is also defined and is given by:

$$\omega_{MFT} = \psi_{MFT,is} \left(\frac{1}{\eta_{is}} - 1 \right) \quad (6.20)$$

where the isentropic work coefficient, $\psi_{MFT,is}$, is obtained by:

$$\psi_{MFT,is} = \frac{h_{out,is}^0 - h_{in}^0}{\frac{1}{2} U_{c,t,in}^2} \quad (6.21)$$

Note that, in Eqs (6.19) and (6.21) the corrected tip speed, $U_{c,t,in}$, is calculated using the tip diameter and total temperature corresponding to the inlet of the first rotor blade.

For the general case of a compressor with a gas bleed at the exit of any row, the compressor power is established by:

$$P_{wr} = - \left[\dot{m}_{out} h_{out}^0 - \dot{m}_{in} h_{in}^0 + \sum_{j=1}^{j=N_{br}} (\dot{m}_{gb} h_{gb}^0)_j \right] \quad (6.22)$$

where the work absorbed by the compressor is assumed negative, and \dot{m}_{gb} and h_{gb}^0 are the gas bleed mass flow rate and absolute total enthalpy, respectively.

Finally, since conventional corrections (subscript “c”) are not sufficient for accounting the effects of different compressor inlet temperatures during a simulation [see AGARD (1995)], appropriate gamma corrections (subscript “ γ ”) are introduced to the compressor corrected inflow ($\dot{m}_{c,in}$), total pressure ratio (PR), and corrected rotational speed ($N_{mech,c}$) according to the following equations [see Walsh et al. (2004)]:

$$\dot{m}_{\gamma,in} = \dot{m}_{c,in} \sqrt{\frac{\gamma_{ref}^0 R_{g,in}}{\gamma_{in}^0 R_{g,ref}}} \quad (6.23)$$

$$PR_{\gamma} = \left\{ \frac{\gamma_{ref}^0 - 1}{\gamma_{in}^0 - 1} \left[PR^{(\gamma_{in}^0 - 1)/\gamma_{in}^0} - 1 \right] \right\}^{\gamma_{ref}^0 / (\gamma_{ref}^0 - 1)} \quad (6.24)$$

$$N_{mech,\gamma} = N_{mech,c} \sqrt{\frac{\gamma_{ref}^0 R_{g,ref}}{\gamma_{in}^0 R_{g,in}}} \quad (6.25)$$

where $\dot{m}_{c,in}$ and $N_{mech,c}$ are obtained by:

$$\dot{m}_{c,in} = \dot{m}_{in} \frac{\sqrt{T_{in}^0/T_{ref}}}{p_{in}^0/p_{ref}} \quad (6.26)$$

$$N_{mech,c} = \frac{N_{mech}}{\sqrt{T_{in}^0/T_{ref}}} \quad (6.27)$$

In Eqs (6.23) through (6.27), the reference temperature and pressure are taken equal to the standard-day sea-level conditions, that is, $T_{ref} = 288.15$ K and $p_{ref} = 101,325$ Pa, respectively. Finally, the reference γ and R_g are evaluated at $T_{ref} = 288.15$ K, $FARB_{ref} = 0$, and $WAR_{ref} = 0$, while γ_{in}^0 and $R_{g,in}$ are estimated using the values of T^0 , $FARB$, and WAR at the compressor inlet.

6.3 Compressor Performance Modelling

MLAC models the performance of multi-row, axial-flow compressors with or without gas bleeds by conducting a 1D calculation. For known compressor geometry, inlet flow conditions (\dot{m}_{in} , T_{in}^0 , p_{in}^0 , a_{in}), and compressor speed (N_{mech}), the mean-line calculation is performed row-by-row, meaning that the calculation starts at the compressor inlet and terminates at the compressor outlet after having passed through every blade row from inlet to outlet. For the calculation to continue on with a downstream blade row, the row inlet conditions must have been already established from the exit conditions of the upstream row, and so forth. At the end of this row-by-row calculation, the compressor exit flow conditions (\dot{m}_{out} , T_{out}^0 , p_{out}^0) are obtained and the compressor overall performance is established by Eqs (6.15)–(6.27).

The building blocks of MLAC are the Blade Row Module (BRM) and the Inter-Volume Module (IVM). BRM models the performance of individual blade rows, while IVM models the flow processes across the “duct” after a blade row (practically, the gap between two successive rows). Figure 6.2 illustrates conceptually the performance modelling of blade rows and the station numbering used in the present chapter. At the inlet and outlet of BRMs and IVMs, the flow condition is fully defined by the vector (\dot{m} , T^0 , p^0 , V , a , $FARB$, WAR). The latter is estimated at stations 1, 2, and 3 (see Figure 6.2) according to the methodology that will be described in paragraphs 6.3.1 and 6.3.2.

Overall, the performance of a blade row is modelled by a BRM followed by an IVM. Thus, the compressor is modelled by a number of BRMs and IVMs equal to the number of the blade rows comprising the compressor. In Figure 6.3, a simplified flow-chart of the row-by-row calculation is shown.

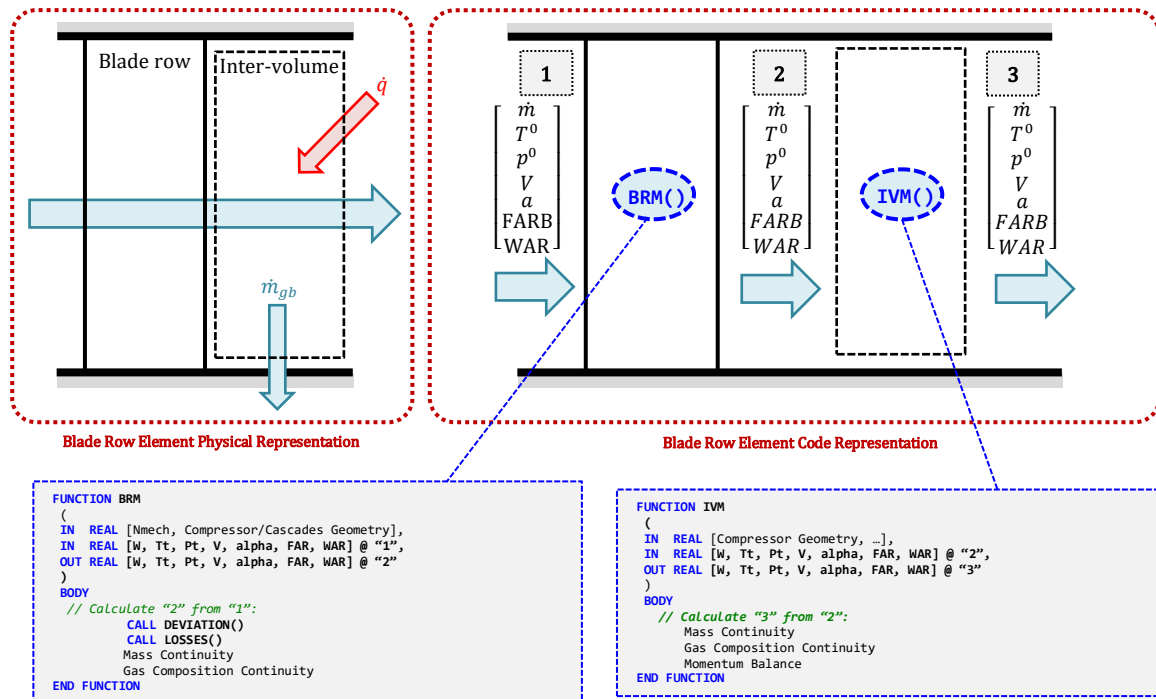


Figure 6.2: Conceptual blade row performance modelling using BRMs and IVMs, and station numbering.

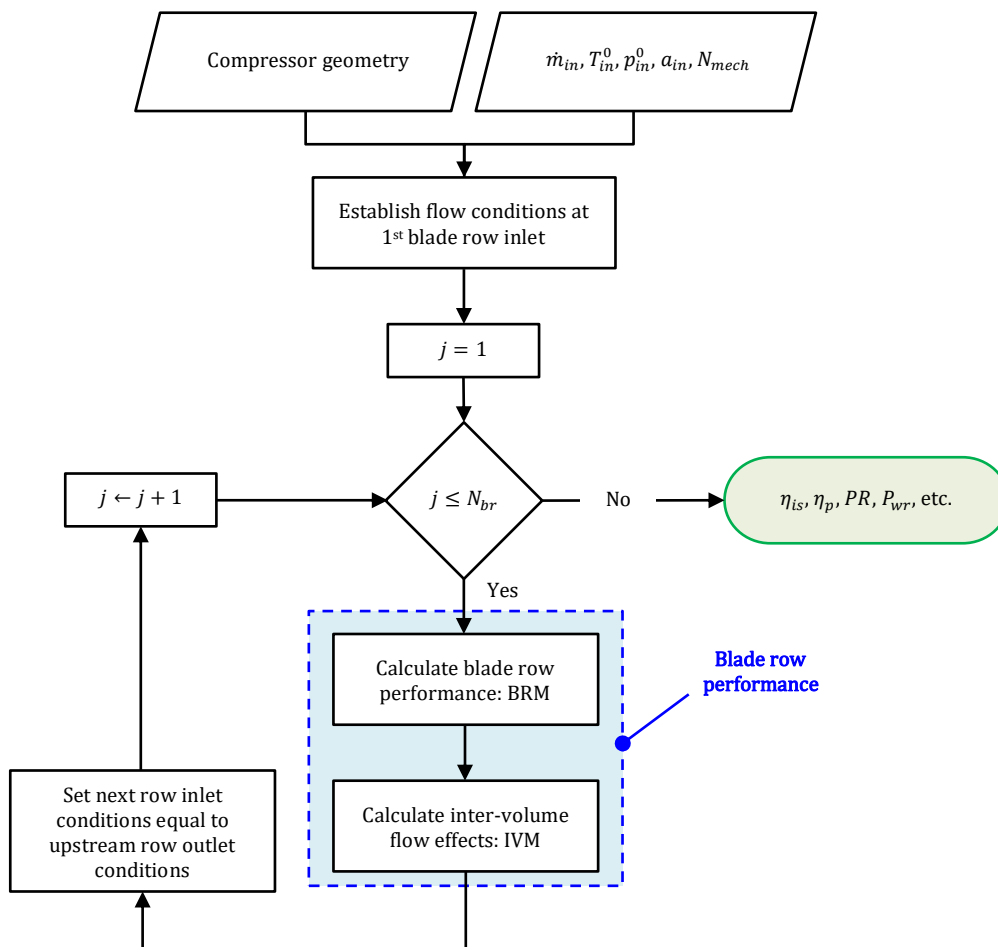


Figure 6.3: Row-by-row calculation to establish the compressor performance. The performance of the individual blade rows is modelled through BRMs and IVMs.

The blade row module estimates the row exit conditions by solving iteratively a system of equations formed by mass and gas composition continuity, the conservation of rothalpy (for rotors) or total enthalpy (for stators), and loss and deviation correlations introduced for modelling the row aerodynamic performance. These equations are summarized below.

Across a row there is no gas bleed and/or injection and, therefore, mass flow and gas composition continuity are expressed by:

$$\dot{m}_2 = \dot{m}_1, \quad \text{FARB}_2 = \text{FARB}_1, \quad \text{WAR}_2 = \text{WAR}_1 \quad (6.30)$$

Across a rotor, the work done by the rotor blades on the working fluid is accounted for by the Euler pump equation, which here is expressed in terms of rothalpy. More specifically, across any rotor row the conservation of rothalpy holds and is expressed by:

$$h_{r,2}^0 = h_{r,1}^0 + \frac{1}{2}(U_2^2 - U_1^2) \quad (6.31)$$

where $h_{r,1}^0 = h_1^s + W_1^2/2$.

Across stators:

$$h_2^0 = h_1^0 \quad (6.32)$$

The entropy increase across a row is accounted for by a total pressure loss coefficient, ω , expressed by:

$$\omega = \begin{cases} \frac{(p_{r,is}^0)_2 - p_{r,2}^0}{p_{r,1}^0 - p_1^s}, & \text{for rotating blade rows} \\ \frac{p_1^0 - p_2^0}{p_1^0 - p_1^s}, & \text{for stationary blade rows} \end{cases} \quad (6.33)$$

where ω is, in general, a function of the meridional density ratio and the axial velocity ratio across the row, ρ_2^s/ρ_1^s and $W_{x,2}/W_{x,1}$, respectively.

Finally, one more equation is required to close the system of equations for estimating the flow across a row. This equation expresses the flow deviation, δ , from the blade metal angle at TE. This is given by:

$$\beta_2 = \kappa_{TE} + \delta \quad (6.34)$$

where δ is, generally, also a function of ρ_2^s/ρ_1^s and $W_{x,2}/W_{x,1}$.

The system of equations formed by Eqs (6.30)–(6.34) is solved iteratively on ρ_2^s/ρ_1^s and $W_{x,2}/W_{x,1}$ until the mass continuity, Eq. (6.30), is satisfied within a user-specified tolerance. For this reason, a PROOSIS built-in Newton-Raphson method is utilized.

The functional forms of the flow deviation (δ) and total pressure loss coefficient (ω) are extremely complicated and, therefore, δ and ω will be discussed in more detail later in dedicated chapter sections.

6.3.2 IVM Modelling

In the inter-volumes, the secondary flow processes that could take place along a compressor are modelled. Example secondary effects are gas bleeds, thermal effects, water-vapor injections, etc. Currently, the only secondary effects modelled in IVMs are gas bleeds and the flow direction change. Figure 6.5 shows a schematic representation of the inter-volume effects that are currently modelled in MLAC.

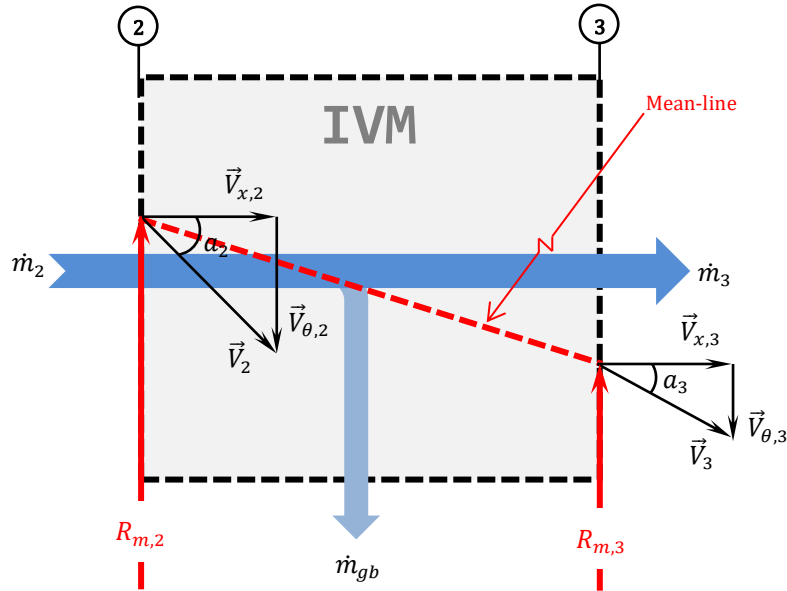


Figure 6.5: Inter-volume effects modelled in MLAC. Currently only gas bleeds and radius changes are modelled in IVMs.

From the known inlet conditions (station 2), IVM estimates the exit ones (station 3) by employing mass continuity, gas composition continuity (no water-vapor and mixing effects are considered), and a moment of momentum balance.

The flow across any inter-volume is considered adiabatic (no thermal effects are modelled) and, since there is no gas composition change:

$$T_3^0 = T_2^0 \quad (6.35)$$

Also, there are no pressure losses for the flow across the inter-volume (no loss model is employed to account for, e.g., wall friction, gas mixing effects, etc.) and, therefore, the total pressure at the exit of the inter-volume is:

$$p_3^0 = p_2^0 \quad (6.36)$$

From mass and gas composition continuity (see Figure 6.5), the inter-volume exit mass flow rate and gas properties are obtained from:

$$\dot{m}_3 = \dot{m}_2 - \dot{m}_{gb}, \quad \text{FARB}_3 = \text{FARB}_2, \quad \text{WAR}_3 = \text{WAR}_2 \quad (6.37)$$

where the gas bleed flow properties (T^0 , p^0 , FARB, WAR, a) are taken equal to those at the blade row outlet (station 2).

Finally, from a moment of momentum balance, the radius change effect on the flow across the inter-volume (see Figure 6.5) is taken into account according to [see Kidikian et al. (2018a)]:

$$\dot{m}_3 R_{m,3} V_{\theta,3} = \dot{m}_2 R_{m,2} V_{\theta,2} \quad (6.38)$$

From Eq. (6.38) $V_{\theta,3}$ is established and, then, V_3 and a_3 are estimated according to paragraph 6.2.3.

6.4 Blade Row Geometry Modelling

For modelling the geometry of a blade section, four (4) airfoil profile shapes are considered in MLAC:

- Equivalent circular-arc NACA-65 profiles
- Equivalent parabolic-arc NACA-63 A₄K₆ profiles (for IGVs)
- Double Circular-Arc (DCA) profiles
- British C-4 (BC4) profiles

Note that traditional NACA profiles have typically infinite camber-line slopes at the leading- (LE) and trailing-edge (TE) and, therefore, geometric and flow parameters such as the airfoil camber angle, the incidence angle, etc., cannot be defined properly unless a suitable approximation for the definition of the mean camber-line shape is used [see Aungier (2003)]. Therefore, the NACA-65 and -63 profiles are defined by an equivalent circular- and parabolic-arc camber-line [see Johnsen et al. (1965)], respectively.

Figure 6.6 illustrates the basic geometry parameters used for defining the geometry of airfoils of axial-flow compressors, while Figure 6.7 illustrates the cascade geometry and flow nomenclature used in the present chapter.

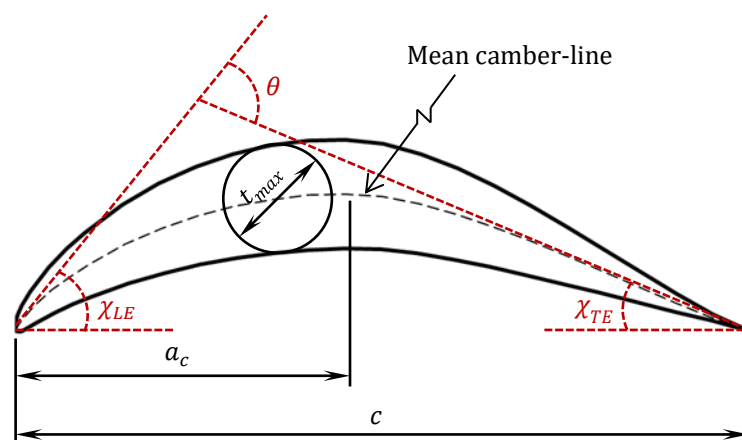


Figure 6.6: Airfoil geometrical modelling and nomenclature for axial-flow compressors [adapted from Aungier (2003)]. Currently MLAC models blade profiles with equivalent circular- and parabolic-arc camber-lines.

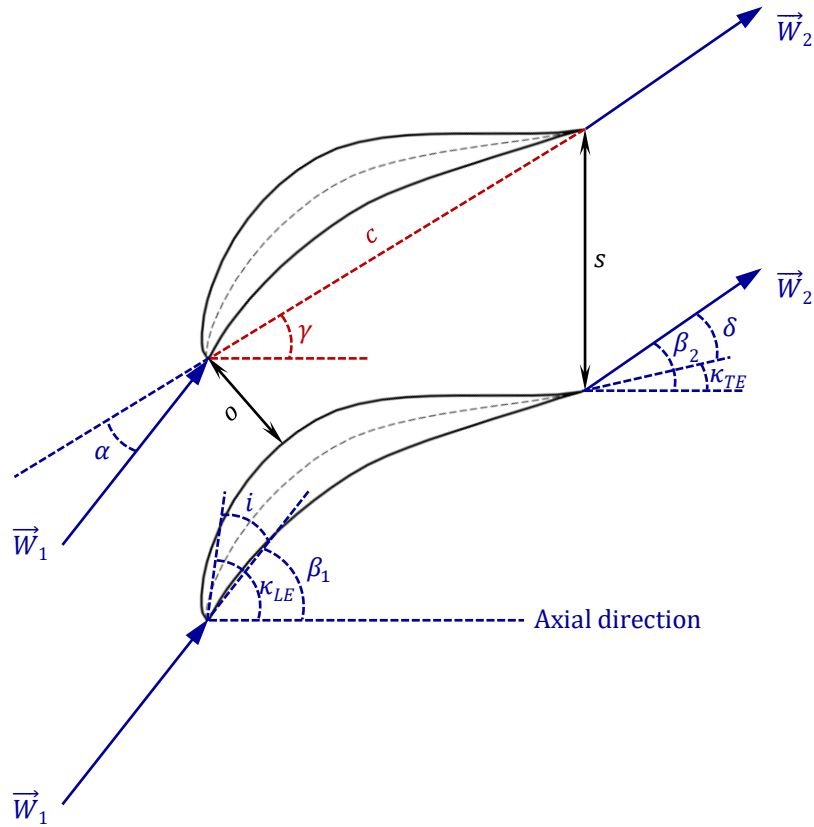


Figure 6.7: Blade row geometrical modelling and nomenclature for axial-flow compressors [adapted from Aungier (2003)].

As it can be seen from Figure 6.6 and Figure 6.7, the airfoil and blade row geometries are defined by a number of parameters which include the blade camber angle (θ), the blade row throat opening (o), the blade row solidity (σ), etc. Hence, useful formulas necessary in subsequent calculations that describe the blade row geometry and the interrelations between different parameters are presented next.

The blade camber angle, θ , for a generic cambered airfoil is calculated using the following geometrical equation:

$$\theta = \chi_{LE} + \chi_{TE} \quad (6.39)$$

For staggered airfoils, camber angle is alternatively related to metal angles κ_{LE} and κ_{TE} by:

$$\theta = \kappa_{LE} - \kappa_{TE} \quad (6.40)$$

with:

$$\kappa_{LE} = \chi_{LE} + \gamma \quad (6.41)$$

$$\kappa_{TE} = \gamma - \chi_{TE} \quad (6.42)$$

where γ is the blade stagger angle. Note that Eqs (6.39) [or (6.40)], (6.41), and (6.42), constitute a system of three (3) independent equations in six (6) unknowns. In the

present implementation, the blade geometry is fully defined by giving any of the following set of angles: $(\chi_{LE}, \chi_{TE}, \gamma)$, $(\chi_{LE}, \theta, \gamma)$, $(\chi_{TE}, \theta, \gamma)$, $(\kappa_{LE}, \kappa_{TE}, \gamma)$, $(\kappa_{LE}, \theta, \gamma)$, or $(\kappa_{TE}, \theta, \gamma)$. The remaining three (3) are established by rearranging properly Eqs (6.39) through (6.42).

Regarding the blade row aspect ratio (AR) and solidity (σ), these are defined by:

$$AR = \frac{\bar{h}_b}{c}, \quad \sigma = \frac{c}{s} \quad (6.43)$$

where \bar{h}_b is given by Eq. (3.25).

The blade row throat opening (o) is the minimum distance between the lower and upper surfaces of two adjacent blades. For compressor blade rows, it appears near the LE region. Throat opening is an important geometry parameter since it defines the maximum flow a blade row can pass as the flow conditions approach the choking ones. For estimating the blade row relative throat opening, o/s , the semi-empirical model formulated by Aungier (2003) is used. Aungier developed a correlation for o/s for the NACA-65 series but he calibrated it to give sufficiently accurate predictions for the other airfoil types used in the present study as well. Aungier's model is illustrated in Figure 6.8 for different values of the stagger angle γ .

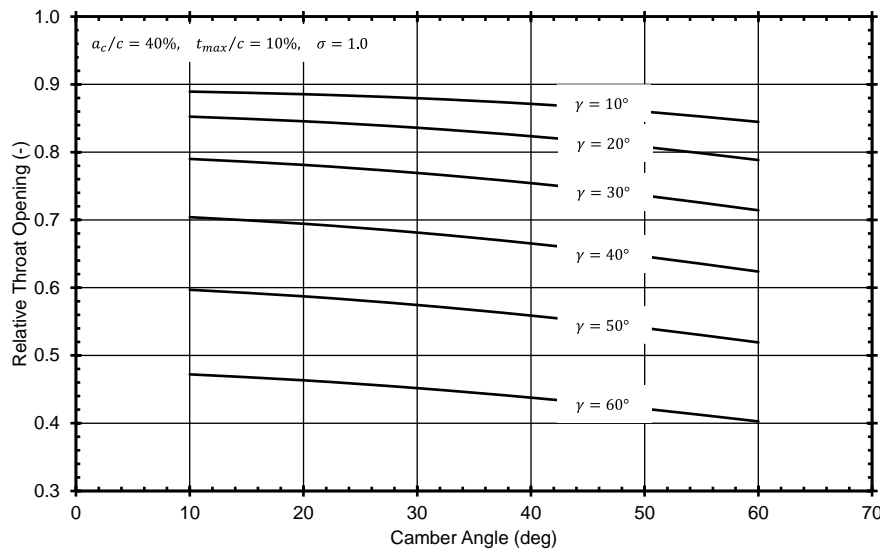


Figure 6.8: Throat opening model, Eq. (6.44), for different stagger angle values [adapted from Aungier (2013)].

The curves shown in Figure 6.8 are expressed analytically by:

$$\frac{o}{s} = s_m \left[\left(1 - \frac{t_{max}}{c} \sqrt{\sigma} \right) \cos \Phi \right]^{\sqrt{\sigma}} + s_a \quad (6.44)$$

where s_m and s_a are user-defined calibration scalars with default values of $s_m = 1$ and $s_a = 0$.

In Eq. (6.44), Φ is a stagger angle parameter which is given by:

$$\Phi = \gamma(1 - 0.05C_{l0}^{1.5}) + 5C_{l0}^{1.5} - 2 \quad (6.45)$$

The design lift coefficient, C_{l0} , is calculated in terms of the camber angle, θ , using the following correlation:

$$C_{l0} = \frac{1}{0.05515} \frac{a_c}{c} \tan \frac{|\theta|}{4} \quad (6.46)$$

Regarding the relative position of maximum camber (a_c/c), this can be a user-input or default values can be assigned to it [see Aungier (2003) and Banjac et al. (2014)]:

$$\frac{a_c}{c} = \begin{cases} 0.5, & \text{for NACA - 65} \\ 0.373, & \text{for NACA - 63 A}_4\text{K}_6 \\ 0.5, & \text{for BC4} \\ 0.5, & \text{for DCA} \end{cases}$$

Finally, from Figure 6.7 it is seen that the flow at the blade row inlet and outlet is characterized by a number of flow angles which are useful in establishing the blade row performance. The flow incidence angle (i), deviation angle (δ), and angle of attack (α), are correlated to the flow and metal angles by:

$$i = \beta_1 - \kappa_{LE} \quad (6.47)$$

$$\delta = \beta_2 - \kappa_{TE} \quad (6.48)$$

$$\alpha = \beta_1 - \gamma = i + \kappa_{LE} - \gamma \quad (6.49)$$

6.5 Design Incidence and Deviation Models

In the present section, models for design⁵³ incidence and design deviation are presented. These models are used in MLAC to establish the design flow angles at the inlet and outlet of blade rows of any type (rotating, stationary, and IGVs) and have primarily been adapted from Aungier (2003).

6.5.1 Design Incidence Angle and Angle of Attack

For modelling the incidence angle at design conditions two (2) models have been programmed in MLAC. These are Lieblein's and Herrig's models.

6.5.1.1 Lieblein's Model

Lieblein's model for estimating the design incidence angle is given by [see Aungier (2003)]:

$$i_d = s_m(K_{sh}K_{ti}i_{010} + n\theta) + s_a \quad (6.50)$$

⁵³The term "design" or "reference" conditions is used to describe the flow conditions (Mach number, Reynolds number, and flow angle) at the inlet of a blade row for which the row operates with minimum losses.

where s_m and s_a are user-specified calibration scalars with default values of $s_m = 1$ and $s_a = 0$.

In Eq. (6.50), K_{sh} is a correction factor accounting for camberline shape deviations from the traditional NACA-65 series. The default values of K_{sh} are given by:

$$K_{sh} = \begin{cases} 1.0, & \text{for NACA - 65} \\ 1.0, & \text{for NACA - 63 A}_4\text{K}_6 \\ 1.1, & \text{for BC4} \\ 0.7, & \text{for DCA} \end{cases} \quad (6.51)$$

Likewise, K_{ti} is a correction factor to account for blade thicknesses other than 10%. Aungier provides an analytical expression for calculating K_{ti} which was developed to match the experimental data presented by Lieblein [see Johnsen et al. (1965)]. This expression reads:

$$K_{ti} = \left(10 \frac{t_{max}}{c}\right)^q \quad (6.52)$$

where the exponent q is defined by:

$$q = \frac{0.288}{0.1 + \left(\frac{t_{max}}{c}\right)^{0.3}} \quad (6.53)$$

In Eq. (6.50), i_{010} is the design incidence angle for blades of zero camber, obtained by the following correlation:

$$i_{010} = \frac{(\beta_{1,d})^p}{5 + 46e^{-2.3\sigma}} - 0.1\sigma^3 \exp\left(\frac{\beta_{1,d} - 70}{4}\right) \quad (6.54)$$

where $\beta_{1,d}$ is the design flow angle at the blade row inlet, and the exponent p is given by:

$$p = 0.914 + \frac{\sigma^3}{160} \quad (6.55)$$

Finally, n is a slope factor expressed by:

$$n = 0.025\sigma - 0.06 - \frac{(\beta_{1,d}/90)^{1+1.2\sigma}}{1.5 + 0.43\sigma} \quad (6.56)$$

As one can observe, Lieblein's model requires the design flow angle, $\beta_{1,d}$, which is not known before the evaluation of Eqs (6.54) and (6.56) [and, ultimately of Eq. (6.50)]. Therefore, Lieblein's model is utilized in an iterative scheme in the following sense. First, a value for the design incidence angle is assumed (typically, a zero or a very small negative value), let i'_d . A value for $\beta_{1,d}$ is then obtained using Eq. (6.47). Next, Lieblein's model is used to estimate a new value for the design incidence angle (i_d) by replacing the known value of $\beta_{1,d}$ in Eqs (6.54) and (6.56). The aforementioned procedure is

repeated until the two incidence angles are matched within a user-specified tolerance, that is, $|i'_d - i_d| \leq \varepsilon$. At the end of this procedure, $\beta_{1,d}$ is also obtained.

6.5.1.2 Herrig's Model

For estimating the design angle of attack, Herrig formulated the model expressed by [see Aungier (2003)]:

$$\alpha_d = s_m \left\{ \left[3.6K_{sh}K_{ti} + 0.3532\theta \left(\frac{a_c}{c} \right)^{0.25} \right] \sigma^{0.65-0.002\theta} \right\} + s_a \quad (6.57)$$

where s_m and s_a are user-specified calibration scalars with default values of $s_m = 1$ and $s_a = 0$ for both models.

Contrary to Lieblein's model, Herrig's model gives the angle of attack instead of the incidence angle. However, having obtain α_d from Eq. (6.57), i_d is established from Eq. (6.49).

Finally, in Eq. (6.57) K_{sh} and K_{ti} are the same as in Lieblein's model and are obtained by using Eq. (6.51) and Eq. (6.52), respectively.

6.5.2 Design Deviation Angle

For modelling the design deviation angle, two (2) models have been programmed in MLAC: Lieblein's and Howell's models. These are presented next.

6.5.2.1 Lieblein's Model

Lieblein's model for estimating the design deviation angle is given by [see Aungier (2003)]:

$$\delta_d = s_m(K_{sh}K_{t\delta}\delta_{010} + m\theta) + s_a \quad (6.58)$$

where the factor K_{sh} is given by Eq. (6.51), and s_m and s_a are user-specified calibration scalars with default values of $s_m = 1$ and $s_a = 0$.

In Eq. (6.58), δ_{010} is the design deviation angle for zero camber blades and is expressed by:

$$\delta_{010} = 0.01\sigma\beta_{1,d} + (0.74\sigma^{1.9} + 3\sigma) \left(\frac{\beta_{1,d}}{90} \right)^{1.67+1.09\sigma} \quad (6.59)$$

Similarly to the K_{ti} correction for the design incidence models described in the preceding paragraph, $K_{t\delta}$ is a correction factor for blade thicknesses other than 10%. This is obtained by the polynomial:

$$K_{t\delta} = 6.25 \frac{t_{max}}{c} + 37.5 \left(\frac{t_{max}}{c} \right)^2 \quad (6.60)$$

Finally, m is a slope factor given by:

$$m = \frac{m_{1.0}}{\sigma^b} \quad (6.61)$$

where the slope $m_{1,0}$ and the exponent b are given by the polynomials expressed by:

$$m_{1,0} = \begin{cases} 0.17 - 0.0333x + 0.333x^2, & \text{for NACA - 65} \\ 0.249 + 0.074x - 0.132x^2 + 0.316x^3, & \text{for DCA, BC4} \end{cases} \quad (6.62)$$

$$b = 0.9625 - 0.17x - 0.85x^3 \quad (6.63)$$

In the above, x is defined as: $x = \beta_{1,d}/100$.

6.5.2.2 Howell's Model

Howell's model is given by [see Aungier (2003)]:

$$\delta_d = s_m \left[\frac{0.92(a_c/c)^2 + 0.002\kappa_{TE} \theta}{1 - 0.02\theta/\sqrt{\sigma}} \frac{\theta}{\sqrt{\sigma}} + (K_{sh}K_{t\delta} - 1)\delta_{010} \right] + s_a \quad (6.64)$$

where s_m and s_a are user-specified calibration scalars with default values of $s_m = 1$ and $s_a = 0$, and K_{sh} , $K_{t\delta}$, and δ_{010} are obtained by Eqs (6.51), (6.60), and (6.59), respectively.

Note that, having established the design deviation angle using either the model described by Eq. (6.58) or the one described by Eq. (6.64), then the design flow angle at the blade row exit, $\beta_{2,d}$, is obtained using Eq. (6.48).

6.6 Aerodynamic Performance of Diffusing Rows

In MLAC, the aerodynamic performance of diffusing rows⁵⁴ is modelled using diffusion factors. Diffusion factors express the loading limit before the boundary layer over a blade separates, thus leading to an abrupt increase in losses. In other words, diffusion factors express the maximum deceleration a flow over a blade can withstand or, equivalently, the maximum pressure rise a blade can achieve without stalling. Historically, the diffusion factors have been used as correlating parameters in developing semi-empirical expressions for loss and deviation⁵⁵. In MLAC, two (2) diffusion factors are employed: the so-called "D-factor" (DF)⁵⁶ and the equivalent diffusion factor (DF_{eq}), both formulated by Lieblein in the 1950's. Next, the correlations used in MLAC for estimating DF and DF_{eq} are presented.

The diffusion factor, DF , is obtained by:

$$DF = 1 - \frac{W_{x,2} \cos \beta_1}{W_{x,1} \cos \beta_2} + \frac{1}{2\sigma} \left(\sin \beta_1 - \frac{W_{x,2}}{W_{x,1}} \cos \beta_1 \tan \beta_2 \right) \quad (6.65)$$

The equivalent diffusion factor, DF_{eq} , is calculated by:

⁵⁴The term "diffusing rows" is used to distinguish the blades of a compressor decelerating the flow, from IGVs that operate like turbine NGVs accelerating the flow.

⁵⁵For a more detailed presentation, see Aungier (2003).

⁵⁶Hereafter, it will simply be called "diffusion factor".

$$DF_{eq} = \frac{W_{max} \cos \beta_2 W_{x,1}}{W_1 \cos \beta_1 W_{x,2}} \quad (6.66)$$

The ratio of the maximum velocity over the airfoil-to-the inlet velocity, W_{max}/W_1 , is calculated by:

$$\frac{W_{max}}{W_1} = s_a + s_{m,1} \frac{\cos^2 \beta_1}{\sigma} \left(\tan a_1 - \frac{R_{m,2} W_{x,2}}{R_{m,1} W_{x,1}} \tan a_2 \right) + K_a s_{m,2} |i - i_d|^{s_{m,3}} \quad (6.67)$$

where s_a , $s_{m,1}$, and $s_{m,2}$ are user-defined calibration scalars with default values:

$$s_a = 1.12, \quad s_{m,1} = 0.61, \quad s_{m,2} = 1.0, \quad s_{m,3} = 1.43$$

and K_a is given by:

$$K_a = \begin{cases} 0.0117, & \text{for NACA - 65} \\ 0.007, & \text{for BC4, DCA} \end{cases} \quad (6.68)$$

Note that, Eq. (6.67) can also be used to compute the design value of W_{max}/W_1 [and, thus, the design value of DF_{eq} by replacing it in Eq. (6.66)] if one sets $i = i_d$ and replaces the flow angles with the design ones.

6.7 Off-Design Deviation Angle Models

In the present section, models for the calculation of the off-design deviation are presented. These are used to estimate the flow angle at the exit of the blade rows when they operate at off-design conditions. Models are given for both diffusing rows (rotating and stationary) and IGVs.

6.7.1 Deviation Angle Models for Diffusing Rows

For modelling the off-design deviation angle (δ) for diffusing rows, two (2) approaches have been programmed in MLAC. These are described in the following.

6.7.1.1 Lieblein's Model

The first one presented is the model developed by Lieblein and modified according to Cumpsty (1989) for taking into account the flow density changes across the row. This model is expressed by [see Aungier (2003)]:

$$\delta = \delta_d + s_{m,1} \left(\frac{\partial \delta}{\partial i} \right)_d (i - i_d) + s_{m,2} (1 - AVDR) \quad (6.69)$$

where $s_{m,1}$ and $s_{m,2}$ are user-defined scalar multipliers for calibrating Eq. (6.69), with default values:

$$s_{m,1} = 1.0, \quad s_{m,2} = 10.0$$

In Eq. (6.69), AVDR is the axial velocity-density ratio defined by:

$$\text{AVDR} = \frac{\rho_2^s W_{x,2}}{\rho_1^s W_{x,1}} \quad (6.70)$$

Finally, the off-design slope, $(\partial\delta/\partial i)_d$, is given by:

$$\left(\frac{\partial\delta}{\partial i}\right)_d = \begin{cases} 0, & \text{for IGVs} \\ \frac{1 + (\sigma + 0.25\sigma^4)(\beta_{1,d}/53)^{2.5}}{\exp(3.1\sigma)}, & \text{for other blade types} \end{cases} \quad (6.71)$$

The above analytical expression was formulated by Aungier for matching the experimental data presented by Lieblein [see Johnsen et al. (1965)].

6.7.1.2 Swan's Model

The second model available in MLAC for estimating the off-design deviation angle for diffusing rows, is the one presented by Swan (1961). This is given by:

$$\delta = \delta_d + [s_{m,1} + s_{m,2}(M_{r,1} - 0.6)](DF_{eq} - DF_{eq,d}) \quad (6.72)$$

where $s_{m,1}$ and $s_{m,2}$ are user-defined calibration scalars with default values:

$$s_{m,1} = 6.40, \quad s_{m,2} = -9.45$$

Note that, in Eq. (6.72) appears the equivalent diffusion factor (both in design and off-design conditions). Having established the design flow conditions, this means that the evaluation of Eq. (6.72) requires the knowledge of β_2 at off-design conditions. Therefore, in a mean-line calculation, Swan's model is always evaluated iteratively in the following sense. First, a value for the off-design deviation angle is assumed (typically, it is set equal to the design value established beforehand), let δ' . A value for β_2 is then obtained by Eq. (6.48) allowing, in turn, the calculation of the off-design DF_{eq} using Eq. (6.66). This value of DF_{eq} is finally used in Eq. (6.72) to establish a new value for the off-design deviation angle δ . This procedure is repeated until the two deviation angles are matched within a user-specified tolerance, that is, $|\delta' - \delta| \leq \varepsilon$. At the end of this procedure, β_2 is also obtained.

6.7.2 Deviation Angle Model for IGVs

For IGVs modelled by equivalent circular-arc NACA-65, or equivalent parabolic-arc NACA-63 A4K6 profiles, Banjac et al. (2014) formulated the following equation for estimating the off-design deviation angle:

$$\delta = \delta_{ref} + \Delta\delta_t + \Delta\delta_\gamma + \Delta\delta_{\text{AVDR}} \quad (6.73)$$

In the above, δ_{ref} is a reference deviation angle, $\Delta\delta_t$ is a correction for IGVs with different thicknesses than reference, $\Delta\delta_\gamma$ is a correction for stagger angle changes from reference, and $\Delta\delta_{\text{AVDR}}$ is a correction accounting for the axial velocity-density ratio. Each term in Eq. (6.73) was formulated by Banjac et al. for matching CFD simulation

results produced for the flow past cascades of different solidities, cambers, thicknesses, and staggers, and exposed to different inlet Mach numbers. Next, the respective equations for calculating each term in Eq. (6.73) are given. Note that, in all equations that follow, the camber angle and the inlet Mach number are limited by:

$$\theta = \max(0, \theta), \quad M_1 = \max(0.2, M_1)$$

The reference deviation angle, δ_{ref} , is given by:

$$\delta_{ref} = (s_{m,1} + s_{m,2}\sigma + s_{m,3}M_1)\theta^{s_{m,4}+s_{m,5}\sigma+s_{m,6}M_1} \quad (6.74)$$

where $s_{m,1}$, $s_{m,2}$, $s_{m,3}$, $s_{m,4}$, $s_{m,5}$, and $s_{m,6}$ are user-defined calibration scalars with default values according to Table 6.1.

Table 6.1: Calibration scalars for Banjac et al.'s deviation angle model for the reference deviation angle equation [adapted from Banjac et al. (2014)]

Scalar	NACA-65	NACA-63 A ₄ K ₆
$s_{m,1}$	0.401695	0.1002060
$s_{m,2}$	-0.081487	-0.0443672
$s_{m,3}$	-0.408090	-0.0675766
$s_{m,4}$	1.101494	1.3524830
$s_{m,5}$	-0.244558	-0.2510492
$s_{m,6}$	0.440575	0.1684732

The correction for thickness, $\Delta\delta_t$, is calculated according to:

$$\Delta\delta_t = \begin{cases} (s_{m,1} + s_{m,2}\sigma) \left(0.1 - \frac{t_{max}}{c}\right) \frac{\theta}{40} (s_{m,3}M_1 + s_{m,4}), & \text{for NACA - 65} \\ (s_{m,1} + s_{m,2}\sigma) \left(0.06 - \frac{t_{max}}{c}\right) \frac{\theta}{56} (s_{m,3}M_1 + s_{m,4}), & \text{for NACA - 63 A}_4\text{K}_6 \end{cases} \quad (6.75)$$

where $s_{m,1}$, $s_{m,2}$, $s_{m,3}$, and $s_{m,4}$ are user-defined calibration scalars with default values as shown in Table 6.2.

Table 6.2: Calibration scalars for Banjac et al.'s deviation angle model for the thickness correction equation [adapted from Banjac et al. (2014)]

Scalar	NACA-65	NACA-63 A ₄ K ₆
$s_{m,1}$	3.0	4.7
$s_{m,2}$	9.44	12.55
$s_{m,3}$	2.0	2.2
$s_{m,4}$	0.6	0.56

The correction for the stagger angle change, $\Delta\delta_\gamma$, is expressed by:

$$\Delta\delta_\gamma = [s_{m,1} + s_{m,2}\theta^2 + s_{m,3}\sigma + s_{m,4}\sigma^2 + s_{m,5}\theta(\Delta\gamma)^{s_{m,6}}]\Delta\gamma \quad (6.76)$$

where $\Delta\gamma$ is the stagger angle change from reference:

$$\Delta\gamma = \gamma - \gamma_{ref}$$

In Eq. (6.76), $s_{m,1}$, $s_{m,2}$, $s_{m,3}$, $s_{m,4}$, $s_{m,5}$, and $s_{m,6}$ are user-defined calibration scalars with default values according to Table 6.3.

Table 6.3: Calibration scalars for Banjac et al.'s deviation angle model for the stagger angle correction equation [adapted from Banjac et al. (2014)]

Scalar	$\Delta\gamma \leq 0$	$\Delta\gamma > 0$
$s_{m,1}$	0.205450	0.272548
$s_{m,2}$	2.9165×10^{-5}	3.7159×10^{-5}
$s_{m,3}$	-0.313651	-0.411102
$s_{m,4}$	0.090360	0.126291
$s_{m,5}$	0.0	7.6708×10^{-8}
$s_{m,6}$	0.0	2.630323

Finally, the correction for the axial velocity-density ratio, $\Delta\delta_{AVDR}$, is calculated using the following expression:

$$\Delta\delta_{AVDR} = s_{m,1}(1 - AVDR) \quad (6.77)$$

where AVDR is given by Eq. (6.70), and $s_{m,1}$ is a user-specified calibration scalar with default value equal to $s_{m,1} = 10.0$.

6.8 Loss Models for Diffusing Rows

In the present section, the models used in MLAC for calculating the losses across diffusing rows are presented. By default, the overall loss across a row is split into the following loss sources:

- Endwall losses
- Secondary losses
- Clearance losses
- Shock losses
- Reynolds number effects
- Mach number effects
- Profile losses

The overall loss coefficient of a row, ω , is thus obtained by summing up the above losses according to:

$$\omega = \omega_{ew} + \omega_{sc} + \omega_{sh} + \omega_{cl} + \omega_{pr} \quad (6.78)$$

where ω_{ew} , ω_{sc} , ω_{sh} , ω_{cl} , and ω_{pr} is the endwall, secondary, shock, clearance, and profile loss, respectively. Profile losses (ω_{pr}) are also corrected for Reynolds and Mach number effects.

Note that MLAC is fully customizable. The user can enable or disable any of the above loss sources (or all of them, in which case $\omega = 0$), or to even use different loss splits by introducing user-defined loss correlations (e.g., obtained by CFD simulations). Next, the equations used to describe the individual loss sources appearing in Eq. (6.78) are presented. The equations were primarily adapted by Aungier (2003), but models from other open source references have also been programmed in MLAC.

6.8.1 Equivalent Drag Coefficient Loss

Some of the traditional loss models used in MLAC have been formulated based on the inviscid flow theory past airfoils and are expressed in terms of equivalent drag and/or lift coefficients. To transform an equivalent drag coefficient (C_D) to the corresponding total pressure loss coefficient (ω), the following equation is used [see Aungier (2003)]:

$$\omega = C_D \sigma \frac{\cos^2 \beta_1}{\cos^3 \bar{\beta}} \quad (6.79)$$

where $\bar{\beta}$ is a “mean” flow angle given by:

$$\bar{\beta} = \tan^{-1} \left[\frac{1}{2} (\tan \beta_1 + \tan \beta_2) \right] \quad (6.80)$$

Finally, the lift coefficient that also appears in some models is given by:

$$C_L = 2 \cos \bar{\beta} \frac{\tan \beta_1 - \tan \beta_2}{\sigma} \quad (6.81)$$

6.8.2 Endwall Loss Models

Endwall losses are due to the boundary layers that develop over the compressor annulus walls. In MLAC, there are two (2) models that can be used to estimate endwall losses. The equations are presented next.

6.8.2.1 Howell’s Model

Howell used the inviscid airfoil theory to express endwall losses in terms of an equivalent drag coefficient. Howell’s model is given by [see Aungier (2003)]:

$$C_{D,ew} = s_m \frac{s}{\bar{h}_b} = s_m \frac{1}{\sigma AR} \quad (6.82)$$

where s_m is a user-specified calibration scalar with a default value of $s_m = 0.02$.

6.8.2.2 Vavra's Model

Similarly to Howell's model, Vavra also formulated an endwall loss model based on the inviscid airfoil theory. This model is given by [see Vavra (1974)]:

$$C_{D,ew} = s_m \frac{c}{h_b} = s_m \frac{1}{AR} \quad (6.83)$$

where s_m is a user-defined calibration scalar with a default value of $s_m = 0.018$.

6.8.3 Secondary Loss Models

Secondary losses are due to flow phenomena developing along the blade span and are associated with the 3D nature of the flow. Secondary losses typically include all loss sources that cannot be classified as endwall or profile losses. In MLAC, there are two (2) models that can be used to estimate secondary losses. The equations of these models are given next.

6.8.3.1 Howell's Model

Similarly to the endwall loss model, Howell developed a model for secondary losses utilizing the inviscid flow theory. Secondary losses are estimated according to [see Aungier (2003)]:

$$C_{D,sc} = s_m C_L^2 \quad (6.84)$$

where C_L is calculated from Eq. (6.81), and s_m is a user-defined calibration scalar with a default value of $s_m = 0.018$.

6.8.3.2 Vavra's Model

Vavra's model for secondary losses also relies on the inviscid flow theory around airfoils. This is given by [see Vavra (1974)]:

$$C_{D,sc} = s_{m,1} C_L^2 \sigma \frac{s}{h_b} + s_{m,2} C_L^2 \sigma \frac{\delta_c}{h_b} \frac{1}{\cos \beta_2} \quad (6.85)$$

where $s_{m,1}$ and $s_{m,2}$ are user-defined calibration scalars with default values of:

$$s_{m,1} = 0.04, \quad s_{m,2} = 0.25$$

As stated by Vavra [and as it can be seen, intuitively, from Eq. (6.85)], Vavra's model presumably accounts for clearance losses too [due to the presence of the radial clearance gap, δ_c , in the second RHS term of Eq. (6.85)]. Theoretically, by zeroing one of the two scalar values, $s_{m,1}$ or $s_{m,2}$, one can estimate any of the secondary or clearance loss parts.

6.8.4 Clearance Loss Model

Clearance losses arise due to the flow around the tip clearance in rotors, and hub clearance in stators. For estimating the clearance loss in MLAC, the model by Lakshminarayana is used. This, similarly to the endwall and secondary loss models,

was also formulated using the inviscid flow theory around airfoils. This model is described by [see Lakshminarayana (1970)]:

$$C_{D,cl} = s_m \frac{C_L^2 \delta_c}{AR s} \quad (6.86)$$

where s_m is a user-defined calibration scalar with a default value of $s_m = 0.7$.

6.8.5 Shock Loss Models

Shock losses appear due to supersonic flow phenomena at the blade row inlet and are related to the development of shock waves in front of the blade row. For calculating shock losses, Steinke et al.'s model [see Steinke et al. (1967)] is primarily utilized in MLAC, but Dixon's model expressed by Eq. (3.89) is also available.

For relative Mach numbers at the row inlet greater or equal to one ($M_{r,1} \geq 1$), shock losses are calculated from:

$$\omega_{sh} = \frac{1 - \left[\frac{(\gamma + 1)\bar{M}_{r,1}^2}{2 + (\gamma - 1)\bar{M}_{r,1}^2} \right]^{\gamma/(\gamma-1)} \left(\frac{\gamma + 1}{1 - \gamma + 2\gamma\bar{M}_{r,1}^2} \right)^{1/(\gamma-1)}}{1 - \left(1 + \frac{\gamma - 1}{2} M_{r,1}^2 \right)^{\gamma/(1-\gamma)}} \quad (6.87)$$

where $\bar{M}_{r,1}$ is given by:

$$\bar{M}_{r,1} = \frac{M_{r,1} + M_{ss}}{2} \quad (6.88)$$

In the above, M_{ss} is the peak Mach number appearing at the blade suction surface. For calculating M_{ss} , Steinke et al. assumed that along the blade suction surface, supersonic turning occurs by means of a Prandtl-Meyer expansion fan. The amount of supersonic turning ($\Delta\nu$) is, in turn, assumed to be proportional to the flow turning ($\Delta\beta = \beta_1 - \beta_2$) and inversely proportional to the row solidity, that is:

$$\Delta\nu = \frac{0.625\Delta\beta}{\sigma} \quad (6.89)$$

As stated by Steinke et al., Eq. (6.89) is an approximation that eliminates the need to know the exact blade geometry for estimating $\Delta\nu$. Thus, the calculation procedure is simplified. Finally, M_{ss} is calculated by:

$$M_{ss} = 1.095 + 0.03395\Delta\nu + 1.086(M_{r,1} - 1)^{1.372} \quad (6.90)$$

which is an approximation of the Prandtl-Meyer function.

If, otherwise, the relative Mach number at the row inlet is less than one ($M_{r,1} < 1$), then a pseudo-peak suction surface Mach number (M'_{ss}) is calculated first given by:

$$M'_{ss} = 1.095 + 0.03395\Delta\nu \quad (6.91)$$

Then, an average Mach number, $\bar{M}_{r,1}$, is calculated using Eq. (6.88), where $M_{r,1}$ is the actual Mach number at the row inlet and $M_{ss} = M'_{ss}$. Shock losses are then calculated from:

$$\omega_{sh} = \begin{cases} \frac{1 - \left[\frac{(\gamma + 1)\bar{M}_{r,1}^2}{2 + (\gamma - 1)\bar{M}_{r,1}^2} \right]^{\gamma/(\gamma-1)} \left(\frac{\gamma + 1}{1 - \gamma + 2\gamma\bar{M}_{r,1}^2} \right)^{1/(\gamma-1)}}{1 - \left(1 + \frac{\gamma - 1}{2} \right)^{\gamma/(1-\gamma)}}, & \bar{M}_{r,1} \geq 1 \\ 0, & \bar{M}_{r,1} < 1 \end{cases} \quad (6.92)$$

In Eq. (6.87), $M_{r,1} = 1$ was used.

6.8.6 Reynolds Number Effects

Reynold's number effects, when activated, are used to correct the profile loss coefficient for different flow Reynolds numbers in the sense:

$$(\Omega_{pr,d})_{Re} = s_{m,Re}(\Omega_{pr,d} + s_{a,Re}) \quad (6.93)$$

where $\Omega_{pr,d}$ is the profile total pressure loss parameter at design conditions (see paragraph 6.8.7), and $s_{m,Re}$ and $s_{a,Re}$ is a Reynolds number correction multiplier and adder, respectively. For estimating $s_{a,Re}$ the model developed by Aungier (2003) is used, while for calculating $s_{m,Re}$ the models by Wright et al. (1991) and Koch et al. (1976) are available. These models are described next.

6.8.6.1 Aungier's Model

The Reynolds number correction, $s_{a,Re}$, is expressed by:

$$s_{a,Re} = s_m \begin{cases} \sqrt{\frac{Re_{ref}}{Re_c}} - 1, & Re_c \leq Re_{ref} \\ \left(\frac{\log_{10} Re_{ref}}{\log_{10} Re_c} \right)^{2.58} - 1, & Re_c > Re_{ref} \end{cases} \quad (6.94)$$

where s_m is a user-specified calibration scalar with a default value of $s_m = 0.04$, and $Re_{ref} = 2.5 \times 10^5$ is a reference Reynolds number.

In Eq. (6.94), Re_c is the flow Reynolds number based on the blade chord and the row inlet flow conditions and is given by:

$$Re_c = \frac{\rho_1^s W_1 c}{\mu_1^s} \quad (6.95)$$

6.8.6.2 Wright et al.'s Model

Wright et al.'s model is an approximation to Koch et al.'s chart [see Koch et al. (1976)] for skin roughness corrections. The Reynolds number correction, $s_{m,Re}$, is calculated by:

$$s_{m,Re} = \begin{cases} 489.8Re_c^{-0.5} & Re_c \leq 1.0 \times 10^5 \\ 13.8Re_c^{-0.19}, & Re_c \leq 1.0 \times 10^6 \\ 1.0, & Re_c > 1.0 \times 10^6 \end{cases} \quad (6.96)$$

where Re_c is given by Eq. (6.95).

6.8.6.3 Koch et al.'s Model

At high chordwise Reynolds numbers (Re_c), the boundary layer characteristics over the blade do not change with varying Reynolds number but depend only on the value of the blade relative roughness (k_s/c) [see Koch et al. (1976)]. Koch et al. used this observation (emanating from the turbulent boundary layer theory) to construct a Moody-type graph to express the variation of the wake momentum thickness in terms of the blade relative roughness and the chordwise Reynolds number. This graph is given in a functional form by:

$$s_{m,Re} = f\left(Re_c, \frac{k_s}{c}\right) \quad (6.97)$$

where k_s is the blade surface equivalent sand-grain roughness. The latter is correlated to the roughness arithmetical average, k_{CLA} , through the following expression [see Koch et al. (1976)]:

$$k_s = 6.2k_{CLA}$$

Note that, Eq. (6.97) represents the graph shown in Figure 6.9, which was digitized, smoothed, and introduced in MLAC in a PROOSIS 2D table format.

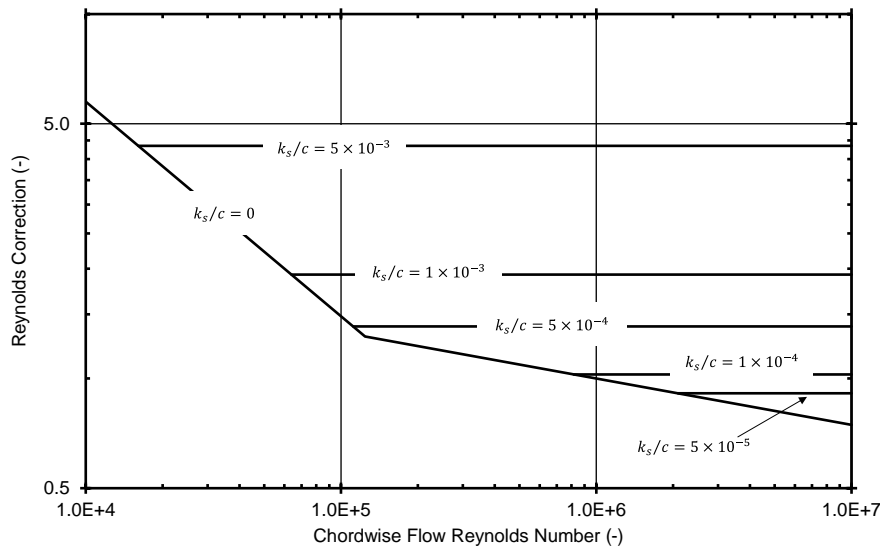


Figure 6.9: Koch et al.'s profile loss Reynolds number correction model [adapted from Koch et al. (1976)].

6.8.7 Design Profile Loss Models

Profile losses are associated with the boundary layer development over the blade. Traditional profile loss models correlate profile losses to the wake momentum thickness which, in turn, was correlated to a diffusion factor [see, e.g., Johnsen et al.

(1965)]. For models correlating profile losses to the diffusion factor, DF , the total pressure loss coefficient (ω) is obtained from the total pressure loss parameter (Ω) using [see Aungier (2003)]:

$$\omega_{pr} = \frac{2\Omega_{pr}\sigma}{\cos\beta_2} \quad (6.98)$$

For models correlating profile losses to the equivalent diffusion factor, DF_{eq} , ω is obtained from Ω using [see Aungier (2003)]:

$$\omega_{pr} = \frac{2\Omega_{pr}\sigma}{\cos\beta_2} \left(\frac{W_{x,2} \cos\beta_1}{W_{x,1} \cos\beta_2} \right)^2 \quad (6.99)$$

Next, two (2) models for obtaining the profile total pressure loss parameter at design conditions ($\Omega_{pr,d}$) are presented. Both models were adapted from Aungier (2003) who, in turn, developed analytical equations for approximating experimental data from 2D cascade tests conducted by Lieblein in the early 1950's [see Johnsen et al. (1965)].

6.8.7.1 $\Omega_{pr} = f(DF)$ Model

The first model presented here correlates the design total pressure loss parameter ($\Omega_{pr,d}$) with the design diffusion factor (DF_d):

$$\Omega_{pr,d} = s_{m,1} \sum_{k=2}^6 s_{m,k} (DF_d)^{k-2} \quad (6.100)$$

In the above, s_m 's are user-defined calibration scalars with default values:

$$\begin{aligned} s_{m,1} &= 0.0035, & s_{m,2} &= 1.0, & s_{m,3} &= 3.5, \\ s_{m,4} &= 0.0, & s_{m,5} &= 0.0, & s_{m,6} &= 37.0 \end{aligned}$$

According to Aungier, Eq. (6.100) presumably accounts for secondary losses too. Finally, the design total pressure loss coefficient, $\omega_{pr,d}$, is obtained by replacing $\Omega_{pr,d}$ into Eq. (6.98).

6.8.7.2 $\Omega_{pr} = f(DF_{eq})$ Model

The second model available in MLAC correlates $\Omega_{pr,d}$ with the design equivalent diffusion factor ($DF_{eq,d}$), and accounts for the Reynolds number corrections introduced in paragraph 6.8.6 [see Eq. (6.93)]. This model is described by:

$$\Omega_{pr,d} = s_{m,Re} \left[s_{m,1} \sum_{k=2}^{10} s_{m,k} (DF_{eq,d} - 1)^{k-2} + s_{a,Re} \right] \quad (6.101)$$

where the s_m 's are user-defined calibration scalars with default values:

$$\begin{aligned} s_{m,1} &= 0.004, & s_{m,2} &= 1.0, & s_{m,3} &= 0.0, & s_{m,4} &= 3.1, & s_{m,5} &= 0.0, \\ s_{m,6} &= 0.0, & s_{m,7} &= 0.0, & s_{m,8} &= 0.0, & s_{m,9} &= 0.0, & s_{m,10} &= 0.4 \end{aligned}$$

Finally, the design total pressure loss coefficient, $\omega_{pr,d}$, is obtained by replacing $\Omega_{pr,d}$ into Eq. (6.99).

6.8.8 Mach Number Effects

The profile loss models presented in the preceding paragraph were developed based on cascade tests conducted in the early 1950's in subsonic wing tunnels where the flow Mach number was no greater than ~ 0.2 . In current technology compressors, the flow is transonic with regions of supersonic flow near the tip of rotor blades. Compressibility effects that physically arise in high Mach number flows tend not only to increase losses (due to, e.g., the formation of shock waves) but, most importantly, to narrow significantly the high-efficiency operating range of blades (Figure 6.10).

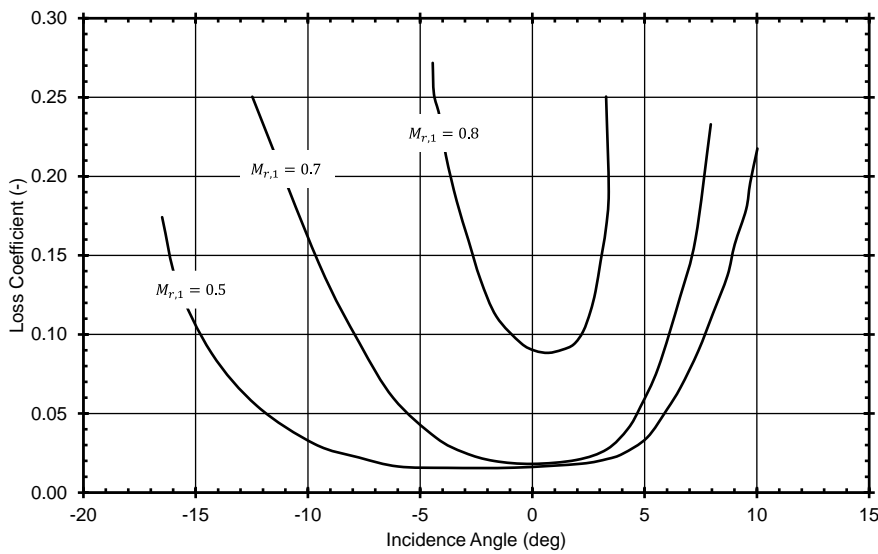


Figure 6.10: Example effect of Mach number on losses [adapted from Saravanamuttoo et al. (2017)].

Following the previous discussion, it is evident that the models described in the preceding paragraphs should be corrected to account for compressibility effects. For this reason, in MLAC the methodology developed and proposed by Aungier (2003) is implemented as described next.

First, negative (R_c) and positive (R_s) stall ranges are calculated according to:

$$R_c = i_d - i_c = \begin{cases} -9 + \left[1 - \left(\frac{30}{\beta_{1,c}} \right)^{0.48} \right] \frac{\theta}{4.176}, & \text{for DCA, BC4, NACA - 65} \\ -10^\circ, & \text{for NACA - 63 A}_4\text{K}_6 \end{cases} \quad (6.102)$$

$$R_s = i_s - i_d = \begin{cases} 10.3 + \left(2.92 - \frac{\beta_{1,s}}{15.6} \right) \frac{\theta}{8.2}, & \text{for DCA, BC4, NACA - 65} \\ +10^\circ, & \text{for NACA - 63 A}_4\text{K}_6 \end{cases} \quad (6.103)$$

These expressions were developed by Aungier to match the experimental observations made by Herrig et al. (1957).

For known blade geometry (θ and κ_{LE}), Eq. (6.103) is solved analytically to obtain the (uncorrected for Mach number effects) positive incidence angle, i_s , by also utilizing the fact that $\beta_{1,s}$ is expressed in terms of i_s and κ_{LE} using Eq. (6.47).

On the other hand, Eq. (6.102) is solved iteratively to obtain the (uncorrected for Mach number effects) negative incidence angle, i_c , in the following sense. First, a value for i_c is assumed (typically is set equal to i_d which is known beforehand), let i'_c . This value for i_c is then replaced into Eq. (6.47) to give a value for the angle $\beta_{1,c}$. The (now) known negative stall inlet flow angle ($\beta_{1,c}$) is then used in Eq. (6.102) to obtain a new value for i_c . The aforementioned procedure is repeated until the two incidence angles, i'_c and i_c , are matched within a user-specified tolerance: $|i'_c - i_c| \leq \varepsilon$. For numerical stability reasons, in the above procedure the constraint,

$$\beta_{1,c} = \max(\beta_{1,c}, 20^\circ)$$

was adopted in MLAC [see Aungier (2003)].

After the uncorrected for Mach number effects negative and positive stall incidence angles are obtained as described above, the corrected for Mach number effects (subscript “Ma”) values for i_c and i_s are estimated by applying the following equations:

$$i_{c, \text{Ma}} = i_d - \frac{R_c}{1 + \sum_{k=1}^3 s_{m,k} M_{r,1}^k} \quad (6.104)$$

$$i_{s, \text{Ma}} = i_d + \frac{R_s}{1 + \sum_{k=1}^3 s_{m,k} (K_{sh} M_{r,1})^k} \quad (6.105)$$

where $s_{m,1}$, $s_{m,2}$, and $s_{m,3}$ are user-defined calibration scalars with default values:

$$s_{m,1} = 0.0, \quad s_{m,2} = 0.0, \quad s_{m,3} = 0.5$$

which apply to both Eq. (6.104) and Eq. (6.105). K_{sh} is the blade profile shape correction factor [see Eq. (6.51)] for which:

$$K_{sh} = \min(K_{sh}, 1)$$

The negative stall incidence angle ($i_{c, \text{Ma}}$) is bounded according to [see Aungier (2003)]:

$$i_{c, \text{Ma}} = \max(i_{c, \text{Ma}}, \beta_1^* - \kappa_{LE} + 1^\circ) \quad (6.106)$$

where the flow angle β_1^* is obtained from mass continuity across the row throat:

$$\cos \beta_1^* = \frac{o \rho_1^{s*} W_1^*}{s \rho_1^s W_1} \quad (6.107)$$

In Eq. (6.107), the sonic gas density and velocity, ρ_1^{s*} and W_1^* , respectively, are obtained using a dedicated PROOSIS built-in thermodynamic function which establishes the sonic (for $M_r = 1$) static conditions for given total temperature (T_r^0), total pressure (p_r^0), and flow angle (β).

After having established the corrected for Mach number effects negative and positive incidence angle, $i_{c, Ma}$ and $i_{s, Ma}$, respectively, the minimum loss incidence angle ($i_{min, Ma}$) is obtained from:

$$i_{min, Ma} = s_{m,1} i_{c, Ma} + s_{m,2} (i_{s, Ma} - i_{c, Ma}) \frac{R_c}{R_c + R_s} \quad (6.108)$$

where $s_{m,1}$ and $s_{m,2}$ are user-defined calibration scalars with default values equal to one. Note that, as it can be seen from Eq. (6.108), if no Mach number corrections are applied then the minimum loss incidence angle is equal to the design incidence angle ($i_{min} = i_d$).

Finally, the design profile loss coefficient ($\omega_{pr,d}$) is corrected for Mach number effects to give a minimum loss coefficient ($\omega_{pr,min}$):

$$\omega_{pr,min} = s_{m, Ma} \omega_{pr,d} + s_{a, Ma} \quad (6.109)$$

where $s_{m, Ma}$ and $s_{a, Ma}$ is a Mach number correction multiplier and adder, respectively.

The Mach number correction multiplier, $s_{m, Ma}$, is calculated irrespective of the value of the flow Mach number at the blade row inlet [see Aungier (2003)], and is given by:

$$s_{m, Ma} = s_{m,1} \left[1 + s_{m,2} \frac{(i_{min, Ma} - i_d)^2}{R_s^2} \right] \quad (6.110)$$

where $s_{m,1}$ and $s_{m,2}$ are user-specified calibration scalars with default values equal to one.

The Mach number correction adder, $s_{a, Ma}$, depends on the row inlet Mach number and is obtained from:

$$s_{a, Ma} = \begin{cases} s_m K_{sh} \left[\left(\frac{M_{r,1}}{M^*} - 1 \right) \frac{W_1^*}{W_1} \right]^2, & M_{r,1} \geq M^* \\ 0, & M_{r,1} < M^* \end{cases} \quad (6.111)$$

where s_m is a user-defined calibration scalar with default value of unity. In the above, M^* is a critical Mach number obtained from:

$$M^* = s_m M_{r,1} \frac{W_1^*}{W_1} \frac{W_1}{W_{max}} \quad (6.112)$$

with s_m being a user-defined calibration scalar (default value equal to one). The ratio W_{max}/W_1 is calculated by Eq. (6.67).

6.8.9 Off-Design Profile Loss Model

After the minimum profile loss coefficient has been obtained, the profile loss away from the minimum loss incidence angles is estimated using the extrapolation technique proposed by Aungier (2003). According to this method, the total pressure loss

coefficient at off-minimum (or off-design) conditions (Figure 6.10) is obtained by the following extrapolation formulas:

$$\omega_{pr} = \omega_{pr,min} \begin{cases} (s_{m,1} + s_{m,2}\xi^2), & -2 \leq \xi \leq 1 \\ [s_{m,3} + s_{m,4}(\xi + 2)], & \xi \leq -2 \\ [s_{m,5} + s_{m,6}(\xi - 2)], & \xi > 1 \end{cases} \quad (6.113)$$

where the s_m 's are user-defined calibration scalars with default values:

$$\begin{aligned} s_{m,1} &= 1.0, & s_{m,2} &= 1.0, & s_{m,3} &= 5.0, \\ s_{m,4} &= -4.0, & s_{m,5} &= 2.0, & s_{m,6} &= 2.0 \end{aligned}$$

In Eq. (6.113), ξ is a normalized incidence angle parameter calculated defined by:

$$\xi = \begin{cases} \frac{i - i_m}{i_s - i_m}, & i \geq i_m \\ \frac{i - i_m}{i_m - i_c}, & i < i_m \end{cases} \quad (6.114)$$

6.8.10 Blockage Modelling

In MLAC, blockage is accounted at the inlet and outlet of any blade row according to values given by Glassman et al. (1995), or by using Eq. (3.33). Alternatively, blockage can be a user-defined input along the compressor.

6.9 Loss Model for IGVs

In the present section, the model used in MLAC for estimating the losses across IGV rows is presented. This was developed (and adopted for the needs of this work) by Banjac et al (2014).

For IGVs modelled by equivalent circular-arc NACA-65, or equivalent parabolic-arc NACA-63 A4K6 profiles, Banjac et al. (2014) formulated the following equation for estimating the losses across IGV rows:

$$\omega = \omega_{ref} + \Delta\omega_t + \Delta\omega_\gamma \quad (6.115)$$

where ω_{ref} is a reference loss coefficient, $\Delta\omega_t$ is a correction for IGVs with different thicknesses than reference, and $\Delta\omega_\gamma$ is a correction for stagger angle changes from reference. Each term in Eq. (6.115) was formulated by Banjac et al. for matching the CFD simulation results produced for the flow past cascades of different solidity, camber, thickness, and stagger positioning, and exposed to different inlet Mach numbers. Next, the respective equations for calculating each term in Eq. (6.115) are given. Note that, similarly to the off-design deviation model presented by the same

authors (see paragraph 6.7.2), in all equations that follow the camber angle and the inlet Mach number are limited by:

$$\theta = \max(0, \theta), \quad M_1 = \max(0.2, M_1)$$

The reference loss coefficient (ω_{ref}) is calculated by:

$$\omega_{ref} = \exp(s_{m,1} + s_{m,2}\theta + s_{m,3}\sigma + s_{m,4}M_1) + s_{m,5}\sigma \quad (6.116)$$

where the default values for the scalar calibration factors, s_m , are given in Table 6.4.

Table 6.4: Calibration scalars for Banjac et al.'s loss model for the reference loss equation [adapted from Banjac et al. (2014)]

Scalar	NACA-65	NACA-63 A ₄ K ₆
$s_{m,1}$	-7.83636	-12.57281
$s_{m,2}$	0.0380755	0.0789899
$s_{m,3}$	1.186934	1.917747
$s_{m,4}$	1.41946	3.68047
$s_{m,5}$	0.00951139	0.0139719

The correction for thickness, $\Delta\omega_t$, is calculated according to:

$$\Delta\omega_t = \begin{cases} (s_{m,1} + s_{m,2}\sigma) \left(0.1 - \frac{t_{max}}{c}\right) \frac{\theta}{40} (s_{m,3}M_1 + s_{m,4}), & \text{for NACA - 65} \\ (s_{m,1} + s_{m,2}\sigma) \left(0.06 - \frac{t_{max}}{c}\right) \frac{\theta}{56} (s_{m,3}M_1 + s_{m,4}), & \text{for NACA - 63 A}_4\text{K}_6 \end{cases} \quad (6.117)$$

where $s_{m,1}$, $s_{m,2}$, $s_{m,3}$, and $s_{m,4}$ are user-defined calibration scalars with default values as shown in Table 6.5.

Table 6.5: Calibration scalars for Banjac et al.'s loss model for the thickness correction equation [adapted from Banjac et al. (2014)]

Scalar	NACA-65	NACA-63 A ₄ K ₆
$s_{m,1}$	0.0429	0.0621
$s_{m,2}$	-0.0704	-0.1006
$s_{m,3}$	6.7	5.0
$s_{m,4}$	-0.34	0.0

Finally, the correction for stagger angle changes, $\Delta\omega_\gamma$, is given by:

$$\Delta\omega_\gamma = \min \left[s_{m,1} (s_{m,2})^{\Delta\gamma} (s_{m,3})^\sigma (1 + s_{m,4}\theta), 1.2 (s_{m,5} + s_{m,6}\theta) \right] \quad (6.118)$$

where the s_m 's are user-defined calibration scalars with default values:

$$\begin{aligned} s_{m,1} &= 0.0002, & s_{m,2} &= 1.48, & s_{m,3} &= 0.09, \\ s_{m,4} &= 0.01, & s_{m,5} &= 1.0, & s_{m,6} &= 0.01 \end{aligned}$$

and $\Delta\gamma = \gamma - \gamma_{ref}$.

6.10 Choke Modelling

A 1D compressor model for off-design performance analysis must be able to determine not only the maximum flow a compressor can deliver, but also the performance over the choked region of operation. Convergence problems in obtaining the solution of the mean-line equations near or beyond choked conditions, must be resolved.

In MLAC, choke conditions are modelled by introducing indices that quantify the “distance” of an operating point along a speed-line from the corresponding limiting value. For this reason, four (4) dedicated indices are defined, three (3) at blade row level and one (1) at compressor level. An appropriate functional of these indices is defined which is numerically zeroed for estimating the choked mass flow. Once the maximum mass flow rate for a speed-line is obtained, the choked part of the map characteristics is established. The procedure followed is presented below.

6.10.1 Indices for Annulus Choke Modelling

For modelling the annulus choke, three indices are defined, two at each blade row (at the inlet and outlet), and one at the compressor exit. These are given by:

$$I_{br,1}^{choke} = \frac{\dot{m}_1^* - \dot{m}_1}{\dot{m}_1^*} \quad (6.119)$$

$$I_{br,2}^{choke} = \frac{\dot{m}_2^* - \dot{m}_2}{\dot{m}_2^*} \quad (6.120)$$

$$I_{out}^{choke} = \frac{\dot{m}_{out}^* - \dot{m}_{out}}{\dot{m}_{out}^*} \quad (6.121)$$

Indices $I_{br,1}^{choke}$ and $I_{br,2}^{choke}$ express, respectively, how far is the actual mass flow (\dot{m}) that passes through the blade row inlet and outlet annuli from the choked one (\dot{m}^*), while index I_{out}^{choke} expresses the same condition for the compressor exit. In each equation, the choked mass flow rate is calculated from the local sonic flow properties by:

$$\dot{m}^* = \rho^{s*} W^* A_g \cos \beta \quad (6.122)$$

where A_g is the flow annulus cross-sectional area. The sonic static density (ρ^{s*}) and flow velocity (W^*) are obtained using a dedicated PROOSIS built-in thermodynamic

function, which establishes the sonic (for $M_r = 1$) static conditions for given total temperature (T_r^0), total pressure (p_r^0), and flow angle (β).

6.10.2 Index for Throat Passage Choke Modelling

The modelling of the blade row throat passage choke is achieved by introducing an index expressed by:

$$I_{br,throat}^{choke} = \frac{\beta_1 - \beta_1^*}{\beta_1^*} \quad (6.123)$$

The above quantity indicates how far the actual flow angle, β_1 , is from a minimum value, β_1^* , below which the row throat passage chokes. For calculating the critical blade row inlet flow angle (β_1^*), two flow conditions were considered at the blade row inlet when developing MLAC: subsonic and supersonic. For modelling them, the approach presented by Cumpsty (1989) and Freeman et al. (1992) was followed. This is shown diagrammatically in Figure 6.11.

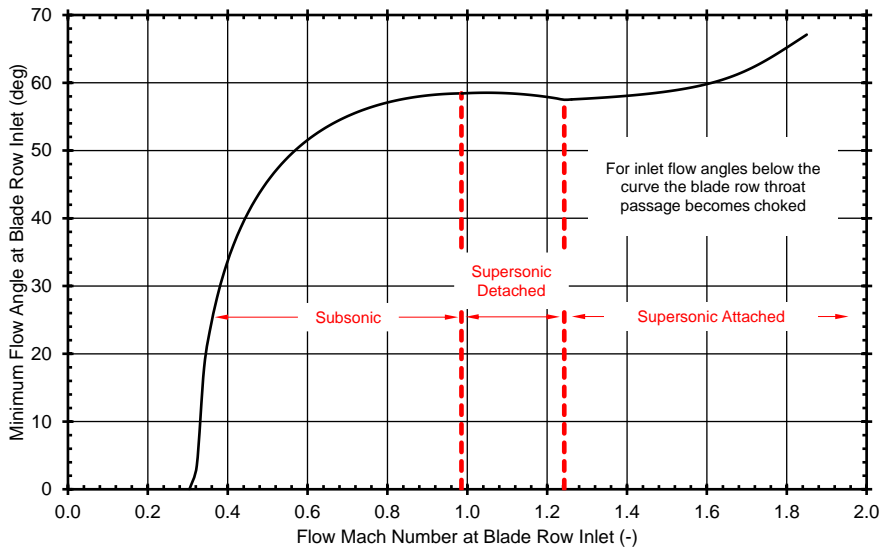


Figure 6.11: Example diagrammatic representation of the blade row throat choking modelling. For inlet flow angles less than the critical inlet flow angle, the row passage is choked.

6.10.2.1 Subsonic Choke Modelling

Choking when the inlet flow to the blade row is subsonic is determined using the simplified analysis described by Cumpsty (1989). When the flow angle at the blade row inlet is reduced, then the mass flow through the throat passage increases and a minimum angle value is obtained for which the blade row becomes choked. This value for β_1^* is obtained from:

$$\frac{o}{s \cos \beta_1^*} = M_{r,1} \left(\frac{1 + \frac{\gamma - 1}{2}}{1 + \frac{\gamma - 1}{2} M_{r,1}^2} \right)^{\frac{\gamma + 1}{2(\gamma - 1)}} \quad (6.124)$$

6.10.2.2 Supersonic Choke Modelling

For supersonic inlet flow, two possible sub-cases can be identified. For the first one, the flow condition appears for which the bow shock that develops ahead of the row is detached from the blade LE. In this case, the modelling proposed by Freeman et al. (1992) was used for obtaining β_1^* . Following a relatively simple control-volume analysis for the conservation of mass, momentum, and energy between the blade row inlet and the throat passage, and assuming that the throat is choked, Cumpsty et al. arrived at the following expression:

$$\frac{\cos \kappa_{LE}}{\cos \beta_1^*} + \gamma M_{r,1}^2 \cos(\beta_1^* - \kappa_{LE}) = M_{r,1} \frac{1 + \gamma(1 - t_{max}/d_g)}{1 - t_{max}/d_g} \sqrt{\frac{1 + \frac{\gamma-1}{2} M_{r,1}^2}{1 + \frac{\gamma-1}{2}}} \quad (6.125)$$

which is solved iteratively to obtain the value of β_1^* . In the above, d_g is the distance between two blades measured normal to the chord line.

Finally, for supersonic inlet there is a unique flow angle for which the bow shock formed is attached to the blade row LE. For this case, an idealized flow was considered by Cumpsty (1989). The modelling approach followed by Cumpsty, led to the following non-linear system of equations between the inlet flow and the end (subscript “e”) of the Prandtl–Meyer expansion fan that develops due to the suction surface curvature in the region of the blade LE:

$$\beta_1^* + \nu(M_{r,1}) = \kappa_{LE} + \nu(M_e) \quad (6.126)$$

$$f(M_{r,1})s \cos \beta_1^* = f(M_e)(s \cos \kappa_{LE} - t_{LE}) \quad (6.127)$$

In the above, $\nu(M)$ is the Prandtl–Meyer function given by:

$$\nu(M) = \sqrt{\frac{\gamma-1}{\gamma+1}} \tan^{-1} \sqrt{\frac{\gamma-1}{\gamma+1} (M^2 - 1)} - \tan^{-1} \sqrt{M^2 - 1} \quad (6.128)$$

and $f(M)$ is a flow function defined by:

$$f(M) = \frac{\gamma}{\sqrt{\gamma-1}} M \left(1 + \frac{\gamma-1}{2} M^2 \right)^{-\frac{\gamma+1}{2(\gamma-1)}} \quad (6.129)$$

For a given blade geometry and inlet Mach number, the system of Eqs (6.126) and (6.127) is solved iteratively (for this, a PROOSIS built-in Newton–Raphson method is utilized) to give the values of M_e and β_1^* . This means that for a given inlet Mach number ($M_{r,1}$) there exists a unique inlet flow angle (β_1^*) that satisfies both Eqs (6.126) and (6.127). Furthermore, if this unique angle cannot be changed then neither the mass flow can change and the flow across the blade row throat passage is choked.

It should be noted that when the blade row operates in the supersonic flow regime, the question arises about the type of flow that prevails, with detached or attached shocks. In MLAC, the type of flow is decided in terms of a Mach number value for which the two flow models give the same value of β_1^* . This Mach number value is obtained

iteratively. For supersonic Mach numbers below this value the detached-shock model is applied, whereas for larger Mach number values the attached-shock model is implemented.

6.10.3 Estimating the Choke Mass Flow Rate

To establish numerically the compressor choking mass flow rate, a secant method is used since it was found to be the most robust. For any compressor speed (N_{mech}) and inlet conditions (T^0, p^0), the secant method updates the compressor inflow (\dot{m}_{in}) until the functional f expressed by Eq. (6.130) is zeroed within a user-specified tolerance, or two successive estimates for \dot{m}_{in} differ less than a prescribed tolerance.

$$f = I_{min}^{choke} - \varepsilon \quad (6.130)$$

In Eq. (6.130), I_{min}^{choke} is the global minimum choke index given by:

$$I_{min}^{choke} = \min \left[|I_{out}^{choke}|, (I_{br,min}^{choke})_{\forall br} \right] \quad (6.131)$$

where the minimum index for each blade row, $I_{br,min}^{choke}$, is given by:

$$I_{br,min}^{choke} = \min(|I_{br,1}^{choke}|, |I_{br,2}^{choke}|, |I_{br,throat}^{choke}|) \quad (6.132)$$

To avoid numerical solutions in the windmilling region of the compressor operation, a constraint is also imposed on the overall total pressure ratio, which should be greater than a minimum, user-specified value ($PR_{min} > 1$).

6.10.4 Choked Part of a Speed-Line

The choked part of a speed-line is vertical to the mass flow axis, since it is characterized by a constant corrected mass flow rate. For operation in this part, a mean-line calculation should be able to provide the flow characteristics (pressure, temperature, velocity magnitude, direction, etc.) at the inlet and outlet of each blade row along a multi-stage compressor gas-path. The approach followed in MLAC for determining the flow characteristics, when the compressor pressure ratio becomes lower than its value at the onset of choke, is based on the assumption that the flow pattern in the part of the compressor downstream of a choked row will be formed so that pressure losses are such that the outlet pressure matches a back pressure specified. Thus, the flow before the choked row is considered frozen, total pressure losses are incrementally added to the choked blade row, and the flow along the downstream blade rows is computed until the compressor back pressure is attained or a downstream row becomes choked. If the compressor back pressure is not reached but a downstream row chokes, then the same procedure is repeated for the new choked row. Note that this approach is similar to the one used by Arolla et al. (2008). However, they only applied it to the case of a single-stage fan and, more importantly, their approach gave no insight as to how the flow conditions evolve when choke occurs along a multi-stage compressor.

For a compressor map to be generated, the last point on the vertical portion of the map characteristics corresponding to the minimum pressure ratio that the compressor

can attain when it operates at the maximum \dot{m}_{in} , is first established. Starting from the first choked blade row, an iterative scheme is employed that modifies the losses of the choked row until a downstream row chokes. The same procedure is then repeated successively for every downstream row that chokes until, eventually, the compressor exit becomes choked. In any case, the last pressure ratio is taken equal to the maximum value between the PR established in the above iterative procedure, and a user-defined value $PR_{min} > 1$ for avoiding solutions in the windmilling regime. Finally, the vertical portion of the map characteristic is refined for any user-defined number of pressure ratio values between the first and the last one, following the algorithmic logic shown in Figure 6.12.

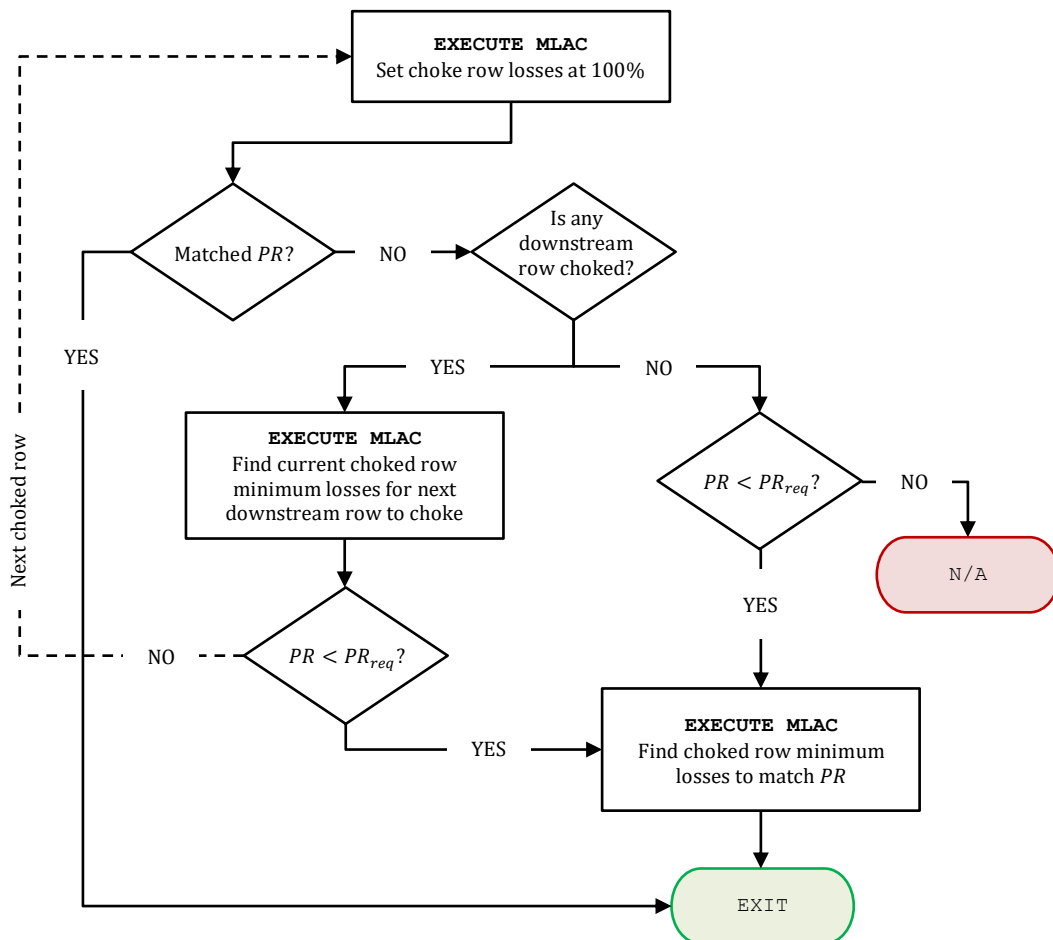


Figure 6.12: MLAC flow-chart to establish the 1D performance in the choked region.

6.11 Stall Modelling

Similarly to the choke indices described in the preceding section, an appropriate index indicating how far a blade row operates from stall is also defined in MLAC. MLAC offers different stall index definitions for estimating the stalled mass flow rate (for given $N_{mech}, T_{in}^0, p_{in}^0$), which will be described in more detail in the following.

6.11.1 Stalling Incidence Criterion

The first stall index defined in MLAC quantifies the difference between the actual (i) and the positive stall incidence (i_s) angles. The latter was defined in paragraph 6.8.8 and, according to Herrig et al. (1957), corresponds to operation with blade losses twice the minimum ones. The stall index is defined by:

$$I_{br}^{stall} = i_s - i \quad (6.133)$$

In Eq. (6.133), the positive stall incidence angle (i_s) can alternatively be calculated according to the model proposed by Miller et al. (1987). In their model, i_s is expressed in terms of the blade stagger angle, camber angle, and blade row solidity. This relationship is given by:

$$i_s = A + B\sigma - C\theta \quad (6.134)$$

where A, B, and C are functions of the blade stagger angle. Their values are given graphically in Figure 6.13. Note that, the curves shown in Figure 6.13 were digitized and introduced in MLAC as PROOSIS 1D tables.

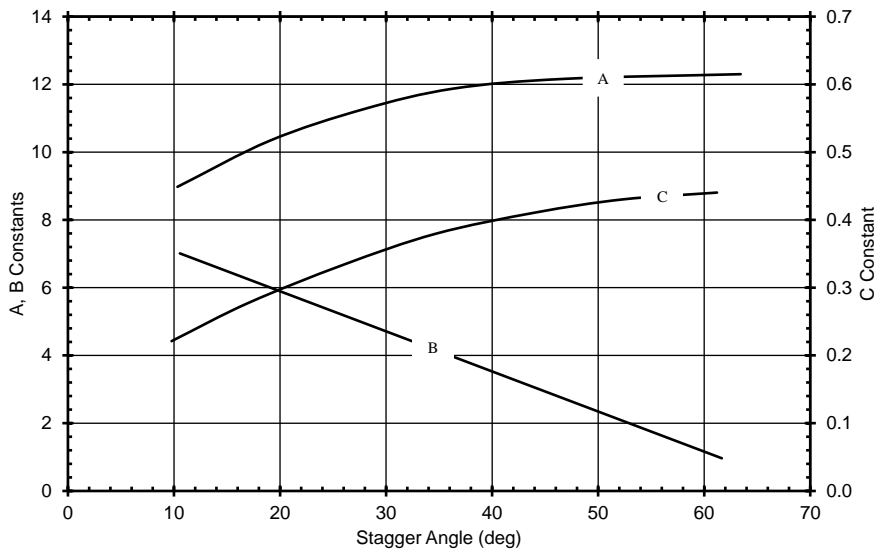


Figure 6.13: Stalling incidence angle correlation constants [adapted from Miller et al. (1987)].

6.11.2 Diffusion Factor Criterion

Another quantity used to define blade stall in MLAC is the diffusion factor (DF). According to the experimental data presented by Lieblein [see Aungier (2003)], blade stall is assumed to occur when the diffusion factor exceeds a limiting value (Lieblein determined it to be around 0.6 for an abrupt increase in blade losses). Therefore, the stall index depending on the diffusion factor is given by:

$$I_{br}^{stall} = DF_{max} - DF \quad (6.135)$$

where DF_{max} is a user-defined maximum value above which stall is assumed to occur, and DF is the current diffusion factor computed using Eq. (6.65).

6.11.3 Minimum Velocity Ratio Criterion

Banjac et al. (2015) utilized the De Haller number to express blade stall. The De Haller number, defined as W_2/W_1 , poses an upper limit on the maximum permissible deceleration that the blade row can attain without stalling. In other words, the blade row must operate with $W_2/W_1 \geq (W_2/W_1)_{min}$. A practical limit for $(W_2/W_1)_{min} \cong 0.72$, while current technology compressors operate with values of about ~ 0.69 [see Saravanamuttoo et al. (2017)].

In Banjac et al.'s method, the minimum velocity ratio, $(W_2/W_1)_{min}$, is calculated in terms of the blade row geometry considering that compressor rows operate like 2D diffusers. The expression for $(W_2/W_1)_{min}$ is given by:

$$\left(\frac{W_2}{W_1}\right)_{min} = \frac{\frac{0.15 + 11(t_{max}/c)}{0.25 + 10(t_{max}/c)}}{1 + 0.4 \left[\max \left(1.1, \frac{K_{sh,b} \theta \sigma}{2 \sin(\theta/2) \cos \gamma} \right) \right]^{0.65}} \quad (6.136)$$

where $K_{sh,b}$ is a shape calibration factor with values given by [see Banjac et al. (2015)]:

$$K_{sh,b} = \begin{cases} 1.0, & \text{for NACA - 65} \\ 1.0, & \text{for NACA - 63 A}_4\text{K}_6 \\ 0.95, & \text{for DCA} \\ 0.82, & \text{for BC4} \end{cases} \quad (6.137)$$

For NACA-65 blades with $DF_{eq} > 2.2$, $(W_2/W_1)_{min}$ is additionally corrected according to [see Aungier (2003)]:

$$\left(\frac{W_2}{W_1}\right)_{min} = \left(\frac{W_2}{W_1}\right)_{min} \left(\frac{2.2}{DF_{eq}}\right)^{0.6} \quad (6.138)$$

Finally, the De Haller number-based stall index is given by:

$$I_{br}^{stall} = \min \left\{ \left[\left(\frac{W_2}{W_1}\right) - s_{ch} \left(\frac{W_2}{W_1}\right)_{min} \right]_h, \left[\left(\frac{W_2}{W_1}\right) - \left(\frac{W_2}{W_1}\right)_{min} \right]_m, \left[\left(\frac{W_2}{W_1}\right) - s_{ct} \left(\frac{W_2}{W_1}\right)_{min} \right]_t \right\} \quad (6.139)$$

Stall is assumed to occur when the De Haller number limit is violated in any of the three characteristic radial positions along the blade span (hub, mean, tip) [see Banjac et al. (2015)].

In Eq. (6.139), the current and minimum velocity ratios are evaluated as average values over a blade span portion. These are given by:

$$\left(\frac{W_2}{W_1}\right) = \frac{1}{\tilde{R}_{h,2} - \tilde{R}_{h,1}} \int_{\tilde{R}_{h,1}}^{\tilde{R}_{h,2}} \frac{W_2}{W_1} d\tilde{r} \quad (6.140)$$

where $\tilde{R}_h = 1 - \tilde{R}_{IMM}$ is the relative spanwise position with $0.0 \leq \tilde{R}_h \leq 1.0$ (0.0 corresponds to hub and 1.0 to tip). In the above, the following spanwise positions are used for evaluating the velocity ratios at the hub, mean, and tip:

$$\tilde{R}_{h,1} = \begin{cases} 0.10, & \text{for hub} \\ 0.15, & \text{for mean,} \\ 0.80, & \text{for tip} \end{cases}, \quad \tilde{R}_{h,2} = \begin{cases} 0.20, & \text{for hub} \\ 0.85, & \text{for mean} \\ 0.90, & \text{for tip} \end{cases}$$

In MLAC, Eq. (6.140) is evaluated numerically using the trapezoidal rule.

The hub and tip correction factors, s_{ch} and s_{ct} , respectively, that appear in Eq. (6.140), are calculated according to Eqs (6.141) and (6.142):

$$s_{ch} = \begin{cases} 1/1.3, & \text{for rotors} \\ C_{tc}/1.3, & \text{for stators} \end{cases} \quad (6.141)$$

$$s_{ct} = \begin{cases} C_{tc}/1.3, & \text{for rotors} \\ 1/1.3, & \text{for stators} \end{cases} \quad (6.142)$$

where the factor 1/1.3 reflects the fact that the blade row can operate stably despite the corner stall appearing in the regions of the hub and the tip, while C_{tc} is a factor accounting for the influence of the tip clearance. The latter is given by [see Koch (1981) and Banjac et al. (2015)]:

$$C_{tc} = \begin{cases} \frac{1}{(W_2/W_1)_{min,m}} \sqrt{1 - K_{tc} \{1 - [(W_2/W_1)_{min,m}]^2\}}, & \text{for unshrouded rows} \\ 1.0, & \text{for shrouded rows} \end{cases} \quad (6.143)$$

with $K_{tc} = \exp(-1.0629x^{0.56226})$ and $x = \delta_c/(s \cos \gamma)$.

6.11.4 Stall Margin Criterion (Maximum Static Pressure Rise Criterion)

The maximum static pressure rise that a blade can achieve is just another measure for the maximum flow deceleration over the blade. This fact was utilized by Schweitzer et al. (1984) who developed a semi-empirical correlation for estimating the stall margin of compressors. In this paragraph, this correlation is presented as adapted from the works of both Schweitzer et al. (1984) and Glassman et al. (1995). Finally, an “overall” stall margin/index (I^{stall}) is defined that can be used to quantify how far the compressor operates from stall.

The primary correlations for developing this index depend on the assumption that a compressor blade passage resembles that of a diffuser. The diffuser performance, in turn, depends strongly on geometric parameters that reflect the quantity and quality of diffusion such as 1) the inlet/outlet area ratio (determines the overall amount of diffusion) and, for conical diffusers, 2) the diffuser angle (determines the rate of diffusion). For frictionless and incompressible flow, the ideal static pressure rise coefficient of diffusers can be expressed in terms of the area ratio alone which, in turn, for a 2D compressor cascade is expressed in terms of the cascade inlet and outlet flow angles according to [see Glassman et al. (1995)]:

$$C_{p,th} = 1 - \left(\frac{\cos \beta_1}{\cos \beta_2} \right)^2 \quad (6.144)$$

Then, for the same cascade, an equivalent diffuser angle can be formulated which is given by [see Glassman et al. (1995)]:

$$\tan \alpha_{eq} = (\sqrt{\cos \beta_2} - \sqrt{\cos \beta_1}) \sqrt{\frac{AR}{\pi \sigma}} \quad (6.145)$$

where AR is the blade aspect ratio.

The above two parameters enabled Schweitzer et al. (1984) to use cascade data to formulate a correlation for determining the maximum static pressure rise coefficient that a blade row can attain. This correlation is given by:

$$C_{p,max} = \left(-0.23355 + \frac{2.7847}{\alpha_{eq}^{1/2}} - \frac{2.0348}{\alpha_{eq}^{3/2}} - 0.019203\Delta\beta \right) C_{p,th} + 0.087858 \quad (6.146)$$

where the flow turning, $\Delta\beta = \beta_1 - \beta_2$, was also included in the correlation since a given area ratio can be obtained for different combinations of inlet/outlet flow angles, as the blade is positioned at different stagger angles [see Glassman et al. (1995)].

Next, a relative loading parameter (RLP) is defined for every individual row which indicates how far that row operates from its maximum loading capacity. RLP is expressed by:

$$RLP = \frac{C_p}{C_{p,max}} \quad (6.147)$$

where C_p is the actual static pressure rise coefficient.

Finally, the stall margin/index is defined by [see Schweitzer et al. (1984)]:

$$I^{stall} = 0.93958 \left\{ 1 - \frac{\overline{RLP}}{2} \left[1 + \left(\frac{RLP_{max}}{\overline{RLP}} \right)^{\frac{j_{max}}{N_{stg}}} \right] \right\} \quad (6.148)$$

where \overline{RLP} is the average loading parameter for the entire compressor, RLP_{max} is the maximum loading parameter that appears among the blade rows, and j_{max} is the stage number where RLP_{max} occurs. In the above, the coefficient 0.93958 is a regression coefficient determined by Schweitzer et al. (1984) using statistical data.

Note that, contrary to the other stall indices that estimate the “stall margin” for every single row [see Eqs (6.133), (6.135), and (6.139)], the stall index given in Eq. (6.148) is an overall indicator of how close (or far) the compressor is to stall.

6.11.5 Estimating the Stall Mass Flow Rate

For stall conditions defined using any of Eqs (6.133), (6.135), or (6.139), an overall stall index is defined which is the minimum value between the stall indices of all blade rows. This minimum index is then zeroed to establish the stall mass flow rate in the same numerical way as with choke.

Alternatively, the overall stall index defined by Eq. (6.148) can be used instead to obtain the stalled mass flow rate.

6.12 MLAC PROOSIS Library Components for Off-Design Simulations

As mentioned in the chapter introduction, the methods and equations presented in the previous sections were used to develop a dedicated PROOSIS library named MLAC. MLAC defines PROOSIS components (see Chapter 2) for estimating the off-design performance of multi-row, axial-flow compressors, by conducting a row-by-row mean-line calculation. Here, the components that are used for conducting off-design analyses, as well as their capabilities, are presented. The PROOSIS symbols defined in MLAC for off-design calculations are shown in Figure 6.14.

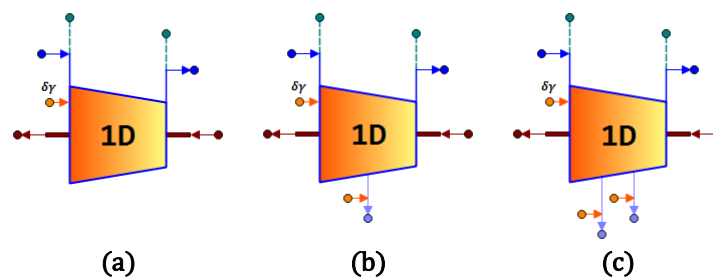


Figure 6.14: MLAC palette defining PROOSIS symbols for off-design performance calculations of axial-flow, multi-row compressors with (a) 0, (b) 1, and (c) 2 gas bleeds.

The symbols shown in Figure 6.14 can be dragged-and-dropped into a PROOSIS schematic canvas for estimating the off-design performance of compressors individually or, as will be explained later, as part of an engine model. As it can be seen from Figure 6.14, components with 0, 1, and 2 gas bleeds are defined by default, but components with more than 2 bleeds can easily be defined utilizing PROOSIS EL's inheritance capability. Note that, more than one symbols of the same MLAC component can be dragged-and-dropped into the same schematic canvas.

Given the compressor geometry, inlet conditions (\dot{m}_{in} , T_{in}^0 , p_{in}^0 , a_{in}), and compressor speed (N_{mech}), the components defined in Figure 6.14 can be used to estimate the overall compressor performance (see paragraph 6.2.4) at a single operating point or, they can be utilized to produce performance maps for different combinations of \dot{m}_{in} and N_{mech} . For the latter case, a dedicated PROOSIS experiment was developed that implements the following four (4) steps for any number of user-defined compressor speeds and values (between 5-120%):

1. The limiting choke mass flow rate is calculated by employing the procedure outlined in paragraph 6.10.3.
2. For speed-lines where choke occurs, the last choke point in the vertical part of that speed-line is first calculated according to the methodology described in paragraph 6.10.4. Then, the vertical part of that speed-line is generated for any user-defined number of points between the first and last choke points.

3. For each rotational speed, the stall mass flow rate is calculated using any of the methods outlined in Section 6.11.
4. The compressor performance is finally estimated in the stable operating range by varying the compressor inlet mass flow rate between the stall and choke values for all the different compressor speeds.

When it comes to engine cycle calculations, the above MLAC components for off-design calculations can be utilized in two (2) different approaches. In the first one, the compressor map is first generated in the full operating range for given compressor geometry, inlet conditions, and different speeds, as explained above. The generated map, is then “uploaded” into the conventional OD components for off-design calculations by replacing the generic maps available in PROOSIS which, among other downsides, must be scaled during a pre-design calculation step (since they do not reflect the actual compressor geometry and inlet operating conditions).

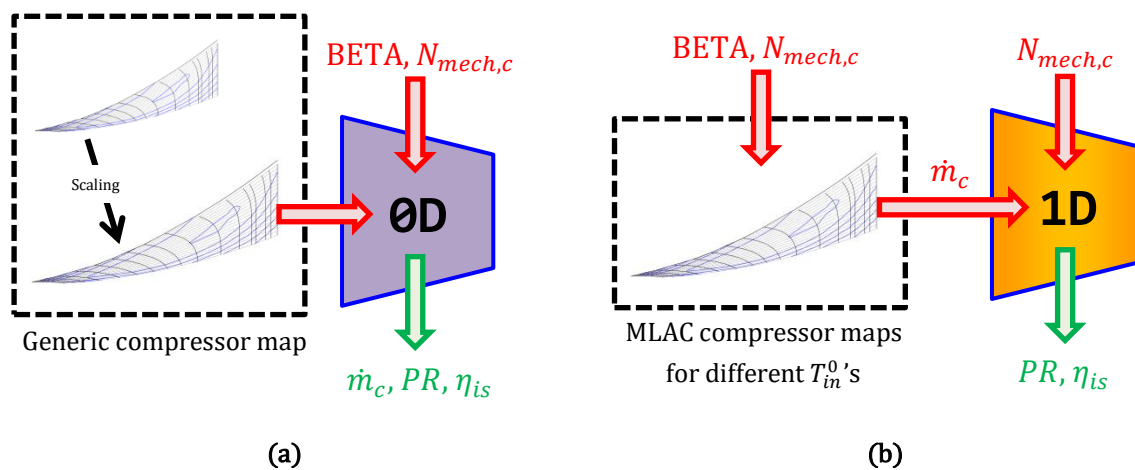


Figure 6.15: Compressor performance at engine simulation level using (a) conventional OD and (b) MLAC 1D components (orange-colored).

The second way that MLAC could be used, is by directly integrating the components in OD cycle calculations in a hybrid OD-1D mode. For this case, special care should be given so that the traditional OD algorithmic logic is maintained when the MLAC components replace the conventional OD components for off-design calculations. In their simplest form, conventional OD compressor components (see Figure 6.15) establish performance (\dot{m}_c, PR, η_{is}) by reading a set of tables (a map) for given values of corrected speed and an auxiliary BETA parameter [see Kurzke et al. (2018)]. BETA is an independent variable at engine model level that a numerical solver adjusts so that mass and power compatibility between connected components is ensured.

MLAC components, on the other hand, require mass flow (\dot{m}_c) and compressor speed ($N_{mech,c}$) as inputs and produce the compressor performance (PR, η_{is}). During a pre-processing step, MLAC is executed to produce a multitude of \dot{m}_c –BETA relationships for different compressor speeds and, in an attempt to improve accuracy, for different T_{in}^0 's (including, of course the ISA one) since conventional gamma corrections are not sufficient [see AGARD (1995)]. Then, when an MLAC component replaces the respective conventional OD component in an engine model, BETA is still

used as an algebraic variable for reading the appropriate \dot{m}_c value that satisfies the mass and power compatibility requirements. This \dot{m}_c value, along with $N_{mech,c}$, are then fed into the MLAC component to obtain the compressor performance (see Figure 6.15) by conducting a mean-line, row-by-row calculation.

6.13 MLAC Validation Studies

In the present section, example calculations are presented to validate and verify the MLAC capability for off-design simulations (map generation) of multi-stage compressors.

6.13.1 MLAC Tuning Test Case

MLAC employs by default loss and deviation models that were mostly developed on the basis of 2D cascade tests in subsonic wind tunnels during the early 1950's. Hence, they cannot fully capture the performance of current transonic compressors, as explained by Neumann et al. (2019). On the other hand, both Kidikian et al. (2018a; 2018b) and Neumann et al. (2019) demonstrated that traditional loss and deviation models, if appropriately calibrated, could reproduce accurately the aerodynamics of current technology compressors. Thus they remain a valuable design and analysis tool.

As shown in Sections 6.4–6.9, in the default MLAC loss and deviation correlations calibration scalars and adders were introduced which offer the capability of tuning the models. To demonstrate this capability, the NASA “Stage-35” compressor [see Reid et al. (1978)] is considered. Stage-35 is a high-aerodynamic loading, transonic compressor with a design pressure ratio of 1.82, that rotates at 17,188.7 rpm.

For the calculations that follow, MLAC is executed with the loss and deviation models summarized in Table 6.6 for both Rotor-35 and Stator-35. Note that, since the diffusion factor model for profile losses is used, both the secondary losses and Reynolds number effects are turned off. Clearance losses are also deactivated (there is no information given on δ_c 's by Reid et al.). For Mach number effects, the default model is used (see paragraph 6.8.8). Finally, blockage is a user input at every row's inlet and outlet.

Table 6.6: Loss and deviation models used in MLAC to reproduce NASA's Stage-35 performance

Loss/Deviation	Model	Remarks
Design incidence	Herrig's model	See paragraph 6.5.1.2
Design deviation	Lieblein's model	See paragraph 6.5.2.1
Off-design deviation	Swan's model	See paragraph 6.7.1.2
Profile loss	Diffusion factor model	See paragraph 6.8.7.1
Endwall loss	Howell's model	See paragraph 6.8.2.1
Shock loss	Steinke's model	See paragraph 6.8.5

First, MLAC is executed considering the default values for the calibration scalars of the loss and deviation models given in Table 6.6, while blockage is set to the defaults given by Glassman et al. (1995) (see paragraph 6.8.10). The generated maps for pressure ratio and isentropic efficiency are shown in Figure 6.16.

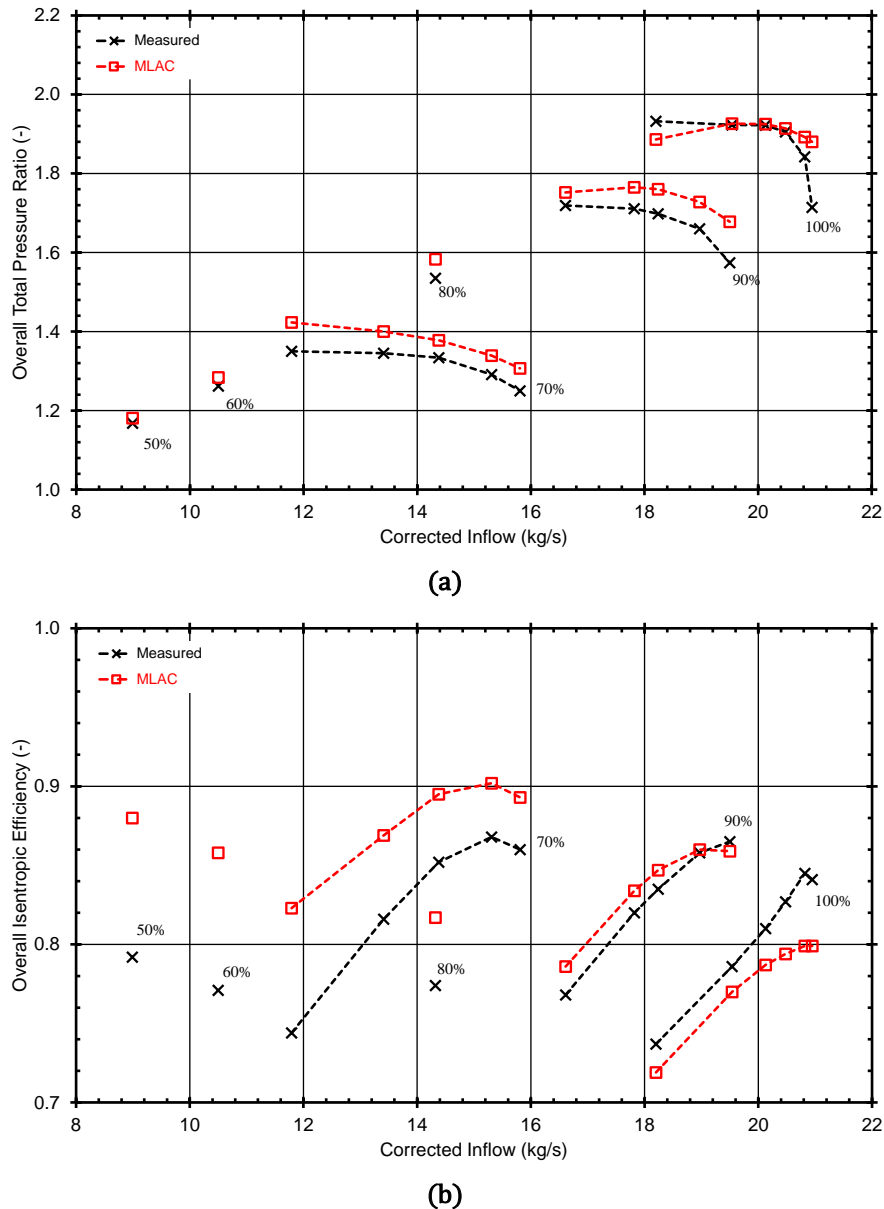


Figure 6.16: Comparison between the uncalibrated MLAC predictions and measured data for the NASA Stage-35 compressor: (a) pressure ratio vs corrected inflow; (b) isentropic efficiency vs corrected inflow.

As it can be seen from Figure 6.16, MLAC can reproduce satisfactorily the physical trends for both the pressure ratio and isentropic efficiency, but the differences in magnitude (especially in isentropic efficiency) are quite high. A source adding to this difference is, of course, the absence of the clearance losses which are deactivated. Thus, MLAC predicts lower losses than the actual ones. This, in turn, results in higher isentropic efficiencies than the measured ones (see, for instance, the 50%, 60%, 70%, and 80% iso-speed lines, where the most apparent differences in efficiency are observed).

Next, the models are calibrated with the aim to match the measured performance of Stage-35. This is done following an approach similar to that presented by Kidikian et al. (2018a; 2018b), but adapted to the MLAC capabilities. To reproduce the performance of Stage-35 (PR , η_{is}), Kidikian et al. employed a numerical procedure to set the loss, deviation angle, and inlet and outlet blockage estimated by their mean-line model, equal to the respective values measured for both Rotor-35 and Stator-35. They repeated this procedure for each individual pair of measurements (rotational speed and inflow), that is, for a total of nineteen (19) operating points.

Here, for matching the Stage-35 pressure ratio and isentropic efficiency in all 19 pairs of compressor speed and inflow, the scalars introduced in the models used by MLAC to calculate loss (ω), deviation (δ), and inlet ($\lambda_{B,1}$) and outlet ($\lambda_{B,2}$) blockage are calibrated instead. In contrast to Kidikian et al. who imposed ω , δ , $\lambda_{B,1}$, and $\lambda_{B,2}$ simultaneously for both Rotor-35 and Stator-35, here the calibration procedure is demonstrated considering only the Rotor-35 for which the flow is fully supersonic at the inlet [at design conditions, the Mach number varies from ~ 1.1 at the hub up to almost ~ 1.5 at the tip according to Reid et al. (1978)]. Therefore, a minimization procedure was followed for the following objective function:

$$f_{OBJ} = \left(1 - \frac{PR}{PR^{R35}}\right)^2 + \left(1 - \frac{\eta_{is}}{\eta_{is}^{R35}}\right)^2$$

In the above, PR and η_{is} is the pressure ratio and the isentropic efficiency obtained by the MLAC, respectively, while PR^{R35} and η_{is}^{R35} is the Rotor-35 pressure ratio and isentropic efficiency measured by Reid et al., respectively.

The minimization was conducted separately for all 19 sets of compressor speed and inflow, using the Nelder-Mead SIMPLEX method [see Nelder et al. (1965)]⁵⁷. The design variables (calibration scalars) and their initial (default) values are shown in Table 6.7.

Table 6.7: Design variables and initial values for matching the Rotor-35 performance

Loss/Deviation	Calibration Scalar(s)
Blockage	$\lambda_{B,1} = 0.99, \lambda_{B,2} = 0.9875$
Off-design deviation	$s_{m,1} = 6.40, s_{m,2} = -9.45$
Endwall loss	$s_m = 0.02$
Profile loss	$s_{m,1} = 0.0035, s_{m,2} = 1.0, s_{m,3} = 3.5, s_{m,6} = 37.0$
Equivalent diffusion factor	$s_a = 1.12, s_{m,1} = 0.61, s_{m,2} = 1.0, s_{m,3} = 1.43$

For the minimization, the following constraints on the value of the blockage factor at the rotor inlet and outlet were imposed:

$$0.95 \leq \lambda_{B,1} \leq 1.0, \quad 0.95 \leq \lambda_{B,2} \leq 1.0$$

⁵⁷It's available as a built-in and validated PROOSIS function.

The optimized values of the design variables (calibration scalars) in terms of corrected inflow for the different iso-speed lines are shown in Figure 6.17 through Figure 6.21. On the graphs, the initial (default value) for the respective variable is also shown for comparison.

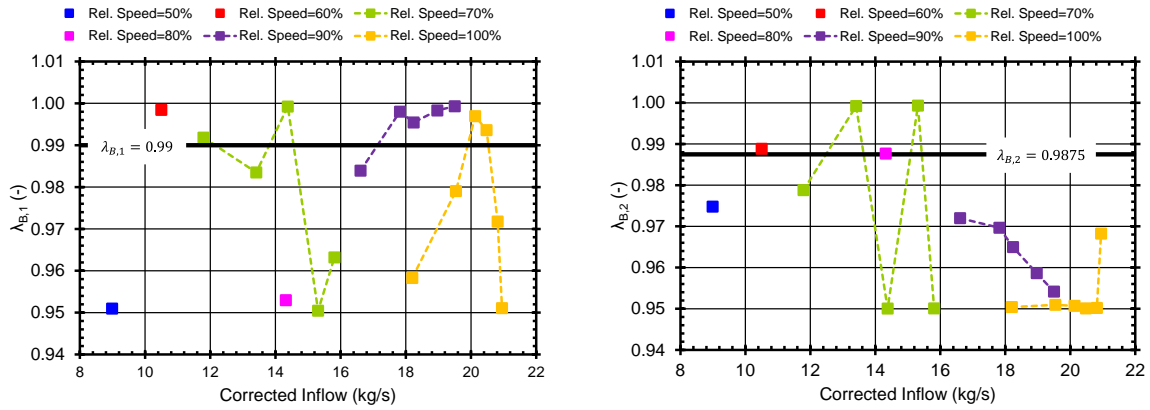


Figure 6.17: Blockage variation to match the performance of Rotor-35.

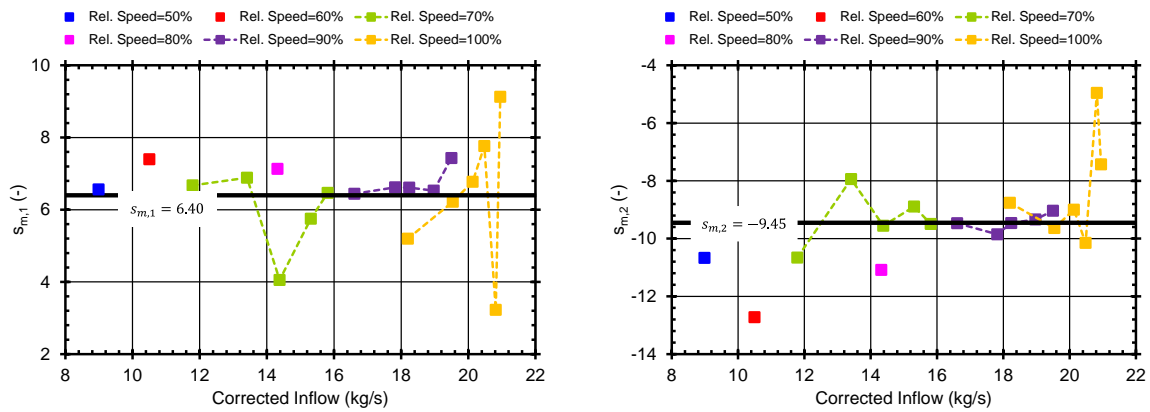


Figure 6.18: Deviation model scalars variation to match the performance of Rotor-35.

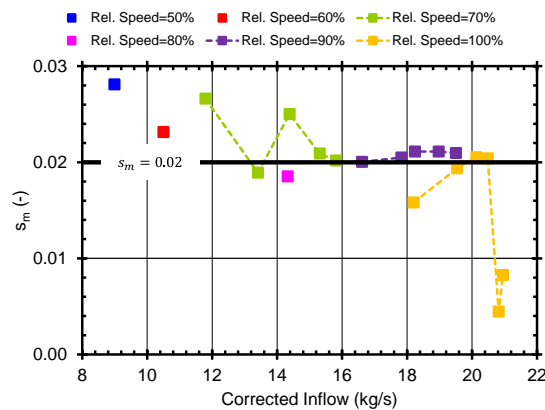


Figure 6.19: Endwall loss model scalar variation to match the performance of Rotor-35.

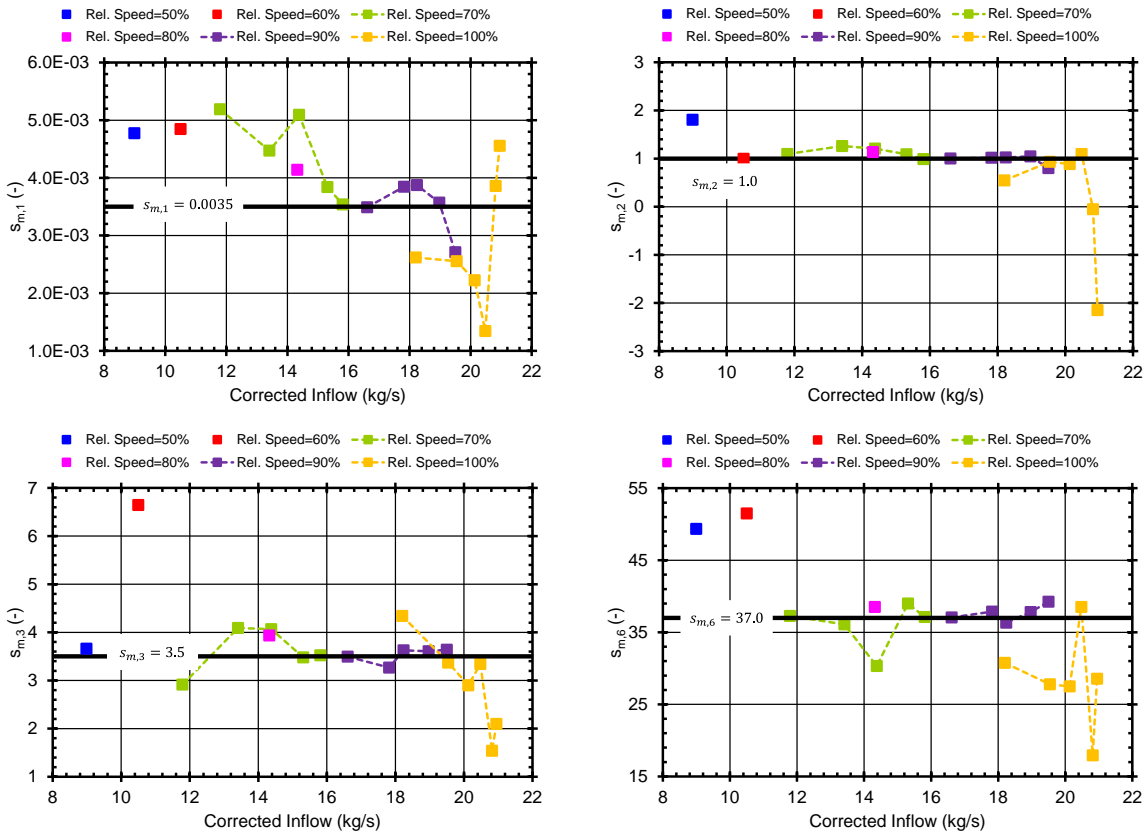


Figure 6.20: Profile loss model scalars variation to match the performance of Rotor-35.

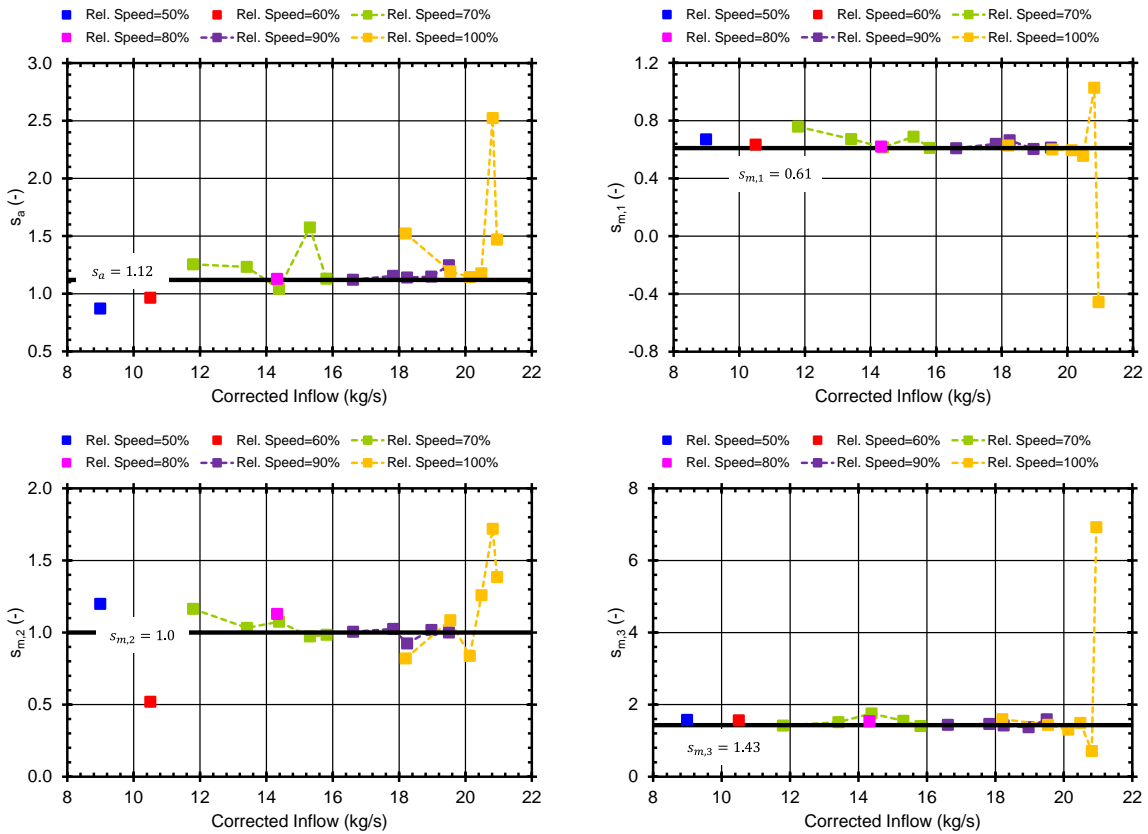


Figure 6.21: Equivalent diffusion factor model scalars variation to match the performance of Rotor-35.

Next, the values for the scalars shown in Figure 6.17–Figure 6.21 are introduced into the loss and deviation models used for estimating the performance of Rotor-35. The loss and deviation models for estimating the performance of Stator-35 are evaluated with their scalars set at the respective default values. Then, executing MLAC for Stage-35 gives the results shown in Figure 6.22.

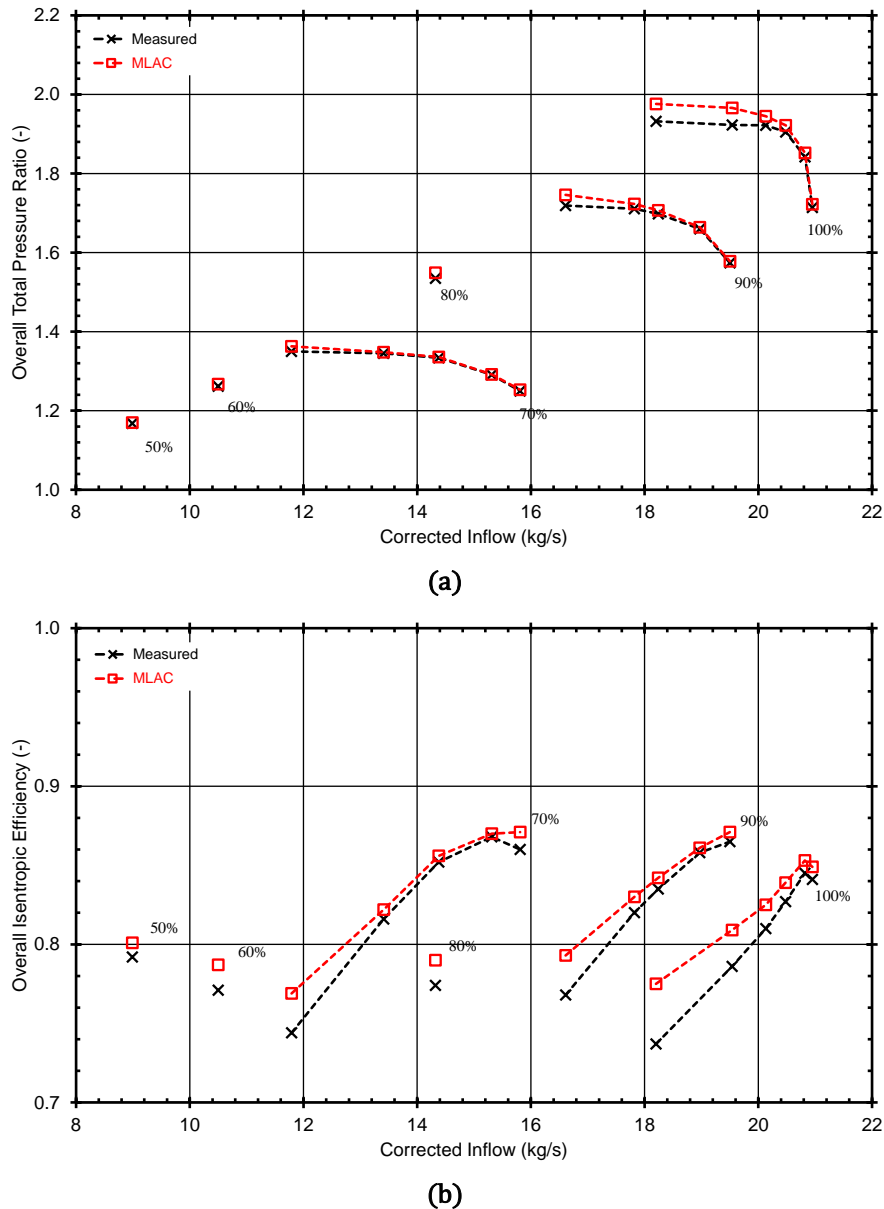


Figure 6.22: Comparison between the calibrated (only for Rotor-35 performance) MLAC predictions and measured data for the NASA Stage-35 compressor: **(a)** pressure ratio vs corrected inflow; **(b)** isentropic efficiency vs corrected inflow.

As it can be seen from Figure 6.22, the calibration of Rotor-35 alone is sufficient for reproducing the stage performance with reasonable accuracy.

Finally, note that no sensitivity analysis was conducted pre- or post- the calibration procedure presented in this paragraph. The present example serves only as a mere demonstration of the MLAC capability to adapt to existing measurements by

calibrating the loss and deviation models that it employs. In the future, however, it is recommended to study how the variations of the individual calibration scalars affect, both qualitatively and quantitatively, the behavior of the respective models relative to publicly available data. This way, possible physical trends could be identified which, in turn, could be utilized for, e.g., constructing correlations for the scalars themselves.

6.13.2 Choke Modelling Test Case

The MLAC choke modelling capability is exemplified using the geometry⁵⁸ of a multi-stage compressor, namely NASA’s “ISG-74A”. ISG-74A is a 3-stage transonic, high-speed compressor developed and tested during the 1980’s with a design pressure ratio of ~ 4.47 , rotating at 16,042.3 rpm [see Steinke (1986)]. ISG-74A includes one row of variable geometry IGVs, and three rows of variable geometry stators. For easy reference, the following designation is used for the compressor blade rows: IGV-R1-S1-R2-S2-R3-S3, where “R” stands for rotors and “S” for stators.

For the calculations that follow, the loss and deviation models shown in Table 6.6 are again employed. Secondary losses, clearance losses, and Reynolds number effects are deactivated. The deviation and losses for the IGVs are calculated according to Banjac et al.’s models (see paragraph 6.7.2 and Section 6.9, respectively). Finally, blockage is an input throughout the compressor and is set equal to the values given by Steinke in graph form (here tabulated in Table 6.8).

Table 6.8: Blockage factor distribution used in MLAC for the choke modelling test case

Row Nr.	Row	Blockage Value	
		@ Inlet	@ Outlet
1	IGV	0.96380	0.95996
2	R1	0.95986	0.95002
3	S1	0.94944	0.93960
4	R2	0.93986	0.92834
5	S2	0.92812	0.91804
6	R3	0.91806	0.90810
7	S3	0.90800	0.89804

The map produced by MLAC is shown in Figure 6.23. It was produced for standard-day inlet conditions, assuming axial flow at the compressor inlet, zero gas bleed extractions, at the design IGVs-VSVs setting (0°). The choked mass flow rate was calculated using a value for $\varepsilon = 10^{-3}$ in Eq. (6.130), while a lower bound on the total pressure ratio of $PR_{min} = 1.001$ was selected when establishing both the first and last point on the choked portion of the map characteristics. Between stall (estimated using the stalling incidence criterion, see paragraph 6.11.1) and choke, PR was calculated for eleven (11) equidistant values of \dot{m}_{in} along each iso-speed line.

⁵⁸The geometry of the NASA ISG-74A compressor serves only for demonstrating the choke modelling capabilities, and not for validating MLAC against the ISG-74A measured performance.

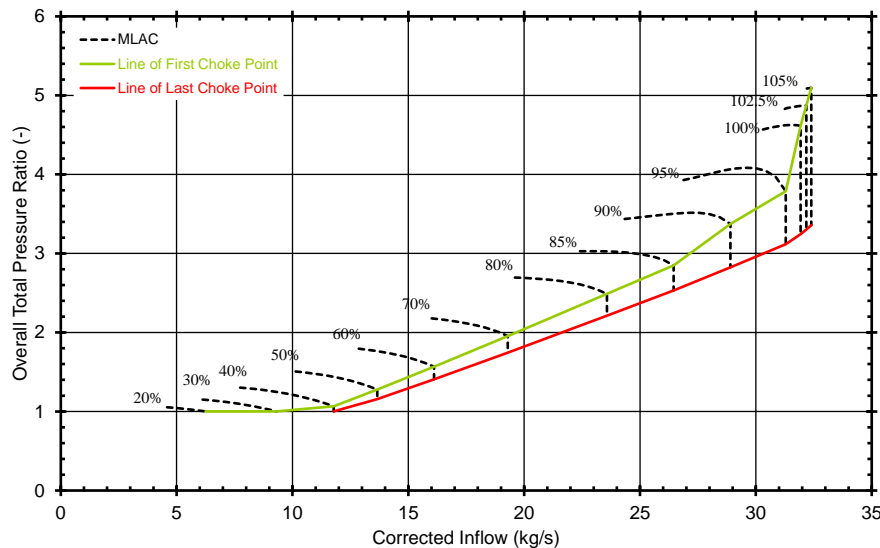


Figure 6.23: MLAC-produced pressure ratio map for the example 3-stage compressor geometry where the first and last choke line is shown.

The lines that connect the respective first and last choke points on every speed-line are also presented in Figure 6.23. These lines define the domain where the compressor operates at the maximum inlet mass flow. For $N_{mech}/N_{mech,d} = 20\%$ and 30% the maximum flow is established from the limiting pressure ratio value of $PR_{min} = 1.001$ and, thus, no vertical portion exists on these characteristics. The compressor works unchoked at these two speeds. Numerically, this means that the secant method cannot zero the functional expressed by Eq. (6.130) for the value of $\varepsilon = 10^{-3}$ while satisfying the constraint $PR > PR_{min}$. At both these points, $I_{R3,2}^{choke}$ has the minimum value which is about two orders of magnitude greater than the value of $\varepsilon = 10^{-3}$ for which choking is assumed to numerically occur. For $N_{mech}/N_{mech,d} = 40\%$, there is a narrow region on the map characteristic where the compressor can work at the maximum mass flow. Here, the compressor chokes for the first time at the throat of S3, while the last choke point is established from the constraint $PR_{min} = 1.001$ which is met before the compressor exit annulus becomes choked. Table 6.9 summarizes the rows and stations where the first and last choke points occur for $N_{mech}/N_{mech,d} > 40\%$.

Table 6.9: MLAC first and last choke point results for the example 3-stage compressor geometry

$N_{mech}/N_{mech,d}$ (%)	First Choke Point (Row-Station)	Last Choke Point (Row-Station)
50, 60, 70, 80, 85	S3-Throat	Compressor exit
90, 95	R3-Throat	Compressor exit
100, 102.5, 105	R1-Throat	Compressor exit

As we can see from Table 6.9, the first choke point progresses from the compressor inlet to the exit as the compressor rotational speed decreases, which is in accordance with the physical intuition [see Saravanamuttoo et al. (2017)].

To illustrate in more detail how the first choke point is established numerically, the 85% speed-line is used as an example. In Figure 6.24 and Figure 6.25, the choke indices values are plotted against the compressor inlet mass flow rate (\dot{m}_{in}) as it increases towards the choking value. Figure 6.24 shows the variation of the global minimum index (I_{min}^{choke}) and the variation of the minimum blade row index ($I_{br,min}^{choke}$) for all blade rows, while Figure 6.25 shows the variation of the individual indices for the third-stage stator (S3): $I_{S3,1}^{choke}$, $I_{S3,2}^{choke}$, $I_{S3,throat}^{choke}$, and $I_{S3,min}^{choke}$.

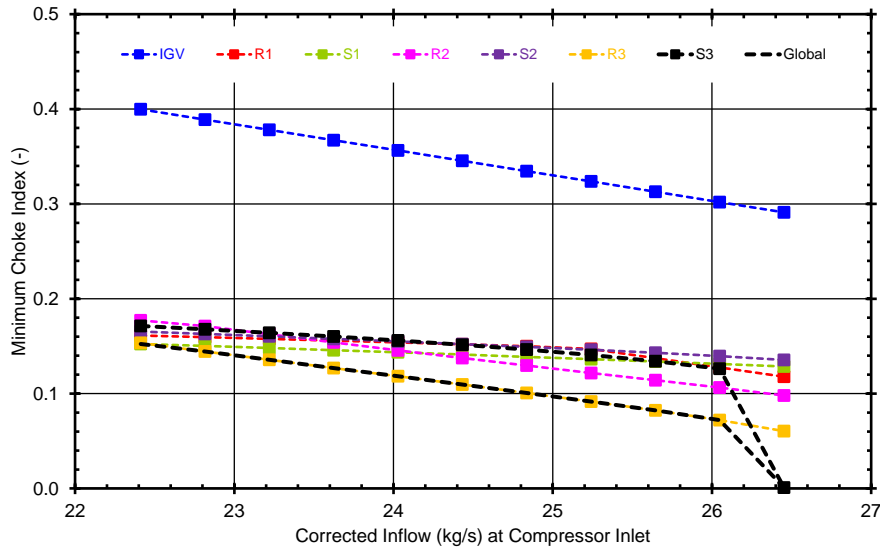


Figure 6.24: Minimum value of choke indices variation for the example 3-stage compressor geometry, for the 85% iso-speed line.

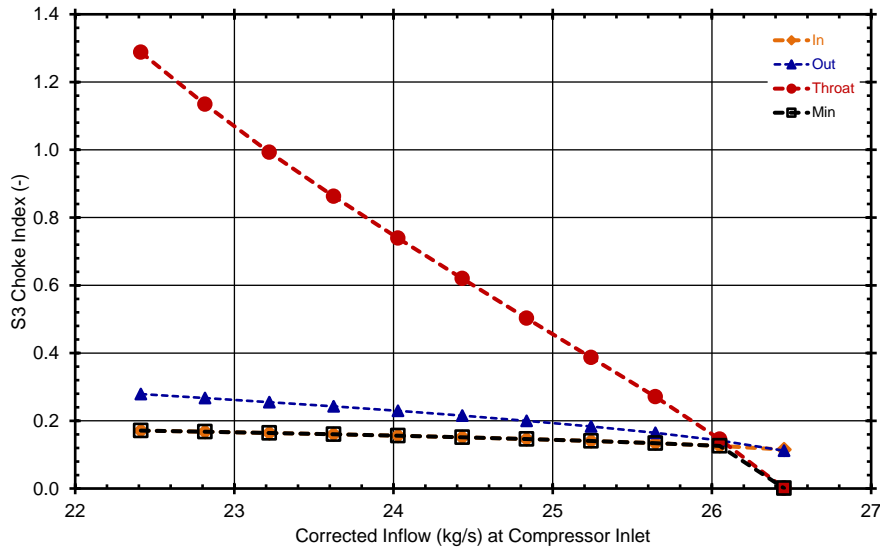


Figure 6.25: S3 individual choke indices variation for the example 3-stage compressor geometry, for the 85% iso-speed line, where: “In” and “Out” is the row inlet and outlet flow annulus, respectively.

From Figure 6.24, it is seen that $I_{min}^{choke} = I_{R3,min}^{choke}$ for \dot{m}_{in} 's between 22 and 26 kg/s, while in the same mass flow range the distance between $I_{R3,min}^{choke}$ and the values of all other indices either increases or remains constant as \dot{m}_{in} is increased. This means that,

if the compressor were to choke for a \dot{m}_{in} value between 22 and 26 kg/s, it would be due to R3 becoming choked. However, as \dot{m}_{in} approaches the choking value (≈ 26.5 kg/s), $I_{S3,min}^{choke}$ experiences an abrupt value drop and becomes less than $I_{R3,min}^{choke}$. This in turn results in an abrupt drop in the value of I_{min}^{choke} , causing the compressor to eventually choke for the first time at S3 as its value becomes equal to that of $I_{S3,min}^{choke}$.

The reason for the drop in $I_{S3,min}^{choke}$ value can be found in Figure 6.25. We see that $I_{S3,min}^{choke} = I_{S3,1}^{choke}$ for \dot{m}_{in} between 22 and 26 kg/s and, using the same rationale as above, if S3 were to choke for a \dot{m}_{in} in this range it would be due to the choking of the flow annulus at the S3's inlet. However, the distance between $I_{S3,1}^{choke}$ and the other indices decreases as the mass flow increases and, for a \dot{m}_{in} value slightly greater than 26 kg/s the difference between $I_{S3,throat}^{choke}$ and $I_{S3,1}^{choke}$ finally becomes negative, therefore causing the drop in $I_{S3,min}^{choke}$ value and S3 to choke at the passage instead.

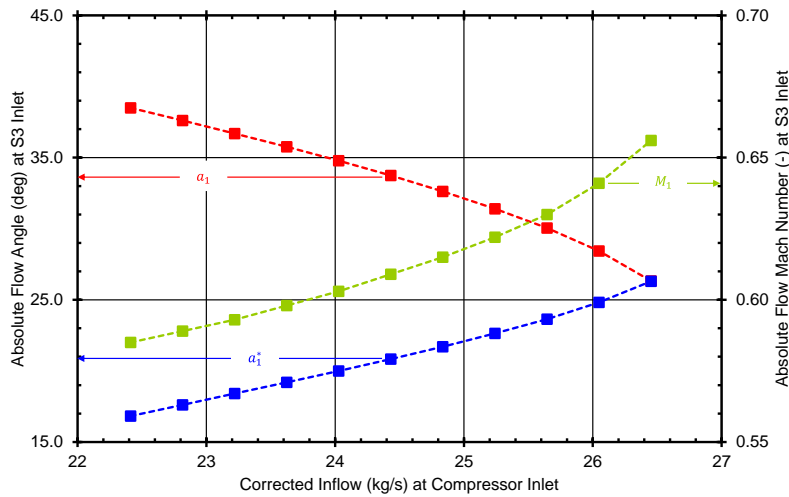


Figure 6.26: Throat passage choking for S3 at 85% compressor speed, for the example 3-stage compressor geometry.

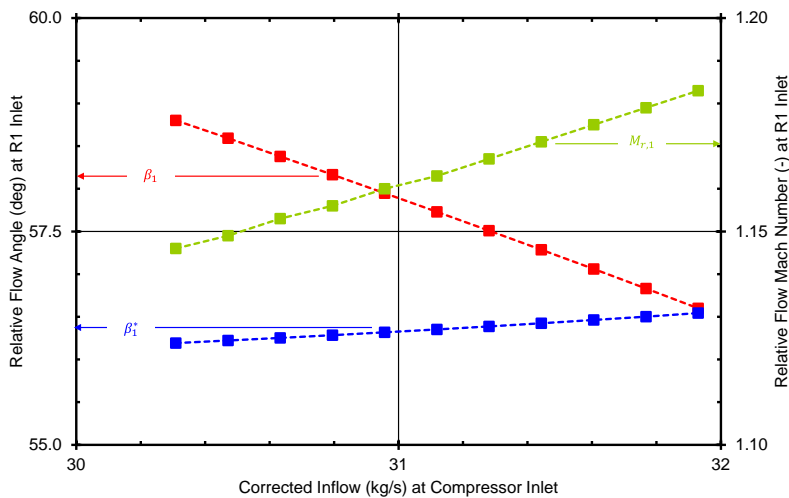


Figure 6.27: Throat passage choking for R1 at 100% compressor speed, for the example 3-stage compressor geometry.

In Figure 6.26, the absolute flow Mach number at S3's inlet is shown to be subsonic, for all $22 \leq \dot{m}_{in} \leq 26$ kg/s. As the flow Mach number increases, the minimum flow angle required for the throat to become choked (a_1^*) increases as well, while the absolute flow angle at the inlet of S3 decreases until the two become equal within the specified tolerance of $\varepsilon = 10^{-3}$. Therefore, the throat passage choking for S3 is realized for subsonic conditions. This is in contrast, for instance, to the R1 throat passage choking for the 100% iso-speed line where, as seen from Figure 6.27, the relative flow Mach number at R1's inlet is supersonic for $30 \leq \dot{m}_{in} \leq 32$ kg/s and the throat passage chokes for supersonic conditions with attached shocks.

The method to extend the choked part described in paragraph 6.10.4 is exemplified considering the speed-lines 100%, 102.5%, and 105%. In all three speed-lines, both the first and last choke points occurred at the throat passage of R1 and the compressor exit, respectively. Thus, these speed-lines were a good example for viewing how the choke point moves from R1 (almost at the compressor inlet) until it reaches the compressor exit flow annulus. Figure 6.28 shows the outcome of the procedure of the flow chart in Figure 6.12. It shows the “iso-choke” lines that denote the different rows and stations that choke successively as the compressor pressure ratio is reduced. It is shown that choking advances from R1 to R2 to R3 to S3 until the compressor exit is reached and the minimum pressure ratio for which the compressor can work is attained. For all blade rows, choking occurs at the respective throat passage. For all three rotors, the flow regime at the respective inlet is supersonic with attached shocks, while the flow at the S3 inlet is subsonic.

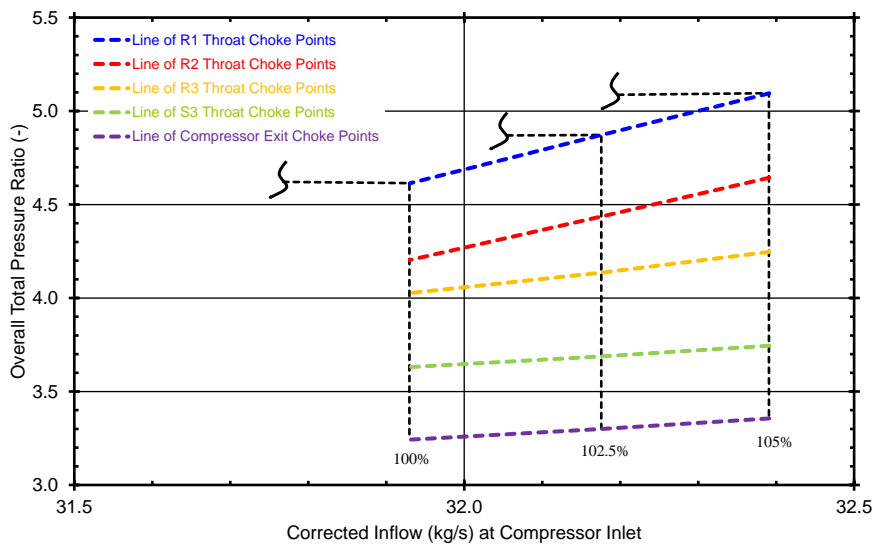


Figure 6.28: “Iso-choke” lines for the 100%, 102.5%, and 105% iso-speed lines for the example 3-stage compressor geometry.

To conclude this paragraph, an overall pressure ratio map illustrating the “iso-choke” lines for the case of the example 3-stage compressor geometry is presented in Figure 6.29.

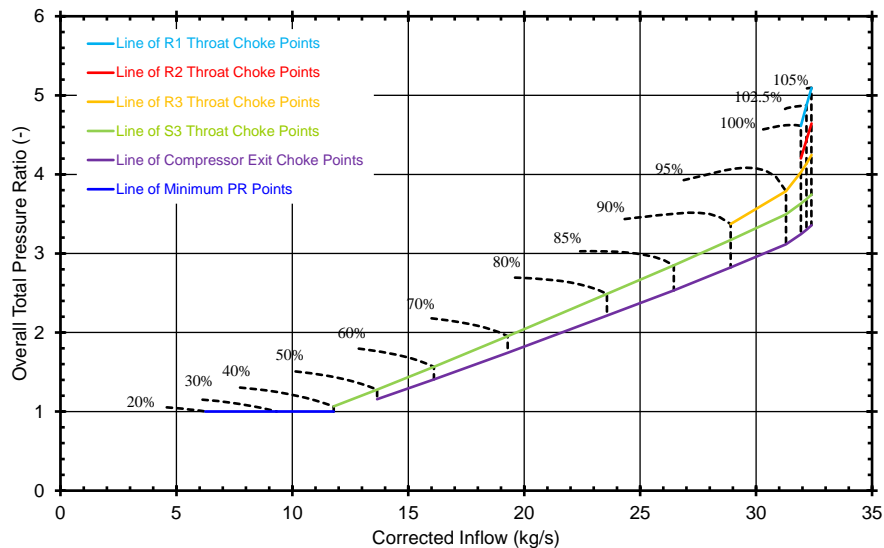


Figure 6.29: MLAC-produced pressure ratio map for the example 3-stage compressor geometry showing the “iso-choke” lines.

6.13.3 MLAC Integration in OD Cycle Calculations Test Case

For demonstrating the integration capability of MLAC in engine performance models, the case of a 2-spool turbofan engine with separate exhausts is considered. In this model, MLAC is used for replacing the HPC OD TURBO component. The engine schematic model in PROOSIS is shown in Figure 6.30.

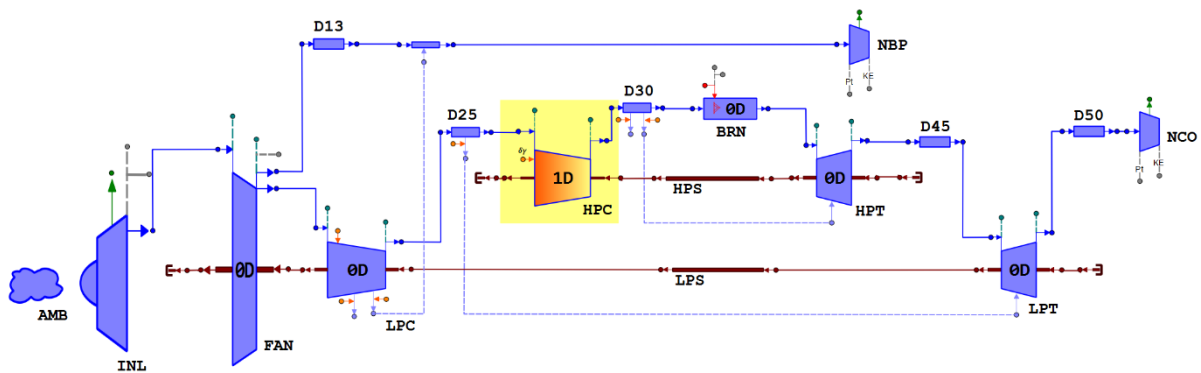


Figure 6.30: Schematic model of a 2-spool, unmixed turbofan engine in PROOSIS, where the MLAC component (orange-colored) shown inside the yellow rectangle (HPC) has replaced the conventional OD TURBO component for the HPC. Other components shown in the schematic are: Atmosphere (AMB), engine inlet (INL), fan (FAN), low-pressure compressor (LPC), high-pressure (HPT) and low-pressure (LPT) turbines, burner (BRN), core (NCO) and bypass (NBP) nozzles, low-pressure (LPS) and high-pressure (HPS) shafts, and ducts (D13-D50).

The 1D component seen in Figure 6.30 was set to represent the NASA/GE’s E³ 10-stage HPC [see Holloway et al. (1982)] as far as the necessary geometry is required for MLAC to run the compressor map. Following the pre-processing step described in Section 6.12, a map (Figure 6.31) is generated for four (4) different compressor inlet temperatures ($T_{in}^0 = 200, 288, 400, \text{ and } 500 \text{ K}$), covering the expected range for the considered application.

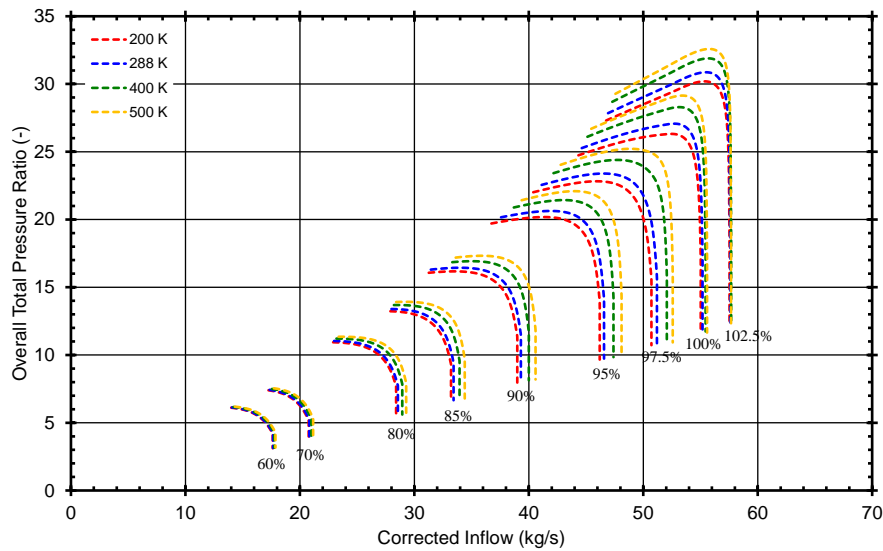


Figure 6.31: MLAC-produced pressure ratio map for different compressor inlet temperatures for the example 10-stage compressor.

Note that the mathematical formulation of the above mixed-fidelity engine model is identical to the conventional, full 0D cycle case, both in terms of boundary conditions (only one handle variable is required, here thrust is selected) and algebraic (turbomachinery component map parameters, bypass ratio, inlet mass flow rate) and dynamic (low- and high-pressure spool rotational speeds) variables. An engine design calculation was performed first to obtain the scaling factors for the 0D map components (fan, LPC, HPT, and LPT) and the throat areas of the convergent core and bypass nozzles. The values of the main engine cycle parameters are shown in Table 6.10.

Table 6.10: Selected engine performance parameters

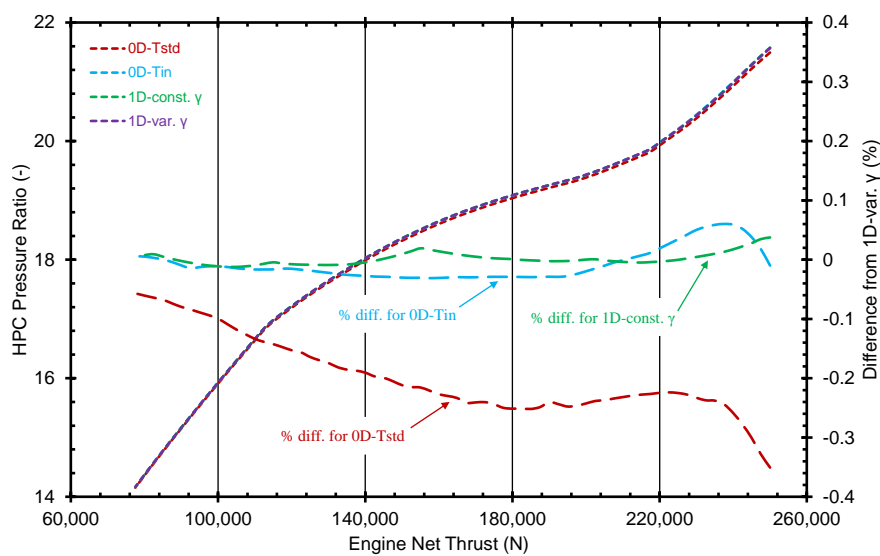
Parameter	Value
Net thrust	59.2 kN
Overall pressure ratio	56.1
Bypass ratio	8.85
HPC pressure ratio	23.9
Turbine inlet temperature	1715 K

Next, off-design simulations were performed to produce a steady-state operating line between low- and high-power conditions at SLS conditions. Simulations were performed in both 0D and 1D mode for the HPC component. In the latter case, the calculations were conducted considering both variable and constant gas properties. The loss and deviation models shown in Table 6.6 were again employed with the exception of shock losses where Dixon’s model was used instead of Steinke’s (see paragraph 6.8.5). Secondary losses, clearance losses, and Reynolds number effects were deactivated, and blockage was set to the default values given by Glassman et al.

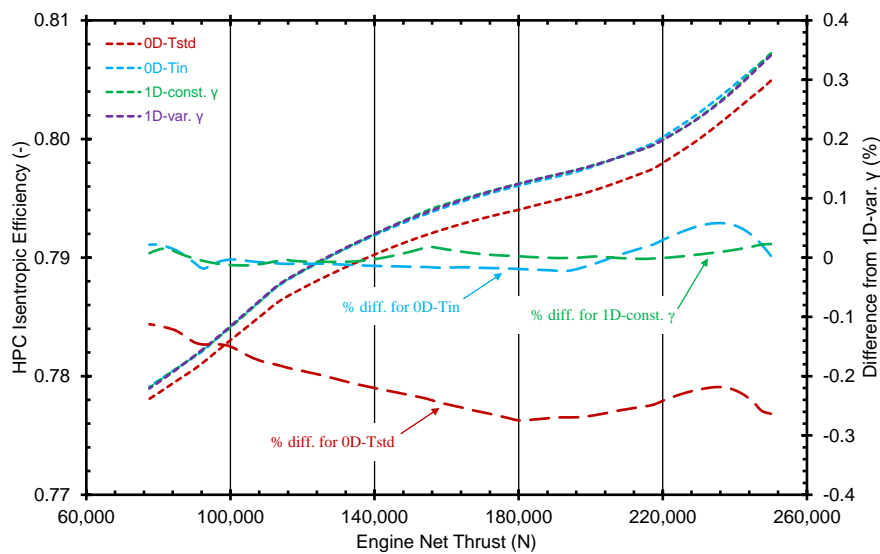
(1995) (see paragraph 6.8.10). Finally, the deviation and losses for the IGVs were calculated according to Banjac et al.'s models, described in paragraph 6.7.2 and Section 6.9, respectively.

Figure 6.32 and Figure 6.33 show the variation of the HPC pressure ratio and isentropic efficiency and that of the engine SFC with the engine thrust (60-260 kN) at SLS conditions for four (4) simulation options which, presented in order of increasing computational complexity, are:

- 0D mode using single MLAC-generated map at standard temperature (0D-Tstd)
- 0D mode using MLAC-generated maps and the actual HPC T_{in}^0 (0D-Tin)
- 1D mode with constant gas properties (1D-const. γ)
- 1D mode with variable gas properties (1D-var. γ)



(a)



(b)

Figure 6.32: Variation at SLS conditions of HPC (a) pressure ratio and (b) isentropic efficiency with engine thrust, for different calculation modes of MLAC HPC component.

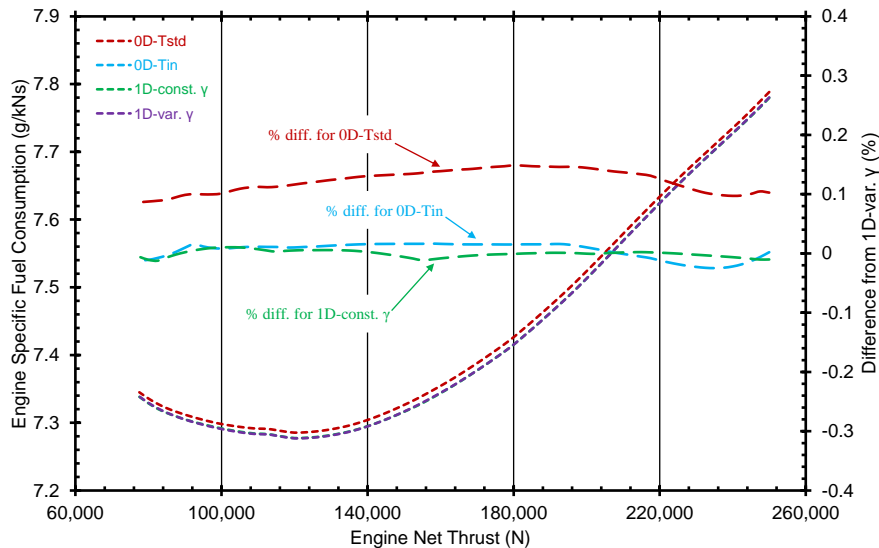


Figure 6.33: Variation at SLS conditions of engine SFC with engine thrust, for different calculation modes of MLAC HPC component.

In Figure 6.32 and Figure 6.33, the differences (%) of the simulation results of the first three cases from the fourth one are also shown. As expected, the first option (0D-Tstd) shows the largest differences (up to -0.35%) from the fourth option (1D-var. γ). The other two are well within the $\pm 0.1\%$ range. The use of the 0D mode with T_{in}^0 as an extra dimension shows the importance of obtaining the compressor performance for the actual inlet conditions and justifies the need for the 1D mode, since otherwise the 0D mode would require the generation and use of multi-dimensional tables/maps where all possible combinations of compressor operation are included.

Finally, the use of the “1D-const. γ ” option proves to be an excellent surrogate to the “1D-var. γ ” mode, as it provides calculations with the same accuracy while it executes much faster ($\sim 45\%$ faster on a PC with Windows 7 64-bit, Intel® CoreTM2 Duo CPU @ 3 GHz and 4GB RAM).

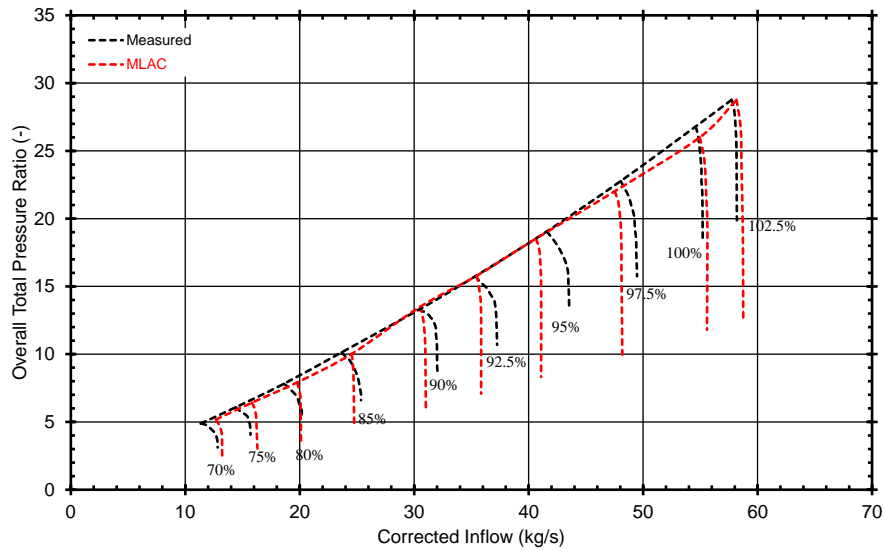
6.13.4 Multi-Stage Compressor Performance Map Validation Test Case

As the last test case, the capability of MLAC to reproduce successfully the entire performance maps of multi-stage, transonic compressors is verified. For this, the well-known NASA/GE E³ 10-stage HPC [see Holloway et al. (1982) and Cline et al. (1983)] is again used. The compressor and blade geometry information in the above references is used as input to MLAC.

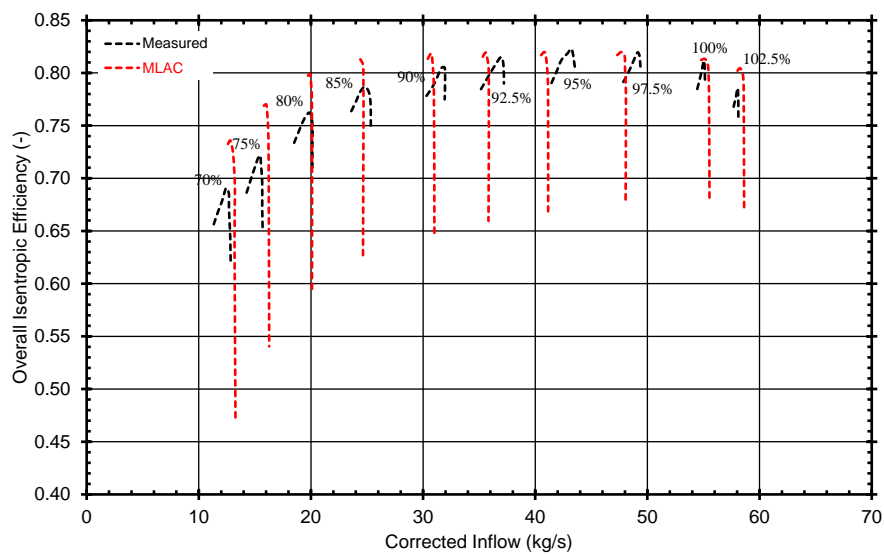
For producing the performance maps, the loss and deviation models shown in Table 6.6 were employed where secondary losses, clearance losses, and Reynolds number effects were deactivated, and blockage was set to the default values given by Glassman et al. (1995) (see paragraph 6.8.10). Finally, the surge line was established using the stall margin method presented in paragraph 6.11.4.

The generated maps are depicted as overall total pressure ratio against corrected inflow and as overall isentropic efficiency versus corrected inflow in Figure 6.34. In both figures, also plotted is the corresponding measured map [see Cline et al. (1983)] for comparison. As it can be seen from Figure 6.34, MLAC predictions are, in general, in

good agreement with measurements. This fact demonstrates the appropriateness of MLAC as a tool for predicting the off-design performance of multi-stage, transonic compressors over their entire operating range.



(a)



(b)

Figure 6.34: Comparison between the measured and the MLAC predicted maps for the NASA/GE E³ HPC: (a) overall total pressure ratio vs corrected inflow; (b) overall isentropic efficiency vs corrected inflow.

6.14 Summary and Discussion

In the present chapter models and procedures were presented for estimating the off-design performance of axial-flow, multi-row compressors, with any number of gas bleeds and any kind of blades (rotating, stationary, IGVs, of variable geometry or not). The performance modelling is accomplished through a mean-line (1D) approach in a row-by-row calculation manner, where loss and deviation models are applied to

estimate the performance of the individual blade rows. This resulted in the development of a PROOSIS library (called MLAC), which defines components for off-design performance calculations of axial compressors with any number of gas bleeds. Calculations can be performed considering variable or constant gas properties.

Given the compressor geometry, the compressor speed and inlet conditions, the components defined in MLAC can be used to estimate the performance of compressors at a single operating point or, using a dedicated PROOSIS experiment, they can be used to produce performance maps in a user-defined operating range (i.e., for any number and values of compressor speeds between 5-120%), between stall and choke, and beyond choke conditions. These maps can then be used in 0D components for conducting engine cycle calculations. Alternatively, MLAC components can directly replace the 0D components in engine models to estimate the compressor performance by utilizing the 1D, row-by-row approach. The latter offers the advantage of establishing the compressor performance at the current inlet temperature, thus producing cycle simulations with higher accuracy.

To establish the conditions where the compressor operation becomes choked, and the vertical (choked) part of a characteristic, MLAC utilizes a novel approach. Appropriate indices are introduced that model choke at both blade row level and compressor level. These indices are then zeroed numerically to establish the choked mass flow in an automated way and, then, the vertical part of the characteristic is computed such that a specified back pressure is attained or the compressor exit annulus becomes choked. The developed method gives insight of the flow pattern across the compressor as the choke progresses from one row to the next. Similarly, appropriately defined indices are used for computing the compressor inlet mass flow that corresponds to stall conditions.

The MLAC capabilities both at component and at engine level were validated and verified through a series of test cases. The choke modelling approach was exemplified by visualizing the progression of choking conditions through a 3-stage, transonic compressor. More importantly, it was shown that MLAC can successfully reproduce the performance of multi-stage, transonic compressors in the entire operating range, while the MLAC integration capability in engine cycle models was proven by considering the performance of the HPC of a 2-spool turbofan engine (calculations conducted with both constant and variable gas properties).

7 Axial Compressor 1D Design Modelling (MLDC)

7.1 Introduction

The present chapter describes a mean-line (1D) formulation and its materialization into PROOSIS component(s) for the preliminary aerothermodynamic design of axial-flow, multi-row compressors, called MLDC (Mean-Line Design Code). The geometry output by MLDC, is the geometry input required by the MLAC components described in Chapter 6 for estimating the off-design performance of compressors.

For known inlet conditions (that is, \dot{m}_{in} , T_{in}^0 , p_{in}^0), compressor speed (N_{mech} , $U_{t,in}$, or both), and design pressure ratio, the MLDC component computes the compressor geometry and performance by conducting a row-by-row calculation where the gas-path and blade dimensions are obtained simultaneously. That is, the gas-path radii are obtained by the aerothermodynamic design of the blade rows, and then these are used to obtain basic blade dimensions such as blade heights and chord lengths; these, in turn, are used to size axially the compressor gas-path, thus moving the design sequence to the next row. MLDC uses the same fluid models, thermodynamic functions, blade models, loss models, and numerical schemes as those employed in the MLAC library (see Chapter 6). Thus, consistent calculations between the design and analysis modes are ensured. The MLDC component also uses the same building blocks (i.e., BRM and IVM) as those utilized in the modelling of the off-design components. Therefore, in the present chapter only the differences in modelling between the design and off-design components will be summarized as well as the necessary design inputs and options.

7.2 Compressor Design Modelling, Options, and Inputs

7.2.1 General Design Approach

For a given pressure ratio (PR), the compressor design is conducted following one of two possible approaches. In the first one, the number of stages is specified by the user. In the second one, the number of stages is an output of the aerothermodynamic design,

where the MLDC component accumulates stages until the required PR is achieved. In either case, if for the current work distribution PR is exceeded, then a follow-on calculation adjusts the overall compressor enthalpy change (for the same work distribution) in order to match the required PR .

7.2.2 Definition of the Compressor Work Distribution

The work distribution across the compressor, expressed as percentage of the stage enthalpy rise to the compressor overall enthalpy rise, can either be an input or can be established according to the following four (4) aerodynamic criteria [see Glassman et al. (1995)]:

- Maximum diffusion factor at rotor tip (default value = 0.50)
- Maximum diffusion factor at stator hub (default value = 0.60)
- Maximum flow angle change at rotor hub (default value = 40°)
- Maximum Mach number at stator hub (default value = 0.85)

7.2.3 Definition of the Axial Velocity Distribution

The axial velocity across the compressor can be described based on one of the following three (3) ways:

1. Axial velocity distribution between the values at compressor inlet and exit using a user-defined axial velocity shape factor ($V_{x,CLICO}$) that describes the shape of a parabola in relation to a straight line according to:

$$V_{x,1} = c_1(j - 1)^2 + c_2(j - 1) + c_3 \quad (7.1)$$

where $V_{x,1}$ is the axial flow velocity at the blade row inlet, j is the blade row number, and the coefficients c_1 , c_2 , and c_3 are given by:

$$c_1 = -\frac{2(V_{x,in} + V_{x,out})(V_{x,CLICO} - 1)}{(N_{br} - 1)^2} \quad (7.2)$$

$$c_2 = \frac{3V_{x,out} + V_{x,in} - 2V_{x,CLICO}(V_{x,in} + V_{x,out})}{N_{br} - 1} + \frac{4N_{br}(V_{x,in} + V_{x,out})(V_{x,CLICO} - 1)}{(N_{br} - 1)^2} \quad (7.3)$$

$$c_3 = V_{x,in} \quad (7.4)$$

In the above equations, the default value for $V_{x,CLICO}$ is unity.

2. Specifying the coefficients of a 4th order polynomial that describes the axial distribution in relation to a user-defined reference value ($\bar{V}_{x,1}$):

$$\frac{V_{x,1}}{\bar{V}_{x,1}} = c_1y^4 + c_2y^3 + c_3y^2 + c_4y + 1 \quad (7.5)$$

where $V_{x,1}$ is the axial flow velocity at the inlet of the rotors, and the auxiliary parameter y is $y = (j - 1)/(N_{stg} - 1)$.

The default values for the coefficients c_1, c_2, c_3, c_4 , and $\bar{V}_{x,1}$ were obtained using as reference the NASA/GE E³ HPC [see Holloway et al. (1982)]:

$$c_1 = 1.237, c_2 = -3.251, c_3 = 2.300, c_4 = -0.389, \bar{V}_{x,1} = 150 \text{ m/s}$$

3. Using Eq. (7.1) but, this time, to describe the axial velocity variation at the rotor inlet between the corresponding values of the first and last stage rotors.

The axial velocities at the component inlet ($V_{x,in}$) and exit ($V_{x,out}$) are specified either by imposing them directly, or by giving the absolute flow Mach number. Note that, for the compressor inlet, imposing the compressor specific flow is a third option.

Finally, for the second and third options, velocity ratios must also be specified that describe the change in axial velocity between the 1) rotor outlet/inlet (default value = 0.914), 2) stator outlet/inlet (default value = 0.980), 3) IGVs outlet/inlet (default value = 1.078), 4) rotor inlet/IGVs inlet (default value = 1.160), and 5) rotor inlet/stator inlet (default value = 1.050).

7.2.4 Definition of the Rotor Inlet Absolute Flow Angle

The rotor inlet absolute flow angle can be a user input in every stage, or it can be described by specifying the coefficients of a 3rd degree polynomial in relation to a user-defined average value (\bar{a}_1) according to:

$$\frac{a_1}{\bar{a}_1} = c_1 y^3 + c_2 y^2 + c_3 y + c_4 \quad (7.6)$$

where a_1 is the absolute flow angle at the inlet of the rotors, and the auxiliary parameter y is again given by $y = (j - 1)/(N_{stg} - 1)$.

The default values for the coefficients c_1, c_2, c_3, c_4 , and \bar{a}_1 were again obtained using as reference the NASA/GE E³ HPC [see Holloway et al. (1982)]:

$$c_1 = 1.806, c_2 = -4.463, c_3 = 2.854, c_4 = 0.642, \bar{a}_1 \cong 14^\circ$$

7.2.5 Compressor Mean-Line Definition

In MLDC, the compressor gas-path can be described in one of the following eight (8) ways:

1. Constant hub radius
2. Constant mean radius
3. Constant tip radius
4. Mean radius distribution as a ratio from the average (calculated) value
5. Constant radius from compressor's inlet up to a stage and then linear up to compressor's exit
6. Linear from compressor's inlet up to a stage and then constant up to compressor's exit

7. Mean radius distribution between compressor's inlet and exit using a single user-defined parameter that, similarly to Eq. (7.1), describes the shape of a parabola in relation to a straight line
8. User-specified distribution of mean radius

In addition to the above, the user must also specify the compressor inlet hub-to-tip ratio (except for the case when N_{mech} and $U_{t,in}$ are both specified). The exit hub-to-tip ratio is only required when the gas-path shape is defined according to options 5-7.

7.2.6 Compressor Axial Positioning and Gas-Path Visualization

Finally, having determined the compressor gas-path radii, the compressor axial sizing and the gas-path visualization are conducted following adapted versions of the methodologies presented in Section 3.4. Note that, the axial gap percentage between two consecutive blade rows is either an input or obtained considering linear interpolation between a first and last row input value. In MLDC, the axial gap percentage is defined as the axial gap length between two rows divided by the average value of the hub and tip axial chord lengths of the upstream row. For rows where bleeds occur, the axial gas is set explicitly to facilitate the necessary mass extraction.

7.3 Blade Row Design Modelling, Options, and Inputs

For predicting the flow (\dot{m} , T^0 , p^0) across any blade row and for estimating the required geometry, MLDC employs the same computational building blocks as those used in MLAC (see Chapter 6), i.e., the Blade Row Module (BRM) and the Inter-Volume Module (IVM).

7.3.1 IVM Modelling

In summary, IVM models the flow in the duct after a blade row. In IVM, gas bleeds are taken into account through mass and gas composition continuity, while gas-path radius changes are accounted for through a moment of momentum balance according to:

$$\dot{m}_3 R_{m,3} V_{\theta,3} = \dot{m}_2 R_{m,2} V_{\theta,2} \quad (7.7)$$

For more information on the IVM modelling, see paragraph 6.3.2.

7.3.2 BRM Modelling

BRM establishes the performance (flow losses and deviation) and geometry (metal angles, chord lengths, blade count) of individual blade rows. BRM can model any type of rotating or stationary blade row, of fixed or variable geometry. In MLDC, there are available four (4) profile shapes for describing the geometry and performance of a blade section: (1) NACA-65, (2) NACA-63 A₄K₆ (for IGVs), (3) DCA, and (4) BC4 (for more information on the different profiles, see Section 6.4).

7.3.2.1 BRM Flow Modelling

In BRM, the flow across a blade row is described by a set of equations including the mass and gas composition continuity, the conservation of energy, and loss (ω) and deviation (δ) correlations for obtaining the flow conditions at the outlet of the blade row knowing the ones at the inlet:

$$\omega = \begin{cases} \frac{(p_{r,is}^0)_2 - p_{r,2}^0}{p_{r,1}^0 - p_1^s}, & \text{for rotating blade rows} \\ \frac{p_1^0 - p_2^0}{p_1^0 - p_1^s}, & \text{for stationary blade rows} \end{cases} \quad (7.8)$$

$$\beta_2 = \kappa_{TE} + \delta \quad (7.9)$$

For the different loss and deviation models applied in both MLAC and MLDC, the reader is referred to Section 6.5 through 6.9.

7.3.2.2 BRM Geometry Modelling

An output of the BRM in MLDC, is the blade geometry. For establishing the blade metal angles at the mean-line (κ_{LE} and κ_{TE}), an iteration scheme on the flow angles at the blade row inlet (β_1) and (β_2) is employed. The residual equations required are given by Eq. (7.9) for the estimated deviation angle, while an additional equation is formulated that requires that the actual incidence angle of the flow be equal to that for which the flow losses across the row are minimum. The latter is expressed according to:

$$i = i_{min, Ma} \quad (7.10)$$

where $i_{min, Ma}$ is calculated according to paragraph 6.8.8.

For estimating the blade chord length at the mean-line, the aspect ratio is required and the blade chord is then estimated by Eq. (7.11):

$$c = \frac{\bar{h}_b}{AR} \quad (7.11)$$

Aspect ratio can either be a user input or is given as a rate of change (δAR) for rotors and stators from their first stage value (δAR_1), and down to a user-specified minimum value (AR_{min}), according to:

$$AR_j = \max[AR_1 + (j - 1)\delta AR, AR_{min}] \quad (7.12)$$

where the default value for AR_{min} is $AR_{min} = 1.0$.

For obtaining the blade geometry along the blade span, first the metal angles at the blade hub and tip have to be established. To do so, the flow along the span of a blade is assumed to approximate a free-vortex flow, described by [see Saravanamuttoo et al. (2017)]:

$$\frac{dV_x}{dr} = 0 \quad (7.13)$$

$$\frac{d}{dr}(rV_\theta) = 0 \quad (7.14)$$

From the above, the flow angles at the blade row inlet and outlet can be established at the blade hub and tip. Then, the metal angles at the blade leading- and trailing-edges are estimated based on the definition of the flow incidence and deviation, or:

$$\kappa_{LE} = \beta_1 - i \quad (7.15)$$

$$\kappa_{TE} = \beta_2 - \delta \quad (7.16)$$

where Eqs (7.15) and (7.16) are applied at both the blade hub and tip.

Having determined κ_{LE} and κ_{TE} at the blade hub, mean, and tip, then the blade stagger angles can also be established. For the blade profiles considered in MLDC, stagger angle can be approximated as [see Aungier (2003)]:

$$\gamma \cong \frac{\kappa_{LE} + \kappa_{TE}}{2}$$

From simple trigonometry it then follows that the blade axial chord lengths at the blade hub, mean, and tip can be estimated from:

$$c_x = c \cos \gamma \quad (7.17)$$

where it is assumed that the blade true chord length remains axially constant, or: $c_h = c_t = c$.

Finally, to estimate the blade count, the estimation of the solidity is required. In MLDC, solidity can either be a user input in every blade row or it can be estimated based on the relative tip Mach number for rotors and the absolute flow turning for stators. These relationships are similar to the ones described in paragraph 3.3.11, but they are again given here for completeness. Therefore, the solidity for a rotor row is given by:

$$\sigma_R = \frac{\bar{R}_t}{\bar{R}_m} (0.5M_{r,t,1} + 0.7) \quad (7.18)$$

while that for a stator row is given by:

$$\sigma_S = \frac{\bar{R}_h}{\bar{R}_m} \begin{cases} (0.0206\Delta a + 0.794), & \Delta a < 44^\circ \\ (0.080\Delta a - 1.82), & 44^\circ \leq \Delta a < 60^\circ \\ 3, & \Delta a \geq 60^\circ \end{cases} \quad (7.19)$$

where $\Delta a = a_1 - a_2$ is the absolute flow turning.

Having determined the solidity, then the blade count is easily established via the ceiling function described by:

$$Z_b = \left\lceil \frac{2\pi\sigma\bar{R}_m}{c} \right\rceil \quad (7.20)$$

7.4 MLDC PROOSIS Library Component for Design Calculations

As mentioned in the chapter introduction, the modelling presented in the previous sections led to the development of a dedicated PROOSIS library named MLDC. MLDC currently defines one (1) PROOSIS component for conducting the aerothermodynamic design of multi-row, axial-flow compressors by conducting a row-by-row mean-line calculation. The PROOSIS symbol defined in MLDC for compressor design calculations is shown in Figure 7.1.

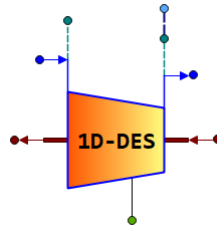


Figure 7.1: MLDC palette defining PROOSIS symbols for the aerothermodynamic design of axial-flow, multi-row compressors with any number of gas bleeds.

As with all components described in the present thesis, the symbol shown in Figure 7.1 can also be dragged-and-dropped into a PROOSIS schematic canvas for conducting compressor design studies. For this reason, a dedicated PROOSIS experiment was also developed that conducts the compressor design for different design strategies.

7.5 MLDC Validation Study

The MLDC component shown in Figure 7.1 was validated against the well-known NASA/GE E³ HPC. The aerodynamic design point data and the design aspects of the compressor have been described analytically in paragraph 3.9.1.

For the validation, all the available information from the relevant public literature [see Holloway et al. (1982)] was used, except for solidity which was calculated according to Eqs (7.18) and (7.19), and the work distribution that was determined from the aerodynamic criteria described in paragraph 7.2.2 with their default values. For the axial velocity distribution, Eq. (7.5) was used with $\bar{V}_{x,1} = 180$ m/s. For the rotor inlet absolute flow angle (a_1), the mean-line radius distribution, the blade aspect ratio, and the axial gap percentage, the information given by Holloway et al. (1982) was used.

The validation was conducted with the loss and deviation models summarized in Table 7.1. Note that, since the diffusion factor model for profile losses is used, both the secondary losses and Reynolds number effects were turned off. Clearance losses were also deactivated (there is no information whatsoever given on δ_c 's by Holloway et al.).

For Mach number effects, the default model was used (see paragraph 5.8.8). Finally, blockage was set to the default values given by Glassman et al. (1995) (see paragraph 6.8.10).

Table 7.1: Loss and deviation models used in validating the MLDC component

Loss/Deviation	Model	Remarks
Design incidence	Herrig's model	See paragraph 6.5.1.2
Design deviation	Lieblein's model	See paragraph 6.5.2.1
Off-design deviation	Swan's model	See paragraph 6.7.1.2
Profile loss	Diffusion factor model	See paragraph 6.8.7.1
Endwall loss	Howell's model	See paragraph 6.8.2.1
Shock loss	Dixon's model	See paragraph 6.8.5

The compressor efficiency estimated by the MLDC component is equal to 82.5%, which gives a (relative) difference of about 3.73% compared to the actual compressor efficiency (85.7%). The derived gas-path is compared with the actual one in Figure 7.2 and shows only minor differences along the axial direction due to small differences in the calculation of the chord lengths (see Figure 7.3e) and the way the gap ratio is defined at the mean radius in MLDC.

As can also be seen from Figure 7.2, the MLDC component is also capable of estimating the correct number of stages (10) for the compressor design pressure ratio (25) and the used aerodynamic criteria to establish the stage loading.

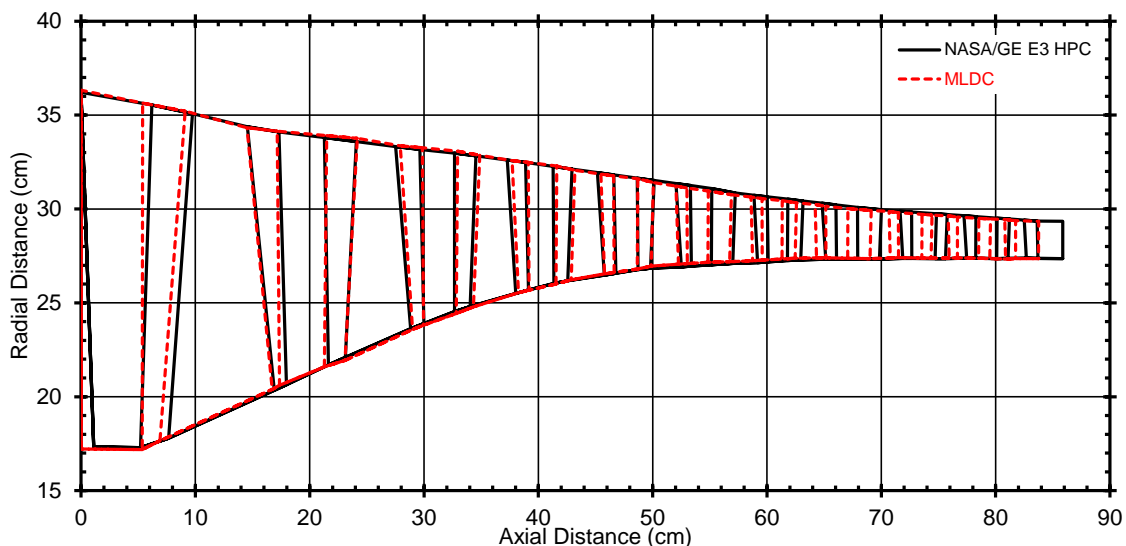


Figure 7.2: Comparison between the actual NASA/GE E³ HPC gas-path and the one obtained by the MLDC compressor component.

Next, Figure 7.3 presents the comparison of the actual and the estimated blade dimensions for the NASA/GE E³ HPC. Comparisons are shown for basic blade dimensions such as blade metal angles at leading- and trailing edge, blade count, etc.

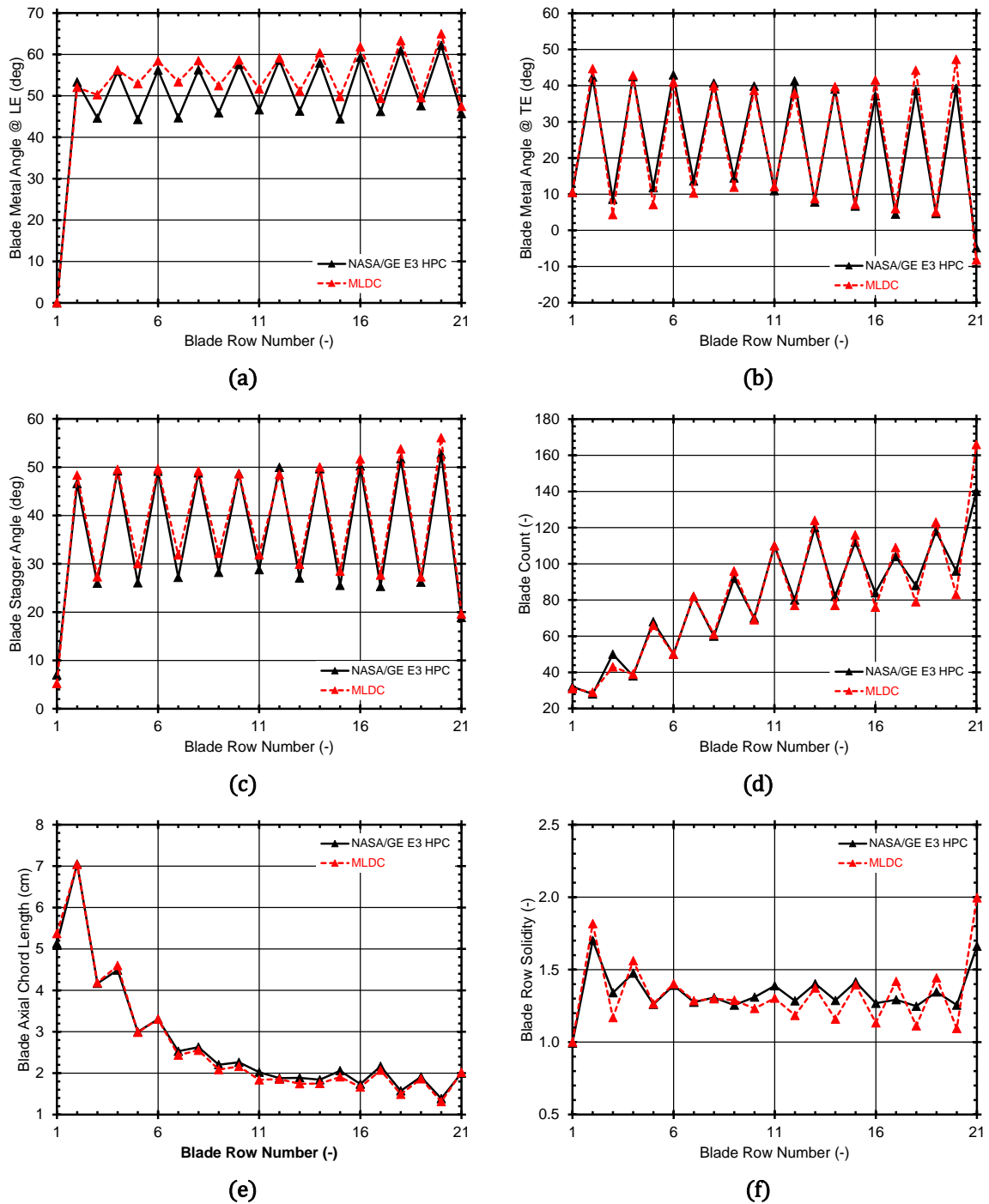


Figure 7.3: Comparison between the actual and MLDC blade geometries for the NASA/GE E³ HPC: (a) Metal angle at LE; (b) metal angle at TE; (c) stagger angle; (d) blade count; (e) blade axial chord length; (f) blade row solidity.

Overall, as it can be seen by both Figure 7.2 and Figure 7.3, as well as by the estimated compressor efficiency, the MLDC component is capable of capturing the correct performance and geometry both at component (Figure 7.2) and blade row level (Figure 7.3). Therefore, the design case results demonstrate the validity and accuracy of the proposed tool for the design of multi-stage, axial-flow compressors.

7.6 Summary and Discussion

In the present chapter, an extension of the MLAC components for off-design performance predictions defined in Chapter 6, was presented. The modelling formulation described here led to the development of a library (MLDC) that defines one component for the aerothermodynamic design of axial-flow, multi-stage compressors. The design is accomplished through a mean-line (1D) approach in a row-by-row calculation manner.

The MLDC component for the aerothermodynamic design of compressors uses the same fluid models, thermodynamic functions, numerical schemes, and building blocks for the performance modelling of blade rows (i.e., BRM and IVM) as those utilized by its MLAC counterparts. Therefore, consistent calculations between the design and off-design modes of the MLC libraries are ensured. In other words, the geometry outputs by the MLDC component can be used by the MLAC components to produce consistent performance maps which, in turn, can replace the generic maps in engine cycle calculations.

Finally, the MLDC component capability was validated using as reference an existing ten-stage compressor. More specifically, it was demonstrated that the MLDC component was able to reproduce the geometry of the compressor both at component and at blade row level.

8 Compressor Trade-Off Design Studies

8.1 Introduction

In the context of the UTOPEA project⁵⁹, a preliminary design study on an ultra-high bypass ratio, 2-spool, geared turbofan engine with separate exhausts was conducted by the LTT/NTUA team for investigating the effects of specific engine design parameters on fuel burn for a specified mission. Basically, a multi-disciplinary optimization calculation was conducted where the engine bypass ratio, fan pressure ratio, and overall pressure ratio were used as design parameters to minimize the block fuel over a specified aircraft mission, while not violating a number of engine performance and structural constraints at different operating points (take-off, top-of-climb, cruise), as well as constraints related to the high-pressure compressor stability at low power conditions (idle). Optimization calculations were conducted for different values of pressure ratio split between the LP and HP spools (n_{PRS}), which gave the boundary values shown in Table 8.1 for the LPC and HPC components for the $n_{PRS} = 0.30$ and $n_{PRS} = 0.40$ design cases [see Alexiou et al. (2022)]. Note that, $n_{PRS} = 0.30$ and $n_{PRS} = 0.40$ are of current interest in aircraft industry. Therefore, these values are the main focus of the studies presented in this and the following chapter.

Table 8.1: LPC and HPC performance boundary conditions for different pressure ratio split values

Component	Parameter	Value	
		$n_{PRS} = 0.30$	$n_{PRS} = 0.40$
LPC	Corrected inflow (kg/s)	39.597	40.171
	Corrected speed (rpm)	9786.6	9855.4
	Overall pressure ratio (-)	2.482	3.690
HPC	Corrected inflow (kg/s)	18.706	13.587
	Corrected speed (rpm)	18,162.2	18,334.4
	Overall pressure ratio (-)	15.084	10.399

⁵⁹<https://cordis.europa.eu/project/id/886840> (accessed: May 5th, 2023)

The pressure ratio split exponent, n_{PRS} , determines how the overall pressure ratio of the engine is split between the LP and HP spools. Here, this is defined by [see Kyrianiadis et al. (2014)]:

$$n_{PRS} = \frac{\log(p_{26}^0/p_2^0)}{\log(p_3^0/p_2^0)} \quad (8.1)$$

where p_2^0 is the total pressure at the fan inlet, p_{26}^0 is the total pressure at the HPC inlet, and p_3^0/p_2^0 is the engine overall pressure ratio with p_3^0 being the HPC exit total pressure.

In the present chapter, the performance specifications given in Table 8.1 are used for conducting compressor design and off-design studies. For this reason, both the design and off-design versions of the MLC libraries (see Chapters 7 and 6, respectively), the weight calculation library for gas turbine components GTWC (see Chapter 5), as well as the mechanical design methods included in the GTMDC library (see Chapter 4), are utilized. The purpose of this chapter is not only to illustrate the integrated capabilities developed in the context of the present thesis, but also to investigate the relative influence (trade-offs) of various design variables on compressor on- and off-design performance, and weight.

For conducting the design and off-design studies which will be presented in the subsequent sections, the ISIGHT⁶⁰ platform was utilized. ISIGHT offers a variety of different methods for parametric and optimization studies. Regarding the available optimization algorithms, these include gradient-based methods, genetic algorithms, and searching techniques, among other. Here, ASA and an evolutionary algorithm were utilized [for more information on both, see Giachos (2019)]. Note that, both these methods formulate any optimization problem with K objectives as a minimization one in the form:

$$\min: f_{OBJ} = \sum_{k=1}^{k=K} \left[\frac{s_w}{s_s} (\pm f) \right]_k \quad (8.2)$$

where s_w is a user-defined weight factor, s_s is a user-defined scale factor, and f is the functional to be minimized or maximized by applying the “+” or “-” sign, respectively.

8.2 Inputs for Aerodynamic, Performance, and Weight Calculations

For the studies conducted in the present chapter, the total temperature and total pressure at the inlet of both the LPC and HPC components correspond to standard-day, sea-level static conditions (288.15 K, 101,325 Pa). For computer memory allocation reasons, the maximum number of blade rows in both the design and off-design components of MLC is set at 21, for both the LPC and HPC. This number corresponds to ten (10) stages and one (1) row of IGVs. Note also, that for the LPC component the IGVs are of variable geometry while for the HPC component both the IGVs and the first two (2) stator rows are variable. The above inputs are summarized in Table 8.2.

⁶⁰<https://www.3ds.com/products-services/simulia/products/isight-simulia-execution-engine> (accessed: May 11th, 2022)

Table 8.2: General inputs for the LPC and HPC design and off-design studies

Parameter	Value(s)
Inlet flow conditions	288.15 K, 101,325 Pa
Max. number of stages	10
Max. number of blade rows	21 ($10 \times 2 + \text{IGVs}$)

Table 8.3 summarizes the design assumptions regarding the mean-line shape and the radial positioning of the LP and HP compressors. As it can be seen from Table 8.3, the LP component is designed for a constant hub diameter, while the HP component is designed assuming a constant mean diameter. In the table are also given the inlet and exit Mach numbers from which and the given mass flow across the compressor the inlet and exit flow-annulus areas are established. Finally, the radial positioning of the gas-path of the compressors is established by specifying the inlet and exit hub-to-tip ratios. As we will see later in the parametric and optimization studies, both the inlet hub-to-tip ratio and the exit Mach number are design variables, where the former is specified indirectly by varying the tip speed of the 1st rotor.

Table 8.3: Compressor geometry assumptions for the LPC and HPC design studies

Component	Parameter	Value
LPC	Configuration	Const. hub
	Inlet hub-to-tip ratio	0.75
	Exit hub-to-tip ratio	0.92
	Inlet Mach number	0.40
	Exit Mach number	0.40
HPC	Configuration	Const. mean
	Inlet hub-to-tip ratio	0.65
	Exit hub-to-tip ratio	0.92
	Inlet Mach number	0.40
	Exit Mach number	0.30

Regarding the shape of the blades, the following are noted and apply to both the LPC and the HPC components. The blade profile for all stator rows is modelled as an equivalent circular-arc NACA-65, while the blade profile for all rotor rows is selected to be that of a double circular-arc (DCA) since it is expected that the rotor blades will operate with transonic flow conditions at their inlet. The relative position of maximum camber (a_c/c) is set to its default values, that is, 50% for both the NACA-65 and DCA profiles (see Section 6.4). These inputs are summarized in Table 8.4, where “R” and “S” stand for rotors and stators, respectively, followed by the stage number for easy reference.

Table 8.4: Blade profile inputs for the LPC and HPC design studies

Blade Row	Blade Profile	Rel. Position of Max. Camber
IGVs, S1-S10	Eq. Circ.-Arc NACA-65	50%
R1-R10	DCA	50%

Regarding the relative maximum thickness (t_{max}/c), this is assumed to be constant for the rotors (5.4%), while for the stators it falls linearly from an inlet (8.3%) to an outlet value (6.2%). For the IGVs, $t_{max}/c = 8.5%$ is used. The blade aspect ratio is defined for both rotors and stators assuming a linear variation from inlet to outlet, given the 1st row aspect ratio value ($AR_{R,1} = 1.7$ and $AR_{S,1} = 2.5$) and an aspect ratio change ($\delta AR_R = -0.07$ and $\delta AR_S = -0.15$), according to Eq. (7.12). For the LPC, the aspect ratio of the IGVs is set to 2.5, while for the HPC to 3.8. As we will see later in the parametric and optimization studies, the blade aspect ratio distribution is defined by varying both AR_1 and δAR (design variables), for both the rotors and the stators. The blade row solidity is calculated according to Glassman's correlations, which correlate the blade solidity to the inlet relative tip Mach number for rotors and the hub absolute flow turning for stators (see paragraph 7.3.2.2). For the IGVs, $\sigma = 1.0$ is used. Finally, for both the LPC and HPC components, the axial gap ratio is assumed constant and equal to 30%. The above inputs and assumptions are summarized in Table 8.5.

Table 8.5: Blade geometry inputs for the LPC and HPC design studies

Parameter	Value (Blade Row)	
	LPC	HPC
Rel. max. thickness	Constant: 5.4% (R1-R10)	Constant: 5.4% (R1-R10)
	Linear var.: 8.3% (S1)-6.2% (S10)	Linear var.: 8.3% (S1)-6.2% (S10)
	8.5% (IGVs)	8.5% (IGVs)
Aspect ratio	Linear Var.: 1.7 (R1), $\delta AR = -0.07$	Linear Var.: 1.7 (R1), $\delta AR = -0.07$
	Linear Var.: 2.5 (S1), $\delta AR = -0.15$	Linear Var.: 2.5 (S1), $\delta AR = -0.15$
	2.5 (IGVs)	3.8 (IGVs)
Solidity	According to Glassman (R1-R10)	According to Glassman (R1-R10)
	According to Glassman (S1-S10)	According to Glassman (S1-S10)
	1.0 (IGVs)	1.0 (IGVs)
Axial gap ratio	Constant: 30%	Constant: 30%

For the axial velocity distribution, Eq. (7.1) is used. However, in the optimization studies that will follow, the shape of the distribution is changed by modifying the axial velocity shape factor $V_{x,CLICO}$ (design variable). For the absolute flow angle at the inlet of the rotors, the 3rd degree polynomial distribution is assumed [see Eq. (7.6)] with the default correlation factors ($\bar{a}_1 = 14.0^\circ$). Finally, to establish the rotor work distribution, the default values for the aerodynamic criteria considered in Chapter 7 are

used [see Glassman et al. (1995)]. The above inputs are summarized in Table 8.6 and are used in designing both the LPC and HPC.

Table 8.6: Aerodynamic inputs for the LPC and HPC design studies

Parameter	Value
Velocity distribution	Using Eq. (7.1)
Absolute flow angle distribution	Using Eq. (7.6)
Max. diffusion factor @ rotor tip	0.50
Max. diffusion factor @ stator hub	0.60
Max. flow angle turning @ rotor hub	40°
Max. Mach number @ stator hub	0.85

Finally, to establish the blade row performance (loss and deviation), the default models with their default calibration scalars are used as described in Chapter 6. More specifically, these are summarized in Table 8.7. Note that Reynolds number effects are deactivated, while clearance losses are also not taken into account in the design and off-design calculations. For Mach number effects, the default model by Aungier (see paragraph 6.8.8) is used, while blockage is set to the default values given by Glassman et al. (1995) (see paragraph 6.8.10).

Table 8.7: Loss and deviation models for the LPC and HPC design and off-design studies

Loss/Deviation	Model	Remarks
Design incidence	Herrig's model	See paragraph 6.5.1.2
Design deviation	Lieblein's model	See paragraph 6.5.2.1
Off-design deviation	Swan's model	See paragraph 6.7.1.2
Profile loss	Equivalent diffusion factor model	See paragraph 6.8.7.2
Endwall loss	Vavra's model	See paragraph 6.8.2.2
Secondary loss	Howell's model	See paragraph 6.8.3.1
Shock loss	Dixon's model	See paragraph 6.8.5

The inputs given in Table 8.2 through Table 8.7 are used in the MLC components for design (MLDC library) and off-design (MLAC library) calculations. Another significant part of the studies presented here is the compressor weight. For this reason, the GTWC library component for compressor weight estimations is utilized running in the CB-GM calculation mode (see Chapter 5).

For estimating the weight of the casings, the thickness for both the inner and outer casings is assumed constant across the compressor and equal to 2.54 mm [the default value according to NASA's WATE, see Pera et al. (1977a)]. For time efficiency, the weight of the disks is estimated according to NASA's WATE correlations (see paragraph 5.3.6). Finally, regarding the materials selection, these are given in Table 8.8 and have

been selected after materials that are typically used in such applications (as described in Table 4.2).

Table 8.8: Material selection for the LPC and HPC design studies

Component	Structural Part	Material (Stages)
LPC	Hardware	Rene-41 (1-10)
	Rotor blades	Ti-6Al-4V (1-10)
	Stator blades	A-286 (1-10)
	IGVs	A-286
	Disks	Ti-6Al-4V (1-10)
	Casings (inner & outer)	A-286 (1-10)
HPC	Hardware	Rene-41 (1-10)
	Rotor blades	Ti-6Al-4V (1-3); Inconel-718 (4-10)
	Stator blades	A-286 (1-10)
	IGVs	A-286
	Disks	Ti-6Al-4V (1-3); Inconel-718 (4-10)
	Casings (inner & outer)	A-286 (1-5); Inconel-718 (6-8); N-155 (9-10)
Shafts	Low-pressure	Inconel-706A
	High-pressure	Ti-6Al-4V

8.3 LPC and HPC Design Studies

In the present section compressor design studies are presented. First, sensitivity (parametric) studies are conducted in order to identify how the selected design variables affect the compressor efficiency and weight. Then, optimization studies are presented to find the compressor geometries that satisfy the required objectives and constraints, including both performance and structural criteria. Note that, production, manufacturability, and detail design aspects are not taken into account neither in the design procedure nor in the post-processing and/or evaluation of the results. For the studies presented here, the corresponding PROOSIS components and experiments are executed using the design inputs and assumptions outlined in the previous section.

Finally, note that the following studies consider design variables that have been used in the past to similar studies limited, however, to the design of single-stage compressors [e.g., see Lim et al. (1989)]. In the studies presented here, constraints regarding the compressor stall and choke limits which, in the studies by, e.g., Lim et al. (1989) are not taken into account, are also included.

8.3.1 PROOSIS Design Model Setup and ISIGHT Implementation

A PROOSIS schematic model is created using the MLDC component for compressor aerothermodynamic design, and the GTWC component for estimating the weight of

compressors. These are connected through their dedicated ports so that the required by the GTWC component data can be transferred from the MLDC one for estimating the compressor weight after its aerothermodynamic design has been completed. This schematic model is shown in Figure 8.1. The model partition is created next which requires the compressor inlet conditions (total temperature, total pressure, mass flow) and the compressor rotational speed as inputs (these are given in Table 8.1 and Table 8.2). Then, a PROOSIS experiment is created that conducts the aerothermodynamic design and weight estimation for the given partition boundaries, specified pressure ratio (see Table 8.1), and design inputs and assumptions (see Table 8.2 through Table 8.8).

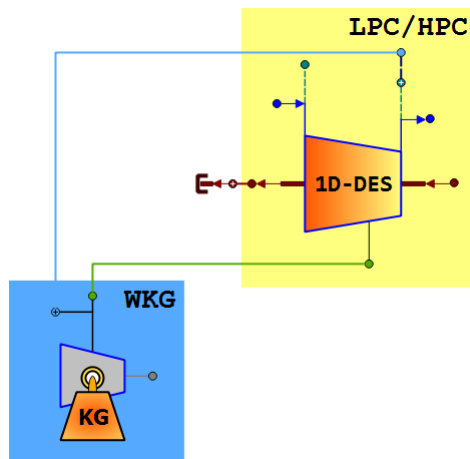


Figure 8.1: PROOSIS schematic model for the LPC and HPC design. Inside the yellow rectangle the MLDC component for the aerothermodynamic design of compressors is shown, while inside the blue one the GTWC component for estimating the weight of compressors is illustrated.

Finally, a deck executable of the above PROOSIS experiment is created which is used to construct an ISIGHT workflow for conducting the parametric and design studies described next. This workflow is presented in Figure 8.2.

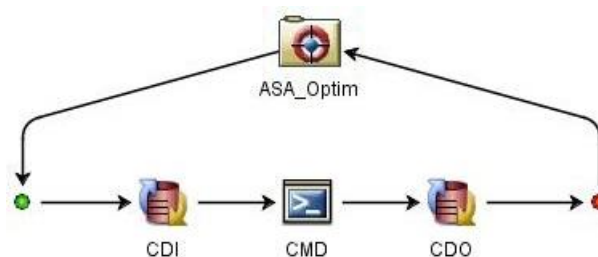


Figure 8.2: ISIGHT implementation and workflow for the LPC and HPC design studies: “CMD” is the deck executable, “CDI” is the input data file (design variables), and “CDO” is the output data file (e.g., compressor efficiency, weight, stall and choke margins, etc.).

8.3.2 Sensitivity Design Studies

Here, parametric design studies are conducted to identify how the design variables (they are later presented in Table 8.10) affect the compressor design and performance, and as a means for validating qualitatively the tools presented in Chapters 4, 5, 6, and 7.

For the following studies, only the $n_{PRS} = 0.30$ case is considered. Apart from the design variables shown in Table 8.10, the blade solidity and the compressor number of stages are also considered. Table 8.9 gives the baseline designs for both the LPC and HPC components, for the 0.30 pressure ratio split value [see Alexiou et al. (2022)].

Table 8.9: Baseline values for LPC and HPC sensitivity studies for the 0.30 pressure ratio split case [see Alexiou et al. (2022)]

Variable	Baseline Value	
	LPC	HPC
Average absolute flow angle (deg)	15.0	15.0
Compressor exit absolute Mach number (-)	0.40	0.30
1 st rotor tip speed (m/s)	346.3	447.3
Axial velocity shape factor (-)	1.0	1.0
Average blade aspect ratio (-)	2.14	1.71
Average blade row solidity (-)	1.29	1.31
Number of stages (-)	4	10
Overall polytropic efficiency (%)	91.45	90.69
Overall weight ⁶¹ (kg)	138.739	96.353
Overall stall margin (-)	0.092	0.050

8.3.2.1 Influence of Aspect Ratio

Figure 8.3 illustrates the variation of the LPC and HPC overall polytropic efficiency (η_p), overall weight (W_{KG}), and overall stall index (I^{stall}) in terms of the blade aspect ratio. Note that the same (average) value of aspect ratio is assigned to all blade rows, rotors and stators alike.

As it can be seen from Figure 8.3, the increase in the blade aspect ratio is beneficial for both η_p and W_{KG} . An increase in aspect ratio tends to reduce the losses and, more specifically, the endwall losses [see Eq. (6.83)], thus leading to better row-wise and, eventually, compressor efficiencies. Regarding the compressor structural weight, an increase in aspect ratio tends to reduce the blade chord for fixed flow-annulus heights (i.e., blade heights) [see Eq. (6.43)]. Thus, for the same blade thickness the blade weight is reduced. Furthermore, the reduced blading weights lead to reduced centrifugal loads on the disks for the same rotational speed which, in turn, leads to disks with less volume (and thus weight) for supporting the reduced loads.

On the other hand, the increase in the aspect ratio presents an adverse effect on the compressor stall margin [see Eq. (6.145)]. That is, increasing the blade aspect ratio across the compressor produces designs with low values of surge margin and, thus, narrower regions of stable operation.

⁶¹Compared to Alexiou et al. (2022), the overall weight quoted here has been calculated considering the CB-GM calculation mode of the GTWC component and the material selection of Table 5.9.

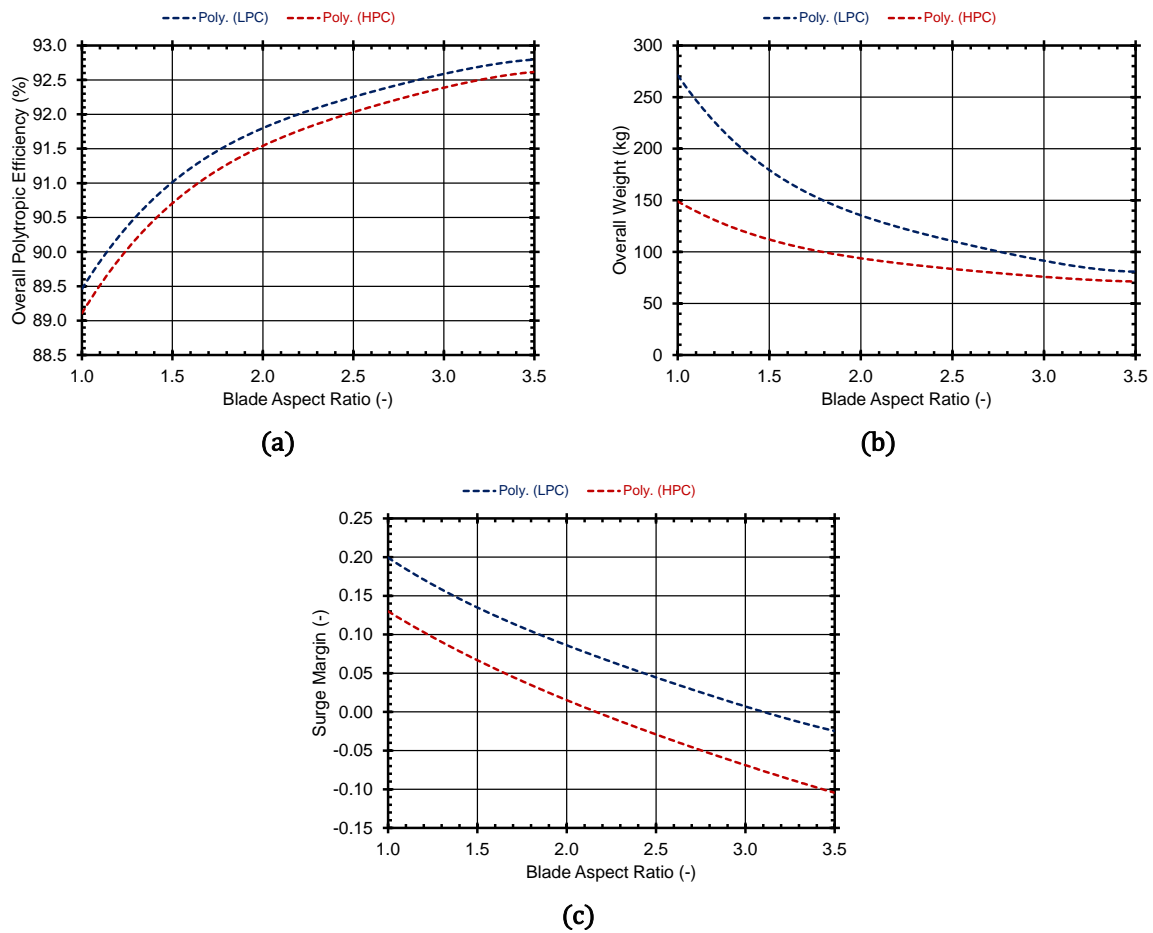


Figure 8.3: Variation of the LPC and HPC (a) overall polytropic efficiency, (b) overall weight, and (c) surge margin with blade aspect ratio (average) for aspect ratios between 1.0 and 3.5.

8.3.2.2 Influence of Solidity

Figure 8.4 illustrates the variation of the LPC and HPC overall polytropic efficiency (η_p), overall weight (W_{KG}), and overall surge index (I^{stall}) in terms of the blade row solidity. Note that the same (average) value of solidity is assigned to all blade rows, rotors and stators alike.

From Figure 8.4 it is seen that the increase in solidity increases η_p up to a value where η_p becomes maximum, and then η_p drops as the solidity continues to increase. In other words, there is an optimal value of solidity for which the row losses are minimized. This is interpreted as follows. For fixed compressor mean-line shape and blade chord, solidity is translated to blade count through Eq. (6.43). Removing or adding blades, that is, reducing or increasing solidity, respectively, increases the losses across the compressor either because there are less blades than those required to drive the flow correctly (i.e., to the exit flow angle for which the losses are minimum), or because there are more blades leading to increased friction losses.

On the other hand, the increase in solidity leads to increasing compressor weights due to the higher blade counts. Furthermore, larger volume (and, thus, weight) disks are required to support the increased centrifugal loads developed by the heavier rotor rows.

Finally, note that the increase in solidity has a positive effect on the overall surge margin [see Eq. (6.145)]. That is, increasing the solidity yields compressor designs with

wider regions of stable operation, contrary to what happens with increasing the blade aspect ratio.

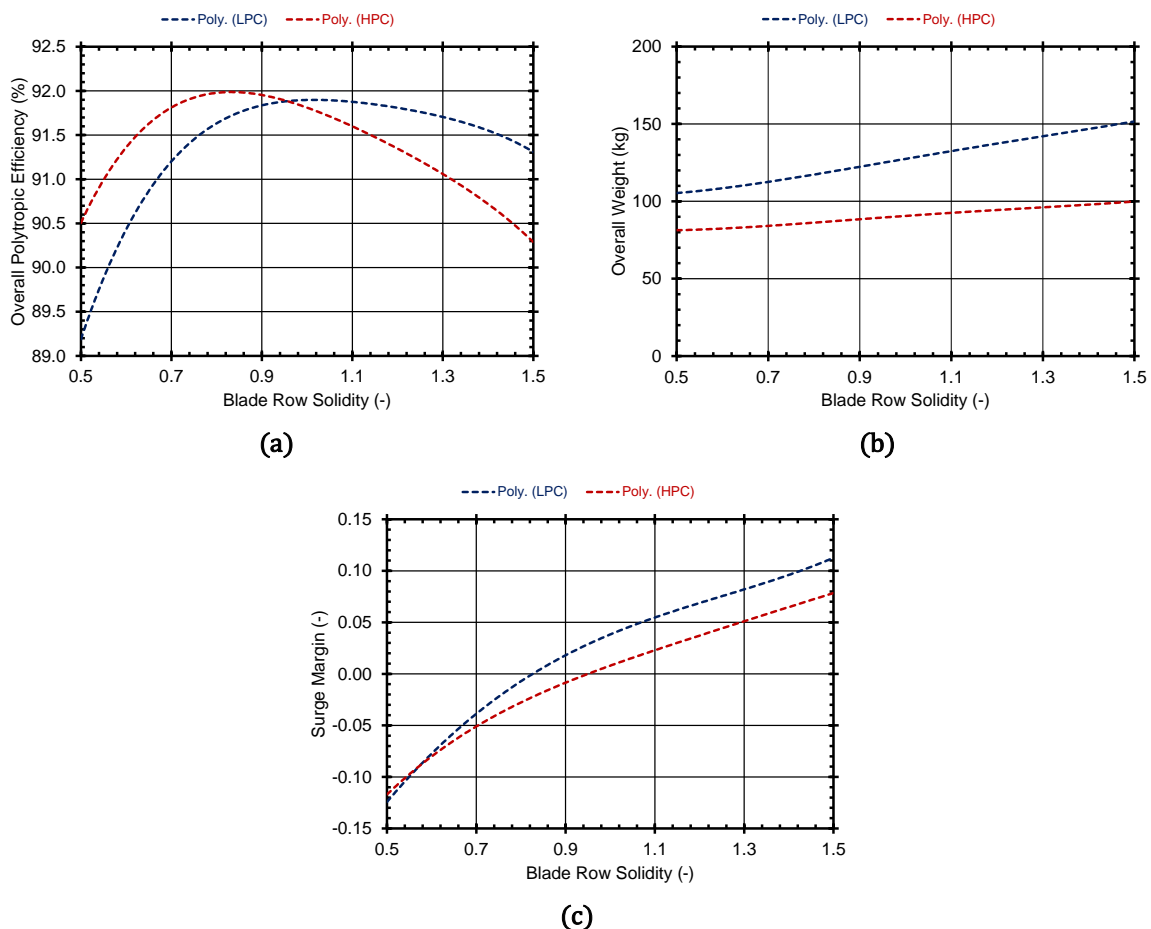


Figure 8.4: Variation of the LPC and HPC (a) overall polytropic efficiency, (b) overall weight, and (c) surge margin with blade row solidity (average) for solidities between 0.5 and 1.5.

8.3.2.3 Influence of Stage Count

Figure 8.5 illustrates the variation of the LPC and HPC overall polytropic efficiency (η_p) and overall weight (W_{KG}) in terms of the stage count.

As we see from Figure 8.5, increasing the number of stages leads to an increase in η_p until a maximum value is reached. From that point on, the addition of stages leads to a drop in compressor efficiency. In other words, for a given pressure ratio (as in the studies conducted in the present chapter), there is an optimal number of stages for which the work distribution yields the best efficiency value. Removing a number of stages from that value means that the remaining stages are loaded more for achieving the same pressure ratio, i.e., the stage efficiency drops resulting in a subsequent reduction in the compressor overall efficiency. On the other hand, adding a number of stages to the optimal one means increased flow losses that, again, reduce the compressor efficiency.

Regarding the compressor weight, from Figure 8.5 it is seen that less stages give reduced values of structural weight for fixed material selection, blade count, etc. This conclusion, of course, is not to be taken light-hearted since it is true for the design

inputs and assumptions used here for the sensitivity studies. According to Wisler et al. (1977), fewer stages do not necessarily translate into reduced weight, although they may give less expensive and shorter compressors.

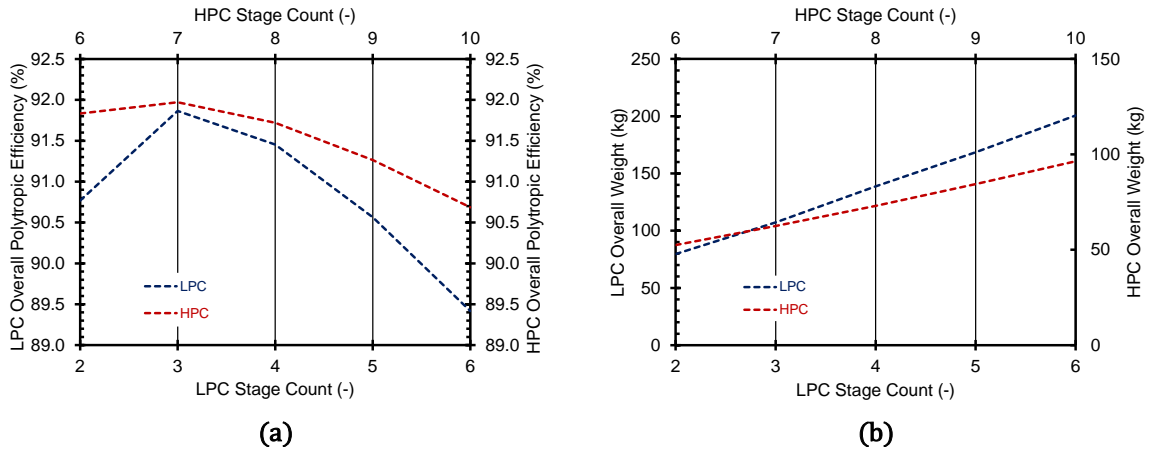


Figure 8.5: Variation of the LPC and HPC (a) overall polytropic efficiency and (b) overall weight with stage count for 2-6 LPC stages and 6-10 HPC stages.

8.3.2.4 Influence of 1st Rotor Tip Speed

Figure 8.6 shows the variation of the LPC and HPC overall polytropic efficiency (η_p) and overall weight (W_{KG}) in terms of the tip speed of the 1st rotor row ($U_{t,in}$). For given compressor speed (N_{mech}), $U_{t,in}$ basically determines the flow-annulus tip radius and, essentially, the shape (hub, mean, tip) of the flow-annulus across the entire compressor for known flow-annulus areas (established from mass continuity and the given mass flow across the compressor). Note that, for both compressors, typical values used in the common design practice for $U_{t,in} \leq 500$ m/s were also adopted here, but the lower value of $U_{t,in}$ for the parametric studies was established by the model being unable to converge below that value (320 m/s for the LPC design and 400 m/s for the HPC design).

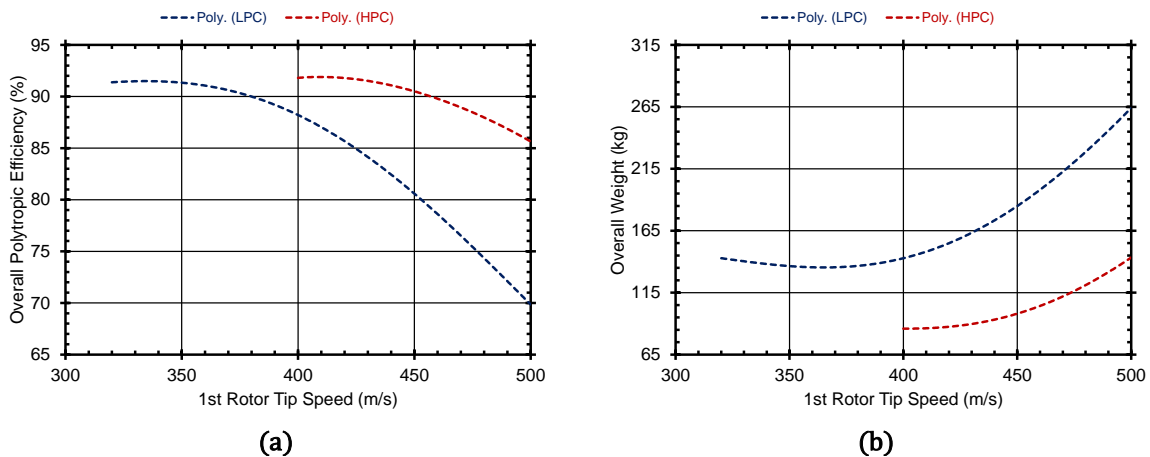


Figure 8.6: Variation of the LPC and HPC (a) overall polytropic efficiency and (b) overall weight with 1st rotor tip speed for tip speeds between 320 and 500 m/s for the LPC, and between 400 and 500 m/s for the HPC.

We can see from Figure 8.6 that there is an optimal $U_{t,in}$ value for which the efficiency becomes maximum and then reduces for values left and right of the optimal one. In other words, for a fixed compressor pressure ratio, number of stages, and rotational speed, there is a value of $U_{t,in}$ for which the stage loading distribution gives the optimal compressor efficiency, and for distributions different than the optimal one the compressor efficiency deteriorates.

On the other hand, from Figure 8.6 we observe a continuous increase in compressor weight with increasing $U_{t,in}$. This is because, for fixed compressor speed and inlet conditions, the increase in $U_{t,in}$ shifts the compressor gas-path towards higher mean radius distributions which, in turn, penalize W_{KG} due to the increase in the weights of casings, hardware, and disks. This effect will be described/interpreted in more detail in paragraph 8.3.3.

8.3.2.5 Influence of Exit Mach Number

Figure 8.7 presents the variation of the LPC and HPC overall polytropic efficiency (η_p) and overall weight (W_{KG}) in terms of the absolute Mach number at the compressor exit (M_{out}). Similarly to $U_{t,in}$, for fixed compressor exit conditions and mass flow, M_{out} determines the exit flow-annulus area and, for a specified hub-to-tip ratio, the flow-annulus shape (hub, mean, tip). Thus, the following are noted.

From Figure 8.7, one sees that the increase in M_{out} is beneficial for W_{KG} , that is, increasing M_{out} reduces the compressor weight. This is because the increase in Mach number (as long as it remains subsonic) reduces the exit annulus area which, subsequently, leads to smaller and thus lighter designs.

Regarding the compressor efficiency, the exit Mach number pretty-much presents the same influence as $U_{t,in}$ (see paragraph 8.3.2.4). Since, practically, the Mach number determines the compressor gas-path, we see from Figure 8.7 that there is an optimal M_{out} value for which the resulting stage loading distribution gives the optimal compressor efficiency (for fixed compressor stages, rotational speed, and pressure ratio). For values of M_{out} other than the optimal one, the compressor efficiency drops. Note also, that the value of M_{out} influences the pressure losses of the downstream duct which, in the present studies, is not part of the compressor design.

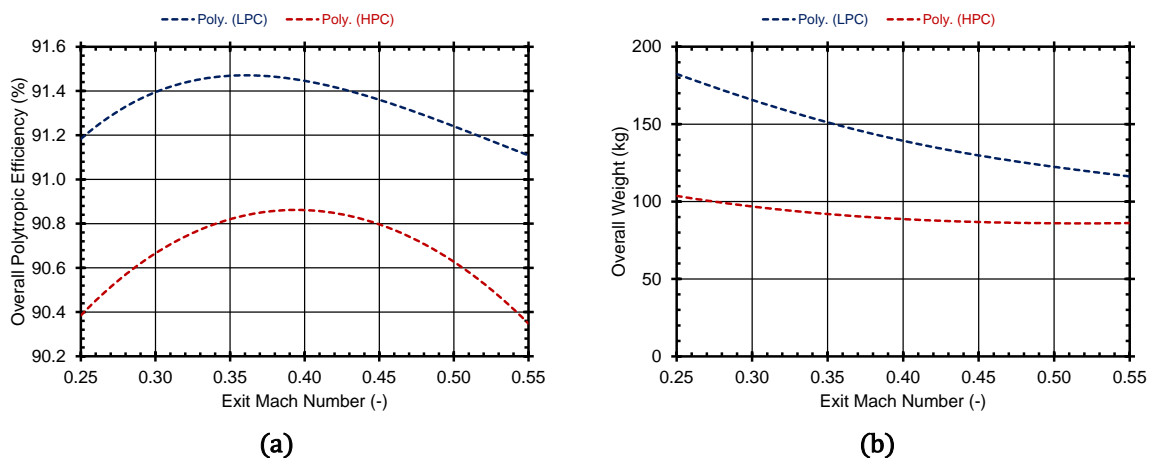


Figure 8.7: Variation of the LPC and HPC (a) overall polytropic efficiency and (b) overall weight with compressor exit Mach number for Mach numbers between 0.25 and 0.55.

8.3.2.6 Influence of Axial Velocity Shape Factor

The axial velocity shape factor ($V_{x,CLICO}$) basically determines the axial velocity distribution across the compressor. This, in turn, means that $V_{x,CLICO}$ effects the velocity triangles across the compressor which effect both the performance (losses) of the blade rows and the compressor geometry (from mass continuity). This combined effect can be seen in Figure 8.8 which illustrates the variation of the LPC and HPC overall polytropic efficiency (η_p) and overall weight (W_{KG}) with $V_{x,CLICO}$. Note that, for both compressors, logical values for $1.0 \leq V_{x,CLICO} \leq 2.0$ were used here, but the upper value of $V_{x,CLICO}$ for the LPC parametric studies was established by the model being unable to converge above that value (1.8).

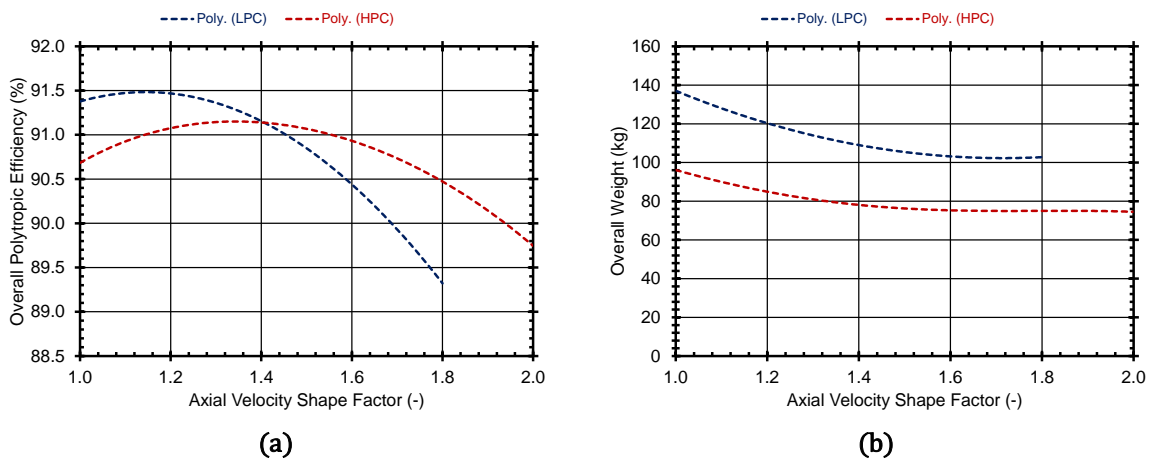


Figure 8.8: Variation of the LPC and HPC (a) overall polytropic efficiency and (b) overall weight with axial velocity shape factor for values between 1.0 and 1.8 for the LPC, and between 1.0 and 2.0 for the HPC.

As we can see from Figure 8.8, there is an optimal axial velocity distribution for which η_p becomes maximum. In other words, there is an optimal distribution for which the resulting combination of geometry, blade losses, and flow and loading coefficients give the best compressor efficiency. At this point, remember that the stage efficiency is a function of blade losses and φ and ψ ⁶² [see Eq. (3.91)].

Regarding the compressor weight, we can see that increasing V_x across the compressor leads to a reduction in W_{KG} . This is directly linked to mass continuity from which an increase in V_x yields a decrease in flow-annulus areas (assuming that flow density across the compressor doesn't change much for the given pressure ratio) and, thus, a reduction in compressor size and weight.

8.3.2.7 Influence of Average Absolute Flow Angle

The average absolute flow angle ($\bar{\alpha}_1$) determines the distribution of the absolute flow angle at the inlet of the rotor blades. Similarly to $V_{x,CLICO}$, $\bar{\alpha}_1$ effects the velocity triangles across the compressor which, in turn, effect both the compressor performance and geometry. This combined effect is shown in Figure 8.9 illustrating the

⁶²The stage reaction is also a function of φ and ψ and the stage inlet flow angle [see Eq. (3.63)] but, according to Lewis (1996), reaction's influence on the stage efficiency is not that profound and, therefore, it can be omitted for interpretation purposes.

variation of the LPC and HPC overall polytropic efficiency (η_p) and overall weight (W_{KG}) with $\bar{\alpha}_1$. Note here, that for both compressors logical values for $0^\circ \leq \bar{\alpha}_1 \leq 45^\circ$ were used, but the upper value of $\bar{\alpha}_1$ for the LPC parametric studies was established by the model being unable to converge above that value (i.e. 40°).

As it can be seen from Figure 8.9, there is an optimal distribution of rotor inlet flow angles for which the compressor η_p is maximized. On the other hand, $\bar{\alpha}_1$ doesn't play a significant role on W_{KG} , although we can see that the lower values of W_{KG} are obtained for the relatively smaller values of $\bar{\alpha}_1$ ($0^\circ \leq \bar{\alpha}_1 \leq 10^\circ$).

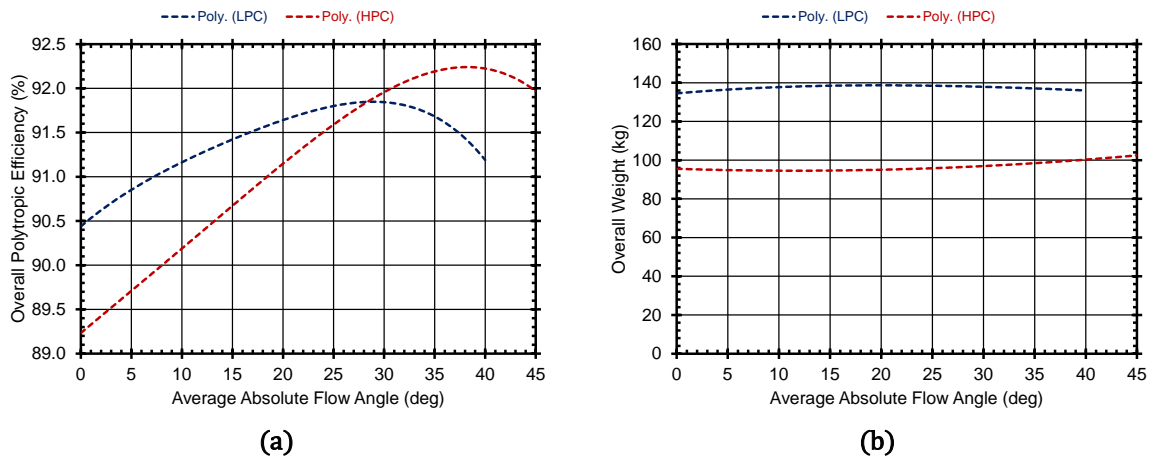


Figure 8.9: Variation of the LPC and HPC (a) overall polytropic efficiency and (b) overall weight with average absolute flow angle for values between 0° and 40° for the LPC, and between 0° and 45° for the HPC.

8.3.3 Optimization Studies

The implementation shown in Figure 8.2 is used next to design the LPC and HPC components considering the following two (2) objectives:

1. Maximum overall polytropic efficiency (η_p), and
2. a balance between the maximum overall η_p and the minimum structural weight (W_{KG}).

In what follows, the above two optimization problems will be referred to as “MPE” (for the “Maximum Polytypic Efficiency” optimization case) and “BEW” (for the “Balanced Efficiency-Weight” optimization case). For the MPE and BEW cases, Eq. (8.2) is formulated as:

$$f_{OBJ} = \begin{cases} -\frac{1.0}{0.9}\eta_p, & \text{for the MPE case} \\ -\frac{0.5}{0.9}\eta_p + \frac{0.5}{75.0}W_{KG}, & \text{for the BEW case} \end{cases}$$

where a scale factor of 0.9 is assumed for the efficiency term and a scale factor of 75 kg is assumed for the weight term [cf. Eq. (8.2)]. For the MPE case, the weight factor is set

equal to 1.0, while for the BEW case the weight factor is set equal to 0.5 for both terms [cf. Eq. (8.2)], hence the “balanced” optimization problem.

Note that, the MPE and BEW optimization cases are conducted for both values of the pressure ratio split parameter, that is, $n_{PRS} = 0.30$ and $n_{PRS} = 0.40$. Thus, a total of eight (8) optimization studies are conducted.

Finally, note that the optimization studies for both the LPC and HPC components were conducted following the next approach. The MPE case was ran prior to the BEW one considering fixed number of compressor stages: $3 \leq N_{stg} \leq 5$ for the LPC and $8 \leq N_{stg} \leq 10$ for the HPC. These values are encountered in LPC and HPC components of contemporary turbofan engines and, therefore, the same values were adopted also in the present study. For the optimal value of the stage count, was opted that one for which the best overall polytropic efficiency was obtained between all the examined values. This number of stages was then used for running the BEW design studies to examine the trade-offs that exist between the compressor efficiency and structural weight. The above approach was mainly followed in order to avoid numerical problems related to the highly discontinuous design spaces produced when the stage count (a discrete variable) is used as a design variable when setting up the optimizer. As a future work, it is suggested that BEW studies are conducted considering also different stage counts.

8.3.3.1 Selection of Design Variables and Constraints

The design variables for both optimization problems are described in Table 8.10. In the same table, the range of validity for each design variable is also shown. As it can be seen from Table 8.10, there are in total eight (8) design variables. The same variables are used in the design of both the LPC and HPC components. Regarding the lower and upper values assigned to each design variable, these were adopted after typical values used in practice (for M_{out} , $AR_{R,1}$, $AR_{S,1}$, $U_{t,in}$), after values used in the parametric studies presented in paragraph 8.3.2 (for \bar{a}_1 and $V_{x,CLICO}$), or after arbitrary (but reasonable) values (for δAR_R , and δAR_S).

Table 8.10: Design variables and range of validity for the design of the LPC and HPC components

Nr.	Design Variable	Range of Validity	
		LPC	HPC
1	Average absolute flow angle (deg)	$0 \leq \bar{a}_1 \leq 45$	$0 \leq \bar{a}_1 \leq 45$
2	Exit absolute Mach number (-)	$0.25 \leq M_{out} \leq 0.55$	$0.25 \leq M_{out} \leq 0.35$
3	1 st rotor tip speed (m/s)	$300 \leq U_{t,in} \leq 500$	$300 \leq U_{t,in} \leq 500$
4	1 st rotor aspect ratio (-)	$1.0 \leq AR_{R,1} \leq 3.5$	$1.0 \leq AR_{R,1} \leq 3.5$
5	1 st stator aspect ratio (-)	$1.0 \leq AR_{S,1} \leq 3.5$	$1.0 \leq AR_{S,1} \leq 3.5$
6	Rotor aspect ratio change per row (-)	$-0.5 \leq \delta AR_R \leq 0.0$	$-0.5 \leq \delta AR_R \leq 0.0$
7	Stator aspect ratio change per row (-)	$-0.5 \leq \delta AR_S \leq 0.0$	$-0.5 \leq \delta AR_S \leq 0.0$
8	Axial velocity shape factor (-)	$1.0 \leq V_{x,CLICO} \leq 2.0$	$1.0 \leq V_{x,CLICO} \leq 2.0$

Constraints are imposed on the minimum choke index (I_{min}^{choke}) (see paragraph 6.10.3) and the overall surge margin/index (I^{stall}) (see paragraph 6.11.4). The requirement for the former is to avoid solutions in the choked part of the compressor characteristics map which is neither a desirable design point condition nor an acceptable numerical result to be used in MLAC that uses the produced geometries from the MLDC calculations to produce the corresponding performance maps. Similarly, the latter controls the distance of the design point from the surge line. Finally, a constraint for the last stage blade height (LSBH) is also imposed, mainly to avoid HPC designs producing very small engine cores. These constraints are expressed in terms of lower values as described in Table 8.11. The selected numerical values for the minimum choke index and the overall stall index were obtained after trial-and-error calculations.

Table 8.11: Constraints for the design of the LPC and HPC components

Nr.	Constraint Variable	Range of Validity	
		LPC	HPC
1	Minimum choke index (-)	$0.010 \leq I_{min}^{choke}$	$0.010 \leq I_{min}^{choke}$
2	Overall stall margin/index (-)	$0.075 \leq I^{stall}$	$0.050 \leq I^{stall}$
3	Last stage blade height (mm)	$13.0 \leq LSBH$	$13.0 \leq LSBH$

8.3.3.2 Optimization Results

Table 8.12 and Table 8.13 show the results obtained from the MPE and BEW calculations, for both $n_{PRS} = 0.30$ and $n_{PRS} = 0.40$ cases.

Table 8.12: MPE and BEW results for the LPC design, where red shaded cells indicate active constraints

Parameter	Value (MPE)		Value (BEW)	
	$n_{PRS} = 0.30$	$n_{PRS} = 0.40$	$n_{PRS} = 0.30$	$n_{PRS} = 0.40$
$\bar{\alpha}_1$ (deg)	19.11	18.34	2.90	1.49
M_{out} (-)	0.46	0.46	0.54	0.55
$U_{t,in}$ (m/s)	349.4	376.2	323.9	335.9
$AR_{R,1}$ (-)	3.50	3.49	3.50	3.49
$AR_{S,1}$ (-)	3.48	3.49	3.50	3.49
δAR_R (-)	-0.0049	-0.0070	-0.0033	-0.1766
δAR_S (-)	-0.0566	-0.1768	-0.0084	-0.0420
$V_{x,CLICO}$ (-)	1.11	1.09	1.46	1.49
I_{min}^{choke} (-)	0.105	0.083	0.028	0.028
I^{stall} (-)	0.075	0.075	0.075	0.087
LSBH (mm)	77.8	51.6	74.3	53.51
N_{stg} (-)	4	5	4	5
η_p (%)	92.78	92.99	91.10	91.22
W_{KG} (kg)	75.9	88.8	59.6	65.9

Table 8.13: MPE and BEW results for the HPC design, where red shaded cells indicate active constraints

Parameter	Value (MPE)		Value (BEW)	
	$n_{PRS} = 0.30$	$n_{PRS} = 0.40$	$n_{PRS} = 0.30$	$n_{PRS} = 0.40$
$\bar{\alpha}_1$ (deg)	22.18	27.55	0.14	0.13
M_{out} (-)	0.33	0.35	0.35	0.35
$U_{t,in}$ (m/s)	448.7	413.3	388.8	346.0
$AR_{R,1}$ (-)	3.11	3.48	3.49	3.50
$AR_{S,1}$ (-)	3.13	2.61	3.50	3.50
δAR_R (-)	-0.1020	-0.0259	-0.2247	-0.1481
δAR_S (-)	-0.2660	-0.1267	-0.0572	-0.0098
$V_{x,CLICO}$ (-)	1.38	1.25	1.61	1.51
I_{min}^{choke} (-)	0.039	0.073	0.054	0.093
I^{stall} (-)	0.050	0.050	0.050	0.050
LSBH (mm)	13.1	13.2	16.3	18.0
N_{stg} (-)	9	9	9	9
η_p (%)	93.11	93.41	92.89	93.03
W_{KG} (kg)	59.1	45.8	36.9	27.8

As it can be seen from Table 8.12 and Table 8.13, in all optimization cases the higher values of the overall polytropic efficiency (η_p) are obtained when the LPC is more loaded and the HPC is less loaded (i.e., for $n_{PRS} = 0.40$). Regarding weight, we observe that the LPC is heavier when is more loaded, whereas the HPC is lighter when is less loaded. LPC requires one additional stage (5 compared to 4) when is more loaded in order to achieve the best η_p , whereas the HPC component requires for both pressure ratio splits 9 stages to achieve the best η_p .

For the LPC component and the $n_{PRS} = 0.30$ case, the MPE optimization gives an overall η_p which is higher by 1.68% (absolute) than the BEW optimization. At the same time, W_{KG} is also greater by 16.3 kg (relative difference $\sim 21.5\%$). Similarly, for the $n_{PRS} = 0.40$ case, the MPE case gives an η_p value higher by 1.77% (absolute) than the one obtained by the BEW calculation while the compressor weight is greater by ~ 23 kg (relative difference $\sim 25.8\%$). Similar observations as the ones for the LPC component can be made for the HPC component (see Table 8.13). For $n_{PRS} = 0.30$, the MPE calculation gives an η_p which is higher by 0.22% (absolute) than the one obtained by the BEW optimization, while the compressor weight is also greater by 22.2 kg (relative difference $\sim 37.5\%$). For $n_{PRS} = 0.40$, the MPE calculation gives an η_p which is higher by 0.38% (absolute) than that obtained by the BEW calculation while W_{KG} is greater by ~ 18 kg (relative difference $\sim 39.3\%$). From the above observations, we can clearly see the trade-off that exists between the compressor efficiency and weight, where the minimization of the compressor weight penalizes the compressor attainable efficiency for a given pressure ratio requirement. This trade-off between weight and efficiency can be explained if we see Figure 8.10, which illustrates the LPC and HPC gas-paths, respectively, as obtained by the MPE and BEW calculations.

The BEW calculation produces compressor gas-paths with lower mean radius distributions which, as will be explained later in more detail, have a beneficial effect on the component weight. On the other hand, this reduction in mean radius reduces the blade speed which, for the same work distribution, increases the stage loading compared to the value for which the best compressor efficiency is attained. Thus, for the same loading case (i.e., pressure ratio split value or, pressure ratio), number of stages, and compressor speed the efficiency of the stages is reduced (in average), leading to the eventual reduction in the overall component efficiency. Figure 8.11 presents the distributions of loading coefficients and stage isentropic efficiencies as obtained for the different design cases. From Figure 8.11, it is seen that this is not the case only for the first and last stages of the HPC where the isentropic efficiency from the MPE calculation is less than that from the BEW calculation. This discrepancy is due to higher stage losses for those two stages.

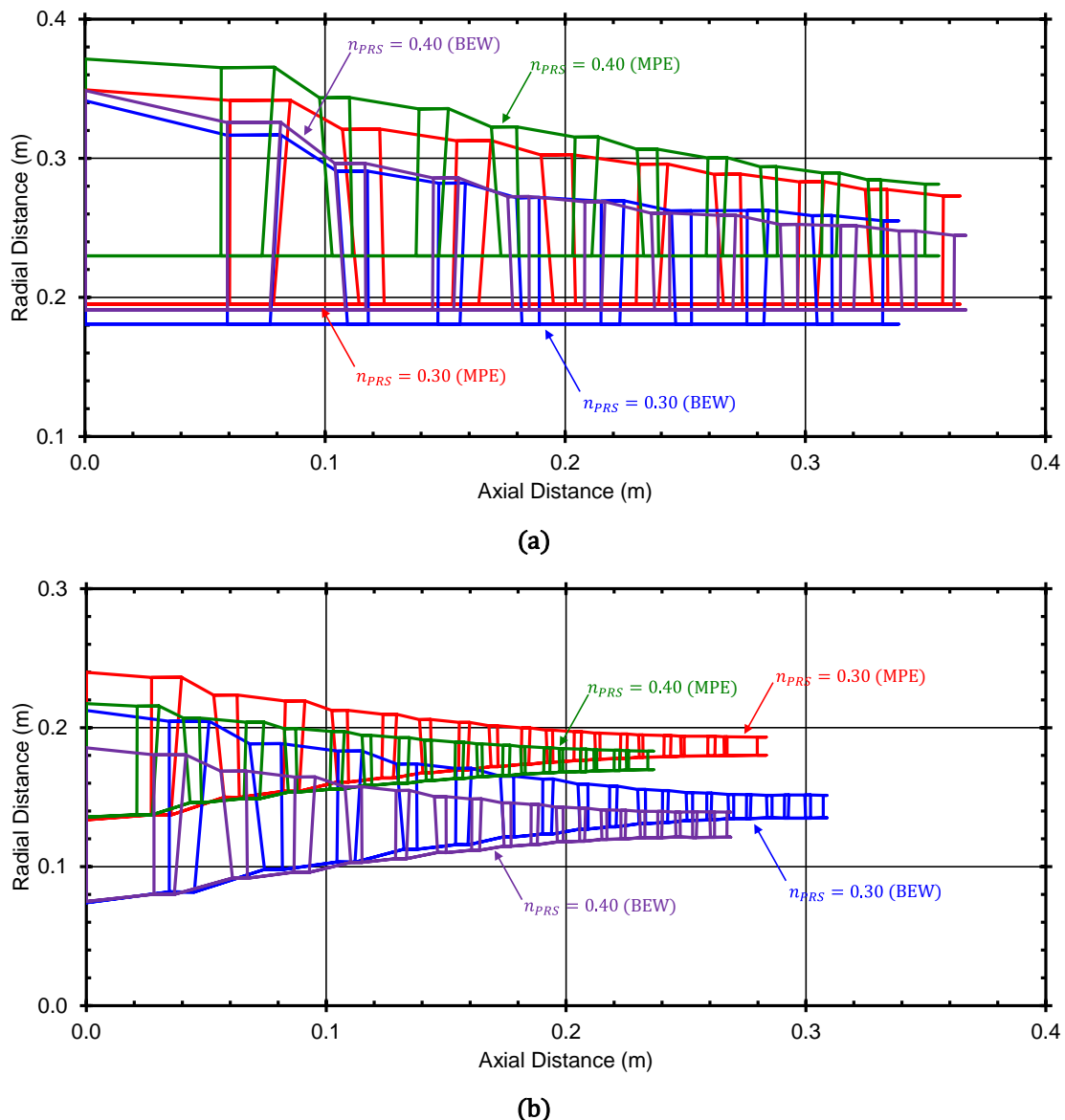


Figure 8.10: Meridional gas-path views computed by MPE and BEW for the (a) LPC and the (b) HPC components.

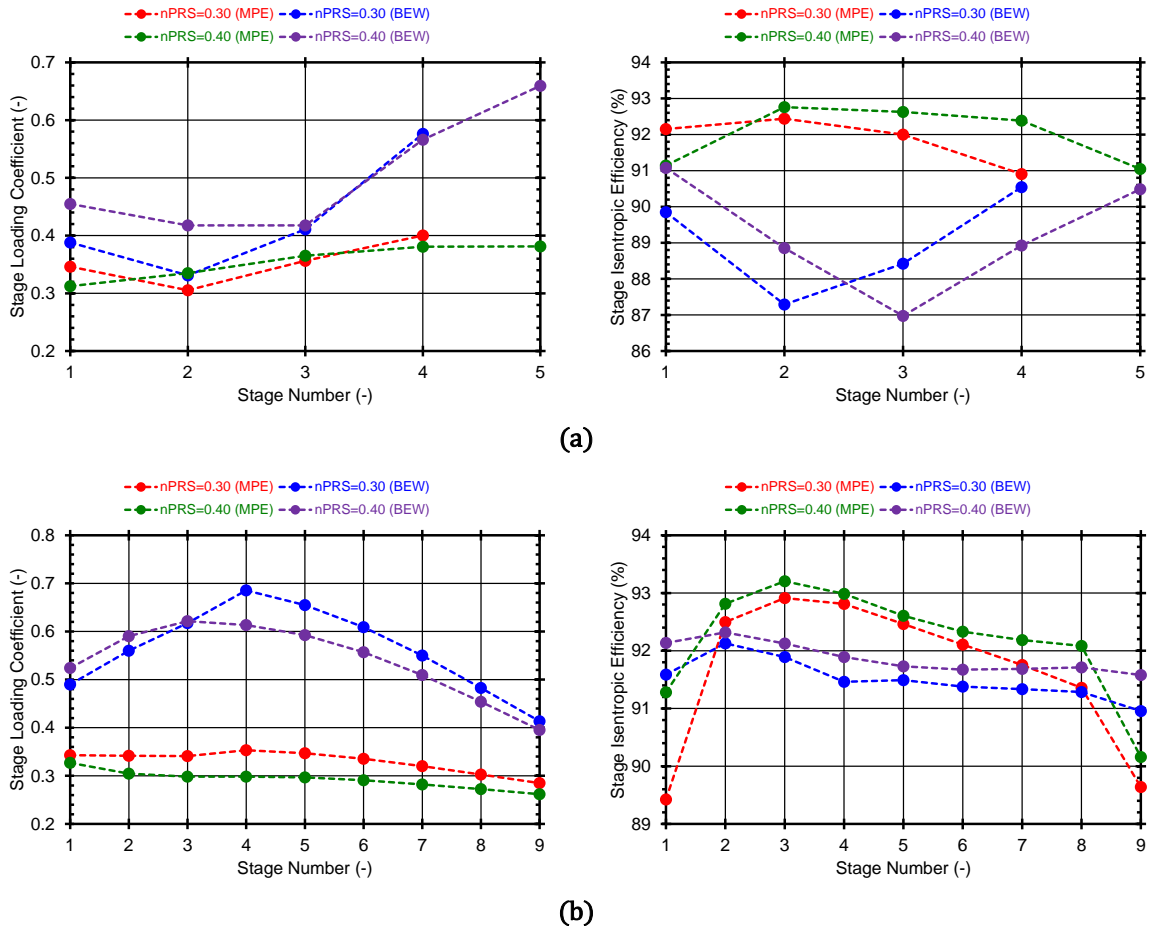


Figure 8.11: Stage loading coefficient and isentropic efficiency distributions computed by MPE and BEW for the (a) LPC and (b) HPC components.

From Table 8.12, it is seen that there are active constraints in three (3) out of the four (4) LPC design problems. From all constraints imposed (i.e., on I_{min}^{choke} , I^{stall} , and LSBH), the only active constraint is the one imposed on I^{stall} , while the other two constraints on I_{min}^{choke} and LSBH are satisfied in all four optimization problems. The only optimization problem where all of the imposed constraints are satisfied is the (BEW, $n_{PRS} = 0.40$) design case. As one observes from Table 8.12, the value of I_{min}^{choke} is well above the imposed lower value of 0.010 (see Table 8.11) in all four optimization problems, while the same is true for the value of LSBH ($LSBH \gg 13.0$ mm).

Regarding the HPC component, from Table 8.13 it is seen that there are active constraints in all four (4) of the optimization problems. However, similarly to the LPC case, the only constraint active is the one imposed on I^{stall} while the other two constraints on I_{min}^{choke} and LSBH are satisfied in all four calculation cases. From Table 8.13, we can observe that $I_{min}^{choke} \gg 0.010$ in all design problems. On the other hand, LSBH is satisfied marginally by only 0.1 mm and 0.2 mm for the (MPE, $n_{PRS} = 0.30$) and (MPE, $n_{PRS} = 0.40$) design cases, respectively.

From both Table 8.12 and Table 8.13 it is also seen that there are optimization cases where the design variables themselves have also reached a specified boundary value. From the eight (8) design variables, however, only three (3) of them have reached a limiting value and, more specifically, the upper one. These variables are the compressor exit Mach number and the 1st rotor and stator aspect ratios.

From Figure 8.10, we can see that for the HPC component the BEW design produces compressors with length slightly greater than the one obtained by the MPE calculation. For reference, the BEW design gives an HPC with length greater by about 2.53 cm (relative difference of about 8.9%) for the $n_{PRS} = 0.30$ case, and by about 3.21 cm (relative difference of about 13.6%) for the $n_{PRS} = 0.40$ case. However, this is true only for the $n_{PRS} = 0.40$ case, where an increase in length between the BEW and MPE calculations is observed by about 1.14 cm (relative difference $\sim 3.2\%$). For the $n_{PRS} = 0.30$ case the BEW calculation produces a gas-path with a slight decrease in length by about 2.56 cm (relative difference $\sim 7\%$). This discrepancy can be interpreted using Figure 8.12 which illustrates the axial chord length distribution for the rotors and stators of the LPC and HPC components.

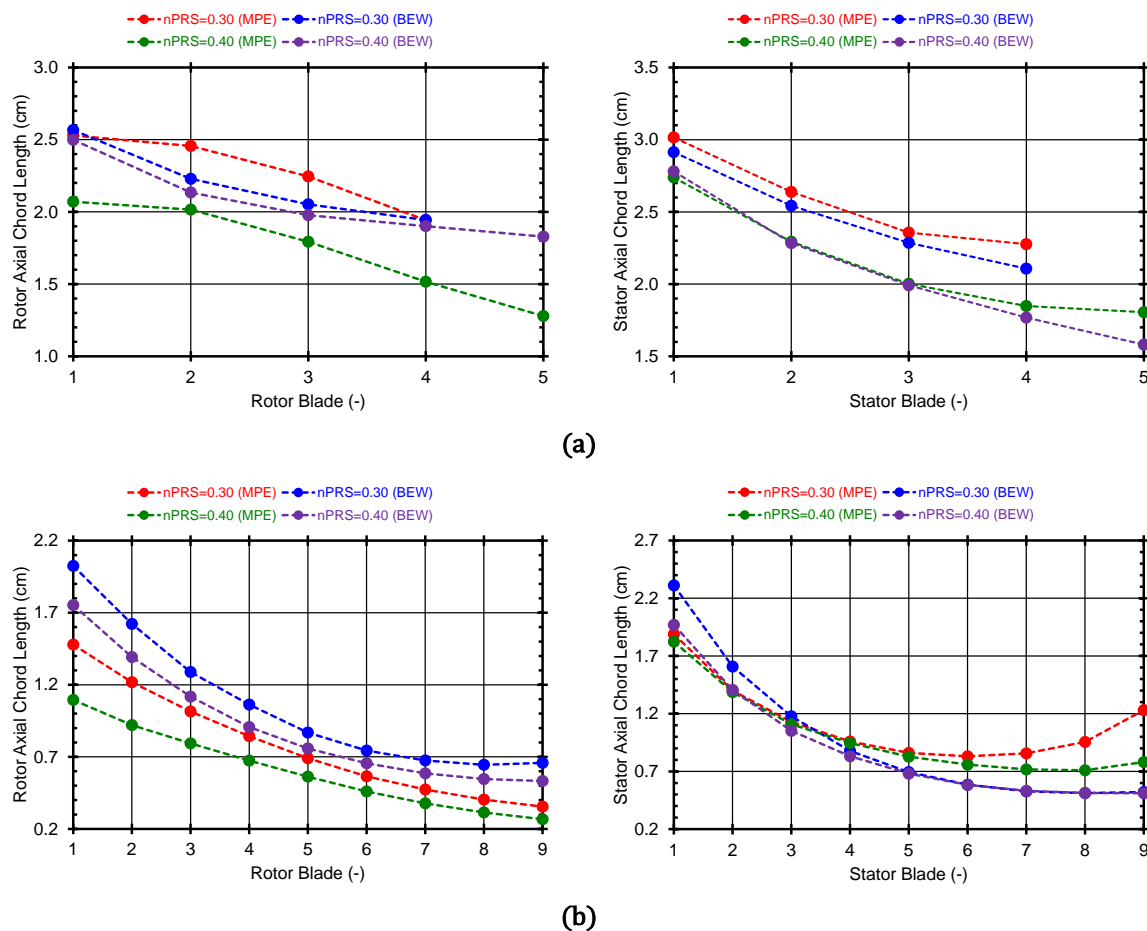
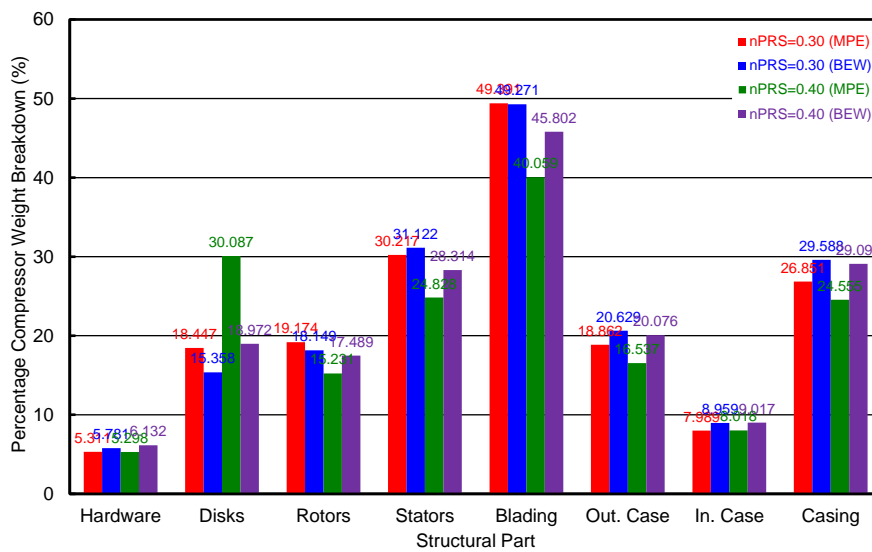


Figure 8.12: Rotor and stator axial chord lengths distributions computed by MPE and BEW for the (a) LPC and (b) HPC components.

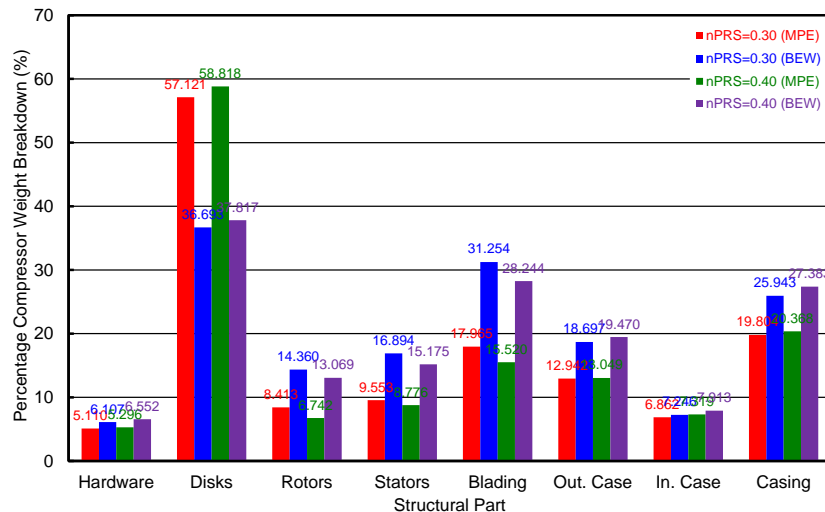
As it can be seen from Figure 8.12, in all cases where an increase in compressor length is produced between the MPE and BEW calculations, this is realized by increasing the axial chord length of the rotors much more compared to the decrease in the axial chord length of the stators. For reference, the average chord length increase between the HPC rotors is of the order of 36% and 51% for the $n_{PRS} = 0.30$ and 0.40 case, respectively, whereas the average decrease between the stators is of the order of 13% ($n_{PRS} = 0.30$) and 11% ($n_{PRS} = 0.40$). We can see that the rotor chord increase overcompensates for

the stator chord decrease for both pressure ratio splits. Note that the larger difference in the order of magnitude which is observed for the $n_{PRS} = 0.40$ case, also justifies the bigger length increase compared to the $n_{PRS} = 0.30$ case (3.21 cm and 2.53 cm, respectively). The same observations are also true for the LPC component regarding the $n_{PRS} = 0.40$ case (the average rotor chord is increased by $\sim 19\%$ while the average stator chord is decreased by $\sim 3\%$). For the $n_{PRS} = 0.30$ case, however, both the (average) rotor and stator chords are decreased by almost 4% between the BEW and MPE calculations, thus the decrease in compressor length.

Regarding the weight distribution of the compressors, this is illustrated in Figure 8.13 (percentage weight breakdown in terms of the compressor overall weight), while Table 8.14 summarizes the physical weight breakdown for both components for easy reference.



(a)



(b)

Figure 8.13: Percentage weight breakdown computed by the MPE and BEW for the (a) LPC and (b) HPC components.

Table 8.14: Physical weight breakdown computed by MPE and BEW for the LPC and the HPC components

Component	Structural Part	Weight (kg) (MPE)		Weight (kg) (BEW)	
		$n_{PRS} = 0.30$	$n_{PRS} = 0.40$	$n_{PRS} = 0.30$	$n_{PRS} = 0.40$
LPC	Hardware	4.0	4.7	3.4	4.0
	Disks	14.0	26.7	9.1	12.5
	Rotors	14.6	13.5	10.8	11.5
	Stators	22.9	22.0	18.5	18.6
	Blading (total)	37.5	35.6	29.4	30.2
	Casing (outer)	14.3	14.7	12.3	13.2
	Casing (inner)	6.1	7.1	5.3	5.9
	Casing (total)	20.4	21.8	17.6	19.2
HPC	Hardware	3.0	2.4	2.3	1.8
	Disks	33.8	26.9	13.6	10.5
	Rotors	5.0	3.1	5.3	3.6
	Stators	5.6	4.0	6.2	4.2
	Blading (total)	10.6	7.1	11.5	7.8
	Casing (outer)	7.7	6.0	6.9	5.4
	Casing (inner)	4.1	3.4	2.7	2.2
	Casing (total)	11.7	9.3	9.6	7.6

As we saw from the optimization results tabulated in Table 8.12 and Table 8.13, the LPC component is heavier than the HPC component (even the lighter LPC design is still heavier than the heavier HPC design: ~ 59.6 kg and ~ 59.1 kg, respectively), even though it comprises almost half the stages of the HPC. This is simply because the LPC is positioned at higher mean radii than the HPC (see Figure 8.10), and has also taller flow-annulus areas (and, thus, taller blades by about 1.5-4 times) than the HPC due to the smaller flow densities.

Although the HPC comprises significantly more blades than the LPC (see Figure 8.14), its blades have significantly smaller chord length (by about 1.3-3.8 times). This difference in blading weight can be seen in Table 8.14.

The lower hub and tip radii and the smaller length of the HPC compared to the respective values of the LPC (see Figure 8.10) gives also lighter hardware and casing weights than the LPC. The only HPC structural part which might be heavier than the LPC is the disks, due to the HPC having significantly more stages than the LPC [the only exception being the (BEW, $n_{PRS} = 0.40$) case, where the LPC has slightly heavier disks than the HPC by about 2 kg].

Finally, as we see from Table 8.14, the weight reduction that takes place between the BEW and MPE calculations is realized for both compressors by a weight reduction in every individual part [the only exception being the blading of the HPC component where a slight increase of less than ~ 1 kg (average) is observed from the MPE to the BEW calculation].

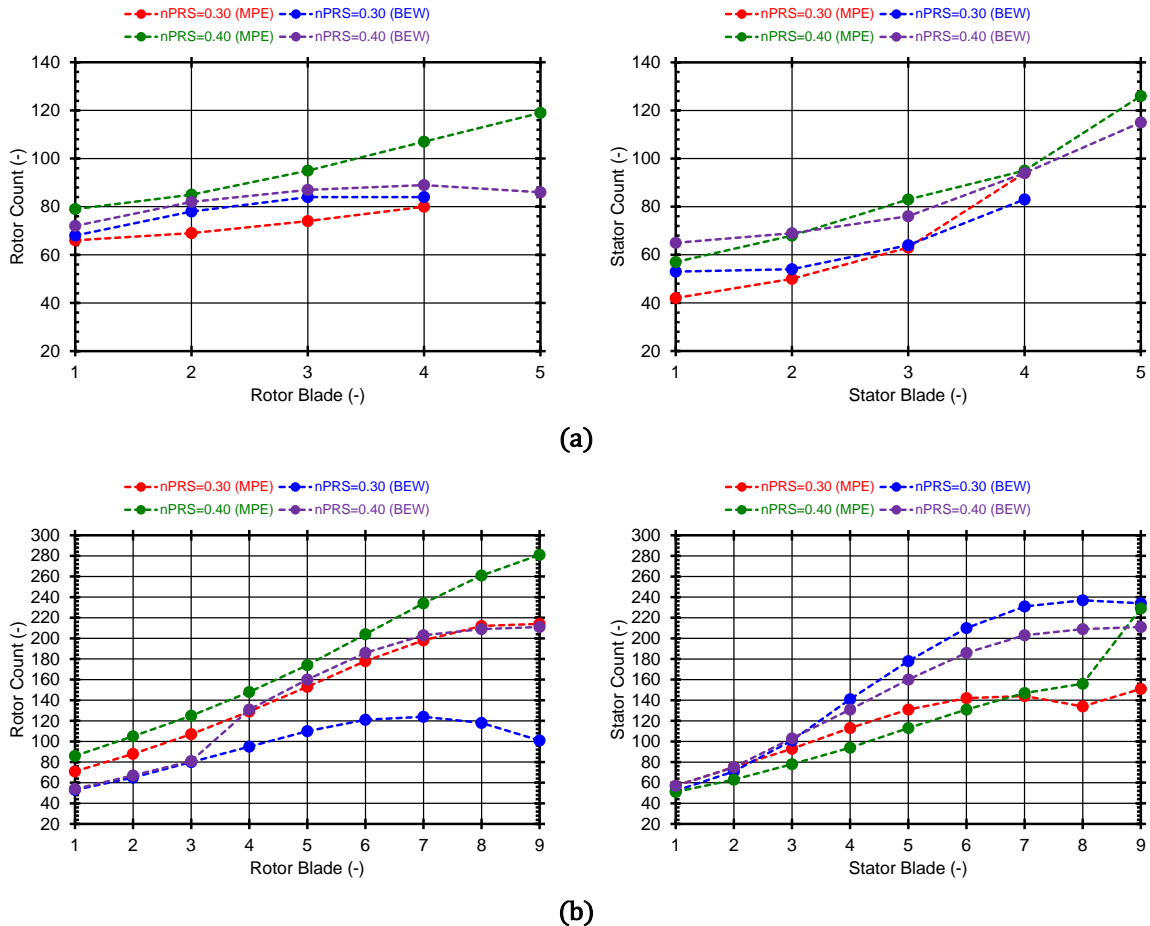


Figure 8.14: Rotor and stator blade counts distributions computed by MPE and BEW for the (a) LPC and (b) HPC components.

Regarding the weight of the connecting hardware, the reduction between the MPE and BEW calculations is of the order of $\sim 15\%$ and $\sim 25\%$ for the LPC and HPC component, respectively. From Eq. (5.28), it is seen that the connecting hardware weight is proportional to the product of $\bar{R}_h L$ (\bar{R}_h and L being the stage average hub radius and axial length, respectively). Therefore, the reduction is mainly due to the lower flow-annulus hub diameter obtained by the BEW calculation (see Figure 8.10), which overcompensates the slight increase in length for some stages between the MPE and BEW designs. For the LPC, the stage length is decreased by about 5.7 mm (average) for the $n_{PRS} = 0.30$ case, while for the $n_{PRS} = 0.40$ case the stage length is increased approximately by about 1.8 mm (average). At the same time, the average hub radius is decreased by about 14.4 mm and 38.7 mm (average values) for the $n_{PRS} = 0.30$ and 0.40 case, respectively. Therefore, for the $n_{PRS} = 0.30$ case the weight of the connecting hardware is reduced because both \bar{R}_h and L are decreased, while for the $n_{PRS} = 0.40$ case the weight is reduced mainly due to the \bar{R}_h reduction which is more than one order of magnitude larger than the increase in the stage length (L).

The same observations can be made for the HPC component too, where the stage length is increased (in average) by about 2.2 mm ($n_{PRS} = 0.30$) and 2.9 mm ($n_{PRS} = 0.40$), whereas the stage hub radius is decreased (in average) by about 46.2 mm ($n_{PRS} = 0.30$) and 48.9 mm ($n_{PRS} = 0.40$).

Similar arguments as the ones above can be made for the casing weight too. The inner and outer casing weights are proportional to $\bar{R}_h L$ and $\bar{R}_t L$, respectively (\bar{R}_h , \bar{R}_t , and L is the stage average hub radius, tip radius, and axial length, respectively). As we see from Figure 8.10, the tip radius reduction is larger than the slight increase in the length of some stages for both compressors, while the same is true for the hub radius. Hence, a $\sim 13\%$ and 19% reduction in the overall casing weight is observed for the LPC and the HPC, respectively, between the MPE and BEW designs.

Regarding the LPC blading weight, for the $n_{PRS} = 0.30$ case the reduction in both the rotor and stator weights is realized by reducing both the blade height (see Figure 8.10) and chord length (see Figure 8.12) despite the slight increase in blade count (see Figure 8.14). For the $n_{PRS} = 0.40$ case, the reduction in weight is realized for both rotors and stators by reducing (in average) simultaneously the blade count, the blade height, and the blade chord length, with the exception of the rotor chord length which (as mentioned above) is slightly increased. The latter observation justifies also the smaller reduction in rotor weight between the $n_{PRS} = 0.30$ and $n_{PRS} = 0.40$ cases ($\sim 26\%$ compared to $\sim 15\%$ as it can be seen from Table 8.14).

As we mentioned above, in contrast to the LPC, the HPC blading weight shows a slight increase. As we can see from Figure 8.10, the blade height between the MPE and BEW calculations is increased for both $n_{PRS} = 0.30$ and 0.40 cases. From Figure 8.14 it is also seen that the stator count increases significantly between the MPE and BEW calculations for both $n_{PRS} = 0.30$ and 0.40 cases. Finally, from Figure 8.12 we observe that the rotor chord is increased (in average) between the MPE and BEW calculations while that for the stators is slightly decreased (the observations are true for both $n_{PRS} = 0.30$ and 0.40). The combination of these trends yields a slight increase in the blading weight from the MPE to the BEW design, which is of the order of 0.9 kg for the $n_{PRS} = 0.30$ case, and ~ 0.7 kg for the $n_{PRS} = 0.40$ case.

Concluding this parenthesis regarding the compressor weight, we see from Table 8.14 that the weight of the compressors is reduced mainly due to the significant reduction in the weight of the rotating disks. For comparison, the disk weight reduction between the MPE and BEW designs for the LPC component is approximately 35% ($n_{PRS} = 0.30$) and 53% ($n_{PRS} = 0.40$). For the HPC, these figures are close to 60% for both pressure ratio split cases! The reduction in the weight of the disks is achieved in the following way. As we have already see, the BEW calculation produces compressor designs with lower mean radius distributions (see Figure 8.10). This, in turn, means that the blade speed is reduced (for fixed compressor speed) while the center of gravity of the blades is also lowered. As we have also seen above, in the LPC the blading weight is also reduced between the MPE to the BEW calculations, while for the HPC there is a slight increase in blading weight (the rotor weight which is of concern when calculating the weight of the disks is increased by only ~ 0.5 kg for both pressure ratio split cases). Thus, in the LPC the reduction in both the blade speed and rotor mass results in the reduction in the centrifugal loads exerted on the disks, while in the HPC component the same is true due to the significant reduction in blade speed which overcompensates the small increase observed in the rotor weight. Therefore, smaller volume disks and, hence, lighter disks (for fixed material) are required for supporting the lower mechanical loads.

The results in Table 8.12 and Table 8.13 indicate that the axial velocity shape factor ($V_{x,CLICO}$) takes values close to the left-to-middle end of the valid range (see Table 8.10) for all MPE optimization problems, while in all BEW problems it claims values around the middle of the valid range. That is, an increase in $V_{x,CLICO}$ takes place between the MPE to the BEW problems. The increased axial velocities result in a reduction in the flow-annulus areas across the compressor, thus leading to a reduction in compressor size and weight. From the MPE to the BEW problems the flow coefficient across the compressor experiences a change (more specifically, an increase which is also due to the lower blade speeds produced by the BEW designs, see Figure 8.15) from the optimal value obtained by the MPE designs which, along with the higher loading coefficients lead to lower stage efficiencies (see Figure 8.11) and overall compressor efficiency. The above trends are inline with those observed in paragraph 8.3.2.6 where, from Figure 8.8 we see that the higher compressor efficiencies are located about the lower-to-middle values of $V_{x,CLICO}$, whereas the lower compressor weights are located about the middle-to-higher values of $V_{x,CLICO}$.

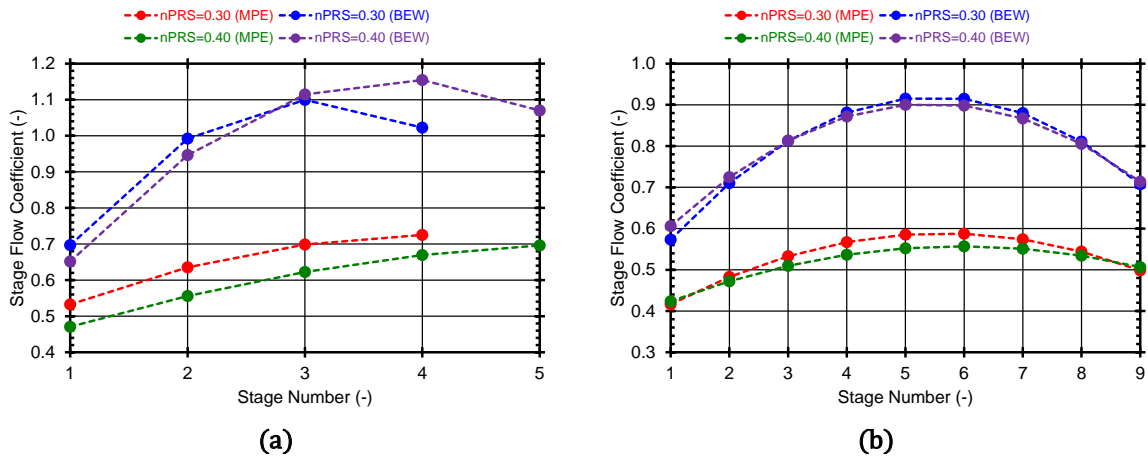


Figure 8.15: Stage flow coefficient distributions computed by MPE and BEW for the (a) LPC and (b) HPC components.

Regarding the average flow angle ($\bar{\alpha}_1$), we see from Table 8.12 and Table 8.13 that $\bar{\alpha}_1$ claims values about the middle of its valid range (see Table 8.10) in the MPE problems, while in the BEW problems it takes very low values (close to zero degrees). These trends are in accordance with those observed in paragraph 8.3.2.7, where from Figure 8.9 we saw that medium $\bar{\alpha}_1$ values maximize the compressor efficiency, while low $\bar{\alpha}_1$ values minimize the compressor weight.

The compressor exit Mach number (M_{out}) obtains high values in all MPE problems, while in all BEW problems it takes the highest specified value for the respective component (see Table 8.12 and Table 8.13). Note that the valid range differs between the LPC and HPC components (see Table 8.10) according to the guidelines given in bibliography (see Appendix A). The above trends are inline with those we saw in paragraph 8.3.2.5 (see also Figure 8.7 in conjunction with Table 8.10).

Finally, regarding the blade aspect ratio, from Table 8.12 and Table 8.13 we see that the optimizer produces (in general) designs with blades of medium-to-high aspect ratios. Figure 8.16 illustrates the rotor and stator aspect ratio distributions for the LPC

and HPC, for the different design cases. It is seen from Figure 8.16 that the LPC has, in average, blades with higher aspect ratio (~ 3.4) than the HPC (~ 2.8) which, of course, is due to the fewer stages comprising the LPC for the same aspect ratio magnitudes.

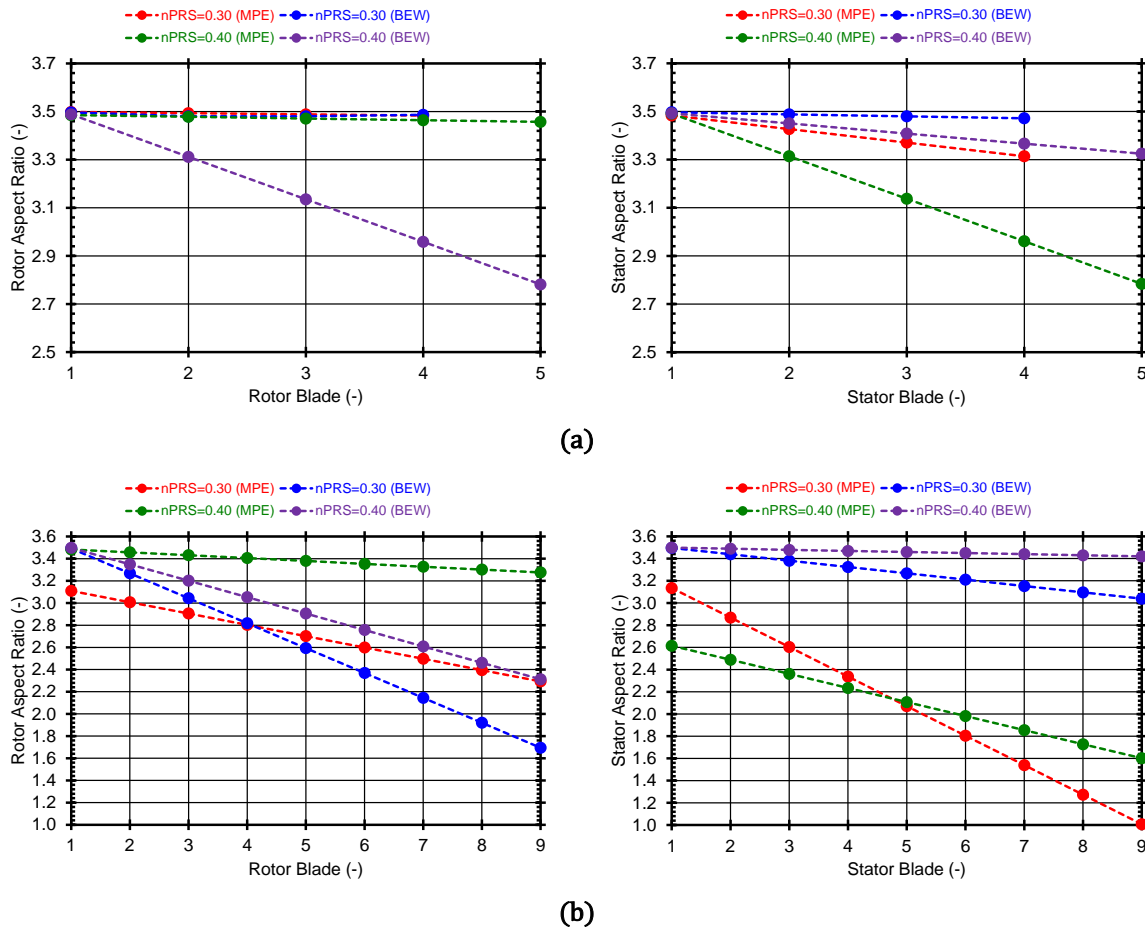


Figure 8.16: Rotor and stator blade aspect ratios distributions computed by MPE and BEW for the (a) LPC and (b) HPC components.

As was explained in paragraph 8.3.2.1, a high aspect ratio value affects positively both the compressor efficiency and weight. At the same time, an increase in aspect ratio reduces the stable working range of the compressor by reducing the available surge margin. This is seen clearly from Table 8.12 and Table 8.13 where almost all design solutions have reached the minimum specified surge margin ($I^{\text{stall}} = 0.075$ for the LPC and $I^{\text{stall}} = 0.050$ for the HPC). To compensate for that, the optimizer increases (in average) the solidity. As we saw in paragraph 8.3.2.2, the increase in solidity may have an adverse effect on both the compressor efficiency and weight but, on the other hand, it also increases the available surge margin. Therefore, the optimizer increases the blade aspect ratios to increase the compressor efficiency (in the MPE problems) or to reduce the compressor weight (in the BEW problems) leading to solutions with low surge margins but, at the same time, it produces flow designs that, although penalizing the maximum possible efficiency increase or weight reduction, they maintain the surge margin above the lower specified value by increasing the blade solidities. Figure 8.17 shows the solidity distributions as obtained by the MPE and BEW calculations. For

reference, the blade solidity for the LPC increases from 1.275 (MPE) to 1.318 (BEW) for the $n_{PRS} = 0.30$ case, while for the HPC it increases from 1.253 (MPE) to 1.380 (BEW). For the $n_{PRS} = 0.40$ case, these figures are 1.270 (MPE) and 1.326 (BEW) for the LPC, and 1.200 (MPE) and 1.350 (BEW) for the HPC.

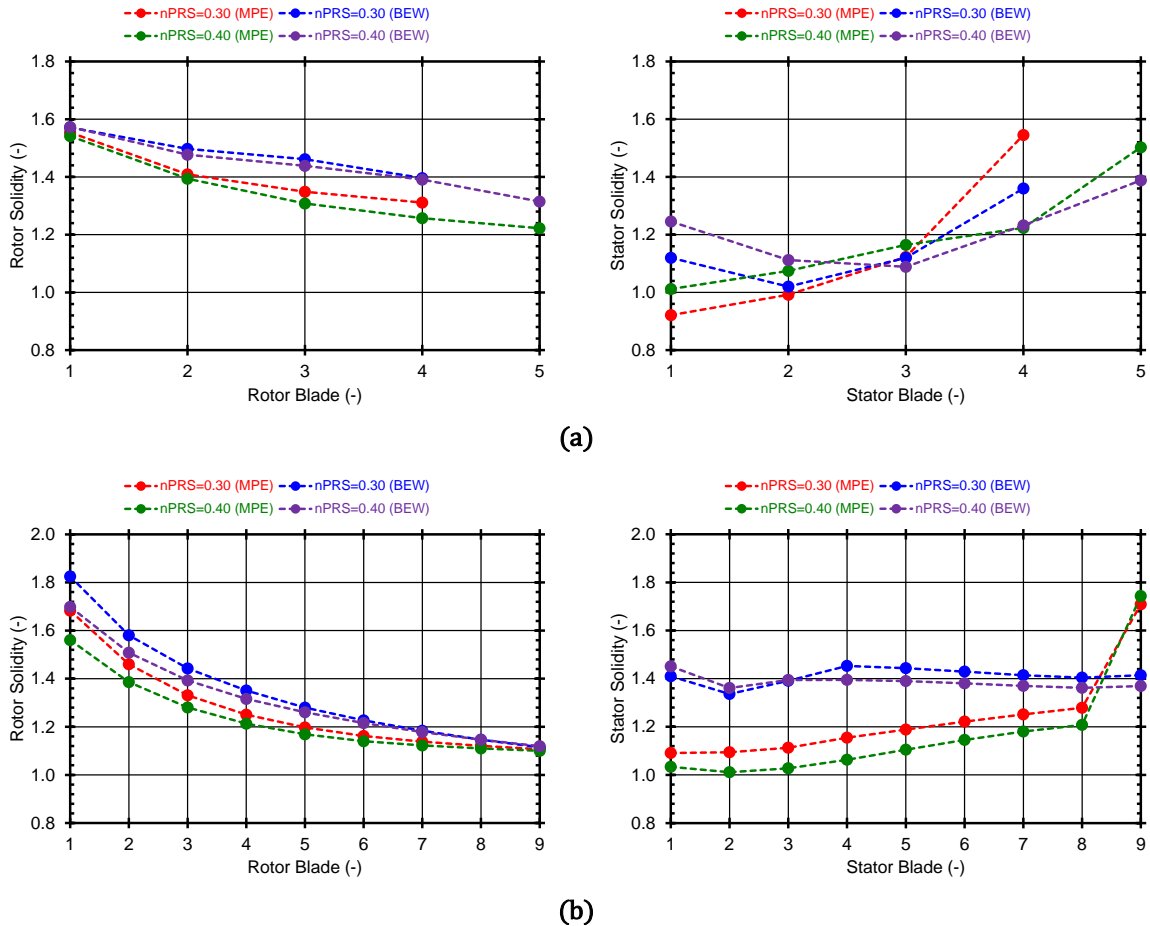


Figure 8.17: Rotor and stator blade solidities distributions computed by MPE and BEW for the (a) LPC and (b) HPC components.

Figure 8.18 shows an example sensitivity study around the optimal η_p obtained by the MPE calculations for both the LPC and HPC components. Sensitivity studies were conducted for both pressure ratio split cases, i.e., for $n_{PRS} = 0.30$ and $n_{PRS} = 0.40$. The sensitivity studies were conducted for visualizing the design space around the optimal η_p value. For this reason, the design variables were varied $\pm 10\%$ around their optimal values (see Table 8.12 and Table 8.13). In the graphs presented in Figure 8.18, the variation of η_p with the aspect ratio changes δAR_R and δAR_S is not shown since, in general, these design variables claim very low values which are close to zero (see Table 8.12 and Table 8.13). Therefore, their variation by $\pm 10\%$ produces η_p curves which are almost horizontal and offer no major information whatsoever. The intersecting point in all graphs is the maximum η_p solution.

As we see from Figure 8.18, the solutions depend strongly on $U_{t,in}$, which affects both the compressor geometry and performance. As we have already observed above, for both the LPC and HPC components the optimal solution is primarily constrained by

the limiting I^{stall} value. This is shown in Figure 8.19, where the value of I^{stall} is plotted against the percent variable change of $U_{t,in}$ which is the most influential design variable (all other design variables are kept fixed and equal to their value corresponding to the optimal η_p solution). As we see from Figure 8.19 in conjunction with Figure 8.18, there are regions with better η_p values which, however, are not obtained because the solution is bounded by the lower specified value on I^{stall} (red dashed lines in Figure 8.19). In all design cases, the region of feasible solutions lies right of the optimal one in terms of $U_{t,in}$. Similar observations can be made for the other design variables too if their variation is examined alone while keeping all other design variables fixed, where regions of feasible solutions can be observed left or right of the optimal solution or, in some cases, no feasible solutions can be found at all. However, the combination of the design variables considered in this study gives the optimal solutions shown in Table 8.12 and Table 8.13. In conclusion, the design space is a rather difficult one in terms of the constraints used, justifying the need for using an exploratory optimization technique for obtaining a solution. Remember that apart from constraints related to the compressor performance and geometry (see Table 8.11), constraints on the design variables themselves have been used in the present study too. This makes the visualization of the design space around the optimal solutions obtained in the present studies a rather difficult task.

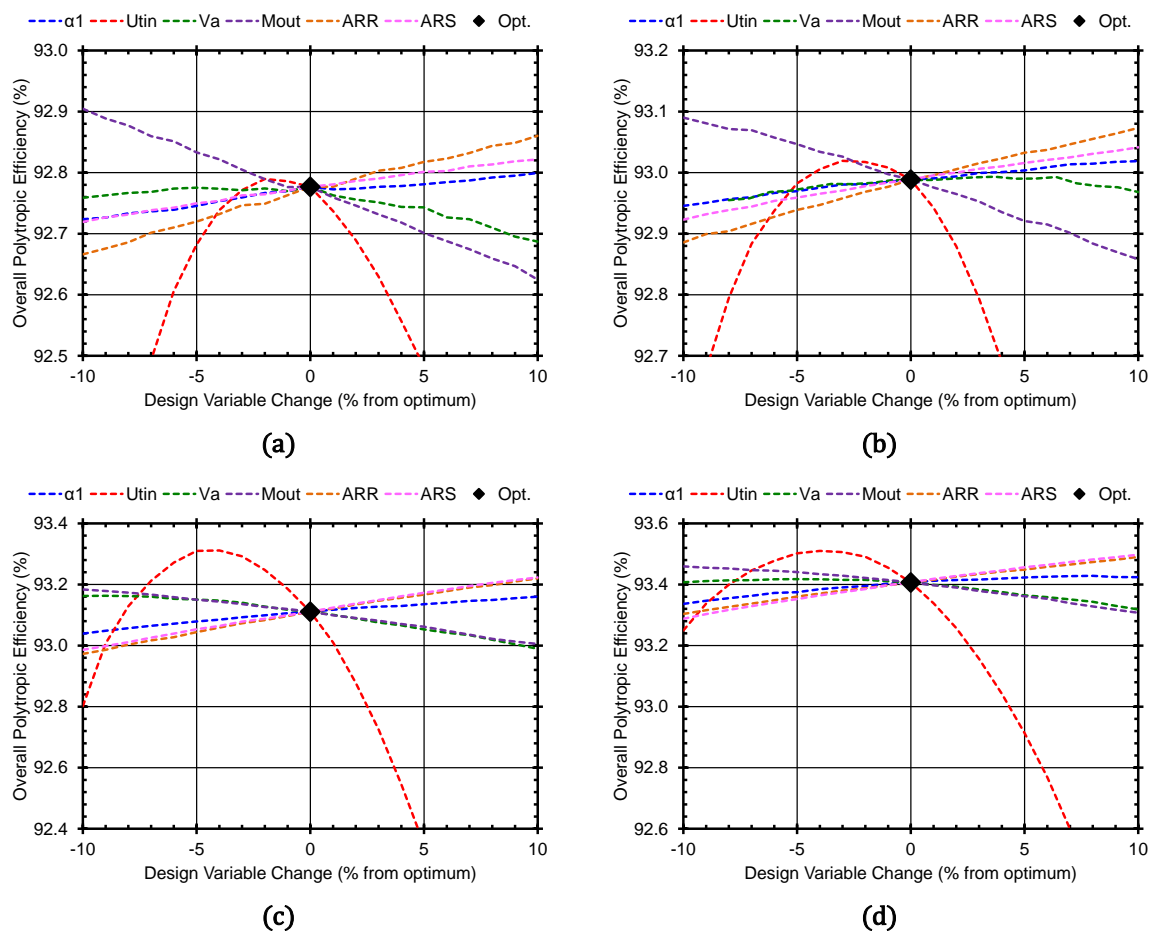


Figure 8.18: Parametric studies around the optimal overall polytopic efficiency solution obtained by the MPE calculation. LPC component: (a) 0.30 and (b) 0.40 pressure ratio split. HPC component: (c) 0.30 and (d) 0.40 pressure ratio split.

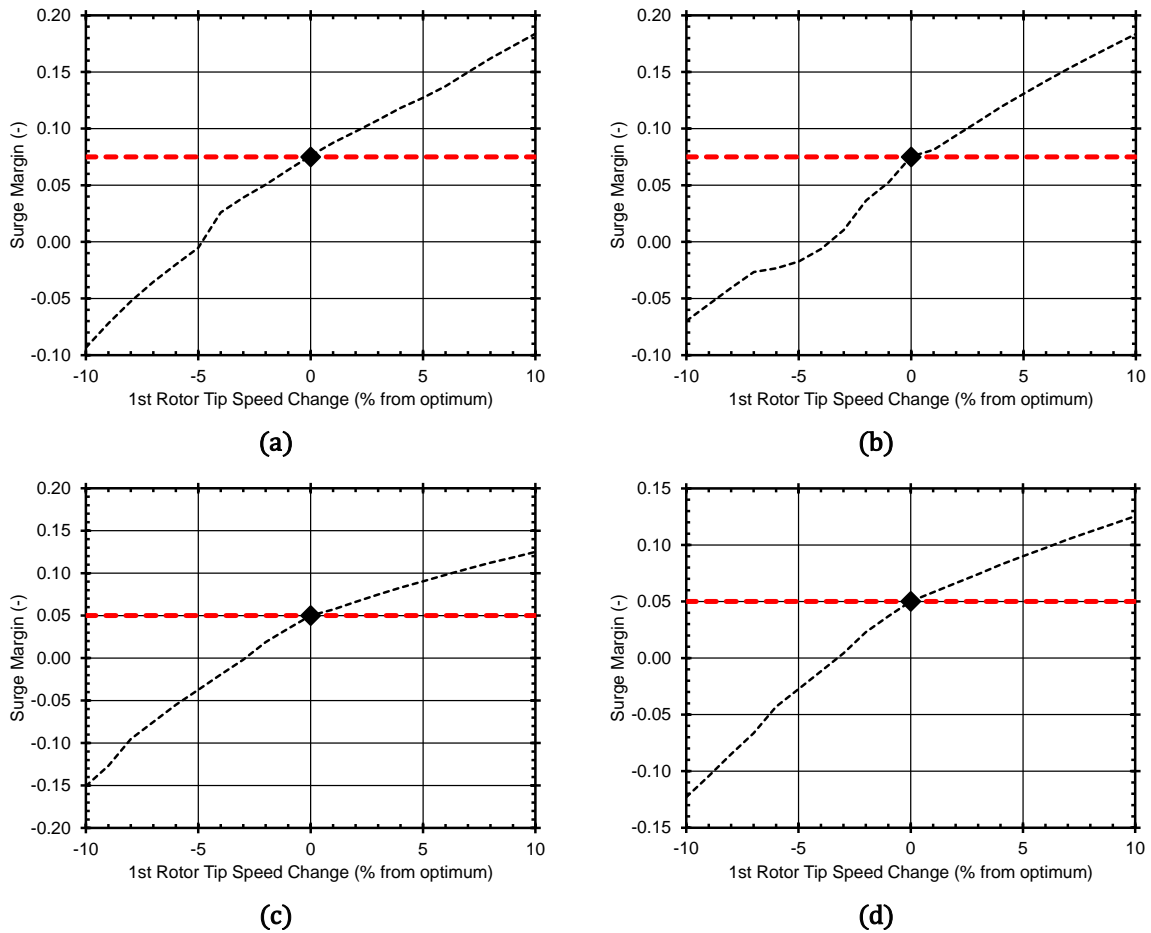


Figure 8.19: Surge margin variation around the optimal overall polytropic efficiency solution (diamond) obtained by the MPE calculation in terms of the 1st rotor tip speed percent change. LPC component: (a) 0.30 and (b) 0.40 pressure ratio split. HPC component: (c) 0.30 and (d) 0.40 pressure ratio split. The red dashed lines are the lower specified surge margin values used in the present study (0.075 for the LPC and 0.050 for the HPC).

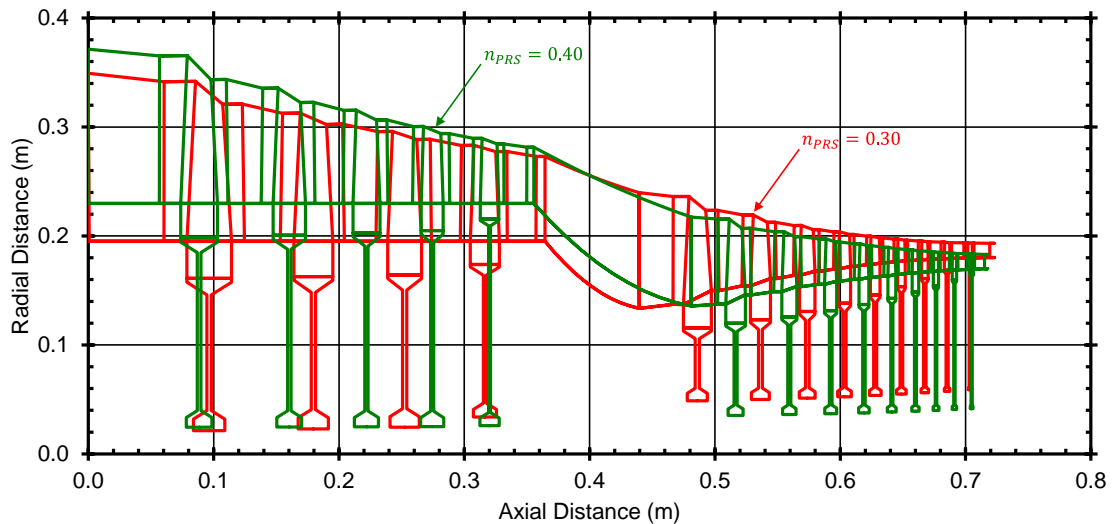


Figure 8.20: Compression system gas-path meridional view as obtained from the MPE calculation for different pressure ratio split cases. The S-duct connecting the two compressors as well as the rotating disks are also shown.

Finally, Figure 8.20 above shows the entire compression system gas-path as obtained for the MPE design case, where the S-duct and the rotating disks can also be seen. The S-duct was designed for a diameter-to-length ratio equal to 0.63 and a tip shape coefficient equal to -0.22 (see Chapter 4). The disks (web-type for both compressors) were designed according to the methodologies presented in Chapter 4 for the default RDO calculation inputs and without considering heat-transfer effects [the material properties were calculated at constant room temperature ($20\text{ }^{\circ}\text{C}$)].

From Figure 8.20, it is seen that the 0.40 pressure ratio split case yields a compression system that has slightly smaller length than the 0.30 one (by about 5.4 mm). Considering a typical material for the duct (A-286) and a typical duct wall thickness of 2.54 mm [see Pera et al. (1977a)], we can obtain the overall weight of the compression system (Table 8.15). We can see that the 0.40 pressure ratio split case yields a slightly heavier compression system than the 0.30 (by about 2.5 kg), which is mainly due to the heavier duct component.

Table 8.15: Physical weight breakdown of the compression system produced by the MPE calculation for different pressure ratio splits

Component	Weight (kg)	
	$n_{PRS} = 0.30$	$n_{PRS} = 0.40$
LPC	75.9	88.8
HPC	59.1	45.8
S-Duct	4	6.9
	$\Sigma = 139.0$	$\Sigma = 141.5$

8.4 HPC Design and Off-Design Optimization Studies

Here, HPC design and off-design optimization studies are presented. For this reason, the MLC components for both aerothermodynamic design (MLDC) and off-design calculations (MLAC) are utilized (as well as the GTWC component for estimating the weight of compressors). The goal of the present section is to investigate the relative influence (trade-off) of the design variables used previously (Table 8.10) in the HPC design while, now, we also take into account the off-design performance of the HPC at low power settings. The optimization studies are again conducted for the two pressure ratio split cases we considered in the preceding section (0.30 and 0.40).

8.4.1 PROOSIS Design Model Setup and ISIGHT Implementation

First, two (2) PROOSIS schematic models are created using the MLDC component for aerothermodynamic design and the MLAC one for map generation. The first schematic model that conducts the HPC design is similar in structure and philosophy to the one shown in Figure 8.1. The model, partition boundaries, and experiment inputs are the same as the ones described in paragraph 8.3.1. Basically, this PROOSIS model works

similarly to the one described in the previous section, which was used for the trade-off design studies of the LPC and HPC components.

The second schematic model is used for generating the compressor performance map and is shown in Figure 8.21. The partition of this model requires the compressor inlet conditions (total temperature and total pressure) as inputs (see Table 8.2), the mass flow at the compressor inlet, and the compressor rotational speed. A PROOSIS experiment is created then that generates the compressor map for different mass flow rates and rotational speeds covering the entire operating range: from stall to choke and beyond choke conditions (see Section 6.12). Here, the HPC performance map is produced for a user-specified range of speeds between 70%-105% of the design speed, while for time efficiency, the calculations are performed considering constant gas properties (see paragraph 6.2.1).

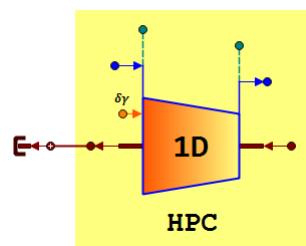


Figure 8.21: PROOSIS schematic model for the HPC off-design (map generation) calculations. Inside the yellow rectangle is shown the MLAC component for off-design performance calculations.

Finally, two (2) deck executables are created: one for the HPC design (see paragraph 8.3.1) and one for the HPC off-design calculations. These decks are then used to construct the ISIGHT workflow shown in Figure 8.22, which is used for conducting HPC design and off-design optimization studies.

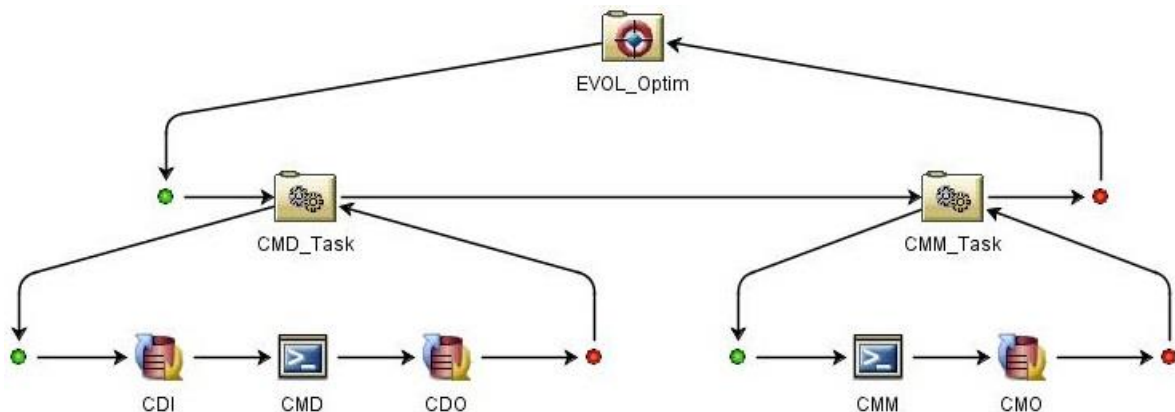


Figure 8.22: ISIGHT implementation and workflow for the HPC design and off-design optimization studies. Compared to Figure 8.2, the new components are: “CMM” is the deck executable for the HPC map generation and “CMO” is the performance output file (surge margin at 70% of design speed).

8.4.2 Optimization Studies

The implementation shown in Figure 8.22 is used to design the HPC component with the aim to obtain simultaneously the maximum overall polytropic efficiency (η_p) and

the maximum surge margin at low power conditions ($SM_{@70\%}$). Here, the low power conditions are considered at 70% of the HPC design speed (as we will see in the following chapter, 70% is close to the idle power setting in the considered aircraft mission). Therefore, Eq. (8.2) is formulated as:

$$f_{OBJ} = -\left(\frac{0.5}{50}SM_{@70\%} + \frac{0.5}{0.9}\eta_p\right) \quad (8.3)$$

where $SM_{@70\%}$ is expressed as percentage. As it can be seen from the above equation, a scale factor of 50% is assumed for the $SM_{@70\%}$ term, while the weight factors for both terms are set equal to 0.5. This calculation will be called “BESM” (from “Balanced Efficiency-Surge Margin”) hereafter.

Here, the HPC surge margin (at 70% of the design speed) is defined as:

$$SM = 100 \times \frac{\dot{m}_{\eta_{is,max}} - \dot{m}_s}{\dot{m}_c - \dot{m}_s}$$

where \dot{m}_c and \dot{m}_s is the HPC choke and stall mass flow rate, respectively, and $\dot{m}_{\eta_{is,max}}$ is the mass flow rate corresponding to the maximum HPC isentropic efficiency (see Figure 8.23). Thus, the above definition is used as a qualitative measure of the HPC surge margin during an acceleration maneuver from low power conditions.

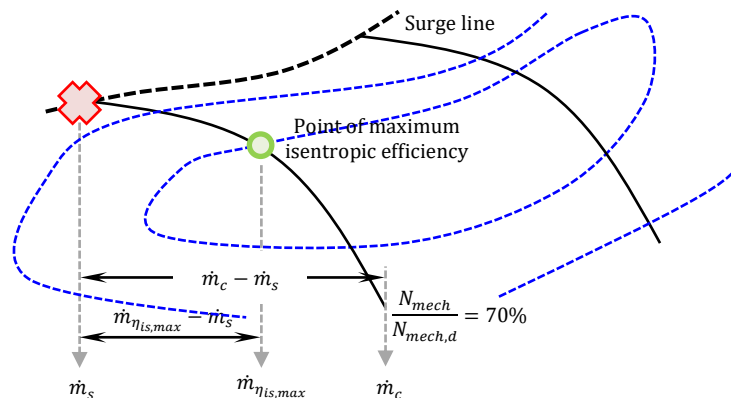


Figure 8.23: Graphical representation of surge margin definition on HPC map (at 70% of design speed).

Note here, that the number of stages of the HPC is set equal to 9 (the optimal value obtained during the design studies). The design variables and their range of validity are the same as those used in the design studies (see Table 8.10), while the same geometry and performance constraints are also applied (see Table 8.11).

8.4.3 Optimization Results

Table 8.16 shows the results obtained from the BESM calculation, for both the $n_{PRS} = 0.30$ and $n_{PRS} = 0.40$ cases. Additionally to Table 8.16, Table 8.17 tabulates the surge margin value at 70% of design speed as obtained by both the MPE and BESM calculations.

Table 8.16: BESM results for the HPC design, where red shaded cells indicate active constraints

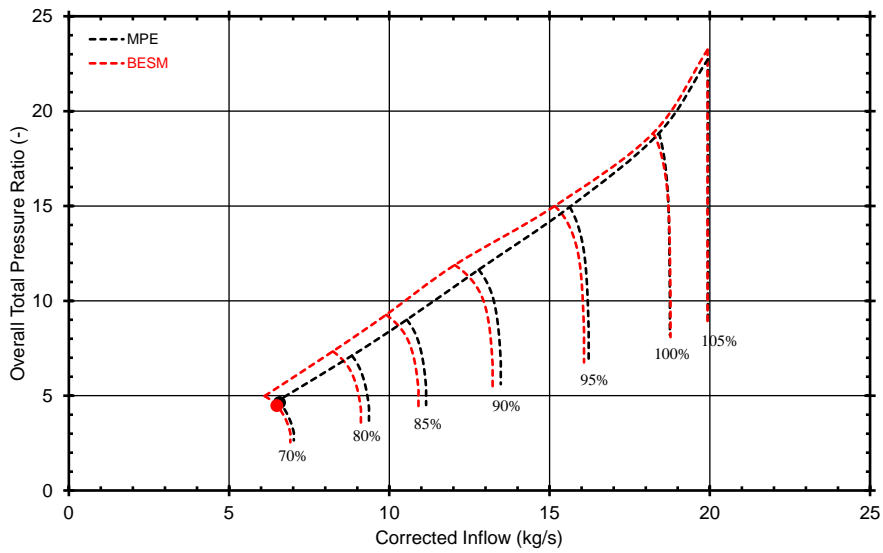
Parameter	$n_{PRS} = 0.30$	$n_{PRS} = 0.40$
$\bar{\alpha}_1$ (deg)	16.78	22.15
M_{out} (-)	0.34	0.35
$U_{t,in}$ (m/s)	444.7	413.3
$AR_{R,1}$ (-)	3.41	3.48
$AR_{S,1}$ (-)	1.78	2.41
δAR_R (-)	-0.0620	-0.0159
δAR_S (-)	-0.2760	-0.0566
$V_{x,CLICO}$ (-)	1.32	1.47
I_{min}^{choke} (-)	0.033	0.036
I^{stall} (-)	0.052	0.065
LSBH (mm)	13.0	13.0
η_p (%)	92.71	93.12
W_{KG} (kg)	65.4	44.1

Table 8.17: MPE and BESM surge margin at 70% of design speed

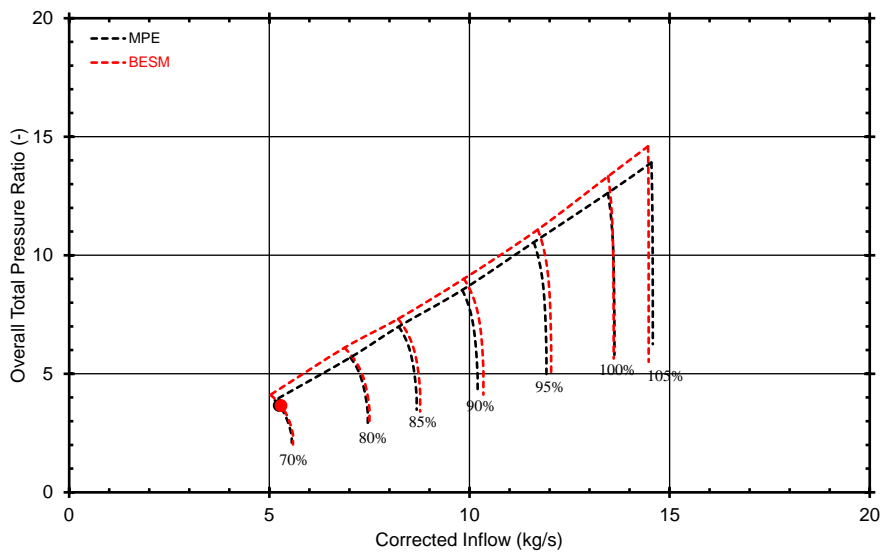
MPE		BESM	
$n_{PRS} = 0.30$	$n_{PRS} = 0.40$	$n_{PRS} = 0.30$	$n_{PRS} = 0.40$
10.53%	26.32%	47.37	47.37

From Table 8.16 we see that, similarly to the MPE calculations, the higher value of overall polytropic efficiency (η_p) is obtained when the HPC is (again) less loaded, that is, for $n_{PRS} = 0.40$. From Table 8.17, we can also see that after the optimization both pressure ratio split cases give about the same surge margin: $SM_{@70\%} \cong 47.4\%$.

Comparing the BESM to the MPE calculations, we can observe that a trade-off between the efficiency and the surge margin exists (see Table 8.13, Table 8.16, and Table 8.17). Considering that when it is less loaded ($n_{PRS} = 0.40$) the HPC has both higher polytropic efficiency and surge margin at low power settings (see Table 8.17), the penalty on η_p when increasing further $SM_{@70\%}$ is smaller for the $n_{PRS} = 0.40$ case compared to the 0.30 one. More specifically, for the $n_{PRS} = 0.30$ case we see that η_p drops by about 0.4% (absolute) while $SM_{@70\%}$ increases by about 36.8% (absolute). For the $n_{PRS} = 0.40$ case, these figures are $\sim 0.29\%$ (absolute) and $\sim 21\%$ (absolute), respectively. From Table 8.13 and Table 8.16, a change in weight can also be identified. For the $n_{PRS} = 0.30$ case the weight is penalized by about 6.3 kg, while for the 0.40 the weight decreases slightly by ~ 1.7 kg. Overall, the $n_{PRS} = 0.40$ case seems to offer HPC designs which have high overall efficiency, good surge margin at low power settings, and they are structurally lighter, while the exchange for better surge margin doesn't penalize much neither efficiency nor weight compared to the 0.30 pressure ratio split case.

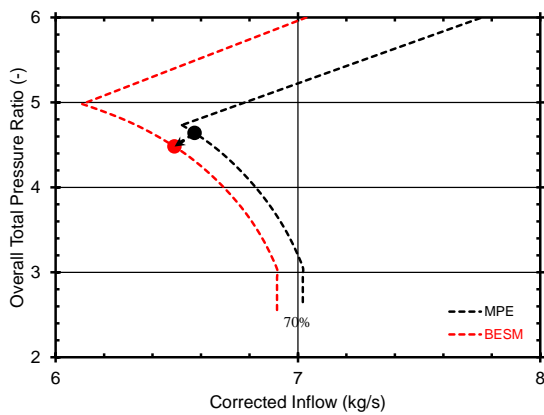


(a)

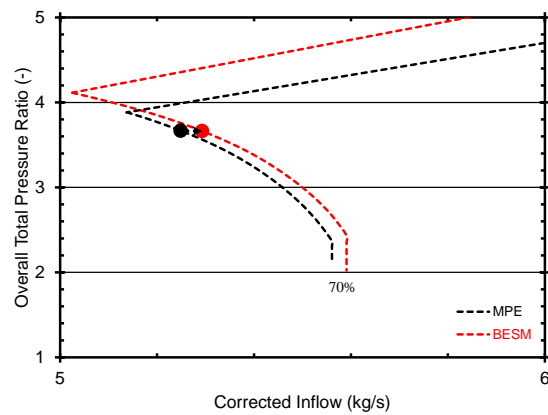


(b)

Figure 8.24: Comparison of the performance maps computed by MPE and BESM for the (a) 0.30 and (b) 0.40 pressure ratio split cases.



(a)



(b)

Figure 8.25: Close-up view of performance maps computed by MPE and BESM for the (a) 0.30 and (b) 0.40 pressure ratio split cases.

Table 8.18: MPE and BESM performance at the maximum isentropic efficiency point on the 70% speed line

Parameter	Value (MPE)		Value (BESM)	
	$n_{PRS} = 0.30$	$n_{PRS} = 0.40$	$n_{PRS} = 0.30$	$n_{PRS} = 0.40$
Corrected inflow (kg/s)	6.574	5.249	6.491	5.293
Overall pressure ratio (-)	4.640	3.667	4.480	3.663
Overall isentropic efficiency (%)	86.71	88.18	85.92	87.81
Overall polytropic efficiency (%)	89.20	90.11	88.50	89.80

Figure 8.24 shows the performance maps obtained by the MPE and BESM calculations for both pressure ratio split cases, Figure 8.25 presents a close-up view of the maps around the 70% speed line while, for completeness, Table 8.18 presents the compressor performance at the point of maximum isentropic efficiency on the 70% speed line. In the graphs, the point of maximum isentropic efficiency on the 70% speed line is also shown (circle) for reference. As we can observe, in both cases the 70% speed line is slightly shifted to the right and left for the $n_{PRS} = 0.30$ and 0.40 case, respectively, while the point of maximum efficiency remains almost at the same pressure ratio value (see also Table 8.18). Basically, the optimizer modifies the performance map such that the maximum efficiency iso-line is moved further apart from the surge line towards lower efficiencies but, at the same time, the distance between $\dot{m}_{\eta_{is,max}}$ and \dot{m}_s is increased sufficiently (more than the increase in the stable operating range, $\dot{m}_c - \dot{m}_s$, that we see from Figure 8.25) to obtain a higher surge margin value compared to the MPE design case.

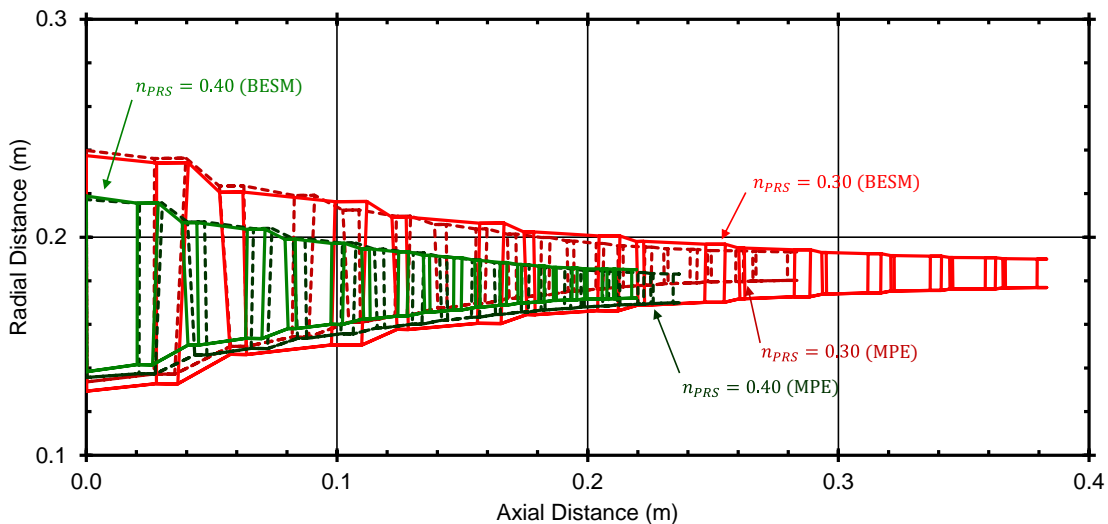


Figure 8.26: Comparison of the HPC meridional gas-path between the MPE and BESM calculations for the different pressure ratio split cases.

Figure 8.26 shows a comparison between the gas-paths computed by the MPE and BESM calculations for the different pressure ratio split cases. We can see that in both pressure ratio split cases, the BESM calculation produces gas-paths with slightly shifted

mean radii compared to the respective MPE calculation. This shift is due to both the change in $U_{t,in}$ and M_{out} which produce a shift on the mean radius⁶³.

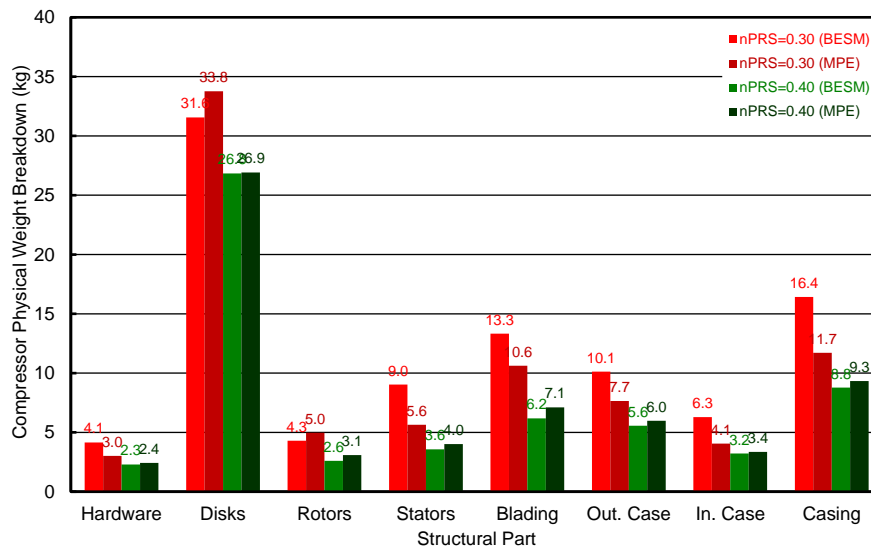


Figure 8.27: Comparison of the HPC weights between the MPE and BESM calculations for the different pressure ratio split cases.

As we see from Figure 8.27 for the $n_{PRS} = 0.30$ case, the weight of the disks reduces by about 2.2 kg between the MPE and BESM designs. This is due to both the lower weight of the rotor blades (by about 0.7 kg) and the lowering of the mean radius across the compressor (see Figure 8.26). The combined effect leads to lower centrifugal loads and, thus, to lighter disk designs. For the $n_{PRS} = 0.40$ case, we see that the weight of the disks reduces by only ~ 0.1 kg. This is mainly due to the reduction in the weight of the rotor blades (by ~ 0.4 kg), while the compressor mean radius essentially remains fixed between the MPE and BESM calculations (see Figure 8.26).

As we also see from Figure 8.27, $n_{PRS} = 0.30$ produces heavier casings and hardware. This is because the BESM calculation produces a compressor which is significantly lengthier (by about 10 cm, see Figure 8.26). On the contrary, $n_{PRS} = 0.40$ gives slightly lighter casing and hardware designs because the slightly higher hub and tip radii are overcompensated by the smaller compressor length (by about 1.7 cm).

Regarding the blading weight, we see from Figure 8.27 that the $n_{PRS} = 0.30$ case produces a total weight which is greater (by about 2.7 kg) than that produced by the

⁶³As we have already explained, the 1st rotor tip speed basically establishes the compressor inlet tip radius (for fixed inlet conditions, mass flow, and compressor speed), while the compressor exit Mach number establishes the compressor exit flow annulus area (for fixed mass flow and known exit conditions) which, for a given hub-to-tip ratio yields the compressor exit tip radius (or hub). More specifically, at the compressor inlet the flow annulus area and the tip radius are known and, thus, the hub radius is given by: $R_h = \sqrt{R_t^2 - A/\pi}$. Therefore, for fixed A the change in R_t (by changing $U_{t,in}$) leads R_h to change and subsequently $R_m = (R_h + R_t)/2$ to change across the compressor (HPC is designed with the assumption of constant mean radius). A similar argument can be made for the compressor exit, where for known A and HTR the tip radius is calculated by: $R_t = \sqrt{A/[\pi(1 - HTR^2)]}$. Therefore, a change in A (by modifying M_{out}) leads R_t to change and subsequently $R_m = R_t(1 + HTR)/2$ to also change across the compressor.

MPE calculation. As we see from Figure 8.27, the weight of the stators is increased by about 3.4 kg while the weight of the rotors is decreased by about 0.7 kg. For the case of the stators, this difference is mainly due to the significant increase in the chord length of the blades (Figure 8.29) which is increased much more than both the (small) increase in annulus (and, thus, blade) height (see Figure 8.26) and decrease in blade count (see Figure 8.28). The opposites are true for the rotor blades, leading to a small decrease in their weight.

On the other hand, the $n_{PRS} = 0.40$ cases produces a design which has a slight reduction in both the weight of the rotors and the stators (the overall blading weight is reduced by about 1 kg). Although the blade counts increase between the MPE and BESM calculations (Figure 8.28), at the same time we observe that both the blade chords (Figure 8.29) and blade heights (Figure 8.26) are reduced.

Overall, the BESM calculation for the $n_{PRS} = 0.30$ case produces an HPC design where the change of the weight of its structural parts gives an overall increase in weight of about 6.3 kg (see Table 8.13 and Table 8.16). For the $n_{PRS} = 0.40$ case, the increase in weight is only ~ 0.3 kg.

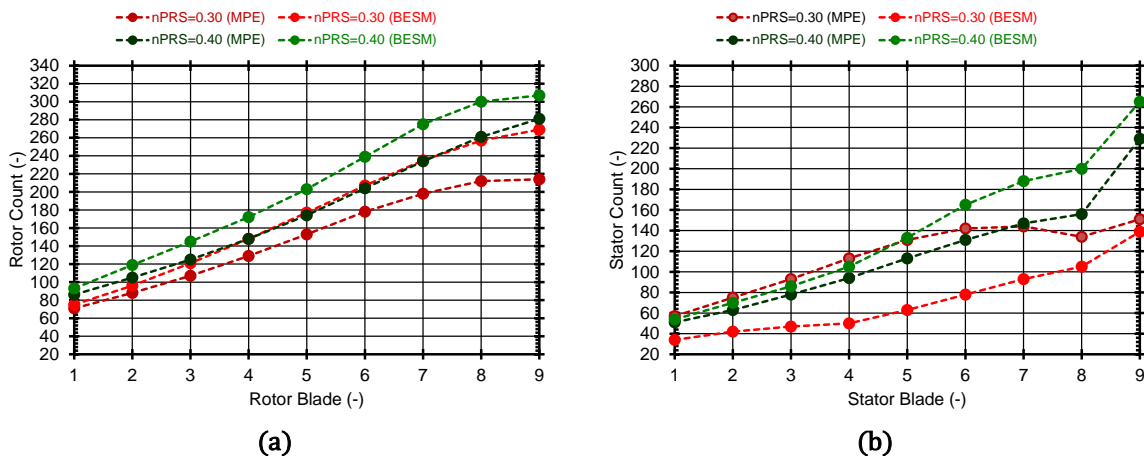


Figure 8.28: Rotor and stator blade counts distributions computed by MPE and BESM.

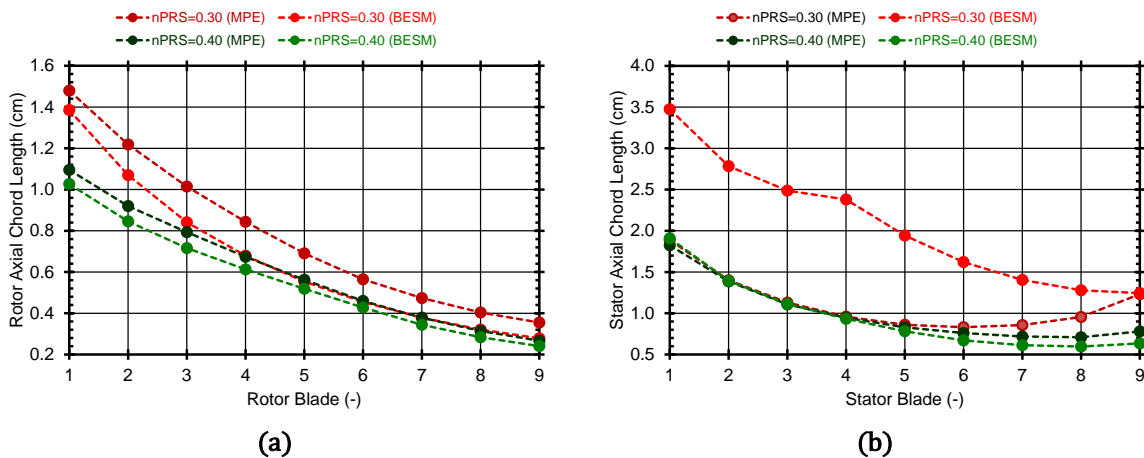


Figure 8.29: Rotor and stator axial chord lengths distributions computed by MPE and BESM.

Figure 8.30 illustrates the entire compression system gas-path. For the visualization, the results obtained by the MPE calculation for the LPC and those obtained by the BESM calculation for the HPC, were used. The S-duct connecting the LPC and HPC components, as well as the rotating disks are also shown. Again, the S-duct was designed for a diameter-to-length ratio equal to 0.63 and a tip shape coefficient equal to -0.22 . The disks (web-type for both compressors) were designed for the default RDO calculation inputs (see Chapter 4) and without considering heat-transfer effects [the material properties were calculated at constant room temperature ($20\text{ }^{\circ}\text{C}$)]. Finally, Table 8.19 presents the compression system weight breakdown for a typical duct material (A-286) and a typical wall thickness (2.54 mm).

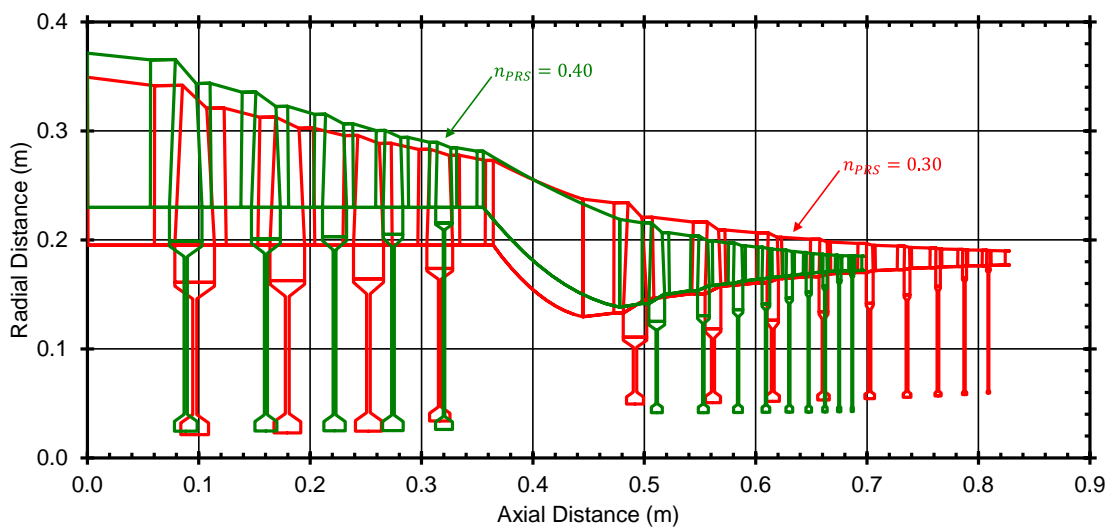


Figure 8.30: Compression system gas-path meridional view as obtained from the MPE (for the LPC) and BESM (for the HPC) calculations for different pressure ratio split cases. The S-duct connecting the two compressors as well as the rotating disks are also shown.

Table 8.19: Physical weight breakdown of the compression system computed by the MPE (for the LPC) and BESM (for the HPC) designs for different pressure ratio splits

Component	Weight (kg)	
	$n_{PRS} = 0.30$	$n_{PRS} = 0.40$
LPC	75.9	88.8
HPC	65.4	44.1
S-Duct	4.2	6.7
	$\Sigma = 145.6$	$\Sigma = 139.6$

From Figure 8.30, we see that the 0.40 pressure ratio split case produces a design with significantly smaller length than the 0.30 one, by about 13.1 cm. Also, from Table 8.19 we see that $n_{PRS} = 0.40$ yields a lighter compression system design than the 0.30 one (by about 6 kg) where, as we have already seen and explained, the major difference is made by the HPC component which for the 0.40 case is lighter by more than 21 kg compared to the 0.30 design. For comparison, Figure 8.31 illustrates the gas-path of the

compression system as obtained by the MPE and BESM calculations for the $n_{PRS} = 0.40$ case (the LPC component in both cases is the one produced by the MPE calculation).

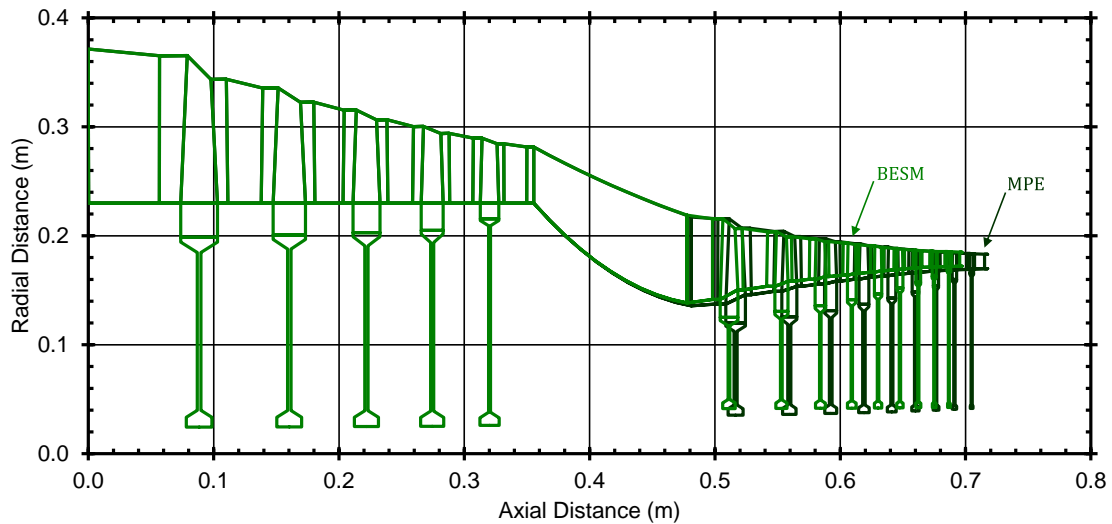


Figure 8.31: Comparison between the compression system gas-paths computed by the MPE and BESM calculations for the 0.40 pressure ratio split case.

8.5 Summary and Discussion

The aim of the present chapter was to showcase the capabilities of the design and analysis tools described in the previous chapters. For this reason, trade-off optimization studies at component level were conducted for the design of the low- and high-pressure compressors of a geared UHBR turbofan engine with separate exhausts. In the studies presented in this chapter, different design objectives were considered, while constraints were imposed on flow, geometry, and performance parameters.

More specifically, both the LPC and HPC components were designed for the following two (2) objectives: 1) maximization of their polytropic efficiency and 2) maximization of their polytropic efficiency with simultaneous minimization of their structural weight. For the HPC component, a third design study was also considered, which aimed at the simultaneous maximization of the polytropic efficiency and surge margin at low power conditions (idle). For all design studies two (2) values of the pressure ratio split between the low- and high-pressure spools were considered: 0.30 and 0.40.

Although the conclusions drawn from the above design studies cannot be generalized due to the specific inputs and assumptions considered when setting-up the calculation cases, the following can be noted. The 0.40 case seems to offer higher polytropic efficiencies for both compressors. Regarding the design of the HPC component, the 0.40 case doesn't penalize much neither efficiency nor weight when we seek to maximize simultaneously the component efficiency and surge margin compared to the case where we seek to only maximize its efficiency. Finally, the 0.40 case seems

to produce compression systems (LPC + S-duct + HPC) which are lighter and have smaller length compared to the 0.30 case.

Overall, the above studies illustrated the trade-off that exists between the compressor efficiency, weight, and stability, as well as the resolution with which the developed tools can predict these trade-offs.

9 Engine Trade-Off Design Studies at Aircraft Mission Level

9.1 Introduction

Following the compressor design studies presented in the previous chapter, this chapter presents engine design studies at aircraft mission level. The engine considered is an ultra-high bypass ratio, 2-spool, geared turbofan engine with separate exhausts. The goal of this chapter is to conduct design studies for investigating the relative effect (trade-offs) of the pressure ratio split between the LP and HP spools (n_{PRS}) on the engine total fuel consumption and on the HP compressor low power performance, at aircraft mission level. The pressure ratio split exponent (n_{PRS}) was defined in Eq. (8.1) and, as with the compressor design studies of the previous chapter, the values 0.30 and 0.40 are also considered here for n_{PRS} ⁶⁴. Note that the engine top-level specifications can be found in Alexiou et al. (2022). Finally, for the optimization studies presented here, the ISIGHT⁶⁵ platform is again utilized. Regarding the optimization studies, ASA and an evolutionary optimization algorithm were used [see Giachos (2019) for more information on both].

9.2 Multi-Disciplinary Design Workflow Setup and ISIGHT Implementation

To enable the design studies presented here, the models, procedures, and PROOSIS components presented in Chapters 3-7 are utilized, as well as the default TURBO library components for OD performance calculations [see Alexiou (2014)].

The design workflow is shown diagrammatically in Figure 9.1 and comprises the following six (6) calculation modules, which will be explained in more detail in the following:

⁶⁴These values correspond to two-spool geared turbofan engines (0.30) and three-spool turbofans (0.40) [see Epstein (2014)] and, therefore, they are of great interest in industry for the design of new engine concepts.

⁶⁵<https://www.3ds.com/products-services/simulia/products/isight-simulia-execution-engine> (accessed: May 11th, 2022)

1. An engine cycle analysis module (TDP),
2. a compressor design module (CMD),
3. a compressor performance map generation module (CMM),
4. an engine multi-point design module (MPD),
5. an engine off-design performance module (ODS), and
6. an aircraft mission analysis module (ACS).

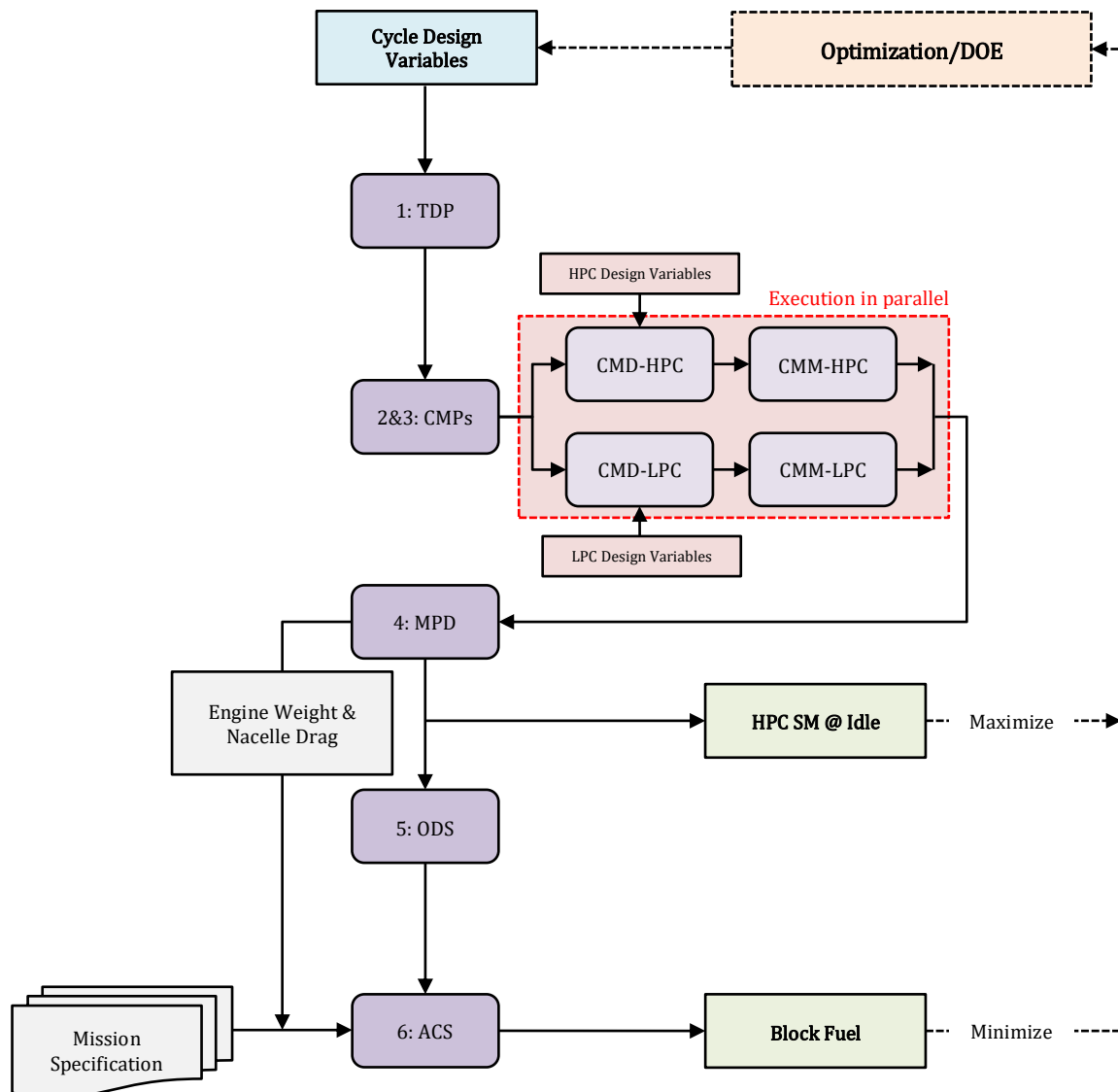


Figure 9.1: Engine design workflow for the studies presented in this chapter.

9.2.1 Engine Cycle Analysis Module (TDP)

The purpose of the engine cycle analysis module is to provide the necessary boundary conditions for the design of the LP and HP compressors. The aerodynamic design point for both compressors is Top-of-Climb (ToC). The engine cycle is thus calculated at ToC conditions for a set of design parameters and a set of structural and flow constraints to establish the speed of the shafts.

As design parameters, the values of the bypass ratio, overall pressure ratio, and fan pressure ratio are selected and are allowed to vary in the context of the optimization studies that will be presented here. To establish the speeds of the LP and HP shafts, the LP turbine stress parameter (AN_{mech}^2) is set equal to a maximum value of 40×10^6 $m^2 \cdot rpm^2$ for an exit Mach number of 0.42, and the HP turbine stress parameter is set equal to 28×10^6 $m^2 \cdot rpm^2$ for an exit Mach number of 0.45. The PROOSIS schematic model that conducts the cycle analysis at ToC conditions is shown in Figure 9.2.

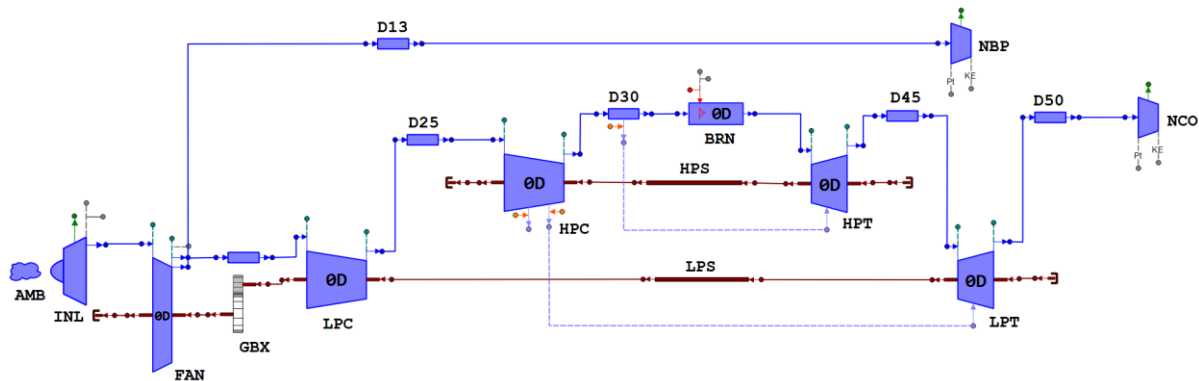


Figure 9.2: PROOSIS schematic model of a 2-spool, geared turbofan engine with separate exhausts to conduct design-point cycle analysis at ToC conditions. In the schematic the following components are shown: Atmosphere (AMB), engine inlet (INL), fan (FAN), low-pressure (LPC) and high-pressure (HPC) compressors, high-pressure (HPT) and low-pressure (LPT) turbines, burner (BRN), core (NCO) and bypass (NBP) nozzles, low-pressure (LPS) and high-pressure (HPS) shafts, gearbox (GBX), and ducts (D13-D50).

9.2.2 Compressor Design (CMD) and Off-Design Analysis (CMM) Modules

The compressor design and map generation (off-design) modules are executed after the cycle analysis module has provided the necessary boundary conditions, that is, the corrected inflow, overall pressure ratio, and corrected speed at ToC conditions.

First, the LPC and HPC design is conducted in the same context as the design studies shown in Chapter 8. Both compressors are optimized for the same design variables and constraints as those considered in Chapter 8, and the optimization aims at finding those compressor geometries that achieve a maximum overall polytropic efficiency (similarly to the MPE calculations described in Chapter 8). Note here, that to avoid numerical and optimization instabilities that are related to the stage count (N_{stg}) when is used as a design variable, the number of stages is set equal to the values obtained in Chapter 8, i.e., 9 for the HPC (irrespective of the n_{PRS} value), and 4 and 5 for the LPC for $n_{PRS} = 0.30$ and $n_{PRS} = 0.40$, respectively.

After the design of the compressors has been completed, the necessary gas-path and blade dimensions are fed into the respective off-design modules for producing the maps of the compressors. The LPC performance maps are produced for speeds between 20-102.5% of the design speed, while the HPC performance maps are obtained for speeds between 65%-105% of the design speed. Calculations are performed with constant gas properties for time efficiency (see paragraph 6.2.1).

Finally, note that the design and off-design calculations are independent between the LPC and HPC components and, therefore, are executed in parallel (see Figure 9.1) to

minimize the waiting time between the different calculations and, thus, to reduce the overall calculation time. In Figure 9.3 the PROOSIS schematic models used to conduct the compressor design and off-design calculations are shown.

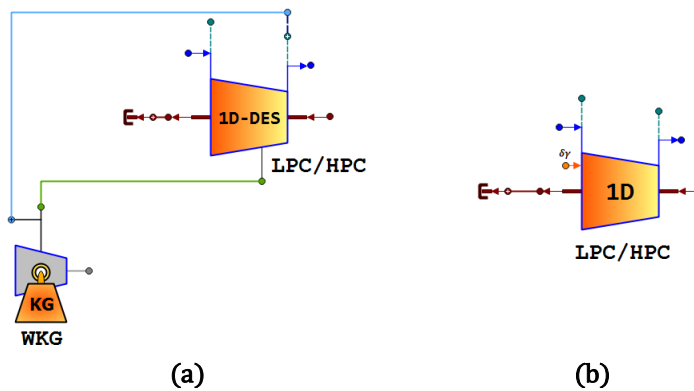


Figure 9.3: PROOSIS schematic models for compressor (a) design and (b) off-design (map generation) calculations.

9.2.3 Engine Multi-Point Design Module (MPD)

The aerodynamic design and performance map outputs for the compressors that are produced by the design (CMD) and off-design (CMM) modules, are then used by the engine multi-point design module. Figure 9.4 illustrates the PROOSIS schematic model that conducts the MPD calculation.

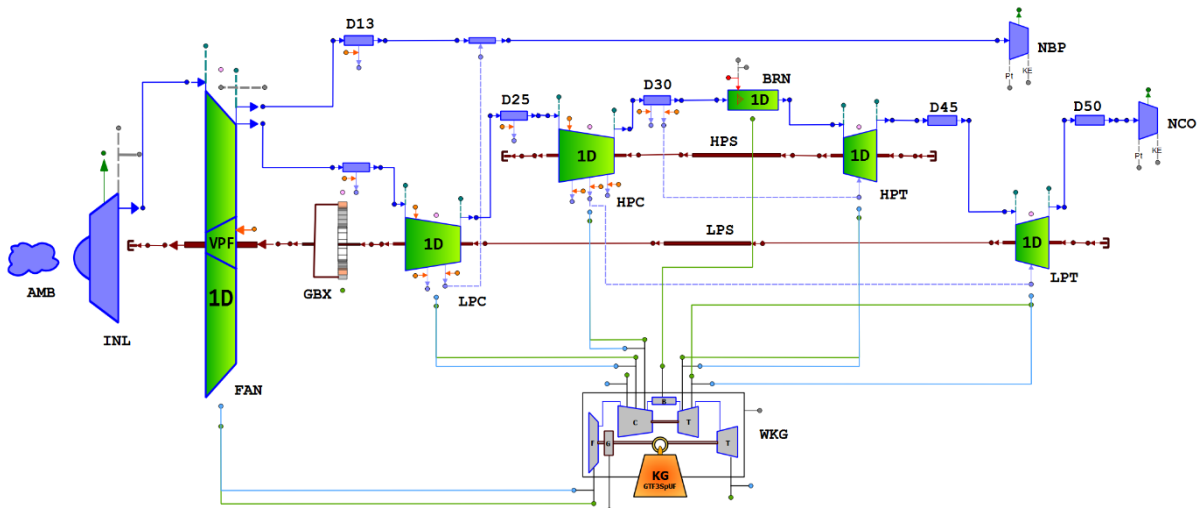


Figure 9.4: PROOSIS schematic model of a 2-spool, geared turbofan engine with separate exhausts to conduct the multi-point design calculations. In the schematic the following components are shown: Atmosphere (AMB), engine inlet (INL), fan (FAN), low-pressure (LPC) and high-pressure (HPC) compressors, high-pressure (HPT) and low-pressure (LPT) turbines, burner (BRN), core (NCO) and bypass (NBP) nozzles, low-pressure (LPS) and high-pressure (HPS) shafts, gearbox (GBX), ducts (D13-D50), and engine weight estimation component (WKG).

The MPD setup is explained in more detail by Alexiou et al. (2017) and Kolias et al. (2018). It basically consists of an extended mathematical model generated by defining a number of independent variables and an equivalent number of closure equations. The

latter can be defined in any number of operating points and are expressed in terms of equalities or groups of inequalities. Here, the Rolling Take-Off (RTO), Top-of-Climb (ToC), and Mid-Cruise (MCR) operating points are considered, while the engine performance is also obtained at Ground Idle (GIDLE) conditions (off-design operating point). Turbine cooling flows and component areas are examples of independent variables. A typical closure equation is the required value for net thrust at each operating point. Other closure equations could include the value for fan pressure ratio at ToC, the values for polytropic or isentropic efficiency of turbomachinery components at MCR, and the values for HPT blade metal temperatures at RTO. A representative group of inequalities may consist of the value for overall pressure ratio at ToC provided that the compressor exit temperature at RTO conditions does not exceed an upper limit (1st inequality), while the HPC LSBH remains above a lower limit (2nd inequality). Through proper initialization of the independent variables, a solution can be obtained that simultaneously satisfies the requirements and constraints defined on all the specified operating points. Figure 9.5 shows diagrammatically the MPD setup and calculation sequence.

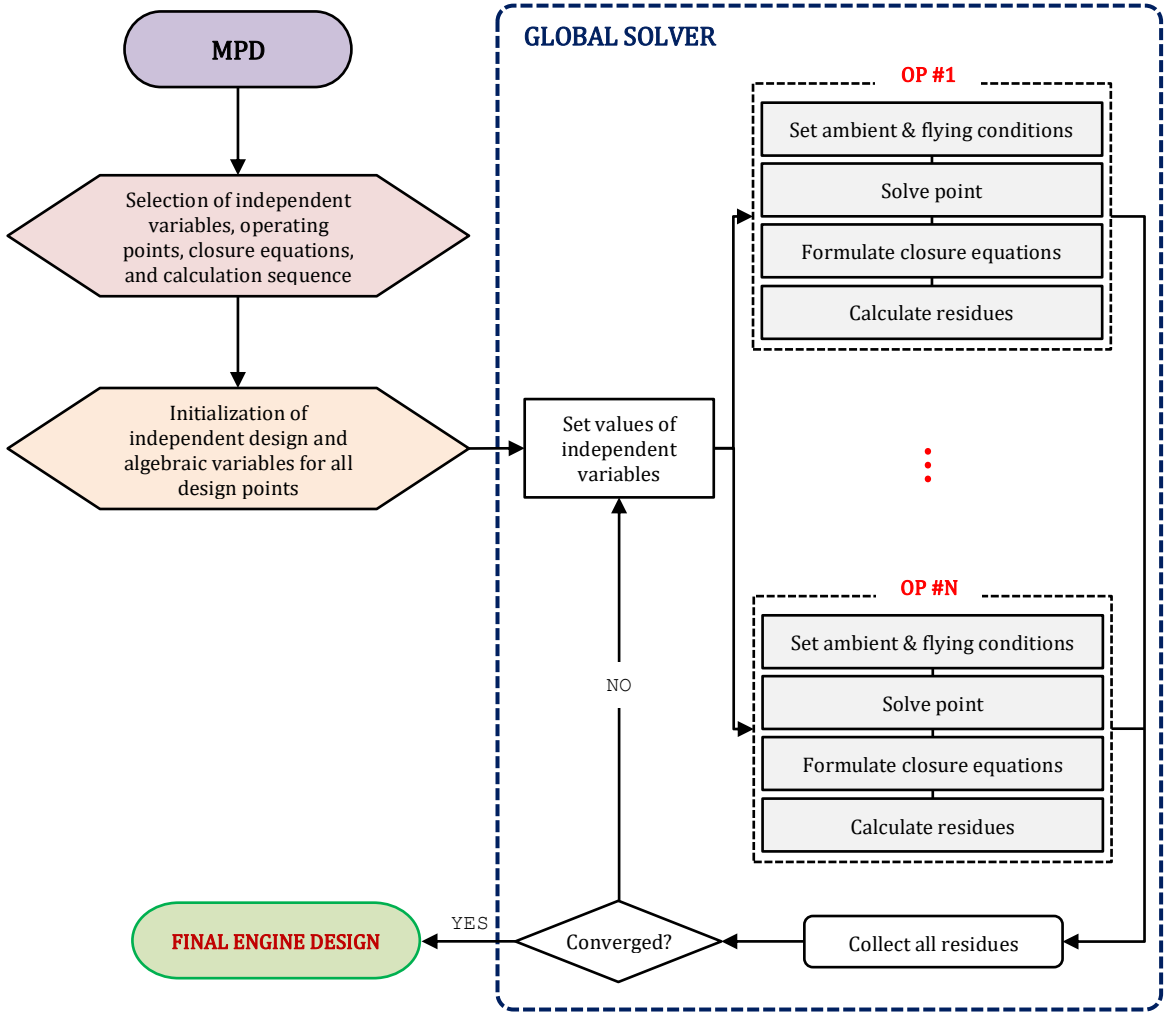


Figure 9.5: MPD calculation flow-chart.

The design variables for the RTO, ToC, and MCR operating points considered in the present studies are summarized in Table 9.1 (by setting a value for each design variable the relevant closure equation is created).

Table 9.1: MPD module design variables for different operating points (OP)

OP	Design Variable
ToC	Overall pressure ratio
	Fan pressure ratio
	Bypass ratio
	Pressure ratio split exponent
	Fan corrected tip speed
	Location of design point on all turbomachinery maps
	Flow Mach number at the inlet and exit of components
	Burner and ducts pressure drops
MCR	Burner efficiency
	Turbomachinery components efficiencies (specified or calculated)
RTO	Blade metal temperatures at each HPT row
	Total amount of HPT cooling flow
	Working potential of HPT cooling flow in equivalent single stage rotor

At the end of the MPD calculation, the engine total weight and the installed engine drag coefficient (see Appendix G) are also obtained (among other), which are required by the aircraft mission module.

9.2.4 Engine Off-Design Performance Module (ODS)

After the completion of the engine (multi-point) design, the engine off-design module is executed. The engine ODS uses the engine design information that was generated by the engine MPD calculation and runs an off-design, steady-state calculation for different combinations of flight altitude, flight Mach number, and thrust setting. The goal of the ODS module is to generate a surrogate to the engine off-design performance. This is realized in the form of a performance matrix of the engine fuel consumption in terms of the engine thrust, for different flight conditions (altitude and Mach number). The PROOSIS schematic model used for this purpose is similar to the one used for the thermodynamic cycle analysis (see Figure 9.2) where, of course, the OD turbomachinery components are replaced by components with performance maps to simulate the off-design operation.

To produce the said performance matrix, the following are noted. The engine mathematical model requires only one (1) boundary (handle) variable for solving the engine cycle. Here, the engine thrust is selected (another typical handle variable is, e.g., the fuel mass flow rate or the fuel-to-air ratio). The variation of thrust (F_N) with flight conditions [altitude (alt_f) and Mach number (M_f)] is modelled using the algebraic equations presented by Mattingly et al. (2002) which express the thrust lapse,

$F_N/F_{N,SLS}$, in terms of the reduced temperature, $\theta = T^0/288.15$, reduced pressure, $\delta = p^0/101,325$, and turbine inlet temperature ratio $TR = T_4^0/T_{4,SLS}^0$. A nested-loop approach from TR to alt_f to M_f is thus implemented to produce a performance table in the form of corrected fuel flow ($\dot{m}_f/\sqrt{\theta}/\delta$) versus corrected thrust (F_N/δ) and M_f . Note that, the use of corrected parameters eliminates the effect of altitude and ambient conditions, but it cannot eliminate the effect of Mach number. A graphical example of a performance matrix, $\dot{m}_f/\sqrt{\theta}/\delta = f(F_N/\delta, M_f)$, is illustrated in Figure 9.6.

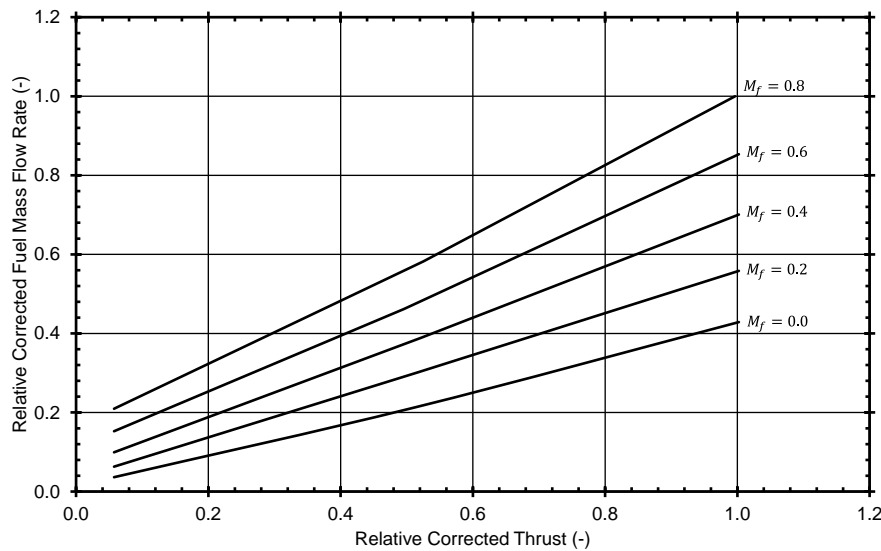


Figure 9.6: Example of surrogate engine off-design performance, in the form of relative corrected fuel mass flow rate versus relative corrected thrust and flight Mach number [adapted from Alexiou et al. (2021)].

The performance matrix produced by the ODS module is then used by the ACS module. Instead of using a surrogate model for the off-design performance of the engine, one could use the full engine thermodynamic model which would run at the current operating point (specified by the flight altitude, flight Mach number, and thrust requirement) on the flight envelope to produce the necessary engine performance required by the ACS module. However, this is time inefficient if the flight envelope has many legs and is discretized with many points and, therefore, the solution with the surrogate performance model was opted for instead. Note that a single off-design calculation requires ~ 30 milliseconds on a typical desktop workstation (Windows 7 64-bit, Intel® Core™2 Duo CPU @ 3 GHz with 4GB RAM).

9.2.5 Aircraft Mission Analysis Module (ACS)

The last step is an aircraft mission analysis for specified aircraft type and mission with the aircraft mass and drag being corrected according to the values obtained by the MPD calculation.

The ACS module is based on CAMACM, a tool developed and validated by LTT/NTUA. The latest version of the tool is available in PROOSIS [see Katsikogiannis et al. (2019)]. In CAMACM, aircraft dynamics is a component and the mission analysis is

conducted through a dedicated experiment (see Chapter 2). Fuel burn at a point (flight altitude, flight Mach number, and thrust requirement) along the mission is calculated from the engine performance matrix produced by the ODS module. The required engine thrust is obtained by the aircraft dynamics determined, in turn, by its aerodynamic performance (lift and drag) and kinematic conditions. The required aircraft performance data are introduced through a dedicated user-file, while the kinematic conditions (Mach number, flight path angle, etc.) at each point are derived from a user-defined flight envelope detailing the mission segments and the procedure with which each individual segment is realized. For more information about CAMACM, the reader could refer to the works by Kelaidis et al. (2009) and Katsikogiannis et al. (2019).

9.2.6 ISIGHT Implementation

The models described in paragraphs 9.2.1–9.2.5 are transformed into executable decks (PROOSIS schematic model → PROOSIS partition → PROOSIS experiment → deck executable). These decks are then used to construct the ISIGHT workflow shown in Figure 9.7, which materializes the schematic workflow shown in Figure 9.1. Note that, one full cycle calculation requires less than 90 seconds on a typical desktop workstation (Windows 7 64-bit, Intel® Core™2 Duo CPU @ 3 GHz with 4GB RAM).

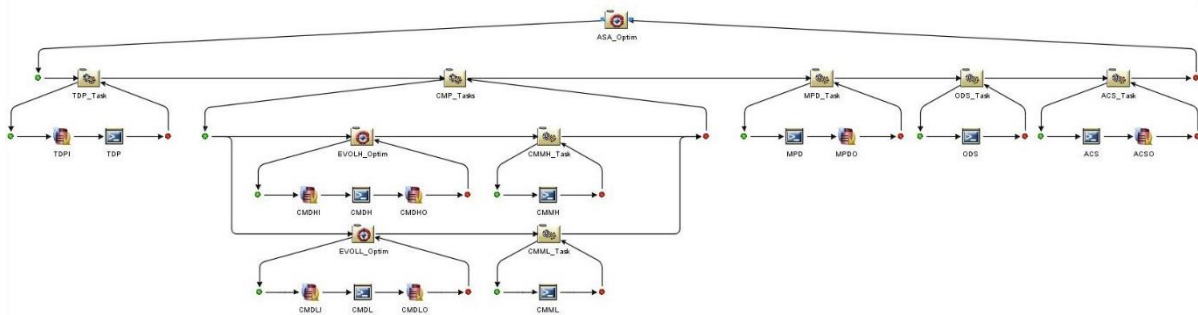


Figure 9.7: ISIGHT implementation and workflow for the engine design studies at aircraft mission level: “TDPi” is the input data file (engine design variables) for the TDP module, “CMDLI” and “CMDHI” are the input data files (compressor design variables) for the respective CMD modules, “CMDLO” and “CMDHO” are the output data files (compressor performance) from the respective CMD modules, MPDO is the output data file from the MPD module (engine performance at different operating points), and “ACSO” is the ACS module output data file (mission results).

9.3 Calculation Inputs and Design Assumptions

In the present section, the necessary inputs and design assumptions used in the models of the different modules are given. Note that the aerodynamic, performance, and weight calculation inputs and assumptions for the design of the engine LP and HP compressors (CMD module), are identical to those described in Section 8.2 and, therefore, they will not be presented again here. For consistency, the design inputs and outputs from the CMD module are assigned as inputs (through generated files) to the TURBO1D compressor components that are used to construct the MPD engine model (see Figure 9.4).

For the aerothermodynamic design (MPD calculation) of the fan component, an inlet hub-to-tip ratio of 0.30 is assumed, while the flow Mach numbers at the fan inlet and outlet (core and bypass streams) are set equal to 0.65 and 0.45, respectively. The rotational speed of the fan is established from Eq. (3.190), and along with the known speed of the LP shaft (from the TDP calculation) the gearbox ratio is also obtained. For the fan gas-path calculation, the default values shown in Table 3.7 are used, while the fan is assumed to have no bypass struts.

For the aerothermodynamic (MPD calculation) design of the turbines, the geometry assumptions shown in Table 9.2 are used. The efficiency for both components is estimated according to Aungier’s method (see paragraph 3.5.8.1) for a technology factor equal to 1.0 and 1.02 for the HPT and LPT, respectively. For determining the velocity diagrams across the turbines, both turbines are designed assuming symmetrical velocity diagrams and the constant ψ option for determining the stage-wise loading distribution. The gap ratios for the axial sizing of the turbines are set to the default values (25%), while the default value for the Zweifel loading coefficient ($\psi_z = 0.8$) is also used in both components. For the HP turbine, the cooling flows at RTO conditions are established by setting the design metal temperature for the HPT nozzles to 1320 K and that for the rotors to 1220 K. The cooling air is provided from the exit of the HPC. Finally, for the LP turbine cooling and/or sealing, the flow is assumed fixed and equal to 2% of the HPC inlet flow and is extracted from mid-stage conditions.

Table 9.2: Geometry assumptions for the HPT and LPT aerothermodynamic design

Component	Parameter	Value
HPT	Nr. of stages	2 (fixed)
	Mean-line shape	Linear
	Inlet hub-to-tip ratio	0.80
	Exit hub-to-tip ratio	0.80
	Inlet Mach number	0.15
	Exit Mach number	0.42
LPT	Nr. of stages	3 (fixed)
	Mean-line shape	Linear
	Inlet hub-to-tip ratio	0.85
	Exit hub-to-tip ratio	0.65
	Inlet Mach number	0.37
	Exit Mach number	0.45

Other necessary inputs (e.g., flow Mach numbers, duct losses, etc.) to the multi-point design module, are given in Table 9.3. For off-design calculations, the duct pressure losses are assumed to vary with the square of corrected flow relative to the respective design value [see Walsh et al. (2004)]. Finally, the thrust and discharge coefficients for both nozzles are estimated based on tables in terms of the nozzle pressure ratio [see Alexiou (2014)].

Table 9.3: Other necessary inputs for the engine design

Component	Parameter	Value
LP shaft	Mechanical efficiency	99.5%
HP shaft	Mechanical efficiency	99.5%
Burner	Design efficiency	99.9%
	Design pressure loss	4.0%
	Design Inlet Mach number	0.10
Bypass duct (D13)	Design pressure loss	2.5%
Swan neck (D25)	Design pressure loss	1.5%
HPC diffuser (D30)	Design pressure loss	1.0%
Inter-turbine duct (D45)	Design pressure loss	1.0%
LPT diffuser (D50)	Design pressure loss	1.5%
Engine inlet	Pressure ratio	99%

For calculating the weight of the engine, typical materials for such applications are used. These are given in Table 9.4 for components other than the compressors. Two (2) frames are considered, a fan rear frame (Type 2) and a LPT rear frame (Type 3), the weight of the disks is estimated according to NASA's WATE semi-empirical approach (see paragraph 5.3.6), while all other inputs for weight calculations are set to their default values.

Table 9.4: Material selection for various engine components

Component	Structural Part	Material (Stages)
Fan	Rotor blades	Ti-6Al-4V
	IGVs	A-286
	OGVs	Kevlar-149
	Disk	Ti-6Al-4V
	Hardware	Rene-41
	Casings (inner & outer)	A-286
HPT	Hardware	Rene-41 (1-2)
	Blading (rotors & stators)	Rene-41 (1-2)
	Disks	Rene-41 (1-2)
	Casings (inner & outer)	Inconel-718 (1-2)
LPT	Hardware	Rene-41 (1-3)
	Blading (rotors & stators)	Rene-41 (1-3)
	Disks	Rene-41 (1-3)
	Casings (inner & outer)	Inconel-718 (1-3)
Ducts		A-286
Shafts	Low-pressure	Inconel-706A
	High-pressure	Ti-6Al-4V

For off-design calculations (in the MPD and ODS modules), component performance maps are required. For the LP and HP compressors, these are obtained by the CMM module after the CMD module has provided the necessary compressor geometry. For the other turbomachinery components (fan, HPT, and LPT), the performance maps shown in Figure 9.8 are used.

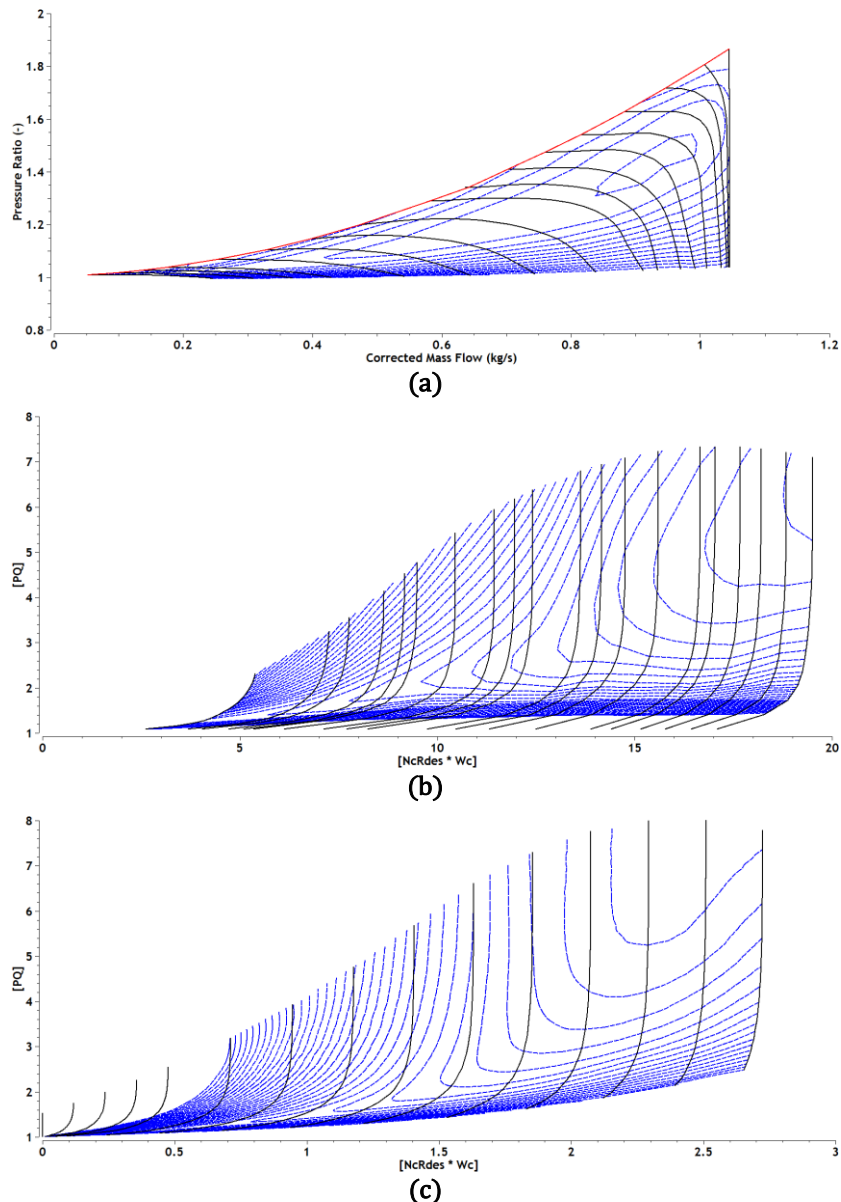


Figure 9.8: Performance maps for off-design calculations for (a) the fan component [see Cornell (1975)], (b) the HPT component [see Timko (1984)], and (c) the LPT component [see Wilfert et al. (2005)].

Finally, the aircraft mission considered in this study is an average, short-range mission of ~ 600 nm (e.g., between London and Barcelona), with a flight duration of ~ 95 minutes. The variation of flight altitude and Mach number with time for the different mission legs is shown in Figure 9.9. A payload of 14,250 kg is assumed that corresponds to a total of 150 passengers, while the fuel reserve is set to 15% of the total fuel load. The aircraft considered in the present application is a 2-engine aircraft similar to A320, with a lift-to-drag ratio equal to 19.

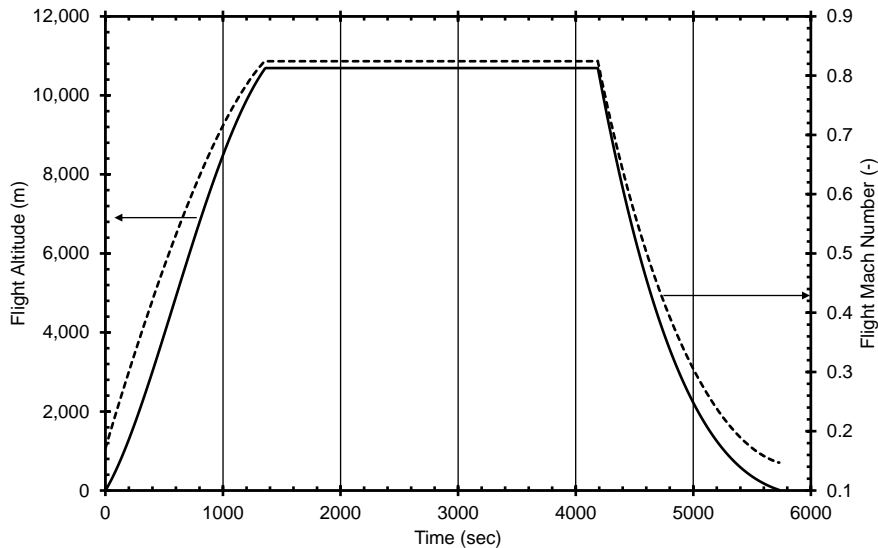


Figure 9.9: Variation of flight altitude and Mach number with flight time for three (3) mission segments: ascend, cruise, and descend.

9.4 Optimization Setup

The implementation seen in Figure 9.7 is used to conduct engine trade-off studies at aircraft mission level for the two pressure ratio splits mentioned in the introduction ($n_{PRS} = 0.30$ and $n_{PRS} = 0.40$). Here, the engine is optimized for minimum block fuel (FB) over the entire flight envelope and maximum HPC surge margin (SM) at GIDLE conditions. Thus, proper formulation of Eq. (8.2) yields:

$$f_{OBJ} = -\frac{0.5}{20} SM_{@GIDLE} + \frac{0.5}{3500} FB \quad (9.1)$$

where FB is expressed in kilograms and $SM_{@GIDLE}$ is expressed as percentage. In the above, a scale factor of 20% is assumed for the $SM_{@GIDLE}$ term and a scale factor of 3500 kg for the FB term. The weight factor for both terms is set to 0.5.

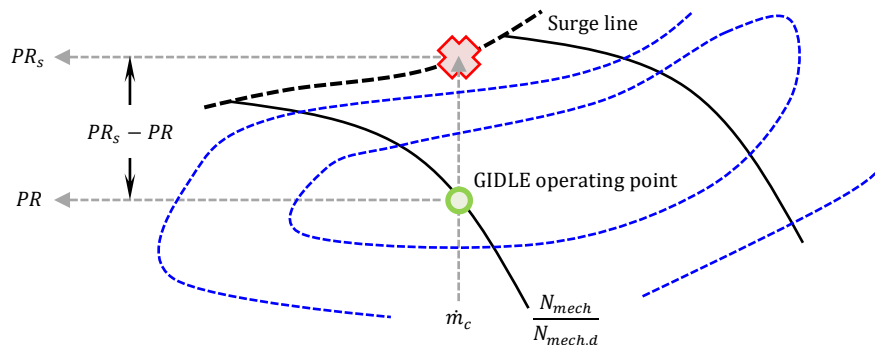


Figure 9.10: Graphical representation of surge margin definition on HPC map (at GIDLE conditions).

The fuel burn is obtained by integrating in time the fuel mass flow rate for the different points along the aircraft mission while the HPC surge margin is defined as:

$$SM = 100 \times \frac{PR_s - PR}{PR}$$

where PR is the HPC pressure ratio at GIDLE conditions, and PR_s is the surge pressure ratio for the same corrected inflow (see Figure 9.10).

To minimize the above objective function, the engine bypass ratio (BPR), overall pressure ratio (OPR), and fan pressure ratio (FPR) are varied at ToC conditions. The engine bypass ratio, overall pressure ratio, and fan pressure ratio are defined as:

$$BPR = \frac{\dot{m}_{cold}}{\dot{m}_{hot}}, \quad OPR = \frac{p_3^0}{p_2^0}, \quad FPR = \frac{p_{13}^0}{p_2^0}$$

where \dot{m}_{cold} and \dot{m}_{hot} are the engine bypass and core stream flows, respectively, and p_2^0 , p_{13}^0 , and p_3^0 is the fan inlet, fan (outer) exit, and HPC exit total pressure, respectively.

For the studies presented here, all three (3) design variables were allowed to vary within a $\pm 5\%$ range from a baseline design (see Table 9.5). For all calculations, the engine specific thrust at ToC conditions was fixed and was set equal to 98 m/s which, along with the specified net thrust (25.35 kN), inlet Mach number (0.65), and fan hub-to-tip ratio (0.30) yields a fixed fan diameter.

Table 9.5: Baseline values for engine bypass ratio, overall pressure ratio, and fan pressure ratio at ToC

Parameter	Value
Bypass ratio	13.3
Overall pressure ratio	49.0
Fan pressure ratio	1.43

Constraints were imposed on both the HPC delivery temperature (T_3^0) and the HPT inlet temperature (T_4^0) at RTO conditions, as well as on the HPC surge margin (SM) at GIDLE conditions. The constraints considered are summarized in Table 9.6.

Table 9.6: Constraints imposed during the engine optimization

Nr.	Constraint Variable	Range of Validity
1	HPC delivery temperature @ RTO	$T_3^0 \leq 955 \text{ K}$
2	HPT inlet temperature @ RTO	$T_4^0 \leq 1850 \text{ K}$
3	HPC surge margin @ GIDLE	$10\% \leq SM^{66}$

⁶⁶Although a conservative value for the surge margin would be 15%, here a 10% value was considered to allow the optimization algorithm to scan more effectively the design space for obtaining initial, feasible designs.

Finally, note that during one engine optimization cycle, an optimization of the LPC and HPC components also takes place. Both compressors are optimized for maximum overall polytropic efficiency (the MPE case in Section 8.3.3) using the design variables and constraints described in Section 8.3.3.

9.5 Optimization Results

Table 9.7 presents the optimization results for the engine (for maximum HPC surge margin at GIDLE conditions and minimum block fuel), while Table 9.8 shows the design results for the LPC and HPC components that correspond to the optimized engine design. From the tabulated results it is obvious that the design of the compressors is driven by the engine design requirements and constraints, and in turn it affects the engine performance, geometry, and weight, as we will see in more detail next.

Table 9.7: Indicative engine optimization results for different pressure ratio splits

Operating Point	Parameter	Value	
		$n_{PRS} = 0.30$	$n_{PRS} = 0.40$
ToC	Bypass ratio (-)	12.940	13.004
	Overall pressure ratio (-)	47.603	48.975
	Fan pressure ratio (-)	1.409	1.409
	LPC pressure ratio (-)	2.520	3.750
	HPC pressure ratio (-)	15.167	10.484
MCR	Fan polytropic efficiency (%)	94.96	94.95
	LPC polytropic efficiency (%)	92.58	92.74
	HPC polytropic efficiency (%)	92.82	93.20
	HPT isentropic efficiency (%)	91.88	92.24
	LPT isentropic efficiency (%)	94.05	94.12
	Uninstalled specific fuel consumption (g/kN·s)	13.940	13.867
	Installed specific fuel consumption (g/kN·s)	16.861	16.755
	Thermal efficiency (%)	47.76	47.99
	Propulsive efficiency (%)	80.19	80.22
	Core efficiency (%)	56.27	56.54
RTO	Transfer efficiency (%)	84.88	84.88
	Compressor delivery temperature (K)	937.3	935.0
GIDLE	Turbine inlet temperature (K)	1751.0	1776.3
	HPC surge margin (%)	18.44	18.17
	HPC relative corrected speed (%)	69.5	71.4
N/A	Gear ratio (-)	3.519	3.532
	Engine total weight (kg)	2895.3	2859.1
	Fuel burn (kg)	3545.8	3522.7

Table 9.8: LPC and HPC design results, where red shaded cells indicate active constraints

Component	Parameter	Value	
		$n_{PRS} = 0.30$	$n_{PRS} = 0.40$
LPC	Average absolute flow angle (deg)	24.01	16.31
	Exit absolute Mach number (-)	0.51	0.51
	1 st rotor tip speed (m/s)	369.4	381.4
	1 st rotor aspect ratio (-)	3.5	3.5
	1 st stator aspect ratio (-)	3.5	3.5
	Rotor aspect ratio change per row (-)	0.0	-0.01
	Stator aspect ratio change per row (-)	-0.05	-0.02
	Axial velocity shape factor (-)	1.01	1.05
	Minimum choke index (-)	0.086	0.083
	Overall stall margin/index (-)	0.075	0.077
	Last stage blade height (mm)	78.3	53.8
Polytropic efficiency (%)	92.63	92.87	
HPC	Average absolute flow angle (deg)	16.78	20.38
	Exit absolute Mach number (-)	0.31	0.31
	1 st rotor tip speed (m/s)	440.7	408.7
	1 st rotor aspect ratio (-)	2.41	3.26
	1 st stator aspect ratio (-)	2.63	2.68
	Rotor aspect ratio change per row (-)	-0.0120	0.0
	Stator aspect ratio change per row (-)	-0.1860	-0.1760
	Axial velocity shape factor (-)	1.52	1.44
	Minimum choke index (-)	0.032	0.032
	Overall stall margin/index (-)	0.054	0.050
	Last stage blade height (mm)	14.0	14.8
Polytropic efficiency (%)	92.79	93.19	

First of all, we can see from both Table 9.7 and Table 9.8 that the higher overall polytropic efficiency for the LPC and the HPC is obtained when the former is more loaded and the latter is less loaded, that is, for $n_{PRS} = 0.40$ for both compressors. This is in accordance with the conclusions drawn in Chapter 8. From Table 9.8, we see that these efficiencies are obtained because the solution has reached a constraint and/or a limiting value for some of the design variables. For example, for the HPC design we see that the constraint on I^{stall} is active for the $n_{PRS} = 0.40$ case ($I^{stall} = 0.050$), while for the LPC design we see that the constraint on I^{stall} is active for the $n_{PRS} = 0.30$ case ($I^{stall} = 0.075$). The values of I_{min}^{choke} and LSBH are well above the imposed lower permissible values (0.010 and 13.0 mm, respectively) in all design calculations.

The effect of the above LPC and HPC designs on the engine (off-design) performance for the two different values of pressure ratio splits examined here is shown in Figure 9.11, where both the change in map shape and the change of the relative location of the different operating points on them can be observed. These

changes eventually lead to different engine cycles (in terms of ToC *BPR*, *OPR*, and *FPR*) for achieving the specified optimization objectives.

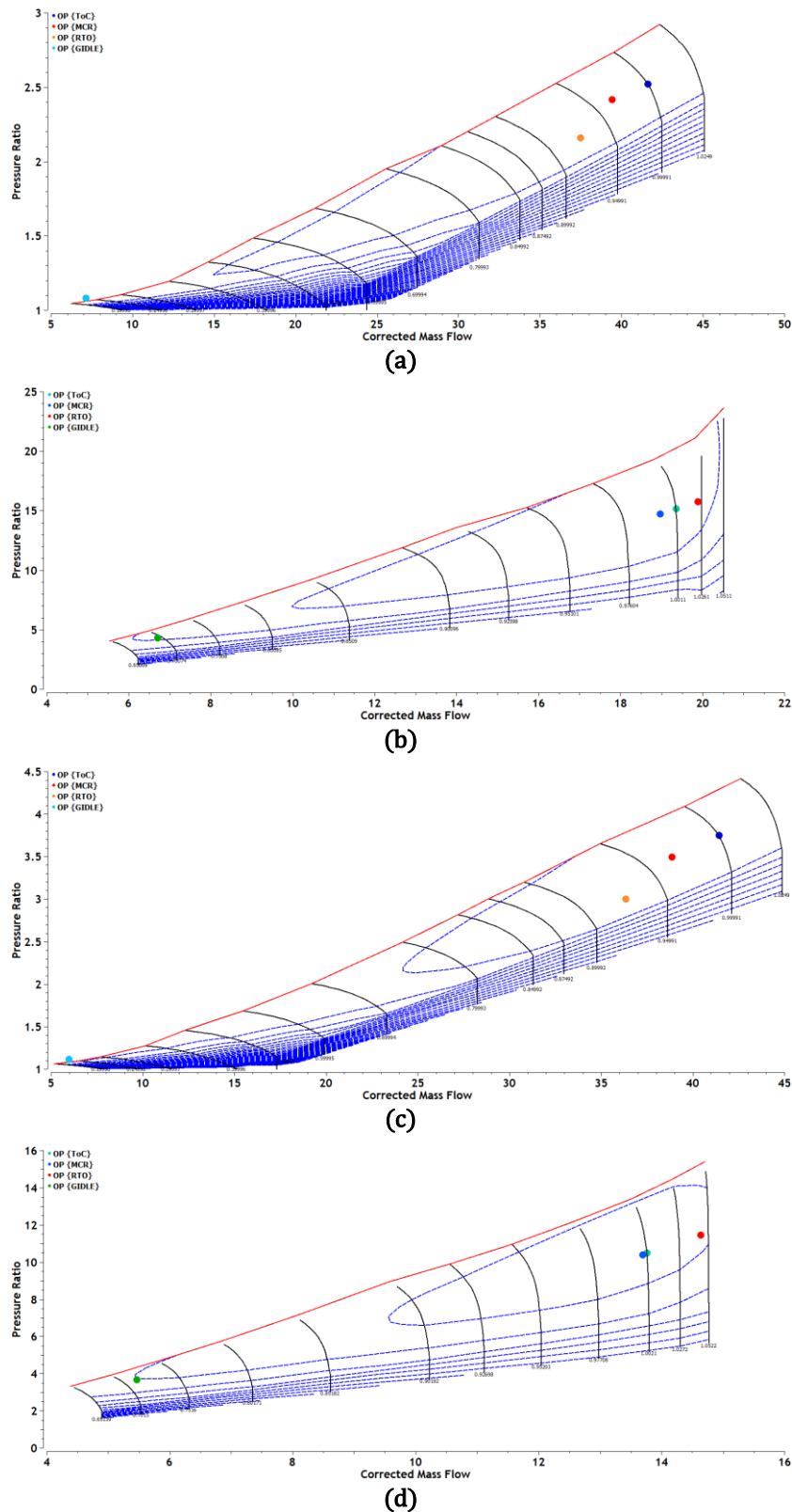


Figure 9.11: Operating points on the (a) LPC and (b) HPC maps for the 0.30 pressure ratio split case, and on the (c) LPC and (d) HPC maps for the 0.40 pressure ratio split case.

An interesting outcome of this study is the fact that the results presented in Table 9.8 correspond to LPC and HPC designs which give the best engine design in terms of minimum block fuel and maximum HPC surge margin at GIDLE conditions (the results presented in Table 9.7), but not the best compressor efficiencies. For reference, Table 9.9 and Table 9.10 present the engine performance corresponding to the best LPC and HPC design, respectively, as they were obtained during the engine optimization procedure (Figure 9.7). The best designs for the LPC and the HPC (in terms of polytropic efficiency) didn't occur at the same optimization cycle, i.e., the best design for each compressor was obtained for different engine cycles (expressed in terms of the *BPR*, *OPR*, and *FPR* at ToC conditions).

Table 9.9: Indicative engine performance results corresponding to the best LPC design for different pressure ratio splits, where red shaded cells indicate active constraints

Operating Point	Parameter	Value	
		$n_{PRS} = 0.30$	$n_{PRS} = 0.40$
ToC	Bypass ratio (-)	12.683	13.527
	Overall pressure ratio (-)	50.410	48.064
	Fan pressure ratio (-)	1.439	1.450
MCR	LPC polytropic efficiency (%)	92.69	92.89
	Uninstalled specific fuel consumption (g/kN·s)	13.799	13.786
	Installed specific fuel consumption (g/kN·s)	16.713	16.686
RTO	Compressor delivery temperature (K)	953.7	928.3
	Turbine inlet temperature (K)	1756.9	1821.2
GIDLE	HPC surge margin (%)	12.24	8.29
N/A	Fuel burn (kg)	3517.7	3521.8

Table 9.10: Indicative engine performance results corresponding to the best HPC design for different pressure ratio splits, where red shaded cells indicate active constraints

Operating Point	Parameter	Value	
		$n_{PRS} = 0.30$	$n_{PRS} = 0.40$
ToC	Bypass ratio (-)	13.057	13.532
	Overall pressure ratio (-)	47.779	50.392
	Fan pressure ratio (-)	1.427	1.421
MCR	HPC polytropic efficiency (%)	93.11	93.46
	Uninstalled specific fuel consumption (g/kN·s)	13.834	13.757
	Installed specific fuel consumption (g/kN·s)	16.735	16.611
RTO	Compressor delivery temperature (K)	937.8	939.8
	Turbine inlet temperature (K)	1764.3	1820.3
GIDLE	HPC surge margin (%)	9.90	9.60
N/A	Fuel burn (kg)	3520.0	3494.4

As we see from Table 9.9 and Table 9.10, there are combinations of engine design parameters (BPR , OPR , and FPR) which give both better compressor efficiencies and engine fuel burn, compared to the results presented in Table 9.7. However, we see that for all n_{PRS} cases the surge margin of the HPC is low (less than, e.g., 15%, which is considered as a conservative value). In fact, we see that for most cases the HPC surge margin is even less than the imposed constraint of 10% (see Table 9.6). For comparison (and verification) purposes, Table 9.11 gives the objective function (f_{OBJ}) value as evaluated by Eq. (9.1) when replacing the values of FB and $SM_{@GIDLE}$ obtained for the different design cases. From Table 9.11 it is seen that, indeed, the best engine designs do not correspond to the best compressor designs. This remark is generally in agreement with the one made by Wisler et al. (1977)⁶⁷, who in their work showed that the best compressor design doesn't necessarily yield the best overall system performance potential.

Table 9.11: Objective function value for the different feasible design cases

Design Case	$FB/HPC\ SM_{@GIDLE}$	f_{OBJ} (-)
Best engine design for $n_{PRS} = 0.30$	3545.8 kg/18.44%	0.04554
Best engine design for $n_{PRS} = 0.40$	3522.7 kg/18.17%	0.04899
Best LPC design for $n_{PRS} = 0.30$	3517.7 kg/12.24%	0.19653
Best HPC design for $n_{PRS} = 0.30$	3520.0 kg/9.90%	0.25546
Best LPC design for $n_{PRS} = 0.40$	3521.8 kg/8.29%	0.29586
Best HPC design for $n_{PRS} = 0.40$	3494.4 kg/9.60%	0.25920

Closing this parenthesis, the discussion that follows will be focused only on the results presented in Table 9.7 and Table 9.8, i.e., for the best engine design.

From Table 9.7 we observe that $n_{PRS} = 0.40$ produces a lighter engine design than $n_{PRS} = 0.30$ (by ~ 36 kg). Figure 9.12 illustrates the percent weight breakdown relative to the engine total weight quoted in Table 9.7. For both n_{PRS} cases, the fan and the gearbox contribute collectively about 41% on the engine total weight (this figure goes up to $\sim 51\%$ if we consider the bare engine weight). The fan alone, comprises almost one-third of the engine total weight, a figure directly linked to the large fan diameters encountered in ultra-high bypass ratio engines (here, the fan diameter is equal to 2.16 m). Other components/parts that contribute significantly to the engine total weight, are the structural parts (shafts + ducts + frames) which account for about 19% of the engine total weight. In this 19%, the frames contribute the most with $\sim 77\%$, shafts account for another $\sim 15\%$, while ducts make up for the remaining $\sim 8\%$. Finally, the engine nacelle accounts for almost 20% of the engine total weight. For completeness, Table 9.12 summarizes the engine physical weight breakdown.

⁶⁷Wisler et al. (1977) conducted compressor parametric calculations to study the effect of various design parameters (geometrical, flow, etc.) on the compressor overall efficiency, weight, etc. They showed that the best compressor design does not (necessarily) yield the best engine performance when integrated into an engine system, since there are other engine components contributing too to the engine performance.

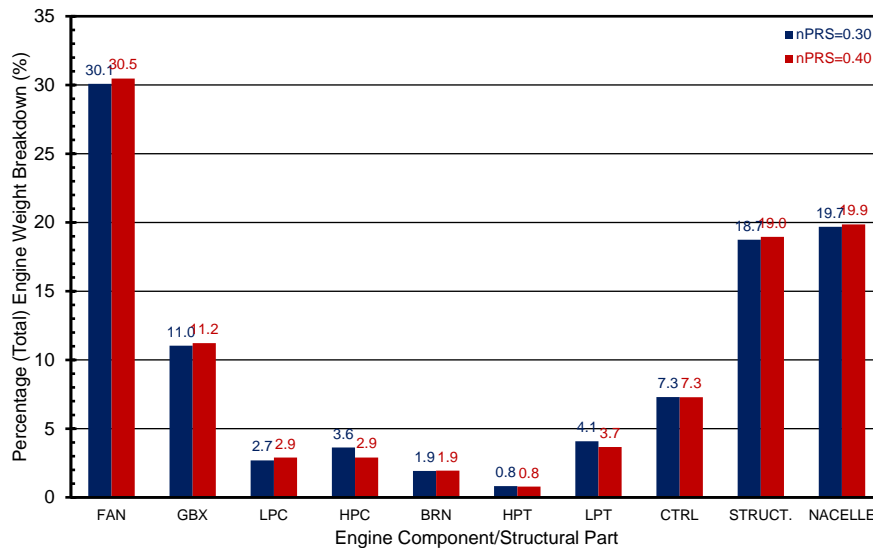


Figure 9.12: Percentage engine weight breakdown for different pressure ratio splits.

Table 9.12: Physical engine weight breakdown for different pressure ratio splits

Component/Part	Weight (kg)	
	$n_{PRS} = 0.30$	$n_{PRS} = 0.40$
Fan	871.0	871.1
Gearbox	319.5	3201.0
LPC	78.1	82.9
HPC	105.0	83.1
Burner	55.7	55.7
HPT	23.8	22.6
LPT	118.2	105.0
Ducts	44.5	44.7
Frames	417.6	416.0
Shafts	80.8	81.1
Control & accessories	211.4	208.3
Bare engine	2325.5	2291.4
Nacelle	569.8	567.7

The effect of the different n_{PRS} values on the engine gas-path can be seen in Figure 9.13, where the disks are also shown. The disks were designed according to the methodologies presented in Chapter 4 for the default RDO calculation inputs. Apart from the HPT disks which were designed considering thermal effects, all other disks were designed without taking into account heat-transfer effects and with material properties calculated at constant room temperature (20 °C). For the fan, a ring-type disk was considered, for the LP and HP compressors the disks were assumed to be of the web-type, for the HPT the disks were assumed to be of the hyperbolic-type and, finally, for the LPT the disks were set to the web-type. The S-duct which connects the

LPC to the HPC was designed for a diameter-to-length ratio equal to 0.63 and a tip shape coefficient equal to -0.22 (see Chapter 4).

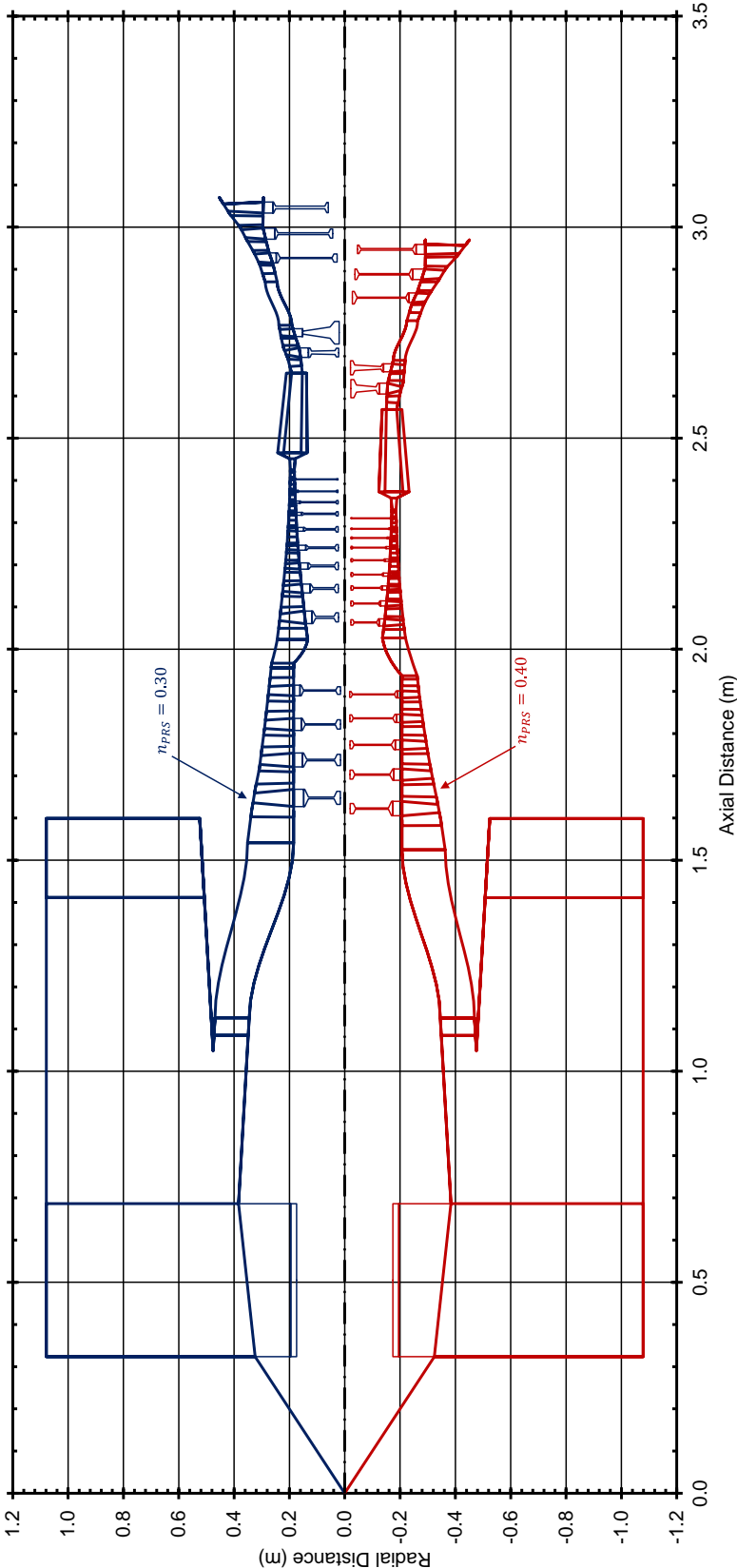


Figure 9.13: Engine gas-path meridional view for different pressure ratio splits.

From Figure 9.13, we can see that the $n_{PRS} = 0.40$ case produces an engine which has slightly smaller (axial) length than that for the $n_{PRS} = 0.30$ design case (about 10 cm), although the LPC compressor has one additional stage (5 compared to 4). This difference is mainly due to the length difference between the HPC components (~ 10 cm), where the HPC for the $n_{PRS} = 0.30$ case is lengthier than that for the $n_{PRS} = 0.40$ case. This result is qualitatively in agreement with the results obtained in Chapter 8. Note that, this difference in length not only leads to a slightly lighter nacelle (see Table 9.12), but also to a smaller engine drag for the same fan diameter⁶⁸.

The $n_{PRS} = 0.40$ case produces an engine design with lower specific fuel consumption at cruise conditions than the $n_{PRS} = 0.30$ one. This, of course, is due to slightly better engine overall efficiency (the product of thermal and propulsive efficiencies) which has a value of about 38.5% compared to $\sim 38.3\%$ (for $n_{PRS} = 0.30$). This difference in *SFC* is mainly responsible for the difference in block fuel between the $n_{PRS} = 0.30$ and 0.40 cases since, as we can see from Figure 9.9, cruise makes up for almost half the flight duration (~ 47 minutes). Figure 9.14 shows the fuel flow in terms of flight time for the different pressure ratio split cases (in the same graph the flight altitude variation with time is also given for reference). From Figure 9.14, the $n_{PRS} = 0.40$ presents slightly better fuel consumption than $n_{PRS} = 0.30$ in all mission segments. Because, as already explained, the total fuel burn is obtained by integrating in time the fuel flow rate, the point differences shown in Figure 9.14 lead to a total difference of 23.1 kg in fuel consumption over the entire flight envelope.

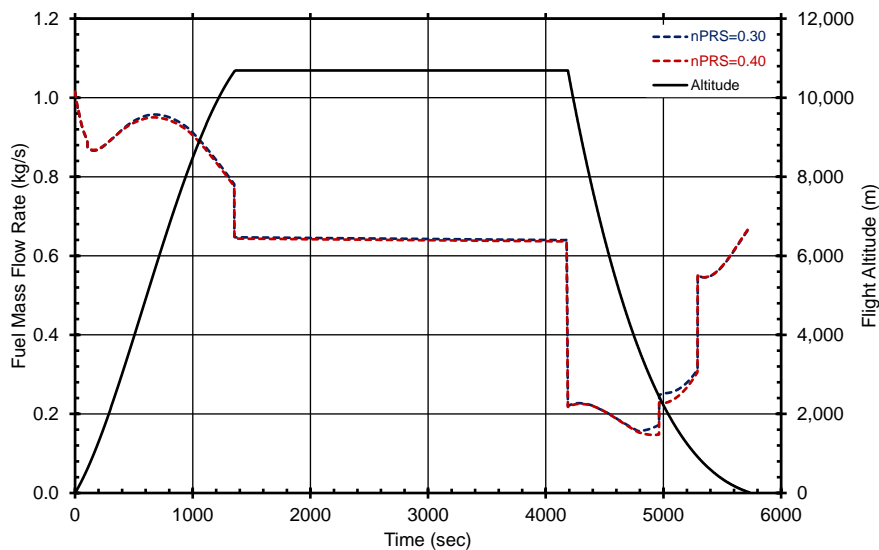


Figure 9.14: Fuel flow rate versus flight time for different pressure ratio splits.

Regarding the HPC performance at low power conditions (GIDLE), from Table 9.7 we see that $n_{PRS} = 0.30$ shows a slightly better surge margin than the 0.40 case by about 0.27% (absolute). For both pressure ratio split cases, the available surge margin is considered sufficient ($>15\%$) for acceleration maneuvers from low power settings. Also, from Figure 9.15 which presents the *RLP* [defined in Eq. (6.147)] and incidence

⁶⁸As we saw in Chapter 5, the engine nacelle is modelled as a cylinder.

angle variations in terms of the blade row number, we see that for both pressure ratio splits it is the first stage that governs the HPC surge. This result is qualitatively inline with what we would expect since, at low compressor speeds, it is always the first compressor stages that govern surge [see Saravanamuttoo et al. (2017)]. More specifically, we can see that in both cases it is the 3rd row (the stator of the 1st stage) that presents both the maximum *RLP* value [the actual pressure rise is ~ 1.6 times greater than the maximum (theoretical) one without the row stalling] and the higher incidence angle. Note that, the 1st stage also bears, overall, the higher pressure losses.

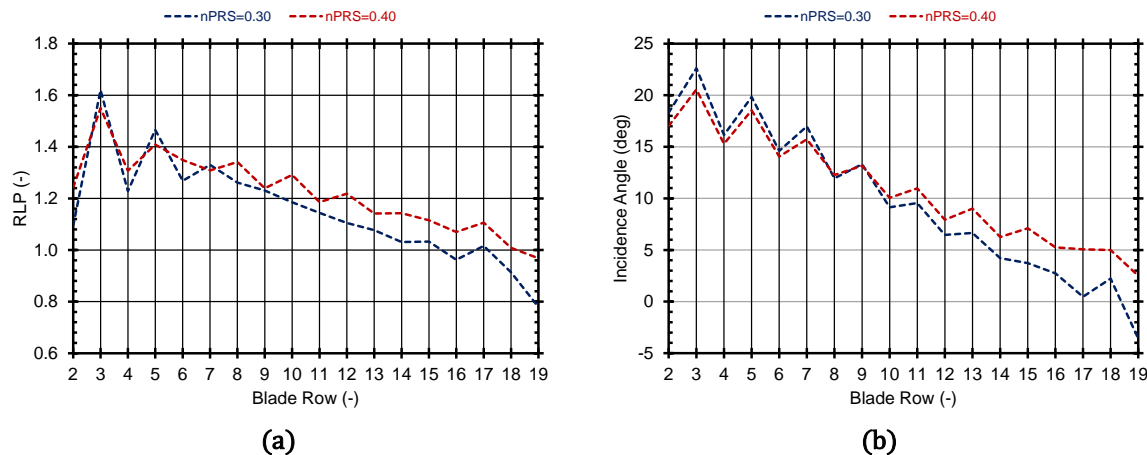


Figure 9.15: HPC blade (a) relative loading parameter and (b) incidence angle variations with blade row number for different pressure ratio splits at GIDLE conditions.

9.6 Summary and Discussion

The developed design workflow presented in Section 2.3 was exploited to conduct trade-off studies at engine level. A geared UHBR turbofan engine was considered for a short-range aircraft mission. The objective of the studies was the minimization of the engine block fuel over the entire flight mission, while maximizing the HPC surge margin at ground-idle conditions. Similarly to studies presented in Chapter 8, the same two (2) values of the pressure ratio split parameter were considered (0.30 and 0.40).

Although the conclusions drawn from the presented studies cannot be generalized due to the specific inputs and assumptions used when setting-up the calculation case, the following can be noted. The 0.40 pressure ratio split case seems to produce geared UHBR turbofans which have lower weight, smaller length (and, therefore, drag), and lower fuel consumption. Although the HPC surge margin at GIDLE conditions is somewhat smaller than the 0.30 case, it is still considered sufficient ($>15\%$). However, it is worth noting that the 0.40 case is of current industrial interest and research efforts, since it seems to deal with most of the design concerns imposed by the high overall pressure ratios envisaged for future UHBR engines.

Overall, the studies presented in this chapter showcased the capability of the developed system of tools to conduct trade-off studies and to identify the relative influence of various parameters on the design of future aircraft gas turbines.

10 Closure

10.1 Summary

The goal of this thesis was the development of an integrated workflow for the preliminary, multi-disciplinary design of aircraft gas turbines. To this end, tools appropriate for such calculations were developed. These comprise models of lower-fidelity (0D/1D) which, compared to higher-fidelity tools (2D or 3D) present a number of advantages when used in preliminary calculations: 1) they are fast, 2) require very few inputs that are typically available during a preliminary design calculation, 3) are relatively easy to use for setting-up a new calculation case, and 4) are easy to integrate in a design workflow.

In the above context, tools and models (0D/1D) were developed which are organized into the following four (4) libraries:

- **TURBO1D:** Includes models for the preliminary aerothermodynamic design of gas turbine components, which are appropriate for multi-point design studies. Models were developed for axial-flow fans, axial-flow, multi-stage compressors and turbines, and combustors.
- **GTMD:** Includes models and tools for the preliminary design and analysis of critical structural parts. Design and analysis models were developed for turbomachinery disks, rotating shafts, turbomachinery casings, and ducts.
- **GTWC:** Includes models for the preliminary weight estimation of gas turbine components and generic turbofan engines. Weight estimation models were developed for burners, axial-flow fans, axial-flow, multi-stage compressors and turbines, while a weight-estimation model for a generic 3-spool, geared turbofan engine with separate exhausts is also defined.
- **MLC:** Includes models and tools for the preliminary aerothermodynamic design (MLDC) and off-design performance estimation (MLAC) of multi-stage, axial-flow compressors with any type of blade rows (rotating, stationary, IGVs, of fixed or variable geometry) and with any number of gas bleeds.

More specifically, the components defined in the TURBO1D library for the aerothermodynamic design of turbomachinery components (fans, compressors, and

turbines), conduct the component design in a stage-by-stage manner. The code offers several options to the user for specifying the component mean-line shape. The stage performance (efficiency and pressure ratio) necessary for establishing the stage exit conditions and, in turn, the stage exit flow-annulus dimensions, can be established based on loss or semi-empirical methods (e.g., Smith-type charts for turbines), among other options. Finally, the components for the design of fans, compressors, and turbines, were validated using as reference the respective components of NASA's energy efficient engine (E³). The validations showed that the developed components can reproduce both the meridional gas-path geometry and the performance of real machines.

The methods and tools defined in the GTMDC library are used for the mechanical design and analysis of critical structural parts, such as shafts and disks. The structural model for the shafts takes into account steady-state loads due to torque, pressure and centrifugal forces. The model used for estimating the mechanical stresses in disks takes into account steady-state loads due to temperature gradients (thermal stresses), centrifugal, and body forces. Both models were validated both qualitatively and quantitatively against a higher-fidelity 3D FEA tool, using the NASA/GE E³ HPC as reference as far as the necessary geometry and performance inputs required. The comparisons showed that the developed tools can reproduce the physical trends of the mechanical stresses in real-engine structural components. A tool for the optimization of the disk geometry aiming at minimum weight while satisfying a number of geometry and stress constraints (RDO) was also programmed in the GTMDC library. The tool's performance was verified by considering different re-design test cases, using as reference the disks of the NASA/GE E³ HPC. Finally, simplified algebraic models were also programmed for the design of ducts and turbomachinery casings.

The GTWC library defines models and methods for estimating the weight of gas turbine engines. More specifically, two (2) approaches were programmed both belonging to the component-based (CB) class of methods. The first one is a semi-empirical method (CB-SE) which estimates the weight of gas turbine components based on simplified algebraic expressions that correlate the component weight to basic performance (e.g., rotational speed) and geometry (e.g., hub-to-tip ratios) inputs. The second one is an "analytical" method (CB-GM) that estimates the weight of gas turbine components based on the geometry that has been produced by the aerothermodynamic and mechanical design tools (TURBO1D, MLDC, and GTMDC) and the material selection specified by the user. Both methods were validated qualitatively using as reference a generic 2-spool high bypass ratio turbofan engine with separate exhausts. The CB-GM method was also validated quantitatively using as reference the CFM56-5A turbofan engine. The validations showed that both methods can produce the correct weight trends, while the CB-GM method can also give precise weight predictions.

In the MLC libraries, components for the aerothermodynamic design (MLDC) and analysis (MLAC) of axial-flow, multi-stage compressors are included. The components defined in these libraries conduct the compressor design and analysis in a row-by-row manner, where the blade row performance is established in terms of loss and deviation models. The user can select from several available loss and deviation correlations, can introduce customized models, or can calibrate the existing ones to match an existing performance. The MLC components can also perform calculations considering constant

or variable gas properties. A novel aspect of the MLC codes is the way that they model and predict the stall and choke flow conditions. The MLDC and MLAC components use the same fluid models, thermodynamic functions, numerical solvers, and building blocks (BRM and IVM) for modelling the performance of blade rows. Thus, the compressor geometry produced by the MLDC component can be used as an input by the MLAC components to produce consistent performance maps, which can then replace the generic maps in engine cycle calculations. Finally, the components defined in the MLC libraries were validated and their utility verified using as reference publicly available data for NASA's multi-stage compressors. From the validations, it was shown that the MLDC component for the aerothermodynamic design of compressors can reproduce the geometry, both at component and at blade row level, of real machines. Similarly, the MLAC component(s) for the generation of performance maps can reproduce the performance of existing compressors in the whole operating range, from stall to choke, and beyond choke conditions.

All the above tools were developed under the same, user-friendly, coding, modelling, and simulation environment, namely PROOSIS. Then, they were combined under PROOSIS to form an integrated system which can be used for the preliminary, multi-disciplinary design of aircraft gas turbines. The system allows the efficient preliminary design and assessment of new engine concepts, where the user can easily define any combination of design metrics and constraints, at any operating point, and for any of the involved design and analysis disciplines. The capabilities, fidelity, efficiency, and resolution of the developed system and of the tools comprising it were demonstrated through trade-off optimization studies at component and at engine level. For this reason, a geared UHBR turbofan engine for a short-range aircraft mission was considered. The design studies were formulated considering different objectives and were conducted for two (2) different values of the engine overall pressure ratio split between the low- and high-pressure compressors (0.30 and 0.40), which are of current industrial interest.

10.2 Conclusions

The conclusions drawn from the present PhD thesis are summarized below:

- The development of a system of tools under a single coding, modelling, and simulation environment is achievable. This way, a number of advantages are ensured. These include: 1) easy code maintainability, 2) easy extendibility, 3) consistent use of physical models and numerical solvers between the different design and analysis modules, and 4) transparent integration and 5) cooperation between the different design and analysis modules, among other. Furthermore, the use of an environment like the one offered by PROOSIS (see Chapter 2), allows any engine model to be easily defined as well as any combination of multi-disciplinary and multi-fidelity calculations to be performed upon it.

- The components (the methodologies and models they employ) for the aerothermodynamic design of fan, compressor, and turbine components can estimate accurately the efficiency of real turbomachinery components which have been through almost all the stages of the development course up to actual manufacturing and testing.
- The components (the methodologies and models they employ) for the aerothermodynamic design of fan, compressor, and turbine components can reproduce the geometry of real machines, both at component and at blade row level. This, in turn, means that the produced geometry outputs can be used as inputs later in the design process (i.e., in the detail design stage), thus minimizing the iterations required between the preliminary and detail design stages.
- The design methods (and the models they employ) for shafts and disks can reproduce the geometry of real gas turbine shafts and disks. That is, the produced dimensions can be used as inputs for the detail design stages, thus minimizing the iterations required between them and the preliminary design stage. Furthermore, the accurate estimation of the geometry (and, thus, material volume) of critical structural components can offer the designer a sufficiently accurate first glance of a machine's production and maintenance costs.
- The analytical or approximate thermal models for estimating the radial temperature profiles in disks can be replaced by a more "detailed" one (D-STM) that takes into account the radial thickness variation of the disk. Although this model needs to be solved numerically, this is accomplished at the same expense of computational time as the simplified thermal models, thus making their use obsolete. Furthermore, its use leads to vastly more accurate predictions for the mechanical stresses developed in disks compared to the simplified ones, which are commonly used in other platforms for the preliminary design of gas turbine engines.
- The design of turbomachinery disks aiming at minimum weight can be formulated as an equivalent stress maximization problem (RDO). This approach leaves as the only constraints to be fulfilled constraints regarding the disk dimensions alone and, thus, allows the production of feasible initial solutions through proper geometry initialization. This, in turn, allows the use of non- evolutionary techniques which are faster when the design of multi-stage machines, or the design of gas turbine engines comprising many spools, is considered.
- Although the component-based, semi-empirical (CB-SE) models for estimating the weight of gas turbine engines have poorer accuracy than the component-based, analytical (CB-GM) ones, they present consistent physical behavior at the engine level and, therefore, are still of great use in preliminary design calculations where, sometimes, the trends are more important than absolute numbers.
- The component-based, analytical (CB-GM) weight estimation models can successfully estimate the weight of high- and ultra-high bypass ratio turbofan engines with separate exhausts (within the $\pm 10\%$ margin used by other similar

tools). Therefore, the designer can draw a sufficiently accurate first conclusion in the engine's production and operational costs.

- The components (the methodologies and models they employ) for the off-design performance prediction of axial-flow, multi-stage compressors can reproduce the performance of real compressor configurations in the whole operating range: from stall to choke, and beyond choke conditions. The produced maps can, therefore, replace the generic maps used in engine cycle calculations which do not correspond to the computed (by the design) compressor geometry, and which require scaling. Thus, performance predictions can be obtained which are consistent with the computed designs. Furthermore, all these are achieved in an automatic way due to the approach used to establish the choke and stall operation limits.
- Overall, it was shown that the lower-fidelity (1D) design and analysis tools developed in this thesis can produce accurate 2D geometry information and performance values, which can then be used in the later stages of the development course of a new gas turbine engine. This, in turn, can minimize the iterations required between the different design stages. Furthermore, this is achieved with reduced computational effort (time, number of inputs required, and user effort to set-up a new calculation case) compared to that required by higher-fidelity (2D/3D) tools.
- The developed design workflow can be used to conduct trade-off optimization studies of novel aircraft engine configurations (both at component and at engine level). The capabilities offered by the developed tools were proven by conducting design studies on a geared UHBR turbofan engine. The results showcased that the developed tool allows the designer/analyst to assess the potential of a new engine concept in terms of different combinations of metrics and constraints.

Finally, for the specific geared UHBR turbofan architecture and for the specific inputs and assumptions used when setting-up the engine design case, it was found that:

- The 0.40 pressure ratio split case seems to produce compression systems (LPC + S-duct + HPC) which are lighter and have smaller length compared to the 0.30 case, while offering higher component efficiencies and higher surge margin for the HPC at low power conditions.
- At aircraft mission level, the 0.40 pressure ratio split case seems to produce geared UHBR turbofans which have lower weight, smaller length (and, therefore drag), and lower fuel consumption. Although the HPC surge margin at low power conditions is somewhat smaller than the 0.30 case, it is still considered sufficient (>15%).

The above conclusions regarding the engine design are not to be generalized, since they depend on the specific inputs and assumptions considered. It is worth noting, however, that the 0.40 case is of current industrial interest and research efforts, since it seems to deal with most of the design concerns imposed by the high overall pressure ratios envisaged for future UHBR engines.

10.3 Novel Contributions

The novel contributions of this PhD thesis are summarized below:

- The system and the individual tools described in the present thesis were developed under the same coding, modelling, and simulation environment. For this reason, PROOSIS was used which is the tool used by the European gas turbine industry. Both the development of a workflow for the preliminary design of gas turbine engines under the same environment, as well as the use of PROOSIS to do so, are reported for the first time in the industrial and research practice.
- The models for the aerothermodynamic design of compressors and turbines defined in the TURBO1D library conduct the aerothermodynamic design in a single step, that is, no iterations are required on the component efficiencies between the thermodynamic analysis and aerodynamic design calculations.
- The numerical model used for estimating the thermal stresses in rotating disks (Numerical D-STM), is proposed and implemented for the first time in the present thesis.
- The formulation used for the design of turbomachinery disks (RDO) is proposed and its efficiency is assessed for the first time in the present thesis.
- The modelling of the flow choke in axial-flow, multi-stage compressors used in the MLAC and MLDC components, is novel and is described for the first time in the present thesis.
- Similarly, the modelling of the flow stall in axial-flow, multi-stage compressors is novel and is described for the first time in the present thesis.
- To the authors' knowledge, the inclusion of constraints regarding the stall and choke operation so that the computed compressor design point is meaningful (see Chapters 8 and 9), is presented for the first time in this thesis.
- To the author's knowledge, the influence of the pressure ratio split between the low- and high-pressure compressors of a geared UHBR turbofan engine considering simultaneously the engine fuel burn and HPC stability (surge margin) at low power conditions (ground idle), is studied for the first time in the present thesis.

10.4 List of Publications and Technical Reports

The aforementioned work led to a number of publications, newsletters, and technical reports, which are summarized below.

- The novel contributions of the present thesis are verified through five (5) publications in international scientific peer-reviewed journals and conferences:
 1. A. Alexiou, N. Aretakis, I. Roumeliotis, **I. Koliass**, and K. Mathioudakis. Performance Modelling of an Ultra-High Bypass Ratio Geared Turbofan.

Proceedings of the 23rd ISABE Conference, Manchester, UK, 3-8 September 2017. ISABE-2017-22512.

2. **I. Koliás**, A. Alexiou, N. Aretakis, and K. Mathioudakis. Direct Integration of Axial Turbomachinery Preliminary Aerodynamic Design Calculations in Engine Performance Component Models. Proceedings of the ASME Turbo Expo 2018, Oslo, Norway, 11-15 June 2018. GT2018-76494. doi: 10.1115/GT2018-76494.
3. A. Alexiou, N. Aretakis, **I. Koliás**, and K. Mathioudakis. Novel Aero-Engine Multi-Disciplinary Preliminary Design Optimization Framework Accounting for Dynamic System Operation and Aircraft Mission Performance. Aerospace 2021, 8(49), 19 pages. doi: 10.3390/aerospace8020049.
4. **I. Koliás**, A. Alexiou, N. Aretakis, and K. Mathioudakis. Axial Compressor Mean-Line Analysis: Chocking Modelling and Fully-Coupled Integration in Engine Performance Simulations. Int. J. Turbomach. Propuls. Power 2021, 6(4), 23 pages. doi: 10.3390/ijtp6010004.
5. **I. Koliás**, N. Aretakis, A. Alexiou, and K. Mathioudakis. A Tool for the Design of Turbomachinery Disks for an Aero-Engine Preliminary Design Framework. Aerospace 2023, 10(5), 17 pages. doi: 10.3390/aerospace10050460.

➤ The value of the tools developed in terms of the underlying software development is verified by the following newsletter publication:

1. **I. Koliás** and A. Alexiou. Axial Turbomachinery Performance-Aerodynamics Integration in PROOSIS. EcosimPro/PROOSIS Newsletter, No. 14, March 2018.

➤ Finally, the industrial worth and applicability of the developed tools is verified by the following technical reports produced in the context of European projects:

1. A. Alexiou, **I. Koliás**, N. Aretakis, and K. Mathioudakis. Integrated Preliminary Sizing and Performance Prediction Models for a Y2025 UBGF Engine Configuration. Project DEMOS: Developing Advanced Engine Multi-Disciplinary Optimisation Simulations (Grant Agreement ID: 686340). Deliverable 3.7, Issue 1.0, 2017.
2. A. Alexiou, **I. Koliás**, N. Aretakis, and K. Mathioudakis. Compressor Stability Studies at Component Level. Project UTOPEA: UHBR Engine Technology for Aircraft Operation, Emissions and Economic Assessments (Grant Agreement ID: 886840). Deliverable 1.1, Issue 1.0, 2021.
3. A. Alexiou, **I. Koliás**, N. Aretakis, and K. Mathioudakis. Compressor Stability Studies at Engine Level. Project UTOPEA: UHBR Engine Technology for Aircraft Operation, Emissions and Economic Assessments (Grant Agreement ID: 886840). Deliverable 1.2, Issue 1.1, 2022.
4. A. Alexiou, **I. Koliás**, N. Aretakis, and K. Mathioudakis. Idle Performance Studies. Project UTOPEA: UHBR Engine Technology for Aircraft Operation, Emissions and Economic Assessments (Grant Agreement ID: 886840). Deliverable 1.3, Issue 1.0, 2022.

10.5 Suggestions for Future Work

A major part of the work presented in this PhD thesis was carried out in the context of LTT/NTUA's collaboration with European gas turbine and aircraft industries. Hopefully, the work presented in this text will be extended and further developed in future projects undertaken by LTT/NTUA. Some ongoing developments and suggestions concerning future work are given in the following list:

- The material database described in Chapter 4 should be enriched with materials of current and future interest in gas turbine applications (e.g., CMCs), should their (mechanical and thermal) properties become publicly available.
- The default loss and deviation models used in the aerothermodynamic design and analysis components (Chapters 3, 6, and 7) could be replaced by newer and more accurate ones established in the context of experimental and/or computational (CFD) calculations. These models could, additionally, correlate the blade performance only to inlet conditions (such as the relative Mach number and flow angle) instead of inlet and outlet conditions like the current ones do. This way, iterations at row level for establishing the row's outlet conditions could be avoided, thus leading to faster calculations.
- It is recommended to study how the variations of the individual calibration scalars introduced in the default loss and deviation correlations in Chapter 6 affect the behavior of the respective models, in relation to publicly available data (experimental or computational). This way, possible physical trends could be identified which, in turn, could be used in the development of correlations for the scalars themselves. This approach could, eventually, improve the accuracy of the default loss and deviation models used currently in the MLC libraries.
- The models described in Chapter 5 for estimating the weight of individual gas turbine components (fans, compressors, burners, turbines) should be validated quantitatively. Due to the disclosure policies followed by OEMs, information for such components is unavailable. Therefore, the validation could be done using publicly available 3D CAD engine cutaways.
- A module for the economic assessment (production, operation, and maintenance costs) should be developed and integrated into the developed system of tools.
- Due to the continuous environmental concerns regarding all new and future engines, the developed system of tools should be extended by including modules for emissions, noise, and carbon footprint estimations.
- Disk lifing (in terms of LCF) should be part of the disk optimization procedure described in Chapter 4.
- Models and methods should be developed for the aerothermodynamic design and off-design performance prediction of axial-flow, multi-stage turbines, similar in logic and structure to the ones presented in Chapters 6 and 7 for compressors. This way, the turbine design and off-design performance prediction (map generation) could be done in a consistent way, while the produced turbine maps could replace the generic ones in the engine models.

- With the increasing interest in new fuel solutions (e.g., hydrogen and biofuels or sustainable alternative fuels), a more detailed model for the aerothermodynamic design and analysis of combustors should be developed. The current model developed and used in this work only conducts the gas-path visualization based on crude inputs used in the relevant bibliography, but does not conduct the burner design based on models for the combustion and the losses of the various burner parts.
- Regarding the trade-off studies conducted in Chapter 8, the design of the compression system should be considered as a whole (LPC + S-duct + HPC + diffuser).
- For the trade-off studies conducted in Chapter 9, the engine design and the design of the compressors should be conducted at the same level, while the design of the turbines should also be taken into account (assuming that appropriate models for their design and off-design performance prediction have been developed and integrated into the existing system of tools).

A Turbomachinery Design Guidelines

The present appendix summarizes parameter values for the preliminary aerothermodynamic and mechanical design of turbomachinery components. These values have been collected from relevant turbomachinery texts and technical reports and handbooks on the design of gas turbine engines.

Table A.1: Design guidelines for axial-flow fan components

Parameter	Value		Reference	Remarks
	Min	Max		
$U_{t,in}$		500 m/s	Walsh et al. (2004)	
	427 m/s	457 m/s	Mattingly (2005)	
\bar{U}_h		180 m/s	Walsh et al. (2004)	
HTR_{in}	0.30	0.40	Walsh et al. (2004)	
	0.40	0.50	Fishbach (1983)	
AR_x	2.0	2.5	Walsh et al. (2004)	Fans without clappers
	2.5	3.5	Walsh et al. (2004)	Fans with clappers
	2.0	2.0	Walsh et al. (2004)	Stators with structural duty
	3.0	5.0	Fishbach (1983)	
σ	1.0	1.5	Fishbach (1983)	
		0.55	Mattingly (2005)	
DF		0.6	Walsh et al. (2004)	@ Blade mean
		0.4	Walsh et al. (2004)	@ Blade tip
M_{in}	0.55	0.65	Walsh et al. (2004)	
	0.50	0.60	Fishbach (1983)	
M_{out}	0.30-0.35	0.40	Walsh et al. (2004)	@ Core inlet
	0.45	0.55	Fishbach (1983)	@ Core inlet
$M_{r,t,in}$	1.40	1.80	Walsh et al. (2004)	

Table A.2: Design guidelines for axial-flow low-pressure compressors

Parameter	Value		Reference	Remarks
	Min	Max		
$U_{t,in}$		500 m/s	Walsh et al. (2004)	
	427 m/s	457 m/s	Mattingly (2005)	
HTR_{in}	0.65		Walsh et al. (2004)	
	0.40	0.50	Fishbach (1983)	
M_{in}	0.45	0.60	Fishbach (1983)	
	0.48	0.60	Mattingly (2005)	
	0.40	0.60	Walsh et al. (2004)	
M_{out}	0.45	0.55	Walsh et al. (2004)	
		0.35	Fishbach (1983)	
$M_{r,t,in}$	0.90	1.30	Walsh et al. (2004)	
	1.5	3.5	Walsh et al. (2004)	
AR_x	3.0	5.0	Fishbach (1983)	@ 1 st stage
	2.0	3.0	Fishbach (1983)	@ N th stage
σ	1.0	1.5	Fishbach (1983)	
		0.55	Mattingly (2005)	
DF		0.60	Walsh et al. (2004)	@ Blade mean
		0.40	Walsh et al. (2004)	@ Blade tip

Table A.3: Design guidelines for axial-flow high-pressure compressors

Parameter	Value		Reference	Remarks
	Min	Max		
$U_{t,in}$		400 m/s	Walsh et al. (2004)	
	350 m/s	460 m/s	Mattingly (2005)	
HTR_{in}	0.65		Walsh et al. (2004)	
	0.60	0.80	Fishbach (1983)	
	0.60	0.75	Mattingly (2005)	
HTR_{out}	0.90	0.92	Mattingly (2005)	
		0.92	Walsh et al. (2004)	
M_{in}	0.40	0.50	Fishbach (1983)	
	0.48	0.60	Mattingly (2005)	
	0.40	0.60	Walsh et al. (2004)	
M_{out}	0.20	0.30	Fishbach (1983)	
		0.35	Walsh et al. (2004)	
$M_{r,t,in}$	0.90	1.30	Walsh et al. (2004)	
	1.5	3.5	Walsh et al. (2004)	
AR_x	2.0	5.0	Fishbach (1983)	@ 1 st stage
	1.0	2.0	Fishbach (1983)	@ N th stage

Table A.3 (cont.): Design guidelines for axial-flow high-pressure compressors

Parameter	Value		Reference	Remarks
	Min	Max		
σ	1.0	1.5	Fishbach (1983)	
DF		0.55	Mattingly (2005)	
		0.60	Walsh et al. (2004)	@ Blade mean
		0.40	Walsh et al. (2004)	@ Blade tip

Table A.4: Design guidelines for axial-flow low-pressure turbines

Parameter	Value		Reference	Remarks
	Min	Max		
AN_{mech}^2		$50 \cdot 10^6$ $m^2 \cdot rpm^2$	Walsh et al. (2004)	@ N^{th} stage
HTR_{in}	0.35	0.50	Mattingly (2005)	
	0.50	0.85	Walsh et al. (2004)	
M_{in}	0.40	0.50	Fishbach (1983)	
		0.20	Walsh et al. (2004)	
M_{out}	0.55	0.60	Fishbach (1983)	
	0.40	0.60	Mattingly (2005)	
	0.30	0.55	Walsh et al. (2004)	
$M_{r,h,in}$		0.70	Walsh et al. (2004)	
$U_{h,out}$		350 m/s	Walsh et al. (2004)	
σ	1.0	1.5	Fishbach (1983)	
AR	2.0	3.0	Fishbach (1983)	@ 1 st stage
	4.0	6.0	Fishbach (1983)	@ N^{th} stage
AR_x		6.0	Walsh et al. (2004)	
	2.5	3.5	Walsh et al. (2004)	

Table A.5: Design guidelines for axial-flow high-pressure turbines

Parameter	Value		Reference	Remarks
	Min	Max		
AN_{mech}^2	$20 \cdot 10^6$ $m^2 \cdot rpm^2$	$50 \cdot 10^6$ $m^2 \cdot rpm^2$	Walsh et al. (2004)	@ N^{th} stage
	$40 \cdot 10^6$ $m^2 \cdot rpm^2$	$50 \cdot 10^6$ $m^2 \cdot rpm^2$	Mattingly (2005)	@ N^{th} stage
HTR_{in}	0.50	0.85	Walsh et al. (2004)	
M_{in}	0.30	0.40	Fishbach (1983)	
		0.20	Walsh et al. (2004)	

Table A.5 (cont.): Design guidelines for axial-flow high-pressure turbines

Parameter	Value		Reference	Remarks
	Min	Max		
M_{out}	0.30	0.55	Walsh et al. (2004)	
	0.40	0.50	Mattingly (2005)	
	0.45	0.50	Fishbach (1983)	
$M_{r,h,in}$		0.70	Walsh et al.(2004)	
$U_{h,out}$		400 m/s	Walsh et al.(2004)	
σ	1.0	1.5	Fishbach (1983)	
AR	1.0	2.0	Fishbach (1983)	@ 1 st stage
	1.0	2.0	Fishbach (1983)	@ N th stage
AR_x	2.5	3.5	Walsh et al. (2004)	

B Polytropic Efficiency for Consistent Preliminary Design

Apart from the aerodynamic design presented in Chapter 3 for establishing the overall performance (isentropic and polytropic efficiencies) of a component, another method used in the present thesis is the one presented by Samuelsson et al. (2015) for consistent preliminary design calculations. Samuelsson et al., following the work conducted by Grieb (2004), developed overall correlations for estimating the polytropic efficiency of turbomachinery components in the form:

$$\eta_p = \eta_{p,ref} + (\Delta\eta_p)_{EIS} + (\Delta\eta_p)_{RNI} + (\Delta\eta_p)_{wc} \quad (B.1)$$

with $\eta_{p,ref}$ being the nominal efficiency for a reference component with characteristics as shown in Table B.1.

Table B.1: Reference component characteristics for Samuelsson et al. (2015) model

Component Characteristic	Reference Value
Entry Into Service (EIS)	1995
Size (Corrected Mass Flow)	70 kg/s
Reynolds Number Index (RNI)	1.0

According to Eq. (B.1), the component polytropic efficiency, η_p , is obtained by correcting the reference polytropic efficiency, $\eta_{p,ref}$, for EIS, $(\Delta\eta_p)_{EIS}$, size, $(\Delta\eta_p)_{wc}$, and Reynolds number $(\Delta\eta_p)_{RNI}$, effects. Next, the equations for calculating the terms appearing in Eq. (B.1) are presented.

For fan components, the reference polytropic efficiency is correlated with the fan outer pressure ratio, p_{13}^0/p_2^0 , and is given by:

$$\eta_{p,ref} = \eta_{A\infty} + \frac{A_1}{1 + e^{-A_2 \left(\frac{p_{13}^0}{p_2^0} - A_3 \right)}} \quad (B.2)$$

For IPC components, $\eta_{p,ref}$ is correlated with the average stage loading, $\bar{\psi}$, and this correlation is given in the form:

$$\eta_{p,ref} = \eta_{A\infty} + \sum_{i=1}^{i=4} A_i (\bar{\psi} - A)^i \quad (\text{B.3})$$

For HPC, HPT, and LPT components, $\eta_{p,ref}$ is correlated with $\bar{\psi}$ as:

$$\eta_{p,ref} = \eta_{A\infty} - \frac{A_1}{2} + \frac{A_1}{1 + e^{-A_2(\bar{\psi}-A_3)}} \quad (\text{B.4})$$

In Eqs (B.3) and (B.4), the average stage loading is defined as:

$$\bar{\psi} = \frac{|h_{out}^0 - h_{in}^0|}{\sum_{j=1}^{j=N_{stg}} U_j^2}$$

The correction for EIS, $(\Delta\eta_p)_{EIS}$, is given for all components by the following equations:

$$(\Delta\eta_p)_{EIS} = \eta_{p,EIS} - \eta_{p,1995} \quad (\text{B.5})$$

$$\eta_{p,EIS} = \eta_{B\infty} - B_1 \left[1 - \frac{1}{1 + e^{-B_2(EIS-B_3)}} \right] \quad (\text{B.6})$$

The correction for Reynolds number, $(\Delta\eta_p)_{RNI}$, is given for all components by:

$$(\Delta\eta_p)_{RNI} = \begin{cases} C_1 \left(1 - \frac{1}{RNI^{C_2}} \right), & RNI \leq 1 \\ 0, & RNI > 1 \end{cases} \quad (\text{B.7})$$

The correction for component size, $(\Delta\eta_p)_{wc}$, is given for all components by:

$$(\Delta\eta_p)_{wc} = \begin{cases} D_1 \left[1 - \left(\frac{70}{\dot{m}_{c,in}} \right)^{D_2} \right], & \dot{m}_{c,in} \leq 70 \text{ kg/s} \\ 0, & \dot{m}_{c,in} > 70 \text{ kg/s} \end{cases} \quad (\text{B.8})$$

In Eqs (B.8) and (B.7), the corrected mass flow, $\dot{m}_{c,in}$, and the Reynolds number index, RNI , are defined, respectively, as:

$$\dot{m}_{c,in} = \dot{m}_{in} \frac{\sqrt{T_{in}^0/T_{ref}}}{p_{in}^0/p_{ref}}$$

and

$$RNI = \frac{p_{in}^0/p_{ref}}{\sqrt{T_{in}^0/T_{ref}}} \frac{\mu_{ref}}{\mu_{in}^0}$$

where T_{ref} , p_{ref} , and μ_{ref} are the reference temperature, pressure, and dynamic viscosity, respectively, used to define the component maps.

The values of the coefficients appearing in Eqs (B.2)–(B.7) are given in Table B.2.

Table B.2: Correlation coefficients for Samuelsson et al. (2015) model

Coeff.	Fan	IPC	HPC	HPT	LPT
$\eta_{A\infty}$	0.95	0.92	0.95	0.97	0.98
A	-	0.65	-	-	-
A_1	-0.3989	0.01942	-0.90	-0.0427	-0.0629
A_2	3.0	-0.4896	0.2102	0.7053	0.6367
A_3	2.50	0	0.20	1.0	1.0
A_4	-	1.425	-	-	-
$\eta_{B\infty}$	0.97	0.96	0.96	0.97	0.98
B_1	0.26	0.14	0.14	0.20	0.14
B_2	0.0366	0.01317	0.007666	0.04925	0.03874
B_3	1952.4	1967.4	1940.2	1956.8	1956.8
C_1	0.095	0.095	0.095	0.055	0.055
C_2	0.14	0.12	0.10	0.18	0.18
D_1	0.095	0.095	0.095	0.055	0.055
D_2	0.063	0.063	0.063	0.236	0.236

C Annular Combustor Preliminary Sizing

C.1 Introduction

In the present appendix, a simplified methodology and the relevant equations employed for the preliminary sizing of single annular combustors are presented. The dimensions obtained from the sizing procedure can then be used for both the estimation of the weight of the combustor (given the material selection), and for visualizing the combustor meridional gas-path. The meridional view of a single annular combustor is illustrated in Figure C.1, where the various combustor sections and the relevant nomenclature are shown.

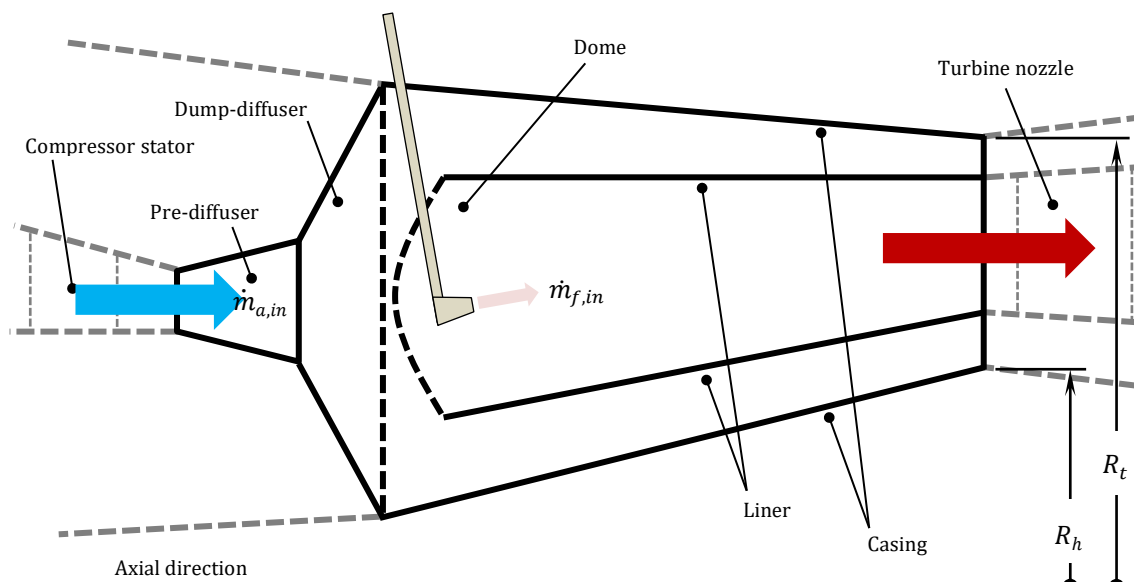


Figure C.1: Single annular combustor meridional view and nomenclature. The combustor inlet is assumed to coincide geometrically with the upstream compressor exit, while the combustor exit coincides geometrically with the downstream turbine inlet.

The sizing methodology and equations presented here were primarily adapted by Mohammad et al. (2009). Note here, that necessary inputs such as the air mass flow

($\dot{m}_{a.in}$), fuel mass flow ($\dot{m}_{f.in}$), and flow conditions at the combustor inlet (T_{in}^0, p_{in}^0) and outlet (T_{out}^0, p_{out}^0), are predetermined from the engine cycle calculation.

Note here, that a deep-dive into the design of modern gas turbine combustors was not in the scope of this thesis. Thus, more information about the configuration, operation, and design of gas turbine combustors can be found in dedicated textbooks as, e.g., by Mellor (1990) and Lefebvre et al. (2010).

C.2 Combustor Sizing

In a typical gas turbine burner, the air at the combustor inlet ($\dot{m}_{a.in}$) flows from the compressor exit and then is divided into two different streams: one through the combustor dome (\dot{m}_{CD}) and the other through the combustor passage (\dot{m}_{CP}). The air flowing through the dome is used 1) for atomizing the liquid fuel (\dot{m}_{CA}), 2) for creating a stabilizing swirling flow (\dot{m}_{CS}), and 3) for cooling the dome itself (\dot{m}_{CDC}). The flow through the passage serves three purposes: 1) provides cooling air to the combustor liner, 2) provides the necessary air for completing the combustion process in the secondary combustion region, and 3) achieves the required gas temperature at the combustor outlet [see Mohammad et al. (2009)].

The atomizing mass flow rate, \dot{m}_{CA} , is calculated by:

$$\dot{m}_{CA} = \text{AFR} \times \dot{m}_{f.in} \quad (\text{C.1})$$

where $\dot{m}_{f.in}$ is the injected fuel mass and AFR is a user-defined atomizing flow rate.

The dome cooling flow, \dot{m}_{CDC} , is calculated according to:

$$\dot{m}_{CDC} = \frac{\text{DCFR}[\%]}{100} \dot{m}_{a.in} \quad (\text{C.2})$$

where DCFR is a user-defined dome cooling flow rate.

The air mass flow required for stabilizing the combustion reaction, \dot{m}_{CS} , is given by the following equation:

$$\dot{m}_{CS} = \frac{\dot{m}_{f.in}}{\phi_p \text{FAR}_{th}} - \dot{m}_{CA} - \dot{m}_{CDC} \quad (\text{C.3})$$

where FAR_{th} is the theoretical (stoichiometric) fuel-to-air ratio assuming kerosene ($\text{FAR}_{th} \cong 0.067$), and ϕ_p is the combustor primary zone equivalence ratio.

From the above, the mass flow through the dome is then determined using the continuity equation:

$$\dot{m}_{CD} = \dot{m}_{CA} + \dot{m}_{CDC} + \dot{m}_{CS} \quad (\text{C.4})$$

while the mass flow through the passage is obtained according to:

$$\dot{m}_{CP} = \dot{m}_{a.in} - \dot{m}_{CD} \quad (\text{C.5})$$

Having obtained the gas mass flow through the combustor dome and passage, the dome and passage heights can then be established. From mass continuity, the dome (A_{CD}) and passage (A_{CP}) cross-sectional areas are obtained by the following equations:

$$A_{CD} = \frac{\dot{m}_{CD}}{\rho_{in}^s V_{CD}} \quad (C.6)$$

$$A_{CP} = \frac{\dot{m}_{CP}}{\rho_{in}^s V_{CP}} \quad (C.7)$$

where ρ_{in}^s is the density of the air at the combustor inlet, estimated using the equation of state:

$$\rho_{in}^s = \frac{p_{in}^s}{R_g T_{in}^s}$$

with $R_g = 287 \text{ J/kg}\cdot\text{K}$, and p_{in}^s and T_{in}^s is the static pressure and static temperature at the combustor inlet, respectively. In Eqs (C.6) and (C.7), V_{CD} and V_{CP} is the gas velocity through the dome and through the passage, respectively, with V_{CD} and V_{CP} being user-specified inputs.

From A_{CD} and A_{CP} , a reference area (A_{ref}) can be estimated according to:

$$A_{ref} = A_{CD} + A_{CP} \quad (C.8)$$

From A_{ref} , a reference gas velocity (V_{ref}) is obtained from mass continuity according to:

$$V_{ref} = \frac{\dot{m}_{a,in}}{\rho_{in}^s A_{ref}} \quad (C.9)$$

The dome (h_{CD}) and passage (h_{CP}) heights are then obtained from:

$$h_{CD} = \frac{A_{CD}}{2\pi R_{m,in}} \quad (C.10)$$

$$h_{CP} = \frac{A_{ref}}{2\pi R_{m,in}} - h_{CD} \quad (C.11)$$

where $R_{m,in}$ is the mean radius at the combustor inlet, given by:

$$R_{m,in} = \frac{1}{2} (R_{h,in} + R_{t,in})$$

Next, the pre-diffuser (subscript “CPD”) and dump-diffuser (subscript “CDD”) dimensions are estimated. The pre-diffuser geometry and nomenclature are shown in Figure C.2. More information about the detailed design of combustor diffusers (taking into account losses and the maximum achievable pressure rise) can be found in Mohammad et al. (2009).

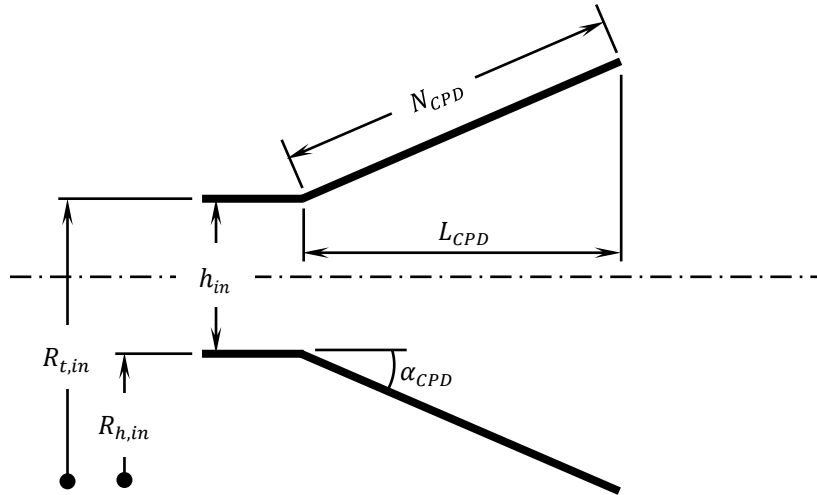


Figure C.2: Pre-diffuser geometry and nomenclature [adapted from Mohammad et al. (2009)].

First, the pre-diffuser length-to-width ratio is estimated for a user-defined diffuser aspect ratio (AR_{CPD})⁶⁹, for which no appreciable stall is obtained. This is estimated from experimental charts provided by Reneau et al. (1967), according to [see Mohammad et al. (2009)]:

$$\frac{N_{CPD}}{h_{in}} = \begin{cases} \left(\frac{AR_{CPD}}{1.044} \right)^{\frac{1}{0.38859}} - 0.26, & AR_{CPD} \leq 2 \\ \frac{44.8535}{1 + 2165.67 \exp(-2.8225 AR_{CPD})}, & AR_{CPD} > 2 \end{cases} \quad (C.12)$$

In the above, $h_{in} = R_{t,in} - R_{h,in}$ is the pre-diffuser width at the inlet (see Figure C.1) and N_{CPD} is the pre-diffuser wall length (see Figure C.2). Then, the pre-diffuser angle (α_{CPD}) is estimated by:

$$\tan \alpha_{CPD} = \frac{1}{2} \frac{AR_{CPD} - 1}{N_{CPD}/h_{in}} \quad (C.13)$$

from which the pre-diffuser axial length (L_{CPD}) is obtained as:

$$L_{CPD} = \frac{N_{CPD}}{h_{in}} h_{in} \cos \alpha_{CPD} \quad (C.14)$$

For estimating the dump-diffuser axial length (L_{CDD}), a user-defined dump gap-to-inlet width ratio (DGIWR) must be provided [see Honami et al. (1990) and Lefebvre et al. (2010)]. Then, L_{CDD} is obtained from:

$$L_{CDD} = \text{DGIWR} \times (R_{t,in} - R_{h,in}) \quad (C.15)$$

Regarding the liner axial length (L_{CL}), the following equation is used for estimating it:

⁶⁹The diffuser aspect ratio is defined as the ratio of the outlet width to the inlet width.

$$L_{CL} = \text{LLDHR} \times h_{CD} \quad (\text{C.16})$$

where LLDHR is a user-specified liner length-to-dome height ratio.

The combustor overall axial length (L) and maximum height (h) are obtained from:

$$L = L_{CL} + L_{CPD} + L_{CDD} \quad (\text{C.17})$$

$$h = h_{CD} + h_{CP} \quad (\text{C.18})$$

Typical values for the user-defined inputs (AFR, DCFR, V_{CD} , V_{CP} , ϕ_p , AR_{CPD} , DGIWR, LLDHR) appearing in the above system of equations are given in Table C.1.

Table C.1: Typical values for user-defined inputs for combustor sizing

Quantity	Value(s)	Reference(s)
AFR	2-3	Mohammad et al. (2009)
DCFR	10-15%	Mohammad et al. (2009)
ϕ_p	1.4-1.5	Mohammad et al. (2009)
V_{CP}	35-60 m/s	Mohammad et al. (2009)
V_{CD}	7-12 m/s	Mohammad et al. (2009)
AR_{CPD}	1.4-3.0	Mohammad et al. (2009)
LLDHR	2-3	Mohammad et al. (2009)
DGIWR	~1	Honami et al. (1990); Lefebvre et al. (2010)

Concluding the combustor sizing, the thickness of both the casing and liner has to be estimated. To do this, the approach used in NASA's WATE [see Onat et al. (1979a)] is adopted.

The thickness of the casing is estimated assuming that the combustor operates like a pressurized container. For containing the pressure of the gas flow, an average casing thickness is then estimated according to:

$$\bar{t} = \frac{\bar{p}^0 \bar{R}_t}{\sigma_\gamma} \quad (\text{C.19})$$

where \bar{p}^0 is the average total pressure between the combustor inlet and outlet, \bar{R}_t is the average outer casing radius (i.e., the annulus tip radius), and σ_γ is the casing material yield strength. Since combustors operate in high temperatures, the latter is taken equal to $\sigma_\gamma = 50,000$ psi assuming steel [see Onat et al. (1979a)].

Finally, the average liner thickness is assumed equal to ~1.4 mm (0.055 inches) according to Onat et al. (1979a).

C.3 Combustor Axial Positioning and Gas-Path Visualization

For visualizing the gas-path of the combustor, the numbering system shown in Figure C.3 is used. Note that, the combustor gas path up to station 3 is obtained assuming that the mean diameter is held constant and equal to that at the combustor inlet (station 1). From station 3 up to station 4 (combustor exit) there is a shift in mean radius since, in general, $R_{m,in} \neq R_{m,out}$. Here, the combustor inlet is assumed to coincide geometrically with the compressor exit at the upstream of the combustor, while the combustor outlet coincides geometrically with the turbine inlet at the downstream of the combustor; that is, $R_{h,in}$ and $R_{t,in}$ are equal to the upstream compressor exit hub and tip radii, and $R_{h,out}$ and $R_{t,out}$ are equal to the downstream turbine inlet hub and tip radii.

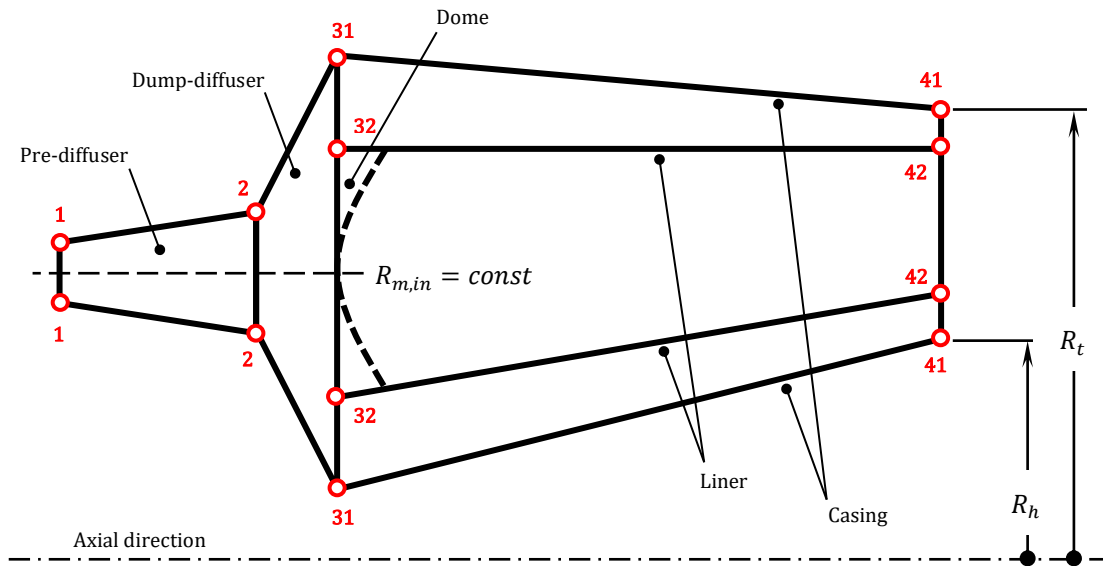


Figure C.3: Numbering system and stations for defining the combustor meridional gas-path contour. For convenience in the calculations, the same indices (i.e., 1, 2, 3, and 4) are used for both the annulus hub and tip, and each number identifies uniquely a gas-path station: 1 → combustor inlet/pre-diffuser inlet, 2 → pre-diffuser outlet/dump-diffuser inlet, 3 → dump-diffuser outlet/dome/liner inlet, 4 → liner outlet/combustor exit. The curve segment representing the combustor dome is visualized, for simplicity, as a straight line (32-32).

First, an origin is selected, let $x_{h,1}$ be the one ($x_{h,1} = 0$). The hub axial coordinates at the different stations shown in Figure C.3 are then obtained by the following equations:

$$x_{h,1} = 0 \quad (C.20)$$

$$x_{h,2} = x_{h,1} + L_{CPD} \quad (C.21)$$

$$x_{h,31} = x_{h,32} = x_{h,2} + L_{CDD} \quad (C.22)$$

$$x_{h,41} = x_{h,42} = x_{h,31} + L_{CL} = x_{h,1} + L \quad (C.23)$$

while the tip axial coordinates at stations 1, 2, 3, and 4 are assumed equal to the respective hub radii or, according to:

$$x_t = x_h \quad (C.24)$$

Next, the hub and tip radii are calculated at the different stations. At station 1, hub and tip radii are given by:

$$R_{h,1} \equiv R_{h,in} \quad (C.25)$$

$$R_{t,1} \equiv R_{t,in} \quad (C.26)$$

The hub and tip radii at station 2 are given by:

$$R_{h,2} = R_{m,in} - \frac{1}{2}AR_{CPD}(R_{t,1} - R_{h,1}) \quad (C.27)$$

$$R_{t,2} = R_{m,in} + \frac{1}{2}AR_{CPD}(R_{t,1} - R_{h,1}) \quad (C.28)$$

The hub and tip radii at station 3 are given by:

$$R_{h,31} = R_{m,in} - \frac{h}{2} \quad (C.29)$$

$$R_{t,31} = R_{m,in} + \frac{h}{2} \quad (C.30)$$

$$R_{h,32} = R_{m,in} - \frac{h_{CD}}{2} \quad (C.31)$$

$$R_{t,32} = R_{m,in} + \frac{h_{CD}}{2} \quad (C.32)$$

Finally, the hub and tip radii at station 4 are given by:

$$R_{h,42} \equiv R_{h,out} \quad (C.33)$$

$$R_{t,42} \equiv R_{t,out} \quad (C.34)$$

$$R_{h,41} = \left\{ 1 - \frac{LCWGR[\%]}{100} \right\} R_{h,42} \quad (C.35)$$

$$R_{t,41} = \left\{ 1 + \frac{LCWGR[\%]}{100} \right\} R_{t,42} \quad (C.36)$$

where LCWGR is a user-defined liner-to-casing gap ratio, with a typical value equal to 10% according to NASA's WATE [see Pera et al. (1977a)].

D NASA/GE E³ HPC Inputs for Mechanical Design and Weight Estimation Validations

In the present appendix, the NASA/GE E³ 10-stage HPC geometry and performance inputs used in mechanical design (Chapter 4) and weight calculations (Chapter 5), are summarized. The data inputs have been primarily found, extrapolated, or estimated by Holloway et al. (1982).

NASA/GE E³ HPC is a 10-stage, high-speed, high-aerodynamic loading compressor designed and tested during the late 1970's-early 1980's, while its basic configuration was selected during a NASA/GE preliminary design and optimization phase conducted in the mid 1970's. The inlet guide vanes and the first four stator rows are of variable geometry, while two bleeds are located at the exit of stages 5 (1.3% of inlet flow for customer needs and turbine cooling) and 7 (2.3% of inlet flow for starting and turbine cooling). The aerodynamic design of the compressor was performed at 100% corrected speed and inlet mass flow rate (maximum climb flight conditions) for standard-day, sea-level inlet static conditions (288.15 K, 101,325 Pa). The efficiency goal for the E³ high-pressure compressor was set at 85.7%; the two rig-tests conducted in the early 80's, however, did not reach 100% speed or this efficiency goal [see Cline et al. (1983)]. Table D.1 presents the compressor design point data.

Table D.1: NASA/GE E³ HPC design point data

Parameter	Value
Corrected inflow	54.4 kg/s
Corrected inlet tip speed	456.0 m/s
Overall total pressure ratio	25.0
Overall total temperature rise ⁷⁰	493.6 K

Table D.2 tabulates basic geometrical data that are used to estimate useful geometry and performance quantities, as will be described next.

⁷⁰See Figure 14 by Holloway et al. (1982).

Table D.2: NASA/GE E³ HPC general geometrical data⁷¹

Parameter	Value (mm)
Compressor inlet hub radius	173.4
Compressor inlet tip radius	362.1
Compressor exit hub radius	273.6
Compressor exit tip radius	293.4
First rotor tip radius	350.7

The compressor rotational speed (N_{mech}), angular velocity (ω), power (P_{wr}), and torque (T_{rq}) can be estimated through:

$$N_{mech} = \frac{60 U}{2\pi R} \quad (D.1)$$

$$\omega = \frac{2\pi N_{mech}}{60} \quad (D.2)$$

$$P_{wr} = \dot{m}_{in} c_p \Delta T^0 \quad (D.3)$$

$$T_{rq} = \frac{P_{wr}}{\omega} \quad (D.4)$$

where, for simplicity, in Eq. (D.3) constant air properties are assumed ($c_p = 1004.5$ J/kg·K) while the mass extractions from the compressor are neglected. In Eq. (D.1), $U = 456$ m/s is the first rotor tip speed and $R = 350.7$ mm is the first rotor tip radius (see Table D.1 and Table D.2, respectively).

Finally, the axial force, $F_{rc,x}$, induced by the compressor is assumed to be due to the pressure difference between the compressor inlet and outlet and is obtained by the following equation:

$$F_{rc,x} = p_{in}^0 A_{in} - p_{out}^0 A_{out} \quad (D.5)$$

where the flow-annulus area, A , is calculated by:

$$A = \frac{\pi}{4} (R_t^2 - R_h^2)$$

and the compressor exit pressure, p_{out}^0 , is given by:

$$p_{out}^0 = PR \times p_{in}^0$$

where $PR = 25$ is the compressor pressure ratio.

Replacing the variables in Table D.1 and Table D.2 into Eqs (D.1)–(D.5), yields the results shown in Table D.3.

⁷¹See Table XXI by Holloway et al. (1982).

Table D.3: NASA/GE E³ HPC calculated performance data

Parameter	Value
Mechanical rotational speed	12,416.5 rpm
Angular velocity	1300.3 rad/s
Power	26.8 MW
Torque	20.7 kN·m
Axial force	-57.5 kN

Next, the relative total temperature at the rotor hub across the compressor is calculated. Table D.4 tabulates the total temperatures and Mach numbers across the compressor, at the rotor hub.

Table D.4: Flow properties across the NASA/GE E³ HPC rotor hub⁷²

Stage	M (-)		M_r (-)		$T^0/288.15$ (-)	
	@ Inlet	@ Outlet	@ Inlet	@ Outlet	@ Inlet	@ Outlet
1	0.448	0.835	0.804	0.554	1.0201	1.2190
2	0.546	0.785	0.830	0.526	1.2190	1.4135
3	0.527	0.735	0.774	0.452	1.4135	1.6042
4	0.507	0.699	0.730	0.413	1.6042	1.7915
5	0.483	0.650	0.698	0.368	1.7914	1.9764
6	0.447	0.587	0.673	0.390	1.9764	2.1408
7	0.427	0.574	0.664	0.390	2.1408	2.3130
8	0.401	0.551	0.644	0.370	2.3130	2.4906
9	0.364	0.516	0.625	0.345	2.4906	2.6721
10	0.333	0.482	0.603	0.329	2.6721	2.8496

The relative total temperature at the rotor hub is taken equal to average between those at the rotor hub inlet and outlet, according to the following system of equations:

$$\bar{T}_r^0 = \frac{T_{r,1}^0 + T_{r,2}^0}{2} \quad (\text{D.6})$$

$$T_r^0 = T^s \left(1 + \frac{\gamma - 1}{2} M_r^2 \right) \quad (\text{D.7})$$

$$T^s = \frac{T^0}{1 + \frac{\gamma - 1}{2} M^2} \quad (\text{D.8})$$

⁷²See Table XXI by Holloway et al. (1982) for 100% immersion.

where in the above constant air properties ($\gamma = 1.4$) are assumed for calculation simplicity.

Replacing the variables in Table D.4 into Eqs (D.6)–(D.8) yields the results shown in Table D.5. Note that, \bar{T}_r^0 is assumed equal to the temperature at the disk rim (T_{rim}), that is, no heat transfer is assumed between the blade root and its surroundings along the root span.

Table D.5: NASA/GE E³ HPC disk rim temperature distribution

Stage	T^s (K)		T_r^0 (K)		\bar{T}_r^0 (K)	T_{rim} (K)
	@ Inlet	@ Outlet	@ Inlet	@ Outlet		
1	282.6	308.3	319.1	327.2	323.2	323.2
2	331.5	362.6	377.2	382.7	379.9	379.9
3	385.9	417.2	432.1	434.2	433.2	433.2
4	439.6	470.3	486.5	486.3	486.4	486.4
5	493.2	525.1	541.2	539.3	540.3	540.3
6	547.6	577.1	597.2	594.7	595.9	595.9
7	595.2	625.3	647.6	644.3	646.0	646.0
8	645.7	676.6	699.3	695.1	697.2	697.2
9	699.1	731.0	753.8	748.4	751.1	751.1
10	753.3	784.7	808.0	801.6	804.8	804.8

Table D.6 summarizes the rotor blading material, count, and weights, while Table D.7 presents the hub and tip radii at the blade row LE and TE [Holloway et al. (1982)].

Table D.6: NASA/GE E³ HPC rotor blade material, count, and weights⁷³

Stage	Material	Z_b (-)	$W_{KG,af}$ (g)	$W_{KG,af+root}$ (g)
1	Ti-8-1-1	28	284.0	550.0
2	Ti-8-1-1	38	78.6	183.3
3	Ti-8-1-1	50	35.6	82.4
4	Ti-8-1-1	60	18.0	47.7
5	Inconel-718	70	19.8	62.8
6	Inconel-718	80	12.2	44.5
7	Inconel-718	82	9.4	43.3
8	Inconel-718	84	6.0	29.5
9	Inconel-718	86	4.5	20.1
10	Inconel-718	94	4.0	15.5

⁷³See Table X by Holloway et al. (1982).

Table D.7: NASA/GE E³ HPC rotor aerofoil hub and tip radii⁷⁴

Stage	R_h (mm)		R_t (mm)	
	@ LE	@ TE	@ LE	@ TE
1	178.0	203.5	350.7	343.8
2	221.0	236.2	335.9	333.2
3	248.1	255.1	328.3	326.0
4	261.7	264.7	321.2	319.3
5	268.4	269.2	315.1	313.5
6	271.0	271.4	308.5	307.3
7	272.9	273.3	304.3	303.1
8	273.2	273.7	299.6	298.9
9	273.6	273.8	297.0	296.4
10	273.6	273.8	294.6	294.1

Table D.8 tabulates the material and type (shape) of the compressor disks. Note that the disks of the last five (5) stages were fabricated from a special R95 powder⁷⁵. Since such a material is not available in the material database created in the scope of this thesis, the material for the disks in stages 6-10 was selected to be Inconel-718, an approximation also followed by other investigators [see Turner et al. (2010)].

Table D.8: NASA/GE E³ HPC disk shape and material⁷⁶

Stage	Type	Material
1	Ring	Ti-8-1-1
2	Hyperbolic	Ti-6Al-4V
3	Web	Ti-6Al-4V
4	Web	Ti-6Al-4V
5	Web	Ti-6Al-4V
6	Web	Inconel-718
7	Web	Inconel-718
8	Web	Inconel-718
9	Web	Inconel-718
10	Web	Inconel-718

Digitization of the NASA/GE E³ HPC 2D cutaway⁷⁷, gave the disk radius and thickness dimensions at the six (6) characteristic radial stations shown in Table D.9 and Table D.10, respectively. Note that, for the 1st stage disk which is of ring type, the disk radius

⁷⁴See Table XXI by Holloway et al. (1982) for 100% (hub) and 0% (tip) immersion.

⁷⁵See Figure 31 by Holloway et al. (1982)

⁷⁶See Figure 31 by Holloway et al. (1982).

⁷⁷See Figure 9 by Holloway et al. (1982).

at stations 2, 3, 4, and 5 was calculated by a linear interpolation between the radius at the disk bore (station 1) and rim (station 6).

Table D.9: NASA/GE E³ HPC disk radii (mm) at the six characteristic radial stations

Stage	Disk Station					
	1 (Bore)	2	3	4	5	6 (Rim)
1	104.1	114.2	124.3	134.4	144.5	154.6
2	106.6	121.0	140.1	169.9	196.7	202.0
3	106.3	120.1	153.6	198.6	217.1	230.3
4	105.9	122.4	159.5	225.1	237.9	246.2
5	85.5	101.7	152.7	238.9	247.0	255.0
6	91.0	128.3	156.4	239.0	249.5	257.4
7	91.0	125.1	152.3	237.6	251.8	258.1
8	91.1	122.1	151.2	248.4	256.5	261.6
9	91.7	120.7	151.0	250.9	258.8	263.5
10	92.2	135.0	167.3	250.7	257.0	265.9

Table D.10: NASA/GE E³ HPC disk thicknesses (mm) at the six characteristic radial stations

Stage	Disk Station					
	1 (Bore)	2	3	4	5	6 (Rim)
1	93.7	93.7	93.7	93.7	93.7	93.7
2	32.9	32.9	15.3	7.5	46.2	46.2
3	24.7	24.7	6.2	6.2	28.1	28.1
4	20.6	20.6	5.8	5.8	22.0	22.0
5	31.7	31.7	8.7	8.7	23.3	23.3
6	25.9	25.9	6.7	6.7	23.3	23.3
7	24.3	24.3	4.6	4.6	16.7	16.7
8	25.5	25.5	5.4	5.4	12.2	12.2
9	25.5	25.5	4.6	4.6	16.7	16.7
10	25.5	25.5	5.0	5.0	15.0	15.0

Replacing the dimensions in Table D.9 and Table D.10 and the materials in Table D.8 into Eq. (D.9) (with $dsf = 1$ in all disk segments), gives the live weight of the NASA/GE E³ HPC disks shown in Table D.11.

$$W_{KG} = 2\pi\rho \sum_{k=1}^{k=5} \left\{ m \left[\frac{(R_o - R_i)^{2+dsf}}{2 + dsf} + \frac{R_i(R_o - R_i)^{1+dsf}}{1 + dsf} \right] + \frac{n}{2}(R_o^2 - R_i^2) \right\}_k \quad (D.9)$$

Table D.11: NASA/GE E³ HPC disk live weight distribution

Stage	Disk Live Weight (kg)
1	16.8
2	9.7
3	8.5
4	7.4
5	11.1
6	18.8
7	14.6
8	14.7
9	14.1
10	17.4
$\Sigma = 133.1$	

The digitization of the NASA/GE E³ HPC 2D cutaway⁷⁸ gave also the total volume of the disk post and the root of the blades. Since from the engine's 2D cutaway [or from Holloway et al. (1982)] could not be extracted any information about the shape of the root of the blades, it was assumed (for simplicity) that the blade root comprises only the fir tree portion. According to GasTurb Details 5 [see Kurzke (2007)], the volume of the fir tree is approximately equal to the volume occupied by the disk post or, in other words, the disk post and the blade root (in this case only the fir tree) are both equal to the half of the total volume estimated by the engine digitization.

Let V_{M3} be the total volume of the disk post and the blade root for a single blade⁷⁹, and $V_{M3,1}$ and $V_{M3,2}$ be the individual volume of the disk post and the blade root for a single blade, respectively. From the above it follows that:

$$V_{M3} = V_{M3,1} + V_{M3,2}$$

where:

$$V_{M3,1} = V_{M3,2} = \frac{1}{2}V_{M3}$$

The total weight of disk post and the blade root for a single blade is then calculated as:

$$W_{kg} = \rho_1 V_{M3,1} + \rho_2 V_{M3,2} = \frac{1}{2}(\rho_1 + \rho_2)V_{M3} \quad (\text{D.10})$$

where ρ_1 is the material density of the disk (given in Table D.8) and ρ_2 is the material density of the blade (given in Table D.6).

Applying Eq. (D.10) yields the results shown in Table D.12 for the total weight of the disk post and the blade root for a single blade.

⁷⁸See Figure 9 by Holloway et al. (1982).

⁷⁹The volume estimated by the engine digitization divided by the blade count given in Table D.6.

Table D.12: NASA/GE E³ HPC total weight of disk post and blade root for a single blade

Stage	$W_{KG,pst+fir}$ (g)
1	581.6
2	200.6
3	81.5
4	45.9
5	49.6
6	55.7
7	41.9
8	24.4
9	29.6
10	18.8

The centrifugal load ($\sigma_{r,rim}$) applied at the rim of a live disk by the disk dead weight is estimated by:

$$\sigma_{r,rim} = \frac{Z_b W_{KG,dw} R_{cg,dw}}{2\pi R_{rim} t_{rim}} \omega^2 \quad (D.11)$$

where $W_{KG,dw}$ is the dead weight and $R_{cg,dw}$ is the center of gravity of the dead weight. The former is estimated by:

$$W_{KG,dw} = W_{KG,af} + W_{KG,pst+fir} \quad (D.12)$$

while latter can be estimated according to:

$$R_{cg,dw} = \frac{R_{cg,af} W_{KG,af} + R_{cg,pst+fir} W_{KG,pst+fir}}{W_{KG,dw}} \quad (D.13)$$

The center of gravity of the combination of the disk post and the blade root ($R_{cg,pst+fir}$) is assumed to be at the half-point between the blade hub and disk rim, or:

$$R_{cg,pst+fir} = \frac{1}{2} (\bar{R}_h + R_{rim}) \quad (D.14)$$

where:

$$\bar{R}_h = \frac{1}{2} (R_{h,LE} + R_{h,TE})$$

whereas the center of gravity of the aerofoil ($R_{cg,af}$) is estimated by:

$$R_{cg,af} = 0.4\bar{R}_t + 0.6\bar{R}_h \quad (D.15)$$

where:

$$\bar{R}_t = \frac{1}{2}(R_{t,LE} + R_{t,TE})$$

Finally, by replacing the variables appearing in Table D.3, Table D.6, Table D.7, Table D.9, Table D.10, and Table D.12 into Eqs (D.11) through (D.15) yields the results shown in Table D.13:

Table D.13: NASA/GE E³ HPC disk rim loading

Stage	$W_{KG,dw}$ (g)	\bar{R}_h (mm)	\bar{R}_t (mm)	$R_{cg,af}$ (mm)	$R_{cg,pst+fir}$ (mm)	$R_{cg,dw}$ (mm)	$\sigma_{r,rim}$ (MPa)
1	865.6	190.7	347.2	253.3	172.6	199.1	89.7
2	279.2	228.6	334.5	271.0	215.3	231.0	70.6
3	117.1	251.6	327.2	281.8	240.9	253.3	61.6
4	63.9	263.2	320.3	286.0	254.7	263.5	50.2
5	69.4	268.8	314.3	287.0	261.9	269.1	59.3
6	67.9	271.2	307.9	285.9	264.3	268.2	65.4
7	51.3	273.1	303.7	285.3	265.6	269.2	70.8
8	30.4	273.5	299.2	283.8	267.5	270.7	58.5
9	34.1	273.7	296.7	282.9	268.6	270.5	48.5
10	22.8	273.7	294.3	281.9	269.8	271.9	39.2

E Blade and Blade Attachment Sizing

E.1 Introduction

To add energy to, or remove energy from the working fluid, turbomachinery components use stages of rotating (rotors) and stationary (stators) blades. Both rotor and stator blades comprise the blade itself (aerofoil + shroud), while rotor blades have also a root section (platform + neck + fir tree) which is used for attaching the aerofoil onto the rotating disks (disk posts) to transfer or receive rotational motion and torque (power). Next, the equations used for calculating the basic dimensions of a blade and of its attachment (in case of rotor blades) are presented. These follow from the simplified approach used in GasTurb Details 5 [see Kurzke (2007)].

E.2 Calculation of Blade Dimensions

The tip radius, R_{tip} , of an aerofoil is estimated according to:

$$R_{tip} = \begin{cases} \frac{R_{t,LE} + R_{t,TE}}{2}, & \text{for rotors} \\ \frac{R_{h,LE} + R_{h,TE}}{2}, & \text{for stators} \end{cases} \quad (\text{E.1})$$

while the root radius, R_{root} , is given by:

$$R_{root} = \begin{cases} \frac{R_{h,LE} + R_{h,TE}}{2}, & \text{for rotors} \\ \frac{R_{t,LE} + R_{t,TE}}{2}, & \text{for stators} \end{cases} \quad (\text{E.2})$$

where R_h and R_t is the flow-annulus hub and tip radius, respectively, at the blade leading- and trailing edges.

The root width, t_{root} , of an aerofoil is given by:

$$t_{root} = \begin{cases} x_{h,TE} - x_{h,LE} = c_{x,h}, & \text{for rotors} \\ x_{t,TE} - x_{t,LE} = c_{x,t}, & \text{for stators} \end{cases} \quad (\text{E.3})$$

where x_h and x_t is the axial positioning of the flow-annulus hub and tip radius, respectively.

The radius of the center of gravity, R_{cg} , is given by:

$$R_{cg,af} = 0.4R_{tip} + 0.6R_{root} \quad (\text{E.4})$$

For blade shrouds (if exist), the center of gravity is given by:

$$R_{cg,srd} = R_{tip} + 0.05t_{root} \quad (\text{E.5})$$

Finally, the blade center of gravity is calculated as a weighted average between $R_{cg,af}$ and $R_{cg,srd}$, given the mass of the aerofoil and that of the shroud:

$$R_{cg,bld} = \frac{\sum_k R_{cg,k} W_{KG,k}}{\sum_k W_{KG,k}}, \quad k = af, srd \quad (\text{E.6})$$

E.3 Calculation of Blade Attachment Dimensions

The attachment of a rotor blade is comprised of the root (platform + neck + fir tree) and the disk post where the blade attaches itself to the disk. Figure E.1 shows the assembly of the blade attachment and its basic dimensions.

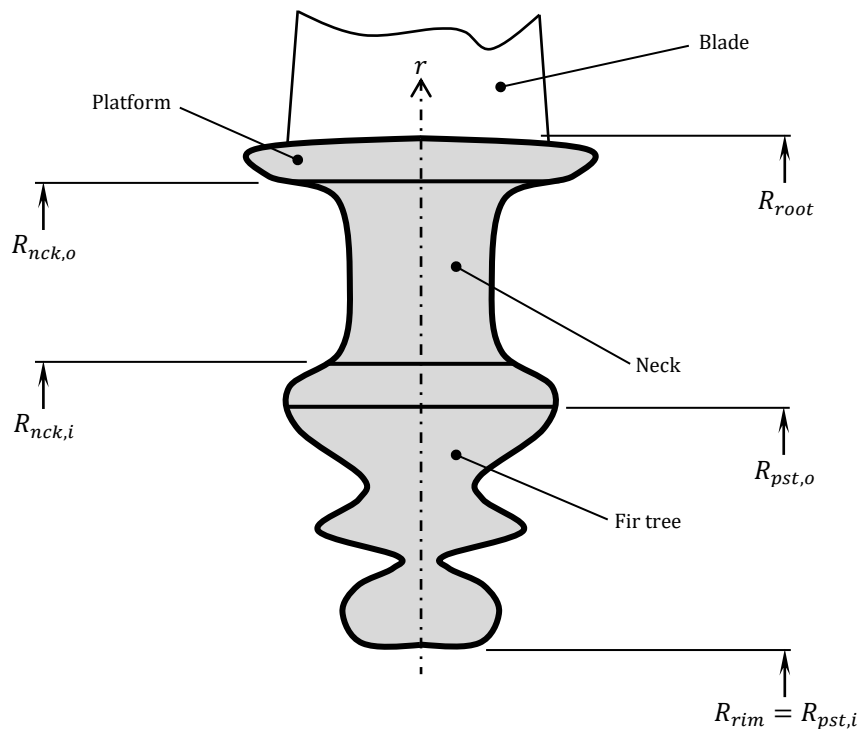


Figure E.1: Blade attachment and nomenclature [adapted from Kurzke (2007)].

First, the height of the blade root is calculated as a percentage of the (average) blade height, or:

$$h_{root} = \frac{K_{RBHR}[\%]}{100} \times \bar{h}_b$$

where K_{RBHR} is, in general, a user input. Default values of K_{RBHR} as function of the disk shape are given by Tong et al. (2004):

$$K_{RBHR} = \begin{cases} 17.65\%, & \text{for ring disks} \\ 25\%, & \text{for web disks} \\ 53.85\%, & \text{for hyperbolic disks} \end{cases}$$

Then, the root rim radius (disk rim radius), R_{rim} , is calculated according to:

$$R_{rim} = \min(R_{h,LE}, R_{h,TE}) - h_{root} \quad (\text{E.7})$$

while the rim width, t_{rim} , is assumed equal to the root width:

$$t_{rim} = t_{root} \quad (\text{E.8})$$

The inner and outer neck radius, $R_{nck,i}$ and $R_{nck,o}$, respectively, are calculated according to the following equations:

$$R_{nck,o} = R_{root} - 0.05t_{rim} \quad (\text{E.9})$$

$$R_{nck,i} = \min\left(R_{nck,o}, R_{rim} + \frac{2\pi R_{root}}{Z_b}\right) \quad (\text{E.10})$$

Finally, the disk post inner and outer radius, $R_{pst,i}$ and $R_{pst,o}$, respectively, are calculated according to:

$$R_{pst,i} = R_{rim} \quad (\text{E.11})$$

$$R_{pst,o} = 0.2R_{rim} + 0.8R_{nck,i} \quad (\text{E.12})$$

The center of gravity of the platform ($R_{cg,plt}$), neck ($R_{cg,nck}$), fir tree ($R_{cg,fir}$), and disk post ($R_{cg,pst}$) are given by the following equations:

$$R_{cg,plt} = 0.5(R_{root} + R_{nck,o}) \quad (\text{E.13})$$

$$R_{cg,nck} = 0.5(R_{nck,i} + R_{nck,o}) \quad (\text{E.14})$$

$$R_{cg,fir} = 0.5(R_{nck,i} + R_{rim}) \quad (\text{E.15})$$

$$R_{cg,pst} = 0.5(R_{pst,i} + R_{pst,o}) \quad (\text{E.16})$$

The center of gravity of the blade root is calculated as a weighted average between $R_{cg,plt}$, $R_{cg,nck}$, and $R_{cg,fir}$ given the mass of the platform, neck, and fir tree. Therefore:

$$R_{cg,root} = \frac{\sum_k R_{cg,k} W_{KG,k}}{\sum_k W_{KG,k}}, \quad k = plt, nck, fir \quad (E.17)$$

The center of gravity of the blade attachment is estimated in the same manner by including also the disk post weight, or:

$$R_{cg,att} = \frac{\sum_k R_{cg,k} W_{KG,k}}{\sum_k W_{KG,k}}, \quad k = plt, nck, fir, pst \quad (E.18)$$

Finally, the center of gravity of the disk dead weight (the combination of the blade and the blade attachment) is given by:

$$R_{cg,dw} = \frac{\sum_k R_{cg,k} W_{KG,k}}{\sum_k W_{KG,k}}, \quad k = af, srd, plt, nck, fir, pst \quad (E.19)$$

F Proof and Validation of Eq. (4.53)

Let a disk be defined by an arbitrary number of radial segments. Each segment is in turn defined by an inner and an outer set of radius and thickness, (R_i, t_i) and (R_o, t_o) , respectively, and a radial variation of thickness which is described by:

$$t = n + m(r - R_i)^{dsf}, \quad n = t_i, \quad m = \frac{t_o - t_i}{(R_o - R_i)^{dsf}} \quad (\text{F.1})$$

where $dsf > 0$ is a shape factor. In Eq. (F.1), R_i, t_i, R_o, t_o, dsf and, therefore, n and m , have, in general, different values in different disk segments.

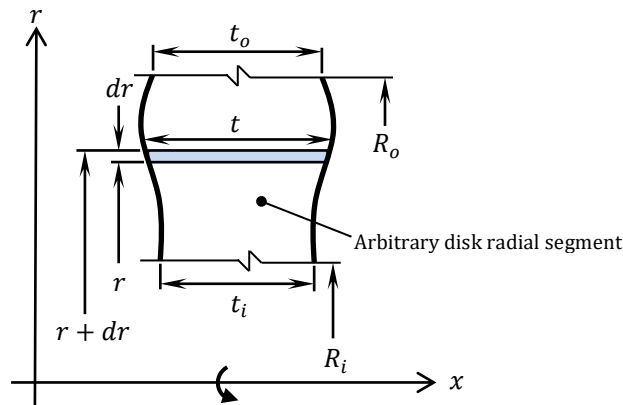


Figure F.1: Volume by revolution of a differential radial segment (blue-shaded rectangle).

The volume of an infinitesimal radial disk segment with a base radius dr and length t (see Figure F.1), produced by revolution of the segment about the x -axis, is given by:

$$dV_{M3} = \pi[(r + dr)^2 - r^2]t \cong 2\pi r t dr$$

where the higher order terms of dr are neglected. Using Eq. (F.1) to substitute the thickness t in the above yields:

$$dV_{M3} = 2\pi[mr(r - R_i)^{dsf} + nr]dr$$

Integrating from R_i to R_o we obtain:

$$V_{M3} = 2\pi \left\{ m \left[\frac{(R_o - R_i)^{2+dsf}}{2 + dsf} + \frac{R_i(R_o - R_i)^{1+dsf}}{1 + dsf} \right] + \frac{n}{2}(R_o^2 - R_i^2) \right\} \quad (F.2)$$

which expresses the total volume of a radial disk segment.

For disks with five (5) radial segments (as the ones examined in the present thesis), the total disk live mass is obtained by summing up the five different V_{M3} 's given by Eq. (F.2) and multiplying the result by the material density (ρ), or:

$$W_{KG} = 2\pi\rho \sum_{k=1}^{k=5} \left\{ m \left[\frac{(R_o - R_i)^{2+dsf}}{2 + dsf} + \frac{R_i(R_o - R_i)^{1+dsf}}{1 + dsf} \right] + \frac{n}{2}(R_o^2 - R_i^2) \right\}_k \quad (F.3)$$

Equation (F.3) was validated against a CAD-like tool⁸⁰ considering the disks of the NASA/GE E³ 10-stage HPC [see Holloway et al. (1982)]. The comparison between the CAD and (the ‘‘Geometrical’’) Eq. (F.3) is shown in Figure F.2. From Figure F.2 it is seen that Eq. (F.3) estimates correctly the mass of disks with thickness distributions described by Eq. (F.1).

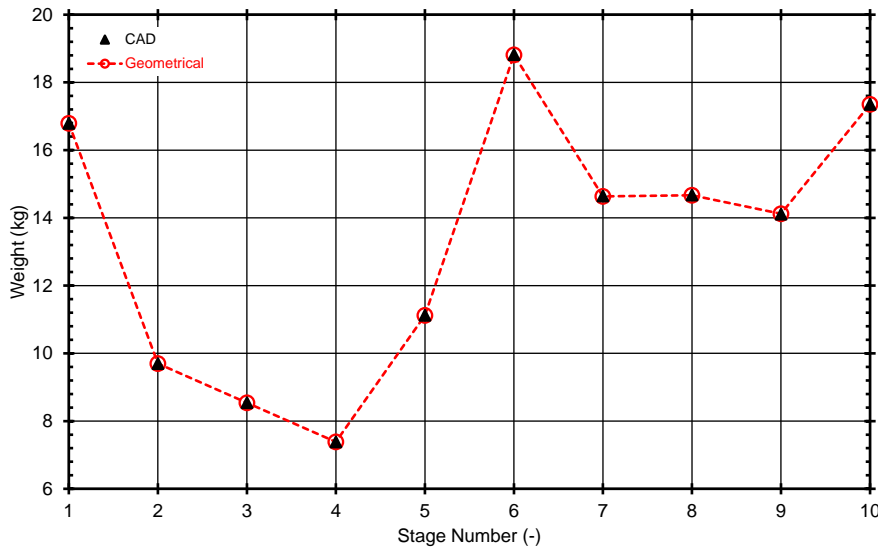


Figure F.2: Disk weight comparison between CAD and Eq. (F.3) for all ten disks of the NASA/GE E³ HPC [Holloway et al. (1982)].

⁸⁰<https://www.solidworks.com/domain/design-engineering> (accessed: May 11th, 2022)

G Nacelle Dimensions and Installed Engine Profile Drag Estimation for Unmixed Turbofans

The present appendix presents the models and approximations used in this thesis for estimating the nacelle dimensions as well as the engine installation (including the nacelle, pylon, and interference effects) profile drag. The discussion is limited to separated exhaust turbofan engines only. Figure G.1 depicts the characteristic nacelle dimensions and nomenclature for typical underwing installations of unmixed turbofan engines.

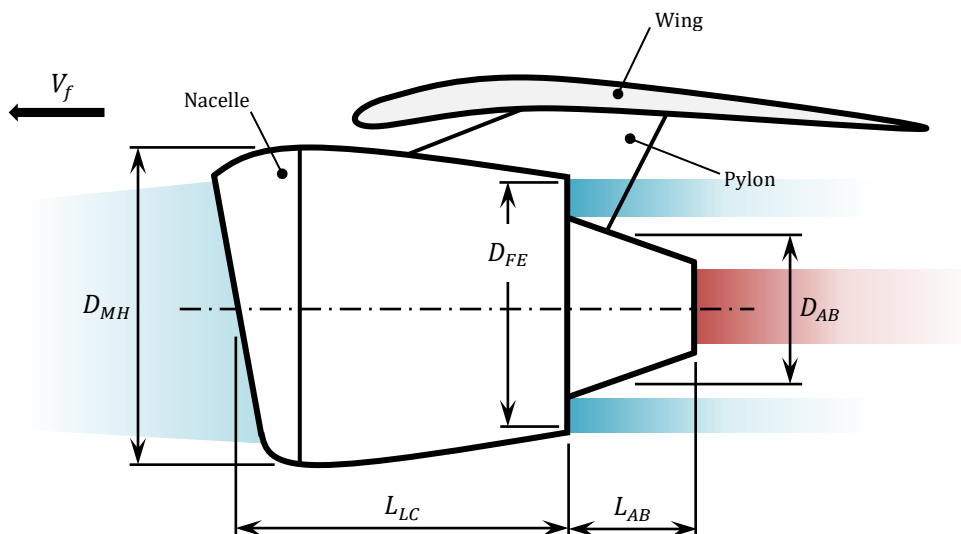


Figure G.1: Engine underwing installation and nomenclature for nacelle dimensions and profile drag estimation for separated exhaust turbofan engines.

G.1 Nacelle Dimensions Estimation

The cowl diameter, D_{MH} , is estimated using a statistical correlation derived by Bijewitz et al. (2014). Bijewitz et al. used a database of existing and future (projected) engines

to perform a non-linear regression analysis to link the nacelle cowl diameter with the fan tip diameter (D_{FAN}). This correlation reads:

$$\frac{D_{MH}}{D_{FAN}} = \frac{0.28}{D_{FAN}} + 1.17 \quad (G.1)$$

As stated by its authors, Eq. (G.1) is valid for $D_{FAN} = 1.0 - 3.5$ m. Note that, due to unavailable correlations for estimating the cowl diameter at the fan exit (D_{FE}), in the present modelling approach is assumed that $D_{FE} \approx D_{MH}$.

The cowl length, L_{LC} , is estimated using the statistical correlation developed by Seitz (2012) in his PhD thesis, which links the cowl length-to-diameter ratio, L_{LC}/D_{MH} , with the fan (outer) pressure ratio (p_{13}^0/p_2^0). This expression is given by:

$$\frac{L_{LC}}{D_{MH}} = 0.95 \frac{p_{13}^0}{p_2^0} - 0.09 \quad (G.2)$$

Note that, Eq. (G.2) is valid for fan pressure ratios in the range $p_{13}^0/p_2^0 = 1.3 - 1.9$.

The afterbody diameter (D_{AB}) is assumed equal to the maximum between the inlet tip diameter of the LP compressor and the outlet tip diameter of the LP turbine. The afterbody length, L_{AB} , is assumed to be a fraction of the afterbody diameter, or:

$$\frac{L_{AB}}{D_{AB}} = K_{AB} \quad (G.3)$$

with K_{AB} being a user-defined quantity. For instance, for the CFM56-5A turbofan engine $K_{AB} \sim 1$.

G.2 Installed Engine Profile Drag Estimation

The profile drag ($C_{D,0}$) of the engine installation includes those of the engine nacelle and pylon, as well as the interference effects between the engine, the wing, and the fuselage. Profile drag is estimated according to [see Jenkinson et al. (1999)]:

$$C_{D,0} = 1.15 C_f F_F F_I \frac{A_{wet}}{A_{ref}} \quad (G.4)$$

where C_f is the nacelle skin friction coefficient, F_F is the nacelle form factor, F_{FI} is the interference factor between the engine nacelle and the aircraft wing and fuselage, A_{wet} is the nacelle wetted area, and A_{ref} is a reference area (typically taken equal to the wing planform area).

Jenkinson et al. (1999) state that the engine installation (e.g., pylon) may account as much as 15% of the engine nacelle profile drag. According to Kundu (2010), the estimation of drag should always lie on the safe side, that is, it's better to overestimate drag than underestimate it. Hence, in Eq. (G.4) a conservative factor of 1.15 is adopted for multiplying the nacelle profile drag to obtain the engine overall drag. Next, the estimation of the individual terms appearing on the RHS of Eq. (G.4) will be described.

First, the nacelle wetted area, A_{wet} , is estimated according to Guha et al. (2012) and is given by:

$$A_{wet} = \frac{1}{2}\pi[(D_{MH} + D_{FAN})L_{LC} + (D_{FE} + D_{AB})L_{AB}] \quad (G.5)$$

The nacelle total skin friction coefficient is calculated as a weighted average by the following equation:

$$C_f = \left\{1 - \frac{K_l[\%]}{100}\right\} C_{f,t} + \frac{K_l[\%]}{100} C_{f,l} \quad (G.6)$$

where $C_{f,t}$ and $C_{f,l}$ is the turbulent and laminar skin friction coefficient, respectively, and K_l is a user-defined laminar flow percentage over the nacelle wetted area. Note that, in the present thesis, is assumed that the condition of the boundary layer over the nacelle surface is purely turbulent and, therefore, $K_l = 0\%$ is used.

The laminar skin friction coefficient, $C_{f,l}$, is estimated from [see Jenkinson et al. (1999)]:

$$C_{f,l} = \frac{1.328}{\sqrt{Re_f}} \quad (G.7)$$

where the flow Reynolds number (Re_f) is calculated by Eq. (G.8) based on the flight conditions (subscript “ f ”) and the nacelle characteristic length (L_{NCL}). The latter is taken equal to the nacelle overall length (that is $L_{NCL} = L_{LC} + L_{AB}$) according to Jenkinson et al.

$$Re_f = \frac{\rho_f V_f L_{NCL}}{\mu_f} \quad (G.8)$$

In Eq. (G.8), V_f is the flight velocity.

The turbulent skin friction coefficient, $C_{f,t}$, is estimated using the Prandtl-Schlichting formula for turbulent boundary layers [see Jenkinson et al. (1999)]:

$$C_{f,t} = \frac{0.455}{(\log_{10} Re_{min})^{2.58} (1 + 0.144 M_f^2)^{0.65}} \quad (G.9)$$

where M_f is the flight Mach number.

Regarding the Reynolds number (Re_{min}) appearing in Eq. (G.9), the following are noted: If the nacelle surface is relatively rough, then the actual friction coefficient will be higher than the one estimated by Eq. (G.9) if we used the flow Reynolds number (Re_f). For this reason, in Eq. (G.9) a minimum Reynolds number is used instead, which is the minimum between the actual flow Reynolds number and a “cutoff” Reynolds number (Re_c). Therefore, $Re_{min} = \min(Re_f, Re_c)$, where the cutoff Reynolds number is obtained [see Raymer (1992)]:

$$\text{Re}_c = \begin{cases} 38.21 \left(\frac{L_{NCL}}{k_s} \right)^{1.053}, & M_f < 1 \\ 44.62 M_f^{1.16} \left(\frac{L_{NCL}}{k_s} \right)^{1.053}, & M_f \geq 1 \end{cases} \quad (\text{G.10})$$

In the above, the nacelle characteristic length (L_{NCL}) is again taken equal to the nacelle overall length ($L_{NCL} = L_{LC} + L_{AB}$), and k_s is the nacelle skin roughness. Typical values for k_s are given in Table G.1 for different nacelle surface finishes and/or materials.

Table G.1: Skin roughness values [adapted from Raymer (1992)]

Surface Finish	k_s (ft)
Camouflage paint	3.33×10^{-5}
Smooth paint	2.08×10^{-5}
Aluminum	3.33×10^{-5}
Production sheet metal	1.33×10^{-5}
Polished sheet metal	0.50×10^{-5}
Smooth molded composite	0.17×10^{-5}

Finally, the nacelle form factor, F_F , is given by [see Raymer (1992)]:

$$F_F = 1 + 0.35 \frac{D_{MH}}{L_{LC}} \quad (\text{G.11})$$

and the interference factor, F_I , is given in Table G.2 for different longitudinal positionings of the nacelle under the aircraft wing.

Table G.2: Interference factor values [adapted from Raymer (1992)]

Nacelle Positioning	F_I (-)
Directly under the wing	1.5
Less than one diameter away	1.3
Much beyond one diameter away	1.0

H Polar Moments of Inertia Estimation

An outcome of the GTWC library (see Chapter 5) when calculating the weight of rotating components utilizing the CB-GM mode, is also values for the polar moment of inertia (required when conducting transient engine calculations). In this appendix, the equations used for estimating the polar moment of inertia (J_p) of rotating components and structural parts are summarized.

For rotating shafts of constant thickness, J_p can be calculated analytically and is given by:

$$J_p = \frac{1}{2} W_{KG} (R_i^2 + R_o^2) \quad (\text{H.1})$$

where W_{KG} is the shaft mass and R_i and R_o are the shaft inner and outer radius, respectively.

For rotating blades (rotors), J_p is approximated by:

$$J_p \cong W_{KG} R_{cg}^2 \quad (\text{H.2})$$

where W_{KG} is the blade weight and R_{cg} is its center of gravity. For rotor blades, W_{KG} accounts for the weight of the blade itself (aerofoil + shroud) and the weight of the root section (platform + neck + fir tree), while R_{cg} is calculated according to Appendix E.

For rotating disks, J_p is approximated by [see Onat et al. (1979a)]:

$$J_p \cong \frac{1}{8} W_{KG} \bar{R}_h^2 \quad (\text{H.3})$$

where W_{KG} is the disk weight and \bar{R}_h is the average hub radius of the flow annulus at the position of the disk.

For fan components, the spinner J_p can be calculated analytically and is given by the following equation:

$$J_p = \frac{1}{2} W_{KG} R^2 \quad (\text{H.4})$$

where W_{KG} is the spinner weight and R is the spinner base radius (assuming that the spinner approximates a right circular cone).

Finally, for VPFs, the pitch changing mechanism J_p is approximated as:

$$J_p \cong W_{KG} \left(\frac{1}{2} \bar{R}_h \right)^2 \quad (\text{H.5})$$

where W_{KG} is the pitch changing mechanism weight and \bar{R}_h is the fan rotor average hub radius. In Eq. (H.5), it is assumed that the pitch changing mechanism center of gravity is placed at the half-point between the fan rotor hub and the fan axis.

For estimating the overall polar moment of inertia of a rotating component, the inertias of the structural parts comprising that component are simply summed up. For instance, for a compressor comprising N_{stg} stages, its total polar moment of inertia is obtained by summing up the N_{stg} inertias for the disks and rotors (the same calculation is performed for turbines too). For fan components, their inertia is obtained by adding together the inertias of the blades, disks, spinner and, for VPFs, the inertia of the pitch changing mechanism.

I 2-Spool Unmixed Flow Turbofan Engine Station Designation

In this appendix the station designation used for 2-spool turbofan engines with separate exhausts is given. This designation is followed in the relevant engine models presented in this text, and is adopted after the SAE standard [see SAE (1997)]. The flow station numbering is shown in Figure I.1 and summarized in Table I.1.

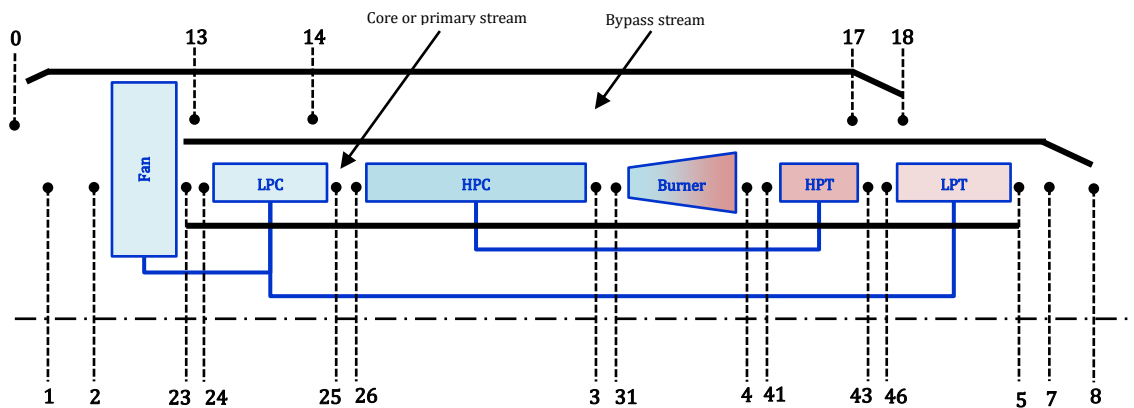


Figure I.1: Flow station designation across 2-spool, unmixed flow turbofan engines with convergent nozzles [see SAE (1997)].

Table I.1: Flow station designation across 2-spool, unmixed turbofan engines with convergent nozzles [see SAE (1997)]

Designation	Flow Station
0	Free-stream conditions
1	Inlet duct front face
2	Fan inlet face
23/24	Fan exit face/LPC inlet face
25/26	LPC exit face/HPC inlet face
3/31	HPC discharge face/Burner inlet face

Table I.1 (cont.): Flow station designation across 2-spool, unmixed turbofan engines with convergent nozzles [see SAE (1997)]

Designation	Flow Station
4/41	Burner discharge face/HPT inlet face
43/46	HPT exit face/LPT inlet face
5	LPT exit face
7	Primary nozzle inlet face
8	Primary nozzle throat
13	Fan bypass exit face
14	Bypass duct
17	Bypass nozzle inlet face
18	Bypass nozzle throat

Abbreviations

0D	0-Dimensional
1D	1-Dimensional
2D	2-Dimensional
3D	3-Dimensional
ACARE	Advisory Council for Aviation Research and Innovation
ACM	Area-Changing Mechanism
ASA	Adaptive Simulated Annealing
BC4	British C-4
BEW	Balanced Efficiency-Weight
BRM	Blade Row Module
C&A	Controls and Accessories
CAD	Computer Aided Design
CAMACM	Commercial Aircraft Mission Analysis Computational Model
CB	Component-Based
CB-GM	Component-Based, Geometry-Material (Analytical)
CB-SE	Component-Based, Semi-Empirical
CFD	Computational Fluid Dynamics
CMC	Ceramic Matrix Composite
DAE	Differential-Algebraic Equation
DCA	Double Circular Arc
DLR	German Aerospace Center
DOC	Direct Operational Cost
EDS	Environmental Design Space
EGV	Exit Guide Vane
EIS	Entry Into Service
EVA	Environmental Assessment
FARB	Fuel-to-Air Ratio
FD	Finite Difference
FEA	Finite Element Analysis
FV	Finite Volume
GE	General Electric
GIDLE	Ground Idle
GTF	Geared Turbofan
GTMDC	Gas Turbine Mechanical Design Code
GTWC	Gas Turbine Weight Code
GUI	Graphical User Interface
HP	High-Pressure

HPC	High-Pressure Compressor
HPT	High-Pressure Turbine
IGV	Inlet Guide Vane
IP	Intermediate-Pressure
IPC	Intermediate-Pressure Compressor
ISA	International Standard Atmosphere
IVM	Inter-Volume Module
LCF	Low Cycle Fatigue
LE	Leading Edge
LP	Low-Pressure
LPC	Low-Pressure Compressor
LPT	Low-Pressure Turbine
LTO	Landing and Take-Off
LTT	Laboratory of Thermal Turbomachines
MCA	Multiple Circular Arc
MCR	Mid-Cruise
MESM	Maximum Efficiency-Surge Margin
MFT	Map Fitting Tool
MLC	Mean-Line Code
MLAC	Mean-Line Analysis Code
MLDC	Mean-Line Design Code
MOPEDS	Modular Performance and Engine Design System
MPE	Maximum Polytropic Efficiency
NASA	National Aeronautics and Space Administration
NGV	Nozzle Guide Vane
NPSS	Numerical Propulsion System Simulation
NTUA	National Technical University of Athens
ODE	Ordinary Differential Equation
OEM	Original Equipment Manufacturer
OGV	Outlet Guide Vane
OTAC	Object-Oriented Turbomachinery Analysis Code
P&W	Pratt & Whitney
PCM	Pitch-Changing Mechanism
PMDO	Preliminary Multi-Disciplinary Design Optimization
PROOSIS	Propulsion Object Oriented Simulation Software
PS	Planetary gearbox
PTO	Power Take-Off
RDO	Rotating Disk Optimizer
RFP	Request for Proposal
RHS	Right Hand Side
RMS	Root-Mean-Square
RNI	Reynolds Number Index
RTO	Rolling Take-Off
SFC	Specific Fuel Consumption
SI	International System of Units
SLS	Sea Level Static

SO	Simple-Offset gearbox
SSM	Simplified Stress Model
STM	Simplified Thermal Model
STOL	Short Take-Off and Landing
TE	Trailing Edge
TERA	Techno-Economic Environmental Risk Assessment
ToC	Top-of-Climb
TURBO1D	Turbo-component Mean-line (1D) Design
UHBR	Ultra-High Bypass Ratio
(U)RANS	(Unsteady) Reynolds-Averaged Navier-Stokes
UTS	Ultimate Tensile Strength
VAN	Variable Area Nozzle
VPF	Variable Pitch Fan
VSV	Variable Stator Vane
VTOL	Vertical Take-Off and Landing
w.r.t.	with respect to
WAR	Water-to-Air Ratio
WATE	Weight Analysis of Turbine Engines
WEB	Whole Engine-Based

Nomenclature

Here the mathematical symbols used throughout the text are listed. Please note the following:

1. The SI system of units is used everywhere in the text unless stated otherwise.
2. Unless explicitly specified in the text, when for a (flow or kinematic) variable the term “relative to frame of reference” is used, then this variable is absolute relative to a stationary frame of reference and relative to a rotating frame of reference. For example, M_r is the Mach number relative to the frame of reference studied, i.e., the absolute Mach number relative to a stationary frame of reference (when, e.g., the flow across a stator vane is studied), or the relative Mach number relative to a rotating frame of reference (when, e.g., the flow across a rotor blade is studied). When the subscript “ r ” is omitted then the respective flow quantity corresponds to a stationary frame of reference (in the above example, M is the absolute Mach number).
3. Unless otherwise specified, the subscript “ m ” is omitted when the text refers to a flow or kinematic variable defined and/or calculated at the mean-line.
4. For the engine station numbering used throughout the text, the reader is referred to Appendix I.

Latin Symbols

a	Absolute flow angle (deg)
a_c	Maximum camber distance from airfoil leading edge (m)
a_{CTE}	Coefficient of thermal expansion ($\mu\text{m}/\text{m}/^\circ\text{C}$)
alt	Altitude (m)
A	Area (m^2)
$A_{rm}, A_{\theta m}$	Stress tensor components (Pa)
A_ω	Stage loss parameter (-)
AFR	Combustor atomizing flow rate (-)
AVDR	Axial velocity-density ratio (-)
AR	Aspect Ratio (-)
BETA	Auxiliary compressor map parameter (-)
BPR	Bypass ratio (-)
$B_{rm}, B_{\theta m}$	Stress tensor components (Pa)
Bi_{met}	Metal Biot number (-)
Bi_{tbc}	Thermal barrier coating Biot number (-)
c	Chord length (m)

c_p	Specific heat capacity at constant pressure (J/kg·K)
C_p	Static pressure rise coefficient (-)
C_D	Drag coefficient (-)
$C_{D,0}$	Nacelle profile drag coefficient (-)
C_L	Lift coefficient (-)
C_{l0}	Airfoil design lift coefficient (-)
$C_{rm}, C_{\theta m}$	Stress tensor components (Pa/K)
C_{tc}	Tip clearance influence factor (-)
C_ω	Blade loss parameter (-)
C_f	Nacelle skin friction coefficient (-)
$C_{f,l}$	Laminar nacelle skin friction coefficient (-)
$C_{f,t}$	Turbulent nacelle skin friction coefficient (-)
D	Diameter (m)
D_{CLICO}	Parabolic mean-line shape factor (-)
DCFR	Combustor/dome cooling flow rate (%)
DGIWR	Combustor dump gap-to-inlet width ratio (-)
DF_{eq}	Equivalent diffusion factor (-)
DF	Diffusion factor (-)
dsf	Disk shape factor (-)
E	Modulus of elasticity (Pa)
E_a	Squared ratio of stage exit-to-stage average axial velocities (-)
E_k	Kinetic energy (J)
EIS	Entry Into Service (years)
f	Function/Functional
FAR	Fuel-to-air ratio (-)
FARB	Burnt fuel-to-air ratio (-)
FB	Fuel burn (kg)
FPR	Fan pressure ratio (-)
F_ω	Blade loss weighting factor (-)
F_N	Net thrust (N)
F_{rc}	Force (N)
F_F	Nacelle form factor (-)
F_I	Nacelle interference factor (-)
g_x	Axial gap percentage (-) between successive blade rows
h	Specific enthalpy (J/kg); Height (m)
HTR	Hub-to-tip ratio (-)
i	Incidence angle (deg)
i_{010}	Design incidence angle for zero camber (deg)
i_{12}	Gear ratio (-)
I	Index
j	Stage number; Blade row number
J_p	Polar moment of inertia (kg·m ²)
k	Counter; Index
k_s	Equivalent sand-grain roughness or skin roughness (m)
k_{CLA}	Roughness arithmetical average (m)
$K_{C\&A}$	Controls and accessories weight proportionality constant (-)

K_{ACM}	Area-changing mechanism weight proportionality constant (-)
K_{AR}	Axial chord model coefficients
K_{AB}	Nacelle afterbody length-to-diameter ratio (-)
K_{comb}	Combustion pattern factor (-)
K_{cool}	Cooling factor (-)
$K_{\Delta h}$	Stage enthalpy change fraction (-)
K_{ψ}	Uncooled turbine stage efficiency factor (-)
K_{ω}	Stage loss proportionality constant (-)
K_{PCM}	Pitch-changing mechanism weight-to-fan weight ratio (-)
K_B	Burner weight proportionality constant (kg/m^2)
K_C	Compressor weight proportionality constant ($\text{kg}/\text{m}^{2.2}$)
K_F	Fan weight proportionality constant ($\text{kg}/\text{m}^{2.7}$)
K_{FNR}	Thrust reversal system proportionality constant (-)
K_{VM3}	Blade volumetric factor (-)
K_{RBHR}	Blade root height-to-blade height ratio (-)
K_T	Turbine weight proportionality constant ($\text{kg} \cdot \text{s}^{0.6}/\text{m}^{3.1}$)
K_S	Structural weight proportionality constant (-)
K_l	Laminar flow percentage over nacelle wetted area (-)
K_G	Gearbox weight proportionality constant
K_{Gp}	Gearbox weight auxiliary parameter ($W^{0.75}/\text{rpm}^{0.75}$)
K_{Gw}	Gearbox weight auxiliary parameter
K_{sh}	Camberline shape correction factor (-)
$K_{ti}, K_{t\delta}$	Thickness correction factors (-)
K_{tc}	Tip clearance auxiliary parameter (-)
L	Length (m)
LLDHR	Combustor liner length-to-dome height ratio (-)
LCWGR	Combustor liner-to-casing gap ratio (-)
LSBH	Last stage blade height (m)
\dot{m}	Mass flow rate (kg/s)
M	Mach number (-)
M_{ss}	Airfoil suction surface peak Mach number (-)
n_{PRS}	Pressure ratio split parameter (-)
N_d	Number of nodes
N_{mech}	Mechanical rotational speed (rpm)
N_{br}	Number of blade rows
N_R	Number of rotor rows
N_{stg}	Number of stages
o	Blade row throat opening (m)
OPR	Overall pressure ratio (-)
p	Pressure (Pa)
PR	Pressure ratio (-)
P_{wr}	Power (W)
r	Radial coordinate (m)
R	Radius (m); Stall range (deg)
RBM	(Reverse) burst margin (-)
RDM	(Reverse) design margin (-)

RLP	Relative loading parameter (-)
Re	Reynolds number (-)
R_g	Gas constant (J/kg·K)
\tilde{R}_{IMM}	Immersion from tip (-)
\tilde{R}_h	Relative spanwise position (-)
RNI	Reynolds Number Index (-)
s	Specific entropy (J/kg·K); Blade row spacing (m)
s_a	Scalar adder
s_m	Scalar multiplier
s_s	Scaling factor
s_w	Weight factor (-)
s_{ch}, s_{ct}	Hub and tip correction factors (-)
$S_{11}, S_{22}, S_{33},$ S_{12}, S_{13}, S_{23}	Stress tensor components (Pa)
SF_Y	Safety factor on yield strength (-)
SF_T	Safety factor on ultimate tensile strength (-)
SF_N	Specific thrust (N·s/kg)
SFC	Specific Fuel Consumption (kg/N·s)
SM	Surge margin (%)
t	Thickness (m)
T	Temperature (K)
TET	Turbine entry temperature
TF	Technology factor (-)
TR	Taper Ratio (-); Temperature ratio (-)
T_{rq}	Torque (N·m)
u	Radial displacement (deformation) (m)
U	Blade speed (m/s)
V	Absolute flow velocity (m/s)
V_{M3}	Volume (m ³)
$V_{x,CLICO}$	Axial velocity shape factor (-)
W	Flow velocity relative to frame of reference (m/s)
W_{KG}	Mass/weight (kg)
WAR	Water-to-air ratio (-)
x	Axial coordinate (m); Auxiliary parameter
y	Auxiliary parameter
X	Dummy variable
Z_b	Blade count (-)

Greek Symbols

α	Angle (deg); Angle of attack (deg)
β	Flow angle relative to frame of reference (deg)
γ	Specific heats ratio (-); Stagger angle (deg)
δ	Deviation angle (deg)
δ_{010}	Design deviation angle for zero camber (deg)
δ_B	Blockage fraction (-)

δ_c	Cooling specific loss for turbine blades (-); Radial clearance (m)
Δ	Variation; Correction; Difference
$\varepsilon > 0$	Tolerance/Threshold
ε_0	Cooling effectiveness
ε_f	Film cooling effectiveness (-)
η	Efficiency (-)
η_{int}	Internal cooling effectiveness (-)
θ	Peripheral coordinate (deg); Camber angle (deg)
θ_w	Wake momentum thickness (m)
κ	Blade camber tangent w.r.t. axial direction (deg)
κ_π	Nacelle material density per unit area (kg/m ²)
λ_B	Blockage factor (-)
Λ	Reaction (-)
μ	Dynamic viscosity (Pa·s)
ν	Poisson's ratio (-); Prandtl-Meyer function (deg)
ξ	Normalized incidence angle (-)
ρ	Density (kg/m ³)
σ	Solidity (-); Normal stress (Pa)
τ	Shear stress (Pa)
ϕ	Specific entropy function (J/kg·K)
ϕ_p	Combustor primary zone equivalence ratio (-)
Φ	Stagger angle parameter (deg)
φ	Flow coefficient (-)
χ	Blade camber tangent w.r.t. chord (deg)
ψ	Loading coefficient (-)
ψ_z	Tangential loading coefficient (-)
ω	Total pressure loss coefficient (-); Angular velocity (rad/s)
Ω	Total pressure loss parameter (-)

Subscripts

1/2/3	Rotor inlet/rotor exit/stator exit (for compressor stages)
1/2/3	Row inlet/row outlet/inter-volume exit (for MLAC and MLDC)
0/1/2	Nozzle inlet/rotor inlet/rotor exit (for turbine stages)
1/2/3/4/5/6	Disk radial station numbering
<i>a</i>	Air
<i>af</i>	Aerofoil
<i>att</i>	Blade attachment
<i>AB</i>	Nacelle afterbody
<i>ACM</i>	Area-changing mechanism
<i>b</i>	Blade
<i>bld</i>	Blade or blading
<i>bo</i>	Nacelle body
<i>bore</i>	Disk bore
<i>br</i>	Blade row
<i>BENG</i>	Bare engine

<i>BRN</i>	Burner
<i>c</i>	Corrected; Negative stall; Choke; Cutoff (for Reynolds numbers)
<i>cf</i>	Coolant flow
<i>cg</i>	Center of gravity
<i>cl</i>	Clearance loss
<i>CA</i>	Combustor atomizing flow
<i>CC</i>	Combustor casing
<i>CD</i>	Combustor dome
<i>CDC</i>	Combustor dome cooling flow
<i>CDD</i>	Combustor dump-diffuser
<i>CL</i>	Combustor liner
<i>CP</i>	Combustor passage
<i>CPD</i>	Combustor pre-diffuser
<i>CS</i>	Combustor stabilizing flow
<i>C&A</i>	Controls and accessories
<i>CMP</i>	Axial-flow compressor component
<i>CNS</i>	Constraint function
<i>d</i>	Design
<i>dw</i>	Disk dead weight
<i>dsk</i>	Disk
<i>DCT</i>	Duct component
<i>e</i>	Effective
<i>eq</i>	Equivalent
<i>ew</i>	Endwall loss
<i>f</i>	Fuel; Flight conditions
<i>fir</i>	Blade fir tree
<i>FAN</i>	Axial-flow fan component
<i>FE</i>	Nacelle cowl height at fan exit
<i>FNR</i>	Thrust reversal system
<i>FRM</i>	Frame component
<i>g</i>	Geometric; Mainstream gas
<i>gb</i>	Gas bleed
<i>GBX</i>	Gearbox component
<i>h</i>	Hub
<i>hw</i>	Connecting hardware
<i>i</i>	Inner
<i>ics</i>	Inner casing
<i>ocs</i>	Outer casing
<i>is</i>	Isentropic process
<i>in</i>	Component inlet
<i>IGV</i>	IGVs
<i>IS</i>	Disk inner shoulder
<i>OBJ</i>	Objective function
<i>OS</i>	Disk outer shoulder
<i>LC</i>	Nacelle cowl (or casing)
<i>LE</i>	Leading edge

<i>m</i>	Mean/Meridional
<i>max</i>	Maximum
<i>MFT</i>	MFT map format
<i>MH</i>	Nacelle cowl maximum height
<i>Ma</i>	Mach number correction
<i>min</i>	Minimum
<i>nck</i>	Blade neck
<i>N</i>	Nozzle (turbine stator blade)
<i>NCL</i>	Nacelle
<i>o</i>	Outer
<i>out</i>	Component exit
<i>opt</i>	Optimum
<i>OGV</i>	OGVs
<i>p</i>	Polytropic process
<i>plt</i>	Blade platform
<i>pr</i>	Profile loss
<i>pst</i>	Disk post
<i>PCM</i>	Pitch-changing mechanism
<i>PNL</i>	Penalty function
<i>r</i>	Relative to frame of reference conditions; Radial direction
<i>rb</i>	Returning gas bleed
<i>req</i>	Required
<i>R</i>	Rotor
<i>RP</i>	Radial position
<i>ref</i>	Reference conditions
<i>rim</i>	Disk rim
<i>Re</i>	Reynolds number correction
<i>root</i>	Blade root radius or blade root section
<i>s</i>	Positive stall; Stall; Surge
<i>srd</i>	Aerofoil shroud
<i>spn</i>	Fan spinner (nose cone)
<i>S</i>	Stator
<i>STR</i>	Structural component
<i>SHF</i>	Shaft component
<i>SLS</i>	Seal Level Static conditions
<i>sc</i>	Secondary loss
<i>sh</i>	Shock loss
<i>t</i>	Tip
<i>th</i>	Theoretical
<i>tip</i>	Blade tip
<i>TE</i>	Trailing edge
<i>TO</i>	Take-off
<i>TRB</i>	Axial-flow turbine component
<i>UTS</i>	Ultimate Tensile Strength
<i>uc</i>	Uncooled (for turbine stages)
<i>vM</i>	von Mises

<i>wet</i>	Wetted (area)
<i>x</i>	Axial direction
<i>Y</i>	Yield
γ	Gamma correction
θ	Peripheral direction

Superscripts

*	Critical (sonic) conditions
0	Total (stagnation) conditions
<i>s</i>	Static conditions
–	Average

References

- 1 **Manson (1947)**: S. S. Manson. Determination of Elastic Stresses in Gas-Turbine Disks. NACA Report No. 871. Flight Propulsion Laboratory, Cleveland, OH, USA.
- 2 **Millenson et al. (1948)**: M. B. Millenson and S. S. Manson. Determination of Stresses in Gas-Turbine Disks Subjected to Plastic Flow and Creep. NACA Report No. 906. Flight Propulsion Laboratory, Cleveland, OH, USA.
- 3 **Carter (1950)**: A. D. S. Carter. The Low Speed Performance of Related Aerofoils in Cascades. Aeronautical Research Council, Technical Report: CP-No. 29.
- 4 **Lieblein et al. (1953)**: S. Lieblein, F. C. Schwenk, and R. L. Broderick. Diffusion Factor for Estimating Losses and Limiting Blade Loadings in Axial-Flow-Compressor Blade Elements. NACA RM-E53D01. Lewis Flight Propulsion Laboratory, Cleveland, OH, USA.
- 5 **Ainley et al. (1955)**: D. G. Ainley and G. C. R. Mathieson. An Examination of the Flow and Pressure Losses in Blade Rows of Axial-Flow Turbines. Aeronautical Research Council, Technical Report: RM-2891.
- 6 **Miser et al. (1956)**: J. W. Miser, W. L. Stewart, and W. J. Whitney. Analysis of Turbomachine Viscous Losses Affected by Changes in Blade Geometry. NACA RM-E56F21. Lewis Flight Propulsion Laboratory, Cleveland, OH, USA.
- 7 **Ainley et al. (1957)**: D. G. Ainley and G. C. R. Mathieson. A Method of Performance Estimation for Axial-Flow Turbines. Aeronautical Research Council, Technical Report: RM-2974.
- 8 **Herrig et al. (1957)**: L. J. Herrig, J. C. Emery, and J. R. Erwin. Systematic Two-Dimensional Cascade Tests of NACA 65-Series Compressor Blades at Low Speeds. NACA Technical Note 3916. Langley Aeronautical Laboratory, Langley, VA, USA.
- 9 **Lieblein (1957)**: S. Lieblein. Analysis of Experimental Low-Speed Loss and Stall Characteristics of Two-Dimensional Compressor Blade Cascades. NACA RM-E57A28. Lewis Flight Propulsion Laboratory, Cleveland, OH, USA.
- 10 **Lieblein (1960)**: S. Lieblein. Incidence and Deviation-Angle Correlations for Compressor Cascades. J. Basic Eng., 82(3), 575-584. doi: 10.1115/1.3662666.
- 11 **Stewart (1961)**: W. L. Stewart. A Study of Axial-Flow Turbine Efficiency Characteristic in Terms of Velocity Diagram Parameters. ASME Paper: 61-WA-37.
- 12 **Swan (1961)**: W. C. Swan. A Practical Method of Predicting Transonic-Compressor Performance. J. Eng. Power, 83(3), 322-330. doi: 10.1115/1.3673194.

- 13 **Johnsen et al. (1965)**: I. A. Johnsen and R. O. Bullock (ed.). Aerodynamic Design of Axial-Flow Compressors. NASA, SP-36. NASA: Washington, DC, USA.
- 14 **Nelder et al. (1965)**: J. A. Nelder and R. Mead. A Simplex Method for Function Minimization. The Computer Journal, 7(4), 308-313. doi: 10.1093/comjnl/7.4.308.
- 15 **Reneau et al. (1967)**: L. R. Reneau, J. P. Johnston, and S. J. Kline. Performance and Design of Straight, Two-Dimensional Diffusers. J. Basic Eng., 89(1), 141-150. doi: 10.1115/1.3609544.
- 16 **Steinke et al. (1967)**: R. J. Steinke and J. E. Crouse. Analytical Studies of Aspect Ratio and Curvature Variations for Axial-Flow-Compressor-Inlet Stages Under High Loading. NASA, TN D-3959. NASA: Lewis Research Center, Cleveland, OH, USA.
- 17 **Creveling et al. (1968a)**: H. F. Creveling and R. H. Carmody. Axial Flow Compressor Design Computer Programs Incorporating Full Radial Equilibrium: Part I-Flow Path and Radial Distribution of Energy Specified (Program II). NASA, CR-54532. NASA: Lewis Research Center, Cleveland, OH, USA.
- 18 **Creveling et al. (1968b)**: H. F. Creveling and R. H. Carmody. Axial Flow Compressor Design Computer Programs Incorporating Full Radial Equilibrium: Part II-Radial Distribution of Total Pressure and Flow Path or Axial Velocity Ratio Specified (Program III). NASA, CR-54531. NASA: Lewis Research Center, Cleveland, OH, USA.
- 19 **Creveling et al. (1968c)**: H. F. Creveling and R. H. Carmody. Axial Flow Compressor Computer Program for Calculating Off-Design Performance (Program IV). NASA, CR-72427. NASA: Lewis Research Center, Cleveland, OH, USA.
- 20 **De Silva (1969)**: D. M. E. De Silva. Minimum Weight Design of Disks Using a Frequency Constraint. J. Eng. Ind., 91(4), 1091-1099. doi: 10.1115/1.3591753.
- 21 **Gerend et al. (1970)**: R. P. Gerend and J. P. Roundhill. Correlation of Gas Turbine Engine Weights and Dimensions. Proceedings of the 6th AIAA Propulsion Joint Specialist Conference, San Diego, CA, USA, 15-19 June 1970. AIAA-70-669. doi: 10.2514/6.1970-669.
- 22 **Lakshminarayana (1970)**: B. Lakshminarayana. Methods of Predicting the Tip Clearance Effects in Axial Flow Turbomachinery. J. Basic Eng., 92(3), 467-480. doi: 10.1115/1.3425036.
- 23 **AGARD (1971)**: Advisory Group for Aerospace Research & Development. High Temperature Turbines. AGARD-CP-73-71.
- 24 **Sagerser et al. (1971)**: D. A. Sagerser, S. Lieblein, and R. P. Krebs. Empirical Expressions for Estimating Length and Weight of Axial-Flow Components of VTOL Powerplants. NASA, TM X-2406. NASA: Lewis Research Center, Cleveland, OH, USA.

- 25 **Brown (1972)**: L. E. Brown. Axial Flow Compressor and Turbine Loss Coefficients: A Comparison of Several Parameters. *J. Eng. Power*, 94(3), 193-201. doi: 10.1115/1.3445672.
- 26 **Dawson et al. (1972)**: L. G. Dawson and T. D. Sills. Turbofan Trends for Short Haul. Proceedings of the ASME 1972 International Gas Turbine and Fluids Engineering Conference and Products Show, San Francisco, CA, USA, 26-30 March 1972. 72-GT-86. doi: 10.1115/72-GT-86.
- 27 **Denning (1972)**: R. M. Denning. Variable Pitch Ducted Fans for STOL Transport Aircraft. Proceedings of the ASME 1972 International Gas Turbine and Fluids Engineering Conference and Products Show, San Francisco, CA, USA, 26-30 March 1972. 72-GT-61. doi: 10.1115/72-GT-61.
- 28 **Edkins et al. (1972)**: D. P. Edkins, R. Hirschcron, and R. Lee. TF34 Turbofan Quiet Engine Study. NASA, CR-120914. NASA: Lewis Research Center, Cleveland, OH, USA.
- 29 **Glassman (1972a)**: A. J. Glassman (ed.). Turbine Design and Application (Vol. I). NASA, SP-290. NASA: Washington, DC, USA.
- 30 **Glassman (1972b)**: A. J. Glassman. Computer Program for Preliminary Design Analysis of Axial-Flow Turbines. NASA, TN D-6702. NASA: Lewis Research Center, Cleveland, OH, USA.
- 31 **Galvas (1973)**: M. R. Galvas. FORTRAN Program for Predicting Off-Design Performance of Centrifugal Compressors. NASA, TN D-7487. NASA: Lewis Research Center, Cleveland, OH, USA.
- 32 **Vavra (1974)**: M. H. Vavra. Aero-Thermodynamics and Flow in Turbomachines. Krieger, NY, USA. ISBN: 0-88275-189-1.
- 33 **Cornell (1975)**: W. G. Cornell. Experimental Quiet Engine Program-Summary Report. NASA, CR-2519. NASA: Lewis Research Center, Cincinnati, OH, USA.
- 34 **Koch et al. (1976)**: C. C. Koch and L. H. Smith. Loss Sources and Magnitudes in Axial-Flow Compressors. *J. Eng. Power*, 98(3), 411-424. doi: 10.1115/1.3446202.
- 35 **Pera et al. (1977a)**: R. J. Pera, E. Onat, G. W. Klees, and E. Tjonneland. A Method to Estimate Weight and Dimensions of Aircraft Gas Turbine Engines-Final Report, Vol. I: Method of Analysis. NASA, CR-135170. NASA: Lewis Research Center, Cleveland, OH, USA.
- 36 **Pera et al. (1977b)**: R. J. Pera, E. Onat, G. W. Klees, and E. Tjonneland. A Method to Estimate Weight and Dimensions of Aircraft Gas Turbine Engines-Final Report, Vol. II: Users Manual. NASA, CR-135171. NASA: Lewis Research Center, Cleveland, OH, USA.
- 37 **Ryan et al. (1977)**: W. P. Ryan, D. M. Black, and A. F. Yates. Variable Pitch Fan System for NASA/Navy Research and Technology Aircraft. NASA, CR-135185. NASA: Lewis Research Center, Cleveland, OH, USA.

- 38 **Waters et al. (1977)**: M. H. Waters and E. T. Schairer. Analysis of Turbofan Propulsion System Weight and Dimensions. NASA, TM X-73,199. NASA: Ames Research Center, Moffett Field, CA, USA.
- 39 **Wisler et al. (1977)**: D. C. Wisler, C. C. Koch, and L. H. Smith. Preliminary Design Study of Advanced Multistage Axial Flow Core Compressors: Final Report. NASA, CR-135133. NASA: Lewis Research Center, Cleveland, OH, USA.
- 40 **Drydale (1978)**: G. V. Drydale. Design of Shafts for General Engineering Applications. MSc Thesis, University of New South Wales, Australia.
- 41 **Howell et al. (1978)**: A. R. Howell and W. J. Calvert. A New Stage Stacking Technique for Axial-Flow Compressor Performance Prediction. J. Eng. Power, 100(4), 698-703. doi: 10.1115/1.3446425.
- 42 **Johnston et al. (1978)**: R. P. Johnston, R. Hirschkron, C. C. Koch, R. E. Neitzel, and P. W. Vinson. Energy Efficient Engine Preliminary Design and Integration Studies. NASA, CR-135444. NASA: Lewis Research Center, Cleveland, OH, USA.
- 43 **Klees et al. (1978)**: Klees G. W. and Fishbach L. H. Aircraft Engine Weight Estimation Method. Proceedings of the 37th Annual Conference of Society of Allied Weight Engineers, Munich, West Germany, 8-10 May 1978. SAWE Paper: 1248.
- 44 **Reid et al. (1978)**: L. Reid and R. D. Moore. Performance of Single-Stage Axial-Flow Transonic Compressor with Rotor and Stator Aspect Ratios of 1.19 and 1.26, Respectively, and with Design Pressure Ratio of 1.82. NASA, TP 1338. NASA: Lewis Research Center, Cleveland, OH, USA.
- 45 **Onat et al. (1979a)**: E. Onat and G. W. Klees. A Method to Estimate Weight and Dimensions of Large and Small Gas Turbine Engines-Final Report. NASA, CR-159481. NASA: Lewis Research Center, Cleveland, OH, USA.
- 46 **Onat et al. (1979b)**: E. Onat and F. F. Tolle. An Extension of Engine Weight Estimation Techniques to Compute Engine Production Cost. Naval Air Systems Command. Contract Number: N62269-78-C0286.
- 47 **Willis (1979)**: W. S. Willis. Quiet Clean Short-Haul Experimental Engine (QCSEE) Final Report. NASA, CR-159473. NASA: Lewis Research Center, Cleveland, OH, USA.
- 48 **Gaunter (1980)**: J. W. Gaunter. Algorithm for Calculating Turbine Cooling Flow and the Resulting Decrease in Turbine Efficiency. NASA, TM 81453. NASA: Lewis Research Center, Cleveland, OH, USA.
- 49 **Luchi et al. (1980)**: M. L. Luchi, A. Poggialini, and F. Persiani. An Interactive Optimization Procedure Applied to the Design of Gas Turbine Disks. J. Computers and Structures, 11(6), 629-637. doi: 10.1016/0045-7949(80)90069-3.
- 50 **AGARD (1981)**: Advisory Group for Aerospace Research & Development. Through Flow Calculations in Axial Turbomachines. AGARD-AR-175.

- 51 **Halle et al. (1981)**: J. E. Halle and C. J. Michael. Energy Efficient Engine Fan Component Detailed Design Report. NASA, CR-165466. NASA: Lewis Research Center, Cleveland, OH, USA.
- 52 **Koch (1981)**: C. C. Koch. Stalling Pressure Rise Capability of Axial Flow Compressor Stages. *J. Eng. Power*, 103(4), 645-656. doi: 10.1115/1.3230787.
- 53 **Holloway et al. (1982)**: P. R. Holloway, G. L. Knight, C. C. Koch, and S. J. Shaffer. Energy Efficient Engine: High Pressure Compressor Detail Design Report. NASA, CR-165558. NASA: Lewis Research Center, Cleveland, OH, USA.
- 54 **Kacker et al. (1982)**: S. C. Kacker and U. Okapuu. A Mean Line Prediction Method for Axial Flow Turbine Efficiency. *J. Eng. Power*, 104(1), 111-119. doi: 10.1115/1.3227240.
- 55 **Steinke (1982)**: R. J. Steinke. A Computer Code for Predicting Multistage Axial-Flow Compressor Performance by a Meanline Stage-Stacking Method. NASA, TP-2020. NASA: Lewis Research Center, Cleveland, OH, USA.
- 56 **Torenbeek (1982)**: E. Torenbeek. Synthesis of Subsonic Airplane Design (1982 ed.). Springer, Dordrecht, Netherlands. ISBN: 978-90-481-8273-2.
- 57 **Bridgeman et al. (1983)**: M. J. Bridgeman, D. G. Cherry, and J. Pedersen. NASA/GE Energy Efficient Engine Low Pressure Turbine Scaled Test Vehicle Performance Report. NASA, CR-168290. NASA: Lewis Research Center, Cleveland, OH, USA.
- 58 **Cline et al. (1983)**: S. J. Cline, W. Fesler, H. S. Liu, R. C. Lovell, and S. J. Shaffer. Energy Efficient Engine: High Pressure Compressor Component Performance Report. NASA, CR-168245. NASA: Lewis Research Center, Cleveland, OH, USA.
- 59 **Fishbach (1983)**: L. H. Fishbach. PREWATE-An Interactive Preprocessing Computer Code to the Weight Analysis of Turbine Engines (WATE) Computer Code. NASA, TM-83545. NASA: Lewis Research Center, Cleveland, OH, USA.
- 60 **Loewenthal (1984)**: S. H. Loewenthal. Design of Power-Transmitting Shafts. NASA, RP 1123. NASA: Lewis Research Center, Cleveland, OH, USA.
- 61 **Schweitzer et al. (1984)**: J. K. Schweitzer and J. E. Garberoglio. Maximum Loading Capability of Axial Flow Compressors. *J. Aircraft*, 21(8), 593-600. doi: 10.2514/3.45028.
- 62 **Timko (1984)**: L. P. Timko. Energy Efficient Engine High Pressure Turbine Component Test Performance Report. NASA, CR-168289. NASA: Lewis Research Center, Cleveland, OH, USA.
- 63 **Davis et al. (1985)**: D. Y. Davis and E. M. Stearns. Energy Efficient Engine: Flight Propulsion System Final Design and Analysis. NASA, CR-168219. NASA: Lewis Research Center, Cleveland, OH, USA.
- 64 **Daini (1986)**: A. J. Al-Daini. Loss and Deviation Model for a Compressor Blade Element. *Int. J. Heat and Fluid Flow*, 7(1), 69-78. doi: 10.1016/0142-727X(86)90046-9.

- 65 **Steinke (1986)**: R. J. Steinke. Design of 9.271-Pressure-Ratio Five-Stage Core Compressor and Overall Performance for First Three Stages. NASA, TP 2597. NASA: Lewis Research Center, Cleveland, OH, USA.
- 66 **AGARD (1987)**: Advisory Group for Aerospace Research & Development. Application of Modified Loss and Deviation Correlations to Transonic Axial Compressors. AGARD-R-745.
- 67 **Casey (1987)**: M. V. Casey. A Mean Line Prediction Method for Estimating the Performance Characteristics of an Axial Compressor Stage. Proc. IMechE: C264/87, 273-285.
- 68 **Dominy (1987)**: J. Dominy. Transmission Efficiency in Advanced Aerospace Powerplant. Proceedings of the 23rd Joint Propulsion Conference, San Diego, CA, USA, 29 June-2 July 1987. AIAA-87-2043. doi: 10.2514/6.1987-2043.
- 69 **Miller et al. (1987)**: D. C. Miller and D. L. Wasdell. Off-Design Prediction of Compressor Blade Losses. Proc. IMechE: C279/87, 249-260.
- 70 **Borradaile (1988)**: J. A. Borradaile. Towards the Optimum Ducted UHBR Engine. Proceedings of the 24th Joint Propulsion Conference, Boston, MA, USA, 11-13 July 1988. AIAA-88-2954. doi: 10.2514/6.1988-2954.
- 71 **Cetin et al. (1989)**: M. Cetin, A. S. Ucer, Ch. Hirsch, and G. K. Serovy. An Off-Design Loss and Deviation Prediction Study for Transonic Axial Compressors. Proceedings of the ASME Gas Turbine and Aeroengine Congress and Exposition 1989, Toronto, Ontario, Canada, 4-8 June 1989. 89-GT-324. doi: 10.1115/89-GT-324.
- 72 **Cumpsty (1989)**: N. A. Cumpsty. Compressor Aerodynamics (1989 ed.). Longman Ltd., Harlow, UK. ISBN: 0-582-01364-X.
- 73 **Lim et al. (1989)**: J. S. Lim and M. K. Chung. Design Point Optimization of an Axial-Flow Compressor Stage. Int. J. Heat and Fluid Flow, 10(1), 48-58. doi: 10.1016/0142-727X(89)90054-4.
- 74 **Honami et al. (1990)**: S. Honami and T. Morioka. Flow Behavior in a Dump Diffuser with Distorted Flow at the Inlet. Proceedings of the ASME Gas Turbine and Aeroengine Congress and Exposition, Brussels, Belgium, 11-14 June 1990. 90-GT-90. doi: 10.1115/90-GT-090.
- 75 **Mellor (1990)**: A. M. Mellor. Design of Modern Turbine Combustors (1990 ed.). Academic Press Ltd., San Diego, CA, USA. ISBN: 0-12-490055-0.
- 76 **Zimbrick et al. (1990)**: R. A. Zimbrick and J. L. Colehour. Investigation of Very High Bypass Ratio Engines for Subsonic Transports. J. Propulsion, 6(4), 490-496. doi: 10.2514/3.25461.
- 77 **Wright et al. (1991)**: P. I. Wright and D. C. Miller. An Improved Compressor Performance Prediction Model. Proc. IMechE: C423/028, 69-82.
- 78 **Glassman (1992a)**: A. J. Glassman. Users Manual for Updated Computer Code for Axial-Flow Compressor Conceptual Design. NASA, CR-189171. NASA: Lewis Research Center, Cleveland, OH, USA.

- 79 **Glassman (1992b)**: A. J. Glassman. Computer Code for Preliminary Sizing Analysis of Axial-Flow Turbines. NASA, CR-4430. NASA: Lewis Research Center, Cleveland, OH, USA.
- 80 **Freeman et al. (1992)**: C. Freeman and N. A. Cumpsty. Method for the Prediction of Supersonic Compressor Blade Performance. *J. Propulsion*, 8(1), 199-208. doi: 10.2514/3.23461.
- 81 **Kerrebrock (1992)**: J. L. Kerrebrock. Aircraft Engines and Gas Turbines. MIT Press Ltd., Cambridge, MA, USA. ISBN: 0-262-11162-4.
- 82 **Raymer (1992)**: D. P. Raymer. Aircraft Design: A Conceptual Approach (2nd ed.). AIAA, Renton, DC, USA. ISBN: 0-930403-51-7.
- 83 **Denton (1993)**: J. D. Denton. Loss Mechanisms in Turbomachines. Proceedings of the ASME International Gas Turbine and Aeroengine Congress and Exhibition 1993, Cincinnati, OH, USA, 24-27 May 1993. 93-GT-435. doi: 10.1115/93-GT-435.
- 84 **Glassman (1993)**: A. J. Glassman. Blading Models for TURBAN and CSPAN Turbomachine Design Codes. NASA, CR-191164. NASA: Lewis Research Center, Cleveland, OH, USA.
- 85 **Glassman (1994)**: A. J. Glassman. Enhanced Capabilities and Updated Users Manual for Axial-Flow Turbine Preliminary Sizing Code TURBAN. NASA, CR-195405. NASA: Lewis Research Center, Cleveland, OH, USA.
- 86 **Konig et al. (1994a)**: W. M. Konig, D. K. Hennecke, and L. Fottner. Improved Blade Profile Loss and Deviation Models for Advanced Transonic Compressor Bladings: Part I-A Model for Subsonic Flow. Proceedings of the ASME International Gas Turbine and Aeroengine Congress and Exhibition 1994, The Hague, Netherlands, 13-16 June 1994. 94-GT-335. doi: 10.1115/94-GT-335.
- 87 **Konig et al. (1994b)**: W. M. Konig, D. K. Hennecke, and L. Fottner. Improved Blade Profile Loss and Deviation Models for Advanced Transonic Compressor Bladings: Part I-A Model for Supersonic Flow. Proceedings of the ASME International Gas Turbine and Aeroengine Congress and Exhibition 1994, The Hague, Netherlands, 13-16 June 1994. 94-GT-336. doi: 10.1115/94-GT-336.
- 88 **Mathioudakis et al. (1994)**: K. Mathioudakis and A. Stamatis. Compressor Fault Identification from Overall Performance Data Based on Adaptive Stage Stacking. *J. Eng. Gas Turbines Power*, 116(1), 156-164. doi: 10.1115/1.2906785.
- 89 **Tsalavoutas et al. (1994)**: A. Tsalavoutas, A. Stamatis, and K. Mathioudakis. Derivation of Compressor Stage Characteristics, for Accurate Overall Performance Map Prediction. Proceedings of the ASME International Gas Turbine and Aerospace Congress and Exposition 1994, The Hague, Netherlands, 13-16 June 1994. 94-GT-372. doi: 10.1115/94-GT-372.
- 90 **AGARD (1995)**: Advisory Group for Aerospace Research & Development. Recommended Practices for the Assessment of the Effects of Atmospheric Water Ingestion on the Performance and Operability of Gas Turbine Engines. AGARD-AR-332.

- 91 **Armand (1995)**: S. C. Armand. Structural Optimization Methodology for Rotating Disks of Aircraft Engines. NASA TM 4693. NASA: Lewis Research Center, Cleveland, OH, USA.
- 92 **Glassman et al. (1995)**: A. J. Glassman and T. M. Lavelle. Enhanced Capabilities and Modified Users Manual for Axial-Flow Compressor Conceptual Design Code CSPAN. NASA, TM 106833. NASA: Lewis Research Center, Cleveland, OH, USA.
- 93 **Dunham (1996)**: J. Dunham. Compressor Off-Design Performance Prediction Using an Endwall Model. Proceedings of the ASME International Gas Turbine and Aeroengine Congress and Exhibition 1996, Birmingham, UK, 10-13 June 1996. 96-GT-62. doi: 10.1115/96-GT-062.
- 94 **Lewis (1996)**: R. I. Lewis. Turbomachinery Performance Analysis (1996 ed.). Elsevier, Oxford, UK. ISBN: 0340631910.
- 95 **Rolls-Royce plc (1996)**: Rolls-Royce plc. The Jet Engine (5th ed.). Rolls-Royce plc. ISBN: 0902121-235.
- 96 **McKenzie (1997)**: A. B. McKenzie. Axial Flow Fans and Compressors (1997 ed.). Ashgate Ltd., Burlington, VT, USA. ISBN: 0-29139-850-2.
- 97 **SAE (1997)**: SAE Aerospace Standard. Aircraft Propulsion System Performance Station Designation and Nomenclature. SAE AS755 (Rev. C).
- 98 **Schobeiri (1997a)**: M. T. Schobeiri. Advanced Compressor Loss Correlations, Part I: Theoretical Aspects. Int. J. Rotating Machinery, 3(3), 163-177. doi: 10.1155/S1023621X9700016X.
- 99 **Schobeiri (1997b)**: M. T. Schobeiri. Advanced Compressor Loss Correlations, Part II: Experimental Verifications. Int. J. Rotating Machinery, 3(3), 179-187. doi: 10.1155/S1023621X97000171.
- 100 **Tannehill et al. (1997)**: J. C. Tannehill, D. A. Anderson, and R. H. Pletcher. Computational Fluid Mechanics and Heat Transfer (2nd ed.). Taylor and Francis Inc., Washington, DC, USA. ISBN: 1-56032-046-X.
- 101 **Dixon (1998)**: S. L. Dixon. Fluid Mechanics and Thermodynamics of Turbomachinery (4th ed.). Elsevier, Oxford, UK. ISBN: 0-7506-7059-2.
- 102 **Shanghi et al. (1998)**: V. Shanghi, S. S. Kumar, V. Sundararajan, and S. K. Sane. Preliminary Estimation of Engine Gas-Flow-Path Size and Weight. J. Propulsion and Power, 14(2), 208-214. doi: 10.2514/2.5269.
- 103 **Bloch et al. (1999)**: G. S. Bloch, W. W. Copenhaver, and W. F. O'Brien. A Shock Loss Model For Supersonic Compressor Cascades. J. Turbomach. 121(1), 28-35. doi: 10.1115/1.2841231.
- 104 **Gallimore (1999)**: S. J. Gallimore. Axial Flow Compressor Design. Proc. IMechE Part C: J. Mechanical Engineering Science, 213(5), 437-449. doi: 10.1243/0954406991522680.
- 105 **Jenkinson et al. (1999)**: L. R. Jenkinson, P. Simpkin, and D. Rhodes. Civil Jet Aircraft Design (1999 ed.). Elsevier, Oxford, UK. ISBN: 0-340-74152-X.

- 106 **Smith (1999)**: S. L. Smith. One-Dimensional Mean Line Code Technique to Calculate Stage-by-Stage Compressor Characteristics. MSc Thesis, University of Tennessee, USA.
- 107 **Papailiou et al. (2000)**: K. Papailiou, K. Mathioudakis, and K. Giannakoglou. Introduction to Thermal Turbomachines. Lectures' textbook from the Laboratory of Thermal Turbomachines, National Technical University of Athens, Greece (in Greek).
- 108 **Svoboda (2000)**: C. Svoboda. Turbofan Engine Database as a Preliminary Design Tool. *J. Aircraft Design*, 3(1), 17-31. doi: 10.1016/S1369-8869(99)00021-X.
- 109 **European Commission (2001)**: Report of the Group of Personalities. European Aeronautics: A Vision for 2020.
- 110 **Guha (2001)**: A. Guha. Optimisation of Aero Gas Turbine Engines. *The Aeronautical Journal*, 105(1049), 345-358. doi: 10.1017/S0001924000012264.
- 111 **Jeschke et al. (2002)**: P. Jeschke, J. Kurzke, R. Schaber, and C. Riegler. Preliminary Gas Turbine Design Using the Multidisciplinary Design System MOPEDS. Proceedings of the ASME Turbo Expo 2002, Amsterdam, The Netherlands, 3-6 June 2002. GT-2002-30496. doi: 10.1115/GT2002-30496.
- 112 **Jones et al. (2002)**: M. J. Jones, S. J. Bradbrook, and K. Nurvey. A Preliminary Engine Design Process for an Affordable Capability. Proceedings of the RTO AVT Symposium 2002, Paris, France, 22-25 April 2002. RTO-MP-089/52-1-22.
- 113 **Kurzke (2002)**: J. Kurzke. Performance Modeling Methodology: Efficiency Definitions for Cooled Single and Multistage Turbines. Proceedings of the ASME Turbo Expo 2002, Amsterdam, The Netherlands, 3-4 June 2002. GT-2002-30497. doi: 10.1115/GT2002-30497.
- 114 **Mattingly et al. (2002)**: J. D. Mattingly, W. H. Heiser, and D. T. Pratt. *Aircraft Engine Design* (2nd ed.). AIAA, Renton, VA, USA. ISBN: 1-56347-538-3.
- 115 **Panchenko et al. (2002)**: Y. Panchenko, H. Moustapha, S. Mah, K. Patel, M. J. Dowhan, and D. Hall. Preliminary Multi-Disciplinary Optimization in Turbomachinery Design. Proceedings of the RTO AVT Symposium 2002, Paris, France, 22-25 April 2002. RTO-MP-089/57-1-22.
- 116 **White et al. (2002)**: N. M. White, A. Tournlidakis, and R. L. Elder. Axial Compressor Performance Modelling with a Quasi-One-Dimensional Approach. *Proc. IMechE Part A: J. Power and Energy*, 216(2), 181-193. doi: 10.1243/09576500260049197.
- 117 **Aungier (2003)**: R. H. Aungier. *Axial-Flow Compressors: A Strategy for Aerodynamic Design and Analysis* (2003 ed.). ASME Press, NY, USA. ISBN: 0-7918-0192-6.
- 118 **Cumpsty (2003)**: N. Cumpsty. *Jet Propulsion: A Simple Guide to the Aerodynamic and Thermodynamic Design and Performance of Jet Engines* (2nd ed.). Cambridge University Press, Cambridge, UK. ISBN: 978-0-521-54144-2.

- 119 **Daggett et al. (2003)**: D. L. Daggett, S. T. Brown, and R. T. Kawai. Ultra-Efficient Engine Diameter Study. NASA, CR-2003-212309. NASA: Glenn Research Center, Cleveland, OH, USA.
- 120 **Ugural et al. (2003)**: A. C. Ugural and S. K. Fenster. Advanced Strength and Applied Elasticity (4th ed.). Prentice Hall, NJ, USA. ISBN: 0-13-047392-8.
- 121 **Grieb (2004)**: H. Grieb. Projektierung von Turboflugtriebwerken. Birkhauser Verlag, Basel, Switzerland. ISBN: 3-7643-6023-2.
- 122 **Gunston (2004)**: B. Gunston (ed.). Jane's Aero-Engines. Jane's Information Group Ltd., Surrey, UK, ISBN: 0-7106-1405-5.
- 123 **Tong et al. (2004)**: M. T. Tong, I. Halliwell, and L. J. Ghosn. A Computer Code for Gas Turbine Engine Weight and Disk Life Estimation. J. Eng. Gas Turbines Power, 126(2), 265-270. doi: 10.1115/1.1691980.
- 124 **Walsh et al. (2004)**: P. P. Walsh and P. Fletcher. Gas Turbine Performance (2nd ed.). ASME Press, NY, USA. ISBN: 0-632-06434-X.
- 125 **Alexiou et al. (2005)**: A. Alexiou and K. Mathioudakis. Development of Gas Turbine Performance Models Using a Generic Simulation Tool. Proceedings of the ASME Turbo Expo 2005, Reno-Tahoe, NV, USA, 6-9 June 2005. GT2005-68678. doi: 10.1115/GT2005-68678.
- 126 **Aungier (2005)**: R. H. Aungier. Turbine Aerodynamics: Axial-Flow and Radial-Inflow Turbine Design and Analysis (2005 ed.). ASME Press, NY, USA. ISBN: 0-7918-0241-8.
- 127 **Mattingly (2005)**: J. D. Mattingly. Elements of Gas Turbine Propulsion (2005 ed.). Tata McGraw-Hill Education Private Ltd., New Delhi, India. ISBN: 0-07-912196-9.
- 128 **Thomas (2005)**: K. D. Thomas. Blade Row and Blockage Modelling in an Axial Compressor Throughflow Code. MSc Thesis, University of Stellenbosch, South Africa.
- 129 **Wilcock et al. (2005)**: R. C. Wilcock, J. B. Young, and J. H. Horlock. The Effect of Turbine Blade Cooling on the Cycle Efficiency of Gas Turbine Power Cycles. J. Eng. Gas Turbines Power, 127(1), 109-120. doi: 10.1115/1.1805549.
- 130 **Wilfert et al. (2005)**: G. Wilfert, B. Kriegl, L. Wald, and O. Johanssen. CLEAN-Validation of a GTF High Speed Turbine and Integration of Heat Exchanger Technology in an Environmental Friendly Engine Concept. Proceedings of the 17th ISABE Conference, Munich, Germany, 4-9 September 2005. ISABE-2005-1156.
- 131 **Alexiou et al. (2006)**: A. Alexiou and K. Mathioudakis. Gas Turbine Engine Performance Model Application Using an Object-Oriented Simulation Tool. Proceedings of the ASME Turbo Expo 2006, Barcelona, Spain, 8-11 May 2006. GT2006-90339. doi: 10.1115/GT2006-90339.
- 132 **Calkins et al. (2006)**: Variable Geometry Chevrons for Jet Noise Reduction. Proceedings of the 12th AIAA/CEAS Aeroacoustics Conference (27th AIAA

- Aeroacoustics Conference), Cambridge, MA, USA, 8-10 May 2006. AIAA 2006-2546. doi: 10.2514/6.2006-2546.
- 133 **Hall et al. (2006):** C. A. Hall and D. Crichton. Engine Design Studies for a Silent Aircraft. Proceedings of the ASME Turbo Expo 2006, Barcelona, Spain, 8-11 May 2006. GT2006-90559. doi: 10.1115/GT2006-90559.
 - 134 **Pachidis et al. (2006):** V. Pachidis, P. Pilidis, I. Templalexis, T. Alexander, and P. Kotsiopoulos. Prediction of Engine Performance Under Compressor Inlet Flow Distortion Using Streamline Curvature. Proceedings of the ASME Turbo Expo 2006, Barcelona, Spain, 8-11 May 2006. GT2006-90806. doi: 10.1115/GT2006-90806.
 - 135 **Templalexis et al. (2006):** I. Templalexis, P. Pilidis, V. Pachidis, and P. Kotsiopoulos. Development of a 2-D Compressor Streamline Curvature Code. Proceedings of the ASME Turbo Expo 2006, Barcelona, Spain, 8-11 May 2006. GT2006-90867. doi: 10.1115/GT2006-90867.
 - 136 **Turner et al. (2006):** M. G. Turner, A. Merchant, and D. Bruna. A Turbomachinery Design Tool for Teaching Design Concepts for Axial-Flow Fans, Compressors, and Turbines. Proceedings of the ASME Turbo Expo 2006, Barcelona, Spain, 8-11 May 2006. GT2006-90105. doi: 10.1115/GT2006-90105.
 - 137 **Alexiou et al. (2007):** A. Alexiou, E. H. Baalbergen, O. Kogenhop, K. Mathioudakis, and P. Arendsen. Advanced Capabilities for Gas Turbine Engine Performance Simulations. Proceedings of the ASME Turbo Expo 2007, Montreal, Canada, 14-17 May 2007. GT2007-27086. doi: 10.1115/GT2007-27086.
 - 138 **Avellan et al. (2007):** R. Avellan and T. Gronstedt. Preliminary Design of Subsonic Transport Aircraft and Engines. Proceedings of the 18th ISABE Conference, Beijing, China, 2-7 September 2007. ISABE-2007-1195.
 - 139 **Bretschneider et al. (2007):** S. Bretschneider, S. Staudacher, and O. Arago. Architecture of a Techno-Economic and Environmental Risk Assessment Tool Using a Multi-Modular Build Approach. Proceedings of the 18th ISABE Conference, Beijing, China, 2-7 September 2007. ISABE-2007-1103.
 - 140 **Bruna et al. (2007):** D. Bruna, M. G. Turner, and A. Merchant. An Educational Software Suite for Teaching Design Strategies for Multistage Axial Flow Compressors. Proceedings of the ASME Turbo Expo 2007, Montreal, Canada, 14-17 May 2007. GT2007-27160. doi: 10.1115/GT2007-27160.
 - 141 **Kurzke (2007):** J. Kurzke. GasTurb Details 5: An Utility for GasTurb 11. GasTurb Details 5 Software Manual. GasTurb GmbH, Aachen, Germany.
 - 142 **Press et al. (2007):** W. H. Press, S. A. Teukolsky, W. T. Vetterling, and B. P. Flannery. Numerical Recipes: The Art of Scientific Computing (3rd ed.). Cambridge University Press, Cambridge, UK. ISBN-13: 978-0-521-88068-8.
 - 143 **Turner et al. (2007):** M. G. Turner, A. Merchant, and D. Bruna. Applications of a Turbomachinery Design Tool for Compressors and Turbines. Proceedings of the 43rd AIAA/ASME/SAE/ASEE Joint Propulsion Conference & Exhibit, Cincinnati, OH, USA, 8-11 July 2007. AIAA 2007-5152. doi: 10.2514/6.2007-5152.

- 144 **Alexiou et al. (2008)**: A. Alexiou and K. Mathioudakis. Secondary Air System Component Modelling for Engine Performance Simulations. Proceedings of the ASME Turbo Expo 2008, Montreal, Canada, 9-13 June 2008. GT2008-50771. doi: 10.1115/GT2008-50771.
- 145 **Arolla et al. (2008)**: S. K. Arolla, G. Jothiprasad, T. H. Wood, and A. B.-Stringfellow. Reduced Order Modeling of Choked Blade-Rows in Axial Flow Compressors. Proceedings of the International Conference on Aerospace Science and Technology, Bangalore, India, 26–28 June 2008. INCAST 2008-002.
- 146 **Bretschneider et al. (2008)**: S. Bretschneider, F. Rothe, M. G. Rose, and S. Staudacher. Compressor Casing Preliminary Design Based on Features. Proceedings of the ASME Turbo Expo 2008, Berlin, Germany 9-13 June 2008. GT2008-50102. doi: 10.1115/GT2008-50102.
- 147 **Dahlquist (2008)**: A. N. Dahlquist. Investigation of Losses Prediction Methods in 1D for Axial Gas Turbines. MSc Thesis, University of Lund, Sweden.
- 148 **Falck (2008)**: N. Falck. Axial Flow Compressor Mean Line Design. MSc Thesis, University of Lund, Sweden.
- 149 **Kirby et al. (2008)**: M. R. Kirby and D. N. Mavris. The Environmental Design Space. Proceedings of the 26th International Congress of the Aeronautical Sciences, Anchorage, AK, USA, 14-19 September 2008. ICAS-2008-4.7.3.
- 150 **Kyprianidis et al. (2008)**: K. G. Kyprianidis, R. F. C. Quintero, D. S. Pascovici, S. O. T. Ogaji, P. Pilidis, and A. I. Kalfas. EVA-A Tool for Environmental Assessment of Novel Propulsion Cycles. Proceedings of the ASME Turbo Expo 2008, Berlin, Germany, 9-13 June 2008. GT2008-50602. doi: 10.1115/GT2008-50602.
- 151 **Madadi et al. (2008)**: A. Madadi and A. H. Benisi. Performance Predicting Modeling of Axial-Flow Compressor at Design and Off-Design Conditions. Proceedings of the ASME Turbo Expo 2008, Berlin, Germany, 9-13 June 2008. GT2008-50550. doi: 10.1115/GT2008-50550.
- 152 **Tong et al. (2008)**: M. T. Tong and B. A. Naylor. An Object-Oriented Computer Code for Aircraft Engine Weight Estimation. Proceedings of the ASME Turbo Expo 2008, Berlin, Germany, 9-13 June 2008. GT2008-50062. doi: 10.1115/GT2008-50062.
- 153 **Cumpsty (2009)**: N. A. Cumpsty. Preparing for the Future: Reducing gas Turbine Environmental Impact. Proceedings of the ASME Turbo Expo 2009, Orlando, FL, USA, 8-12 June 2009. GT2009-60367. doi: 10.1115/GT2009-60367.
- 154 **Gutzwiller (2009)**: D. Gutzwiller. Automated Design, Analysis, and Optimization of Turbomachinery Disks. MSc Thesis, University of Cincinnati, USA.
- 155 **Gutzwiller et al. (2009)**: D. P. Gutzwiller, M. G. Turner, and M. J. Downing. Educational Software for Blade and Disk Design. Proceedings of the ASME Turbo Expo 2009, Orlando, FL, USA, 8-12 June 2009. GT2009-59692. doi: 10.1115/GT2009-59692.

- 156 **Guynn et al. (2009)**: M. D. Guynn, J. J. Berton, K. L. Fisher, W. J. Haller, M. T. Tong, and D. R. Thruman. Engine Concept Study for an Advanced Single-Aisle Transport. NASA, TM-2009-215784. NASA: Langley Research Center, Hampton, VA, USA.
- 157 **Jackson (2009)**: A. J. B. Jackson. Optimisation of Aero and Industrial Gas Turbine Design for the Environment. PhD Thesis, Cranfield University, UK.
- 158 **Kelaidis et al. (2009)**: M. Kelaidis, N. Aretakis, A. Tsalavoutas, and K. Mathioudakis. Optimal Mission Analysis Accounting for Engine Aging and Emissions. *J. Eng. Gas Turbines Power*, 131(1), 011201 (10 pages). doi: 10.1115/1.2969095.
- 159 **Kurzke (2009)**: J. Kurzke. Fundamental Differences Between Conventional and Geared Turbofans. Proceedings of the ASME Turbo Expo 2009, Orlando, FL, USA, 8-12 June 2009. GT2009-59745. doi: 10.1115/GT2009-59745.
- 160 **Mohammad et al. (2009)**: B. S. Mohammad and S. M. Jeng. Design Procedures and a Developed Computer Code for Preliminary Single Annular Combustor Design. Proceedings of the 45th AIAA/ASME/SAE/ASEE Joint Propulsion Conference and Exhibit, Denver, CO, USA, 2-5 August 2009. AIAA-2009-5208. doi: 10.2514/6.2009-5208.
- 161 **Ogaji et al. (2009)**: S. Ogaji, P. Pilidis, and V. Sethi. Advanced Power Plant Selection: The TERA (Techno-economic Environmental Risk Analysis) Framework. Proceedings of the 19th ISABE Conference, Montreal, Canada, 7-11 September 2009. ISABE-2009-1115.
- 162 **Petrovic et al. (2009)**: M. V. Petrovic, A. Wiedermann, and M. B. Banjac. Development and Validation of a New Universal Through Flow Method for Axial Compressors. Proceedings of the ASME Turbo Expo 2009, Orlando, FL, USA, 8-12 June 2009. GT2009-59938. doi: 10.1115/GT2009-59938.
- 163 **Veres (2009)**: J. P. Veres. Axial and Centrifugal Compressor Mean Line Flow Analysis. Proceedings of the 47th AIAA Aerospace Sciences Meeting, Orlando, FL, USA, 5-8 January 2009. AIAA-2009-1641. doi: 10.2514/6.2009-1641.
- 164 **Alexiou et al. (2010)**: A. Alexiou, N. Aretakis, I. Roumeliotis, and K. Mathioudakis. Short and Long Range Mission Analysis for a Geared Turbofan with Active Core Technologies. Proceedings of the ASME Turbo Expo 2010, Glasgow, UK, 14-18 June 2010. GT2010-22701. doi: 10.1115/GT2010-22701.
- 165 **Berton et al. (2010)**: J. J. Berton and M. D. Guynn. Multi-Objective Optimization of Turbofan Design Parameters for an Advanced, Single-Aisle Transport. Proceedings of the 10th AIAA Aviation Technology, Integration, and Operations (ATIO) Conference, Fort Worth, TX, USA, 13-15 September 2010. AIAA-2010-9168. doi: 10.2514/6.2010-9168.
- 166 **Donus et al. (2010)**: F. Donus, R. Schaber, K.-J. Schmidt, and S. Staudacher. Accuracy of Analytical Engine Weight Estimation During the Conceptual Design Phase. Proceedings of the ASME Turbo Expo 2010, Glasgow, UK, 14-18 June 2010. GT2010-23774. doi: 10.1115/GT2010-23774.

- 167 **Gutzwiller et al. (2010a)**: D. P. Gutzwiller and M. G. Turner. Low Fidelity Turbomachinery Disk Design Studies. Proceedings of the ASME Turbo Expo 2010, Glasgow, UK, 14-18 June 2010. GT2010-22733. doi: 10.1115/GT2010-22733.
- 168 **Gutzwiller et al. (2010b)**: D. P. Gutzwiller and M. G. Turner. Rapid Low Fidelity Turbomachinery Disk Optimization. J. Advances in Engineering Software, 41(5), 779-791. doi: 10.1016/j.advengsoft.2009.12.019.
- 169 **Greitzer et al. (2010a)**: E. M. Greitzer, P. A. Bonney, E. R. Blanco, C. S. Dorbian, M. Drela, D. K. Hall, R. J. Hansman, J. L. Hileman, R. H. Liebeck, J. Lovegren, P. Mody, J. A. Pertuze, S. Sato, Z. S. Spakovszky, C. S. Tan, J. S. Hollman, J. E. Duda, N. Fitzgerald, J. Houghton, J. L. Kerrebrock, G. F. Kiwada, D. Kordonowy, J. C. Parrish, J. Tylko, E. A. Wen, and W. K. Lord. N+3 Aircraft Concept Designs and Trade Studies-Final Report, Vol. I. NASA, CR-2010-216794/VOL1. NASA: Glenn Research Center, Cleveland, OH, USA.
- 170 **Greitzer et al. (2010b)**: E. M. Greitzer, P. A. Bonney, E. R. Blanco, C. S. Dorbian, M. Drela, D. K. Hall, R. J. Hansman, J. L. Hileman, R. H. Liebeck, J. Lovegren, P. Mody, J. A. Pertuze, S. Sato, Z. S. Spakovszky, C. S. Tan, J. S. Hollman, J. E. Duda, N. Fitzgerald, J. Houghton, J. L. Kerrebrock, G. F. Kiwada, D. Kordonowy, J. C. Parrish, J. Tylko, E. A. Wen, and W. K. Lord. N+3 Aircraft Concept Designs and Trade Studies-Final Report, Vol. II. NASA, CR-2010-216794/VOL2. NASA: Glenn Research Center, Cleveland, OH, USA.
- 171 **Holman (2010)**: J. P. Holman. Heat Transfer (10th ed.). McGraw-Hill Inc., NY, USA. ISBN: 978-0-07-352936-3.
- 172 **Kundu (2010)**: A. K. Kundu. Aircraft Design (2010 ed.). Cambridge University Press, Cambridge, UK. ISBN-13: 978-0-521-88516-4.
- 173 **Kyprianidis (2010)**: K. G. Kyprianidis. Multi-Disciplinary Conceptual Design of Future Jet Engine Systems. PhD Thesis, Cranfield University, UK.
- 174 **Lefebvre et al. (2010)**: A. H. Lefebvre and D. R. Ballal. Gas Turbine Combustion: Alternative Fuels and Emissions (3rd ed.). CRC Press Inc., Boca Roca, USA, ISBN-13: 978-1-4200-8605-8.
- 175 **Mazzawy (2010)**: R. S. Mazzawy. Performance Study for Benefits of Variable Pitch Composite Fan. Proceedings of the ASME Turbo Expo 2010, Glasgow, UK, 14-18 June 2010. GT2010-22148. doi: 10.1115/GT2010-22148.
- 176 **Turner et al. (2010)**: M. G. Turner, K. Park, K. Siddappaji, S. Dey, D. P. Gutzwiller, A. Merchant, and D. Bruna. Framework for Multidisciplinary Optimization of Turbomachinery. Proceedings of the ASME Turbo Expo 2010, Glasgow, UK, 14-18 June 2010. GT2010-22228. doi: 10.1115/GT2010-22228.
- 177 **Violette et al. (2010)**: J. A. Violette and E. S. Loos. Mechanical Design of a Variable Pitch Fan for Turbofan Engines. Proceedings of the ASME Turbo Expo 2010, Glasgow, UK, 14-18 June 2010. GT2010-22969. doi: 10.1115/GT2010-22969.
- 178 **Boresi et al. (2011)**: A. P. Boresi, K. P. Chong, J. D. Lee. Elasticity in Engineering Mechanics (3rd ed.). Wiley and Sons Ltd., Hoboken, NJ, USA. ISBN: 978-0-470-40255-9.

- 179 **Dickens et al. (2011)**: T. Dickens and I. Day. The Design of Highly Loaded Axial Compressors. *J. Turbomach.*, 133(3), 031007 (10 pages). doi: 10.1115/1.4001226.
- 180 **Eftari et al. (2011)**: M. Eftari, H. J. Jouybari, M. R. Shahhoseini, F. Ghadak, and M. Rad. Performance Prediction Modeling of Axial-Flow Compressor by Flow Equations. *J. Mechanical Research and Application*, 3(1), 49-55. ISSN: 2251-7383.
- 181 **Felder et al. (2011)**: J. L. Felder, H. D. Kim, G. V. Brown, and J. Chu. An Examination of the Effect of Boundary Layer Ingestion on Turboelectric Distributed Propulsion Systems. Proceedings of the 49th AIAA Aerospace Sciences Meeting Including the New Horizons Forum and Aerospace Exposition, Orlando, FL, USA, 4-7 January 2011. AIAA-2011-300. doi: 10.2514/6.2011-300.
- 182 **Guynn et al. (2011)**: M. D. Guynn, J. J. Berton, K. L. Fisher, W. J. Haller, M. T. Tong, and D. R. Thurman. Refined Exploration of Turbofan Design Options for an Advanced Single-Aisle Transport. NASA, TM-2011-216883. NASA: Langley Research Center, Hampton, VA, USA.
- 183 **Larsson et al. (2011a)**: L. Larsson, R. Avellan, and T. Gronstedt. Mission Optimization of the Geared Turbofan Engine. Proceedings of the 20th ISABE Conference, Gothenburg, Sweden, 12-16 September 2011. ISABE-2011-1314.
- 184 **Larsson et al. (2011b)**: L. Larsson, T. Gronstedt, and K. G. Kyprianidis. Conceptual Design and Mission Analysis for a Geared Turbofan and an Open Rotor Configuration. Proceedings of the ASME Turbo Expo 2011, Vancouver, British Columbia, Canada, 6-10 June 2011. GT2011-46451. doi: 10.1115/GT2011-46451.
- 185 **Rousis (2011)**: D. A. Rousis. A Pareto Frontier Intersection-Based Approach for Efficient Multiobjective Optimization of Competing Concept Alternatives. PhD Thesis, Georgia Institute of Technology, USA.
- 186 **Alexiou et al. (2012)**: A. Alexiou, A. Tsalavoutas, B. Pons, N. Aretakis, I. Roumeliotis, and K. Mathioudakis. Assessing Alternative Fuels for Helicopter Operation. Proceedings of the ASME Turbo Expo 2012, Copenhagen, Denmark, 11-15 June 2012. GT2012-69417. doi: 10.1115/GT2012-69417.
- 187 **ACARE (2012)**: Advisory Group for Aerospace Research & Innovation in Europe. Strategic Research & Innovation Agenda, Volume 1.
- 188 **Guha et al. (2012)**: A. Guha, D. Boylan, and P. Gallagher. Determination of Optimum Specific Thrust for Civil Aero Gas Turbine Engines: A Multidisciplinary Design Synthesis and Optimisation. *Proc. IMechE Part G: J. Aerospace Engineering*, 227(3), 502-527. doi: 10.1177/0954410011435623.
- 189 **Hendricks et al. (2012)**: E. S. Hendricks and M. T. Tong. Performance and Weight Estimates for an Advanced Open Rotor Engine. NASA, TM-2012-217710. NASA: Glenn Research Center, Cleveland, OH, USA.
- 190 **Kurzke (2012)**: J. Kurzke. GasTurb 12 Design and Off-Design Performance of Gas Turbines. GasTurb 12 Software Manual. GasTurb GmbH: Aachen, Germany.

- 191 **McKay et al. (2012):** B. McKay and A. Barlow. The Ultrafan Engine and Aircraft Based Thrust Reversing. Proceedings of the 48th AIAA/ASME/SAE/ASEE Joint Propulsion Conference and Exhibit, Atlanta, GA, USA, 30 July-1 August 2012. AIAA-2012-3919. doi: 10.2514/6.2012-3919.
- 192 **Seitz (2012):** A. Seitz. Advanced Methods for Propulsion System Integration in Aircraft Conceptual Design. PhD Thesis, Technical University of Munich. Germany.
- 193 **Tomita et al. (2012):** J. T Tomita and. Numerical Tools for High Performance Axial Compressor Design for Teaching Purpose. Proceedings of the ASME Turbo Expo 2012, Copenhagen, Denmark, 11-15 June 2012. GT2012-69987. doi: 10.1115/GT2012-69987.
- 194 **Alexiou et al. (2013):** A. Alexiou, B. Pons, P. Cobas, and K. Mathioudakis. Helicopter Engine Optimization for Minimum Mission Fuel Burn. Proceedings of the 21st ISABE Conference, Busan, Korea, 9-13 September 2013. ISABE-2013-1427.
- 195 **Becker et al. (2013):** R. Becker, M. Schaefer, and S. Reitenbach. Assessment of the Efficiency Gains Introduced by Novel Aero Engine Concepts. Proceedings of the 21st ISABE Conference, Busan, Korea, 9-13 September 2013. ISABE-2013-1720.
- 196 **Giannakakis (2013):** P. Giannakakis. Design Space Exploration and Performance Modelling of Advanced Turbofan and Open-Rotor Engines. PhD Thesis, Cranfield University, UK.
- 197 **Krishnan et al. (2013):** G. Krishnan, C. A. Perullo, and D. N. Mavris. An Assessment of Relative Technology Benefits of a Variable Pitch Fan and Variable Area Nozzle. Proceedings of the 49th AIAA/ASME/SAE/ASEE Joint Propulsion Conference, San Jose, CA, USA, 14-17 July 2013. AIAA-2013-3604. doi: 10.2514/6.2013-3604.
- 198 **SAE (2013):** SAE Aerospace Recommended Practice. Gas Turbine Engine Performance Presentation and Nomenclature for Object-Oriented Computer Programs. SAE ARP5571 (Rev. C).
- 199 **Sethi et al. (2013):** V. Sethi, G. Doulgeris, P. Pilidis, A. Nind, M. Doussinault, P. Cobas, and A. Rueda. The Map Fitting Tool Methodology: Gas Turbine Compressor Off-Design Performance Modeling. *J. Turbomach.*, 135(6), 061010 (15 pages). doi: 10.1115/1.4023903.
- 200 **Zhu et al. (2013):** X. C. Zhu, J. F. Hu, H. Ou-Yang, J. Tian, X. Q. Qiang, and Z. H. Du. The Off-Design Performance Prediction of Axial Compressor Based on a 2D Approach. *J. Theoretical Applied Mechanics*, 51(3), 523-531.
- 201 **Alexiou (2014):** A. Alexiou. TURBO 4.0 Library Reference Manual (4th ed.). Empresarios Agrupados International (EAI) SA.
- 202 **Aretakis et al. (2014):** N. Aretakis, I. Roumeliotis, A. Alexiou, C. Romesis, and K. Mathioudakis. Turbofan Engine Health Assessment from Flight Data. Proceedings of the ASME Turbo Expo 2014, Dusseldorf, Germany, 16-20 June 2014. GT2014-26443. doi: 10.1115/GT2014-26443.

- 203 **Banjac et al. (2014)**: M. Banjac, M. V. Petrovic, and A. Wiedermann. A New Loss and Deviation Model for Axial Compressor Inlet Guide Vanes. *J. Turbomach.*, 136(7), 071011 (13 pages). doi: 10.1115/1.4025956.
- 204 **Bijewitz et al. (2014)**: J. Bijewitz, A. Seitz, and M. Hornung. Architectural Comparison of Advanced Ultra-High Bypass Ratio Turbofans for Medium to Long Range Application. Deutscher Luft- und Raumfahrtkongress 2014. DLR-340105.
- 205 **Callister et al. (2014)**: W. D. Callister and D. G. Rethwisch. *Material Science and Engineering: An Introduction* (9th ed.). John Wiley and Sons Inc., NY, USA. ISBN: 978-1-118-32457-8.
- 206 **Dixon et al. (2014)**: S. L. Dixon and C. A. Hall. *Fluid Mechanics and Thermodynamics of Turbomachinery* (7th ed.). Elsevier, Woburn, MA, USA. ISBN: 978-0-12-415954-9.
- 207 **Epstein (2014)**: A. H. Epstein. Aeropropulsion for Commercial Aviation in the Twenty-First Century and Research Directions Needed. *J. Aeronautics and Astronautics*, 52(5), 901-911. doi: 10.2514/1.J052713.
- 208 **Jones (2014)**: S. M. Jones. Development of an Object-Oriented Turbomachinery Analysis Code Within the NPSS Framework. NASA, TM-2014-216621. NASA: Glenn Research Center, Cleveland, OH, USA.
- 209 **Kyprianidis et al. (2014)**: K. G. Kyprianidis and A. M. Rolt. On the Optimization of a Geared Fan Intercooled Core Engine Design. Proceedings of the ASME Turbo Expo 2014, Dusseldorf, Germany, 16-20 June 2014. GT2014-22064. doi: 10.1115/GT2014-22064.
- 210 **Leylekian et al. (2014)**: L. Leylekian, M. Lebrun, and P. Lempereur. An Overview of Aircraft Noise Reduction Technologies. *Onera J. AerosaceLab*, 7, 15 pages.
- 211 **Lolis (2014)**: P. Lolis. Development of a Preliminary Weight Estimation Method for Advanced Turbofan Engines. PhD Thesis, Cranfield University, UK.
- 212 **Banjac et al. (2015)**: M. Banjac, M. V. Petrovic, and A. Wiedermann. Secondary Flows, Endwall Effects, and Stall Detection in Axial Compressor Design. *J. Turbomach.* 137(5), 051004 (12 pages). doi: 10.1115/1.4028648.
- 213 **Becker et al. (2015)**: R.-G. Becker, S. Reitenbach, C. Klein, T. Otten, M. Nauroz, and M. Siggel. An Integrated Method for Propulsion System Conceptual Design. Proceedings of the ASME Turbo Expo 2015, Montreal, Canada, 15-19 June 2015. GT2015-43251. doi: 10.1115/GT2015-43251.
- 214 **Bellocq et al. (2015)**: P. Bellocq, I. Garmendia, and V. Sethi. Preliminary Design Assessments of Pusher Geared Counter-Rotating Open Rotors-Part I: Low Pressure System Design Choices, Engine Preliminary Design Philosophy and Modelling Methodology. Proceedings of the ASME Turbo Expo 2015, Montreal, Canada, 15-19 June 2015. GT2015-43812. doi: 10.1115/GT2015-43812.
- 215 **Cengel et al. (2015)**: Y. A. Cengel and A. J. Ghajar. *Heat and Mass Transfer: Fundamentals and Applications* (5th ed.). McGraw-Hill Inc., Singapore, Singapore. ISBN: 978-0-07-339818-1.

- 216 **Jones (2015)**: S. M. Jones. Design of an Object-Oriented Turbomachinery Analysis Code: Initial Results. Proceedings of the 22nd ISABE Conference, Phoenix, AZ, USA, 25-30 October 2015. ISABE-2015-20015.
- 217 **Samuelsson et al. (2015)**: S. Samuelsson, K. G. Kyprianidis, and T. Gronstedt. Consistent Conceptual Design and Performance Modeling of Aero Engines. Proceedings of the ASME Turbo Expo 2015, Montreal, Canada, 15-19 June 2015. GT2015-43331. doi: 10.1115/GT2015-43331.
- 218 **Schnoes et al. (2015)**: M. Schnoes and E. Nicke. Automated Calibration of Compressor Loss and Deviation Correlations. Proceedings of the ASME Turbo Expo 2015, Montreal, Canada, 15-19 June 2015. GT2015-42644. doi: 10.1115/GT2015-42644.
- 219 **Sieber (2015)**: J. Sieber. European Technology Programs for Eco-Efficient Ducted Turbofans. Proceedings of the 22nd ISABE Conference, Phoenix, AZ, USA, 25-30 October 2015. ISABE-2015-20029.
- 220 **Sun et al. (2015)**: X. Sun, S. Yang, and Q. Zhao. Shock Loss Model and Blade Profile Optimization Design of a Supersonic Cascade. Proc. IMechE Part G: J. Aerospace Engineering, 229(7), 1325-1329. doi: 10.1177/0954410014550050.
- 221 **Hendricks (2016)**: E. S. Hendricks. Meanline Analysis of Turbines with Choked Flow in Object-Oriented Turbomachinery Analysis Code. Proceedings of the 54th AIAA Aerospace Sciences Meeting, San Diego, CA, USA, 4-8 January 2016. AIAA-2016-0119. doi: 10.2514/6.2016-0119.
- 222 **Kalathakis et al. (2016a)**: C. Kalathakis, N. Aretakis, I. Roumeliotis, A. Alexiou, and K. Mathioudakis. Assessment of Solar Steam Injection in Gas Turbines. Proceedings of the ASME Turbo Expo 2016, Seoul, South Korea, 13-17 June 2016. GT2016-57272. doi: 10.1115/GT2016-57272.
- 223 **Kalathakis et al. (2016b)**: C. Kalathakis, N. Aretakis, I. Roumeliotis, A. Alexiou, and K. Mathioudakis. Investigation of Different Solar Hybrid Gas Turbines and Exploitation of Rejected Sun Power. Proceedings of the ASME Turbo Expo 2016, Seoul, South Korea, 13-17 June 2016. GT2016-57700. doi: 10.1115/GT2016-57700.
- 224 **Mathioudakis (2016)**: K. Mathioudakis. Introduction to Aircraft Engines. Lectures' textbook from the Laboratory of Thermal Turbomachines, National Technical University of Athens, Greece (in Greek).
- 225 **Pantalone et al. (2016)**: G. Pantalone, E. Blanco, and K. Willcox. TASOPT Engine Model Development. PARTNER Project 48 Report, PARTNER-COE-2016-004.
- 226 **Peyvan et al. (2016)**: A. Peyvan and A. H. Benisi. Axial-Flow Compressor Performance Prediction in Design and Off-Design Conditions Through 1-D and 3-D Modeling and Experimental Study. J. Applied Fluid Mechanics, 9(5), 2149-2160. doi: acadpub.jafm.68.236.25222.
- 227 **Templalexis et al. (2016)**: I. Templalexis, A. Alexiou, V. Pachidis, I. Roumeliotis, and N. Aretakis. Direct Coupling of a Two-Dimensional Fan Model in a Turbofan Engine Performance Simulation. Proceedings of the ASME Turbo Expo 2016,

- Seoul, South Korea, 13-17 June 2016. GT2016-56617. doi: 10.1115/GT2016-56617.
- 228 **Tiemstra (2016)**: J. C. Tiemstra. On the Conceptual Engine Design and Sizing Tool. MSc Thesis, TU Delft University of Technology, Netherlands.
- 229 **Rozendaal (2016)**: A. V. Rozendaal. A Computer Program for the Coupled Implementation of Meanline and Throughflow Methods to Simplify the Aerodynamic Design of Multistage Axial Compressors. MSc Thesis, Embry-Riddle Aeronautical University, USA.
- 230 **White (2016)**: F. M. White. Fluid Mechanics (8th ed.). McGraw-Hill Inc., NY, USA. ISBN: 978-0-07-339827-3.
- 231 **Xiaoxiong et al. (2016)**: W. Xiaoxiong, B. Liu, S. Lei, Z. Guochen, and M. Xiaochen. Development of an Improved Streamline Curvature Approach for Transonic Axial Compressor. Proceedings of the ASME Turbo Expo 2016, Seoul, South Korea, 13-17 June 2016. GT2016-57072. doi: 10.1115/GT2016-57072.
- 232 **Alexiou et al. (2017)**: A. Alexiou, N. Aretakis, I. Roumeliotis, I. Koliass, and K. Mathioudakis. Performance Modelling of an Ultra-High Bypass Ratio Geared Turbofan. Proceedings of the 23rd ISABE Conference, Manchester, UK, 3-8 September 2017. ISABE-2017-22512.
- 233 **Chaquet et al. (2017)**: J. M. Chaquet, R. Corral, and A. Fernandez. Accurate Method to Reproduce Throughflow Results with a Meanline Solver. Proceedings of the ASME Turbo Expo 2017, Charlotte, NC, USA, 26-30 June 2017. GT2017-63153. doi: 10.1115/GT2017-63153.
- 234 **Denton (2017)**: J. D. Denton. MULTALL-An Open Source, CFD Based, Turbomachinery Design System. Proceeding of the ASME Turbo Expo 2017, Charlotte, NC, USA, 26-30 June 2017. GT2017-63993. doi: 10.1115/GT2017-63993.
- 235 **El-Sayed (2017)**: A. F. El-Sayed. Aircraft Propulsion and Gas Turbine Engines (2nd ed.). CRC Press Inc., Boca Roca, USA, ISBN: 978-1-4665-9516-3.
- 236 **Jones et al. (2017)**: S. M. Jones, W. J. Haller, and M. T. Tong. An N+3 Technology Level Reference Propulsion System. NASA, TM-2017-219501. NASA: Glenn Research Center, Cleveland, OH, USA.
- 237 **Kalathakis et al. (2017)**: C. Kalathakis, N. Aretakis, I. Roumeliotis, A. Alexiou, and K. Mathioudakis. Concentrated Solar Power Components Toolbox in an Object Oriented Environment. J. Simulation Modelling Practice and Theory, 70, 21-35. doi: 10.1016/j.simpat.2016.10.002.
- 238 **Kyprianidis et al. (2017)**: G. K. Kyprianidis and E. Dahlquist. On the Trade-Off Between Aviation NO_x and Energy Efficiency. J. Applied Energy, 185(2), 1506-1516. doi: 10.1016/j.apenergy.2015.12.055.
- 239 **Liu et al. (2017a)**: B. Liu, H. Shi, and X. Yu. A New Method for Rapid Shock Loss Evaluation and Reduction for the Optimization Design of a Supersonic Cascade.

- Proc. IMechE Part G: J. Aerospace Engineering, 0(0), 1-19. doi: 10.1177/0954410017715277.
- 240 **Liu et al. (2017b)**: B. Liu, D. Fu, and X. Yu. Development of a Preliminary Design Method for Subsonic Splittered Blades in Highly Loaded Axial-Flow Compressors. *Appl. Sci.*, 7(3), 22 pages. doi: 10.3390/app7030283.
- 241 **Mishra et al. (2017)**: A. Mishra, Y. Neumeier, J. V. R. Prasad, and D. K. James. Modelling of Multistage Axial Compressor Using Successive Diffusers with Velocity Sources: Part I-Steady State Results. Proceedings of the 53rd AIAA/SAE/ASEE Joint Propulsion Conference, Atlanta, GA, USA, 10-12 July 2017. AIAA 2017-4734. doi: 10.2514/6.2017-4734.
- 242 **Saravanamuttoo et al. (2017)**: H. I. H. Saravanamuttoo, G. F. C. Rogers, H. Cohen, P. V. Straznicky, and A. C. Nix. *Gas Turbine Theory* (7th ed.). Pearson, Harlow, UK. ISBN: 9781-292-09309-3.
- 243 **Altenbach et al. (2018)**: H. Altenbach, J. Altenbach, and W. Kissing. *Mechanics of Composite Structural Elements* (2nd ed.). Springer Verlag, Singapore, Singapore. ISBN: 978-981-10-8934-3.
- 244 **Banjac et al. (2018a)**: M. Banjac and M. V. Petrovic. Development of Method and Computer Program for Multistage Axial Compressor Design: Part I-Mean Line Design and Example Cases. Proceedings of the ASME Turbo Expo 2018, Oslo, Norway, 11-15 June 2018. GT2018-75410. doi: 10.1115/GT2018-75410.
- 245 **Banjac et al. (2018b)**: M. Banjac and M. V. Petrovic. Development of Method and Computer Program for Multistage Axial Compressor Design: Part II-Two-Dimensional Design and Validation Using CFD. Proceedings of the ASME Turbo Expo 2018, Oslo, Norway, 11-15 June 2018. GT2018-75412. doi: 10.1115/GT2018-75412.
- 246 **Cadreja et al. (2018)**: D. Cadreja, J. M. Chaquet, R. Corral, and V. P. Timon. Robust Method to Solve Meanline Equations for Choked Flows. Proceedings of the ASME Turbo Expo 2018, Oslo, Norway, 11-15 June 2018. GT2018-75362. doi: 10.1115/GT2018-75362.
- 247 **EASA (2018)**: European Union Aviation Safety Agency. Type-Certificate Data Sheet No. E.067 for CFM56-5 Series Engines. TDCS No.: E.067. Issue: 02.
- 248 **He et al. (2018)**: Y. He, J. Sun, P. Song, X. Wang, and D. Xu. Development of a Multi-Objective Preliminary Design Optimization Approach for Axial Flow Compressors. Proceedings of the ASME Turbo Expo 2018, Oslo, Norway, 11-15 June 2018. GT2018-76155. doi: 10.1115/GT2018-76155.
- 249 **Kidikian et al. (2018a)**: J. Kidikian and M. Reggio. Off-Design Prediction of Transonic Axial Compressors, Part 1: Mean-Line Code and Tuning Factors. Proceedings of the ASME Turbo Expo 2018, Oslo, Norway, 11-15 June 2018. GT2018-75124. doi: 10.1115/GT2018-75124.
- 250 **Kidikian et al. (2018b)**: J. Kidikian and M. Reggio. Off-Design Prediction of Transonic Axial Compressors, Part 2: Generalized Mean-Line Loss Modelling

- Methodology. Proceedings of the ASME Turbo Expo 2018, Oslo, Norway, 11-15 June 2018. GT2018-75125. doi: 10.1115/GT2018-75125.
- 251 **Kiss et al. (2018)**: A. Kiss and Z. Spakovszky. Effects of Transient Heat Transfer on Compressor Stability. Proceedings of the ASME Turbo Expo 2018, Oslo, Norway, 11-15 June 2018. GT2018-75413. doi: 10.1115/GT2018-75413.
- 252 **Kolias et al. (2018)**: I. Kolias, A. Alexiou, N. Aretakis, and K. Mathioudakis. Direct Integration of Axial Turbomachinery Preliminary Aerodynamic Design Calculations in Engine Performance Component Models. Proceedings of the ASME Turbo Expo 2018, Oslo, Norway, 11-15 June 2018. GT2018-76494. doi: 10.1115/GT2018-76494.
- 253 **Kurzke et al. (2018)**: J. Kurzke and I. Halliwell. Propulsion and Power: An Exploration of Gas Turbine Performance Modeling (1st ed.). Springer, Cham, Switzerland. ISBN: 978-3-319-75977-7.
- 254 **Li et al. (2018)**: T. Li, Y. Wu, H. Quoyang, and X. Qiang. Axial Compressor Performance Prediction Using Improved Streamline Curvature Approach. Proceedings of the ASME Turbo Expo 2018, Oslo, Norway, 11-15 June 2018. GT2018-75450. doi: 10.1115/GT2018-75450.
- 255 **Lions (2018)**: A. Lions. Improving the Representation of 1D Performance Compressor Model. MSc Thesis, KTH Royal Institute of Technology, Sweden.
- 256 **Mishra et al. (2018)**: A. Mishra, Y. Neumeier, J. V. R. Prasad, and D. K. James. Modelling of Multistage Axial Compressor Using Successive Diffusers with Velocity Sources: Part II-Unsteady Results. Proceedings of the 2018 AIAA Joint Propulsion Conference, Cincinnati, OH, USA, 9-11 July 2018. AIAA 2018-4826. doi: 10.2514/6.2018-4826.
- 257 **Ntanakas et al. (2018)**: G. Ntanakas, M. Meyer, and K. C. Giannakoglou. Employing the Time-Domain Unsteady Discrete Adjoint Method for Shape Optimization of Three-Dimensional Multirow Turbomachinery Configurations. *J. Turbomach.*, 140(8), 081006 (11 pages). doi: 10.1115/1.4040564.
- 258 **Reitenbach et al. (2018)**: S. Reitenbach, A. Krumme, T. Behrendt, M. Schnos, T. Schmidt, S. Honig, R. Mischke, and E. Moerland. Design and Application of a Multi-Disciplinary Pre-Design Process for Novel Engine Concepts. Proceedings of the ASME Turbo Expo 2018, Oslo, Norway, 11-15 June 2018. GT2018-76880. doi: 10.1115/GT2018-76880.
- 259 **Wu et al. (2018)**: D. Wu, J. Teng, X. Qiang, and T. Zheng. Development of an Off-Design Deviation Angle Prediction Model for Full Blade Span in Axial Flow Compressors. *Proc. IMechE Part G: J. Aerospace Engineering*, 0(0), 1-14. doi: 10.1177/0954410018793265.
- 260 **Cengel et al. (2019)**: Y. A. Cengel, M. A. Boles, and M. Kanoglu. *Thermodynamics: An Engineering Approach* (9th ed.). McGraw-Hill Education, NY, USA. ISBN: 978-1-259-82267-4.
- 261 **EASA (2019)**: European Union Aviation Safety Agency. Type-Certificate Data Sheet No. E.004 for CFM56-7B Series Engines. TDCS No.: E.004. Issue: 06.

- 262 **Giachos (2019)**: G. Giachos. Optimization Studies of Aircraft Propulsion System. BSc Thesis, National Technical University of Athens, Greece (in Greek).
- 263 **Katsikogiannis et al. (2019)**: D. Katsikogiannis, M. Thoma, K. Mathioudakis, and N. Aretakis. Optimal Civil Aircraft Missions Exploiting Free Routing Possibilities. Proceedings of the 9th EASN International Conference, 05004, Athens, Greece, 3-6 September 2019. doi: 10.1051/mateconf/201930405004.
- 264 **Mishra (2019)**: A. Mishra. Modelling of Multistage Axial-Centrifugal Compressor Configuration Using the Streamtube Approach. PhD Thesis, Georgia Institute of Technology, USA.
- 265 **Neumann et al. (2019)**: N. Neumann and D. Peitsch. Introduction and Validation of a Mean Line Solver for Present and Future Turbomachines. Proceedings of the 24th ISABE Conference, Canberra, Australia, 22-27 September 2019. ISABE-2019-24441.
- 266 **Peng et al. (2019)**: C. Peng, J. Yang, M. Zhang, Y. Liu, and F. Zhang. An Effective Empirical Model Calibration Procedure for Axial Compressor Performance Prediction. Proceedings of the ASME Turbo Expo 2019, Phoenix, AZ, USA 17-21 June 2019. GT2019-91315. doi: 10.1115/GT2019-91315.
- 267 **Ricci et al. (2019)**: M. Ricci, R. Pacciani, M. Marconcini, P. Macelloni, S. Cecchi, and C. Bettini. CFD-Based Throughflow Analysis of Transonic Flows in Steam Turbines. Proceedings of the ASME Turbo Expo 2019, Phoenix, AZ, USA, 17-21 June 2019. GT2019-90851. doi: 10.1115/GT2019-90851.
- 268 **Saito et al. (2019)**: S. Saito, M. Furukawa, K. Yamada, K. Watanabe, A. Matsuoka, and N. Niwa. Mechanisms and Quantitative Evaluation of Flow Loss Generation in a Multi-Stage Transonic Axial Compressor. Proceedings of the ASME Turbo Expo 2019, Phoenix, AZ, USA 17-21 June 2019. GT2019-90439. doi: 10.1115/GT2019-90439.
- 269 **Schaber et al. (2019)**: R. Schaber, C. Salpingidou, and H. Klingels. From Interdisciplinary Propulsion System Parameter Studies to Initial Module Design- An Integrated Approach for Conceptual Design. Proceedings of the 24th ISABE Conference, Canberra, Australia, 22-27 September 2019. ISABE-2019-24040.
- 270 **Vieweg et al. (2019)**: M. Vieweg, F. Wolters, S. Reitenbach, C. Hollmann, and R.-G. Becker. Multi-Disciplinary Tool Coupling for the Determination of Turbofan Transients During Preliminary Design. Proceedings of the ASME Turbo Expo 2019, Phoenix, AZ, USA, 17-21 June 2019. GT2019-91402. doi: 10.1115/GT2019-91402.
- 271 **Alexiou (2020)**: A. Alexiou. Introduction to Gas Turbine Modelling with PROOSIS (4th ed.). Empresarios Agrupados International (EAI) SA.
- 272 **Salpingidou et al. (2020)**: C. Salpingidou, R. Schaber, H. Klingels, and P. Geiger. Mechanical Design in an Interdisciplinary Predesign Tool. Proceedings of the ASME Turbo Expo 2020, Virtual, Online, 21-25 September 2020. GT2020-14633. doi: 10.1115/GT2020-14633.

- 273 **Vidal et al. (2020)**: L. E. F.-Vidal, V. Pachidis, and R. J. Tunstall. Generating Axial Compressor Maps to Zero Speed. *Proc. IMechE Part A: J. Power and Energy*, 0(0), 1-18. doi: 10.1177/0957650920976052.
- 274 **Vieweg et al. (2020)**: M. Vieweg, C. Hollmann, S. Reitenbach, M. Schnoes, T. Behrendt, A. Krumme, R. Meier zu Ummeln, and T. Otten. Collaborative Aircraft Engine Preliminary Design Using a Virtual Engine Platform, Part B: Application. *Proceedings of the AIAA Scitech Forum, Orlando, FL, USA, 6-10 January 2020*. AIAA-2020-0124. doi: 10.2514/6.2020-0124.
- 275 **Zhang et al. (2020a)**: Y. Zhang, S. Zhang, and Y. Xiao. Aerodynamic Performance Prediction of Transonic Axial Multistage Compressors Based on One-Dimensional Meanline Method. *Proceedings of the ASME Turbo Expo 2020, Virtual, Online, 21-25 September 2020*. GT2020-14571. doi: 10.1115/GT2020-14571.
- 276 **Zhang et al. (2020b)**: X. Zhang, Y. Ju, C. Zhang. Accuracy and Sensitivity Analysis of Aerodynamic Performance Prediction Models for Transonic Axial-Flow Compressors. *Proceedings of the ASME Turbo Expo 2020, Virtual, Online, 21-25 September 2020*. GT2020-15172. doi: 10.1115/GT2020-15172.
- 277 **Alexiou et al. (2021)**: A. Alexiou, N. Aretakis, I. Koliass, and K. Mathioudakis. Novel Aero-Engine Multi-Disciplinary Preliminary Design Optimization Framework Accounting for Dynamic System Operation and Aircraft Mission Performance. *Aerospace*, 8(49), 19 pages. doi: 10.3390/aerospace8020049.
- 278 **Anastasiou (2021)**: A. Anastasiou. Turbofan Inter-Compressor Duct Pressure Loss Model Using CFD. BSc Thesis, National Technical University of Athens, Greece.
- 279 **Bakogianni (2021)**: A. Bakogianni. Design of Disks in Thermal Turbomachines. BSc Thesis, National Technical University of Athens, Greece.
- 280 **Gambini et al. (2021)**: M. Gambini and M. Vellini. *Turbomachinery: Fundamentals, Selection and Preliminary Design (1st ed.)*. Springer, Cham, Switzerland. ISBN: 978-3-030-51298-9.
- 281 **Koliass et al. (2021)**: I. Koliass, A. Alexiou, N. Aretakis, and K. Mathioudakis. Axial Compressor Mean-Line Analysis: Chocking Modelling and Fully-Coupled Integration in Engine Performance Simulations. *Int. J. Turbomach. Propuls. Power*, 6(4), 23 pages. doi: 10.3390/ijtp6010004.
- 282 **Lei et al. (2021a)**: F. Lei, Y. Ju, and C. Zhang. A Rapid and Automatic Optimal Design Method for Six-Stage Axial-Flow Industry Compressor. *J. Therm. Sci.*, 30(5), 1658-1673. doi: 10.1007/s11630-021-1496-2.
- 283 **Lei et al. (2021b)**: F. Lei and C. Zhang. Preliminary Optimization of Multi-Stage Axial-Flow Industrial Process Compressors Using Aero-Engine Compressor Design Strategy. *Appl. Sci.*, 11(19), 19 pages. doi: 10.3390/app11199248.
- 284 **Ntonas et al. (2021)**: K. Ntonas, N. Aretakis, and K. Mathioudakis. A Marine Turbocharger Compressor Multi-Point 3D Design Optimization Tool. *Proceedings of the ASME Turbo Expo 2021, Virtual, Online, 7-11 June 2021*. GT2021-59518. doi: 10.1115/GT2021-59518.

- 285 **Wells et al. (2021)**: K. Wells and M. G. Turner. Open Source Axial Compressor Mean-Line Design Tool for Supercritical Carbon Dioxide. Proceedings of the ASME Turbo Expo 2021, Virtual, Online, 7-11 June 2021. GT2021-59961. doi: 10.1115/GT2021-59961.
- 286 **Zhang et al. (2021)**: Y. Zhang and S. Zhang. Performance Prediction of Transonic Axial Multistage Compressor Based on One-Dimensional Meanline Method. Proc. IMechE Part A: J. Power and Energy, 0(0), 1-15. doi: 10.1177/0957650921998819.
- 287 **Alexiou et al. (2022)**: A. Alexiou, I. Koliass, N. Aretakis, and K. Mathioudakis. Compressor Stability Studies at Engine Level. Project UTOPEA: UHBR Engine Technology for Aircraft Operation, Emissions and Economic Assessments (Grant Agreement ID: 886840). Deliverable 1.2, Issue 1.1.
- 288 **Haßy et al. (2022)**: J. Haßy and J. Schmeink. Knowledge-Based Conceptual Design Methods for Geometry and Mass Estimation of Rubber Aero Engines. Proceedings of the 33rd International Congress of the Aeronautical Sciences, Stockholm, Sweden, 4-9 September 2022. ISSN 2958-4647.
- 289 **Ntonas et al. (2022)**: K. Ntonas, N. Aretakis, O. A. Koskoletos, and K. Mathioudakis. 1D Multi-Point Marine Turbocharger Design, for Optimal Performance Recovery. Proc. IMechE Part A: J. Power and Energy, 0(0), 1-19. doi: 10.1177/09576509221100177.
- 290 **Koliass et al. (2023)**: I. Koliass, N. Aretakis, A. Alexiou, and K. Mathioudakis. A Tool for the Design of Turbomachinery Disks for an Aero-Engine Preliminary Design Framework. Aerospace 2023, 10(5), 17 pages. doi: 10.3390/aerospace10050460.

